



HAL
open science

Régulation du cytosquelette par MAP6

Christian Delphin

► **To cite this version:**

Christian Delphin. Régulation du cytosquelette par MAP6. Sciences cognitives. UGA (Université Grenoble Alpes), 2022. tel-04796648

HAL Id: tel-04796648

<https://hal.science/tel-04796648v1>

Submitted on 21 Nov 2024

HAL is a multi-disciplinary open access archive for the deposit and dissemination of scientific research documents, whether they are published or not. The documents may come from teaching and research institutions in France or abroad, or from public or private research centers.

L'archive ouverte pluridisciplinaire **HAL**, est destinée au dépôt et à la diffusion de documents scientifiques de niveau recherche, publiés ou non, émanant des établissements d'enseignement et de recherche français ou étrangers, des laboratoires publics ou privés.



Université Grenoble Alpes

Habilitation à Diriger des Recherches

Régulation du cytosquelette par MAP6

Christian Delphin

Chargé de Recherche, INSERM

Grenoble Institut des Neurosciences
Université Grenoble Alpes
Inserm U1216, Equipe Arnal/Andrieux

Soutenance prévue le 13 Juin 2022

Membres du jury :

Monsieur Vincent Gache

Rapporteur

Monsieur Benoît Gigant

Rapporteur

Monsieur Alphée Michelot

Rapporteur

Mme Laurence Lafanechère

Examinatrice

Mme Marylin Vantard

Examinatrice

Sommaire

1. CURRICULUM VITAE	1
----------------------------------	----------

2. ACTIVITE DE RECHERCHE POST-THESE	6
--	----------

2.1 Activités de recherche post-doctorales (1995-1998) : Etude des mécanismes de transport actif de protéines entre le cytoplasme et le noyau	6
---	---

2.2 Activités de recherche en tant que chargé de recherche entre 1998 et 2006 : Signalisation calcique et membrane plasmique	7
--	---

2.3 Activités de recherche depuis 2007 : Etude du rôle de la protéine MAP6 dans la régulation du cytosquelette.....	8
---	---

2.3.1 Introduction	8
---------------------------------	----------

2.3.1.1 La protéine MAP6	8
--------------------------------	---

2.3.1.1.1 MAP6, une famille de protéines issues d'un seul gène	8
--	---

2.3.1.1.2 Organisation structurale de MAP6.....	9
---	---

2.3.1.1.3 Rôle de MAP6 dans le développement et les fonctions neuronales	10
--	----

- Rôle de MAP6 dans la plasticité synaptique
- Rôle de MAP6 dans la plasticité neurotransmission
- Rôle de MAP6 dans le développement cérébral

2.3.1.1.4 Rôle de MAP6 dans le comportement	11
---	----

2.3.1.1.5 MAP6 : Modèle animal et implication en pathologies neuronales	11
---	----

2.3.1.1.6 Importance de la régulation de la dynamique des microtubules dans les fonctions neuronales de MAP6.....	12
---	----

2.3.1.2 Cytosquelette d'actine et microtubules	12
--	----

2.3.1.2.1 Localisation et fonction cellulaire des microtubules et des filaments d'actine	12
--	----

2.3.1.2.2 Composition et formation des microtubules et des filaments d'actine.....	13
--	----

2.3.1.2.3 Dynamiques d'assemblage des microtubules et filaments d'actine	14
--	----

2.3.1.2.4 Nucléation des microtubules et filaments d'actine	15
---	----

2.3.1.2.5 Formation de faisceaux de microtubules ou de filaments d'actine.....	16
--	----

2.3.1.2.6 Coordination entre le cytosquelette d'actine et les microtubules	16
--	----

2.3.2 Résultats	17
2.3.2.1 PARTIE I : Mécanisme de stabilisation par MAP6F des microtubules exposés au froid	17
2.3.2.1.1 MAP6F protège les microtubules d'une dépolymérisation température dépendante comprise entre 25 °C et 4 °C.....	18
2.3.2.1.2 <i>In vivo</i> , MAP6F se relocalise du cytoplasme vers les microtubules de façon température-dépendante et rapidement lors d'une chute de température de 37 °C à 4 °C	18
2.3.2.1.3 Le domaine Mc de MAP6F se lie de façon température-dépendante aux microtubules	19
2.3.2.1.4 La conformation de MAP6F est dépendante de la température	19
2.3.2.1.5 Un rôle physiologique de MAP6F dans la protection des microtubules exposés à une baisse de température ?	19
2.3.2.2 PARTIE II : Etude de l'activité de MAP6N sur la dynamique et la structure des microtubules	20
2.3.2.2.1 MAP6N interagit directement avec les microtubules et favorise leur polymérisation.....	21
2.3.2.2.2 MAP6N induit la polymérisation de microtubules hélicoïdaux	21
2.3.2.2.3 MAP6N favorise la fermeture des feuilletts à l'extrémité des microtubules.....	21
2.3.2.2.4 MAP6N est une MIP (<i>Microtubule Inner Particule</i>) <i>in vitro</i> et <i>in vivo</i>	21
2.3.2.2.5 MAP6N favorise la formation de microtubule avec des ouvertures.....	22
2.3.2.2.6 Modèle de déformation des microtubules par l'incorporation de MAP6N.....	22
2.3.2.2.7 Quel rôle pour des microtubules hélicoïdaux avec des trous persistants et des densités intraluminales dans les neurones ?	23
2.3.2.3 PARTIE III : Rôle de MAP6N sur la nucléation des microtubules et des filaments d'actine et sur la formation de faisceaux d'actine.....	23
2.3.2.3.1 MAP6N promeut la nucléation des microtubules <i>in vitro</i>	23
2.3.2.3.2 MAP6N stimule la nucléation des filaments d'actine	24

2.3.2.3.3 MAP6N se lie aux filaments d'actine et les organise en faisceaux denses.....	25
2.3.2.3.4 MAP6N favorise la co-nucléation et le co-alignement des filaments d'actine et des microtubules	26
2.3.2.3.5 Déterminants moléculaires de l'interaction de MAP6N avec l'actine et la tubuline	27

3. PROJET DE RECHERCHE 30

3.1 Analyse des domaines d'interaction de MAP6 avec les microtubules : de nouveaux modules Mn ?	30
3.2 La famille des protéines de MAP6 : une famille de MIP ?	31
3.3 MAP6 : MIP, MAP, MIPMAP ?	31
3.4 Coordination des réseaux d'actine et microtubules par MAP6N.....	33
3.5 Analyse structurale des noyaux de nucléation	33
3.6 Une fonction spécifique pour l'isoforme neuronale embryonnaire MAP6E ?	34
3.7 Quel rôle cellulaire pour MAP6 ?	34

4. BIBLIOGRAPHIE 34

5. ANNEXE (sélection de publications au format pdf) 42

1. CURRICULUM VITAE

Christian DELPHIN

Né le 28-06-1967

Nationalité française

Christian.delphin@univ-grenoble-alpes.fr

Tél : 33- (0)4-56-52-05-39

Fax : 33- (0)4-56-52-06-57

Grenoble Institut des Neurosciences

Inserm U1216, UGA, CEA

Equipe Physiopathologie du cytosquelette

Bât. Edmond J. Safra, Ch. Fortuné Ferrini

38700 La Tronche

France

DIPLOMES

Doctorat (1994)

Université Joseph Fourier Grenoble I Spécialité Biologie.

Etude des modes de régulation post-traductionnelle de l'activité de la protéine p53 : la phosphorylation de p53 par la protéine kinase C

Expérimentation animale niveau 1 (2005)

Université Joseph Fourier Grenoble I

PARCOURS PROFESSIONNEL

Stage post-doctoral (1995-1997)

Prof. Larry Gerace (Scripps Research Institute, San Diego-USA)

Etude du transport nucléo-cytoplasmique.

Chargé de recherche INSERM (depuis 1998)

1998-2001 Lab. Prof E. Chambaz (CEA-Grenoble, DBMS)

Implication de la S100B et de Ahnak dans la signalisation calcique.

2002-2006 Equipe Dr. J. Baudier (CEA-Grenoble, DRDC)

Implication du complexe Annexine 2/S100A10 dans la régulation de l'architecture cellulaire.

Depuis 2007 Equipe Dr. A Andrieux puis Dr I. Arnal/A. Andrieux (Institut des Neurosciences-Grenoble).

Rôle de la protéine MAP6 dans la régulation du cytosquelette neuronal.

ENCADREMENT

• Post-doctorant :

- Sandrine De Serrano (1 publication), 2005-2006

• Doctorants :

- Benoit Gentil (5 publications), 1999-2002, co-direction J. Baudier
- Maxime Seggio (2 publications) 2012-2016, co-direction A. Andrieux
- Camille Cuveillier, (3 publications) en cours depuis 2018, co-direction A. Andrieux

- **Master 2 :**
 - Sami Khedhiri (1 publication) 2003
 - Pascal Stuelsatz (1 publication) 2006
 - Melina Petrel, 2008
 - Maxime Seggio, 2012
 - Sawssan Saffiedine, 2016
 - Marion Carcel 2017
- **IUT/BTS :**
 - Sylvie Cholet, 2001
 - Valérie Chavanat, 2002
 - Alexis Benmalek, 2016
 - Lisa Demacedo, 2017, 2018

FINANCEMENTS

- Allocation de recherche doctorale MRT (1991-1994)
- Bourses post-doctorales :
 - EMBO (#ALTF539-1994, 1995)
 - HFSP (#LT-394/95, 1996-1997)
- Contrat ARC #5643 (*Rôle de AHNAK et TAF1 dans l'ancrage cytoplasmique et le transport nucléaire de p53*), 2000-2003, 300 000 F.
- Participation à des ANRs:
 - CBioS (*Cell biology of STOP protein*), 2010-2013, 400 000 €.
 - MAMA (*Microtubule and actin coordination by structural MAPs*), 2017-2021, 492 000 €.
 - FidgetIn Turning (*From guidance signals to cytoskeleton remodeling: Fidgetin-like 1 as an integrator for axon repulsion*), 2021-2024, 669 700 €
 - MIP-MAP (*microtubule inner proteins (MIPs): from molecular identification to structural properties and functions*), 2021-2024, 490 000 €

RESPONSABILITES COLLECTIVES

- Co-organisateur du 3^{ème} congrès du réseau microtubule français (Grenoble 2015)

COMMUNICATIONS ORALES DANS DES CONGRES

- Sur invitation :
RanGTP targets p97 to RanBP2 a filamentous protein localized at the cytoplasmic periphery of the nuclear pore complex - Third congress of Asian-Pacific Organization for Cell Biology, Osaka 1998
- Sur sélection de résumé :
The microtubule inner protein MAP6 promotes microtubule lattice deformation – 4nd French Microtubule network, Rennes 2019

PUBLICATIONS (en italique, les étudiants que j'ai encadrés)

31-Boulan B, Ravello C, Peyrel A, Bosc C, **Delphin C**, Appaix F, Denarier E, Kraut A, Jacquier-Sarlin M, Fournier A, Andrieux A, Gory-Fauré S, Deloulme JC. CRMP4-mediated fornix development involves Semaphorin-3E signaling pathway.

Elife. 2021, 10:e70361

30-Denarier E, Ecklund KH, Berthier G, Favier A, O'Toole ET, Gory-Fauré S, De Macedo L, **Delphin C**, Andrieux A, Markus SM, Boscheron C. Modeling a disease-correlated tubulin mutation in budding yeast reveals insight into MAP-mediated dynein function.

Mol Biol Cell. 2021, 32:ar10

29-**Cuveillier C**, Boulan B, Ravello C, Denarier E, Deloulme J-C, Gory-Fauré S, **Delphin C**, Bosc C, Arnal I and Andrieux A (2021) Beyond Neuronal Microtubule Stabilization: MAP6 and CRMPs, Two Converging Stories.

Front. Mol. Neurosci. 2021, 14:665693.

28-**Cuveillier C**, Saoudi Y, Arnal I, **Delphin C**. Imaging Microtubules *in vitro* at High Resolution while Preserving their Structure.

Bio Protoc. 2021 Apr 5;11:e3968.

27- **Cuveillier C**, Delaroche J, **Seggio M**, Gory-Fauré S, Bosc C, Denarier E, Bacia M, Schoehn G, Mohrbach H, Kulić I, Andrieux A, Arnal I, **Delphin C**. MAP6 is an intraluminal protein that induces neuronal microtubules to coil.

Science Advances 2020, 6: eaaz4344

26- Peris L, Bisbal M, Martinez-Hernandez J, Saoudi Y, Jonckheere J, Rolland M, Sebastien M, Brocard J, Denarier E, Bosc C, Guerin C, Gory-Fauré S, Deloulme JC, Lanté F, Arnal I, Buisson A, Goldberg Y, Blanchoin L, **Delphin C**, Andrieux A. A key function for microtubule-associated-protein 6 in activity-dependent stabilisation of actin filaments in dendritic spines.

Nat Commun. 2018, 9:3775.

25- Fassier C, Fréal A, Gasmi L, **Delphin C**, Ten Martin D, De Gois S, Tambalo M, Bosc C, Mailly P, Revenu C, Peris L, Bolte S, Schneider-Maunoury S, Houart C, Nothias F, Larcher JC, Andrieux A, Hazan J. Motor axon navigation relies on Fidgetin-like 1-driven microtubule plus end dynamics.

J Cell Biol. 2018, 217:1719-1738.

24- Mas L, Cieren A, **Delphin C**, Journet A, Aubry L. Calcium influx mediates the chemoattractant-induced translocation of the arrestin-related protein AdcC in *Dictyostelium*.

J Cell Sci. 2018, 131:jcs207951.

23- Aillaud C, Bosc C, Peris L, Bosson A, Heemeryck P, Van Dijk J, Le Fric J, Boulan B, Vossier F, Sanman LE, Syed S, Amara N, Couté Y, Lafanechère L, Denarier E, **Delphin C**, Pelletier L, Humbert S, Bogyo M, Andrieux A, Rogowski K, Moutin MJ. Vasohibins/SVBP are tubulin carboxypeptidases (TCPs) that regulate neuron differentiation.

Science. 2017, 358:1448-1453.

22- Gay O, Gilquin B, Assard N, **Stuelsatz P**, **Delphin C**, Lachuer J, Gidrol X, Baudier J. Refilins are short-lived Actin-bundling proteins that regulate lamellipodium protrusion dynamics.

Biol Open. 2016, 5:1351-1361.

21- Li S, Lamarche F, Charton R, **Delphin C**, Gires O, Hubstenberger A, Schlattner U, Rousseau D. Expression analysis of ATAD3 isoforms in rodent and human cell lines and tissues.

Gene. 2014, 535:60-9.

20- **Delphin C**, Bouvier D, **Seggio M**, Couriol E, Saoudi Y, Denarier E, Bosc C, Valiron O, Bisbal M, Arnal I, Andrieux A. MAP6-F is a temperature sensor that directly binds to and protects microtubules from cold-induced depolymerization.

J Biol Chem. 2012, 287:35127-38.

19- Arama J, Boulay AC, Bosc C, **Delphin C**, Loew D, Rostaing P, Amigou E, Ezan P, Wingertsmann L, Guillaud L, Andrieux A, Giaume C, Cohen-Salmon M. Bmcc1s, a novel brain-isoform of Bmcc1, affects cell morphology by regulating MAP6/STOP functions.

PLoS One. 2012;7:e35488.

18- Raponi E, Agenes F, **Delphin C**, Assard N, Baudier J, Legraverend C, Deloulme JC. S100B expression defines a state in which GFAP-expressing cells lose their neural stem cell potential and acquire a more mature developmental stage.

Glia. 2007, 55:165-77.

17- **De Seranno S**, Benaud C, Assard N, **Khediri S**, Gerke V, Baudier J, **Delphin C**. Identification of an AHNAK binding motif specific for the Annexin2/S100A10 tetramer.

J Biol Chem. 2006, 281:35030-8.

16- **Gentil BJ**, Benaud C, **Delphin C**, Remy C, Berezowski V, Cecchelli R, Feraud O, Vittet D, Baudier J. Specific AHNAK expression in brain endothelial cells with barrier properties.

J Cell Physiol. 2005, 203:362-71.

15- Benaud C, **Gentil BJ**, Assard N, Court M, Garin J, **Delphin C**, Baudier J. AHNAK interaction with the annexin 2/S100A10 complex regulates cell membrane cytoarchitecture.

J Cell Biol. 2004, 164:133-44.

14- **Gentil BJ**, **Delphin C**, Benaud C, Baudier J. Expression of the giant protein AHNAK (desmoyokin) in muscle and lining epithelial cells.

J Histochem Cytochem. 2003, 51:339-48.

13- Mbele GO, Deloulme JC, **Gentil BJ**, **Delphin C**, Ferro M, Garin J, Takahashi M, Baudier J. The zinc- and calcium-binding S100B interacts and co-localizes with IQGAP1 during dynamic rearrangement of cell membranes.

J Biol Chem. 2002, 277:49998-50007.

12- **Gentil BJ**, **Delphin C**, Mbele GO, Deloulme JC, Ferro M, Garin J, Baudier J. The giant protein AHNAK is a specific target for the calcium- and zinc-binding S100B protein: potential implications for Ca²⁺ homeostasis regulation by S100B.

J Biol Chem. 2001, 276:23253-61.

11- **Delphin C**, Ronjat M, Deloulme JC, Garin G, Debussche L, Higashimoto Y, Sakaguchi K, Baudier J. Calcium-dependent interaction of S100B with the C-terminal domain of the tumor suppressor p53.

J Biol Chem. 1999, 274:10539-44.

10- Scotto C, **Delphin C**, Deloulme JC, Baudier J. Concerted regulation of wild-type p53 nuclear accumulation and activation by S100B and calcium-dependent protein kinase C.
Mol Cell Biol. 1999, 19:7168-80.

9- **Delphin C**, Huang KP, Scotto C, Chapel A, Vincon M, Chambaz E, Garin J, Baudier J. The in vitro phosphorylation of p53 by calcium-dependent protein kinase C--characterization of a protein-kinase-C-binding site on p53.
Eur J Biochem. 1997, 245:684-92.

8- Mahajan R, **Delphin C**, Guan T, Gerace L, Melchior F. A small ubiquitin-related polypeptide involved in targeting RanGAP1 to nuclear pore complex protein RanBP2.
Cell. 1997, 88:97-107.

7- **Delphin C**, Guan T, Melchior F, Gerace L. RanGTP targets p97 to RanBP2, a filamentous protein localized at the cytoplasmic periphery of the nuclear pore complex.
Mol Biol Cell. 1997, 8:2379-90.

6- Paschal BM, **Delphin C**, Gerace L. Nucleotide-specific interaction of Ran/TC4 with nuclear transport factors NTF2 and p97.
Proc Natl Acad Sci U S A. 1996, 93:7679-83.

5- **Delphin C**, Baudier J. The protein kinase C activator, phorbol ester, cooperates with the wild-type p53 species of Ras-transformed embryo fibroblasts growth arrest.
J Biol Chem. 1994, 269:29579-87.

4- **Delphin C**, Cahen P, Lawrence JJ, Baudier J. Characterization of baculovirus recombinant wild-type p53. Dimerization of p53 is required for high-affinity DNA binding and cysteine oxidation inhibits p53 DNA binding.
Eur J Biochem. 1994, 223:683-92.

3- Colbeau A, Richaud P, Toussaint B, Caballero FJ, Elster C, **Delphin C**, Smith RL, Chabert J, Vignais PM. Organization of the genes necessary for hydrogenase expression in *Rhodobacter capsulatus*. Sequence analysis and identification of two hyp regulatory mutants.
Mol Microbiol. 1993, 8:15-29

2- Baudier J, **Delphin C**, Grunwald D, Khochbin S, Lawrence JJ. Characterization of the tumor suppressor protein p53 as a protein kinase C substrate and a S100b-binding protein.
Proc Natl Acad Sci U S A. 1992, 89:11627-31.

1- Filhol O, Baudier J, **Delphin C**, Loue-Mackenbach P, Chambaz EM, Cochet C. Casein kinase II and the tumor suppressor protein P53 associate in a molecular complex that is negatively regulated upon p53 phosphorylation.
J Biol Chem. 1992, 267:20577-83.

2. ACTIVITE DE RECHERCHE POST-THESE

2.1 Activités de recherche post-doctorales (1995-1998) : Etude des mécanismes de transport actif de protéines entre le cytoplasme et le noyau

En 1994, j'ai soutenu ma thèse de Biologie sur la régulation de la translocation nucléaire et l'activité de la protéine p53 par la Protéine Kinase C (PKC) et la calciprotéine S100B. Par la suite, j'ai choisi d'effectuer un stage post-doctoral dans le laboratoire du professeur Larry Gerace au Scripps Research Institut (San Diego, USA). Ce laboratoire s'intéressait alors aux mécanismes de régulation du transport de protéines et ARNs entre le noyau et le cytoplasme. Le transport à travers les pores nucléaires se fait soit par diffusion passive pour les petites molécules (< 30 kDa), soit par transport actif pour celles de taille plus importante. Le transport actif met en jeu l'importine β pour l'import et l'exportine pour l'export. La directionnalité du transport est contrôlée par Ran, une petite protéine G qui lie le GTP dans le noyau et l'hydrolyse dans le cytoplasme. Dans le cadre de mon activité post-doctorale, j'ai cherché à comprendre le rôle de la protéine RanBP2 (ou NUP358) dans les mécanismes de transport nucléocytoplasmiques. RanBP2 est une protéine d'environ 350 kDa, constituant majeur des fibres présentes sur la face cytoplasmique des pores nucléaires par lesquels transitent les molécules.

Une partie de mon travail a abouti à la purification de RanBP2 endogène à partir de foie de rat et à l'étude des différentes interactions mises en jeu au cours du transport. Avec mes collègues de l'équipe, nous avons ainsi pu montrer que Ran sous la forme GTP se lie à l'importine β alors qu'associée au GDP, elle interagit avec NTF2 (*Nuclear Transport Factor 2*), un facteur impliqué dans le recyclage de RanGDP du cytoplasme vers le noyau (Pascal et al., P.N.A.S., 1996, p224). Nous avons montré que RanGTP, en interagissant à la fois avec l'importine β et RanBP2, empêche l'interaction de l'importine β avec différentes protéines du pore nucléaire tout en favorisant son interaction avec RanBP2 (Delphin et al., Mol. Biol. Cell, 1997, p212).

Enfin, nous avons établi que RanGAP, un régulateur de l'activité de Ran qui catalyse l'hydrolyse du GTP par Ran, peut être modifié de façon covalente par une protéine qui a des ressemblances avec l'ubiquitine et que nous avons nommé SUMO-1 (*Small Ubiquitin-related Modifier 1*) (Mahajan et al., Cell, 1997, p201). La sumoylation de RanGAP permet son association avec RanBP2 et le couplage entre l'hydrolyse du GTP par Ran et la progression du complexe d'import au niveau du pore nucléaire.

2.2 Activités de recherche en tant que chargé de recherche entre 1998 et 2006 : Signalisation calcique et membrane plasmique

Suite à mon recrutement à l'Inserm en 1998, comme chargé de recherche, j'ai rejoint l'équipe de Jacques Baudier associé alors au laboratoire d'Edmond Chambaz (CEA, Grenoble). Au cours des 8 années passées dans cette équipe, j'ai développé différents projets en accord avec la progression thématique du groupe :

J'ai tout d'abord repris des études sur la régulation de l'activité de l'anti-oncogène p53 par la calciprotéine S100B et la PKC. Nous avons identifié le domaine de p53 impliqué dans l'interaction calcium-spécifique avec S100B (Delphin et al., *J. Biol. Chem.*, 1999 (p182)). Ce domaine est situé dans la partie C-terminale impliquée dans la séquestration cytoplasmique de p53. Nous avons également montré une coopération entre la PKC et la S100B dans la stimulation de la translocation nucléaire et de l'activité de p53 (Scotto et al., *Mol. Cell. Biol.*, 1999 (p188)). Ces résultats ont mis en lumière le mécanisme d'activation de p53 en réponse à une stimulation calcique.

Nous avons ensuite identifié deux nouvelles cibles cellulaires de la protéine S100B: IQGAP1 et Ahnak. IQGAP1 est une protéine d'échafaudage impliquée dans la signalisation cellulaire entre des récepteurs membranaires et des molécules de signalisation intracellulaires conduisant à un remodelage actine- et microtubule-dépendant de la membrane plasmique. IQGAP1 est un effecteur des petites protéines G, Ras, Cdc42 et Rac. IQGAP1 possède un domaine IQ d'interaction avec la calmoduline et de phosphorylation par la PKC. Nous avons mis en évidence une interaction calcium- et zinc-dépendante de S100B avec le motif IQ. Cette interaction se produit dans des zones de réarrangement de la membrane plasmique reliant l'activité de S100B au remodelage de la membrane plasmique et au contrôle des interactions inter-cellulaires (Mbele et al., *J. Biol. Chem.*, 2002 (p163)). Ahnak, une molécule géante d'environ 700 kDa, interagit avec plusieurs molécules impliquées dans la signalisation calcique : les canaux calciques de type L, la phospholipase C et la PKC. Nous avons montré qu'Ahnak est une cible majeure de la S100B (Gentil et al., *J. Biol. Chem.*, 2001 (p173)). Nous avons également observé qu'Ahnak est une protéine spécifique des tissus soumis à des contraintes physiques ou présentant des propriétés de barrière (Gentil et al., *J. Histochem. Cytochem.*, 2003 (p153)). Ahnak s'accumule aux interfaces cellule-cellule homo- et hétérotypiques et est spécifique au niveau du système nerveux central et périphérique des jonctions vasculaires imperméables. Dans les tumeurs, les néo-vaisseaux qui se caractérisent par une perte des propriétés de barrière en sont dépourvus (Gentil et al., *J. Cell Physiol.*, 2005 (p131)). Ces observations suggèrent donc un rôle pour Ahnak dans l'organisation des propriétés de barrière de l'endothélium vasculaire. Nous avons identifié comme partenaire d'Ahnak au niveau de la membrane plasmique, le complexe S100A10/Annexine 2 (Benaud et al., *J. Cell Biol.*, 2004 (p141)). Ce complexe permet d'ancrer Ahnak à des domaines de la membrane

plasmique riches en cholestérol où elle joue un rôle dans l'organisation et le remodelage du cytosquelette d'actine cortical. Ahnak est donc un régulateur de la cytoarchitecture cellulaire interagissant avec la membrane plasmique et le cytosquelette cortical. Enfin, nous avons caractérisé biochimiquement et par triple-hybride chez la levure, l'interaction entre Ahnak et le complexe S100A10/Annexine 2 (De Seranno et al., J. Biol. Chem., 2006 (p122)).

2.3 Activités de recherche depuis 2007 : Etude du rôle de la protéine MAP6 dans la régulation du cytosquelette

En 2007, j'ai rejoint le groupe « Physiopathologie du cytosquelette » dirigé par Didier Job, puis par Annie Andrieux, et alors localisé sur le CEA-Grenoble. Cette équipe s'intéressait déjà à la dynamique du cytosquelette dont les dysfonctionnements sont associés à de nombreuses pathologies neuronales. Elle est à l'origine notamment de la découverte de MAP6 et cherche à comprendre comment son invalidation cause des troubles cognitifs et de comportement dans un modèle murin. Mon activité de recherche s'est focalisée sur le volet moléculaire de l'étude de la fonction de la régulation du cytosquelette par MAP6. Elle s'est poursuivie à l'institut des Neurosciences de Grenoble après le déménagement du groupe d'Annie Andrieux sur le site et actuellement dans le groupe codirigé par Annie et Isabelle Arnal.

2.3.1 Introduction

2.3.1.1 La protéine MAP6

Les microtubules sont des structures intrinsèquement très dynamiques. Cependant, dans certaines structures telles que les cils et les flagelles, les microtubules peuvent être extrêmement stables. C'est également le cas pour une partie des microtubules neuronaux. Cette stabilité peut être due à la composition en tubuline, à des modifications post-traductionnelles ou à l'association avec des facteurs protéiques. C'est de la recherche de facteurs protéiques responsables de la forte stabilité des microtubules neuronaux et notamment de leur résistance à une dépolymérisation induite par une exposition à basse température que fut identifiée MAP6 ((Job et al., 1981; Job et al., 1982; Margolis and Rauch, 1981; Pabion et al., 1984).

2.3.1.1.1 MAP6, une famille de protéines issues d'un seul gène

MAP6 est exprimée uniquement chez les vertébrés (Bosc et al., 2001). Chez la souris, en fonction des tissus considérés, plusieurs isoformes de MAP6 peuvent être exprimées. Elles sont produites à partir d'un gène unique, par épissage alternatif et départs de transcription différentiels

(Aguazzoul et al., 2003; Bosc et al., 1996; Denarier et al., 1998a). Les formes N et E sont principalement exprimées dans les neurones. MAP6E est exprimée au cours du développement et reste chez l'adulte alors que MAP6N, la plus longue isoforme, est exprimée après la naissance et est la forme majoritaire chez l'adulte (Galiano et al., 2004; Guillaud et al., 1998; Tortosa et al., 2017). MAP6O et MAP6A sont exprimées dans les oligodendrocytes et les astrocytes respectivement (Galiano et al., 2004). Enfin MAP6F est ubiquitaire.

2.3.1.1.2 Organisation structurale de MAP6

L'analyse de la séquence de MAP6 (Bosc et al., 1996) a montré qu'elle comporte les caractéristiques des MAP structurales : c'est une protéine basique (pHi ~ 9.5) très peu structurée et multi-modulaire. Elle ne comporte pas de domaines de liaison aux microtubules communs à d'autres MAP. Cependant, elle est composée de plusieurs séquences répétées impliquées dans la stabilisation des microtubules (Figure 1). Les modules Mn, identifiés au nombre de trois (Mn1-3), stabilisent les microtubules contre la dépolymérisation induite par le froid et le nocodazole (Bosc et al., 2001). En plus de ses modules Mn, MAP6 contient des modules Mc. Ces modules ne sont présents que chez les mammifères et leur nombre peut varier selon l'espèce ou même selon la souche (3-6 chez la souris, 1 chez l'homme) (Bosc et al., 2003). Ces modules sont capables de conférer aux microtubules une stabilité au froid mais pas à des drogues dépolymérisantes, par absence d'interaction avec les microtubules à températures physiologiques (Bosc et al., 1996; Denarier et al., 1998b).

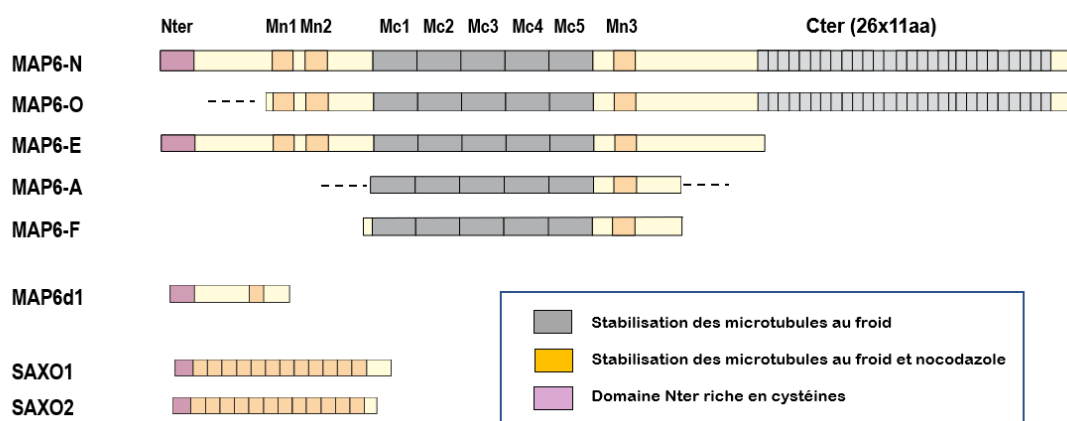


Figure 1 : Organisation multimodulaire des protéines MAP6, MAP6d1 et SAXO1/2

Enfin, MAP6N possède une longue queue C-terminale constituée d'une répétition imparfaite d'une séquence de 11 aa (28 répétitions chez la souris) (Bosc et al., 1996) et dont la fonction est inconnue. En plus des motifs répétés impliqués dans la stabilisation des microtubules, MAP6N possède

à son extrémité N-terminale une séquence riche en cystéines. Ces cystéines peuvent être palmitoylées et dépalmitoylées favorisant ainsi une association réversible de MAP6 avec des structures membranaires (golgi, membrane plasmique, vésicules) (Gory-Faure et al., 2006; Gory-Faure et al., 2014; Tortosa et al., 2017). MAP6 possède également des séquences riches en prolines (PRD) capable de lier des molécules à SH3 impliquées dans la signalisation de la sémaphorine 3E au cours du développement (Deloulme et al., 2015). Enfin, 12 domaines de liaison à la calmoduline ont été identifiés sur MAP6 suggérant une forte régulation de l'activité de MAP6 en réponse à une signalisation calcique (Gory-Faure et al., 2006; Job et al., 1981; Pirollet et al., 1992a; Pirollet et al., 1983; Pirollet et al., 1992b). Trois autres protéines possèdent également des domaines Mn et le domaine N-terminal riche en cystéines. La première, MAP6d1 (MAP6-domain-containing protein 1, anciennement SL21), a une séquence N-terminale et un domaine Mn très conservés par rapport à MAP6 (80% et 72% d'homologies pour la séquence N-terminale et le Mn (avec Mn3 de MAP6N) respectivement) (Bosc et al., 2001; Gory-Faure et al., 2006). La palmitoylation du domaine N-terminal de MAP6d1 régule son interaction avec le golgi et la membrane plasmique mais pas son interaction avec les mitochondries (Gory-Faure et al., 2006; Gory-Faure et al., 2014). MAP6d1 est capable de stabiliser les microtubules d'une dépolymérisation induite par le nocodazole ou le froid (Gory-Faure et al., 2006). Plus récemment, ont été découverts chez le protozoaire *Trypanosoma brucei* deux nouveaux homologues de MAP6, les protéines SAXO1 et SAXO2 (Dacheux et al., 2012). Les protéines SAXO possèdent un domaine N-terminal riche en cystéines et un nombre important de domaines Mn (12 chez la souris) présentant des homologies avec les modules Mn de MAP6. Ces domaines sont impliqués dans la liaison de la protéine aux microtubules et leur stabilisation au froid (Dacheux et al., 2012). Les protéines SAXOs sont présentes chez tous les eucaryotes possédant des cils ou des flagelles, des structures présentant une forte résistance à la dépolymérisation induite par le froid et le nocodazole. L'isoforme humaine hSAXO1 est exprimée de manière ubiquitaire et s'associe spécifiquement aux centrioles, aux corps basaux et aux cils (Dacheux et al., 2015).

2.3.1.1.3 Rôle de MAP6 dans le développement et les fonctions neuronales

L'obtention de souris déficientes dans l'expression de MAP6 (MAP6-KO) a permis une étude exhaustive de l'implication de MAP6 dans différents aspects du fonctionnement neuronal (Andrieux et al., 2002).

- Rôle de MAP6 dans la plasticité synaptique

MAP6 est impliquée dans la plasticité synaptique avec une diminution importante chez les souris MAP6-KO de la LTD (*long-term depression*) et LTP (*long-term potentiation*) des neurones hippocampiques glutamatergiques de la région CA1, du nombre de vésicules pré-synaptiques et du nombre d'épines dendritiques (Andrieux et al., 2002; Peris et al., 2018).

- Rôle de MAP6 dans la neurotransmission

La neurotransmission des souris MAP6-KO est largement affectée avec une hypo-glutamatergie due à une diminution du niveau de glutamate et de son transporteur Vglut1 (Brenner et al., 2007; Eastwood et al., 2007) à l'origine des défauts de plasticité synaptique décrits plus haut. Les souris présentent aussi une hyper-dopaminergie de la voie mésolimbique (Bouvrais-Veret et al., 2007; Bouvrais-Veret et al., 2008; Brun et al., 2005) conduisant à une activité locomotrice accrue (Andrieux et al., 2002; Bouvrais-Veret et al., 2007; Brun et al., 2005; Fradley et al., 2005), une hypersensibilité à la nouveauté ou aux amphétamines (Begou et al., 2007; Bouvrais-Veret et al., 2008; Brun et al., 2005), ainsi qu'à une perturbation importante du sommeil (Profitt et al., 2016). La transmission sérotoninergique des souris MAP6-KO est également fortement dérégulée au niveau de la production de sérotonine et de l'expression de son récepteur (5-HT) dans différentes régions du cerveau (Fournet et al., 2010; Fournet et al., 2012b).

- Rôle de MAP6 dans le développement cérébral

Les souris MAP6 KO présentent une réduction de leur volume cérébral, du cervelet et du thalamus (Deloulme et al., 2015; Powell et al., 2007). Elles ont une diminution du volume des voies myélinisées ainsi que de la fasciculation des voies cortico-spinales et la perte de la partie post-commissurale du fornix (Deloulme et al., 2015 ; Gimenez et al., 2017). L'absence du fornix entraîne une déconnexion entre l'hippocampe et l'hypothalamus et contribue certainement aux défauts comportementaux observés chez les souris MAP6-KO (voir plus bas).

2.3.1.1.4 Rôles de MAP6 dans le comportement

Les troubles précédemment décrits chez les souris MAP6-KO sont associés/participent à des troubles du comportement observés tels qu'une hyperactivité, une fragmentation de l'activité normale, un comportement de type anxieux, un retrait social et un comportement maternel altéré conduisant à la mort des petits (Andrieux et al., 2002; Bouvrais-Veret et al., 2007; Brun et al., 2005; Fradley et al., 2005).

2.3.1.1.5 MAP6 : Modèle animal et implication en pathologies neuronales humaines

Ces défauts biologiques et comportementaux répondent à un traitement à long terme par des antipsychotiques couramment utilisés pour le traitement de la schizophrénie, ce qui a amené à proposer les souris MAP6-KO comme un modèle d'étude de cette pathologie (Andrieux et al., 2002). Allant dans ce sens, des défauts d'expression de MAP6 ont été associés à des pathologies humaines dans des études portant sur des cas de retard de développement, de dysgénésie du corps calleux et

de symptômes autistiques ou schizophréniques (Chen et al., 2021; Choi et al., 2009; Martins-de-Souza et al., 2009; Shimizu et al., 2006; Wei et al., 2016; Xiao et al., 2015).

2.3.1.1.6 Importance de la régulation de la dynamique des microtubules dans les fonctions neuronales de MAP6

En plus des neuroleptiques, il a été montré qu'une partie des déficits observés chez les souris MAP6-KO pouvaient être améliorés par traitement à long terme avec de l'épothilone D (Andrieux et al., 2006; Daoust et al., 2014; Fournet et al., 2012a). L'épothilone D est un modulateur de la dynamique des microtubules, capable de stabiliser les microtubules *in vitro* (Chou et al., 1998; Kolman, 2004). De même, le NAP, un motif de l'ADNP (*Activity-Dependant Neuroprotective Protein*), qui favorise la croissance et la stabilisation des microtubules, atténue partiellement les déficiences cognitives chez les souris hétérozygotes pour MAP6 (Merenlender-Wagner et al., 2010; Volle et al., 2013). Le NAP interagit avec la tubuline (Divinski et al., 2004), les protéines EB (Gozes and Divinski, 2007; Oz et al., 2014) et Tau (Ivashko-Pachima and Gozes, 2019; Ivashko-Pachima et al., 2019; Ivashko-Pachima et al., 2017). Son expression est dérégulée dans la schizophrénie et l'autisme (Gozes, 2011; Hacoheh-Kleiman et al., 2018; Van Dijck et al., 2019).

Ces observations mettent en évidence un rôle important de la régulation de la dynamique des microtubules par MAP6 dans la plasticité synaptique et le comportement.

2.3.1.2 Cytosquelette d'actine et microtubules

Le cytosquelette des cellules eucaryotes comprend les filaments d'actine, les filaments intermédiaires et les microtubules qui forment des réseaux distincts. Bien qu'issues d'un ancêtre commun, l'actine et la tubuline ont divergé pour donner aujourd'hui des protéines qui forment des polymères différents tout en préservant des modes de fonctionnement et de régulation similaires.

2.3.1.2.1 Localisation et fonctions cellulaire des microtubules et des filaments d'actine

Les microtubules, polymères longs et rigides, forment un réseau qui rayonne depuis le centrosome ou centre organisateur des microtubules (MTOC) jusqu'à la périphérie de la cellule. Dans les neurones matures, des microtubules non-centrosomiques sont orientés vers les extrémités dans les axones ou ont une orientation mixte dans les dendrites (Kapitein and Hoogenraad, 2015). Les microtubules forment l'échafaudage de l'appareil mitotique (McIntosh, 2016), des axonèmes, des cils et des flagelles (Loreng and Smith, 2017). Ils servent aussi de rails pour les moteurs moléculaires dynéine et kinésine qui transportent sur de longues distances des complexes protéiques ou des vésicules (Barlan and Gelfand, 2017; Sweeney and Holzbaur, 2018). Ces mouvements sont

responsables des distributions caractéristiques du réticulum endoplasmique, de l'appareil de Golgi et d'autres organites dans le cytoplasme.

Les filaments d'actine se concentrent principalement à la périphérie de la cellule, au niveau du cortex sous-jacent à la membrane plasmique (Svitkina, 2020). Dans les neurones, l'actine s'accumule au niveau des cônes de croissance et dans les épines dendritiques. La polymérisation des filaments d'actine produit des forces pour les mouvements cellulaires et le trafic membranaire. Les myosines transportent des vésicules sur de courtes distances le long des filaments d'actine et tirent sur les câbles d'actine pendant la locomotion, la cytokinèse et d'autres changements de forme de la cellule (Svitkina, 2018).

2.3.1.2.2 Composition et formation des microtubules et des filaments d'actine

Microtubules et filaments d'actine sont des structures polarisées formées par l'assemblage en tête à queue de sous-unité protéiques.

L'unité de base des microtubules est un hétérodimère stable constitué d'une molécule de tubuline α et une molécule de tubuline β . Les dimères de tubuline s'associent pour former des protofilaments qui, à leur tour, établissent des liaisons latérales entre sous-unités voisines identiques (α/α et β/β) pour former un cylindre d'environ 25 nm de diamètre. Les protofilaments sont légèrement décalés les uns par rapport aux autres, formant une hélice latérale. Le nombre de protofilaments qui composent les microtubules peut varier *in vitro* de 11 à 17 (Pierson et al., 1978). *In vivo*, la plupart des microtubules cytoplasmiques sont composés de 13 protofilaments. Selon le nombre de protofilaments qui constitue le microtubule, le décalage après un tour d'hélice latérale varie, imposant une contrainte différente sur la fermeture du tube. Dans le cas d'un microtubule à 13 protofilaments, cas le plus courant *in vivo*, le décalage correspond pratiquement à la dimension de trois sous-unités de tubuline. En conséquence, à la fermeture, chaque sous-unités α va se trouver à côté d'une sous-unité β formant une couture (*seam*) dans laquelle les interactions latérales seront entre des sous-unités différentes (α/β) à la différence du reste du microtubule. Une deuxième conséquence du décalage est que la couture va se faire en induisant un angle différent de rotation entre l'axe des protofilaments et l'axe du microtubule produisant ainsi une hélice longitudinale des protofilaments autour du microtubule.

La molécule d'actine est plate, composée de quatre domaines avec au centre, une cavité profonde où se fixe l'ATP (Pollard, 2016). Les monomères d'actine s'associent pour former des filaments qui décrivent une hélice droite constituée de deux brins parallèles décalés d'une demi-unité. Toutes les sous-unités d'actine asymétriques sont orientées dans la même direction le long du polymère, conférant une polarité au filament. Les deux extrémités des filaments d'actine sont appelées extrémités "barbées" et "pointues", du fait de l'aspect des filaments en microscopie électronique lorsqu'ils sont décorés par la myosine.

2.3.1.2.3 Dynamique d'assemblage des microtubules et des filaments d'actine

La nucléation de la polymérisation des microtubules et de l'actine peut se faire spontanément mais elle est thermodynamiquement défavorisée. Les cellules utilisent des protéines régulatrices pour spécifier quand et où de nouveaux polymères se forment. Une fois amorcés, les filaments d'actine et les microtubules peuvent s'allonger aux deux extrémités par l'addition de monomères ATP-actine ou de dimères de GTP-tubuline respectivement. L'extrémité barbée du filament d'actine et l'extrémité « plus » du microtubule se développent plus rapidement que l'extrémité pointue du filament d'actine et « moins » du microtubule. Les nucléotides liés à l'actine et à la tubuline ont un impact sur leurs propriétés de polymérisation. Chacune des sous-unités du dimère $\alpha\beta$ de tubuline a un site de liaison pour un nucléotide guanine qui se situe à l'extrémité « plus ». Le GTP, qui est lié à la sous-unité α à l'interface stable entre les deux sous-unités, est stable. Le site exposé sur la sous-unité β se lie soit au GTP soit au GDP. La présence de GTP sur la sous-unité β est favorable à l'assemblage du dimère à l'extrémité du microtubule. Les dimères de tubuline s'associent ou se dissocient essentiellement aux extrémités, généralement plus rapidement aux extrémités « plus » qu'aux extrémités « moins » (Goodson and Jonasson, 2018). Suite à l'assemblage, le GTP de la sous-unité β est hydrolysé et le phosphate γ se dissocie. La GDP-tubuline, si elle est exposée à l'extrémité d'un microtubule se dissocie très rapidement mais elle peut être stabilisée par la présence d'une coiffe de sous-unités de GTP-tubuline présente à l'extrémité du microtubule. La perte de la coiffe GTP déstabilise l'extrémité d'un microtubule et entraîne une dépolymérisation rapide par dissociation de courts morceaux de protofilaments. Dans la cellule, de nombreux microtubules peuvent alterner entre des phases d'élongation et de désassemblage (interrompues respectivement par des événements de « catastrophe » ou « sauvetage »), un comportement appelé instabilité dynamique (Desai and Mitchison, 1997; Mitchison and Kirschner, 1984). Après qu'un dimère se dissocie d'un microtubule, le GDP de la sous-unité β est échangé contre du GTP dans le cytoplasme en vue d'un autre cycle d'assemblage. La dépolymérisation des microtubules peut également être catalysée à partir des extrémités par des kinésines dépolymérisantes (Walczak et al., 2013) ou par clivage interne par la Katanine, la Spastine ou la Fidgetine (Kuo and Howard, 2021).

Les deux extrémités du filament d'actine peuvent croître ou rétrécir, mais l'extrémité barbée croît plus rapidement que l'extrémité pointue. Après assemblage, l'ATP lié à l'actine est rapidement hydrolysé en ADP, suivi d'une lente dissociation du γ -phosphate. L'actine ADP-Pi ressemble beaucoup à l'actine ATP, mais l'ADP-actine se dissocie plus rapidement des filaments que l'ATP-actine. Par conséquent, la réaction cruciale est la dissociation du phosphate plutôt que l'hydrolyse de l'ATP (Pollard, 2016). La dépolymérisation des filaments d'actine peut être catalysée par fragmentation par la cofiline (Blanchoin et al., 2014).

2.3.1.2.4 Nucléation des microtubules et des filaments d'actine

In vivo, la nucléation des microtubules se fait majoritairement au niveau du MTOC à partir du complexe γ -TuRC (*γ -Tubulin Ring Complex*) qui agit à la fois comme noyau de nucléation et coiffe de l'extrémité moins. Cependant, dans les neurones, en absence de MTOC central, la nucléation est régulée localement. Les Golgi « outpost » dans les dendrites de neurones en cours de développement ont notamment été décrits comme centre de nucléation des microtubules impliquant le complexe γ -TuRC (Ori-McKenney et al., 2012). La nucléation de nouveaux microtubules à partir de la surface d'un microtubule préexistant a également été décrite : le complexe Augmine dont l'interaction avec la surface des microtubules est favorisée en présence de TPX2, peut promouvoir l'attachement du complexe γ -TuRC sur un microtubule existant, favorisant ainsi la formation localisée d'un nouveau microtubule (Cunha-Ferreira et al., 2018; Petry et al., 2013; Sanchez-Huertas et al., 2016). D'autres mécanismes participant à la formation de microtubules indépendamment du complexe γ -TuRC ont été proposés. Des protéines qui coupent les microtubules, comme la Katanine ou la Spastine peuvent produire des bouts de microtubules susceptibles de polymériser pour former de nouveaux microtubules. La protéine CAMSAP en stabilisant les bouts « moins » peut favoriser ce processus (Akhmanova and Hoogenraad, 2015; Goodwin and Vale, 2010; Liu et al., 2021). Beaucoup de protéines qui stabilisent les microtubules ont une activité de nucléation des microtubules *in vitro* mais ce n'est pas clair si elles agissent *in vivo* en favorisant la nucléation ou en stabilisant des microtubules nucléés par d'autres mécanismes.

In vitro, la nucléation d'un filament d'actine consiste en la formation au minimum d'un trimère d'actine qui sert de base à la polymérisation. La formation de ces noyaux, très instables, peut être favorisée par différents facteurs protéiques. On dénombre trois types de facteurs de nucléation : 1) le complexe ARP2/3 se fixe sur des filaments existants et mime une extrémité barbée d'où va polymériser un nouveau filament avec un angle constant par rapport au filament mère, ce qui conduit à la formation d'un réseau branché. Ce réseau situé dessous la membrane plasmique joue un rôle dans la formation de protrusions cellulaires (Gautreau et al., 2021; Papalazarou and Machesky, 2021). 2) Les formines constituent une large famille de protéines qui favorisent la nucléation et l'élongation des filaments d'actine (Valencia and Quinlan, 2021). Ce sont de homodimères caractérisés par un domaine FH2 et un domaine FH1 riche en prolines. Le domaine FH2 favorise la nucléation en stabilisant les dimères d'actine (Pring et al., 2003) et interagit avec l'extrémité barbée (Goode and Eck, 2007; Paul and Pollard, 2009). Le domaine FH1 favorise l'élongation en interagissant avec la profiline. Les formines permettent la nucléation de filaments non-branchés présents dans les anneaux contractiles, les fibres de stress et les filopodes, 3) une troisième famille de nucléateurs de filaments d'actine est constituée des protéines à plusieurs domaines WH2 (Dominguez, 2016). Les domaines WH2 constitués d'une hélice α suivi d'une petite séquence LKKV sont des domaines qui peuvent interagir avec de

l'actine-ATP avec une forte affinité. Présents en plusieurs copies dans des protéines comme Spire (4 WH2), Cordon bleu (3 WH2) ou VopL/VopF (3 WH2), ils favoriseraient la formation de dimères ou trimères d'actine (Ahuja et al., 2007; Liverman et al., 2007; Quinlan et al., 2005; Tam et al., 2007). Comme pour les microtubules, la génération de nouveaux filaments peut aussi se faire pas coupure de fragments existants par la cofiline (Ichetovkin et al., 2002).

2.3.1.2.5 Formation de faisceaux de microtubules ou de filaments d'actine

Les microtubules peuvent s'associer en larges faisceaux (*bundles*) sous l'activité de protéines de pontage présents au niveau du fuseau mitotique comme MAP65/ASE1/PRC1 ou CENP-V (Nabi et al., 2021; Walczak and Shaw, 2010). Dans les prolongements neuronaux, les protéines Tau, MAP2 et Ankyrine B pontent les microtubules en régulant leur espacement (Chen et al., 1992; Chen et al., 2020; Harada et al., 1994; Stephan et al., 2015). Trim 1 et MTCL1 au niveau de l' AIS (*Axon Initial Segment*) sont d'autres protéines pouvant participer à la formation de faisceaux de microtubules (Harterink et al., 2019; Satake et al., 2017).

La formation de faisceaux d'actine est importante dans le rôle structural de l'actine, la génération de force (De La Cruz and Gardel, 2015), la division cellulaire et la motilité (Mitchison and Cramer, 1996; Pollard and Cooper, 2009) et dans la formation des filopodes (Blanchoin et al., 2014; Mogilner and Rubinstein, 2005). Les filaments d'actine peuvent être pontés par de nombreuses protéines (Matsudaira, 1994). Par exemple, la Fascine et la Fimbrine forment des faisceaux denses d'actine dans les filopodes (Gallop, 2020) alors que la filamine au niveau des lamellipodes, pontent un réseau moins compact (Razinia et al., 2012).

2.3.1.2.6 Coordination entre le cytosquelette d'actine et les microtubules

La communication entre les filaments d'actine et les microtubules est essentielle pour le bon fonctionnement de mécanismes tels que la cytokinèse, la génération et le maintien de la polarité cellulaire (Dogterom and Koenderink, 2019; Rodriguez et al., 2003). Elle met en jeu de grosses molécules d'échafaudage comme la protéine APC (Efimova et al., 2020) et la famille des plakines (Suozzi et al., 2012). Elle inclut aussi la famille des formines (Bartolini et al., 2012; Gaillard et al., 2011), la myosine 10 (Weber et al., 2004) et des MAP structurales comme TAU (Cabral Fontela et al., 2017; Elie et al., 2015). Durant le développement neuronal, l'interaction entre des microtubules dynamiques et les faisceaux de filaments d'actine au niveau des filopodes, est essentielle pour la formation de branches collatérales (Dent and Kalil, 2001; Kalil and Dent, 2014; Ketschek et al., 2016; Pacheco and Gallo, 2016). L'interaction entre les microtubules dynamiques et les filaments d'actine dans les filopodes ainsi que dans les épines dendritiques fait intervenir la drébrine (Ketschek et al., 2016; Merriam et al., 2013). Les microtubules dynamiques peuvent également pénétrer dans les épines

dendritiques et modifier leur morphologie en interagissant avec les filaments d'actine à travers des protéines de bouts « plus » des microtubules comme EB3 (Dent, 2017; Gu et al., 2008; Jaworski et al., 2009) ou CLIPs (Neukirchen and Bradke, 2011; Swiech et al., 2011).

2.3.2 Résultats

2.3.2.1 PARTIE I : Mécanisme de stabilisation par MAP6F des microtubules exposés au froid

Dans cette étude, nous nous sommes intéressés au mécanisme de reconnaissance et de stabilisation des microtubules par l'isoforme ubiquitaire de MAP6, MAP6F, à basse température.

Des informations complémentaires, détails expérimentaux et figures pourront être trouvés dans l'article original joint en annexe (p110): « *MAP6-F is a temperature sensor that directly binds to and protects microtubules from cold-induced depolymerization* » par C. Delphin, D. Bouvier, M. Seggio*, E. Couriol, Y. Saoudi, E. Denarier, C. Bosc, O. Valiron, M. Bisbal, I. Arnal and A. Andrieux, *Journal of Biochemical Chemistry*, 2012.

*Doctorant sous ma co-direction.

In vitro, la dynamique des microtubules est sous le contrôle de la concentration en tubuline et de nombreux autres paramètres physico-chimiques (Lee and Timasheff, 1977; Olmsted and Borisy, 1975; Regula et al., 1981). Parmi ceux-ci, la température joue un rôle crucial car les microtubules se dépolymérisent lors d'un changement de température de 37 °C à 4 °C. Cela pourrait être dû à la modification de différents paramètres de la dynamique, dont l'augmentation du nombre de catastrophes et la disparition des événements de sauvetage à ces températures (Fygenson et al., 1994; Modig et al., 2000). Parmi les organismes endothermes qui contiennent des microtubules sensibles au froid, certains peuvent subir une baisse significative de leur température corporelle dans des conditions naturelles. Le maintien d'un réseau minimal de microtubules est alors nécessaire pour les fonctions cellulaires de base. Il avait été démontré que la protéine MAP6 est la principale protéine capable de protéger les microtubules contre la dépolymérisation induite par le froid (Andrieux et al., 2002; Denarier et al., 1998b). Cependant, la sensibilité au froid des microtubules cellulaires à des températures variables entre 37 °C et 4 °C était peu connue et le mécanisme de leur protection par MAP6 n'était pas compris.

Dans les cellules fibroblastiques NIH/3T3 qui expriment la plus petite isoforme de MAP6, MAP6F, les microtubules sont dynamiques à 37 °C (comme révélé par leur sensibilité au nocodazole) (Lieuvin et al., 1994) alors qu'ils sont stables à 4 °C. Cette stabilité s'accompagne d'une relocalisation de MAP6F du cytosol à 37 °C vers le réseau de microtubulaire à 4 °C (Denarier et al., 1998a). Ces données

suggèrent que la stabilisation des microtubules par MAP6F dépend de la liaison de la protéine aux microtubules.

2.3.2.1.1 MAP6F protège les microtubules d'une dépolymérisation température dépendante comprise entre 25 °C et 4 °C.

L'effet du froid sur la dépolymérisation des microtubules et leur protection par MAP6 ont été documentés dans des conditions de diminution rapide de la température de 37 °C à 4 °C. Ici, nous avons analysé l'effet de l'exposition des microtubules à des températures intermédiaires. Les cellules ont donc été incubées à des températures variables entre 37 °C et 4 °C puis nous avons quantifié par immunofluorescence les microtubules présents après exposition. Ceci a été fait après élimination de la fraction de tubuline libre soluble par perméabilisation des cellules en présence de glycérol (pour préserver les microtubules). Dans ces conditions, en absence de MAP6F (HeLa, naturellement dépourvues de MAP6F ou MEF KO pour MAP6 (MEF-/-)), la quantité de microtubules cellulaires décroît progressivement lorsque la température diminue en dessous de 25 °C jusqu'à une quantité très faible à 4 °C. Par contre, en présence de MAP6F (3T3, MEF+/+), une quantité résiduelle importante de microtubules est préservée même à très basse température. Ceci indique que MAP6F protège les microtubules d'une dépolymérisation induite par des température comprises entre 25 °C et 4 °C.

2.3.2.1.2 *In vivo*, MAP6F se relocalise du cytoplasme vers les microtubules de façon température-dépendante et rapidement lors d'une chute de température de 37 °C à 4 °C

Pour mieux caractériser les mécanismes de stabilisation des microtubules par MAP6 durant le refroidissement, nous avons cherché à établir une corrélation entre les conditions qui déstabilisent les microtubules et celles qui permettent l'interaction de MAP6 avec les microtubules et leur stabilisation. Il était connu que MAP6 se relocalisait du cytoplasme vers le réseau microtubulaire lors d'un passage de 37 °C à 4 °C, nous avons également observé qu'une telle relocalisation se produit déjà à 15 °C. Pour analyser l'association de MAP6F avec les microtubules, nous avons utilisé des approches de fractionnement subcellulaire et quantifié la part de MAP6F dans la fraction soluble et la fraction insoluble. En parallèle, nous avons analysé l'activité de MAP6F dans les cellules 3T3 en quantifiant les microtubules protégés d'une dépolymérisation induite par le froid. En effet, comme MAP6 n'est pas associée avec les microtubules à 37 °C, elle est éliminée lors de la perméabilisation des cellules et les microtubules deviennent sensibles au froid. Au contraire, si les cellules sont exposées au froid avant perméabilisation, MAP6F s'associe aux microtubules qui deviennent résistants au froid. On peut donc, en quantifiant la résistance des microtubules à une dépolymérisation induite par le froid, identifier les conditions nécessaires à une interaction de MAP6F avec les microtubules. Dans ces conditions, nous

avons observé une relocalisation progressive de MAP6F de la fraction soluble vers la fraction insoluble lorsque la température décroît par paliers de 37 °C à 4 °C. Nous avons également observé que la réponse de MAP6 à un changement de température est très rapide (-15 s à 4 °C) et réversible avec la même cinétique suggérant que la température influence directement l'interaction de MAP6 avec les microtubules.

2.3.2.1.3 Le domaine Mc de MAP6F se lie de façon température-dépendante aux microtubules.

Nous avons ensuite purifié à partir de cellules d'insecte, MAP6F ou le domaine Mc de MAP6 connus pour protéger les microtubules d'une dépolymérisation induite par le froid en condition de surexpression dans des cellules HeLa. La liaison *in vitro* du domaine Mc aux microtubules est dépendante de la température. Elle est très faible à 37 °C et augmente de manière significative lorsque la température diminue en dessous de 20 °C pour atteindre une haute affinité ($K_{d_{app}}$ 70 nM) à 4 °C. Ainsi, *in vivo* et *in vitro*, le domaine Mc de MAP6 reconnaît et stabilise les microtubules dès que la température descend en dessous de 20 °C. Ces résultats montrent également pour la première fois une interaction directe de MAP6F avec les microtubules.

2.3.2.1.4 La conformation de MAP6F est dépendante de la température

Les résultats précédents suggèrent que MAP6F adopte une conformation dépendante du froid permettant son interaction avec les microtubules, et/ou que MAP6-F reconnaît une caractéristique structurale des microtubules qui dépolymérisent sous l'effet du froid. En particulier, les microtubules qui dépolymérisent présentent à leurs extrémités, des protofilaments enroulés, mais nous n'avons observé aucune accumulation de MAP6F à l'extrémité des microtubules en voie de désassemblage, ni dans les cellules ni dans les essais *in vitro* suggérant que la reconnaissance spécifique des protofilaments enroulés vers l'extérieur par MAP6F est un mécanisme peu probable. Par contre, une analyse structurale du domaine Mc faite en collaboration avec Denis Bouvier (IBS-Grenoble) par dichroïsme circulaire indique que les domaines Mc ont tendance à se structurer en feuillets bêta qui se désorganisent à basses températures.

Ces résultats indiquent que MAP6 se comporte comme un « détecteur de température » en adaptant sa conformation pour permettre la liaison et la préservation des microtubules lors d'une baisse de température.

2.3.1.2.5 Un rôle physiologique de MAP6F dans la protection des microtubules exposés à une baisse de température ?

Nous avons observé que les microtubules sont sensibles au froid et en absence de MAP6 dépolymérisent graduellement à des températures allant de 20 °C à 4 °C. Chez les animaux, des températures aussi basses peuvent être atteintes pendant les épisodes de torpeur ou d'hibernation (Geiser, 1988; Heldmaier et al., 2004) et MAP6 pourrait être nécessaire pour préserver un niveau minimal de microtubules dans de telles conditions. En accord avec cette hypothèse, nous avons trouvé une corrélation relativement bonne entre le nombre de motifs Mc (de 1 à 9) dans le domaine Mc des mammifères et la capacité des animaux à hiberner ou à entrer en torpeur. Par exemple, presque tous les rongeurs dont le génome a été séquencé (souris domestique, rat de Norvège, écureuil terrestre) qui présentent une MAP6 avec 3 à 9 répétitions de Mc sont capables d'hiberner ou de se mettre en torpeur, alors que le rat taupe, qui ne présente qu'un seul motif est très sensible à l'exposition au froid. De même, chez les primates, seule la branche lémurienne qui contient plusieurs motifs de Mc (3 à 6 pour le galago à petites oreilles et le lémurien souris grise) peut entrer en torpeur alors que tous les autres primates incluant l'homme, l'ourang-outan de Sumatra, le chimpanzé, le gorille, le singe rhésus et le babouin Hamadryas n'entrent pas en torpeur et expriment une MAP6 à un seul motif. Chez l'homme, bien que minimale, la stabilisation des microtubules par MAP6 peut encore être utile lors d'épisodes d'hypothermie accidentels ou même pendant l'hypothermie périopératoire après une anesthésie.

2.3.2.2 PARTIE II : Etude de l'activité de MAP6N sur la dynamique et la structure des microtubules

Dans cette étude, nous nous sommes intéressés au rôle de MAP6 sur la dynamique et la structure des microtubules à température physiologique. Cette étude a été entreprise pour essayer de trouver une explication moléculaire aux défauts observés dans les souris MAP6 KO et sensibles à des traitements qui modifient la dynamique des microtubules. Nous avons donc travaillé avec MAP6N, la forme de MAP6 majoritaire dans les neurones et nous avons étudié son activité sur la dynamique des microtubules à température physiologique (35 °C - 37 °C).

Des informations complémentaires, détails expérimentaux et les figures pourront être trouvés dans l'article original joint en annexe (p78) : « *MAP6 is an intraluminal protein that induces neuronal microtubules to coil* » C. Cuveillier*, M. Seggio*, J. Delaroche, S. Gory-Fauré, C. Bosc, E. Denarier, M. Bacia, G. Schoehn, H. Mohrbach, I. Kulić, A. Andrieux, I. Arnal and C. Delphin. Science Advances, 2020.

*Co-premier auteurs, doctorants sous ma co-direction.

2.3.2.2.1 MAP6N interagit directement avec les microtubules et favorise leur polymérisation

Nous avons, dans un premier temps, purifié MAP6 recombinante étiquetée ou non avec la GFP, et exprimée en cellules d'insectes, puis analysé son interaction avec les microtubules. A température physiologique (35 °C), MAP6N interagit avec les microtubules avec une forte affinité ($K_{d_{app}}$ 50 nM). Ajoutée sur des microtubules polymérisés, elle décore rapidement et uniformément les microtubules (observation en microscopie TIRF). Nous avons constaté qu'une faible quantité de MAP6 a une forte activité de stabilisation des microtubules en ralentissant la vitesse de dépolymérisation et en induisant des « sauvetages ». Cette activité est similaire à celle décrite pour d'autres MAP structurales. Nous avons aussi observé une augmentation de la fréquence de survenue de « catastrophes » en présence de MAP6N, ce qui indique une activité déstabilisatrice de MAP6N sur l'extrémité des microtubules en croissance. La combinaison de ces deux activités conduit à la polymérisation de microtubules stables à extrémité dynamique.

2.3.2.2.2 MAP6N induit la polymérisation de microtubules hélicoïdaux

Etonnement, avec une concentration modérée de MAP6N (50-100 nM), les microtubules adoptent une conformation en spirale gauche avec un pas et une largeur d'environ 5,5 μ m et 700 nm respectivement, observable en microscopie TIRF ou airyscan. Cet effet de MAP6N sur la structure des microtubules nécessite la présence de MAP6N durant la polymérisation et n'est pas observé lors de l'ajout de MAP6N sur des microtubules déjà formés. Encore une fois, ces données suggèrent une activité de MAP6 à l'extrémité des microtubules.

2.3.2.2.3 MAP6N favorise la fermeture des feuillets à l'extrémité des microtubules

Au vu de ces résultats, nous avons analysé l'effet de MAP6N sur les feuillets présents aux extrémités des microtubules en croissance. Les microtubules ont été polymérisés en présence de DMSO et GMPcPP, conditions favorisant l'observation des feuillets. Alors que de nombreux feuillets sont observables en conditions contrôle, la présence de MAP6N diminue de façon significative la proportion de feuillets par rapport aux tubes indiquant que MAP6N favorise la fermeture du feuillet à l'extrémité du microtubule.

2.3.2.2.4 MAP6N est une MIP (*Microtubule Inner Particule*) *in vitro* et *in vivo*

Mais le plus surprenant est qu'au cours de nos études de microscopie électronique à transmission, nous avons observé la présence d'une succession de petites structures ponctiformes de forte densité électronique régulièrement espacés le long des microtubules polymérisés en présence

de MAP6N. Nous avons pu montrer par tomographie cryo-électronique que ces particules sont localisées à l'intérieur des microtubules. Nous avons également observé la présence de ces particules intraluminales lorsque les microtubules sont copolymérisés avec MAP6N dans des conditions standard en présence de GTP. La participation de MAP6 dans la formation des particules intraluminales a été confirmée *in vivo* par l'analyse par cryo-microscopie électronique de microtubules de cultures primaires de neurones issus de souris sauvage ou déficientes en MAP6. La présence des particules intraluminales est fortement réduite dans les microtubules des neurones dépourvus de MAP6 par rapport aux neurones sauvages. Cela indique que MAP6 est un composant principal des particules intraluminales des microtubules dans les neurones et que la présence de ces structures pourrait définir une population spécifique de microtubules.

2.3.2.2.5 MAP6N favorise la formation de microtubule avec des ouvertures

Une autre observation que nous avons faite par cryo-microscopie électronique est la présence de nombreux trous stables dans le réseau des microtubules polymérisés en présence de MAP6N. Nos données suggèrent que MAP6N peut avoir deux activités différentes sur les microtubules : une première activité, stabilisatrice, comme d'autres MAP structurale et une seconde, qui se produirait lors de la polymérisation à l'extrémité du microtubule, conduisant à l'incorporation de MAP6N dans la face interne du microtubule, à une déformation hélicoïdale du microtubule, à la formation de trous et à l'induction de catastrophes. En accord avec cette hypothèse, nous avons identifié un mutant de MAP6N qui porte une délétion de 32 acides aminés dans son domaine N-terminal, MAP6 Δ 4-35, et qui conserve une activité stabilisatrice des microtubules mais aucune de ses autres fonctions.

2.3.2.2.6 Modèle de déformation des microtubules par l'incorporation de MAP6N

En collaboration avec Igor Kulic et Herve Morhbach (Strasbourg), nous avons établi un modèle à partir des données de l'équipe et de la littérature, de déformation des microtubules en présence de MAP6N. Ce modèle est basé sur l'état conformationnel bistable des dimères de tubuline : une conformation allongée, énergétiquement favorisée par liaison au GTP et une conformation courte et compacte favorisée en présence GDP. En condition standard, la tubuline liée au GDP (après hydrolyse du GTP suite à l'incorporation dans le microtubule) adopte la conformation courte et le microtubule est droit. MAP6N se lierait à la GTP-tubuline pendant la polymérisation et formerait un noyau élastique qui favoriserait la forme allongée de la tubuline, même après hydrolyse du GTP. Ceci introduirait un stress au niveau de la tubuline entre une conformation compacte favorisée par l'hydrolyse du GTP et la conformation allongée favorisée par la présence de MAP6N. Ces deux situations étant énergétiquement défavorables, le microtubule réduirait son énergie interne en permettant à une

partie des protofilaments d'être dans la forme allongée tandis que les autres adopteraient la forme compactée. Ceci introduirait une courbure qui se propagerait le long des protofilaments. Nous avons observé que MAP6N favorise la polymérisation de microtubules à 14 protofilaments connus pour avoir une hélicité gauche avec un pas de 5,6 μm . Cette hélicité, combinée à la courbure induite par MAP6N, forcerait le microtubule à adopter une forme en spirale.

2.3.2.2.7 Quel rôle pour des microtubules hélicoïdaux avec des trous persistants et des densités intraluminales dans les neurones ?

Nous avons observé que les microtubules qui polymérisent en présence de MAP6N peuvent adopter une structure hélicoïdale. *In vivo*, à cause de leur faible amplitude, ces déformations sont difficiles à observer. Ces structures pourraient influencer l'organisation spatiale du réseau de microtubules, par exemple, en modifiant le co-alignement et la formation de faisceaux de microtubules, contribuer à déterminer la largeur des neurites ou des axones, ou conférer une résistance aux charges compressives rencontrées au cours du développement ou de la régénération.

In vivo, la plupart des microtubules observés sont constitués de 13 protofilaments. Et des facteurs protéiques autres que MAP6N tels que la doublecortine favorisent ce type de microtubules (Bechstedt and Brouhard, 2012). Dans les microtubules possédant 13 protofilament, les protofilaments ont un angle de rotation très faible autour de l'axe du microtubule. Dans ce cas, une torsion induite par MAP6N induirait la formation d'une courbure en arc de cercle. Une localisation de MAP6N pourrait alors favoriser des changements de direction des microtubules.

La présence de particules intraluminales dans les microtubules cellulaires avait été observée par cryo-microscopie électronique depuis longtemps (Burton, 1984; Garvalov et al., 2006). Au niveau des cônes de croissance, ces particules semblent être enrichies dans les microtubules stables et pourraient participer à cette stabilisation (Atherton et al., 2018; Foster et al., 2022).

2.3.2.3 PARTIE III : Rôle de MAP6N sur la nucléation des microtubules et des filaments d'actine et sur la formation de faisceaux d'actine

2.3.2.3.1 MAP6N promeut la nucléation des microtubules *in vitro*

Au cours de l'étude décrite précédemment, nous avons observé en microscopie TIRF qu'en absence d'amorces, MAP6N, à une concentration supérieure à 200 nM, est capable d'induire la nucléation des microtubules. Nous avons analysé cet effet par des expériences de polymérisation en solution, sédimentation, et quantification de la masse de microtubules obtenus, conditions standard d'évaluation de la concentration critique de nucléation (Figure 2).

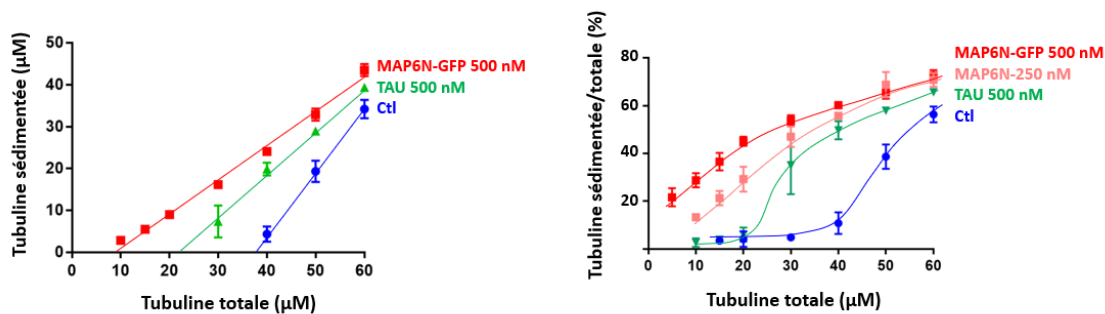


Figure 2 : MAP6N favorise la nucléation des microtubules

Les résultats obtenus indiquent que dans ces conditions, la concentration critique de nucléation de la tubuline passe de 38 µM en absence de MAP6 à 8 µM en présence de 500 nM de MAP6N. Lorsque l'on analyse la proportion de tubuline polymérisée par rapport à la tubuline totale présente dans l'essai, on remarque que la courbe obtenue en présence de MAP6N a une allure différente de celle de la condition contrôle ou en présence de TAU. En effet, des microtubules, observables en microscopie électronique, sont présents à de très faibles concentrations en tubuline. Ceci indique que l'effet de MAP6N sur la concentration critique de nucléation des microtubules est sous-estimé lorsque l'on quantifie cet effet en mesurant la quantité totale de tubuline polymérisée, et qu'avec MAP6N des événements de polymérisation peuvent se produire à des concentrations en tubuline de l'ordre du micromolaire. Quoiqu'il en soit, la capacité de MAP6N à nucléer des microtubules est nettement supérieure à celle observée pour TAU, une autre MAP structurale qui présente pourtant des effets sur la dynamique des microtubules comparables à MAP6N (Ramirez-Rios 2016). Ces résultats suggèrent que MAP6N pourrait avoir une capacité particulière à induire la nucléation des microtubules qui pourrait être due en partie à sa capacité à interagir avec la face interne des microtubules.

2.3.2.3.2 MAP6N stimule la nucléation des filaments d'actine

Parallèlement à ce travail, nous avons également observé au laboratoire une réduction de la densité en épines dendritiques présentes sur les neurones cultivés à partir de cerveaux de souris MAP6-KO. Nous avons montré que cette activité pouvait être restaurée par surexpression du domaine Mc de MAP6 dans ces neurones. Ce domaine interagit avec l'actine dans les cônes de croissance et les épines dendritiques et permet la stabilisation de l'actine des épines dendritiques en réponse à une activation synaptique. *In vitro*, ce domaine favorise la nucléation des filaments d'actine. Ces résultats suggèrent qu'une partie des défauts observés chez les souris MAP6-KO pourrait être liée à une perturbation de la régulation du cytosquelette d'actine (Peris et al., Nature com., 2018 (p89)).

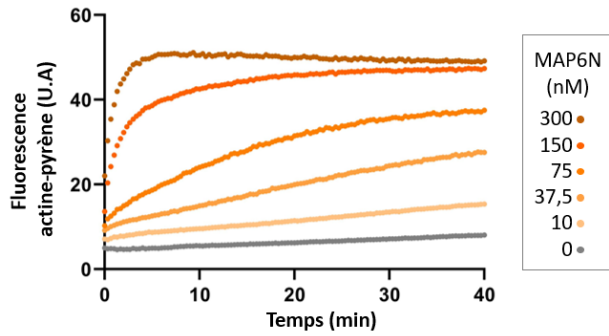


Figure 3 : MAP6N stimule la nucléation des filaments d'actine

Au cours de cette étude, nous avons observé sur des courbes d'assemblage d'actine/pyrène que MAP6N présente une activité de nucléation bien supérieure à celle des domaines Mc isolés. Ceci indique que la protéine contient d'autres domaines impliqués dans cette activité et que le rôle de MAP6 sur le cytosquelette d'actine pourrait dépasser celui décrit précédemment au niveau des

épinés dendritiques. Nous avons alors entrepris une étude *in vitro* sur la régulation du cytosquelette d'actine par MAP6N. Nous avons suivi, par mesure de la fluorescence d'actine-pyrène (2 μ M), la polymérisation de l'actine en présence d'une concentration croissante de MAP6N et observé que MAP6N favorise fortement et de manière dose-dépendante la nucléation des filaments d'actine (Figure 3). Cet effet de MAP6N sur l'induction de la polymérisation de l'actine a aussi été observé en microscopie TIRF.

2.3.2.3.3 MAP6N se lie aux filaments d'actine et les organise en faisceaux denses

Nous avons également observé, dans des expériences de co-sédimentation, que MAP6N lie les filaments d'actine. Pour ces expériences, des concentrations croissantes d'actine polymérisée et stabilisée avec de la phalloïdine (de 0 à 6 μ M) sont incubées avec MAP6N (500 nM) puis sédimentées par centrifugation à haute vitesse (100 000 g). La quantité de MAP6N ayant interagi avec les filaments et co-sédimenté est ensuite quantifiée. Les résultats indiquent une interaction dose-dépendante de MAP6N avec les filaments d'actine et une affinité apparente associée d'environ 200 nM (Figure 4).

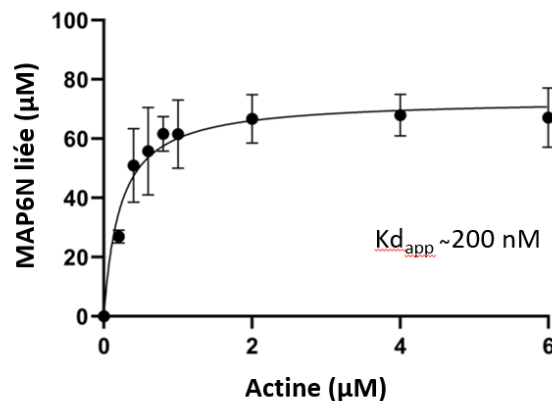


Figure 4 : MAP6N interagit avec les filaments d'actine

De la même façon, nous avons étudié la capacité de MAP6N à induire la formation de faisceaux de filaments d'actine (Figure 5). Dans ce cas, une concentration fixe d'actine/phalloïdine (2 μM) est incubée avec une concentration croissante de MAP6N puis centrifugée à faible vitesse (15 000 xg) pour sédimenter les faisceaux d'actine plus lourd (C) alors que les filaments isolés restent dans le surnageant (S). Les résultats montrent que MAP6N induit de façon dose-dépendante la formation de faisceaux d'actine. Ces faisceaux d'actine formés en présence de MAP6N et observés par microscopie électronique après coloration négative présentent une structure compacte. Ils sont constitués majoritairement de 8 filaments d'actine avec la présence de structures ponctiformes denses aux électrons qui semblent être au centre des faisceaux. Ces structures bien que de taille différente (~15 nm) évoquent celles observées avec MAP6N à l'intérieur des microtubules.

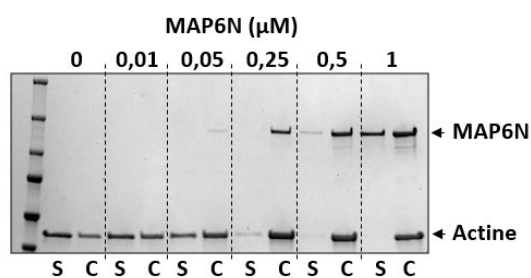
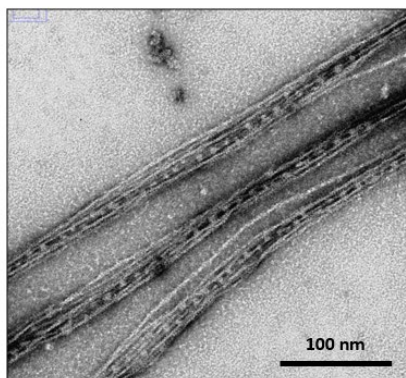


Figure 5 : MAP6N induit la formation dose-dépendante de faisceaux d'actine. En haut, analyse sur gel SDS-PAGE et Coomassie de la quantité de filaments en faisceaux (C) ou non (S). En bas, observation des faisceaux par microscopie électronique.



2.3.2.3.4 MAP6N favorise la co-nucléation et le co-alignement des filaments d'actine et des microtubules

Nous avons cherché à savoir ce qui se passe lorsque MAP6N se retrouve en présence conjointe de tubuline et d'actine, comme c'est le cas dans les cellules. Pour répondre à cette question, de la tubuline (7 μM) et de l'actine (0.3 μM) à des concentrations où il n'y a pas ou très peu de polymérisation en l'absence de MAP6N, ont été incubées en présence de 250 nM MAP6N et observées en microscopie TIRF (Figure 6). Dans ces conditions, nous observons que des microtubules et des filaments d'actine polymérisent rapidement et se co-localisent partiellement. Ces résultats montrent que MAP6N peut à la fois favoriser la nucléation des microtubules et des filaments d'actine et induire leur co-alignement.

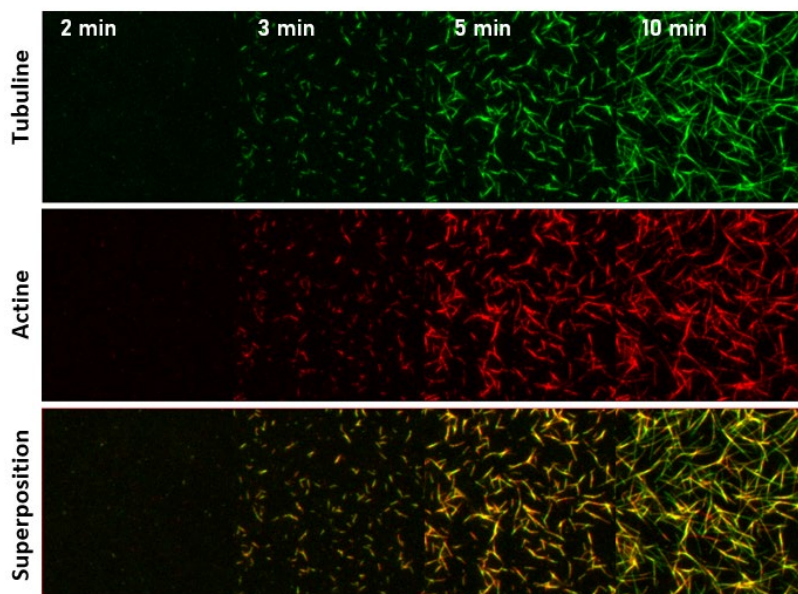


Figure 6 : Co-nucléation et alignement des filaments d'actine et des microtubules en présence de MAP6N

2.3.2.3.5 Déterminants moléculaires de l'interaction de MAP6N avec l'actine et la tubuline.

Afin de déterminer les domaines fonctionnels de MAP6N impliqués dans son interaction avec la tubuline (dimères de tubuline/microtubules) et l'actine (monomérique/filaments), nous avons divisé la protéine en 4 grands fragments : le fragment LNT (long N-terminal, résidus 1 à 221) comprenant le domaine N-terminal et les deux premiers Mn, Mn1 et Mn2, le fragment Mc constitué des cinq modules Mc (résidus 222 à 450), le domaine KR (globalement plus riche en lysines et arginines que le reste de la protéine) comprenant le Mn3 (résidus 451 à 614) et le domaine C-terminal (résidus 615 à 952). Ces régions ont été délétées, seules ou en combinaison, à partir de la MAP6N-GFP (Figure 7).

Nous avons également produit des mutants de délétion plus ciblés. Le fragment C-terminal a été préservé dans toute l'étude car il confère une meilleure solubilité à la protéine produite. Dans aucune de nos expériences, nous n'avons pu déceler une quelconque interaction ou activité du fragment C-terminal avec l'actine ou les microtubules. Ces mutants de délétion ont été analysés pour leur capacité à promouvoir la nucléation des microtubules et des filaments d'actine, à se lier aux filaments d'actine et à induire la formation de faisceaux d'actine. Les résultats obtenus sont résumés dans la Figure 7.

En ce qui concerne l'interaction de MAP6N avec les dimères de tubuline, le domaine KR semble avoir une activité prépondérante puisqu'il est le seul à pouvoir se lier de manière significative lorsqu'il

est seul. Cette activité est potentialisée par le domaine N-terminal et dans une moindre mesure par la présence du domaine Mc.

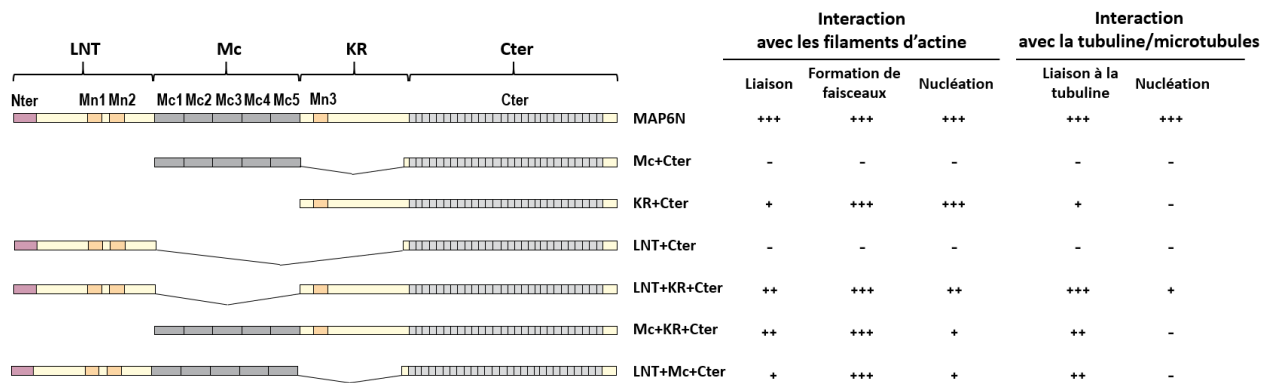


Figure 7 : Implication des différents domaines de MAP6N dans son activité sur l'actine et la tubuline

- = 0-25%, + = 25-50%, ++ = 50-75%, +++ = 75-100% de l'activité de MAP6N

L'induction de la nucléation des microtubules par MAP6N est un phénomène qui nécessite la présence des domaines LNT et KR. Dans les conditions de l'essai réalisé en présence de 12 μ M de tubuline et 300 nM de fragment en microscopie TIRF, le domaine Mc n'est pas indispensable mais sa délétion impacte la capacité de MAP6N à potentialiser la nucléation des microtubules. Cependant, cette implication du domaine Mc dans la nucléation des microtubules induite par MAP6N n'est pas retrouvée dans d'autres conditions (conditions de détermination des concentration critiques). Ceci indique que le domaine Mc, qui n'interagit pas significativement avec la tubuline ni avec les microtubules à la température de l'essai (35 °C, voir plus haut), n'est pas directement impliqué dans cette fonction. Sa délétion pourrait affecter l'activité de la protéine indirectement en modifiant par exemple la distance entre les domaines LNT et KR.

Comme avec la tubuline, l'interaction de MAP6N avec les filaments d'actine est impactée par la délétion de chacun des fragments. Le fragment KR a une activité de liaison supérieure aux deux autres et peut à lui seul permettre une interaction.

En accord avec les résultats obtenus pour l'interaction, la formation de faisceaux d'actine, quantifiée par sédimentation à basse vitesse nécessite l'association d'au moins deux fragments sauf pour le fragment KR qui peut induire des faisceaux seul. Cependant, l'observation par microscopie électronique montre que ces faisceaux obtenus en absence des fragments LNT et Mc sont beaucoup moins denses et organisés que ceux obtenus avec la protéine entière (Figure 8).

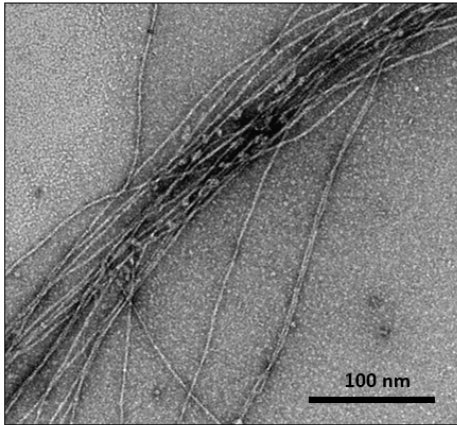


Figure 8 : Effet du domaine LCT + KR sur la formation de faisceaux de filaments d'actine.

En ce qui concerne la nucléation de l'actine, le fragment KR peut à lui seul exercer une activité similaire à la protéine entière. Les 2 autres fragments présentent soit une faible activité en tandem soit une diminution de l'activité du fragment KR lorsqu'ils lui sont associés. Ceci suggère un mécanisme d'autorégulation interne de l'activité de nucléation des filaments d'actine par MAP6 ou une gêne due à la production d'une protéine anormalement structurée.

Dans l'ensemble, ces résultats montrent une implication majeure du domaine KR dans les activités de MAP6N sur les cytosquelettes d'actine et microtubulaire

Des mutations qui touchent des domaines plus précis de MAP6N ont également été testées. De façon inattendue, la mutation simultanée des Mn 1, 2 et 3, les trois domaines d'interaction avec les microtubules identifiés, n'affecte que partiellement la nucléation des microtubules (concentration critique d'environ 8 μ M, 20 μ M et 38 μ M pour MAP6N, MAP6N Δ Mn1,2,3 et le contrôle sans MAP6 respectivement). Ce résultat indique que d'autres domaines de la protéine sont impliqués dans l'interaction de MAP6N avec la tubuline. La délétion des trois domaines Mn n'a pas d'influence sur la nucléation des filaments d'actine par MAP6N, ni sur son interaction avec les filaments d'actine et leur organisation en faisceaux, indiquant que contrairement à d'autres MAPs, les domaines d'interaction de MAP6N avec l'actine seraient distincts de ses domaines d'interaction avec les microtubules (Cabral Fontela et al., 2017; Correas et al., 1990).

La mutation Δ 4-35 dans la partie N-terminale de MAP6N est nécessaire à la fonction MIP de MAP6 (voir plus haut). Cette mutation abolit également la capacité de MAP6N à stimuler la nucléation des microtubules, ce qui indique que ces deux activités ont des bases structurales communes. Comme pour la délétion des Mn, la délétion Δ 4-35 n'a pas d'impact sur l'activité de MAP6N sur le réseau d'actine. Ce domaine pourrait être impliqué dans la formation d'oligomères de MAP6N qui seraient favorisés en présence de tubuline.

3. Projet de Recherche

Les résultats obtenus, associés aux données de la littérature, amènent de nouvelles questions auxquelles on cherchera à répondre dans les années qui viennent et dont une partie fait l'objet d'un contrat de financement ANR du laboratoire.

3.1 Analyse des domaines d'interaction de MAP6 avec les microtubules : de nouveaux modules Mn ?

La découverte récente des nouveaux membres de la famille de MAP6, les protéines SAXOs, a fait évoluer la définition des domaines Mn, originellement basée sur la stabilisation des microtubules dans des expériences de surexpression dans des cellules HeLa (Bosc et al. 2001), et dont les résidus impliqués dans l'interaction avec les microtubules avaient été confirmés par RMN (Lefèvre et al 2013). L'analyse informatique de comparaison de séquences d'un nombre important de domaines Mn présents en de multiples copies dans chaque protéine SAXO et dans de nombreuses espèces a permis de définir une nouvelle séquence consensus de 15 résidus pour les domaines Mn (Dacheux 2012). Basé sur ce consensus, deux nouveaux modules Mn, Mn4 et Mn5 situés en aval du module Mn3 ont été retrouvés sur MAP6N (Figure 9). L'implication fonctionnelle de ces modules dans la stabilisation des microtubules reste à démontrer mais cela pourrait expliquer les résultats obtenus sur l'effet partiel de la mutation des domaines Mn1, 2 et 3 sur la nucléation des microtubules. Dans le cas de protéines

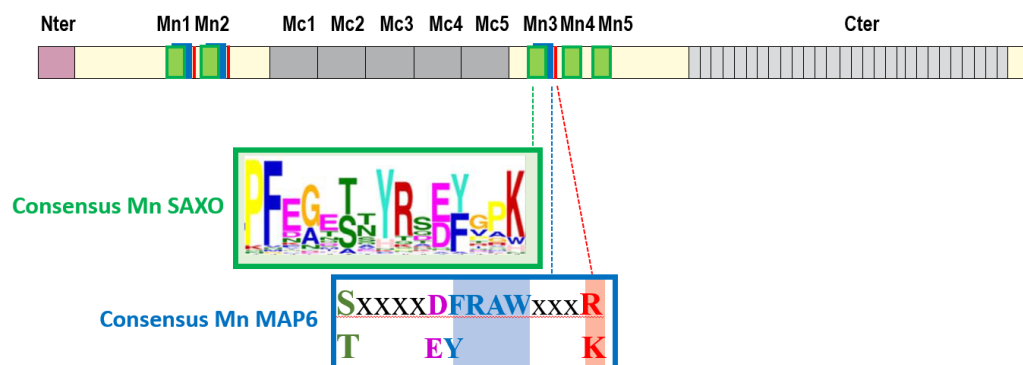


Figure 9 : Evolution des domaines Mn de MAP6N

capables de lier à la fois actine et microtubules, les mêmes domaines sont impliqués (Corréas 1990, Wu 2022). Nos premiers résultats suggèrent que cela pourrait être différent pour MAP6. Cependant, ils montrent aussi que le fragment KR joue un rôle majeur et c'est là que se situe les nouveaux domaines Mn de MAP6N, Mn4 et Mn5. De nouvelles constructions de MAP6N portant des mutations

au niveau de ces domaines seuls ou en association avec les autres domaines Mn seront produites et testées pour leur implication dans les activités de MAP6N sur les microtubules et l'actine.

3.2 La famille des protéines de MAP6 : une famille de MIP ?

De façon intéressante, une étude récente d'analyse structurale par cryo-electron microscopie des MIPs contenues dans les doublets de microtubules de cils de *Chlamydomonas reinhardtii* (Ma et al., 2019) a identifié un orthologue de la famille de MAP6. Cette protéine, FAP363, possède six domaines Mn directement impliqués dans l'interaction de la protéine le long de la surface interne des microtubules, chaque domaine se fixant à l'interface entre les sous-unités α et β d'un dimère de tubuline. Cette observation renforce l'hypothèse d'un rôle fonctionnel de MAP6N en tant que MIP et suggère que l'ensemble des protéines de la famille de MAP6 possédant des domaines Mn seraient des MIPs. Les protéines SAXO sont exprimées dans des cellules portant des cils ou flagelles. Il est très probable que, comme pour FAP363 chez *C. reinhardtii*, elles soient localisées dans les doublets de microtubules et servent à leur stabilisation mécanique.

Nous avons obtenu au laboratoire un financement ANR (MIPMAP) pour analyser la possibilité que les autres membres de la famille de MAP6, MAP6d1 et SAXO1 et 2 soient des MIPs et étudier leur rôle *in vivo* dans la stabilité/fonction des microtubules. Ces protéines sont en cours de production pour mener des analyses *in vitro* semblables à ce qui a été fait pour MAP6N, étudier leur effet sur la dynamique des microtubules et leur capacité à former des densités intraluminales. Parallèlement, nous avons débuté la production de souris déficientes en ces gènes pour observer leurs rôles dans des processus où l'activité ciliaire/flagellaire est importante (reproduction, circulation du fluide cérébrospinal, système respiratoire...)

3.3 MAP6 : MIP, MAP, MIPMAP ?

La nouvelle séquence consensus des domaines Mn établie à partir des séquences de l'ensemble des domaines Mn présents dans la famille de MAP6 et constitué très majoritairement de Mn de SAXOs est différente de celle établie originellement à partir des séquences des protéines MAP6 des vertébrés. Notamment, les résidus RAWxxxR/K présents dans le consensus établi à partir des séquences de MAP6 et montrés comme impliqués dans l'interaction avec les microtubules, ne font pas partie du consensus établi avec les séquences des SAXOs. Ceci suggère qu'au cours de l'évolution, MAP6 a modifié son mode d'interaction avec les microtubules par rapport à SAXO, permettant soit une modification/régulation de son interaction sur la face luminale des microtubules soit une nouvelle fonction, telle qu'une interaction sur la face externe des microtubules. Les nouveaux modules Mn

identifiés sur MAP6, Mn4 et Mn5 n'ont pas la séquence RAWxxxR/K et n'auraient donc pas suivi la même évolution que les domaines Mn1, 2 et 3.

En accord avec leur orthologue FAP363, les protéines SAXO du fait de leurs domaines Mn sont probablement des MIPs. Dans le cas de MAP6 et MAP6d1, l'évolution a fait apparaître au niveau de ces domaines, une séquence supplémentaire importante pour l'interaction avec les microtubules et que l'on pensait être impliquée dans l'interaction de MAP6 avec la face externe du microtubule. Est-il possible que MAP6 soit à la fois une MAP et une MIP ?

Le fait que l'on obtienne des résultats différents selon que MAP6N est présente pendant ou uniquement après polymérisation indique qu'il existe pour MAP6N plusieurs modes d'interaction avec les microtubules. La présence *in vitro* de particules à l'intérieur des microtubules polymérisés en présence de MAP6N, la diminution du nombre de particules intraluminales dans les neurones dépourvues en MAP6 et l'analogie avec FAP363 indiquent clairement une possibilité d'une fonction de MIP pour MAP6N. Nous avons également des arguments suggérant une interaction de MAP6N avec la surface externe des microtubules : la vitesse d'association de MAP6N avec les microtubules pré-polymérisés et stabilisés qui laisse peu de place à la possibilité d'une diffusion à partir des extrémités ou des trous présents dans la paroi des microtubules, la capacité du mutant MAP6N Δ 4-35 à décorer les microtubules tout en ayant perdu sa capacité à se comporter comme une MIP et à stimuler la nucléation des microtubules et les effets de MAP6N sur la dynamique des microtubules semblables à ceux d'autres MAP structurales qui interagissent avec la surface externe des microtubules.

Une étude structurale de l'interaction de MAP6N avec les microtubules a été entreprise au laboratoire par cyo-EM. Cette analyse pourra préciser si MAP6N se fixe préférentiellement sur la face externe des microtubules ou la face luminale et si la résolution le permet, identifier les résidus de MAP6N impliqués. Ces résultats sont importants car ils permettront d'envisager de nouveaux mutants qui pourront être utilisés pour étudier le rôle de chacune de ces interactions dans les fonctions de MAP6 *in vitro* et *in vivo*.

Nous pouvons d'ores et déjà produire des mutants de MAP6N en ciblant les domaines Mn soit dans leur partie N-terminale correspondant au consensus de Mn « SAXO », soit à leur extrémité C-terminale spécifique de MAP6 (consensus RAWxxxR/K) dans le cas des Mn 1, 2 et 3. Nous analyserons leur interaction avec les microtubules et leur implication dans les différentes fonctions de MAP6N sur les microtubules (liaison, stabilisation, torsion, particules intraluminales, nucléation) afin de discriminer clairement les fonctions MIP des fonctions MAP.

3.4 Coordination des réseaux d'actine et de microtubules par MAP6N

Nos résultats montrent que MAP6N peut favoriser la nucléation à la fois des filaments d'actine et des microtubules et leur co-alignement *in vitro*. Nous analyserons comment la présence d'un des deux réseaux peut influencer la dynamique de l'autre (coopération ou compétition pour MAP6) et si MAP6N peut utiliser l'un des deux réseaux pour favoriser la polymérisation de l'autre. Le co-alignement des filaments d'actine et des microtubules sera observé par microscopie électronique et nous chercherons à savoir si MAP6N est capable de favoriser la polymérisation de filaments d'actine à l'intérieur des microtubules comme cela a déjà été observé *in vivo* (Paul 2020).

Un des éléments importants de l'activité de MAP6N pourrait être son oligomérisation. Nos expériences, utilisant des approches de chromatographie d'exclusion de taille, de couplage chimique et de fractionnement sur gradient de sucrose, suggèrent que MAP6N peut former des oligomères. Cette oligomérisation serait favorisée en présence de tubuline et impliquerait le domaine N-terminal. Ces observations apportent un élément de réponse pour expliquer l'incapacité de MAP6N délétée des résidus 4-35 à présenter une activité de type MIP et à favoriser la nucléation des microtubules.

3.5 Analyse structurale des noyaux de nucléation

Les mécanismes de nucléation des microtubules en absence du complexe γ TURC sont très peu compris et leur implication *in vivo* est difficile à démontrer. *In vitro*, les MAP structurales favorisent probablement la nucléation en stabilisant les noyaux de nucléation qui se forment spontanément. MAP6N, en se liant à la fois sur la face des dimères de tubuline qui se retrouvent à l'intérieur et à celle qui se retrouve à l'extérieur du microtubule, pourrait avoir un mode de fonctionnement différent dans la nucléation des microtubules. De même, pour la nucléation des filaments d'actine. Elle nécessite la formation d'un noyau qui mime l'extrémité d'un filament. Un complexe de nucléation devrait donc être composé *a minima* d'une molécule de MAP6 et de deux molécules d'actine.

L'analyse des noyaux de polymérisation des filaments d'actine et des microtubules est importante pour comprendre les mécanismes moléculaires qui sous-tendent ces activités. Pour l'instant, les tentatives d'identification de noyaux de nucléation de microtubules et de filaments d'actine en présence de MAP6N par microscopie électronique n'ont pas abouti. Ces observations sont difficiles à mettre en place car les événements de nucléation sont difficiles à isoler. Plusieurs approches pourront être testées pour réaliser ces expériences : 1) changement de l'agent de contraste : l'utilisation du SST (*sodium silico tungstate*) par exemple, qui peut être utilisé à différents pHs contrairement à l'acétate d'uranyle, pourrait favoriser l'observation de ces complexes, 2) changement des conditions expérimentales pour limiter les interactions « parasites » qui amènent de

l'hétérogénéité dans les complexes observés, 3) utilisation d'un mutant de l'actine (DVD actine, Zahm et al., 2013) que nous avons produit au laboratoire pour restreindre la polymérisation à partir des noyaux de nucléation.

3.6 Une fonction spécifique pour l'isoforme neuronale embryonnaire MAP6E ?

La souris MAP6-KO présente des défauts développementaux qui prennent leur origine avant la naissance à un stade où l'isoforme MAP6N n'est pas encore exprimée et où la forme E est prépondérante. La différence entre les deux isoformes est une absence chez MAP6E de l'extrémité C-terminale contenant un grand nombre de séquences répétées. *In vitro*, cette isoforme fusionnée à la GFP a une très forte propension à s'agréger, ce qui rend son étude impossible. Cependant, il serait intéressant de comprendre la différence fonctionnelle due à cette extrémité. *In vitro*, nous pourrions chercher à améliorer sa solubilité en l'exprimant seule ou en modifiant la position ou les séquences ajoutées pour la purification et la détection. Cette forte tendance à former des agrégats pourrait refléter une capacité de la protéine à faire des condensats comme cela est de plus en plus fréquemment montré pour les MAPs (Boyko and Surewicz, 2022; King and Petry, 2020).

3.7 Quel rôle cellulaire pour MAP6 ?

Nous avons vu que MAP6 est exprimée dans des neurones ou des cellules gliales (pour les isoformes O et A). Dans ces cellules, MAP6 pourrait jouer un rôle dans la stabilisation des doublets de microtubules du cil primaire. Dans les neurones, MAP6 est associée aux microtubules dans le cytoplasme. Des expériences d'immunofluorescence en microscopie super-résolution, couplant expansion de l'échantillon et microscopie Airyscan ou STED, sont en cours dans le laboratoire pour caractériser la localisation précise de MAP6 (faisceaux d'actine, sous-populations de microtubules, sites particuliers qui contiennent MAP6) et des défauts du réseau de cytosquelette après manipulation de l'expression de MAP6. Des mutants de MAP6 ainsi que des stimulations des neurones pourront aussi être utilisés pour mettre en évidence un rôle précis de MAP6 dans les neurones.

4. BIBLIOGRAPHIE

- Aguezoul, M., A. Andrieux, and E. Denarier. 2003. Overlap of promoter and coding sequences in the mouse STOP gene (*Mtap6*). *Genomics*. 81:623-627.
- Ahuja, R., R. Pinyol, N. Reichenbach, L. Custer, J. Klingensmith, M.M. Kessels, and B. Qualmann. 2007. Cordon-bleu is an actin nucleation factor and controls neuronal morphology. *Cell*. 131:337-350.

- Akhmanova, A., and C.C. Hoogenraad. 2015. Microtubule minus-end-targeting proteins. *Curr Biol.* 25:R162-171.
- Andrieux, A., P. Salin, A. Schweitzer, M. Begou, B. Pachoud, P. Brun, S. Gory-Faure, P. Kujala, M.F. Suaud-Chagny, G. Hofle, and D. Job. 2006. Microtubule stabilizer ameliorates synaptic function and behavior in a mouse model for schizophrenia. *Biol Psychiatry.* 60:1224-1230.
- Andrieux, A., P.A. Salin, M. Vernet, P. Kujala, J. Baratier, S. Gory-Faure, C. Bosc, H. Pointu, D. Proietto, A. Schweitzer, E. Denarier, J. Klumperman, and D. Job. 2002. The suppression of brain cold-stable microtubules in mice induces synaptic defects associated with neuroleptic-sensitive behavioral disorders. *Genes Dev.* 16:2350-2364.
- Atherton, J., M. Stouffer, F. Francis, and C.A. Moores. 2018. Microtubule architecture in vitro and in cells revealed by cryo-electron tomography. *Acta Crystallogr D Struct Biol.* 74:572-584.
- Barlan, K., and V.I. Gelfand. 2017. Microtubule-Based Transport and the Distribution, Tethering, and Organization of Organelles. *Cold Spring Harb Perspect Biol.* 9.
- Bartolini, F., N. Ramalingam, and G.G. Gundersen. 2012. Actin-capping protein promotes microtubule stability by antagonizing the actin activity of mDia1. *Mol Biol Cell.* 23:4032-4040.
- Bechstedt, S., and G.J. Brouhard. 2012. Doublecortin recognizes the 13-protofilament microtubule cooperatively and tracks microtubule ends. *Dev Cell.* 23:181-192.
- Begou, M., P. Brun, J.B. Bertrand, D. Job, A. Schweitzer, T. D'Amato, M. Saoud, A. Andrieux, and M.F. Suaud-Chagny. 2007. Post-pubertal emergence of alterations in locomotor activity in stop null mice. *Synapse.* 61:689-697.
- Blanchoin, L., R. Boujemaa-Paterski, C. Sykes, and J. Plastino. 2014. Actin dynamics, architecture, and mechanics in cell motility. *Physiol Rev.* 94:235-263.
- Bosc, C., A. Andrieux, and D. Job. 2003. STOP proteins. *Biochemistry.* 42:12125-12132.
- Bosc, C., J.D. Cronk, F. Pirollet, D.M. Watterson, J. Haiech, D. Job, and R.L. Margolis. 1996. Cloning, expression, and properties of the microtubule-stabilizing protein STOP. *Proc Natl Acad Sci U S A.* 93:2125-2130.
- Bosc, C., R. Frank, E. Denarier, M. Ronjat, A. Schweitzer, J. Wehland, and D. Job. 2001. Identification of novel bifunctional calmodulin-binding and microtubule-stabilizing motifs in STOP proteins. *J Biol Chem.* 276:30904-30913.
- Bouvrais-Veret, C., S. Weiss, A. Andrieux, A. Schweitzer, J.M. McIntosh, D. Job, B. Giros, and M.P. Martres. 2007. Sustained increase of alpha7 nicotinic receptors and choline-induced improvement of learning deficit in STOP knock-out mice. *Neuropharmacology.* 52:1691-1700.
- Bouvrais-Veret, C., S. Weiss, N. Hanoun, A. Andrieux, A. Schweitzer, D. Job, M. Hamon, B. Giros, and M.P. Martres. 2008. Microtubule-associated STOP protein deletion triggers restricted changes in dopaminergic neurotransmission. *J Neurochem.* 104:745-756.
- Boyko, S., and W.K. Surewicz. 2022. Tau liquid-liquid phase separation in neurodegenerative diseases. *Trends Cell Biol.*
- Brenner, E., U. Sonnewald, A. Schweitzer, A. Andrieux, and A. Nehlig. 2007. Hypoglutamatergic activity in the STOP knockout mouse: a potential model for chronic untreated schizophrenia. *J Neurosci Res.* 85:3487-3493.
- Brun, P., M. Begou, A. Andrieux, L. Mouly-Badina, M. Clerget, A. Schweitzer, H. Scarna, B. Renaud, D. Job, and M.F. Suaud-Chagny. 2005. Dopaminergic transmission in STOP null mice. *J Neurochem.* 94:63-73.
- Burton, P.R. 1984. Luminal material in microtubules of frog olfactory axons: structure and distribution. *J Cell Biol.* 99:520-528.
- Cabrales Fontela, Y., H. Kadavath, J. Biernat, D. Riedel, E. Mandelkow, and M. Zweckstetter. 2017. Multivalent cross-linking of actin filaments and microtubules through the microtubule-associated protein Tau. *Nat Commun.* 8:1981.
- Chen, C.P., S.P. Lin, S.R. Chern, P.S. Wu, S.W. Chen, F.T. Wu, D.D. Town, and W. Wang. 2021. Tetrasomy of 11q13.4-q14.3 due to an intrachromosomal triplication associated with paternal uniparental isodisomy for 11q14.3-qter, intrauterine growth restriction, developmental delay,

- corpus callosum dysgenesis, microcephaly, congenital heart defects and facial dysmorphism. *Taiwan J Obstet Gynecol.* 60:169-172.
- Chen, J., Y. Kanai, N.J. Cowan, and N. Hirokawa. 1992. Projection domains of MAP2 and tau determine spacings between microtubules in dendrites and axons. *Nature.* 360:674-677.
- Chen, K., R. Yang, Y. Li, J.C. Zhou, and M. Zhang. 2020. Giant ankyrin-B suppresses stochastic collateral axon branching through direct interaction with microtubules. *J Cell Biol.* 219.
- Choi, K.H., M.E. Zepp, B.W. Higgs, C.S. Weickert, and M.J. Webster. 2009. Expression profiles of schizophrenia susceptibility genes during human prefrontal cortical development. *J Psychiatry Neurosci.* 34:450-458.
- Chou, T.C., X.G. Zhang, A. Balog, D.S. Su, D. Meng, K. Savin, J.R. Bertino, and S.J. Danishefsky. 1998. Desoxyepothilone B: an efficacious microtubule-targeted antitumor agent with a promising in vivo profile relative to epothilone B. *Proc Natl Acad Sci U S A.* 95:9642-9647.
- Correas, I., R. Padilla, and J. Avila. 1990. The tubulin-binding sequence of brain microtubule-associated proteins, tau and MAP-2, is also involved in actin binding. *Biochem J.* 269:61-64.
- Cunha-Ferreira, I., A. Chazeau, R.R. Buijs, R. Stucchi, L. Will, X. Pan, Y. Adolfs, C. van der Meer, J.C. Wolthuis, O.I. Kahn, P. Schatzle, M. Altelaar, R.J. Pasterkamp, L.C. Kapitein, and C.C. Hoogenraad. 2018. The HAUS Complex Is a Key Regulator of Non-centrosomal Microtubule Organization during Neuronal Development. *Cell Rep.* 24:791-800.
- Dacheux, D., N. Landrein, M. Thonnus, G. Gilbert, A. Sahin, H. Wodrich, D.R. Robinson, and M. Bonhivers. 2012. A MAP6-related protein is present in protozoa and is involved in flagellum motility. *PLoS One.* 7:e31344.
- Dacheux, D., B. Roger, C. Bosc, N. Landrein, E. Roche, L. Chansel, T. Trian, A. Andrieux, A. Papaxanthos-Roche, R. Marthan, D.R. Robinson, and M. Bonhivers. 2015. Human FAM154A (SAXO1) is a microtubule-stabilizing protein specific to cilia and related structures. *J Cell Sci.* 128:1294-1307.
- Daoust, A., S. Bohic, Y. Saoudi, C. Debacker, S. Gory-Faure, A. Andrieux, E.L. Barbier, and J.C. Deloulme. 2014. Neuronal transport defects of the MAP6 KO mouse - a model of schizophrenia - and alleviation by Epothilone D treatment, as observed using MEMRI. *Neuroimage.* 96:133-142.
- De La Cruz, E.M., and M.L. Gardel. 2015. Actin Mechanics and Fragmentation. *J Biol Chem.* 290:17137-17144.
- Deloulme, J.C., S. Gory-Faure, F. Mauconduit, S. Chauvet, J. Jonckheere, B. Boulan, E. Mire, J. Xue, M. Jany, C. Maucler, A.A. Deparis, O. Montigon, A. Daoust, E.L. Barbier, C. Bosc, N. Deglon, J. Brocard, E. Denarier, I. Le Brun, K. Pernet-Gallay, I. Vilgrain, P.J. Robinson, H. Lahrech, F. Mann, and A. Andrieux. 2015. Microtubule-associated protein 6 mediates neuronal connectivity through Semaphorin 3E-dependent signalling for axonal growth. *Nat Commun.* 6:7246.
- Denarier, E., M. Aguezoul, C. Jolly, C. Vourc'h, A. Roure, A. Andrieux, C. Bosc, and D. Job. 1998a. Genomic structure and chromosomal mapping of the mouse STOP gene (Mtap6). *Biochem Biophys Res Commun.* 243:791-796.
- Denarier, E., A. Fourest-Lieuvin, C. Bosc, F. Pirollet, A. Chapel, R.L. Margolis, and D. Job. 1998b. Nonneuronal isoforms of STOP protein are responsible for microtubule cold stability in mammalian fibroblasts. *Proc Natl Acad Sci U S A.* 95:6055-6060.
- Dent, E.W. 2017. Of microtubules and memory: implications for microtubule dynamics in dendrites and spines. *Mol Biol Cell.* 28:1-8.
- Dent, E.W., and K. Kalil. 2001. Axon branching requires interactions between dynamic microtubules and actin filaments. *J Neurosci.* 21:9757-9769.
- Desai, A., and T.J. Mitchison. 1997. Microtubule polymerization dynamics. *Annu Rev Cell Dev Biol.* 13:83-117.
- Divinski, I., L. Mittelman, and I. Gozes. 2004. A femtomolar acting octapeptide interacts with tubulin and protects astrocytes against zinc intoxication. *J Biol Chem.* 279:28531-28538.
- Dogterom, M., and G.H. Koenderink. 2019. Actin-microtubule crosstalk in cell biology. *Nat Rev Mol Cell Biol.* 20:38-54.

- Dominguez, R. 2016. The WH2 Domain and Actin Nucleation: Necessary but Insufficient. *Trends Biochem Sci.* 41:478-490.
- Eastwood, S.L., L. Lyon, L. George, A. Andrieux, D. Job, and P.J. Harrison. 2007. Altered expression of synaptic protein mRNAs in STOP (MAP6) mutant mice. *J Psychopharmacol.* 21:635-644.
- Efimova, N., C. Yang, J.X. Chia, N. Li, C.J. Lengner, K.L. Neufeld, and T.M. Svitkina. 2020. Branched actin networks are assembled on microtubules by adenomatous polyposis coli for targeted membrane protrusion. *J Cell Biol.* 219.
- Elie, A., E. Prezel, C. Guerin, E. Denarier, S. Ramirez-Rios, L. Serre, A. Andrieux, A. Fourest-Lieuvin, L. Blanchoin, and I. Arnal. 2015. Tau co-organizes dynamic microtubule and actin networks. *Sci Rep.* 5:9964.
- Foster, H.E., C. Ventura Santos, and A.P. Carter. 2022. A cryo-ET survey of microtubules and intracellular compartments in mammalian axons. *J Cell Biol.* 221.
- Fournet, V., G. de Lavilleon, A. Schweitzer, B. Giros, A. Andrieux, and M.P. Martres. 2012a. Both chronic treatments by epothilone D and fluoxetine increase the short-term memory and differentially alter the mood status of STOP/MAP6 KO mice. *J Neurochem.* 123:982-996.
- Fournet, V., M. Jany, V. Fabre, F. Chali, D. Orsal, A. Schweitzer, A. Andrieux, F. Messanvi, B. Giros, M. Hamon, L. Lanfumey, J.C. Deloulme, and M.P. Martres. 2010. The deletion of the microtubule-associated STOP protein affects the serotonergic mouse brain network. *J Neurochem.* 115:1579-1594.
- Fournet, V., A. Schweitzer, C. Chevarin, J.C. Deloulme, M. Hamon, B. Giros, A. Andrieux, and M.P. Martres. 2012b. The deletion of STOP/MAP6 protein in mice triggers highly altered mood and impaired cognitive performances. *J Neurochem.* 121:99-114.
- Fradley, R.L., G.F. O'Meara, R.J. Newman, A. Andrieux, D. Job, and D.S. Reynolds. 2005. STOP knockout and NMDA NR1 hypomorphic mice exhibit deficits in sensorimotor gating. *Behav Brain Res.* 163:257-264.
- Fygenson, D.K., E. Braun, and A. Libchaber. 1994. Phase diagram of microtubules. *Phys Rev E Stat Phys Plasmas Fluids Relat Interdiscip Topics.* 50:1579-1588.
- Gaillard, J., V. Ramabhadran, E. Neumann, P. Gurel, L. Blanchoin, M. Vantard, and H.N. Higgs. 2011. Differential interactions of the formins INF2, mDia1, and mDia2 with microtubules. *Mol Biol Cell.* 22:4575-4587.
- Galiano, M.R., C. Bosc, A. Schweitzer, A. Andrieux, D. Job, and M.E. Hallak. 2004. Astrocytes and oligodendrocytes express different STOP protein isoforms. *J Neurosci Res.* 78:329-337.
- Gallop, J.L. 2020. Filopodia and their links with membrane traffic and cell adhesion. *Semin Cell Dev Biol.* 102:81-89.
- Garvalov, B.K., B. Zuber, C. Bouchet-Marquis, M. Kudryashev, M. Gruska, M. Beck, A. Leis, F. Frischknecht, F. Bradke, W. Baumeister, J. Dubochet, and M. Cyrklaff. 2006. Luminal particles within cellular microtubules. *J Cell Biol.* 174:759-765.
- Gautreau, A.M., F.E. Fregoso, G. Simanov, and R. Dominguez. 2021. Nucleation, stabilization, and disassembly of branched actin networks. *Trends Cell Biol.*
- Geiser, F. 1988. Reduction of metabolism during hibernation and daily torpor in mammals and birds: temperature effect or physiological inhibition? *J Comp Physiol B.* 158:25-37.
- Goode, B.L., and M.J. Eck. 2007. Mechanism and function of formins in the control of actin assembly. *Annu Rev Biochem.* 76:593-627.
- Goodson, H.V., and E.M. Jonasson. 2018. Microtubules and Microtubule-Associated Proteins. *Cold Spring Harb Perspect Biol.* 10.
- Goodwin, S.S., and R.D. Vale. 2010. Patronin regulates the microtubule network by protecting microtubule minus ends. *Cell.* 143:263-274.
- Gory-Faure, S., V. Windscheid, C. Bosc, L. Peris, D. Proietto, R. Franck, E. Denarier, D. Job, and A. Andrieux. 2006. STOP-like protein 21 is a novel member of the STOP family, revealing a Golgi localization of STOP proteins. *J Biol Chem.* 281:28387-28396.

- Gory-Faure, S., V. Windscheid, J. Brocard, S. Montessuit, R. Tsutsumi, E. Denarier, Y. Fukata, C. Bosc, J. Delaroché, N. Collomb, M. Fukata, J.C. Martinou, K. Pernet-Gallay, and A. Andrieux. 2014. Non-microtubular localizations of microtubule-associated protein 6 (MAP6). *PLoS One*. 9:e114905.
- Gozes, I. 2011. Microtubules, schizophrenia and cognitive behavior: preclinical development of davunetide (NAP) as a peptide-drug candidate. *Peptides*. 32:428-431.
- Gozes, I., and I. Divinski. 2007. NAP, a neuroprotective drug candidate in clinical trials, stimulates microtubule assembly in the living cell. *Curr Alzheimer Res*. 4:507-509.
- Gu, J., B.L. Firestein, and J.Q. Zheng. 2008. Microtubules in dendritic spine development. *J Neurosci*. 28:12120-12124.
- Guillaud, L., C. Bosc, A. Fourest-Lieuvain, E. Denarier, F. Pirollet, L. Lafanechère, and D. Job. 1998. STOP proteins are responsible for the high degree of microtubule stabilization observed in neuronal cells. *J Cell Biol*. 142:167-179.
- Hacohen-Kleiman, G., S. Sragovich, G. Karmon, A.Y.L. Gao, I. Grigg, M. Pasmanik-Chor, A. Le, V. Korenkova, R.A. McKinney, and I. Gozes. 2018. Activity-dependent neuroprotective protein deficiency models synaptic and developmental phenotypes of autism-like syndrome. *J Clin Invest*. 128:4956-4969.
- Harada, A., K. Oguchi, S. Okabe, J. Kuno, S. Terada, T. Ohshima, R. Sato-Yoshitake, Y. Takei, T. Noda, and N. Hirokawa. 1994. Altered microtubule organization in small-calibre axons of mice lacking tau protein. *Nature*. 369:488-491.
- Harterink, M., K. Vocking, X. Pan, E.M. Soriano Jerez, L. Slenders, A. Freal, R.P. Tas, W.J. van de Wetering, K. Timmer, J. Motshagen, S.F.B. van Beuningen, L.C. Kapitein, W.J.C. Geerts, J.A. Post, and C.C. Hoogenraad. 2019. TRIM46 Organizes Microtubule Fasciculation in the Axon Initial Segment. *J Neurosci*. 39:4864-4873.
- Heldmaier, G., S. Ortmann, and R. Elvert. 2004. Natural hypometabolism during hibernation and daily torpor in mammals. *Respir Physiol Neurobiol*. 141:317-329.
- Ichetovkin, I., W. Grant, and J. Condeelis. 2002. Cofilin produces newly polymerized actin filaments that are preferred for dendritic nucleation by the Arp2/3 complex. *Curr Biol*. 12:79-84.
- Ivashko-Pachima, Y., and I. Gozes. 2019. A Novel Microtubule-Tau Association Enhancer and Neuroprotective Drug Candidate: Ac-SKIP. *Front Cell Neurosci*. 13:435.
- Ivashko-Pachima, Y., M. Maor-Nof, and I. Gozes. 2019. NAP (davunetide) preferential interaction with dynamic 3-repeat Tau explains differential protection in selected tauopathies. *PLoS One*. 14:e0213666.
- Ivashko-Pachima, Y., C.L. Sayas, A. Malishkevich, and I. Gozes. 2017. ADNP/NAP dramatically increase microtubule end-binding protein-Tau interaction: a novel avenue for protection against tauopathy. *Mol Psychiatry*. 22:1335-1344.
- Jaworski, J., L.C. Kapitein, S.M. Gouveia, B.R. Dortland, P.S. Wulf, I. Grigoriev, P. Camera, S.A. Spangler, P. Di Stefano, J. Demmers, H. Krugers, P. Defilippi, A. Akhmanova, and C.C. Hoogenraad. 2009. Dynamic microtubules regulate dendritic spine morphology and synaptic plasticity. *Neuron*. 61:85-100.
- Job, D., E.H. Fischer, and R.L. Margolis. 1981. Rapid disassembly of cold-stable microtubules by calmodulin. *Proc Natl Acad Sci U S A*. 78:4679-4682.
- Job, D., C.T. Rauch, E.H. Fischer, and R.L. Margolis. 1982. Recycling of cold-stable microtubules: evidence that cold stability is due to substoichiometric polymer blocks. *Biochemistry*. 21:509-515.
- Kalil, K., and E.W. Dent. 2014. Branch management: mechanisms of axon branching in the developing vertebrate CNS. *Nat Rev Neurosci*. 15:7-18.
- Kapitein, L.C., and C.C. Hoogenraad. 2015. Building the Neuronal Microtubule Cytoskeleton. *Neuron*. 87:492-506.
- Ketschek, A., M. Spillane, X.P. Dun, H. Hardy, J. Chilton, and G. Gallo. 2016. Drebrin coordinates the actin and microtubule cytoskeleton during the initiation of axon collateral branches. *Dev Neurobiol*. 76:1092-1110.

- King, M.R., and S. Petry. 2020. Phase separation of TPX2 enhances and spatially coordinates microtubule nucleation. *Nat Commun.* 11:270.
- Kolman, A. 2004. BMS-310705 Bristol-Myers Squibb/GBF. *Curr Opin Investig Drugs.* 5:1292-1297.
- Kuo, Y.W., and J. Howard. 2021. Cutting, Amplifying, and Aligning Microtubules with Severing Enzymes. *Trends Cell Biol.* 31:50-61.
- Lee, J.C., and S.N. Timasheff. 1977. In vitro reconstitution of calf brain microtubules: effects of solution variables. *Biochemistry.* 16:1754-1764.
- Lieuvin, A., J.C. Labbe, M. Doree, and D. Job. 1994. Intrinsic microtubule stability in interphase cells. *J Cell Biol.* 124:985-996.
- Liu, H., J. Zheng, L. Zhu, L. Xie, Y. Chen, Y. Zhang, W. Zhang, Y. Yin, C. Peng, J. Zhou, X. Zhu, and X. Yan. 2021. Wdr47, Camsaps, and Katanin cooperate to generate ciliary central microtubules. *Nat Commun.* 12:5796.
- Liverman, A.D., H.C. Cheng, J.E. Trosky, D.W. Leung, M.L. Yarbrough, D.L. Burdette, M.K. Rosen, and K. Orth. 2007. Arp2/3-independent assembly of actin by Vibrio type III effector VopL. *Proc Natl Acad Sci U S A.* 104:17117-17122.
- Loreng, T.D., and E.F. Smith. 2017. The Central Apparatus of Cilia and Eukaryotic Flagella. *Cold Spring Harb Perspect Biol.* 9.
- Ma, M., M. Stoyanova, G. Rademacher, S.K. Dutcher, A. Brown, and R. Zhang. 2019. Structure of the Decorated Ciliary Doublet Microtubule. *Cell.* 179:909-922 e912.
- Margolis, R.L., and C.T. Rauch. 1981. Characterization of rat brain crude extract microtubule assembly: correlation of cold stability with the phosphorylation state of a microtubule-associated 64K protein. *Biochemistry.* 20:4451-4458.
- Martins-de-Souza, D., W.F. Gattaz, A. Schmitt, C. Rewerts, G. Maccarrone, E. Dias-Neto, and C.W. Turck. 2009. Prefrontal cortex shotgun proteome analysis reveals altered calcium homeostasis and immune system imbalance in schizophrenia. *Eur Arch Psychiatry Clin Neurosci.* 259:151-163.
- Matsudaira, P. 1994. Actin crosslinking proteins at the leading edge. *Semin Cell Biol.* 5:165-174.
- McIntosh, J.R. 2016. Mitosis. *Cold Spring Harb Perspect Biol.* 8.
- Merenlender-Wagner, A., R. Pikman, E. Giladi, A. Andrieux, and I. Gozes. 2010. NAP (davunetide) enhances cognitive behavior in the STOP heterozygous mouse--a microtubule-deficient model of schizophrenia. *Peptides.* 31:1368-1373.
- Merriam, E.B., M. Millette, D.C. Lumbard, W. Saengsawang, T. Fothergill, X. Hu, L. Ferhat, and E.W. Dent. 2013. Synaptic regulation of microtubule dynamics in dendritic spines by calcium, F-actin, and drebrin. *J Neurosci.* 33:16471-16482.
- Mitchison, T., and M. Kirschner. 1984. Dynamic instability of microtubule growth. *Nature.* 312:237-242.
- Mitchison, T.J., and L.P. Cramer. 1996. Actin-based cell motility and cell locomotion. *Cell.* 84:371-379.
- Modig, C., M. Wallin, and P.E. Olsson. 2000. Expression of cold-adapted beta-tubulins confer cold-tolerance to human cellular microtubules. *Biochem Biophys Res Commun.* 269:787-791.
- Mogilner, A., and B. Rubinstein. 2005. The physics of filopodial protrusion. *Biophys J.* 89:782-795.
- Nabi, D., H. Drechsler, J. Pschirer, F. Korn, N. Schuler, S. Diez, R. Jessberger, and M. Chacon. 2021. CENP-V is required for proper chromosome segregation through interaction with spindle microtubules in mouse oocytes. *Nat Commun.* 12:6547.
- Neukirchen, D., and F. Bradke. 2011. Cytoplasmic linker proteins regulate neuronal polarization through microtubule and growth cone dynamics. *J Neurosci.* 31:1528-1538.
- Olmsted, J.B., and G.G. Borisy. 1975. Ionic and nucleotide requirements for microtubule polymerization in vitro. *Biochemistry.* 14:2996-3005.
- Ori-McKenney, K.M., L.Y. Jan, and Y.N. Jan. 2012. Golgi outposts shape dendrite morphology by functioning as sites of acentrosomal microtubule nucleation in neurons. *Neuron.* 76:921-930.
- Oz, S., O. Kapitansky, Y. Ivashco-Pachima, A. Malishkevich, E. Giladi, N. Skalka, R. Rosin-Arbesfeld, L. Mittelman, O. Segev, J.A. Hirsch, and I. Gozes. 2014. The NAP motif of activity-dependent

- neuroprotective protein (ADNP) regulates dendritic spines through microtubule end binding proteins. *Mol Psychiatry*. 19:1115-1124.
- Pabion, M., D. Job, and R.L. Margolis. 1984. Sliding of STOP proteins on microtubules. *Biochemistry*. 23:6642-6648.
- Pacheco, A., and G. Gallo. 2016. Actin filament-microtubule interactions in axon initiation and branching. *Brain Res Bull*. 126:300-310.
- Papalazarou, V., and L.M. Machesky. 2021. The cell pushes back: The Arp2/3 complex is a key orchestrator of cellular responses to environmental forces. *Curr Opin Cell Biol*. 68:37-44.
- Paul, A.S., and T.D. Pollard. 2009. Review of the mechanism of processive actin filament elongation by formins. *Cell Motil Cytoskeleton*. 66:606-617.
- Peris, L., M. Bisbal, J. Martinez-Hernandez, Y. Saoudi, J. Jonckheere, M. Rolland, M. Sebastien, J. Brocard, E. Denarier, C. Bosc, C. Guerin, S. Gory-Faure, J.C. Deloulme, F. Lante, I. Arnal, A. Buisson, Y. Goldberg, L. Blanchoin, C. Delphin, and A. Andrieux. 2018. A key function for microtubule-associated-protein 6 in activity-dependent stabilisation of actin filaments in dendritic spines. *Nat Commun*. 9:3775.
- Petry, S., A.C. Groen, K. Ishihara, T.J. Mitchison, and R.D. Vale. 2013. Branching microtubule nucleation in *Xenopus* egg extracts mediated by augmin and TPX2. *Cell*. 152:768-777.
- Pierson, G.B., P.R. Burton, and R.H. Himes. 1978. Alterations in number of protofilaments in microtubules assembled in vitro. *J Cell Biol*. 76:223-228.
- Pirollet, F., J. Derancourt, J. Haiech, D. Job, and R.L. Margolis. 1992a. Ca(2+)-calmodulin regulated effectors of microtubule stability in bovine brain. *Biochemistry*. 31:8849-8855.
- Pirollet, F., D. Job, E.H. Fischer, and R.L. Margolis. 1983. Purification and characterization of sheep brain cold-stable microtubules. *Proc Natl Acad Sci U S A*. 80:1560-1564.
- Pirollet, F., R.L. Margolis, and D. Job. 1992b. Ca(2+)-calmodulin regulated effectors of microtubule stability in neuronal tissues. *Biochim Biophys Acta*. 1160:113-119.
- Pollard, T.D. 2016. Actin and Actin-Binding Proteins. *Cold Spring Harb Perspect Biol*. 8.
- Pollard, T.D., and J.A. Cooper. 2009. Actin, a central player in cell shape and movement. *Science*. 326:1208-1212.
- Powell, K.J., S.E. Hori, R. Leslie, A. Andrieux, H. Schellinck, M. Thorne, and G.S. Robertson. 2007. Cognitive impairments in the STOP null mouse model of schizophrenia. *Behav Neurosci*. 121:826-835.
- Pring, M., M. Evangelista, C. Boone, C. Yang, and S.H. Zigmond. 2003. Mechanism of formin-induced nucleation of actin filaments. *Biochemistry*. 42:486-496.
- Profitt, M.F., S. Deurveilher, G.S. Robertson, B. Rusak, and K. Semba. 2016. Disruptions of Sleep/Wake Patterns in the Stable Tubule Only Polypeptide (STOP) Null Mouse Model of Schizophrenia. *Schizophr Bull*. 42:1207-1215.
- Quinlan, M.E., J.E. Heuser, E. Kerkhoff, and R.D. Mullins. 2005. Drosophila Spire is an actin nucleation factor. *Nature*. 433:382-388.
- Razinia, Z., T. Makela, J. Ylanne, and D.A. Calderwood. 2012. Filamins in mechanosensing and signaling. *Annu Rev Biophys*. 41:227-246.
- Regula, C.S., J.R. Pfeiffer, and R.D. Berlin. 1981. Microtubule assembly and disassembly at alkaline pH. *J Cell Biol*. 89:45-53.
- Rodriguez, O.C., A.W. Schaefer, C.A. Mandato, P. Forscher, W.M. Bement, and C.M. Waterman-Storer. 2003. Conserved microtubule-actin interactions in cell movement and morphogenesis. *Nat Cell Biol*. 5:599-609.
- Sanchez-Huertas, C., F. Freixo, R. Viais, C. Lacasa, E. Soriano, and J. Luders. 2016. Non-centrosomal nucleation mediated by augmin organizes microtubules in post-mitotic neurons and controls axonal microtubule polarity. *Nat Commun*. 7:12187.
- Satake, T., K. Yamashita, K. Hayashi, S. Miyatake, M. Tamura-Nakano, H. Doi, Y. Furuta, G. Shioi, E. Miura, Y.H. Takeo, K. Yoshida, H. Yahikozawa, N. Matsumoto, M. Yuzaki, and A. Suzuki. 2017. MTCL1 plays an essential role in maintaining Purkinje neuron axon initial segment. *EMBO J*. 36:1227-1242.

- Shimizu, H., Y. Iwayama, K. Yamada, T. Toyota, Y. Minabe, K. Nakamura, M. Nakajima, E. Hattori, N. Mori, N. Osumi, and T. Yoshikawa. 2006. Genetic and expression analyses of the STOP (MAP6) gene in schizophrenia. *Schizophr Res.* 84:244-252.
- Stephan, R., B. Goellner, E. Moreno, C.A. Frank, T. Hugenschmidt, C. Genoud, H. Aberle, and J. Pielage. 2015. Hierarchical microtubule organization controls axon caliber and transport and determines synaptic structure and stability. *Dev Cell.* 33:5-21.
- Suozi, K.C., X. Wu, and E. Fuchs. 2012. Spectraplakins: master orchestrators of cytoskeletal dynamics. *J Cell Biol.* 197:465-475.
- Svitkina, T. 2018. The Actin Cytoskeleton and Actin-Based Motility. *Cold Spring Harb Perspect Biol.* 10.
- Svitkina, T.M. 2020. Actin Cell Cortex: Structure and Molecular Organization. *Trends Cell Biol.* 30:556-565.
- Sweeney, H.L., and E.L.F. Holzbaur. 2018. Motor Proteins. *Cold Spring Harb Perspect Biol.* 10.
- Swiech, L., M. Blazejczyk, M. Urbanska, P. Pietruszka, B.R. Dortland, A.R. Malik, P.S. Wulf, C.C. Hoogenraad, and J. Jaworski. 2011. CLIP-170 and IQGAP1 cooperatively regulate dendrite morphology. *J Neurosci.* 31:4555-4568.
- Tam, V.C., D. Serruto, M. Dziejman, W. Briehner, and J.J. Mekalanos. 2007. A type III secretion system in *Vibrio cholerae* translocates a formin/spire hybrid-like actin nucleator to promote intestinal colonization. *Cell Host Microbe.* 1:95-107.
- Tortosa, E., Y. Adolfs, M. Fukata, R.J. Pasterkamp, L.C. Kapitein, and C.C. Hoogenraad. 2017. Dynamic Palmitoylation Targets MAP6 to the Axon to Promote Microtubule Stabilization during Neuronal Polarization. *Neuron.* 94:809-825 e807.
- Valencia, D.A., and M.E. Quinlan. 2021. Formins. *Curr Biol.* 31:R517-R522.
- Van Dijck, A., A.T. Vulto-van Silfhout, E. Cappuyns, I.M. van der Werf, G.M. Mancini, A. Tzschach, R. Bernier, I. Gozes, E.E. Eichler, C. Romano, A. Lindstrand, A. Nordgren, A. Consortium, M. Kvarnung, T. Kleefstra, B.B.A. de Vries, S. Kury, J.A. Rosenfeld, M.E. Meuwissen, G. Vandeweyer, and R.F. Kooy. 2019. Clinical Presentation of a Complex Neurodevelopmental Disorder Caused by Mutations in ADNP. *Biol Psychiatry.* 85:287-297.
- Volle, J., J. Brocard, M. Saoud, S. Gory-Faure, J. Brunelin, A. Andrieux, and M.F. Suaud-Chagny. 2013. Reduced expression of STOP/MAP6 in mice leads to cognitive deficits. *Schizophr Bull.* 39:969-978.
- Walczak, C.E., S. Gayek, and R. Ohi. 2013. Microtubule-depolymerizing kinesins. *Annu Rev Cell Dev Biol.* 29:417-441.
- Walczak, C.E., and S.L. Shaw. 2010. A MAP for bundling microtubules. *Cell.* 142:364-367.
- Weber, K.L., A.M. Sokac, J.S. Berg, R.E. Cheney, and W.M. Bement. 2004. A microtubule-binding myosin required for nuclear anchoring and spindle assembly. *Nature.* 431:325-329.
- Wei, H., S. Sun, Y. Li, and S. Yu. 2016. Reduced plasma levels of microtubule-associated STOP/MAP6 protein in autistic patients. *Psychiatry Res.* 245:116-118.
- Xiao, B., H. Xu, H. Ye, Q. Hu, Y. Chen, and W. Qiu. 2015. De novo 11q13.4q14.3 tetrasomy with uniparental isodisomy for 11q14.3qter. *Am J Med Genet A.* 167A:2327-2333.
- Zahm, J.A., S.B. Padrick, Z. Chen, C.W. Pak, A.A. Yunus, L. Henry, D.R. Tomchick, Z. Chen, and M.K. Rosen. 2013. The bacterial effector VopL organizes actin into filament-like structures. *Cell.* 155:423-434.

5. ANNEXE

Ci-après figure une sélection de mes publications.

- Page 44 **Cuveillier C**, Boulan B, Ravello C, Denarier E, Deloulme J-C, Gory-Fauré S, **Delphin C**, Bosc C, Arnal I and Andrieux A (2021) Beyond Neuronal Microtubule Stabilization: MAP6 and CRMPs, Two Converging Stories. **Front. Mol. Neurosci.** 2021, 14:665693.
- Page 64 **Cuveillier C**, Saoudi Y, Arnal I, **Delphin C**. Imaging Microtubules *in vitro* at High Resolution while Preserving their Structure. **Bio Protoc.** 2021 Apr 5;11:e3968.
- Page 78 **Cuveillier C**, Delaroche J, **Seggio M**, Gory-Fauré S, Bosc C, Denarier E, Bacia M, Schoehn G, Mohrbach H, Kulić I, Andrieux A, Arnal I, **Delphin C**. MAP6 is an intraluminal protein that induces neuronal microtubules to coil. **Science Advances** 2020, 6: eaaz4344
- Page 89 Peris L, Bisbal M, Martinez-Hernandez J, Saoudi Y, Jonckheere J, Rolland M, Sebastien M, Brocard J, Denarier E, Bosc C, Guerin C, Gory-Fauré S, Deloulme JC, Lanté F, Arnal I, Buisson A, Goldberg Y, Blanchoin L, **Delphin C**, Andrieux A. A key function for microtubule-associated-protein 6 in activity-dependent stabilisation of actin filaments in dendritic spines. **Nat Commun.** 2018, 9:3775.
- Page 104 Aillaud C, Bosc C, Peris L, Bosson A, Heemeryck P, Van Dijk J, Le Fric J, Boulan B, Vossier F, Sanman LE, Syed S, Amara N, Couté Y, Lafanechère L, Denarier E, **Delphin C**, Pelletier L, Humbert S, Bogyo M, Andrieux A, Rogowski K, Moutin MJ. Vasohibins/SVBP are tubulin carboxypeptidases (TCPs) that regulate neuron differentiation. **Science.** 2017, 358:1448-1453.
- Page 110 **Delphin C**, Bouvier D, **Seggio M**, Couriol E, Saoudi Y, Denarier E, Bosc C, Valiron O, Bisbal M, Arnal I, Andrieux A. MAP6-F is a temperature sensor that directly binds to and protects microtubules from cold-induced depolymerization. **J Biol Chem.** 2012, 287:35127-38.
- Page 122 **De Seranno S**, Benaud C, Assard N, **Khediri S**, Gerke V, Baudier J, **Delphin C**. Identification of an AHNAK binding motif specific for the Annexin2/S100A10 tetramer. **J Biol Chem.** 2006, 281:35030-8.
- Page 131 **Gentil BJ**, Benaud C, **Delphin C**, Remy C, Berezowski V, Cecchelli R, Feraud O, Vittet D, Baudier J. Specific AHNAK expression in brain endothelial cells with barrier properties. **J Cell Physiol.** 2005, 203:362-71.
- Page 141 Benaud C, **Gentil BJ**, Assard N, Court M, Garin J, **Delphin C**, Baudier J. AHNAK interaction with the annexin 2/S100A10 complex regulates cell membrane cytoarchitecture. **J Cell Biol.** 2004, 164:133-44.
- Page 153 **Gentil BJ**, **Delphin C**, Benaud C, Baudier J. Expression of the giant protein AHNAK (desmoyokin) in muscle and lining epithelial cells. **J Histochem Cytochem.** 2003, 51:339-48.

- Page 163 Mbele GO, Deloulme JC, **Gentil BJ, Delphin C**, Ferro M, Garin J, Takahashi M, Baudier J. The zinc- and calcium-binding S100B interacts and co-localizes with IQGAP1 during dynamic rearrangement of cell membranes. **J Biol Chem.** 2002, 277:49998-50007.
- Page 173 **Gentil BJ, Delphin C**, Mbele GO, Deloulme JC, Ferro M, Garin J, Baudier J. The giant protein AHNAK is a specific target for the calcium- and zinc-binding S100B protein: potential implications for Ca²⁺ homeostasis regulation by S100B. **J Biol Chem.** 2001, 276:23253-61.
- Page 182 **Delphin C**, Ronjat M, Deloulme JC, Garin G, Debussche L, Higashimoto Y, Sakaguchi K, Baudier J. Calcium-dependent interaction of S100B with the C-terminal domain of the tumor suppressor p53. **J Biol Chem.** 1999, 274:10539-44.
- Page 188 Scotto C, **Delphin C**, Deloulme JC, Baudier J. Concerted regulation of wild-type p53 nuclear accumulation and activation by S100B and calcium-dependent protein kinase C. **Mol Cell Biol.** 1999, 19:7168-80.
- Page 201 Mahajan R, **Delphin C**, Guan T, Gerace L, Melchior F. A small ubiquitin-related polypeptide involved in targeting RanGAP1 to nuclear pore complex protein RanBP2. **Cell.** 1997, 88:97-107.
- Page 212 **Delphin C**, Guan T, Melchior F, Gerace L. RanGTP targets p97 to RanBP2, a filamentous protein localized at the cytoplasmic periphery of the nuclear pore complex. **Mol Biol Cell.** 1997, 8:2379-90.
- Page 224 Paschal BM, **Delphin C**, Gerace L. Nucleotide-specific interaction of Ran/TC4 with nuclear transport factors NTF2 and p97. **Proc Natl Acad Sci U S A.** 1996, 93:7679-83.



Beyond Neuronal Microtubule Stabilization: MAP6 and CRMPs, Two Converging Stories

Camille Cuveillier, Benoit Boulan, Charlotte Ravanello, Eric Denarier, Jean-Christophe Deloulme, Sylvie Gory-Fauré, Christian Delphin, Christophe Bosc, Isabelle Arnal* and Annie Andrieux*

Univ. Grenoble Alpes, Inserm U1216, CEA-IRIG, CNRS, Grenoble Institut Neurosciences, Grenoble, France

OPEN ACCESS

Edited by:

David Blum,
INSERM U1172 Centre de
Recherche Jean Pierre Aubert,
France

Reviewed by:

Christian Gonzalez-Billaud,
University of Chile, Chile
C Laura Sayas,
University of La Laguna, Spain

*Correspondence:

Annie Andrieux
annie.andrieux@univ-grenoble-
alpes.fr
Isabelle Arnal
isabelle.arnal@univ-grenoble-alpes.fr

Specialty section:

This article was submitted to
Molecular Signalling and Pathways,
a section of the journal
Frontiers in Molecular Neuroscience

Received: 08 February 2021

Accepted: 09 April 2021

Published: 05 May 2021

Citation:

Cuveillier C, Boulan B, Ravanello C,
Denarier E, Deloulme J-C,
Gory-Fauré S, Delphin C, Bosc C,
Arnal I and Andrieux A (2021) Beyond
Neuronal Microtubule Stabilization:
MAP6 and CRMPs, Two
Converging Stories.
Front. Mol. Neurosci. 14:665693.
doi: 10.3389/fnmol.2021.665693

The development and function of the central nervous system rely on the microtubule (MT) and actin cytoskeletons and their respective effectors. Although the structural role of the cytoskeleton has long been acknowledged in neuronal morphology and activity, it was recently recognized to play the role of a signaling platform. Following this recognition, research into Microtubule Associated Proteins (MAPs) diversified. Indeed, historically, structural MAPs—including MAP1B, MAP2, Tau, and MAP6 (also known as STOP);—were identified and described as MT-binding and -stabilizing proteins. Extensive data obtained over the last 20 years indicated that these structural MAPs could also contribute to a variety of other molecular roles. Among multi-role MAPs, MAP6 provides a striking example illustrating the diverse molecular and cellular properties of MAPs and showing how their functional versatility contributes to the central nervous system. In this review, in addition to MAP6's effect on microtubules, we describe its impact on the actin cytoskeleton, on neuroreceptor homeostasis, and its involvement in signaling pathways governing neuron development and maturation. We also discuss its roles in synaptic plasticity, brain connectivity, and cognitive abilities, as well as the potential relationships between the integrated brain functions of MAP6 and its molecular activities. In parallel, the Collapsin Response Mediator Proteins (CRMPs) are presented as examples of how other proteins, not initially identified as MAPs, fall into the broader MAP family. These proteins bind MTs as well as exhibiting molecular and cellular properties very similar to MAP6. Finally, we briefly summarize the multiple similarities between other classical structural MAPs and MAP6 or CRMPs. In summary, this review revisits the molecular properties and the cellular and neuronal roles of the classical MAPs, broadening our definition of what constitutes a MAP.

Keywords: microtubule, microtubule-associated-proteins, actin, neuron, synapse, psychiatric disease, cognition

INTRODUCTION

Microtubule-Associated Proteins (MAPs) were discovered in the context of the study of microtubule (MT) stability in neurons during the 1970s (Weingarten et al., 1975; Sloboda et al., 1976). Indeed, in neurons, MTs composed of α - and β -tubulin heterodimers forming 25 nm wide hollow tubes can either exhibit dynamic properties with phases of

polymerization/depolymerization (Mitchison and Kirschner, 1984), or be particularly stable with a slow tubulin turnover (Okabe and Hirokawa, 1990; Li and Black, 1996). In testimony to their stability, neuronal MTs can resist conditions usually causing MT depolymerization, such as exposure to tubulin poison (nocodazole) or to cold temperatures (Webb and Wilson, 1980; Brady et al., 1984; Baas and Black, 1990). The search for the neuronal effectors leading to this stability has long been a focus of research. Various factors were shown to modulate neuronal MT stability, including: (1) the nature of tubulin isoforms, (2) post-translational tubulin modifications, and (3) binding of MAPs (Baas et al., 2016).

The nature of tubulin isoforms was clearly demonstrated in mice, where α and β tubulin are each coded by eight genes (Findeisen et al., 2014; Hausrat et al., 2020). The different isoforms combine to produce MTs with distinct dynamic parameters. For example, the β III/ β II tubulin MT isoform displays antagonist effects on dynamicity/stability (Panda et al., 1994; Pamula et al., 2016; Vemu et al., 2016; Ti et al., 2018).

Post-translational modifications of tubulin—including tyrosination, polyamination, polyglutamylation, and acetylation—were shown to modulate MT stability by altering their dynamic properties (Moutin et al., 2020), resistance to cold exposure (Song et al., 2013), sensitivity to severing enzymes (Lacroix et al., 2010; Valenstein and Roll-Mecak, 2016), and flexibility (Portran et al., 2017; Xu et al., 2017). Finally, the so-called structural MAPs which bind throughout the MT lattice also influence MT stabilization. As indicated above, these structural MAPs were first discovered in the 1970s, when they were found to be associated with purified brain tubulin preparations. The group includes MAP1, MAP2, MAP4, Tau, and MAP6 (also known as STOP; Cleveland et al., 1977; Herzog and Weber, 1978; Huber and Matus, 1984; Margolis et al., 1986; Job et al., 1987; Chapin and Bulinski, 1994). Other members were identified more recently: DCX, MAP7, and MAP9 (Gleeson et al., 1999; Yadav et al., 2014; Monroy et al., 2020).

Since the initial discovery of these MAPs based on their ability to bind and stabilize MTs, studies have increasingly pointed toward a wide array of other cellular functions (Dehmelt and Halpain, 2005; Morris et al., 2011; Dent and Baas, 2014; Bodakuntla et al., 2019). Thus, structural MAPs have been shown to: regulate actin cytoskeleton dynamics; be amenable to post-translational modifications which target them to membrane compartments; interact with a huge number of partners which are then involved in neuroreceptor homeostasis and signaling cascades. These additional abilities stem from molecular features including actin-binding domains, stretches of cysteine residues for palmitoylation-driven membrane association, and Proline-Rich-Domain (PRDs) to mediate binding to SH3-containing signaling proteins.

In this review, we will present results obtained over almost 40 years of research on MAP6 proteins to illustrate the wide range of MT-dependent and -independent molecular properties that MAPs can exhibit. Using the Collapsin Response Mediator Proteins (CRMPs) as an example, we will show how other proteins not initially identified as MAPs also fulfill molecular and cellular functions initially attributed to the classical

structural MAPs. We will also discuss the multiple cellular and physiological roles of MAPs in neurons and in the central nervous system. The review will, in particular, illustrate the crucial implication of MAPs in neuronal plasticity and cognition in accordance with their dysfunctions in neuropsychiatric diseases. Overall, we aim at demonstrating that the initial definition of classical MAPs (i.e., MT binding and stabilization) should now encompass the MT-dependent and -independent functions of these proteins.

MAP6 PROTEIN IS A MULTI-FUNCTIONAL PROTEIN

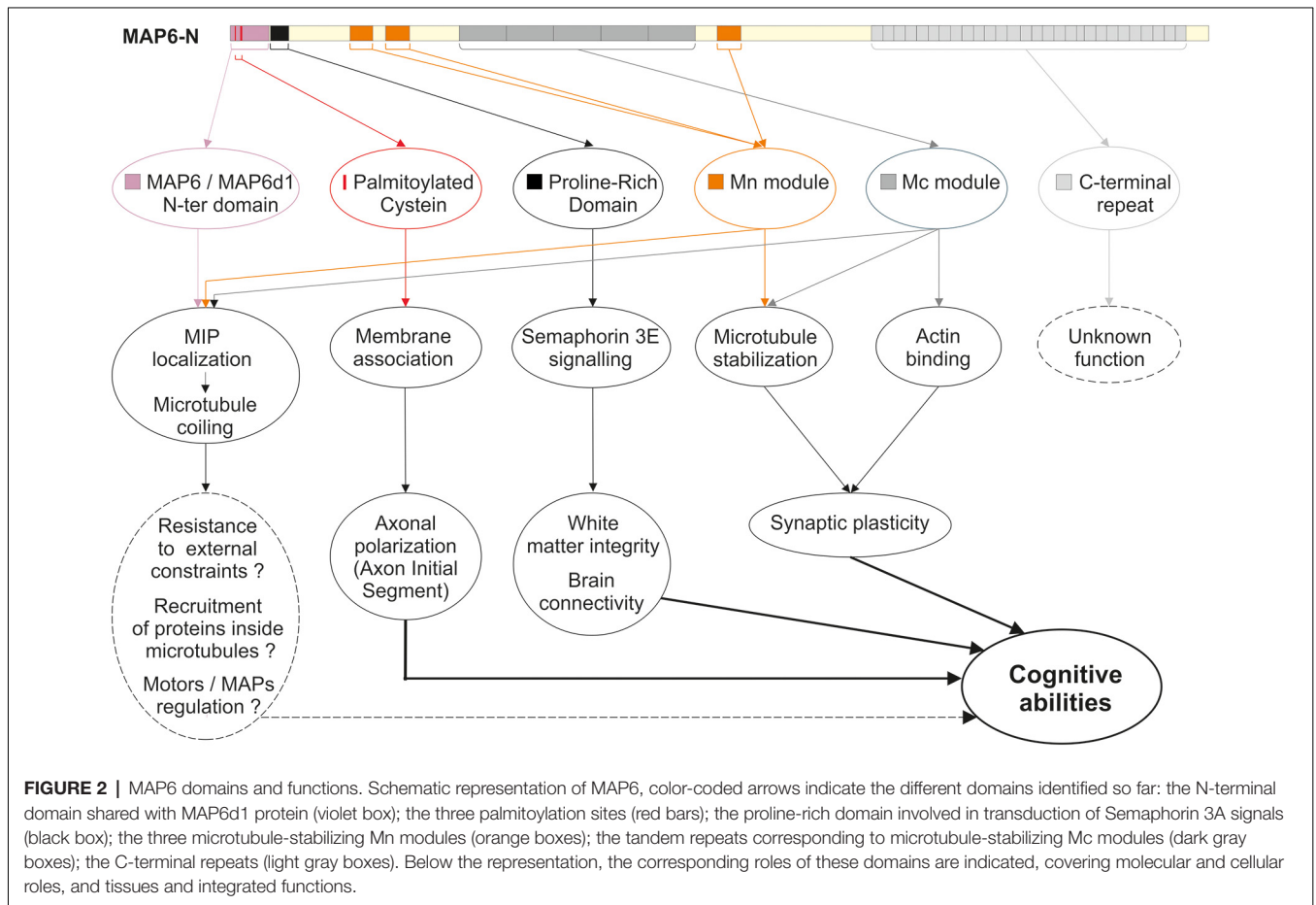
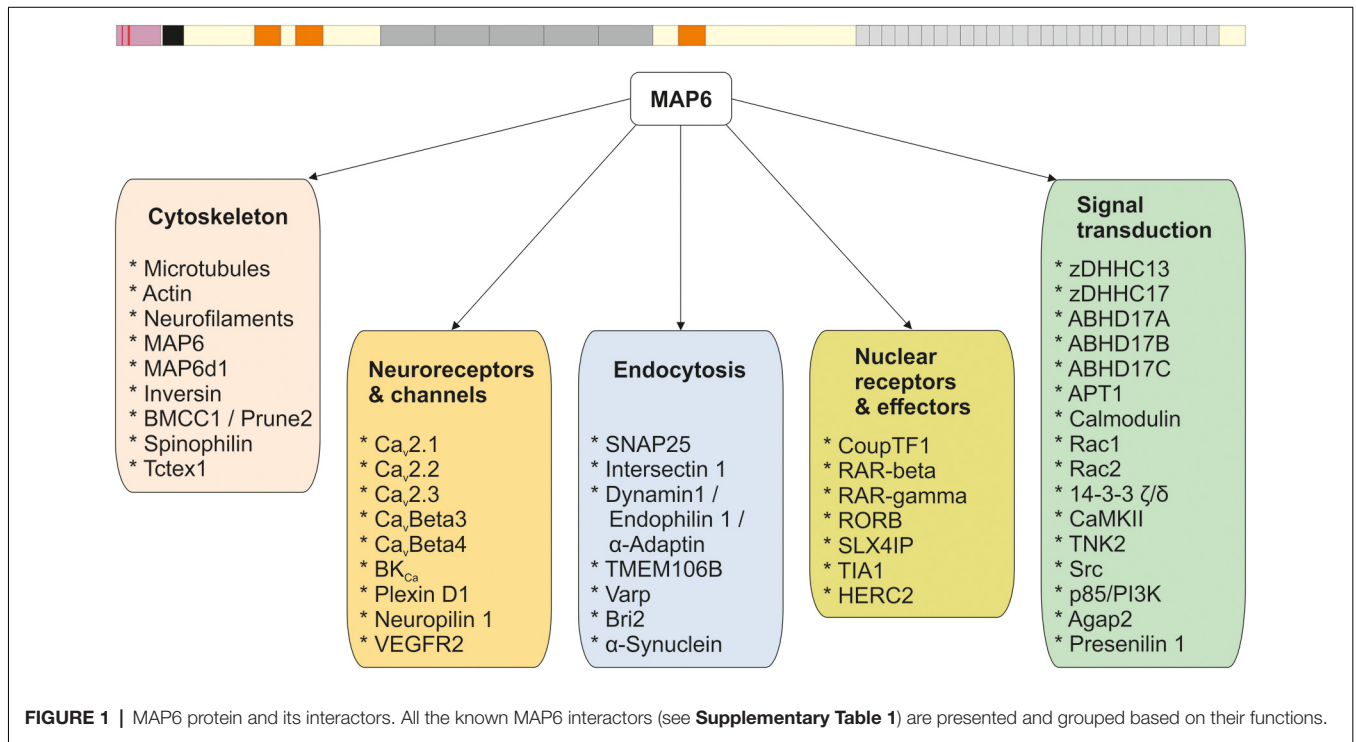
Like the other structural MAPs, MAP6 protein was initially identified thanks to its ability to interact with tubulin/MTs. Subsequent studies identified a large number of MAP6 partners related to various cellular functions including neuroreceptor homeostasis, endocytosis, nuclear function, and signaling pathways. The different partners are summarized in **Figure 1**, and further details are provided in **Supplementary Table 1**. In the following sections, the contribution of each MAP6 sub-domain to its molecular, cellular, and physiological functions are detailed. A summary of MAP6 domains and their roles is presented in **Figure 2**.

MAP6 Binds and Stabilizes Microtubules Discovery of MAP6 as a Microtubule (MT)-Associated Protein

The exceptional stability of brain-extracted MTs when exposed to cold was first described almost half a century ago (Brinkley and Cartwright, 1975; Lee et al., 1975; Webb and Wilson, 1980). Subsequent work led to the identification of several polypeptides that co-purify with cold-stable MTs (Job et al., 1981, 1982; Margolis and Rauch, 1981; Pabion et al., 1984) and are retained on calmodulin-affinity columns (Job et al., 1982; Pirollet et al., 1983). The unique ability of these polypeptides to confer cold stability on MTs led Job and collaborators to call them STOP proteins, for Stable-Tubule-Only Polypeptides (they were later renamed MAP6 proteins). The MT stabilization properties of MAP6 are Ca^{2+} -calmodulin sensitive (Job et al., 1981; Pirollet et al., 1983, 1992a,b) and the 145-kDa STOP isoform from the rat brain was shown to confer a super-stable state on MTs, in a dose-dependent manner (Job et al., 1987).

Molecular Cloning of MAP6 and Identification of MAP6 Isoforms

Bosc et al. (1996) first cloned MAP6 cDNA by immunoscreening of a DNA expression library with MAP6 monoclonal antibodies (Pirollet et al., 1989). These experiments provided clear identification of MAP6 and made further studies to gather specific information on the protein possible. MAP6 isoforms are restricted to vertebrates, where they are expressed in several tissues (Pirollet et al., 1989; Bosc et al., 2001). In mice, a single four-exon gene, *Map6* (formerly *Mtap6*), produces several isoforms of MAP6 proteins as a result of RNA splicing and the use of alternative promoters (Bosc et al., 1996; Denarier et al., 1998a; Aguezoul et al., 2003). Murine neurons express MAP6-E



(MAP6-Early, formerly E-STOP, apparent MW 79 kDa) from early developmental stages to adulthood at constant expression levels, whereas expression of the longest isoform MAP6-N (MAP6-Neuronal, formerly N-STOP, apparent MW 120 kDa) increases between birth and adulthood (up to 10-fold higher expression than MAP6-E in adults) (Guillaud et al., 1998; Galiano et al., 2004; Tortosa et al., 2017). These two variants can be found associated with MTs in neurons and stabilize neuronal MTs when exposed to cold or nocodazole (Pirrollet et al., 1989; Margolis et al., 1990; Bosc et al., 1996; Guillaud et al., 1998; Andrieux et al., 2002). Glial cells also express some MAP6 isoforms, with MAP6-O (apparent MW 89 kDa) found in oligodendrocytes, where they provide resistance to both cold and nocodazole. In contrast, astrocytes express MAP6-A (apparent MW 66 kDa), which only provides cold resistance (Galiano et al., 2004). Like MAP6-A, the ubiquitous MAP6-F isoform (apparent MW 42 kDa) provides only cold resistance (Denarier et al., 1998b).

Identification of MAP6 MT-Binding Domains and Their Role in MT Stabilization

The identification of 12 calmodulin-binding domains on MAP6-N revealed the existence of three domains that partially overlap some of the calmodulin-binding motifs. These three domains are known as Mn modules (Mn1–3, **Figure 2**) and stabilize MTs against both cold and nocodazole-induced depolymerization (Bosc et al., 2001). Mn1 and Mn2 modules were shown to reproduce the function of full-length MAP6-N with regard to MT stabilization, both *in vitro* and *in cellulo* (Bosc et al., 2001; Lefevre et al., 2013). Thus, these modules may stabilize MTs exposed to cold and nocodazole by forming bridges with adjacent tubulin heterodimers either between protofilaments, or longitudinally within the same protofilament (Lefevre et al., 2013).

In addition to its Mn modules, MAP6-N contains central repeats, or Mc modules, each of which encompass a calmodulin-binding domain (**Figure 2**). As indicated above, MAP6 proteins are found only in vertebrates, but Mc modules are further restricted. Thus, these domains have only been identified in mammals and are absent from MAP6 homologs expressed in fish, frogs, lizards or birds (Bosc et al., 2001, 2003). Among mammals, the number of Mc modules varies depending on the species and/or individual (4–6 in non-inbred rats, 3–6 in mice depending on the strain, and only 1 in higher primates) (Bosc et al., 2003). Mc modules have been shown to be responsible for conferring cold-stability of MTs in cells, even though they display no MT-binding capacity at physiological temperatures (Denarier et al., 1998b; Delphin et al., 2012). *In vitro* studies demonstrated that cold temperatures induce conformational changes in the Mc modules which allow them to interact with MTs (Delphin et al., 2012). Thus, Mc modules behave like cold sensors, stabilizing MTs when temperatures drop, for example during hibernation or torpor.

The high abundance of calmodulin-binding domains overlapping the Mn and Mc modules in MAP6 hints that MAP6 binding to MTs is likely to be tightly regulated in cells. Indeed, it was shown *in vitro* that Ca²⁺-Calmodulin (CaM)

binding to MAP6 occurs in an unusual manner (Bouvier et al., 2003) and prevents MAP6 binding to MTs (Lefevre et al., 2013). MAP6/MTs interaction is also prevented by phosphorylation of MAP6 by CAMKII and favors MAP6/F-actin interaction in neurons (Baratier et al., 2006). Based on the available experimental data and as proposed by Ramkumar and collaborators (Ramkumar et al., 2018), the regulation of MAP6 by Ca²⁺-CaM in dendritic spines might follow this sequence: upon synaptic activity, the Ca²⁺-CaM complex forms, detaches MAP6 from adjacent MTs and activates CAMKII (Fink and Meyer, 2002). When Ca²⁺ level decreases, CaM is released from MAP6 allowing its phosphorylation by CAMKII. Then phosphorylated MAP6 is unable to re-associate with MTs but rather binds and stabilizes the synaptic F-actin (Baratier et al., 2006; Peris et al., 2018).

Recently, in cell-free systems, recombinant MAP6-N was shown to exert some stabilizing effects on MT dynamics by promoting rescue (Cuveillier et al., 2020), although the precise contribution of the various MAP6-N MT-binding domains (Mn and/or Mc modules) remains to be clarified. Indeed, the specific role of MAP6-related MT stabilization in developing neurons remains unclear. For example, MT-dependent parameters of neuronal differentiation and morphology (e.g., neurite elongation and branching, axonal polarization) are not dramatically altered in neurons expressing reduced MAP6 levels. Indeed, MAP6 deficient neurons exhibited only moderate morphological defects with a slight increase of the axonal length and a decreased spine density (Andrieux et al., 2002, 2006; Peris et al., 2018; Boulan et al., 2020), as well as a reduced growth cone size and an increased dendrite branching (Schwenk et al., 2014; Qiang et al., 2018). Those defects are not striking possibly due to compensatory mechanisms by other MAPs. Indeed, double-KO neurons for Tau/MAP1B or MAP2/MAP1B display stronger alterations of neuronal differentiation (Takei et al., 2000; Teng et al., 2001) than single KO neurons (Harada et al., 1994; Takei et al., 1997; Gonzalez-Billault et al., 2001). In this respect, an increased expression of Tau has been observed when MAP6 expression is knocked-down even though Tau and MAP6 role in MT stabilization are not similar in neurons (Qiang et al., 2018). In developing neurons, MAP6 was found enriched in the proximal part of the future axon (Tortosa et al., 2017) and a recent proteomic analysis pointed out MAP6 as a specific component of the AIS (Hamdan et al., 2020). MAP6-N localization in the proximal part of axons has been shown to be protective toward the formation of axonal varicosities induced by mechanical stress (Gu et al., 2017). Still, the exact relationships between MAP6-dependent MT stabilization, axonal polarization and AIS functions remains elusive.

MAP6 Belongs to a Family of Proteins

Although most structural MAPs exhibit repeated MT-binding motifs, the repeated motifs in MAP6—its Mn and Mc modules—are unique, and share no homology with MT-binding domains found in Tau or MAP1B (Bosc et al., 1996). However, bioinformatic analysis of the MAP6 sequence has revealed three proteins that share homology in MAP6 functional domains.

The first one is MAP6d1, for MAP6-domain-containing protein 1 (formerly SL21 for 21-kDa STOP-like protein). MAP6d1 is expressed at high levels in the brain and shares two major similarities with MAP6: 80% sequence homology in its N-terminal domain, and 72% sequence homology with the Mn3 module of MAP6 (Bosc et al., 2001; Gory-Fauré et al., 2006). Since the N-terminal domain of both proteins contains the main calmodulin-binding site (Bosc et al., 2001), its functional role might be important.

The original MAP6 family was enlarged following the discovery of homologs of SAXO proteins (SAXO1 and SAXO2 in mammals, formerly named FAM154A and FAM154B, respectively). These proteins were originally identified in the protozoan *Trypanosoma brucei* and in ciliated/flagellated cells (Dacheux et al., 2012). Like neuronal MTs, cilia and flagella are characterized by a high level of MT stability displaying resistance to cold- and nocodazole-induced depolymerization. The human isoform hSAXO1 is ubiquitously expressed and specifically associates with centrioles, basal bodies and cilia (Dacheux et al., 2015). Little is known about SAXO2 beyond the fact that its expression appears to be enriched in ciliated cells.

SAXO proteins share homologies with the Mn modules of MAP6/MAP6d1, and their N-terminal sequence, although distinct, is also rich in cysteines (Dacheux et al., 2012). Interestingly, 80% of hSAXO1 consists of 12 tandem Mn modules that, like the equivalent modules in MAP6 and MAP6d1, are involved in MT binding and cold stabilization. The high number of Mn modules is important since hSAXO1 overexpression results in an increased primary cilia length in RPE1 cells, through a mechanism requiring the Mn modules (Dacheux et al., 2015).

MAP6 Is a Microtubule Inner Protein (MIP)

Cryo-EM experiments revealed neuronal MTs to contain visible intraluminal densities (Burton, 1984; Garvalov et al., 2006; Atherton et al., 2018). These densities correspond to Microtubule Inner Proteins (MIPs), the molecular identity of which was totally unknown until MAP6 was identified as a MIP (Cuveillier et al., 2020). The capacity of MAP6 to enter the lumen of MTs was demonstrated using cell-free systems in which MTs were copolymerized with MAP6, yielding MTs with regularly spaced intraluminal densities. When using MTs derived from murine MAP6 KO neurons, a net reduction in the numbers of intraluminal densities was observed. The presence of MAP6 inside MTs would explain, in part, the extremely slow turnover of MAP6 on neuronal microtubules described by Tortosa et al. (2017). Strikingly, intraluminal MAP6 induced MT coiling *in vitro*, leading to the formation of helical MTs with a highly conserved pitch and width associated with a specific tubulin compaction state in the MT lattice. This coiling pattern requires the Mn and Mc modules, as well as the first 35 N-terminal residues.

In neurons, the functions of such stable helical MAP6-containing MTs remains to be determined. By occupying a greater width, helical MTs could influence the spatial organization of the MT network, help determine neurite or axonal width, or confer resistance to compressive loads, such as those encountered during development. The unhabitual

tubulin compaction state of helical MTs could also be a mean to specifically recruit a set of proteins such as molecular motors.

From an evolutionary point of view, it will be interesting to discover when did the ability of mammalian neuronal MAP6 to behave as a MIP emerge? In other words, does the MAP6 ancestor SAXO in *Trypanosoma* (Dacheux et al., 2012) behave as a MIP only, as a MAP only, or does it exhibit both properties?

MAP6 Associates With Actin

The first indication that MAP6 can bind to actin was obtained when CaMKII-phosphorylated MAP6 was found to be unable to bind MTs, but that it binds actin *in vitro* and in the growth cones of neurons (Baratier et al., 2006). More recently, the central Mc modules of MAP6 were shown to bind actin and to induce specific rearrangements—leading to straightening and bundling of actin filaments (Peris et al., 2018). Moreover, MAP6-mediated stabilization of synaptic actin following synaptic activation was shown to be crucial for maintaining mature dendritic spines, the postsynaptic compartments of synapses (Peris et al., 2018). Other effects of MAP6 on the dynamic parameters of actin, such as nucleation, remain to be investigated, as does the possibility that MAP6 mediates cross-linking between actin and MT networks in neurons. MAP6 may also indirectly influence the actin cytoskeleton through an effect on signaling cascades as it has been shown to interact with the small GTPase protein Rac2 (Figure 1; Capala et al., 2015). Several MAP6 partners have also been shown to interact with actin (Supplementary Table 1), such as spinophilin (Grossman et al., 2004) or α -synuclein (Oliveira da Silva and Liz, 2020). These interactions support specific actin-related cellular functions for MAP6 and its partners.

MAP6 Associates With Membranes and Neuroreceptors

MAP6 and Membranous Compartments

The N-terminal domains of MAP6 and MAP6d1 contain a stretch of cysteines with C5, C10, and C11 residues (Figure 2). These positions have been shown to be palmitoylated by a subset of palmitoylating enzymes containing a DHHC motif. The proteins are then targeted to the Golgi apparatus or the plasma membrane (Gory-Fauré et al., 2006, 2014). In addition, MAP6 interacts directly with ankyrin repeats present in the palmitoylating enzymes zDHHC13 and zDHHC17 (Lemonidis et al., 2015). During neuronal development, palmitoylated forms of MAP6 were identified on the Golgi and on secretory vesicles, and depalmitoylation by α/β hydrolase-domain-containing 17 proteins (ABHD17 proteins) induced MAP6 relocation to MTs in the proximal part of the axon (Tortosa et al., 2017). In neurons, non-centrosomal MT nucleation is crucial, and through its interactions with MTs as well as with the Golgi apparatus or Golgi outposts which are nucleation sites for non-centrosomal MTs (Sanders and Kaverina, 2015; Valenzuela et al., 2020; Yang and Wildonger, 2020), MAP6 might contribute to such events.

MAP6 and MAP6d1 proteins were also shown to localize to mitochondria. This localization involved their N-terminal domain, but not palmitoylation (Gory-Fauré et al., 2014).

Finally, indirect evidence links MAP6 to lysosomes: KIF5B (Kinesin 1 heavy-chain) preferentially binds to MAP6-positive MTs (Tortosa et al., 2017) and lysosomal transport—which is dependent on KIF5B and on TMEM106B, a MAP6 partner (**Figure 1**)—is perturbed when MAP6 expression is impaired (Schwenk et al., 2014).

Overall, these results show that MAP6's association with membranous compartments plays important roles in establishing and maintaining neuronal morphology. The several endocytosis-related proteins such as Varp, dynamin 1 or endophilin 1 (Craft et al., 2008; Vikhreva et al., 2009) which have been found to interact with MAP6 (**Supplementary Table 1**) suggests that the roles played by MAP6 in intracellular organelle trafficking still holds many secrets.

MAP6 and Calcium Channels

Proteomic analysis of the nano-environment of calcium channels ($Ca_v2.1$, $Ca_v2.2$, $Ca_v2.3$, $Ca_v\text{Beta}3$, $Ca_v\text{Beta}4$) revealed the presence of MAP6 (Müller et al., 2010; **Figure 1**). More recently, MAP6, through its Mn3 module, was found to associate with Tctex1 (Brocard et al., 2017), a dynein light chain interacting with $Ca_v2.2/N$ -type calcium channels (Lai et al., 2005). In conjunction with Tctex1, MAP6 is involved in sorting and trafficking $Ca_v2.2$ channels, as shown by impaired calcium signaling in MAP6 KO neurons (Brocard et al., 2017).

MAP6 and Neuroreceptors

Even if MTs are only transiently present in both pre- and post-synaptic compartments of synapses (axonal boutons and dendritic spines), MAP6 was consistently identified in synaptic proteomes, suggesting MT-independent roles (Peng et al., 2004; Baratier et al., 2006; Cheng et al., 2006; Collins et al., 2006; Munton et al., 2007; Weingarten et al., 2014). In a study related to subicular neurons from the hippocampus, MAP6 was associated with the receptors Neuropilin1, Plexin D1, and VEGFR2—which together make up the tripartite Semaphorin 3E receptor (Deloulme et al., 2015; **Figure 1**).

MAP6 Is Involved in Signaling Cascades

In addition to its associations with subcellular compartments and receptors, MAP6 protein contains proline-rich domains (PRD), which are involved in the binding of SH3-domain-containing proteins (**Figure 1** and **Supplementary Table 1**). Binding of Intersectin 1, cSrc, PLC- γ , or PI3K have all been described (Morderer et al., 2012; Deloulme et al., 2015). One of the PRD domains in MAP6 is essential to the Semaphorin 3E signaling cascade (Deloulme et al., 2015), driving the formation of the fornix, an axonal tract which requires Semaphorin 3E signaling.

Although some interactions with kinases and phosphatases have been reported (**Figure 1**), almost nothing is known about how MAP6's functions are regulated by phosphorylation enzymes, with the exception of CaMKII. MAP6-N protein contains four CaMKII phosphorylation sites located within its calmodulin/MT-binding domains. These domains can be phosphorylated *in vitro* and *in vivo*. Phosphorylation induces MAP6 to detach from MTs and delocalize to actin within

growth cones or dendritic spines (Baratier et al., 2006; Peris et al., 2018).

Finally, MAP6 was shown to associate with the highly brain-enriched BCH (Cdc42GAP Homology)-domain-containing protein Bmcc1/Prune2 (**Figure 1**) which negatively regulates the actin cytoskeleton regulator RhoA (Soh and Low, 2008). This association promotes the emergence of membrane protrusions (Arama et al., 2012). However, the relationship between a direct or indirect effect on the cytoskeleton is not clear.

Physio-pathological Roles of MAP6 in the Central Nervous System

As neuronal MAPs, especially MAP6, were thought to be strong MT stabilizers, its deletion in mice was expected to be lethal due to major MT-breakdown in neurons. But in fact, MAP6 KO mice (also known as STOP KO mice) are viable, with an apparently normal brain organization (Andrieux et al., 2002). However, these mice display a wide range of biological and behavioral impairments reminiscent of symptoms displayed by patients suffering from psychiatric disorders, especially schizophrenia, as detailed below.

MAP6 KO Mice as a Model for the Study of Schizophrenia

MAP6 KO mice show hyperactivity, fragmentation of normal activity, anxiety-like behavior, social withdrawal, and impaired maternal behavior leading to the death of pups (Andrieux et al., 2002). These defects are associated with altered synapse-functioning, particularly during synaptic plasticity events when the synapses need to adapt their reactivity. These alterations lead, for example, to strong deficits in potentiation or depression of the synaptic responses. These biological and behavioral defects were shown to respond to long-term treatment with antipsychotics, the gold standard in schizophrenia treatment, thus positioning MAP6 KO mice as a useful model for the study of the physiopathology of this disease (Andrieux et al., 2002).

Schizophrenia is a chronic debilitating neurodevelopmental disorder that affects approximately 1% of the population worldwide; the first symptoms emerge during adolescence and early adulthood. It is characterized by a combination of positive (auditory and visual hallucination), negative (social withdrawal, anxiety), and cognitive symptoms (impaired memory, decision-making difficulties; Joseph et al., 2015). Following our seminal 2002 article (Andrieux et al., 2002), numerous studies were performed and their findings reinforced the validity of the MAP6 KO model for the study of schizophrenia. Indeed, MAP6 KO mice fulfill the three—construct/face/predictive—criteria for the validity of an animal model (Belzung and Lemoine, 2011; Jones et al., 2011) with similar underlying molecular defects/phenotypes/pharmacological responses, respectively (Delotterie et al., 2010; Volle et al., 2013; Deloulme et al., 2015; Bouet et al., 2021).

In further support of the validity of this model, subsequent studies revealed defects in MAP6 expression in humans presenting developmental delay, corpus callosum dysgenesis, autistic or schizophrenic symptoms (Shimizu et al., 2006;

Choi et al., 2009; Martins-de-Souza et al., 2009; Xiao et al., 2015; Coumans et al., 2016; Wei et al., 2016a,b; Chen et al., 2021).

MAP6 Roles in Neurotransmission and Impact on Behavior

In tight correlation with the hyper-dopaminergia observed in schizophrenic patients (Carlsson et al., 2000; Kapur, 2003), MAP6 KO mice present increased dopamine overflow in the mesolimbic pathway. This system plays a significant role in mediating pleasure and rewarding experiences (Brun et al., 2005; Bouvrais-Veret et al., 2007, 2008). Schizophrenia also presents positive symptoms, and MAP6 KO mice exhibited increased locomotor activity (Andrieux et al., 2002; Brun et al., 2005; Fradley et al., 2005; Bouvrais-Veret et al., 2007) associated with hypersensitivity to novelty or to the psychostimulant amphetamine (Brun et al., 2005; Bégou et al., 2007; Bouvrais-Veret et al., 2008), along with extensive disruption of sleep patterns (Proffitt et al., 2016). All these processes crucially depend on dopaminergic neurotransmission.

Negative symptoms in schizophrenia are mediated by alterations in both the glutamatergic and serotonergic (5-HT) neurotransmission systems (Aghajanian and Marek, 2000; Carlsson et al., 2000). MAP6 KO mice exhibited abnormal glutamatergic neurotransmission with altered synaptic plasticity in the hippocampus, leading to totally defective Long-Term Potentiation (LTP) and Long-Term Depression (LTD), as measured by electrophysiology techniques (Andrieux et al., 2002). These defects are related to a smaller presynaptic vesicle pool (Andrieux et al., 2002), a decreased level of glutamate and the glutamate precursor glutamine in the forebrain (Brenner et al., 2007), as well as decreased mRNA levels of the glutamate transporter-1, Vglut1 (Eastwood et al., 2007). MAP6 KO mice are thus characterized by an overall hypo-glutamatergia.

If we now focus on serotonergic neurotransmission, serotonin biosynthesis and expression of the serotonin (5-HT) receptors are highly perturbed in MAP6 KO mice, with a 70% increase in 5HT-1A expression in the raphe nuclei for example (Fournet et al., 2010), as well as half reduction of serotonin (5-HT) in the substantia nigra, the ventral tegmental area and the hippocampus (Fournet et al., 2012b). In addition, the levels of serotonin transporters (SERT) recapturing the serotonin (5-HT) released into the synaptic cleft is very severely affected in MAP6 KO mice with a decreased expression ranging from 30% to 90% in some brain areas whereas the expression increase up to 120% in other brain regions (Fournet et al., 2010). MAP6 KO mice thus display an extreme imbalance in serotonergic transmission.

Finally, sensory-motor gating is also altered in MAP6 KO mice (Fradley et al., 2005; Volle et al., 2013). This effect might be linked to perturbed dopamine-, glutamate-, and serotonin-mediated neurotransmission, but could also be related to activation of opioid mu receptors (Quednow et al., 2008) which is altered in MAP6 KO mice (Charlet et al., 2010).

In summary, basal neurotransmission for all the major neurotransmitters is strongly perturbed in MAP6 KO mice. Strikingly, serotonergic neurons—the longest and most extensively branched neurons in the brain—display very

severe morphological defects, suggesting complementary roles of MAP6 in these neurons. These roles may include MT stabilization, modulation of serotonin neuroreceptors/transporters, and involvement in signaling cascades.

MAP6 Roles in Synaptic Plasticity

In terms of cognitive symptoms, MAP6 KO mice exhibit severe defects in both short- and long-term hippocampal synaptic plasticity. Indeed, glutamatergic hippocampal neurons in the CA1 region display severely defective Post-Tetanus Potentiation (PTP), and, as indicated above, cannot support LTP and LTD (Andrieux et al., 2002). Synaptic deficits exist in the presynaptic compartment, the axonal bouton, where a two-fold decrease in synaptic vesicles is reported (Andrieux et al., 2002) with a possible glutamate-release defect due to the absence of interaction between MAP6 and the SNARE protein SNAP25 (Figure 1). One can speculate on the formation of a transient complex between MAP6 and SNAP25 at the plasma membrane, in the presynaptic release zone, as the membrane targeting of both proteins is induced by similar palmitoylating enzymes (Greaves and Chamberlain, 2011; Gory-Fauré et al., 2014). In addition, the absence of MAP6 induces a general decrease in spine density which is related to altered actin dynamics in dendritic spines (Peris et al., 2018). MAP6 could also contribute to the entry of MTs into the synaptic compartments, and their residence time, thus influencing synaptic strength. Overall, these synaptic defects are most probably a consequence of MAP6's involvement in signaling cascades, receptor homeostasis, and cytoskeleton regulation.

MAP6 Roles in Neuroanatomy

Although the first rough anatomical study of MAP6 KO mice revealed no obvious defects in brain anatomy (Andrieux et al., 2002), subsequent detailed studies showed that MAP6 KO mice have a reduced brain volume associated with an increased ventricular volume and a reduced cerebellum and thalamus size (Powell et al., 2007; Deloulme et al., 2015). Through the use of brain imaging techniques, MAP6 KO mice were found to exhibit a decrease in myelinated tract volumes (e.g., in the internal capsule and cerebellar peduncle) as well as a strong decrease in cortico-spinal tract fasciculation (Deloulme et al., 2015; Gimenez et al., 2017). A very intriguing structural defect is the absence of an important component of the limbic system in MAP6 KO mice—the post-commissural part of the fornix (Deloulme et al., 2015). The fornix is a tract that emerges from the subiculum, the most inferior component of the hippocampal formation of both hemispheres and extends to the mammillary bodies, within the hypothalamus. As part of the Papez circuit, the lack of the fornix leads to a dis-connectivity between the hippocampus and the hypothalamus and certainly contributes to the behavioral defects observed in MAP6 KO mice. During the formation of the fornix, Semaphorin 3E is an attractive guidance molecule for subicular neurons (Chauvet et al., 2007) as it binds to its tripartite receptor (Neuropilin 1/PlexinD1/VEGFR2) to induce activation of downstream signaling cascades involving SH3-containing proteins. Interestingly, the impaired fornix formation observed in MAP6 KO mice is not dependent on MAP6's MT-binding

domains; rather it is driven by the interaction of MAP6 PRD domains with key SH3-domain-containing proteins, including Intersectin 1, PI3K, and Src (**Figure 1**; Deloulme et al., 2015). The axonal tract defects identified in MAP6 KO mice correlate to a striking extent with anomalies identified on brain images from patients with schizophrenia (McCarley et al., 1999; De Peri et al., 2012; Shepherd et al., 2012; Bopp et al., 2017), including alteration of the fornix or of the cortico-spinal tract (Douaud et al., 2007; Kendi et al., 2008; Fitzsimmons et al., 2009; Luck et al., 2010; Davidson et al., 2012; Lee et al., 2013).

MAP6 Role in Neurogenesis

MAP6 is highly expressed in the olfactory bulb and the hippocampus (Couégnas et al., 2007; Richard et al., 2009), two regions where adult neurogenesis is known to occur. Several studies investigated adult neurogenesis in MAP6 KO mice. Benardais et al. (2010) reported an increased number of proliferating cells in the olfactory epithelium with increased apoptosis, whereas Fournet et al. (2010) discovered decreased cell proliferation in the hippocampus. At the molecular level, how MAP6 regulates neurogenesis remains a completely open question, although it is possible that MAP6 through its binding to the retinoic receptors RAR-beta and RAR-gamma (**Figure 1**) can modulate their functions known to be active during neurogenesis (Jacobs et al., 2006; Maden, 2007; Mishra et al., 2018).

MAP6 KO Mice Deficits and Therapeutic Approaches

As the defects observed in MAP6 KO mice are reminiscent of schizophrenia symptoms, the gold standard treatments for psychiatric diseases were the most obvious approach to try in an attempt to alleviate MAP6 KO deficiencies. Alternatively, new pharmacological approaches targeting the neuro-cytoskeleton represent promising avenues of investigation.

Classical treatments of psychiatric diseases. In accordance with their defects in almost all neuro-transmission systems, the defects observed in MAP6 KO mice are sensitive to neuroactive molecules. Thus, long-term treatments with both typical antipsychotics, such as haloperidol (Haldol) (dopamine antagonist), and atypical antipsychotics, such as risperidone (Risperdal) or clozapine (dopamine and serotonin antagonists), alleviate behavioral defects in MAP6 KO mice (Andrieux et al., 2002; Bégou et al., 2008; Delotterie et al., 2010). Moreover, clozapine improves alterations to synaptic plasticity (Delotterie et al., 2010) *via* its known positive effect on glutamatergic synapses (Fukuyama et al., 2019). Similarly, treatment of MAP6 KO mice with anti-depressants such as fluoxetine/Prozac (a Selective Serotonin Reuptake Inhibitor, gold standard treatment for depression) alleviated anxiety-like behavior and cognitive defects (Fournet et al., 2012a). The depressive-like behavior of MAP6 KO mice and their impaired hippocampal neurogenesis were alleviated by the use of electroconvulsive stimulation (ECS) (Jonckheere et al., 2018). ECS is the animal equivalent of Electroconvulsive Therapy (ECT), which remains a very powerful and useful treatment for major depression.

Cytoskeleton-related drugs represent a new pharmacological approach to psychiatric disorders. MAP6 KO mice were the first animal model to establish a link between cytoskeleton defects and

the cognitive impairment characteristics of psychiatric disorders, in particular schizophrenia (Andrieux et al., 2002). Subsequently, other cytoskeletal components including actin and tubulin themselves, as well as CRMP1, CRMP2, MAP2, MAP1B, and LIM kinases were also linked to psychiatric disorders (see below and for review: Benitez-King et al., 2007; Gardiner et al., 2011; Zhao et al., 2015; Marchisella et al., 2016; Lasser et al., 2018). In addition, proteins that were initially identified as risk factors for mental illnesses, such as DISC1 (Disrupted In Schizophrenia) or dysbindin, were later shown to interact with MTs, MAPs, and actin (Morris et al., 2003; Hayashi et al., 2005; Talbot et al., 2006; Taya et al., 2007; Shimizu et al., 2008; Marley and von Zastrow, 2010; Bader et al., 2012).

In this context, cytoskeleton-related drugs have been investigated to determine their ability to influence biological and behavioral defects in MAP6 KO mice. Firstly, chronic exposure of MAP6 KO mice to Epothilone D (EpoD), a modulator of MT dynamics known to stabilize MTs *in vitro* (Chou et al., 1998; Kolman, 2004), leads to behavioral changes (improved maternal behavior, and concomitant pup survival), and improves short-term memory, associated with restoration of synaptic plasticity (LTP) in the hippocampus (Andrieux et al., 2006; Fournet et al., 2012a), as well as restoring neuronal transport deficits (Daoust et al., 2014). Second, a small peptide motif called NAP—present in Activity-Dependent Neuroprotective Protein (ADNP), which is dysregulated in schizophrenia and in autism (Gozes, 2011; Hacoheh-Kleiman et al., 2018; Van Dijk et al., 2019)—partially alleviates cognitive impairments in MAP6 heterozygous mice (Merenlender-Wagner et al., 2010; Volle et al., 2013). NAP directly interacts with tubulin (Divinski et al., 2004) and also promotes MT growth and stability by its interaction with MT plus-end binding proteins of EB family (+TIPs proteins) (Gozes and Divinski, 2007; Oz et al., 2014). In addition, NAP has been shown to bind to Tau (Ivashko-Pachima et al., 2019) and to enhance its binding to MTs in cells (Ivashko-Pachima et al., 2017; Ivashko-Pachima and Gozes, 2019). Thus, NAP protective activity involves MT dynamics modulation *via* direct binding to tubulin and interaction with MT-associated proteins (Oz et al., 2014; Ivashko-Pachima et al., 2017). However, NAP's effects in MAP6 KO mice might not be exclusively related to its MT-related properties as chronic NAP treatment restores normal levels of Beclin1 mRNA in MAP6-deficient mice (Merenlender-Wagner et al., 2014). Beclin1 is a key regulator of autophagy and its expression is strongly decreased in brains from patients with schizophrenia (Merenlender-Wagner et al., 2015).

Overall, these studies with EpoD and NAP highlight MAP6-mediated MT stabilization as an important feature for synaptic plasticity and behavior. The results presented also suggest that the cytoskeleton might be a relevant target for drug development to treat psychiatric disorders including schizophrenia.

Is MAP6 Present in Cilia and Linked to Schizophrenia Phenotypes?

MAP6 was the first neuronal MIP to be identified (Cuveillier et al., 2020). MIPs were originally described in the MT doublet of motile cilia and flagella axonemes (Kirima and Oiwa, 2018;

Owa et al., 2019), where MTs needed to be highly stable to support the strong deformations required to produce a beating motion. The question of whether MAP6 also localizes to non-motile (primary) cilia or to motile cilia within the brain remains open. Future studies assessing these possibilities may provide additional molecular explanations for some of the cognitive impairments observed in MAP6 KO mice. Indeed, ciliopathies can lead to brain malformation and/or mental retardation (Reiter and Leroux, 2017). More precisely, primary cilia which act as signaling platforms participating in Sonic hedgehog or Wnt signaling pathways for example (Lee and Gleeson, 2010) have been shown to modulate neurotransmission through dopamine receptors expressed on their surface (Domire et al., 2011; Iwanaga et al., 2011; Leaf and Von Zastrow, 2015). Interestingly, Inversin and APT1—both MAP6 partners—have been shown to be part of the Wnt pathway (**Supplementary Table 1**). More directly, a reduced number of primary cilia was observed in the olfactory neuroepithelium in patients with schizophrenia (Muñoz-Estrada et al., 2018) and DISC1 was shown to be necessary for the formation of neuronal cilia (Marley and von Zastrow, 2010; Wang and Brandon, 2011). It would be interesting to investigate a possible role for MAP6 acting as a MIP in controlling the number and integrity of neuronal primary cilia.

CRMPs: FROM SIGNALING PATHWAYS TO CYTOSKELETON FUNCTIONS

Research on the structural MAPs revealed over time that their functions are not restricted to MT regulation. Simultaneously, other proteins that were first identified in signaling cascades, for example, were subsequently found to belong to the family of structural MAPs. Collapsin Response Mediator Proteins (CRMPs) are a perfect example of such proteins. Indeed, in addition to their well-known roles in signal transduction and neuronal physiology, we will summarize how, since the 1990s, CRMPs have been documented to play roles in regulating the cytoskeleton and especially in MT dynamics.

CRMP Proteins as Signaling Proteins

Originally discovered in *C. elegans* and named ULIP (UNC-33 like phosphoprotein), members of the CRMP family are involved in neuronal connectivity for sensory and motor neurons (Brenner, 1974; Hedgecock et al., 1985). These proteins originated from various genes and were subsequently renamed Collapsin Response Mediator Proteins (CRMPs) due to their involvement in Semaphorin 3A guidance molecule signaling (Collapsin was the original name of Semaphorin 3A; Goshima et al., 1995).

CRMPs are substrates for a large number of kinases, and high levels of phosphorylation have been reported, mostly in the C-terminal domain (Cole et al., 2004, 2006; Zheng et al., 2018); CRMP phosphorylation has been extensively studied in the context of the axonal guidance signaling pathway induced by Semaphorin 3A. Several kinases involved in this signaling pathway phosphorylate CRMPs. First, Cdk5 acts as the priming kinase, phosphorylating CRMP1, 2, 4, and 5 in response to a Semaphorin 3A-signal *in vitro* and *in vivo*

(Brown et al., 2004; Uchida et al., 2005). This phosphorylation is required for subsequent phosphorylation of CRMPs by GSK3 β , shown to be a key factor in modulating CRMPs' interaction with the cytoskeleton (Uchida et al., 2005; Yoshimura et al., 2005). Thus, the Semaphorin 3A-induced phosphorylation of CRMP2 by Cdk5 and GSK3 β blocks its capacity to bind tubulin and MTs (Uchida et al., 2005; Yoshimura et al., 2005). This lack of interaction leads to cytoskeleton breakdown and the resulting collapse of the growth cone, as the functional consequences of Semaphorin 3A signaling.

Semaphorin 3A-stimulation of the growth of dendritic spines also involves CRMP1 phosphorylation by Cdk5, blocking its interaction with actin (Yamashita et al., 2011; Yao et al., 2016).

Phosphorylation events on CRMPs, thus regulate the proteins' capacity to interact with the cytoskeleton while also modulating their interaction with other partners, such as RhoA (Alabed et al., 2007), the guidance cue co-receptor PlexinA1 (Deo et al., 2004), or the ion channels Cav2.2 (Brittain et al., 2009), and Nav1.7 (Dustrude et al., 2016).

At the same time, the C-terminal part of CRMP2 shares similarities with Tau PRD domains (Hensley and Kursula, 2016), opening up the possibility that CRMPs can bind to SH3-domain-containing proteins.

CRMPs Bind and Stabilize Microtubules

From the time of their discovery in 1985, CRMPs were linked to MTs since mutations induced an over-abundance of MTs in axonal shafts (Hedgecock et al., 1985). It was therefore proposed that CRMP could modulate axonal outgrowth by stabilizing the cytoskeleton (Hedgecock et al., 1985). More recent work has indicated that all CRMPs bind tubulin both *in vitro* and *in vivo* (Fukata et al., 2002a; Lin et al., 2011; Khazaei et al., 2014), although the interaction between CRMP2 and MTs has been the focus of this particular study. Indeed, for CRMP2, its interaction with MTs was recently found to involve two distinct domains: the N-terminal domain, which is essential for binding to soluble tubulin, thus promoting MT polymerization; and the C-terminal region, which interacts with and stabilizes polymerized microtubules (Niwa et al., 2017). Although the ability to bind MTs is shared by all CRMPs, the MT-stabilizing capacity reported for CRMP2 is only shared by CRMP1 and CRMP4 (Lin et al., 2011). In contrast, CRMP5 does not influence MT dynamics (Brot et al., 2010), and CRMP3 was shown to inhibit MT polymerization (Aylsworth et al., 2009). The role of CRMP2 in MT assembly was found to be crucial for neurite formation and axon development (Fukata et al., 2002b) whereas CRMP4-dependent MT organizations contribute to growth-cone dynamics (progression, pausing, and retraction) as well as to axon elongation and regeneration (Khazaei et al., 2014).

CRMPs Associate With Actin

Of all the isoforms, only CRMP3 presents weaker or no interaction with actin (Tan et al., 2015). All other CRMPs have an actin-binding site located at their C-terminal end, adjoining their MT-binding site. This actin-binding site was initially characterized in CRMP4 and promotes the formation of F-actin

both *in vitro* and *in vivo* (Rosslenbroich et al., 2005; Khazaei et al., 2014; Cha et al., 2016). In neurons, through their action on the actin cytoskeleton, CRMP4 and CRMP5 contribute to neurite outgrowth and growth-cone remodeling (Khazaei et al., 2014; Gong et al., 2016), and CRMP4's actin-binding capacity also contributes to dendrite maturation in hippocampal neurons (Cha et al., 2016). The effects of CRMP1 and CRMP2 on actin dynamics are more indirect, as interactions with VASP family proteins or the Sra-1 / WAVE1 complex are required for these proteins to influence axon formation and growth (Kawano et al., 2005; Yu-Kemp and Briehner, 2016; Yu-Kemp et al., 2017).

CRMPs Associate With Membranes and Neuroreceptors

The role of CRMPs in vesicular trafficking and plasma membrane targeting of several transmembrane proteins is well-documented. Thus, CRMP2 is known to bind to the vesicle-associated proteins Slp1 and Rab27 allowing anterograde transport of BDNF receptor TrkB (Arimura et al., 2009). It also binds to the endocytic adaptor Eps15, the ubiquitin ligase Nedd4.2, and to α -adaptin which regulates clathrin-dependent endocytosis of the cellular adhesion molecule L1 and the sodium channel Nav1.7 (Nishimura et al., 2003; Kawano et al., 2005; Dustrude et al., 2016). CRMP1 modulates Na⁺ currents by interacting with Nav1.7 (Yamane et al., 2017) whereas, like MAP6, CRMP2, and CRMP3 respectively interact with voltage-gated Cav2.2/N-type and L-type channels (Brittain et al., 2009; Chi et al., 2009; Quach et al., 2013). CRMP4 is involved in vesicular trafficking through mechanisms involving binding to the SH3 domains of the scaffolding protein Intersectin 1 (Quinn et al., 2003)—which is also a MAP6 partner (Figure 1).

Despite the early discovery of the involvement of CRMPs in the Semaphorin 3A signaling pathway (Goshima et al., 1995), little is known about direct interactions between CRMPs and the numerous semaphorin receptors represented by the Neuropilin and Plexin families. CRMP1, 2, 3, and 4 complexes with Plexin-A1 have been reported following over-expression of the different isoforms in the COS7 cell line (Deo et al., 2004), and associations with the mono-oxygenases MICALs have also been described (Schmidt et al., 2008). In addition, CRMP2 was shown to interact with Plexin-A2 and A3 in the Nogo and Semaphorin 3A signaling pathways, respectively (Sekine et al., 2019; Jiang et al., 2020).

Physio-pathological Roles of CRMPs in the Central Nervous System

As part of their regulation of neuronal development and plasticity, CRMPs are involved in many neurodevelopmental processes including neural progenitor proliferation (Charrier et al., 2006), neuronal migration (Yamashita et al., 2006), and neuronal morphogenesis with both axonal and dendritic maturation influences. The study of CRMP1, CRMP2, and CRMP4 KO neurons revealed morphological defects, especially in dendritic development and branching, but also in migration and positioning (Yamashita et al., 2006, 2007; Niisato et al., 2012). These phenotypes are more severe in double KO neurons, whether the combination is CRMP1 and CRMP4, or

CRMP2 and CRMP4 (Tan et al., 2015; Yamazaki et al., 2020). *In vivo*, KO of any CRMP (CRMP1, CRMP2, CRMP3, or CRMP4) leads to robust alteration of dendritic morphogenesis in several brain regions including the hippocampus and the cortex (Yamashita et al., 2007; Quach et al., 2008; Niisato et al., 2012, 2013; Yamashita and Goshima, 2012; Tsutiya et al., 2015, 2016). CRMP2 is also strongly associated with axonal specification (Nishimura et al., 2003; Kawano et al., 2005; Yoshimura et al., 2005; Morita and Sobue, 2009). The extensive effects of CRMPs on neuronal differentiation are stronger than those observed for the deletion of classical MAPs. This enhanced effect might be due to the crucial roles of CRMPs at the interface between elements of the cytoskeleton and signaling proteins. Impairment of CRMPs functions also leads to synaptic-plasticity defects with abnormal LTP (Su et al., 2007; Quach et al., 2008, 2011; Yamashita et al., 2011), linked to impaired learning and memory (Su et al., 2007; Yamashita et al., 2013).

In humans, CRMPs are associated with several psychiatric disorders, with striking numbers of publications providing evidence of links between CRMPs and schizophrenia (Nakata et al., 2003; Nakata and Ujike, 2004; Ujike et al., 2006; Koide et al., 2010; Hensley et al., 2011; Bader et al., 2012; Lee et al., 2015; Quach et al., 2015; Toyoshima et al., 2019). For example, polymorphisms in the genes encoding CRMP1 and CRMP2, as well as altered hippocampal expression of CRMP2 and CRMP4 have been reported in patients with schizophrenia (Edgar et al., 2000; Beasley et al., 2006; Föcking et al., 2011; Bader et al., 2012). In addition, the abnormal sensory-motor gating abilities reported in psychiatric patients and described for MAP6 KO mice (Fradley et al., 2005), were also replicated in CRMP1 and CRMP3 KO mice (Quach et al., 2008; Yamashita et al., 2013). Importantly, these defects could be alleviated through the use of the antipsychotic chlorpromazine (Yamashita et al., 2013), and CRMP2 and CRMP4 phosphorylation states were shown to be downregulated by the antipsychotics Clozapine and Risperidone (Kedracka-Krok et al., 2015).

Which Proteins Can Be Classified as MAPs?

In summary, the ability of CRMPs to bind MTs, and thus promote their polymerization and stabilization, are major arguments to consider them as members of the wider MAP family. Moreover, and as indicated above, like other MAPs, CRMPs can also bind actin and are involved in signaling cascades. As for conventional MAPs, deletion of CRMPs in mice does not lead to severe cytoskeleton alterations, but rather to subtler neurodevelopmental defects and cognitive dysfunctions similar to those encountered in psychiatric diseases. The history of protein identification draws attention toward specific research. In the case of CRMPs, although data regarding their interactions with MTs have been produced they have not been extensively investigated in the field of cytoskeleton research. In particular, they have never been used in *in vitro* cell-free systems. Several basic questions thus remain open, such as: Do CRMPs modulate specific parameters of

microtubule dynamics? Do they induce MT bundling or simply MT polymerization?

Our demonstration that CRMPs can be considered as MAPs could be extended to other proteins like for example, the Huntingtin protein or α -synuclein. These two proteins have been actively studied in the context of neurodegenerative diseases. Indeed, HTT binds to MTs and actin, is involved in signaling cascades, is palmitoylated by the same DHCC as MAP6 (Lemonidis et al., 2015), and interacts with neuroreceptors (for review see Saudou and Humbert, 2016). Similarly, α -synuclein, a MAP6 partner (**Figure 1**), interacts with and nucleates MTs (Cartelli et al., 2016). α -synuclein also interacts with actin and reduces F-actin polymerization speed (Sousa et al., 2009; Cartelli et al., 2016; Oliveira da Silva and Liz, 2020). It also participates in signaling cascades and neuroreceptor functions (for review see Emamzadeh, 2016; Bernal-Conde et al., 2019). In addition to these examples, proteins related to schizophrenia susceptibility could be mentioned, such as DISC1 (Disrupted In Schizophrenia) or dysbindin, both of which have been shown to interact with MTs, MAPs, and actin (Morris et al., 2003; Hayashi et al., 2005; Talbot et al., 2006; Taya et al., 2007; Shimizu et al., 2008; Marley and von Zastrow, 2010; Bader et al., 2012).

COMMON PROPERTIES OF THE NEURONAL STRUCTURAL MAPs

In this section, we will briefly summarize the properties of the classical neuronal structural MAPs (Tau, MAP1, and MAP2) and compare them to those described for MAP6 and CRMPs. We will focus particularly on properties that are just coming to light.

All the classical MAPs bind to MTs and induce various levels of stability (Baas et al., 1994; Bulinski and Bossler, 1994; Vandecandelaere et al., 1996; Faller et al., 2009; Kadavath et al., 2015; Qiang et al., 2018). Recent advances in cryo-EM have made it possible to visualize how Tau binds along protofilaments at the interface between tubulin dimers (Kellogg et al., 2018). Elucidating the near-atomic structure of complexes between the other MAPs and MTs is essential if we wish to reveal the common and specific mechanisms behind MT stabilization for each MAP. Interestingly, several classical MAPs such as MAP1B, MAP2, and Tau, are also able to indirectly modulate MT dynamics *via* their interaction with EB proteins (Kapitein et al., 2011; Tortosa et al., 2013; Sayas et al., 2015; Ramirez-Rios et al., 2016). Such a possibility regarding MAP6 and CRMPs has not yet been investigated and could be of interest.

With regard to the ability of MAP6 to behave as a MIP, future studies will reveal whether this property is shared by other structural MAPs. Although some previous works suggested that Tau binds to the luminal side of MTs (Kar et al., 2003; Inaba et al., 2019), the answer to this question remains elusive. Interestingly, actin was very recently discovered inside the MT lumen (Paul et al., 2020), opening the possibility that MAPs/MIPs might be involved in the crosstalk between

the two cytoskeletons in the MT lumen like they are in the cytoplasm.

Like MAP6, the other structural MAPs—Tau, MAP1, and MAP2—were shown to bind actin (Griffith and Pollard, 1982; Pedrotti et al., 1994; Ozer and Halpain, 2000; Roger et al., 2004; Ding et al., 2006) and to regulate synaptic plasticity through actin-dependent mechanisms (Davidkova and Carroll, 2007; Tortosa et al., 2011; Benoist et al., 2013; Takei et al., 2015). Interestingly, Tau was directly shown to co-organize actin and MT networks *in vitro* and in the neuronal growth cone (Elie et al., 2015; Biswas and Kalil, 2018), this ability may be shared by the other MAPs (Mohan and John, 2015).

In relation to neuroreceptors, like MAP6 (**Figure 1**), MAP1 and MAP2 proteins interact with the Cav2.2/N-type calcium channel or with BKCa potassium channels (Davare et al., 1999; Park et al., 2004; Leenders et al., 2008). In terms of membrane-association, Tau and MAP2 interact with the membranes of the Golgi and the endoplasmic reticulum (Farah et al., 2005, 2006), whereas MAP1S was shown to link mitochondria and autophagosomes to MTs (Xie et al., 2011).

Several other MAPs in addition to MAP6 contain PRD domains and thus interact with SH3-containing proteins. For example, Tau and MAP2 bind to various SH3-containing proteins including the non-receptor tyrosine kinase Src (MAP6 partner, **Figure 1**; Lim and Halpain, 2000). Interestingly, in link with Alzheimer's disease, a general inhibition of Tau's interactions with SH3-domain-containing proteins was shown to reduce Amyloid β -induced membrane trafficking abnormalities and neurite degeneration (Rush et al., 2020).

Finally, as with MAP6 deletion, invalidation of other MAPs in mice did not result in major MT-breakdown or in lethal neurodevelopmental defects but rather produced viable mice (Harada et al., 1994; Takei et al., 1997, 2015; Teng et al., 2001). However, all KO mice display cognitive dysfunctions similar to those associated with psychiatric diseases. Thus, Tau KO mice exhibit impaired neurogenesis (Dioli et al., 2017), hippocampal synaptic plasticity, and cognitive defects (Ikegami et al., 2000; Lei et al., 2012; Ahmed et al., 2014; Ma et al., 2014; Regan et al., 2015), as well as age-dependent brain atrophy associated with loss of neurons and synapses (Lei et al., 2012). MAP1B-deficient mice also display abnormal synapse maturation (Tortosa et al., 2011; Bodaleo et al., 2016), along with synaptic transmission defects due to deregulation of AMPA receptor trafficking (Benoist et al., 2013; Palenzuela et al., 2017), and impaired synaptic plasticity with abnormal LTP (Zervas et al., 2005). Importantly, MAP1B has been linked to the protein KIRREL3 which is associated with autism/intellectual disability (Liu et al., 2015). This protein is associated with the altered working memory observed in young people with attention-deficit/hyperactivity disorder (Salatino-Oliveira et al., 2016). Mutated forms of MAP1B have been linked to intellectual disability and extensive white-matter deficits in humans (Walters et al., 2018).

A review of the literature relating to MAPs, in particular, Tau (which is by far the most extensively studied MAP), reveals that some MAP features have not yet been reported

for MAP6 and CRMPs. Firstly, it is quite clear that Tau is a *bona fide* nuclear protein (for review see Bukar Maina et al., 2016) mainly contributing to defending the genome against cellular stress. As shown in **Supplementary Table 1**, MAP6 has been shown to interact with various nuclear receptors and effectors, but nothing is known about its possible roles in the nucleus. Secondly, Tau is an unstructured protein that has been shown to promote phase-separation events in cells, both as part of physiological processes such as axonal transport and in pathological conditions such as during Tau aggregation (Hernández-Vega et al., 2017; Wegmann et al., 2018; Siahaan et al., 2019). How the capacity of Tau to promote phase separation affects its non-cytoskeleton-related functions still remains to be determined. As most MAPs including MAP6 are unstructured proteins, it appears logical that the ability to contribute to phase separation events will be shared by many MAPs.

CONCLUSION

Structural MAPs, presented here through the examples of MAP6 and CRMPs, are highly versatile proteins with multiple partners and functions, playing major roles in several brain functions.

The original classification of MAPs was based on their ability to bind MTs. This binding may contribute to MT stability, but it might also be crucial to ensure MAPs presence all over the cell in order to be available to promote signal propagation and/or

to form multi-protein complexes (post-synaptic densities) or regulate the protein composition of membrane compartments. In other words, the MT-binding ability of MAPs is probably required for all their other functions as it is essential to ensure specific spatial and temporal localization. These dual abilities of MAPs to stabilize MTs and to use them as a means to gain access to all regions of the cell for other functions makes it experimentally impossible to distinguish between their MT-related and -unrelated functions.

AUTHOR CONTRIBUTIONS

CC, BB, CR, ED, J-CD, SG-F, CD, CB, IA and AA wrote the manuscript. All authors contributed to the article and approved the submitted version.

FUNDING

This work was supported by funding from INSERM, CEA, CNRS, University Grenoble Alpes and in part by awards from the French Agence Nationale de la Recherche to AA and IA (2017-CE11-0026, MAMAs).

SUPPLEMENTARY MATERIAL

The Supplementary Material for this article can be found online at: <https://www.frontiersin.org/articles/10.3389/fnmol.2021.665693/full#supplementary-material>.

REFERENCES

- Aghajanian, G. K., and Marek, G. J. (2000). Serotonin model of schizophrenia: emerging role of glutamate mechanisms. *Brain Res. Brain Res. Rev.* 31, 302–312. doi: 10.1016/s0165-0173(99)00046-6
- Aguezoul, M., Andrieux, A., and Denarier, E. (2003). Overlap of promoter and coding sequences in the mouse STOP gene (Mtap6). *Genomics* 81, 623–627. doi: 10.1016/s0888-7543(03)00053-3
- Ahmed, T., Van der Jeugd, A., Blum, D., Galas, M. C., D’Hooge, R., Buee, L., et al. (2014). Cognition and hippocampal synaptic plasticity in mice with a homozygous tau deletion. *Neurobiol. Aging* 35, 2474–2478. doi: 10.1016/j.neurobiolaging.2014.05.005
- Alabed, Y. Z., Pool, M., Tone, S. O., and Fournier, A. E. (2007). Identification of CRMP4 as a convergent regulator of axon outgrowth inhibition. *J. Neurosci.* 27, 1702–1711. doi: 10.1523/JNEUROSCI.5055-06.2007
- Andrieux, A., Salin, P., Schweitzer, A., Bégou, M., Pachoud, B., Brun, P., et al. (2006). Microtubule stabilizer ameliorates synaptic function and behavior in a mouse model for schizophrenia. *Biol. Psychiatry* 60, 1224–1230. doi: 10.1016/j.biopsych.2006.03.048
- Andrieux, A., Salin, P. A., Vernet, M., Kujala, P., Baratier, J., Gory-Faure, S., et al. (2002). The suppression of brain cold-stable microtubules in mice induces synaptic defects associated with neuroleptic-sensitive behavioral disorders. *Genes Dev.* 16, 2350–2364. doi: 10.1101/gad.223302
- Arama, J., Boulay, A. C., Bosc, C., Delphin, C., Loew, D., Rostaing, P., et al. (2012). Bmcc1s, a novel brain-isoform of Bmcc1, affects cell morphology by regulating MAP6/STOP functions. *PLoS One* 7:e35488. doi: 10.1371/journal.pone.0035488
- Arimura, N., Kimura, T., Nakamura, S., Taya, S., Funahashi, Y., Hattori, A., et al. (2009). Anterograde transport of TrkB in axons is mediated by direct interaction with Slp1 and Rab27. *Dev. Cell* 16, 675–686. doi: 10.1016/j.devcel.2009.03.005
- Atherton, J., Stouffer, M., Francis, F., and Moores, C. A. (2018). Microtubule architecture *in vitro* and in cells revealed by cryo-electron tomography. *Acta Crystallogr. D Struct. Biol.* 74, 572–584. doi: 10.1107/S205979831801948
- Aylsworth, A., Jiang, S. X., Desbois, A., and Hou, S. T. (2009). Characterization of the role of full-length CRMP3 and its calpain-cleaved product in inhibiting microtubule polymerization and neurite outgrowth. *Exp. Cell Res.* 315, 2856–2868. doi: 10.1016/j.yexcr.2009.06.014
- Baas, P. W., and Black, M. M. (1990). Individual microtubules in the axon consist of domains that differ in both composition and stability. *J. Cell Biol.* 111, 495–509. doi: 10.1083/jcb.111.2.495
- Baas, P. W., Pienkowski, T. P., Cimbalnik, K. A., Toyama, K., Bakalis, S., Ahmad, F. J., et al. (1994). Tau confers drug stability but not cold stability to microtubules in living cells. *J. Cell Sci.* 107, 135–143.
- Baas, P. W., Rao, A. N., Matamoros, A. J. and Leo, L. (2016). Stability properties of neuronal microtubules. *Cytoskeleton (Hoboken)* 73, 442–460. doi: 10.1002/cm.21286
- Bader, V., Tomppio, L., Trossbach, S. V., Bradshaw, N. J., Prikulis, I., Leliveld, S. R., et al. (2012). Proteomic, genomic and translational approaches identify CRMP1 for a role in schizophrenia and its underlying traits. *Hum. Mol. Genet.* 21, 4406–4418. doi: 10.1093/hmg/ddc273
- Baratier, J., Peris, L., Brocard, J., Gory-Faure, S., Dufour, F., Bosc, C., et al. (2006). Phosphorylation of microtubule-associated protein STOP by calmodulin kinase II. *J. Biol. Chem.* 281, 19561–19569. doi: 10.1074/jbc.M509602200
- Beasley, C. L., Pennington, K., Behan, A., Wait, R., Dunn, M. J., and Cotter, D. (2006). Proteomic analysis of the anterior cingulate cortex in the major psychiatric disorders: evidence for disease-associated changes. *Proteomics* 6, 3414–3425. doi: 10.1002/pmic.200500069
- Bégou, M., Brun, P., Bertrand, J. B., Job, D., Schweitzer, A., D’Amato, T., et al. (2007). Post-pubertal emergence of alterations in locomotor

- activity in stop null mice. *Synapse* 61, 689–697. doi: 10.1002/syn.20409
- Bégou, M., Volle, J.-B., Bertrand, J. B., Brun, P., Job, D., Schweitzer, A., et al. (2008). The stop null mice model for schizophrenia displays [corrected] cognitive and social deficits partly alleviated by neuroleptics. *Neuroscience* 157, 29–39. doi: 10.1016/j.neuroscience.2008.07.080
- Belzung, C., and Lemoine, M. (2011). Criteria of validity for animal models of psychiatric disorders: focus on anxiety disorders and depression. *Biol. Mood Anxiety Disord.* 1:9. doi: 10.1186/2045-5380-1-9
- Benardais, K., Kasem, B., Couegnas, A., Samama, B., Fernandez, S., Schaeffer, C., et al. (2010). Loss of STOP protein impairs peripheral olfactory neurogenesis. *PLoS One* 5:e12753. doi: 10.1371/journal.pone.0012753
- Benitez-King, G., Ramirez-Rodriguez, G., and Ortiz-López, L. (2007). Altered microtubule associated proteins in schizophrenia. *Neuroquantology* 5:1. doi: 10.14704/nq.2007.5.1.117
- Benoist, M., Palenzuela, R., Rozas, C., Rojas, P., Tortosa, E., Morales, B., et al. (2013). MAP1B-dependent Rac activation is required for AMPA receptor endocytosis during long-term depression. *EMBO J.* 32, 2287–2299. doi: 10.1038/emboj.2013.166
- Bernal-Conde, L. D., Ramos-Acevedo, R., Reyes-Hernandez, M. A., Balbuena-Olvera, A. J., Morales-Moreno, I. D., Arguero-Sanchez, R., et al. (2019). α -synuclein physiology and pathology: a perspective on cellular structures and organelles. *Front. Neurosci.* 13:1399. doi: 10.3389/fnins.2019.01399
- Biswas, S., and Kalil, K. (2018). The microtubule-associated protein tau mediates the organization of microtubules and their dynamic exploration of actin-rich lamellipodia and filopodia of cortical growth cones. *J. Neurosci.* 38, 291–307. doi: 10.1523/JNEUROSCI.2281-17.2017
- Bodakuntla, S., Jijumon, A. S., Villablanca, C., Gonzalez-Billault, C., and Janke, C. (2019). Microtubule-associated proteins: structuring the cytoskeleton. *Trends Cell Biol.* 29, 804–819. doi: 10.1016/j.tcb.2019.07.004
- Bodaleo, F. J., Montenegro-Venegas, C., Henriquez, D. R., Court, F. A., and Gonzalez-Billault, C. (2016). Microtubule-associated protein 1B (MAP1B)-deficient neurons show structural presynaptic deficiencies *in vitro* and altered presynaptic physiology. *Sci. Rep.* 6:30069. doi: 10.1038/srep30069
- Bopp, M. H. A., Zöllner, R., Jansen, A., Dietsche, B., Krug, A., and Kircher, T. T. J. (2017). White matter integrity and symptom dimensions of schizophrenia: a diffusion tensor imaging study. *Schizophr. Res.* 184, 59–68. doi: 10.1016/j.schres.2016.11.045
- Bosc, C., Andrieux, A., and Job, D. (2003). STOP proteins. *Biochemistry* 42, 12125–12132. doi: 10.1021/bi0352163
- Bosc, C., Cronk, J. D., Pirollet, F., Watterson, D. M., Haiech, J., Job, D., et al. (1996). Cloning, expression and properties of the microtubule-stabilizing protein STOP. *Proc. Natl. Acad. Sci. U S A* 93, 2125–2130. doi: 10.1073/pnas.93.5.2125
- Bosc, C., Frank, R., Denarier, E., Ronjat, M., Schweitzer, A., Wehland, J., et al. (2001). Identification of novel bifunctional calmodulin-binding and microtubule-stabilizing motifs in STOP proteins. *J. Biol. Chem.* 276, 30904–30913. doi: 10.1074/jbc.M011614200
- Bouet, V., Percelay, S., Leroux, E., Diarra, B., Leger, M., Delcroix, N., et al. (2021). A new 3-hit mouse model of schizophrenia built on genetic, early and late factors. *Schizophr. Res.* 228, 519–528. doi: 10.1016/j.schres.2020.11.043
- Boulan, B., Beghin, A., Ravanello, C., Deloulme, J. C., Gory-Faure, S., Andrieux, A., et al. (2020). AutoNeurite: an ImageJ plugin for measurement and classification of neuritic extensions. *PLoS One* 15:e0234529. doi: 10.1371/journal.pone.0234529
- Bouvier, D., Vanhaverbeke, C., Simorre, J. P., Arlaud, G. J., Bally, I., Forge, V., et al. (2003). Unusual Ca^{2+} -calmodulin binding interactions of the microtubule-associated protein F-STOP. *Biochemistry* 42, 11484–11493. doi: 10.1021/bi034746w
- Bouvrais-Veret, C., Weiss, S., Andrieux, A., Schweitzer, A., McIntosh, J. M., Job, D., et al. (2007). Sustained increase of $\alpha 7$ nicotinic receptors and choline-induced improvement of learning deficit in STOP knock-out mice. *Neuropharmacology* 52, 1691–1700. doi: 10.1016/j.neuropharm.2007.03.015
- Bouvrais-Veret, C., Weiss, S., Hanoun, N., Andrieux, A., Schweitzer, A., Job, D., et al. (2008). Microtubule-associated STOP protein deletion triggers restricted changes in dopaminergic neurotransmission. *J. Neurochem.* 104, 745–756. doi: 10.1111/j.1471-4159.2007.05025.x
- Brady, S. T., Tytell, M., and Lasek, R. J. (1984). Axonal tubulin and axonal microtubules: biochemical evidence for cold stability. *J. Cell Biol.* 99, 1716–1724. doi: 10.1083/jcb.99.5.1716
- Brenner, S. (1974). The genetics of *Caenorhabditis elegans*. *Genetics* 77, 71–94. doi: 10.1093/genetics/77.1.71
- Brenner, E., Sonnwald, U., Schweitzer, A., Andrieux, A., and Nehlig, A. (2007). Hypoglutamatergic activity in the STOP knockout mouse: a potential model for chronic untreated schizophrenia. *J. Neurosci. Res.* 85, 3487–3493. doi: 10.1002/jnr.21200
- Brinkley, B. R., and Cartwright, J. Jr. (1975). Cold-labile and cold-stable microtubules in the mitotic spindle of mammalian cells. *Ann. N Y Acad. Sci.* 253, 428–439. doi: 10.1111/j.1749-6632.1975.tb19218.x
- Brittain, J. M., Piekarz, A. D., Wang, Y., Kondo, T., Cummins, T. R., and Khanna, R. (2009). An atypical role for collapsin response mediator protein 2 (CRMP-2) in neurotransmitter release *via* interaction with presynaptic voltage-gated calcium channels. *J. Biol. Chem.* 284, 31375–31390. doi: 10.1074/jbc.M109.009951
- Brocard, J., Dufour, F., Gory-Fauré, S., Arnoult, C., Bosc, C., Denarier, E., et al. (2017). MAP6 interacts with Tctex1 and $Ca_v2.2/N$ -type calcium channels to regulate calcium signalling in neurons. *Eur. J. Neurosci.* 46, 2754–2767. doi: 10.1111/ejn.13766
- Brot, S., Rogemond, V., Perrot, V., Chounlamountri, N., Auger, C., Honnorat, J., et al. (2010). CRMP5 interacts with tubulin to inhibit neurite outgrowth, thereby modulating the function of CRMP2. *J. Neurosci.* 30, 10639–10654. doi: 10.1523/JNEUROSCI.0059-10.2010
- Brown, M., Jacobs, T., Eickholt, B., Ferrari, G., Teo, M., Monfries, C., et al. (2004). $\alpha 2$ -chimaerin, cyclin-dependent kinase 5/p35 and its target collapsin response mediator protein-2 are essential components in semaphorin 3A-induced growth-cone collapse. *J. Neurosci.* 24, 8994–9004. doi: 10.1523/JNEUROSCI.3184-04.2004
- Brun, P., Begou, M., Andrieux, A., Mouly-Badina, L., Clerget, M., Schweitzer, A., et al. (2005). Dopaminergic transmission in STOP null mice. *J. Neurochem.* 94, 63–73. doi: 10.1111/j.1471-4159.2005.03166.x
- Bukar Maina, M., Al-Hilaly, Y. K., and Serpell, L. C. (2016). Nuclear tau and its potential role in Alzheimer's disease. *Biomolecules* 6:9. doi: 10.3390/biom6010009
- Bulinski, J. C., and Bossler, A. (1994). Purification and characterization of ensconsin, a novel microtubule stabilizing protein. *J. Cell Sci.* 107, 2839–2849.
- Burton, P. R. (1984). Luminal material in microtubules of frog olfactory axons: structure and distribution. *J. Cell Biol.* 99, 520–528. doi: 10.1083/jcb.99.2.520
- Capala, M. E., Maat, H., Bonardi, F., van den Boom, V., Kuipers, J., Vellenga, E., et al. (2015). Mitochondrial dysfunction in human leukemic stem/progenitor cells upon loss of RAC2. *PLoS One* 10:e0128585. doi: 10.1371/journal.pone.0128585
- Carlsson, A., Waters, N., Waters, S., and Carlsson, M. L. (2000). Network interactions in schizophrenia—therapeutic implications. *Brain Res. Brain Res. Rev.* 31, 342–349. doi: 10.1016/s0165-0173(99)00050-8
- Cartelli, D., Aliverti, A., Barbiroli, A., Santambrogio, C., Ragg, E. M., Casagrande, F. V., et al. (2016). α -synuclein is a novel microtubule dynamase. *Sci. Rep.* 6:33289. doi: 10.1038/srep33289
- Cha, C., Zhang, J., Ji, Z., Tan, M., Li, S., Wu, F., et al. (2016). CRMP4 regulates dendritic growth and maturation *via* the interaction with actin cytoskeleton in cultured hippocampal neurons. *Brain Res. Bull.* 124, 286–294. doi: 10.1016/j.brainresbull.2016.06.008
- Chapin, S. J., and Bulinski, J. C. (1994). Cellular microtubules heterogeneous in their content of microtubule-associated protein 4 (MAP4). *Cell Motil. Cytoskeleton.* 27, 133–149. doi: 10.1002/cm.970270205
- Charlet, A., Muller, A. H., Laux, A., Kemmel, V., Schweitzer, A., Deloulme, J. C., et al. (2010). Abnormal nociception and opiate sensitivity of STOP null mice exhibiting elevated levels of the endogenous alkaloid morphine. *Mol. Pain* 6:96. doi: 10.1186/1744-8069-6-96
- Charrier, C., Coronas, V., Fombonne, J., Roger, M., Jean, A., Krantic, S., et al. (2006). Characterization of neural stem cells in the dorsal vagal complex of adult rat by *in vivo* proliferation labeling and *in vitro* neurosphere assay. *Neuroscience* 138, 5–16. doi: 10.1016/j.neuroscience.2005.10.046
- Chauvet, S., Cohen, S., Yoshida, Y., Fekrane, L., Livet, J., Gayet, O., et al. (2007). Gating of Sema3E/PlexinD1 signaling by neuropilin-1 switches axonal

- repulsion to attraction during brain development. *Neuron* 56, 807–822. doi: 10.1016/j.neuron.2007.10.019
- Chen, C. P., Lin, S. P., Chern, S. R., Wu, P. S., Chen, S. W., Wu, F. T., et al. (2021). Tetrasomy of 11q13.4–q14.3 due to an intrachromosomal triplication associated with paternal uniparental isodisomy for 11q14.3–qter, intrauterine growth restriction, developmental delay, corpus callosum dysgenesis, microcephaly, congenital heart defects and facial dysmorphism. *Taiwan J. Obstet. Gynecol.* 60, 169–172. doi: 10.1016/j.tjog.2020.11.027
- Cheng, D., Hoogenraad, C. C., Rush, J., Ramm, E., Schlager, M. A., Duong, D. M., et al. (2006). Relative and absolute quantification of postsynaptic density proteome isolated from rat forebrain and cerebellum. *Mol. Cell. Proteomics* 5, 1158–1170. doi: 10.1074/mcp.D500009-MCP200
- Chi, X. X., Schmutzler, B. S., Brittain, J. M., Wang, Y., Hingtgen, C. M., Nicol, G. D., et al. (2009). Regulation of N-type voltage-gated calcium channels (Cav2.2) and transmitter release by collapsin response mediator protein-2 (CRMP-2) in sensory neurons. *J. Cell Sci.* 122, 4351–4362. doi: 10.1242/jcs.053280
- Choi, K. H., Zepp, M. E., Higgs, B. W., Weickert, C. S., and Webster, M. J. (2009). Expression profiles of schizophrenia susceptibility genes during human prefrontal cortical development. *J. Psychiatry Neurosci.* 34, 450–458.
- Chou, T. C., Zhang, X. G., Balog, A., Su, D. S., Meng, D., Savin, K., et al. (1998). Desoxyepothilone B: an efficacious microtubule-targeted antitumor agent with a promising *in vivo* profile relative to epothilone B. *Proc. Natl. Acad. Sci. U S A* 95, 9642–9647. doi: 10.1073/pnas.95.16.9642
- Cleveland, D. W., Hwo, S. Y., and Kirschner, M. W. (1977). Purification of tau, a microtubule-associated protein that induces assembly of microtubules from purified tubulin. *J. Mol. Biol.* 116, 207–225. doi: 10.1016/0022-2836(77)90213-3
- Cole, A. R., Causeret, F., Yadirgi, G., Hastie, C. J., McLaughlan, H., McManus, E. J., et al. (2006). Distinct priming kinases contribute to differential regulation of collapsin response mediator proteins by glycogen synthase kinase-3 *in vivo**. *J. Biol. Chem.* 281, 16591–16598. doi: 10.1074/jbc.M513344200
- Cole, A. R., Knebel, A., Morrice, N. A., Robertson, L. A., Irving, A. J., Connolly, C. N., et al. (2004). GSK-3 phosphorylation of the Alzheimer epitope within collapsin response mediator proteins regulates axon elongation in primary neurons. *J. Biol. Chem.* 279, 50176–50180. doi: 10.1074/jbc.C400412200
- Collins, M. O., Husi, H., Yu, L., Brandon, J. M., Anderson, C. N., Blackstock, W. P., et al. (2006). Molecular characterization and comparison of the components and multiprotein complexes in the postsynaptic proteome. *J. Neurochem.* 97, 16–23. doi: 10.1111/j.1471-4159.2005.03507.x
- Couégnas, A., Schweitzer, A., Andrieux, A., Ghandour, M. S., and Boehm, N. (2007). Expression pattern of STOP lacZ reporter gene in adult and developing mouse brain. *J. Neurosci. Res.* 85, 1515–1527. doi: 10.1002/jnr.21278
- Coumans, J. V., Palanisamy, S. K., McFarlane, J., and Moens, P. D. (2016). Proteomic and microscopic strategies towards the analysis of the cytoskeletal networks in major neuropsychiatric disorders. *Int. J. Mol. Sci.* 17:581. doi: 10.3390/ijms17040581
- Craft, G. E., Graham, M. E., Bache, N., Larsen, M. R., and Robinson, P. J. (2008). The *in vivo* phosphorylation sites in multiple isoforms of amphiphysin I from rat brain nerve terminals. *Mol. Cell Proteomics* 7, 1146–1161. doi: 10.1074/mcp.M700351-MCP200
- Cuveillier, C., Delaroché, J., Seggio, M., Gory-Faure, S., Bosc, C., Denarier, E., et al. (2020). MAP6 is an intraluminal protein that induces neuronal microtubules to coil. *Sci. Adv.* 6:eaz4344. doi: 10.1126/sciadv.aaz4344
- Dacheux, D., Landrein, N., Thonnus, M., Gilbert, G., Sahin, A., Wodrich, H., et al. (2012). A MAP6-related protein is present in protozoa and is involved in flagellum motility. *PLoS One* 7:e31344. doi: 10.1371/journal.pone.0031344
- Dacheux, D., Roger, B., Bosc, C., Landrein, N., Roche, E., Chansel, L., et al. (2015). Human FAM154A (SAXO1) is a microtubule-stabilizing protein specific to cilia and related structures. *J. Cell Sci.* 128, 1294–1307. doi: 10.1242/jcs.155143
- Daoust, A., Bohic, S., Saoudi, Y., Debacker, C., Gory-Faure, S., Andrieux, A., et al. (2014). Neuronal transport defects of the MAP6 KO mouse—a model of schizophrenia—and alleviation by Epithilone D treatment, as observed using MEMRI. *NeuroImage* 96, 133–142. doi: 10.1016/j.neuroimage.2014.03.071
- Davare, M. A., Dong, F., Rubin, C. S., and Hell, J. W. (1999). The A-kinase anchor protein MAP2B and cAMP-dependent protein kinase are associated with class C L-type calcium channels in neurons. *J. Biol. Chem.* 274, 30280–30287. doi: 10.1074/jbc.274.42.30280
- Davidkova, G., and Carroll, R. C. (2007). Characterization of the role of microtubule-associated protein 1B in metabotropic glutamate receptor-mediated endocytosis of AMPA receptors in hippocampus. *J. Neurosci.* 27, 13273–13278. doi: 10.1523/JNEUROSCI.3334-07.2007
- Davidson, C. A., Kuroki, N., Alvarado, J. L., Niznikiewicz, M. A., McCarley, R. W., and Levitt, J. J. (2012). An MRI study of septi pellucidi in relation to hippocampus volume and fornix integrity in schizophrenia. *Schizophr. Res.* 134, 165–170. doi: 10.1016/j.schres.2011.11.012
- De Peri, L., Crescini, A., Deste, G., Fusar-Poli, P., Sacchetti, E., and Vita, A. (2012). Brain structural abnormalities at the onset of schizophrenia and bipolar disorder: a meta-analysis of controlled magnetic resonance imaging studies. *Curr. Pharm. Des.* 18, 486–494. doi: 10.2174/138161212799316253
- Dehmelt, L., and Halpain, S. (2005). The MAP2/Tau family of microtubule-associated proteins. *Genome Biol.* 6:204. doi: 10.1186/gb-2004-6-1-204
- Delotterie, D., Ruiz, G., Brocard, J., Schweitzer, A., Roucard, C., Roche, Y., et al. (2010). Chronic administration of atypical antipsychotics improves behavioral and synaptic defects of STOP null mice. *Psychopharmacology* 208, 131–141. doi: 10.1007/s00213-009-1712-3
- Deloulme, J.-C., Gory-Fauré, S., Mauconduit, F., Chauvet, S., Jonckheere, J., Boulan, B., et al. (2015). Microtubule-associated protein 6 mediates neuronal connectivity through Semaphorin 3E-dependent signalling for axonal growth. *Nat. Commun.* 6:7246. doi: 10.1038/ncomms8246
- Delphin, C., Bouvier, D., Seggio, M., Couriol, E., Saoudi, Y., Denarier, E., et al. (2012). MAP6-F is a temperature sensor that directly binds to and protects microtubules from cold-induced depolymerization. *J. Biol. Chem.* 287, 35127–35138. doi: 10.1074/jbc.M112.398339
- Denarier, E., Aguezoul, M., Jolly, C., Vourc'h, C., Roure, A., Andrieux, A., et al. (1998a). Genomic structure and chromosomal mapping of the mouse STOP gene (Mtap6). *Biochem. Biophys. Res. Commun.* 243, 791–796. doi: 10.1006/bbrc.1998.8179
- Denarier, E., Forest-Lieuvin, A., Bosc, C., Pirollet, F., Chapel, A., Margolis, R. L., et al. (1998b). Nonneuronal isoforms of STOP protein are responsible for microtubule cold stability in mammalian fibroblasts. *Proc. Natl. Acad. Sci. U S A* 95, 6055–6060. doi: 10.1073/pnas.95.11.6055
- Dent, E. W., and Baas, P. W. (2014). Microtubules in neurons as information carriers. *J. Neurochem.* 129, 235–239. doi: 10.1111/jnc.12621
- Deo, R. C., Schmidt, E. F., Elhabazi, A., Togashi, H., Burley, S. K., and Strittmatter, S. M. (2004). Structural bases for CRMP function in plexin-dependent semaphorin3A signaling. *EMBO J.* 23, 9–22. doi: 10.1038/sj.emboj.7600021
- Ding, J., Valle, A., Allen, E., Wang, W., Nardine, T., Zhang, Y., et al. (2006). Microtubule-associated protein 8 contains two microtubule binding sites. *Biochem. Biophys. Res. Commun.* 339, 172–179. doi: 10.1016/j.bbrc.2005.10.199
- Dioli, C., Patrício, P., Trindade, R., Pinto, L. G., Silva, J. M., Morais, M., et al. (2017). Tau-dependent suppression of adult neurogenesis in the stressed hippocampus. *Mol. Psychiatry* 22, 1110–1118. doi: 10.1038/mp.2017.103
- Divinski, I., Mittelman, L., and Gozes, I. (2004). A femtomolar acting octapeptide interacts with tubulin and protects astrocytes against zinc intoxication. *J. Biol. Chem.* 279, 28531–28538. doi: 10.1074/jbc.M403197200
- Domire, J. S., Green, J. A., Lee, K. G., Johnson, A. D., Askwith, C. C., and Mykityn, K. (2011). Dopamine receptor 1 localizes to neuronal cilia in a dynamic process that requires the Bardet-Biedl syndrome proteins. *Cell. Mol. Life Sci.* 68, 2951–2960. doi: 10.1007/s00018-010-0603-4
- Douaud, G., Smith, S., Jenkinson, M., Behrens, T., Johansen-Berg, H., Vickers, J., et al. (2007). Anatomically related grey and white matter abnormalities in adolescent-onset schizophrenia. *Brain* 130, 2375–2386. doi: 10.1093/brain/awm184
- Dustrude, E. T., Moutal, A., Yang, X., Wang, Y., Khanna, M., and Khanna, R. (2016). Hierarchical CRMP2 posttranslational modifications control Nav1.7 function. *Proc. Natl. Acad. Sci. U S A* 113, E8443–E8452. doi: 10.1073/pnas.1610531113
- Eastwood, S. L., Lyon, L., George, L., Andrieux, A., Job, D., and Harrison, P. J. (2007). Altered expression of synaptic protein mRNAs

- in STOP (MAP6) mutant mice. *J. Psychopharmacol.* 21, 635–644. doi: 10.1177/0269881106068825
- Edgar, P. F., Douglas, J. E., Cooper, G. J., Dean, B., Kydd, R., and Faull, R. L. (2000). Comparative proteome analysis of the hippocampus implicates chromosome 6q in schizophrenia. *Mol. Psychiatry* 5, 85–90. doi: 10.1038/sj.mp.4000580
- Elie, A., Prezel, E., Guerin, C., Denarier, E., Ramirez-Rios, S., Serre, L., et al. (2015). Tau co-organizes dynamic microtubule and actin networks. *Sci. Rep.* 5:9964. doi: 10.1038/srep09964
- Emamzadeh, F. N. (2016). α -synuclein structure, functions, and interactions. *J. Res. Med. Sci.* 21:29. doi: 10.4103/1735-1995.181989
- Faller, E. M., Villeneuve, T. S., and Brown, D. L. (2009). MAP1a associated light chain 3 increases microtubule stability by suppressing microtubule dynamics. *Mol. Cell. Neurosci.* 41, 85–93. doi: 10.1016/j.mcn.2009.02.001
- Farah, C. A., Liazoghli, D., Perreault, S., Desjardins, M., Guimont, A., Anton, A., et al. (2005). Interaction of microtubule-associated protein-2 and p63: a new link between microtubules and rough endoplasmic reticulum membranes in neurons. *J. Biol. Chem.* 280, 9439–9449. doi: 10.1074/jbc.M412304200
- Farah, C. A., Perreault, S., Liazoghli, D., Desjardins, M., Anton, A., Lauzon, M., et al. (2006). Tau interacts with Golgi membranes and mediates their association with microtubules. *Cell Motil. Cytoskeleton* 63, 710–724. doi: 10.1002/cm.20157
- Findeisen, P., Muhlhausen, S., Dempewolf, S., Hertzog, J., Zietlow, A., Carlomagno, T., et al. (2014). Six subgroups and extensive recent duplications characterize the evolution of the eukaryotic tubulin protein family. *Genome Biol. Evol.* 6, 2274–2288. doi: 10.1093/gbe/evu187
- Fink, C. C., and Meyer, T. (2002). Molecular mechanisms of CaMKII activation in neuronal plasticity. *Curr. Opin. Neurobiol.* 12, 293–299. doi: 10.1016/s0959-4388(02)00327-6
- Fitzsimmons, J., Kubicki, M., Smith, K., Bushell, G., Estepar, R. S., Westin, C. F., et al. (2009). Diffusion tractography of the fornix in schizophrenia. *Schizophr. Res.* 107, 39–46. doi: 10.1016/j.schres.2008.10.022
- Föcking, M., Dicker, P., English, J. A., Schubert, K. O., Dunn, M. J., and Cotter, D. R. (2011). Common proteomic changes in the hippocampus in schizophrenia and bipolar disorder and particular evidence for involvement of cornu ammonis regions 2 and 3. *Arch. Gen. Psychiatry* 68, 477–488. doi: 10.1001/archgenpsychiatry.2011.43
- Fournet, V., de Lavilleon, G., Schweitzer, A., Giros, B., Andrieux, A., and Martres, M. P. (2012a). Both chronic treatments by epothilone D and fluoxetine increase the short-term memory and differentially alter the mood status of STOP/MAP6 KO mice. *J. Neurochem.* 123, 982–996. doi: 10.1111/jnc.12027
- Fournet, V., Jany, M., Fabre, V., Chali, F., Orsal, D., Schweitzer, A., et al. (2010). The deletion of the microtubule-associated STOP protein affects the serotonergic mouse brain network. *J. Neurochem.* 115, 1579–1594. doi: 10.1111/j.1471-4159.2010.07064.x
- Fournet, V., Schweitzer, A., Chevarin, C., Deloulme, J. C., Hamon, M., Giros, B., et al. (2012b). The deletion of STOP/MAP6 protein in mice triggers highly altered mood and impaired cognitive performances. *J. Neurochem.* 121, 99–114. doi: 10.1111/j.1471-4159.2011.07615.x
- Fradley, R. L., O'Meara, G. F., Newman, R. J., Andrieux, A., Job, D., and Reynolds, D. S. (2005). STOP knockout and NMDA NR1 hypomorphic mice exhibit deficits in sensorimotor gating. *Behav. Brain Res.* 163, 257–264. doi: 10.1016/j.bbr.2005.05.012
- Fukata, Y., Itoh, T. J., Kimura, T., Menager, C., Nishimura, T., Shiromizu, T., et al. (2002a). CRMP-2 binds to tubulin heterodimers to promote microtubule assembly. *Nat. Cell Biol.* 4, 583–591. doi: 10.1038/ncb825
- Fukata, Y., Kimura, T., and Kaibuchi, K. (2002b). Axon specification in hippocampal neurons. *Neurosci. Res.* 43, 305–315. doi: 10.1016/s0168-0102(02)00062-7
- Fukuyama, K., Kato, R., Murata, M., Shiroyama, T., and Okada, M. (2019). Clozapine normalizes a glutamatergic transmission abnormality induced by an impaired NMDA receptor in the thalamocortical pathway via the activation of a group III metabotropic glutamate receptor. *Biomolecules* 9:234. doi: 10.3390/biom9060234
- Galiano, M. R., Bosc, C., Schweitzer, A., Andrieux, A., Job, D., and Hallak, M. E. (2004). Astrocytes and oligodendrocytes express different STOP protein isoforms. *J. Neurosci. Res.* 78, 329–337. doi: 10.1002/jnr.20260
- Gardiner, J., Overall, R., and Marc, J. (2011). The microtubule cytoskeleton acts as a key downstream effector of neurotransmitter signaling. *Synapse* 65, 249–256. doi: 10.1002/syn.20841
- Garvalov, B. K., Zuber, B., Bouchet-Marquis, C., Kudryashev, M., Gruska, M., Beck, M., et al. (2006). Luminal particles within cellular microtubules. *J. Cell Biol.* 174, 759–765. doi: 10.1083/jcb.200606074
- Gimenez, U., Boulan, B., Mauconduit, F., Taurel, F., Leclercq, M., Denarier, E., et al. (2017). 3D imaging of the brain morphology and connectivity defects in a model of psychiatric disorders: MAP6-KO mice. *Sci. Rep.* 7:10308. doi: 10.1038/s41598-017-10544-2
- Gleeson, J. G., Lin, P. T., Flanagan, L. A., and Walsh, C. A. (1999). Doublecortin is a microtubule-associated protein and is expressed widely by migrating neurons. *Neuron* 23, 257–271. doi: 10.1016/s0896-6273(00)80778-3
- Gong, X., Tan, M., Gao, Y., Chen, K., and Guo, G. (2016). CRMP-5 interacts with actin to regulate neurite outgrowth. *Mol. Med. Rep.* 13, 1179–1185. doi: 10.3892/mmr.2015.4662
- Gonzalez-Billault, C., Avila, J., and Cáceres, A. (2001). Evidence for the role of MAP1B in axon formation. *Mol. Biol. Cell* 12, 2087–2098. doi: 10.1091/mbc.12.7.2087
- Gory-Fauré, S., Windscheid, V., Bosc, C., Peris, L., Proietto, D., Franck, R., et al. (2006). STOP-like protein 21 is a novel member of the STOP family, revealing a Golgi localization of STOP proteins. *J. Biol. Chem.* 281, 28387–28396. doi: 10.1074/jbc.M603380200
- Gory-Fauré, S., Windscheid, V., Brocard, J., Montessuit, S., Tsutsumi, R., Denarier, E., et al. (2014). Non-microtubular localizations of microtubule-associated protein 6 (MAP6). *PLoS One* 9:e114905. doi: 10.1371/journal.pone.0114905
- Goshima, Y., Nakamura, F., Strittmatter, P., and Strittmatter, S. M. (1995). Collapse-induced growth cone collapse mediated by an intracellular protein related to UNC-33. *Nature* 376, 509–514. doi: 10.1038/376509a0
- Gozes, I. (2011). Microtubules, schizophrenia and cognitive behavior: preclinical development of davunetide (NAP) as a peptide-drug candidate. *Peptides* 32, 428–431. doi: 10.1016/j.peptides.2010.10.030
- Gozes, I., and Divinski, I. (2007). NAP, a neuroprotective drug candidate in clinical trials, stimulates microtubule assembly in the living cell. *Curr. Alzheimer Res.* 4, 507–509. doi: 10.2174/156720507783018208
- Greaves, J., and Chamberlain, L. H. (2011). DHHC palmitoyl transferases: substrate interactions and (patho)physiology. *Trends Biochem. Sci.* 36, 245–253. doi: 10.1016/j.tibs.2011.01.003
- Griffith, L. M., and Pollard, T. D. (1982). Cross-linking of actin filament networks by self-association and actin-binding macromolecules. *J. Biol. Chem.* 257, 9135–9142. doi: 10.1016/s0021-9258(18)34253-4
- Grossman, S. D., Futter, M., Snyder, G. L., Allen, P. B., Nairn, A. C., Greengard, P., et al. (2004). Spinophilin is phosphorylated by Ca^{2+} /calmodulin-dependent protein kinase II resulting in regulation of its binding to F-actin. *J. Neurochem.* 90, 317–324. doi: 10.1111/j.1471-4159.2004.02491.x
- Gu, Y., Jukkola, P., Wang, Q., Esparza, T., Zhao, Y., Brody, D., et al. (2017). Polarity of varicosity initiation in central neuron mechanosensation. *J. Cell Biol.* 216, 2179–2199. doi: 10.1083/jcb.201606065
- Guillaud, L., Bosc, C., Fourest-Lieuvain, A., Denarier, E., Pirollet, F., Lafanechere, L., et al. (1998). STOP proteins are responsible for the high degree of microtubule stabilization observed in neuronal cells. *J. Cell Biol.* 142, 167–179. doi: 10.1083/jcb.142.1.167
- Hacohen-Kleiman, G., Sragovich, S., Karmon, G., Gao, A. Y. L., Grigg, I., Pasmanik-Chor, M., et al. (2018). Activity-dependent neuroprotective protein deficiency models synaptic and developmental phenotypes of autism-like syndrome. *J. Clin. Invest.* 128, 4956–4969. doi: 10.1172/JCI98199
- Hamdan, H., Lim, B. C., Torii, T., Joshi, A., Konning, M., Smith, C., et al. (2020). Mapping axon initial segment structure and function by multiplexed proximity biotinylation. *Nat. Commun.* 11:100. doi: 10.1038/s41467-019-13658-5
- Harada, A., Oguchi, K., Okabe, S., Kuno, J., Terada, S., Ohshima, T., et al. (1994). Altered microtubule organization in small-calibre axons of mice lacking tau protein. *Nature* 369, 488–491. doi: 10.1038/369488a0
- Hausrat, T. J., Radwitz, J., Lombino, F. L., Breiden, P., and Kneussel, M. (2020). α - and β -tubulin isoforms are differentially expressed during brain development. *Dev. Neurobiol.* doi: 10.1002/dneu.22745. [Epub ahead of print].

- Hayashi, M. A., Portaro, F. C., Bastos, M. F., Guerreiro, J. R., Oliveira, V., Gorrao, S. S., et al. (2005). Inhibition of NUDEL (nuclear distribution element-like)-oligopeptidase activity by disrupted-in-schizophrenia 1. *Proc. Natl. Acad. Sci. U S A* 102, 3828–3833. doi: 10.1073/pnas.0500330102
- Hedgecock, E. M., Culotti, J. G., Thomson, J. N., and Perkins, L. A. (1985). Axonal guidance mutants of *Caenorhabditis elegans* identified by filling sensory neurons with fluorescein dyes. *Dev. Biol.* 111, 158–170. doi: 10.1016/0012-1606(85)90443-9
- Hensley, K., and Kursula, P. (2016). Collapsin response mediator protein-2 (CRMP2) is a plausible etiological factor and potential therapeutic target in Alzheimer's disease: comparison and contrast with microtubule-associated protein tau. *J. Alzheimers Dis.* 53, 1–14. doi: 10.3233/JAD-160076
- Hensley, K., Venkova, K., Christov, A., Gunning, W., and Park, J. (2011). Collapsin response mediator protein-2: an emerging pathologic feature and therapeutic target for neurodegeneration indications. *Mol. Neurobiol.* 43, 180–191. doi: 10.1007/s12035-011-8166-4
- Hernández-Vega, A., Braun, M., Scharrel, L., Jahnel, M., Wegmann, S., Hyman, B. T., et al. (2017). Local nucleation of microtubule bundles through tubulin concentration into a condensed tau phase. *Cell Rep.* 20, 2304–2312. doi: 10.1016/j.celrep.2017.08.042
- Herzog, W., and Weber, K. (1978). Fractionation of brain microtubule-associated proteins. Isolation of two different proteins which stimulate tubulin polymerization *in vitro*. *Eur. J. Biochem.* 92, 1–8. doi: 10.1111/j.1432-1033.1978.tb12716.x
- Huber, G., and Matus, A. (1984). Differences in the cellular distributions of two microtubule-associated proteins, MAP1 and MAP2, in rat brain. *J. Neurosci.* 4, 151–160. doi: 10.1523/JNEUROSCI.04-01.00151.1984
- Ikegami, S., Harada, A., and Hirokawa, N. (2000). Muscle weakness, hyperactivity and impairment in fear conditioning in tau-deficient mice. *Neurosci. Lett.* 279, 129–132. doi: 10.1016/S0304-3940(99)00964-7
- Inaba, H., Yamamoto, T., Iwasaki, T., Kabir, A. M. R., Kakugo, A., Sada, K., et al. (2019). Stabilization of microtubules by encapsulation of the GFP using a Tau-derived peptide. *Chem. Commun.* 55, 9072–9075. doi: 10.1039/c9cc04345d
- Ivashko-Pachima, Y., and Gozes, I. (2019). A novel microtubule-tau association enhancer and neuroprotective drug candidate: Ac-SKIP. *Front. Cell. Neurosci.* 13:435. doi: 10.3389/fncel.2019.00435
- Ivashko-Pachima, Y., Maor-Nof, M., and Gozes, I. (2019). NAP (davunetide) preferential interaction with dynamic 3-repeat Tau explains differential protection in selected tauopathies. *PLoS One* 14:e0213666. doi: 10.1371/journal.pone.0213666
- Ivashko-Pachima, Y., Sayas, C. L., Malishkevich, A., and Gozes, I. (2017). ADNP/NAP dramatically increase microtubule end-binding protein-Tau interaction: a novel avenue for protection against tauopathy. *Mol. Psychiatry* 22, 1335–1344. doi: 10.1038/mp.2016.255
- Iwanaga, T., Hozumi, Y., and Takahashi-Iwanaga, H. (2011). Immunohistochemical demonstration of dopamine receptor D2R in the primary cilia of the mouse pituitary gland. *Biomed. Res.* 32, 225–235. doi: 10.2220/biomedres.32.225
- Jacobs, S., Lie, D. C., DeCicco, K. L., Shi, Y., DeLuca, L. M., Gage, F. H., et al. (2006). Retinoic acid is required early during adult neurogenesis in the dentate gyrus. *Proc. Natl. Acad. Sci. U S A* 103, 3902–3907. doi: 10.1073/pnas.0511294103
- Jiang, T., Zhang, G., Liang, Y., Cai, Z., Liang, Z., Lin, H., et al. (2020). PlexinA3 interacts with CRMP2 to mediate sema3A signalling during dendritic growth in cultured cerebellar granule neurons. *Neuroscience* 434, 83–92. doi: 10.1016/j.neuroscience.2020.02.008
- Job, D., Fischer, E. H., and Margolis, R. L. (1981). Rapid disassembly of cold-stable microtubules by calmodulin. *Proc. Natl. Acad. Sci. U S A* 78, 4679–4682. doi: 10.1073/pnas.78.8.4679
- Job, D., Rauch, C. T., Fischer, E. H., and Margolis, R. L. (1982). Recycling of cold-stable microtubules: evidence that cold stability is due to substoichiometric polymer blocks. *Biochemistry* 21, 509–515. doi: 10.1021/bi00532a015
- Job, D., Rauch, C. T., and Margolis, R. L. (1987). High concentrations of STOP protein induce a microtubule super-stable state. *Biochem. Biophys. Res. Commun.* 148, 429–434. doi: 10.1016/0006-291x(87)91129-6
- Jonckheere, J., Deloulme, J.-C., Dall'Igna, G., Chauhac, N., Pelluet, A., Nguon, A.-S., et al. (2018). Short- and long-term efficacy of electroconvulsive stimulation in animal models of depression: the essential role of neuronal survival. *Brain Stimul.* 11, 1336–1347. doi: 10.1016/j.brs.2018.08.001
- Jones, C., Watson, D., and Fone, K. (2011). Animal models of schizophrenia: animal models of schizophrenia. *Br. J. Pharmacol.* 164, 1162–1194. doi: 10.1111/j.1476-5381.2011.01386.x
- Joseph, B., Narayanaswamy, J. C., and Venkatasubramanian, G. (2015). Insight in schizophrenia: relationship to positive, negative and neurocognitive dimensions. *Indian J. Psychol. Med.* 37, 5–11. doi: 10.4103/0253-7176.150797
- Kadavath, H., Hofele, R. V., Biernat, J., Kumar, S., Tepper, K., Urlaub, H., et al. (2015). Tau stabilizes microtubules by binding at the interface between tubulin heterodimers. *Proc. Natl. Acad. Sci. U S A* 112, 7501–7506. doi: 10.1073/pnas.1504081112
- Kapitein, L. C., Yau, K. W., Gouveia, S. M., van der Zwan, W. A., Wulf, P. S., Keijzer, N., et al. (2011). NMDA receptor activation suppresses microtubule growth and spine entry. *J. Neurosci.* 31, 8194–8209. doi: 10.1523/JNEUROSCI.6215-10.2011
- Kapur, S. (2003). Psychosis as a state of aberrant salience: a framework linking biology, phenomenology, and pharmacology in schizophrenia. *Am. J. Psychiatry* 160, 13–23. doi: 10.1176/appi.ajp.160.1.13
- Kar, S., Fan, J., Smith, M. J., Goedert, M., and Amos, L. A. (2003). Repeat motifs of tau bind to the insides of microtubules in the absence of taxol. *EMBO J.* 22, 70–77. doi: 10.1093/emboj/cdg001
- Kawano, Y., Yoshimura, T., Tsuboi, D., Kawabata, S., Kaneko-Kawano, T., Shirataki, H., et al. (2005). CRMP-2 is involved in kinesin-1-dependent transport of the Sra-1/WAVE1 complex and axon formation. *Mol. Cell. Biol.* 25, 9920–9935. doi: 10.1128/MCB.25.22.9920-9935.2005
- Kedracka-Krok, S., Swiderska, B., Jankowska, U., Skupien-Rabian, B., Solich, J., Buczak, K., et al. (2015). Clozapine influences cytoskeleton structure and calcium homeostasis in rat cerebral cortex and has a different proteomic profile than risperidone. *J. Neurochem.* 132, 657–676. doi: 10.1111/jnc.13007
- Kellogg, E. H., Hejab, N. M. A., Poepsel, S., Downing, K. H., DiMaio, F., and Nogales, E. (2018). Near-atomic model of microtubule-tau interactions. *Science* 360, 1242–1246. doi: 10.1126/science.aat1780
- Kendi, M., Kendi, A. T. K., Lehericy, S., Ducros, M., Lim, K. O., Ugurbil, K., et al. (2008). Structural and diffusion tensor imaging of the fornix in childhood- and adolescent-onset schizophrenia. *J. Am. Acad. Child Adolesc. Psychiatry* 47, 826–832. doi: 10.1097/CHI.0b013e318172ef36
- Khazaei, M. R., Girouard, M. P., Alchini, R., Ong Tone, S., Shimada, T., Bechstedt, S., et al. (2014). Collapsin response mediator protein 4 regulates growth cone dynamics through the actin and microtubule cytoskeleton. *J. Biol. Chem.* 289, 30133–30143. doi: 10.1074/jbc.M114.570440
- Kirima, J., and Oiwa, K. (2018). Flagellar-associated Protein FAP85 is a microtubule inner protein that stabilizes microtubules. *Cell Struct. Funct.* 43, 1–14. doi: 10.1247/csf.17023
- Koide, T., Aleksic, B., Ito, Y., Usui, H., Yoshimi, A., Inada, T., et al. (2010). A two-stage case-control association study of the dihydropyrimidinase-like 2 gene (DPYSL2) with schizophrenia in Japanese subjects. *J. Hum. Genet.* 55, 469–472. doi: 10.1038/jhg.2010.38
- Kolman, A. (2004). BMS-310705 bristol-myers squibb/GBF. *Curr. Opin. Investig. Drugs* 5, 1292–1297.
- Lacroix, B., van Dijk, J., Gold, N. D., Guizzetti, J., Aldrian-Herrada, G., Rogowski, K., et al. (2010). Tubulin polyglutamylation stimulates spastin-mediated microtubule severing. *J. Cell Biol.* 189, 945–954. doi: 10.1083/jcb.201001024
- Lai, M., Wang, F., Rohan, J. G., Maeno-Hikichi, Y., Chen, Y., Zhou, Y., et al. (2005). A tctex1-Ca²⁺ channel complex for selective surface expression of Ca²⁺ channels in neurons. *Nat. Neurosci.* 8, 435–442. doi: 10.1038/nn1418
- Lasser, M., Tiber, J., and Lowery, L. A. (2018). The role of the microtubule cytoskeleton in neurodevelopmental disorders. *Front. Cell. Neurosci.* 12:165. doi: 10.3389/fncel.2018.00165
- Leaf, A., and Von Zastrow, M. (2015). Dopamine receptors reveal an essential role of IFT-B, KIF17 and Rab23 in delivering specific receptors to primary cilia. *Elife* 4:e06996. doi: 10.7554/eLife.06996

- Lee, J. C., Frigon, R. P., and Timasheff, S. N. (1975). Structural stability of calf brain microtubule protein. *Ann. N Y Acad. Sci.* 253, 284–291. doi: 10.1111/j.1749-6632.1975.tb19207.x
- Lee, J. H., and Gleeson, J. G. (2010). The role of primary cilia in neuronal function. *Neurobiol. Dis.* 38, 167–172. doi: 10.1016/j.nbd.2009.12.022
- Lee, H., Joo, J., Nah, S. S., Kim, J. W., Kim, H. K., Kwon, J. T., et al. (2015). Changes in Dpysl2 expression are associated with prenatally stressed rat offspring and susceptibility to schizophrenia in humans. *Int. J. Mol. Med.* 35, 1574–1586. doi: 10.3892/ijmm.2015.2161
- Lee, S.-H., Kubicki, M., Asami, T., Seidman, L. J., Goldstein, J. M., Meshulam-Gately, R. I., et al. (2013). Extensive white matter abnormalities in patients with first-episode schizophrenia: a diffusion tensor imaging (DTI) study. *Schizophr. Res.* 143, 231–238. doi: 10.1016/j.schres.2012.11.029
- Leenders, A. G., Lin, L., Huang, L.-D., Gerwin, C., Lu, P. H., and Sheng, Z. H. (2008). The role of MAP1A light chain 2 in synaptic surface retention of Cav2.2 channels in hippocampal neurons. *J. Neurosci.* 28, 11333–11346. doi: 10.1523/JNEUROSCI.3078-08.2008
- Lefevre, J., Savarin, P., Gans, P., Hamon, L., Clement, M. J., David, M. O., et al. (2013). Structural basis for the association of MAP6 protein with microtubules and its regulation by calmodulin. *J. Biol. Chem.* 288, 24910–24922. doi: 10.1074/jbc.M113.457267
- Lei, P., Ayton, S., Finkelstein, D. I., Spoerri, L., Ciccotosto, G. D., Wright, D. K., et al. (2012). Tau deficiency induces parkinsonism with dementia by impairing APP-mediated iron export. *Nat. Med.* 18, 291–295. doi: 10.1038/nm.2613
- Lemonidis, K., Sanchez-Perez, M. C., and Chamberlain, L. H. (2015). Identification of a novel sequence motif recognized by the ankyrin repeat domain of zDHHC17/13 S-acyltransferases. *J. Biol. Chem.* 290, 21939–21950. doi: 10.1074/jbc.M115.657668
- Li, Y., and Black, M. (1996). Microtubule assembly and turnover in growing axons. *J. Neurosci.* 16, 531–544. doi: 10.1523/JNEUROSCI.16-02-00531.1996
- Lim, R. W., and Halpain, S. (2000). Regulated association of microtubule-associated protein 2 (MAP2) with Src and Grb2: evidence for MAP2 as a scaffolding protein. *J. Biol. Chem.* 275, 20578–20587. doi: 10.1074/jbc.M001887200
- Lin, P.-C., Chan, P. M., Hall, C., and Manser, E. (2011). Collapsin response mediator proteins (CRMPs) are a new class of microtubule-associated protein (MAP) that selectively interacts with assembled microtubules via a taxol-sensitive binding interaction. *J. Biol. Chem.* 286, 41466–41478. doi: 10.1074/jbc.M111.283580
- Liu, Y. F., Sowell, S. M., Luo, Y., Chaubey, A., Cameron, R. S., Kim, H. G., et al. (2015). Autism and intellectual disability-associated KIRREL3 interacts with neuronal proteins MAPIB and MYO16 with potential roles in neurodevelopment. *PLoS One* 10:e0123106. doi: 10.1371/journal.pone.0123106
- Luck, D., Malla, A. K., Joobar, R., and Lepage, M. (2010). Disrupted integrity of the fornix in first-episode schizophrenia. *Schizophr. Res.* 119, 61–64. doi: 10.1016/j.schres.2010.03.027
- Ma, Q.-L., Zuo, X., Yang, F., Ubeda, O. J., Gant, D. J., Alaverdyan, M., et al. (2014). Loss of MAP function leads to hippocampal synapse loss and deficits in the Morris Water Maze with aging. *J. Neurosci.* 34, 7124–7136. doi: 10.1523/JNEUROSCI.3439-13.2014
- Maden, M. (2007). Retinoic acid in the development, regeneration and maintenance of the nervous system. *Nat. Rev. Neurosci.* 8, 755–765. doi: 10.1038/nrn2212
- Marchisella, F., Coffey, E. T., and Hollos, P. (2016). Microtubule and microtubule associated protein anomalies in psychiatric disease. *Cytoskeleton* 73, 596–611. doi: 10.1002/cm.21300
- Margolis, R. L., and Rauch, C. T. (1981). Characterization of rat brain crude extract microtubule assembly: correlation of cold stability with the phosphorylation state of a microtubule-associated 64K protein. *Biochemistry* 20, 4451–4458. doi: 10.1021/bi00518a033
- Margolis, R. L., Rauch, C. T., and Job, D. (1986). Purification and assay of cold-stable microtubules and STOP protein. *Methods Enzymol.* 134, 160–170. doi: 10.1016/0076-6879(86)34085-0
- Margolis, R. L., Rauch, C. T., Pirollet, F., and Job, D. (1990). Specific association of STOP protein with microtubules *in vitro* and with stable microtubules in mitotic spindles of cultured cells. *EMBO J.* 9, 4095–4102. doi: 10.1002/j.1460-2075.1990.tb07631.x
- Marley, A., and von Zastrow, M. (2010). DISC1 regulates primary cilia that display specific dopamine receptors. *PLoS One* 5:e10902. doi: 10.1371/journal.pone.0010902
- Martins-de-Souza, D., Gattaz, W. F., Schmitt, A., Rewerts, C., Maccarrone, G., Dias-Neto, E., et al. (2009). Prefrontal cortex shotgun proteome analysis reveals altered calcium homeostasis and immune system imbalance in schizophrenia. *Eur. Arch. Psychiatry Clin. Neurosci.* 259, 151–163. doi: 10.1007/s00406-008-0847-2
- McCarley, R. W., Wible, C. G., Frumin, M., Hirayasu, Y., Levitt, J. J., Fischer, I. A., et al. (1999). MRI anatomy of schizophrenia. *Biol. Psychiatry* 45, 1099–1119. doi: 10.1016/s0006-3223(99)00018-9
- Merenlender-Wagner, A., Malishkevich, A., Shemer, Z., Udawela, M., Gibbons, A., Scarr, E., et al. (2015). Autophagy has a key role in the pathophysiology of schizophrenia. *Mol. Psychiatry* 20, 126–132. doi: 10.1038/mp.2013.174
- Merenlender-Wagner, A., Pikman, R., Giladi, E., Andrieux, A., and Gozes, I. (2010). NAP (davunetide) enhances cognitive behavior in the STOP heterozygous mouse—a microtubule-deficient model of schizophrenia. *Peptides* 31, 1368–1373. doi: 10.1016/j.peptides.2010.04.011
- Merenlender-Wagner, A., Shemer, Z., Touloumi, O., Lagoudaki, R., Giladi, E., Andrieux, A., et al. (2014). New horizons in schizophrenia treatment: autophagy protection is coupled with behavioral improvements in a mouse model of schizophrenia. *Autophagy* 10, 2324–2332. doi: 10.4161/15548627.2014.984274
- Mishra, S., Kelly, K. K., Rumian, N. L., and Siegenthaler, J. A. (2018). Retinoic acid is required for neural stem and progenitor cell proliferation in the adult hippocampus. *Stem Cell Reports* 10, 1705–1720. doi: 10.1016/j.stemcr.2018.04.024
- Mitchison, T., and Kirschner, M. (1984). Dynamic instability of microtubule growth. *Nature* 312, 237–242. doi: 10.1038/312237a0
- Mohan, R., and John, A. (2015). Microtubule-associated proteins as direct crosslinkers of actin filaments and microtubules. *IUBMB Life* 67, 395–403. doi: 10.1002/iub.1384
- Monroy, B. Y., Tan, T. C., Oclaman, J. M., Han, J. S., Simo, S., Niwa, S., et al. (2020). A combinatorial MAP code dictates polarized microtubule transport. *Dev. Cell* 53, 60.e4–72.e4. doi: 10.1016/j.devcel.2020.01.029
- Morderer, D., Nikolaienko, O., Skrypikina, I., Cherkas, V., Tsyba, L., Belan, P., et al. (2012). Endocytic adaptor protein intersectin 1 forms a complex with microtubule stabilizer STOP in neurons. *Gene* 505, 360–364. doi: 10.1016/j.gene.2012.06.061
- Morita, T., and Sobue, K. (2009). Specification of neuronal polarity regulated by local translation of CRMP2 and Tau via the mTOR-p70S6K pathway. *J. Biol. Chem.* 284, 27734–27745. doi: 10.1074/jbc.M109.008177
- Morris, J. A., Kandpal, G., Ma, L., and Austin, C. P. (2003). DISC1 (Disrupted-In-Schizophrenia 1) is a centrosome-associated protein that interacts with MAP1A, MIPT3, ATF4/5 and NUDEL: regulation and loss of interaction with mutation. *Hum. Mol. Genet.* 12, 1591–1608. doi: 10.1093/hmg/ddg162
- Morris, M., Maeda, S., Vossel, K., and Mucke, L. (2011). The many faces of tau. *Neuron* 70, 410–426. doi: 10.1016/j.neuron.2011.04.009
- Moutin, M.-J., Bosc, C., Peris, L., and Andrieux, A. (2020). Tubulin post-translational modifications control neuronal development and functions. *Dev. Neurobiol.* doi: 10.1002/dneu.22774 [Epub ahead of print].
- Müller, C. S., Haupt, A., Bildl, W., Schindler, J., Knaus, H. G., Meissner, M., et al. (2010). Quantitative proteomics of the Cav2 channel nano-environments in the mammalian brain. *Proc. Natl. Acad. Sci. U S A* 107, 14950–14957. doi: 10.1073/pnas.1005940107
- Muñoz-Estrada, J., Lora-Castellanos, A., Meza, I., Alarcón Elizalde, S., and Benítez-King, G. (2018). Primary cilia formation is diminished in schizophrenia and bipolar disorder: a possible marker for these psychiatric diseases. *Schizophr. Res.* 195, 412–420. doi: 10.1016/j.schres.2017.08.055
- Munton, R. P., Tweedie-Cullen, R., Livingstone-Zatchej, M., Weinandy, F., Waidelich, M., Longo, D., et al. (2007). Qualitative and quantitative analyses of protein phosphorylation in naive and stimulated mouse synaptosomal preparations. *Mol. Cell. Proteomics* 6, 283–293. doi: 10.1074/mcp.M600046-MCP200

- Nakata, K., and Ujike, H. (2004). [The human dihydropyrimidinase-related protein 2 (DRP-2) gene on chromosome 8p21 is associated with paranoid-type schizophrenia]. *Nihon Shinkei Seishin Yakurigaku Zasshi* 24, 33–37.
- Nakata, K., Ujike, H., Sakai, A., Takaki, M., Imamura, T., Tanaka, Y., et al. (2003). The human dihydropyrimidinase-related protein 2 gene on chromosome 8p21 is associated with paranoid-type schizophrenia. *Biol. Psychiatry* 53, 571–576. doi: 10.1016/s0006-3223(02)01729-8
- Niisato, E., Nagai, J., Yamashita, N., Abe, T., Kiyonari, H., Goshima, Y., et al. (2012). CRMP4 suppresses apical dendrite bifurcation of CA1 pyramidal neurons in the mouse hippocampus. *Dev. Neurobiol.* 72, 1447–1457. doi: 10.1002/dneu.22007
- Niisato, E., Nagai, J., Yamashita, N., Nakamura, F., Goshima, Y., and Ohshima, T. (2013). Phosphorylation of CRMP2 is involved in proper bifurcation of the apical dendrite of hippocampal CA1 pyramidal neurons. *Dev. Neurobiol.* 73, 142–151. doi: 10.1002/dneu.22048
- Nishimura, T., Fukata, Y., Kato, K., Yamaguchi, T., Matsuura, Y., Kamiguchi, H., et al. (2003). CRMP-2 regulates polarized Numb-mediated endocytosis for axon growth. *Nat. Cell Biol.* 5, 819–826. doi: 10.1038/ncb1039
- Niwa, S., Nakamura, F., Tomabechi, Y., Aoki, M., Shigematsu, H., Matsumoto, T., et al. (2017). Structural basis for CRMP2-induced axonal microtubule formation. *Sci. Rep.* 7:10681. doi: 10.1038/s41598-017-11031-4
- Okabe, S., and Hirokawa, N. (1990). Turnover of fluorescently labelled tubulin and actin in the axon. *Nature* 343, 479–482. doi: 10.1038/343479a0
- Oliveira da Silva, M. I., and Liz, M. A. (2020). Linking α -synuclein to the actin cytoskeleton: consequences to neuronal function. *Front. Cell Dev. Biol.* 8:787. doi: 10.3389/fcell.2020.00787
- Owa, M., Uchihashi, T., Yanagisawa, H. A., Yamano, T., Iguchi, H., Fukuzawa, H., et al. (2019). Inner lumen proteins stabilize doublet microtubules in cilia and flagella. *Nat. Commun.* 10:1143. doi: 10.1038/s41467-019-09051-x
- Oz, S., Kapitanov, O., Ivashco-Pachima, Y., Malishkevich, A., Giladi, E., Skalka, N., et al. (2014). The NAP motif of activity-dependent neuroprotective protein (ADNP) regulates dendritic spines through microtubule end binding proteins. *Mol. Psychiatry* 19, 1115–1124. doi: 10.1038/mp.2014.97
- Ozer, R. S., and Halpain, S. (2000). Phosphorylation-dependent localization of microtubule-associated protein MAP2c to the actin cytoskeleton. *Mol. Biol. Cell* 11, 3573–3587. doi: 10.1091/mbc.11.10.3573
- Pabion, M., Job, D., and Margolis, R. L. (1984). Sliding of STOP proteins on microtubules. *Biochemistry* 23, 6642–6648. doi: 10.1021/bi00321a055
- Palenzuela, R., Gutiérrez, Y., Draffin, J. E., Lario, A., Benoist, M., and Esteban, J. A. (2017). MAPIB light chain modulates synaptic transmission via AMPA receptor intracellular trapping. *J. Neurosci.* 37, 9945–9963. doi: 10.1523/JNEUROSCI.0505-17.2017
- Pamula, M. C., Ti, S.-C., and Kapoor, T. M. (2016). The structured core of human β tubulin confers isotype-specific polymerization properties. *J. Cell Biol.* 213, 425–433. doi: 10.1083/jcb.201603050
- Panda, D., Miller, H. P., Banerjee, A., Ludueña, R. F., and Wilson, L. (1994). Microtubule dynamics *in vitro* are regulated by the tubulin isotype composition. *Proc. Natl. Acad. Sci. U S A* 91, 11358–11362. doi: 10.1073/pnas.91.24.11358
- Park, S. M., Liu, G., Kubal, A., Fury, M., Cao, L., and Marx, S. O. (2004). Direct interaction between BKCa potassium channel and microtubule-associated protein 1A. *FEBS Lett.* 570, 143–148. doi: 10.1016/j.febslet.2004.06.037
- Paul, D. M., Mantell, J., Borucu, U., Coombs, J., SurrIDGE, K. J., Squire, J. M., et al. (2020). In situ cryo-electron tomography reveals filamentous actin within the microtubule lumen. *J. Cell Biol.* 219:e201911154. doi: 10.1083/jcb.2019.11154
- Pedrotti, B., Colombo, R., and Islam, K. (1994). Interactions of microtubule-associated protein MAP2 with unpolymerized and polymerized tubulin and actin using a 96-well microtiter plate solid-phase immunoassay. *Biochemistry* 33, 8798–8806. doi: 10.1021/bi00195a023
- Peng, J., Kim, M. J., Cheng, D., Duong, D. M., Gygi, S. P., and Sheng, M. (2004). Semiquantitative proteomic analysis of rat forebrain postsynaptic density fractions by mass spectrometry. *J. Biol. Chem.* 279, 21003–21011. doi: 10.1074/jbc.M400103200
- Peris, L., Bisbal, M., Martínez-Hernández, J., Saoudi, Y., Jonckheere, J., Rolland, M., et al. (2018). A key function for microtubule-associated-protein 6 in activity-dependent stabilisation of actin filaments in dendritic spines. *Nat. Commun.* 9:3775. doi: 10.1038/s41467-018-05869-z
- Pirollet, F., Derancourt, J., Haiech, J., Job, D., and Margolis, R. L. (1992a). Ca^{2+} -calmodulin regulated effectors of microtubule stability in bovine brain. *Biochemistry* 31, 8849–8855. doi: 10.1021/bi00152a022
- Pirollet, F., Job, D., Fischer, E. H., and Margolis, R. L. (1983). Purification and characterization of sheep brain cold-stable microtubules. *Proc. Natl. Acad. Sci. U S A* 80, 1560–1564. doi: 10.1073/pnas.80.6.1560
- Pirollet, F., Margolis, R. L., and Job, D. (1992b). Ca^{2+} -calmodulin regulated effectors of microtubule stability in neuronal tissues. *Biochim. Biophys. Acta* 1160, 113–119. doi: 10.1016/0167-4838(92)90044-e
- Pirollet, F., Rauch, C. T., Job, D., and Margolis, R. L. (1989). Monoclonal antibody to microtubule-associated STOP protein: affinity purification of neuronal STOP activity and comparison of antigen with activity in neuronal and nonneuronal cell extracts. *Biochemistry* 28, 835–842. doi: 10.1021/bi00428a064
- Portran, D., Schaedel, L., Xu, Z., Thery, M., and Nachury, M. V. (2017). Tubulin acetylation protects long-lived microtubules against mechanical ageing. *Nat. Cell Biol.* 19, 391–398. doi: 10.1038/ncb3481
- Powell, K. J., Hori, S. E., Leslie, R., Andrieux, A., Schellinck, H., Thorne, M., et al. (2007). Cognitive impairments in the STOP null mouse model of schizophrenia. *Behav. Neurosci.* 121, 826–835. doi: 10.1037/0735-7044.121.5.826
- Proffitt, M. F., Deurveilher, S., Robertson, G. S., Rusak, B., and Semba, K. (2016). Disruptions of sleep/wake patterns in the stable tubule only polypeptide (STOP) null mouse model of schizophrenia. *Schizophr. Bull.* 42, 1207–1215. doi: 10.1093/schbul/sbw017
- Qiang, L., Sun, X., Austin, T. O., Muralidharan, H., Jean, D. C., Liu, M., et al. (2018). Tau does not stabilize axonal microtubules but rather enables them to have long labile domains. *Curr. Biol.* 28, 2181.e4–2189.e4. doi: 10.1016/j.cub.2018.05.045
- Quach, T. T., Honnorat, J., Kolattukudy, P. E., Khanna, R., and Duchemin, A. M. (2015). CRMPs: critical molecules for neurite morphogenesis and neuropsychiatric diseases. *Mol. Psychiatry* 20, 1037–1045. doi: 10.1038/mp.2015.77
- Quach, T. T., Massicotte, G., Belin, M. F., Honnorat, J., Gaspard, E. R., Devries, A. C., et al. (2008). CRMP3 is required for hippocampal CA1 dendritic organization and plasticity. *FASEB J.* 22, 401–409. doi: 10.1096/fj.07-9012com
- Quach, T. T., Wang, Y., Khanna, R., Chounlamountri, N., Auvergnon, N., Honnorat, J., et al. (2011). Effect of CRMP3 expression on dystrophic dendrites of hippocampal neurons. *Mol. Psychiatry* 16, 689–691. doi: 10.1038/mp.2011.6
- Quach, T. T., Wilson, S. M., Rogemond, V., Chounlamountri, N., Kolattukudy, P. E., Martinez, S., et al. (2013). Mapping CRMP3 domains involved in dendrite morphogenesis and voltage-gated calcium channel regulation. *J. Cell Sci.* 126, 4262–4273. doi: 10.1242/jcs.131409
- Quednow, B. B., Csomor, P. A., Chmiel, J., Beck, T., and Vollenweider, F. X. (2008). Sensorimotor gating and attentional set-shifting are improved by the mu-opioid receptor agonist morphine in healthy human volunteers. *Int. J. Neuropsychopharmacol.* 11, 655–669. doi: 10.1017/S146114570708322
- Quinn, C. C., Chen, E., Kinjo, T. G., Kelly, G., Bell, A. W., Elliott, R. C., et al. (2003). TUC-4b, a novel TUC family variant, regulates neurite outgrowth and associates with vesicles in the growth cone. *J. Neurosci.* 23, 2815–2823. doi: 10.1523/JNEUROSCI.23-07-02815.2003
- Ramirez-Rios, S., Denarier, E., Prezel, E., Vinit, A., Stoppin-Mellet, V., Devred, F., et al. (2016). Tau antagonizes end-binding protein tracking at microtubule ends through a phosphorylation-dependent mechanism. *Mol. Biol. Cell* 27, 2924–2934. doi: 10.1091/mbc.E16-01-0029
- Ramkumar, A., Jong, B. Y., and Ori-McKenney, K. M. (2018). ReMAPping the microtubule landscape: how phosphorylation dictates the activities of microtubule-associated proteins: phosphorylation of microtubule-associated proteins. *Dev. Dyn.* 247, 138–155. doi: 10.1002/dvdy.24599
- Regan, P., Piers, T., Yi, J.-H., Kim, D.-H., Huh, S., Park, S. J., et al. (2015). Tau phosphorylation at serine 396 residue is required for hippocampal LTD. *J. Neurosci.* 35, 4804–4812. doi: 10.1523/JNEUROSCI.2842-14.2015
- Reiter, J. F., and Leroux, M. R. (2017). Genes and molecular pathways underpinning ciliopathies. *Nat. Rev. Mol. Cell Biol.* 18, 533–547. doi: 10.1038/nrm.2017.60

- Richard, M., Sacquet, J., Jany, M., Schweitzer, A., Jourdan, F., Andrieux, A., et al. (2009). STOP proteins contribute to the maturation of the olfactory system. *Mol. Cell. Neurosci.* 41, 120–134. doi: 10.1016/j.mcn.2009.02.004
- Roger, B., Al-Bassam, J., Dehmelt, L., Milligan, R. A., and Halpain, S. (2004). MAP2c, but not tau, binds and bundles F-actin via its microtubule binding domain. *Curr. Biol.* 14, 363–371. doi: 10.1016/j.cub.2004.01.058
- Rosslénbroich, V., Dai, L., Baader, S. L., Noegel, A. A., Gieselmann, V., and Kappler, J. (2005). Collapsin response mediator protein-4 regulates F-actin bundling. *Exp. Cell Res.* 310, 434–444. doi: 10.1016/j.yexcr.2005.08.005
- Rush, T., Roth, J. R., Thompson, S. J., Aldaher, A. R., Cochran, J. N., and Roberson, E. D. (2020). A peptide inhibitor of Tau-SH3 interactions ameliorates amyloid- β toxicity. *Neurobiol. Dis.* 134:104668. doi: 10.1016/j.nbd.2019.104668
- Salatino-Oliveira, A., Wagner, F., Akutagawa-Martins, G. C., Bruxel, E. M., Genro, J. P., Zeni, C., et al. (2016). MAP1B and NOS1 genes are associated with working memory in youths with attention-deficit/hyperactivity disorder. *Eur. Arch. Psychiatry Clin. Neurosci.* 266, 359–366. doi: 10.1007/s00406-015-0626-9
- Sanders, A. A. W. M., and Kaverina, I. (2015). Nucleation and dynamics of golgi-derived microtubules. *Front. Neurosci.* 9:431. doi: 10.3389/fnins.2015.00431
- Saudou, F., and Humbert, S. (2016). The biology of huntingtin. *Neuron* 89, 910–926. doi: 10.1016/j.neuron.2016.02.003
- Sayas, C. L., Tortosa, E., Bollati, F., Ramirez-Rios, S., Arnal, I., and Avila, J. (2015). Tau regulates the localization and function of End Binding proteins in neuronal cells. *Springerplus* 4:L16. doi: 10.1186/2193-1801-4-S1-L16
- Schmidt, E. F., Shim, S.-O., and Strittmatter, S. M. (2008). Release of MICAL autoinhibition by semaphorin-plexin signaling promotes interaction with collapsin response mediator protein. *J. Neurosci.* 28, 2287–2297. doi: 10.1523/JNEUROSCI.5646-07.2008
- Schwenk, B. M., Lang, C. M., Hogl, S., Tahirovic, S., Orozco, D., Rentzsch, K., et al. (2014). The FTL risk factor TMEM106B and MAP6 control dendritic trafficking of lysosomes. *EMBO J.* 33, 450–467. doi: 10.1002/emboj.201385857
- Sekine, X. Y., Algarate, P. T., Cafferty, X. W. B. J., and Strittmatter, X. S. M. (2019). Plexina2 and CRMP2 signaling complex is activated by nogo-a-liganded Ngr1 to restrict corticospinal axon sprouting after trauma. *J. Neurosci.* 39, 3204–3216. doi: 10.1523/JNEUROSCI.2996-18.2019
- Shepherd, A. M., Laurens, K. R., Matheson, S. L., Carr, V. J., and Green, M. J. (2012). Systematic meta-review and quality assessment of the structural brain alterations in schizophrenia. *Neurosci. Biobehav. Rev.* 36, 1342–1356. doi: 10.1016/j.neubiorev.2011.12.015
- Shimizu, H., Iwayama, Y., Yamada, K., Toyota, T., Minabe, Y., Nakamura, K., et al. (2006). Genetic and expression analyses of the STOP (MAP6) gene in schizophrenia. *Schizophr. Res.* 84, 244–252. doi: 10.1016/j.schres.2006.03.017
- Shimizu, S., Matsuzaki, S., Hattori, T., Kumamoto, N., Miyoshi, K., Katayama, T., et al. (2008). DISC1-kendrin interaction is involved in centrosomal microtubule network formation. *Biochem. Biophys. Res. Commun.* 377, 1051–1056. doi: 10.1016/j.bbrc.2008.10.100
- Siahaan, V., Krattenmacher, J., Hyman, A. A., Diez, S., Hernandez-Vega, A., Lansky, Z., et al. (2019). Kinetically distinct phases of tau on microtubules regulate kinesin motors and severing enzymes. *Nat. Cell Biol.* 21, 1086–1092. doi: 10.1038/s41556-019-0374-6
- Sloboda, R. D., Dentler, W. L., and Rosenbaum, J. L. (1976). Microtubule-associated proteins and the stimulation of tubulin assembly *in vitro*. *Biochemistry* 15, 4497–4505. doi: 10.1021/bi00665a026
- Soh, U. J. K., and Low, B. C. (2008). BNIP2 extra long inhibits RhoA and cellular transformation by Lbc RhoGEF via its BCH domain. *J. Cell Sci.* 121, 1739–1749. doi: 10.1242/jcs.021774
- Song, Y., Kirkpatrick, L. L., Schilling, A. B., Helseth, D. L., Chabot, N., Keillor, J. W., et al. (2013). Transglutaminase and polyamination of tubulin: posttranslational modification for stabilizing axonal microtubules. *Neuron* 78, 109–123. doi: 10.1016/j.neuron.2013.01.036
- Sousa, V. L., Bellani, S., Giannandrea, M., Yousuf, M., Valtorta, F., Meldolesi, J., et al. (2009). α -synuclein and its A30P mutant affect actin cytoskeletal structure and dynamics. *Mol. Biol. Cell* 20, 3725–3739. doi: 10.1091/mbc.e08-03-0302
- Su, K.-Y., Chien, W.-L., Fu, W.-M., Yu, I.-S., Huang, H.-P., Huang, P.-H., et al. (2007). Mice deficient in collapsin response mediator protein-1 exhibit impaired long-term potentiation and impaired spatial learning and memory. *J. Neurosci.* 27, 2513–2524. doi: 10.1523/JNEUROSCI.4497-06.2007
- Takei, Y., Kikkawa, Y. S., Atapour, N., Hensch, T. K., and Hirokawa, N. (2015). Defects in synaptic plasticity, reduced NMDA-receptor transport, and instability of postsynaptic density proteins in mice lacking microtubule-associated protein 1A. *J. Neurosci.* 35, 15539–15554. doi: 10.1523/JNEUROSCI.2671-15.2015
- Takei, Y., Kondo, S., Harada, A., Inomata, S., Noda, T., and Hirokawa, N. (1997). Delayed development of nervous system in mice homozygous for disrupted microtubule-associated protein 1B (MAP1B) gene. *J. Cell Biol.* 137, 1615–1626. doi: 10.1083/jcb.137.7.1615
- Takei, Y., Teng, J., Harada, A., and Hirokawa, N. (2000). Defects in axonal elongation and neuronal migration in mice with disrupted tau and map1b genes. *J. Cell Biol.* 150, 989–1000. doi: 10.1083/jcb.150.5.989
- Talbot, K., Cho, D.-S., Ong, W.-Y., Benson, M. A., Han, L.-Y., Kazi, H. A., et al. (2006). Dysbindin-1 is a synaptic and microtubular protein that binds brain snapin. *Hum. Mol. Genet.* 15, 3041–3054. doi: 10.1093/hmg/ddl246
- Tan, M., Cha, C., Ye, Y., Zhang, J., Li, S., Wu, F., et al. (2015). CRMP4 and CRMP2 interact to coordinate cytoskeleton dynamics, regulating growth cone development and axon elongation. *Neural Plast.* 2015:947423. doi: 10.1155/2015/947423
- Taya, S., Shinoda, T., Tsuboi, D., Asaki, J., Nagai, K., Hikita, T., et al. (2007). DISC1 regulates the transport of the NUDEL/LIS1/14-3-3-epsilon complex through kinesin-1. *J. Neurosci.* 27, 15–26. doi: 10.1523/JNEUROSCI.3826-06.2006
- Teng, J., Takei, Y., Harada, A., Nakata, T., Chen, J., and Hirokawa, N. (2001). Synergistic effects of MAP2 and MAP1B knockout in neuronal migration, dendritic outgrowth, and microtubule organization. *J. Cell Biol.* 155, 65–76. doi: 10.1083/jcb.200106025
- Ti, S.-C., Alushin, G. M., and Kapoor, T. M. (2018). Human β -tubulin isoforms can regulate microtubule protofilament number and stability. *Dev. Cell* 47, 175.e5–190.e5. doi: 10.1016/j.devcel.2018.08.014
- Tortosa, E., Adolfs, Y., Fukata, M., Pasterkamp, R. J., Kapitein, L. C., and Hoogenraad, C. C. (2017). Dynamic palmitoylation targets MAP6 to the axon to promote microtubule stabilization during neuronal polarization. *Neuron* 94, 809.e7–825.e7. doi: 10.1016/j.neuron.2017.04.042
- Tortosa, E., Galjart, N., Avila, J., and Sayas, C. L. (2013). MAP1B regulates microtubule dynamics by sequestering EB1/3 in the cytosol of developing neuronal cells. *EMBO J.* 32, 1293–1306. doi: 10.1038/emboj.2013.76
- Tortosa, E., Montenegro-Venegas, C., Benoist, M., Härtel, S., González-Billault, C., Esteban, J. A., et al. (2011). Microtubule-associated protein 1B (MAP1B) is required for dendritic spine development and synaptic maturation. *J. Biol. Chem.* 286, 40638–40648. doi: 10.1074/jbc.M111.271320
- Toyoshima, M., Jiang, X., Ogawa, T., Ohnishi, T., Yoshihara, S., Balan, S., et al. (2019). Enhanced carbonyl stress induces irreversible multimerization of CRMP2 in schizophrenia pathogenesis. *Life Sci. Alliance* 2:e201900478. doi: 10.26508/lsa.201900478
- Tsutiya, A., Nishihara, M., Goshima, Y., and Ohtani-Kaneko, R. (2015). Mouse pups lacking collapsin response mediator protein 4 manifest impaired olfactory function and hyperactivity in the olfactory bulb. *Eur. J. Neurosci.* 42, 2335–2345. doi: 10.1111/ejn.12999
- Tsutiya, A., Watanabe, H., Nakano, Y., Nishihara, M., Goshima, Y., and Ohtani-Kaneko, R. (2016). Deletion of collapsin response mediator protein 4 results in abnormal layer thickness and elongation of mitral cell apical dendrites in the neonatal olfactory bulb. *J. Anat.* 228, 792–804. doi: 10.1111/joa.12434
- Uchida, Y., Ohshima, T., Sasaki, Y., Suzuki, H., Yanai, S., Yamashita, N., et al. (2005). Semaphorin3A signalling is mediated via sequential Cdk5 and GSK3 β phosphorylation of CRMP2: implication of common phosphorylating mechanism underlying axon guidance and Alzheimer's disease. *Genes Cells* 10, 165–179. doi: 10.1111/j.1365-2443.2005.00827.x
- Ujike, H., Sakai, A., Nakata, K., Tanaka, Y., Kodaka, T., Okahisa, Y., et al. (2006). Association study of the dihydropyrimidinase-related protein 2 gene and methamphetamine psychosis. *Ann. N Y Acad. Sci.* 1074, 90–96. doi: 10.1196/annals.1369.008
- Valenstein, M. L., and Roll-Mecak, A. (2016). Graded control of microtubule severing by tubulin glutamylation. *Cell* 164, 911–921. doi: 10.1016/j.cell.2016.01.019

- Valenzuela, A., Meservey, L., Nguyen, H., and Fu, M. M. (2020). Golgi outposts nucleate microtubules in cells with specialized shapes. *Trends Cell Biol.* 30, 792–804. doi: 10.1016/j.tcb.2020.07.004
- Van Dijk, A., Vulto-van Silfhout, A. T., Cappuyns, E., van der Werf, I. M., Mancini, G. M., Tzschach, A., et al. (2019). Clinical presentation of a complex neurodevelopmental disorder caused by mutations in ADNP. *Biol. Psychiatry* 85, 287–297. doi: 10.1016/j.biopsych.2018.02.1173
- Vandecandelaere, A., Pedrotti, B., Utton, M. A., Calvert, R. A., and Bayley, P. M. (1996). Differences in the regulation of microtubule dynamics by microtubule-associated proteins MAP1B and MAP2. *Cell Motil. Cytoskeleton.* 35, 134–146. doi: 10.1002/(SICI)1097-0169(1996)35:2<134::AID-CM6>3.0.CO;2-A
- Vemu, A., Atherton, J., Spector, J. O., Szyk, A., Moores, C. A., and Roll-Mecak, A. (2016). Structure and dynamics of single-isoform recombinant neuronal human tubulin. *J. Biol. Chem.* 291, 12907–12915. doi: 10.1074/jbc.C116.731133
- Vikhreva, P. N., Korobko, E. V., and Korobko, I. V. (2009). Identification of novel proteins, possible interaction partners for guanine nucleotide exchange factor Varp. *Dokl. Biochem. Biophys.* 429, 323–325. doi: 10.1134/s160767290906009x
- Volle, J., Brocard, J., Saoud, M., Gory-Faure, S., Brunelin, J., Andrieux, A., et al. (2013). Reduced expression of STOP/MAP6 in mice leads to cognitive deficits. *Schizophr. Bull.* 39, 969–978. doi: 10.1093/schbul/sbs113
- Walters, G. B., Gustafsson, O., Sveinbjornsson, G., Eiriksdottir, V. K., Agustsdottir, A. B., Jonsdottir, G. A., et al. (2018). MAP1B mutations cause intellectual disability and extensive white matter deficit. *Nat. Commun.* 9:3456. doi: 10.1038/s41467-018-05595-6
- Wang, Q., and Brandon, N. J. (2011). Regulation of the cytoskeleton by Disrupted-in-schizophrenia 1 (DISC1). *Mol. Cell. Neurosci.* 48, 359–364. doi: 10.1016/j.mcn.2011.06.004
- Webb, B. C., and Wilson, L. (1980). Cold-stable microtubules from brain. *Biochemistry* 19, 1993–2001. doi: 10.1021/bi00550a041
- Wegmann, S., Eftekhazadeh, B., Tepper, K., Zoltowska, K. M., Bennett, R. E., Dujardin, S., et al. (2018). Tau protein liquid-liquid phase separation can initiate tau aggregation. *EMBO J.* 37:e98049. doi: 10.15252/embj.201798049
- Wei, H., Ma, Y., Liu, J., Ding, C., Hu, F., and Yu, L. (2016a). Proteomic analysis of cortical brain tissue from the BTBR mouse model of autism: evidence for changes in STOP and myelin-related proteins. *Neuroscience* 312, 26–34. doi: 10.1016/j.neuroscience.2015.11.003
- Wei, H., Sun, S., Li, Y., and Yu, S. (2016b). Reduced plasma levels of microtubule-associated STOP/MAP6 protein in autistic patients. *Psychiatry Res.* 245, 116–118. doi: 10.1016/j.psychres.2016.08.024
- Weingarten, J., Lassek, M., Mueller, B. F., Rohmer, M., Lunger, I., Baumlisberger, D., et al. (2014). The proteome of the presynaptic active zone from mouse brain. *Mol. Cell. Neurosci.* 59, 106–118. doi: 10.1016/j.mcn.2014.02.003
- Weingarten, M. D., Lockwood, A. H., Hwo, S. Y., and Kirschner, M. W. (1975). A protein factor essential for microtubule assembly. *Proc. Natl. Acad. Sci. U S A* 72, 1858–1862. doi: 10.1073/pnas.72.5.1858
- Xiao, B., Xu, H., Ye, H., Hu, Q., Chen, Y., and Qiu, W. (2015). De novo 11q13.4q14.3 tetrasomy with uniparental isodisomy for 11q14.3qter. *Am. J. Med. Genet. A* 167A, 2327–2333. doi: 10.1002/ajmg.a.37179
- Xie, R., Nguyen, S., McKeehan, K., Wang, F., McKeehan, W. L., and Liu, L. (2011). Microtubule-associated protein 1S (MAP1S) bridges autophagic components with microtubules and mitochondria to affect autophagosomal biogenesis and degradation. *J. Biol. Chem.* 286, 10367–10377. doi: 10.1074/jbc.M110.206532
- Xu, Z., Schaedel, L., Portran, D., Aguilar, A., Gaillard, J., Marinkovich, M. P., et al. (2017). Microtubules acquire resistance from mechanical breakage through intraluminal acetylation. *Science* 356, 328–332. doi: 10.1126/science.aai8764
- Yadav, S., Verma, P. J., and Panda, D. (2014). C-terminal region of MAP7 domain containing protein 3 (MAP7D3) promotes microtubule polymerization by binding at the C-terminal tail of tubulin. *PLoS One* 9:e99539. doi: 10.1371/journal.pone.0099539
- Yamane, M., Yamashita, N., Hida, T., Kamiya, Y., Nakamura, F., Kolattukudy, P., et al. (2017). A functional coupling between CRMP1 and Nav1.7 for retrograde propagation of Semaphorin3A signaling. *J. Cell Sci.* 130, 1393–1403. doi: 10.1242/jcs.199737
- Yamashita, N., and Goshima, Y. (2012). Collapsin response mediator proteins regulate neuronal development and plasticity by switching their phosphorylation status. *Mol. Neurobiol.* 45, 234–246. doi: 10.1007/s12035-012-8242-4
- Yamashita, N., Morita, A., Uchida, Y., Nakamura, F., Usui, H., Ohshima, T., et al. (2007). Regulation of spine development by semaphorin3A through cyclin-dependent kinase 5 phosphorylation of collapsin response mediator protein 1. *J. Neurosci.* 27, 12546–12554. doi: 10.1523/JNEUROSCI.3463-07.2007
- Yamashita, N., Mosinger, B., Roy, A., Miyazaki, M., Ugajin, K., Nakamura, F., et al. (2011). CRMP5 (collapsin response mediator protein 5) regulates dendritic development and synaptic plasticity in the cerebellar Purkinje cells. *J. Neurosci.* 31, 1773–1779. doi: 10.1523/JNEUROSCI.5337-10.2011
- Yamashita, N., Takahashi, A., Takao, K., Yamamoto, T., Kolattukudy, P., Miyakawa, T., et al. (2013). Mice lacking collapsin response mediator protein 1 manifest hyperactivity, impaired learning and memory, and impaired prepulse inhibition. *Front. Behav. Neurosci.* 7:216. doi: 10.3389/fnbeh.2013.00216
- Yamashita, N., Uchida, Y., Ohshima, T., Hirai, S. I., Nakamura, F., Taniguchi, M., et al. (2006). Collapsin response mediator protein 1 mediates reelin signaling in cortical neuronal migration. *J. Neurosci.* 26, 13357–13362. doi: 10.1523/JNEUROSCI.4276-06.2006
- Yamazaki, Y., Nagai, J., Akinaga, S., Koga, Y., Hasegawa, M., Takahashi, M., et al. (2020). Phosphorylation of CRMP2 is required for migration and positioning of Purkinje cells: redundant roles of CRMP1 and CRMP4. *Brain Res.* 1736:146762. doi: 10.1016/j.brainres.2020.146762
- Yang, S. Z., and Wildonger, J. (2020). Golgi outposts locally regulate microtubule orientation in neurons but are not required for the overall polarity of the dendritic cytoskeleton. *Genetics* 215, 435–447. doi: 10.1534/genetics.119.302979
- Yao, L., Liu, Y.-H., Li, X., Ji, Y.-H., Yang, X.-J., Hang, X.-T., et al. (2016). CRMP1 interacted with Spyl during the collapse of growth cones induced by Sema3A and acted on regeneration after sciatic nerve crush. *Mol. Neurobiol.* 53, 879–893. doi: 10.1007/s12035-014-9049-2
- Yoshimura, T., Kawano, Y., Arimura, N., Kawabata, S., Kikuchi, A., and Kaibuchi, K. (2005). GSK-3 β regulates phosphorylation of CRMP-2 and neuronal polarity. *Cell* 120, 137–149. doi: 10.1016/j.cell.2004.11.012
- Yu-Kemp, H.-C., and Briehner, W. M. (2016). Collapsin response mediator protein-1 regulates Arp2/3-dependent actin assembly. *J. Biol. Chem.* 291, 658–664. doi: 10.1074/jbc.C115.689265
- Yu-Kemp, H.-C., Kemp, J. P. Jr., and Briehner, W. M. (2017). CRMP-1 enhances EVL-mediated actin elongation to build lamellipodia and the actin cortex. *J. Cell Biol.* 216, 2463–2479. doi: 10.1083/jcb.201606084
- Zervas, M., Opitz, T., Edelmann, W., Wainer, B., Kucherlapati, R., and Stanton, P. K. (2005). Impaired hippocampal long-term potentiation in microtubule-associated protein 1B-deficient mice. *J. Neurosci. Res.* 82, 83–92. doi: 10.1002/jnr.20624
- Zhao, Z., Xu, J., Chen, J., Kim, S., Reimers, M., Bacanu, S. A., et al. (2015). Transcriptome sequencing and genome-wide association analyses reveal lysosomal function and actin cytoskeleton remodeling in schizophrenia and bipolar disorder. *Mol. Psychiatry* 20, 563–572. doi: 10.1038/mp.2014.82
- Zheng, Y., Sethi, R., Mangala, L. S., Taylor, C., Goldsmith, J., Wang, M., et al. (2018). Tuning microtubule dynamics to enhance cancer therapy by modulating FER-mediated CRMP2 phosphorylation. *Nat. Commun.* 9:476. doi: 10.1038/s41467-017-02811-7

Conflict of Interest: The authors declare that the research was conducted in the absence of any commercial or financial relationships that could be construed as a potential conflict of interest.

Copyright © 2021 Cuveillier, Boulan, Ravello, Denarier, Deloulme, Gory-Fauré, Delphin, Bosc, Arnal and Andrieux. This is an open-access article distributed under the terms of the Creative Commons Attribution License (CC BY). The use, distribution or reproduction in other forums is permitted, provided the original author(s) and the copyright owner(s) are credited and that the original publication in this journal is cited, in accordance with accepted academic practice. No use, distribution or reproduction is permitted which does not comply with these terms.

Imaging Microtubules *in vitro* at High Resolution while Preserving their Structure

Camille Cuveillier*, Yasmina Saoudi, Isabelle Arnal and Christian Delphin*

Univ. Grenoble Alpes, Inserm, U1216, CNRS, Grenoble Institut Neurosciences, GIN, France

*For correspondence: camille.cuveillier@univ-grenoble-alpes.fr; christian.delphin@univ-grenoble-alpes.fr

[Abstract] Microtubules (MT) are the most rigid component of the cytoskeleton. Nevertheless, they often appear highly curved in the cellular context and the mechanisms governing their overall shape are poorly understood. Currently, *in vitro* microtubule analysis relies primarily on electron microscopy for its high resolution and Total Internal Reflection Fluorescence (TIRF) microscopy for its ability to image live fluorescently-labelled microtubules and associated proteins. For three-dimensional analyses of microtubules with micrometer curvatures, we have developed an assay in which MTs are polymerized *in vitro* from MT seeds adhered to a glass slide in a manner similar to conventional TIRF microscopy protocols. Free fluorescent molecules are removed and the MTs are fixed by perfusion. The MTs can then be observed using a confocal microscope with an Airyscan module for higher resolution. This protocol allows the imaging of microtubules that have retained their original three-dimensional shape and is compatible with high-resolution immunofluorescence detection.

Keywords: Microtubules, Microtubule-Associated Proteins, TIRF microscopy, High resolution imaging, Airyscan.

[Background] Microtubules (MT) are polymers made by the combination of the heterodimers α - and β -tubulins and are a major component of the cell cytoskeleton. They are involved in fundamental mechanisms of cell function such as mitosis, intracellular transport, cytokinesis and maintenance of cell shape (Akhmanova and Steinmetz, 2015). Although inherently very rigid, MTs often appear curved in cells and few proteins have been described to bend microtubules (Brangwynne *et al.*, 2006; Bechstedt *et al.*, 2014; Leung *et al.*, 2020; Cuveillier *et al.*, 2020). Since the early 1970s (Weisenberg, 1972), the study of MTs *in vitro* has led to a better understanding of the molecular mechanism involved in the formation and dynamics of MTs. However, a detailed analysis of the shape of the microtubules remains technically difficult. Two main approaches are currently used: electron microscopy for the very detailed images obtained (up to a separation limit of a few Angstrom) (Alushin *et al.*, 2014; Harris, 2015), and TIRF microscopy which allows the live observation of dynamic microtubules using fluorescently-labelled molecules (separation limit of about 200 nm) (Al-Bassam, 2014). However, these techniques are not suitable for the complete observation of microtubules with large three-dimensional curvatures such as the helical shape they adopt in the presence of MAP6 (Cuveillier *et al.*, 2020). In order to obtain more clues on the structure of the MTs, we developed an assay that combines the use of fluorescent proteins and high-resolution imaging by Airyscan confocal microscopy (achievable resolution down to 120 nm in XY), while preserving the original shape of the MTs which is very sensitive to manipulation. This protocol

has the advantage of avoiding unusual equipment and material. Moreover, it can be adapted to different super-resolution techniques such as expansion microscopy or stimulated-emission-depletion (STED) microscopy which would allow to increase the resolution up to 10 times (Blom and Brismar, 2014) and reach a separation limit of 50-20 nm.

Materials and Reagents

1. Tubulin, Atto-565 labelled tubulin, and biotinylated tubulin are prepared as already fully described in Ramirez-Rios *et al.* (2017). Store up to 1 year in liquid nitrogen
2. Cover glasses 26 × 76 mm #1 (VWR, catalog number: 630-2910)
3. Double-face precut tape 70 µm thick, 3 mm wide (LIMA Company, catalog number: 0000P70PC3003)
4. Siligum wax plate (VWR, MODU140013)
5. 1.5 ml Eppendorf tubes (Fisher Scientific, catalog number: 11558232)
6. 0.5 ml Eppendorf tubes (Fisher Scientific, catalog number: 10318661)
7. Petri dishes (Greiner Bio-One, catalog number: 663102)
8. Polycarbonate centrifuge tubes (Beckman, catalog number: 343775)
9. 0.22 µm filters (Merck Millipore, catalog number: SLGP033RS)
10. Silane-PEG (MW 30k) (Creative PEG-Works, catalog number: PSB-2014)
11. Silane-PEG-biotin (MW 3,400) (LaysanBio, catalog number: BIOTIN-PEF-SIL, MW 3,400)
12. NeutrAvidin (ThermoScientific, catalog number: 31000)
13. PLL20K-G35-PEG2K (PLL-g-PEG) (Jenkem, catalog number: 13022755)
14. Pluronic F-127 (Sigma-Aldrich, catalog number: P2443)
15. Bovine Serum Albumin (BSA) (Sigma-Aldrich, catalog number: A7030)
16. Acetone 100% (VWR, catalog number: 20066.321)
17. Ethanol 96% (VWR, catalog number: 20823362)
18. Hellmanex III (Sigma-Aldrich, catalog number: Z805939-1EA)
19. Phosphate buffer saline (PBS) (Sigma-Aldrich, catalog number: P4417)
20. 1,4-Piperazinediethanesulfonic acid (PIPES) (Sigma-Aldrich, catalog number: P6757)
21. Potassium hydroxide (KOH) (Sigma-Aldrich, catalog number: 484016)
22. Potassium chloride (KCl) (Sigma-Aldrich, catalog number: P9541)
23. Ethylene glycol-bis(2-aminoethylether)-N,N,N',N'-tetraacetic acid (EGTA) (Sigma-Aldrich, catalog number: E3889)
24. Magnesium chloride (MgCl₂) (Sigma-Aldrich, catalog number: 2670)
25. Sodium hydroxide (NaOH) (Carlo Erba, catalog number: 480507)
26. DL-Dithiothreitol (DTT) (Sigma-Aldrich, catalog number: D0632)
27. Guanosine 5'-triphosphate (GTP) (Sigma-Aldrich, catalog number: G8877)
28. Methyl cellulose 1,500 cP (Sigma-Aldrich, catalog number: M0387)
29. GMPCPP (Euromedex, JE-NU-405S)

30. HEPES (Sigma-Aldrich, catalog number: H3375)
31. Glucose (Sigma-Aldrich, catalog number: G8270)
32. Glucose oxidase (Sigma-Aldrich, catalog number: G6766-10KU)
33. Catalase (Sigma-Aldrich, catalog number: C9322-1G)
34. Diamond pencil (Agar Scientific, catalog number: AGT5347)
35. Glutaraldehyde solution 25% (Sigma-Aldrich, catalog number: G5882)
36. Clean nitrogen air flow (Air Liquide)
37. Liquid nitrogen (Air Liquide)
38. 5× BRB80 (see Recipes)
39. BSA 10% (see Recipes)
40. Neutravidine (see Recipes)
41. DTT, 200 mM (see Recipes)
42. KCl, 500 mM (see Recipes)
43. PLL-PEG (see Recipes)
44. Silane-PEG or Silane-PEG-biotin (see Recipes)
45. GTP, 20 mM (see Recipes)
46. Glucose, 450 mg/ml (see Recipes)
47. Deoxymix (catalase and glucose oxydase) (see Recipes)
48. NaOH, 1 M (see Recipes)
49. BSA 1%/BRB80 (see Recipes)
50. Methyl cellulose 1,500 cP (see Recipes)
51. HEPES, 10 mM (see Recipes)
52. Pluronic F27, 10% (see Recipes)
53. PBS (see Recipes)
54. Neutravidin stock solution (see Recipes)
55. Red tubulin mix (see Recipes)
56. Imaging buffer (see Recipes)

Equipment

1. Inverted Eclipse Ti microscope (Nikon) with PSF focus
2. Apochromat 100×/1.49 N.A. oil immersion objective (Nikon) with heated objective (Okolab)
3. Temperature chamber (Technico Plast)
4. Ilas2 TIRF system (Roper Scientific)
5. Cooled Charged-coupled device camera (Evolve 512, Photometrics)
6. Temperature Stage Controller (Linkam Scientific)
7. LSM 710 confocal (Zeiss) Airyscan
8. Plan Apochromat 100×/1.4 N.A. oil immersion objective (Zeiss)
9. Ultracentrifuge (Beckman Coulter Optima, Model Max-XP, catalog number: 393315)

10. Rotor (Beckman, model: TLA100-1, catalog number: 343837)
11. Plasma cleaner FEMTO Diener Electric (Germany) coupled to a vacuum pump Trivac D2.5E Oerliken (Germany)
12. Sonicator (Elmasonic S30, Elma, Germany)
13. Glass staining dishes and tray (VWR, catalog number: MARI4200004)
14. Plastic box for glass microscopy (any brand)
15. Diamond Pencil (Oxford Instruments, catalog number: T5347)
16. Tweezers (Dutscher, catalog numbers: 076100 and 005093)
17. Gloves powder-free (any brand)
18. Water-bath (any brand)

Software

1. MetaMorph 7.8.5 software (Molecular Devices, <https://www.moleculardevices.com>)
2. Zen Black 2.1 (Zeiss)

Procedure

A. Flow chamber preparation

Note: This procedure is adapted from Portran et al. (2013) and Leslie et al. (2013). Cover glasses are used to make both sides of the perfusion chambers. Cover glasses are handled with tweezers or by hand with non-powdered gloves on the edges when drying with airflow so as not to damage their surface by more than 1 cm.

1. Glass cleaning
 - a. Immerse the cover glasses in a clean glass staining dish (105 × 85 × 70 mm) filled with 200-250 ml acetone and sonicate for 30 min in sweep mode.

Note: 6 cover glasses are required to make 10 flow chambers, but some glass breakage may occur during the procedure, so it is advisable to start with a little more cover glasses.
 - b. Replace acetone and incubate for an additional 30 min with orbital shaking (80 rpm).

Note: Acetone from the second bath can be recycled for the first bath of the next cleaning procedure.
 - c. Incubate 15 min with ethanol and rinse 10 times with deionized filtered water.
 - d. Incubate 2 h in prewarmed (60 °C) 2% (v/v) Hellmanex on an orbital shaker (80 rpm), then rinse 10 times with deionized filtered water.
 - e. Sonicate 15 min in 1 M NaOH solution.
 - f. Rinse 10 times with deionized filtered water.
 - g. Sonicate 15 min in ethanol and rinse each coverslip 10 times in a large volume (2 × 2 L) of deionized filtered water.
 - h. Dry the cover glasses with a clean air flow (nitrogen gas).

- i. Dispense the glasses into two clean, dry glass staining tray for activation and silanization (see the next step below).
Note: 5 silane-PEG-biotin-coated glasses and 1 silane-PEG-coated glass are used to prepare 10 perfusion chambers (see below paragraph 3).
2. Glasses activation and silanization
 - a. Plasma activate the glasses for 3 min at 80% of maximum power at a pressure of 0.7 mbar.
 - b. Rapidly immerse the glasses in either silane-PEG-biotin or silane-PEG solutions and incubate overnight on an orbital shaker.
Note: Identify the glass staining dishes containing either silane-PEG-biotin or silane-PEG to avoid mistakes.
 - c. Recover the coating solutions (they can be reused for several months as long as they remain clean) and replace them with ethanol (Figure 1A).
 - d. Wash each coating slide 10 times in a beaker containing ethanol (Figure 1B) and 10 times in a large volume (2 × 2 L) of water (Figure 1C, 1D).
Note: We recommend to wash first the silane-PEG slides then the silane-PEG-biotin ones to avoid potential silane-PEG-biotin binding to silane-PEG slides.



Figure 1. Washing of coated slides. In A we have coated slides in ethanol. B contains ethanol. C and D contain deionized filtered water. E containing deionized filtered water is used to keep rinsed slides before drying.

- e. Dry the coverglasses with a stream of nitrogen.
 - f. Store the silanized lamellae at 4 °C in a plastic box sealed with plastic film for a maximum of one week.
3. Construction of the flow chamber
Note: When handling the silanized cover glasses, make sure that the face inside the chamber remains clean and un-touched.

- a. Transfer 1 silane-PEG-biotin-coated slide to a clean Petri dish and, using the diamond pencil, cut the glass into four parts (approx. 19/26 mm) (Figures 2A, 2B).

Note: When cutting with the diamond pencil, the Petri dish bottom bends leading to slide breaking. To avoid this, we use a thin plastic that we put under the Petri dish (Figure 2A).

- b. Similarly, transfer the silane-PEG-coated slide to another Petri dish and cut them into 7 parts of about 11 mm width. Discard the two end parts and cut the others in half to make fourteen 11 × 13 mm pieces (Figures 2C, 2D).

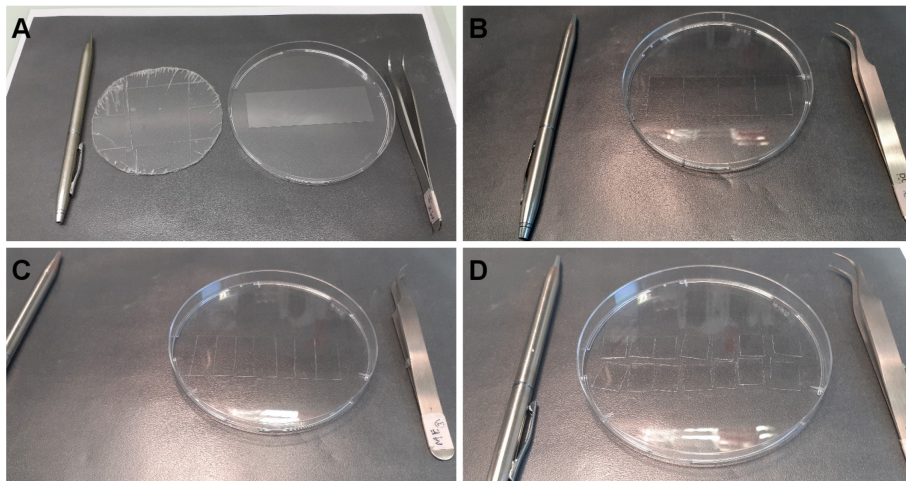


Figure 2. Cutting coated slides. A. From left to right, diamond pencil, plastic to avoid breaking, Petri dish containing silane-PEG-biotin slide, tweezers. B. The slide is cut in four equal parts. C. A silane-PEG slide is cut in 7 parts. D. Each part is cut in half.

- c. Place two pieces of double-sided adhesive tape, 5 mm apart, in the center of a piece of silane-PEG-biotin coated coverslips (Figure 3A).
- d. Tape one piece of PEG-silane-coated strips above the two pieces of tape (the volume of the chamber is about 5 μ l) (Figure 3B).

Note: Carefully press the silane-PEG-coated strip on the tape to ensure correct sealing. You might gently remove excess tape (Figure 3D).

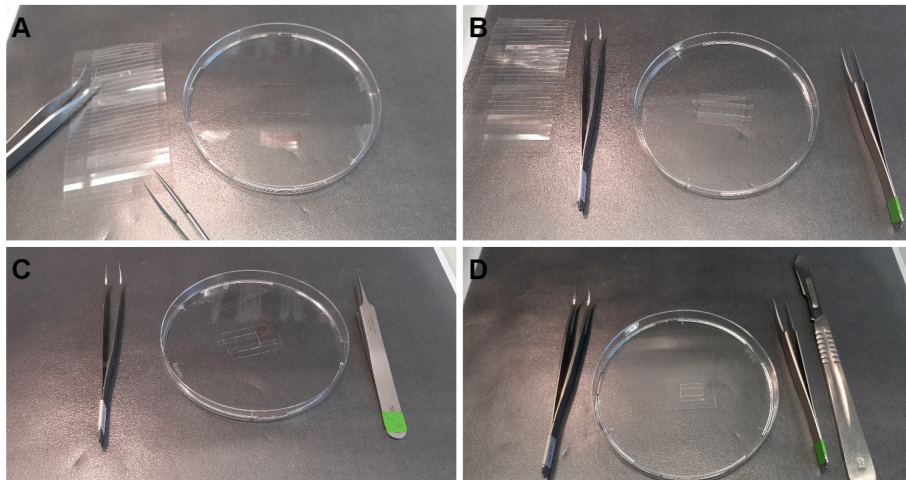


Figure 3. Construction of the flow chamber. A. One piece of silane-PEG-biotin is put in a Petri dish. B. Adhesive tape is stuck to the slide. C. Protective plastic above the tape is removed and one piece of silane-PEG slide is placed onto the tape. D. Excessive tape is cut and removed.

B. Preparation of GMPCPP seeds

Note: GMPCPP seeds tend to depolymerize at low temperatures, try to keep them warm all along the procedure.

1. Prepare a mix of freshly thawed ATTO-565 tubulin and biotinylated tubulin at a 1:1 molar ratio for a final concentration of 10 μM tubulin in BRB80 supplemented with 0.5 mM GMPCPP.

Note: Usually, 300 μl of seeds are necessary for at least 500 experiments.

2. The mix is placed at 35 $^{\circ}\text{C}$ in a water-bath during 1 h to allow polymerization.
3. Spin down the GMPCPP seeds at 130,000 $\times g$ using a TLA 100 rotor during 5 min at 35 $^{\circ}\text{C}$.
4. Discard supernatant and gently rinse with 2 \times 100 μl of prewarmed BRB80.

Note: After the centrifugation, the red seeds are visible in the pellet. Avoid resuspending the pellet during washing steps.

5. Gently resuspend the pellet in prewarmed BRB80 containing 1 mM GMPCPP.

Note: Resuspending might take some time. For 300 μl of polymerization solution, resuspend the pellet in 500 μl .

6. Aliquot by 1-2 μl in 0.5 ml Eppendorf and quickly freeze in liquid nitrogen.
7. Store in liquid nitrogen up to one year.

C. Microtubule polymerization and fixation

Note: The perfusion is performed by loading the solution into one side of the chamber while wiping the other side with a piece of paper (Figure 4).

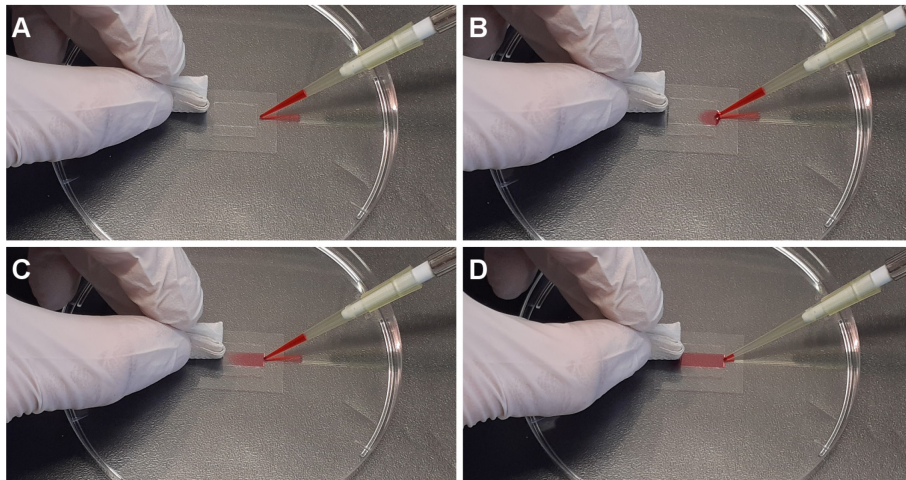


Figure 4. Perfusion in flow chamber. From A to D are sequential images of perfusion of the desired solution into the flow chamber.

1. GMPCPP seeds immobilization in the flow chamber
 - a. Perfuse 10 μ l of Neutravidin (25 μ g/ml in 1% (w/v) BSA/BRB80) in the flow chamber and wait for 2 min.
 - b. Perfuse 30 μ l of PLL-PEG (0.1 mg/ml in 10 mM HEPES, pH 7.4) and wait for 30 s.
 - c. Wash by perfusing 60 μ l of 1% (w/v) pluronic in 1% (w/v) BSA/BRB80.
 - d. Wash by perfusing 2 times with 70 μ l 1% (w/v) BSA/BRB80.
 - e. Quickly thaw GMPCPP seeds and dilute in 1% (w/v) BSA/BRB80.
Note: Adjust seeds dilution if needed, usually start with a 1/100 to 1/500 dilution.
 - f. Perfuse 30 μ l of diluted GMPCPP seeds and let them adhere for 5 min at RT.
 - g. Wash unbound seeds 3 times with 70 μ l 1% (w/v) BSA/BRB80.
2. Microtubule polymerization and fixation
 - a. Perfuse freshly prepared polymerization mix (Recipe 19).
Note: Adjust tubulin/associated proteins concentration if needed. It depends on the affinity and effects of the associated proteins of interest. For tubulin, a concentration of 5 to 20 μ M is a good start and for associated proteins from 5 nM to 500 nM should be informative.
 - b. Put the flow chamber in a warm (32-35 $^{\circ}$ C) place with a water-saturated atmosphere to avoid desiccation for MT polymerization (usually at least 30 min).
 - c. After polymerization, fix MTs by gently perfusing approximately 30 μ l of 0.1% Methyl cellulose 1,500 cP, 0.5% (v/v) Glutaraldehyde/BRB80.
Note: Critical step, fast perfusion will alter MT structure. Put the chamber inside a Petri dish (you might use tape to prevent it from moving). Then, slightly tilt the Petri dish and add drop by drop the fixing buffer at the top of the chamber. The solution will slowly flow down the chamber. You can use blotting paper to clean excess liquid. The fixation buffer should be at least 3 min inside the chamber for proper fixation. Even if the fixation occurs rapidly, dilution might induce MT depolymerization. To overcome this issue, use MT stabilizing compounds

such as taxol (taxol affects MT persistence length) or grow MT longer.

- d. Wash fixation buffer with 50 μ l of 0.1% (v/v) Methyl cellulose 1,500 cP/BRB80.
- e. Perfuse imaging buffer (BRB80 supplemented with 0.1% Methyl cellulose 1,500 cP, 2 mg/ml glucose, 1mg/ml glucose oxidase and 150 μ g/ml catalase).
- f. Seal the flow chamber with the siligum wax.

Note: Imaging of the chambers should be done within one week.

D. Imaging of the microtubules

1. Control fixation: TIRF Microscopy

Note: To estimate the effect of the fixation process on the sample, it is necessary to compare the sample before/after fixation.

- a. Place the flow chamber on the inverted microscope.

Note: For imaging before fixation, set the temperature of the stage at 35 °C to avoid MT depolymerization.

- b. Adjust laser intensity, exposure and focus in order to observe the microtubules.
- c. Acquire images both before (Figure 5A) and after fixation (Figure 5B) of the sample.

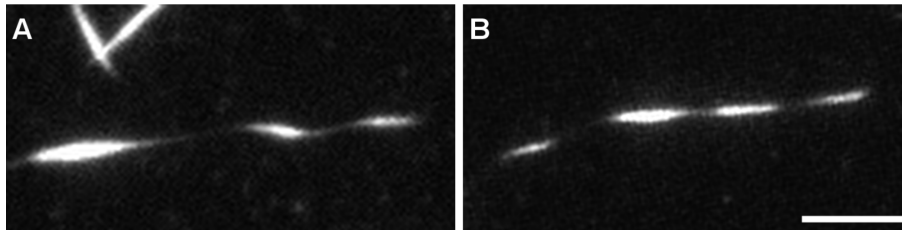


Figure 5. Structure of helical microtubules is not altered by the fixation process. TIRFM image of a helical MT before (A) and after (B) fixation. MTs were grown from GMPCPP seeds with 12 μ M tubulin (9:1 non-labeled tubulin:ATTO-565 labelled tubulin) with 200 nM MAP6-N-GFP. At this concentration, MAP6-N-GFP induces microtubule coiling. Scale bar: 5 μ m.

2. Confocal imaging with Airyscan processing

- a. Place the chamber above the objective.
- b. Adjust focus and laser intensity in order to observe MTs.
- c. Perform acquisition (z-stack series using 220 nm step-size).
- d. Use Zen built-in Airyscan processing. See Figure 6 for TIRF versus confocal imaging with Airyscan processing of helical MT. Figure 7 shows the advantage of performing z-stacks on MTs with a particular shape.
- e. Analyse images using Zen Blue.

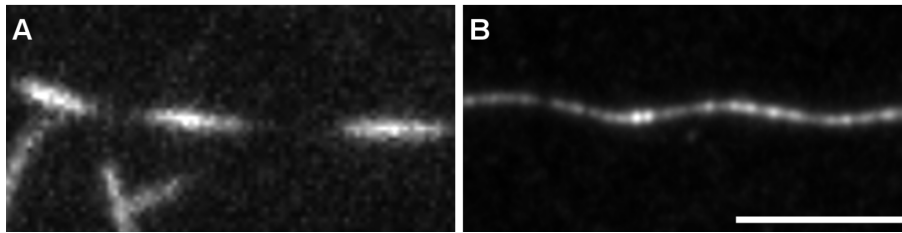


Figure 6. Observation of helical MTs with TIRFM or confocal Airyscan. MTs were grown as in Figure 5 and fixed using the described protocol. A. Fixed helical MTs observed using TIRF microscopy. B. z-projection of a fixed helical MT observed using confocal microscope followed by Airyscan processing. Scale bar: 5 μ m.

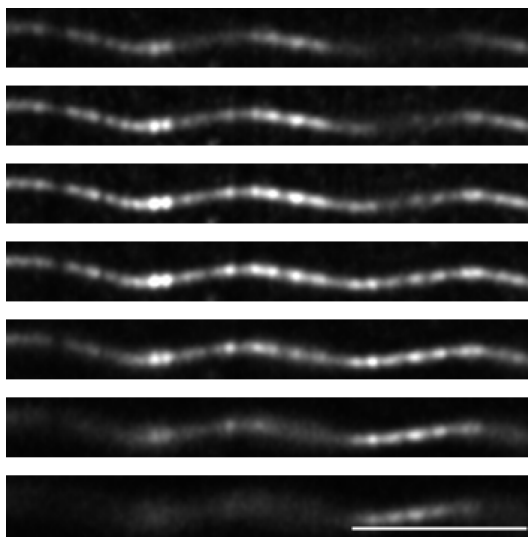


Figure 7. z-stack of a helical MT observed using confocal imaging with Airyscan processing. Images of the z-stack of the same MT as in Figure 6B, with a step of 220 nm between each plane. Scale bar: 5 μ m.

Recipes

All solutions were conserved at indicated temperature without any observable deterioration along time unless stated otherwise. Most solutions were aliquoted to avoid freezing-thawing cycles.

1. 5 \times BRB80

36.28 g PIPES

1.5 ml of MgCl₂ (1 M)

570.6 mg EGTA

Dissolve in 250 ml of deionized water and adjust pH to 6.85 with KOH

Add deionized water to 300 ml, filtrate, aliquot (1 ml and 50 ml) and store at -20 $^{\circ}$ C

Note: The 5 \times BRB80 is used to make the BRB80 solution and to adjust the final concentration of the reaction to 1 \times BRB80. Upon 5 \times dilution the pH drops to 6.75.

2. BSA 10%
Dissolve 2 g of BSA in 20 ml PBS
Filter and store at -20 °C up to 1 year
3. Neutravidine
Dissolve 10 mg Neutravidine in 10 ml H₂O, aliquot (5 and 100 µl) and store at -20 °C
Before the experiment, predilute 5 µl with 195 µl of 1% BSA/BRB80 (final concentration 25 µg/ml)
4. DTT, 200 mM
Dissolve 617 mg DTT powder in 4 ml deionized H₂O, filtrate, aliquot and store at -20 °C
The day of use, dilute 1/5 in H₂O or BRB80. Discard aliquot after each day of use
5. KCl, 500 mM
Dissolve 1 g KCl into 50 ml deionized H₂O (-20 °C) filtrate, aliquot and store at -20 °C
6. PLL-PEG
 - a. Make aliquot of the powder of known weight (20-30 mg) under argon gas and store at -20 °C.
 - b. To make stock solution, dissolve the powder in 10 mM HEPES (pH 7.4) at 1 mg/ml, make 50 µl aliquots and store at -20 °C.
 - c. The day of use, dilute one 50 µl aliquot with 450 µl of 10 mM HEPES (pH 7.4). Diluted PLL-PEG can be stored at 4 °C for one week.
7. Silane-PEG or Silane-PEG-biotin
Notes:
 - i. *Silane-PEG or Silane-PEG-biotin powders are weighted and aliquoted in 200 mg per eppendorf tube under argon gas. The tubes are tightly sealed with parafilm and stored at -20 °C.*
 - ii. *Silane-PEG and Silane-PEG-biotin solutions must be kept anhydrous and in the dark.*
 - a. Dissolve 200 mg powder in 200 ml of 96% ethanol plus 0.4 ml of 37% HCl.
 - b. To solubilize the Silane-PEG solution, heat to 50 °C in a water-bath. Keep the solution in a glass bottle.
 - c. Silane-PEG and silane-PEG-biotin solution are stored at room temperature in the dark for up to 4 months or around 15 coating. If experiments look dirty in the background, use freshly prepared coating solutions.
8. GTP 20 mM
Dissolve 250 mg GTP in 5 ml H₂O
Make aliquots and store at -20 °C
Before use, dilute the stock solution to 20 mM in H₂O or BRB80
9. Glucose 450 mg/ml
Dissolve 2.250 g of glucose in 5 ml of BRB80
Filtrate, aliquot and store at -80 °C
The day of use pre-dilute 1/10 in BRB80 and keep on ice
10. Deoxymix (catalase and glucose oxydase)

Dissolve 35 mg of catalase plus 250 mg of glucose-oxidase in 10 ml of BRB80
Filtrate, make 25 μ l aliquots, freeze in liquid nitrogen and store at -80 °C
Discard thawed aliquot after each day of use

11. NaOH, 1 M

Dissolve 8 g of NaOH in 200 ml deionized water
Discard after each use

12. BSA 1%/BRB80

Dilute 500 μ l of 10% BSA with 1 ml of BRB80 5 \times in 3.5 ml of filtrated deionized water

13. Methyl cellulose 1,500 cP

Dissolve 100 mg of methyl cellulose 1,500 cP in 10 ml of prewarm (60 °C) deionized water
Gently shake on rotating wheel for 30 min
Store at 4 °C for two weeks

14. HEPES, 10 mM

Dissolve 477 mg in 200 ml deionized water
Adjust pH to 7.4 with KOH
Store in aliquots at -20 °C

15. Pluronic F27, 10%

Dissolve 100 mg in 1 ml of deionized water
Store at 4 °C up to 2 months

16. PBS

Dissolve 1 tablet in 200 ml of deionized water
Store at -20 °C

17. Neutravidin stock solution

Dissolve Neutravidin in deionized water at a final concentration of 1 mg/ml
Store at -20 °C

18. Red tubulin mix

Dilute purified non-labelled and ATTO-565 tubulin at a 9:1 molar ratio in BRB80
Spin down aggregates at 100,000 $\times g$, 4 °C using TLA100 rotor
Estimate tubulin concentration by measuring the OD_{280nm} (1OD_{280nm} = 1 mg/ml = 10 μ M of tubulin)
Aliquot, quickly freeze and store in liquid nitrogen for up to 1 year

19. Polymerization mix

BRB80 supplemented with:

50 mM KCl

1% BSA

4 mM DTT

1 mM GTP

1 mM glucose

0.05% Methyl cellulose 1,500 cP

1/50 deoxy mix (70 μ g/ml catalase, 500 μ g/ml glucose oxidase, 1 mg/ml glucose)

12 μ M red tubulin mix
200 nM MAP6-N-GFP

Acknowledgments

Fundings: This work was supported by INSERM (Institut National de la Santé Et de la Recherche Médicale), CEA (Commissariat à l'Energie Atomique), CNRS (Centre National de la Recherche Scientifique), Université Grenoble Alpes, by grants from the Agence Nationale de la Recherche ANR MAMAs 2017-CE11-0026, ANR-15-IDEX-02 NeuroCoG in the framework of the "Investissements d'avenir" program and by fundings from the Ministère de l'enseignement supérieur et de la recherche. GIN is a member of the Grenoble Center of Excellence in Neurodegeneration (GREEN). The Photonic Imaging Center of Grenoble Institute Neuroscience (Univ. Grenoble Alpes–Inserm U1216) is part of the ISdV core facility and certified by the IBISA label.

This protocol is derived from Cuveillier *et al.* (2020).

Competing interests

The authors declare no competing interests.

References

1. Akhmanova, A. and Steinmetz, M. O. (2015). [Control of microtubule organization and dynamics: two ends in the limelight](#). *Nat Rev Mol Cell Biol* 16(12): 711-726.
2. Al-Bassam, J. (2014). [Reconstituting Dynamic Microtubule Polymerization Regulation by TOG Domain Proteins](#). In: *Methods in Enzymology* (Vol. 540, p. 131-148). Elsevier.
3. Alushin, G. M., Lander, G. C., Kellogg, E. H., Zhang, R., Baker, D. and Nogales, E. (2014). [High-Resolution Microtubule Structures Reveal the Structural Transitions in \$\alpha\beta\$ -Tubulin upon GTP Hydrolysis](#). *Cell* 157(5): 1117-1129.
4. Bechstedt, S., Lu, K. and Brouhard, G. J. (2014). [Doublecortin Recognizes the Longitudinal Curvature of the Microtubule End and Lattice](#). *Curr Biol* 24(20): 2366-2375.
5. Blom, H. and Brismar, H. (2014). [STED microscopy : Increased resolution for medical research?](#) *J Intern Med* 276(6): 560-578.
6. Brangwynne, C. P., MacKintosh, F. C., Kumar, S., Geisse, N. A., Talbot, J., Mahadevan, L., Parker, K. K., Ingber, D. E. and Weitz, D. A. (2006). [Microtubules can bear enhanced compressive loads in living cells because of lateral reinforcement](#). *J Cell Biol* 173(5): 733-741.
7. Cuveillier, C., Delaroche, J., Seggio, M., Gory-Fauré, S., Bosc, C., Denarier, E., Bacia, M., Schoehn, G., Mohrbach, H., Kulić, I., Andrieux, A., Arnal, I. and Delphin, C. (2020). [MAP6 is an intraluminal protein that induces neuronal microtubules to coil](#). *Sci Adv* 6(14): eaaz4344.

8. Harris, J. R. (2015). [Transmission electron microscopy in molecular structural biology: A historical survey](#). *Arch Biochem Biophys* 581: 3-18.
9. Leslie, K. and Galjart, N. (2013). [Going Solo: measuring the motions of microtubules with an in vitro assay for TIRF microscopy](#). In: *Methods in Cell Biology* (Vol. 115, p. 109-124). Elsevier.
10. Leung, J. M., Nagayasu, E., Hwang, Y.-C., Liu, J., Pierce, P. G., Phan, I. Q., Prentice, R. A., Murray, J. M. and Hu, K. (2020). [A doublecortin-domain protein of Toxoplasma and its orthologues bind to and modify the structure and organization of tubulin polymers](#). *BMC Mol Cell Biol* 21(1): 8.
11. Portran, D., Gaillard, J., Vantard, M. and Thery, M. (2013). [Quantification of MAP and molecular motor activities on geometrically controlled microtubule networks](#). *Cytoskeleton* 70(1): 12-23.
12. Ramirez-Rios, S., Serre, L., Stoppin-Mellet, V., Prezel, E., Vinit, A., Courriol, E., Fourest-Lieuvin, A., Delaroche, J., Denarier, E. and Arnal, I. (2017). [A TIRF microscopy assay to decode how tau regulates EB's tracking at microtubule ends](#). In: *Methods in Cell Biology* (Vol. 141, p. 179-197). Elsevier.
13. Weisenberg, R. C. (1972). [Microtubule Formation *in vitro* in Solutions Containing Low Calcium Concentrations](#). *Science* 177(4054): 1104-1105.

CELL BIOLOGY

MAP6 is an intraluminal protein that induces neuronal microtubules to coil

Camille Cuveillier^{1*}, Julie Delaroche^{1*}, Maxime Seggio^{1*}, Sylvie Gory-Fauré¹, Christophe Bosc¹, Eric Denarier¹, Maria Bacia², Guy Schoehn², Hervé Mohrbach³, Igor Kulić⁴, Annie Andrieux^{1†}, Isabelle Arnal^{1†‡}, Christian Delphin^{1†‡}

Neuronal activities depend heavily on microtubules, which shape neuronal processes and transport myriad molecules within them. Although constantly remodeled through growth and shrinkage events, neuronal microtubules must be sufficiently stable to maintain nervous system wiring. This stability is somehow maintained by various microtubule-associated proteins (MAPs), but little is known about how these proteins work. Here, we show that MAP6, previously known to confer cold stability to microtubules, promotes growth. More unexpectedly, MAP6 localizes in the lumen of microtubules, induces the microtubules to coil into a left-handed helix, and forms apertures in the lattice, likely to relieve mechanical stress. These features have not been seen in microtubules before and could play roles in maintaining axonal width or providing flexibility in the face of compressive forces during development.

INTRODUCTION

There is perhaps no cell type that must meet more extreme demands than neurons. From their birth and migration within the tight quarters of the developing neural crest to the precise navigation of axons tips extending toward targets that may be meters away, neurons must both maintain a proper shape and be sufficiently flexible to adapt their morphology to new functional demands. This dual capacity for persistence and plasticity derives largely from microtubules, which themselves can be stable, labile, or a combination of both (1).

Microtubules are hollow cylinders that are constantly being made and disassembled according to the cell's needs to grow, change shape, and move organelles or cargo within the intracellular space. They are composed of tubulin heterodimers, consisting of α -tubulin and β -tubulin, which join end to end to form protofilaments that associate laterally around a 25-nm-wide core. The β subunit is key to the microtubule's renowned dynamic instability: Guanosine triphosphate (GTP) bound to the β subunit is quickly hydrolyzed to guanosine diphosphate (GDP) soon after assembly, leading to a conformational change of tubulin that makes the microtubule more prone to depolymerization (2, 3). In purified tubulin preparations, microtubules alternate between phases of growth and shrinkage, known rather colorfully as rescues and catastrophes. In terminally differentiated neurons, however, dynamic microtubules coexist with long-lived microtubules characterized by slow turnover. These stable microtubules are thought to be crucial for the maintenance of axonal and dendritic architecture. Recent studies indicate that there is actually a whole repertoire of stable microtubule subtypes, but the specific roles of these subpopulations in neurons are not yet known (4). Further complicating this picture is the fact that different regions

of the same microtubule can have different degrees of lability or stability (1). A number of proteins and posttranslational modifications are thought to influence microtubule perdurance, particularly the microtubule-associated proteins (MAPs) (1), but their mechanisms remain elusive.

Our laboratory has been studying MAP6 (also known as stable tubule-only peptide), a structural MAP that has the unusual property of protecting microtubules against drug- and cold-induced depolymerization (5–8). This extreme stability appears to be a property unique to MAP6, and it serves a physiological purpose: MAP6-deficient mice suffer severe deficits in synaptic plasticity similar to those seen in schizophrenia, along with concomitant cognitive deficits (9). They also display axonal tract growth defects (10, 11), possibly due to microtubule lability that can be alleviated by microtubule-stabilizing drugs (12, 13). To better understand the mechanism by which neuronal microtubules acquire stability, we decided to study MAP6 activity at the level of individual microtubules.

RESULTS AND DISCUSSION

MAP6 forms microtubule intraluminal particles

We first analyzed microtubules extracted from primary cultured neurons of either wild-type or MAP6-deficient mouse embryos by cryo-electron microscopy. We observed the coexistence of two populations of microtubules in the wild-type condition (Fig. 1A): 64% contained intraluminal particles, and 36% did not. By contrast, the majority (73%) of MAP6-KO (knockout) neurons contained no visible intraluminal particles at all. This observation caught our attention for three reasons. First, MAP6 has been thought to be a structural MAP and thus to bind to the exterior of the microtubule lattice. Second, although intraluminal particles have been previously reported in microtubules observed in certain neuronal compartments (14), their identity has been completely unknown. Third, there is evidence that microtubules are regulated, at least in part, through the lumen: Tubulin acetylation, which occurs on long-lived microtubules, occurs within the lumen, and taxol, the major stabilizing agent, binds to the microtubule lumen (15); furthermore, so-called microtubule inner proteins (MIPs) within cilia and flagella have been found to be

Copyright © 2020
The Authors, some
rights reserved;
exclusive licensee
American Association
for the Advancement
of Science. No claim to
original U.S. Government
Works. Distributed
under a Creative
Commons Attribution
NonCommercial
License 4.0 (CC BY-NC).

¹Univ. Grenoble Alpes, Inserm U1216, CEA, CNRS, Grenoble Institut Neurosciences, GIN, 38000 Grenoble, France. ²Univ. Grenoble Alpes, CNRS, CEA, Institut for Structural Biology (IBS), 38000 Grenoble, France. ³Laboratoire de Chimie et Physique Théorique, UMR 7019, Université de Lorraine. ⁴Institut Charles Sandron, CNRS-Uds, 67034 Strasbourg, France.

*These authors contributed equally to this work.

†Corresponding author. Email: annie.andrieux@univ-grenoble-alpes.fr (A.A.); isabelle.arnal@univ-grenoble-alpes.fr (I.A.); christian.delphin@univ-grenoble-alpes.fr (C.D.)

‡These authors contributed equally to this work.

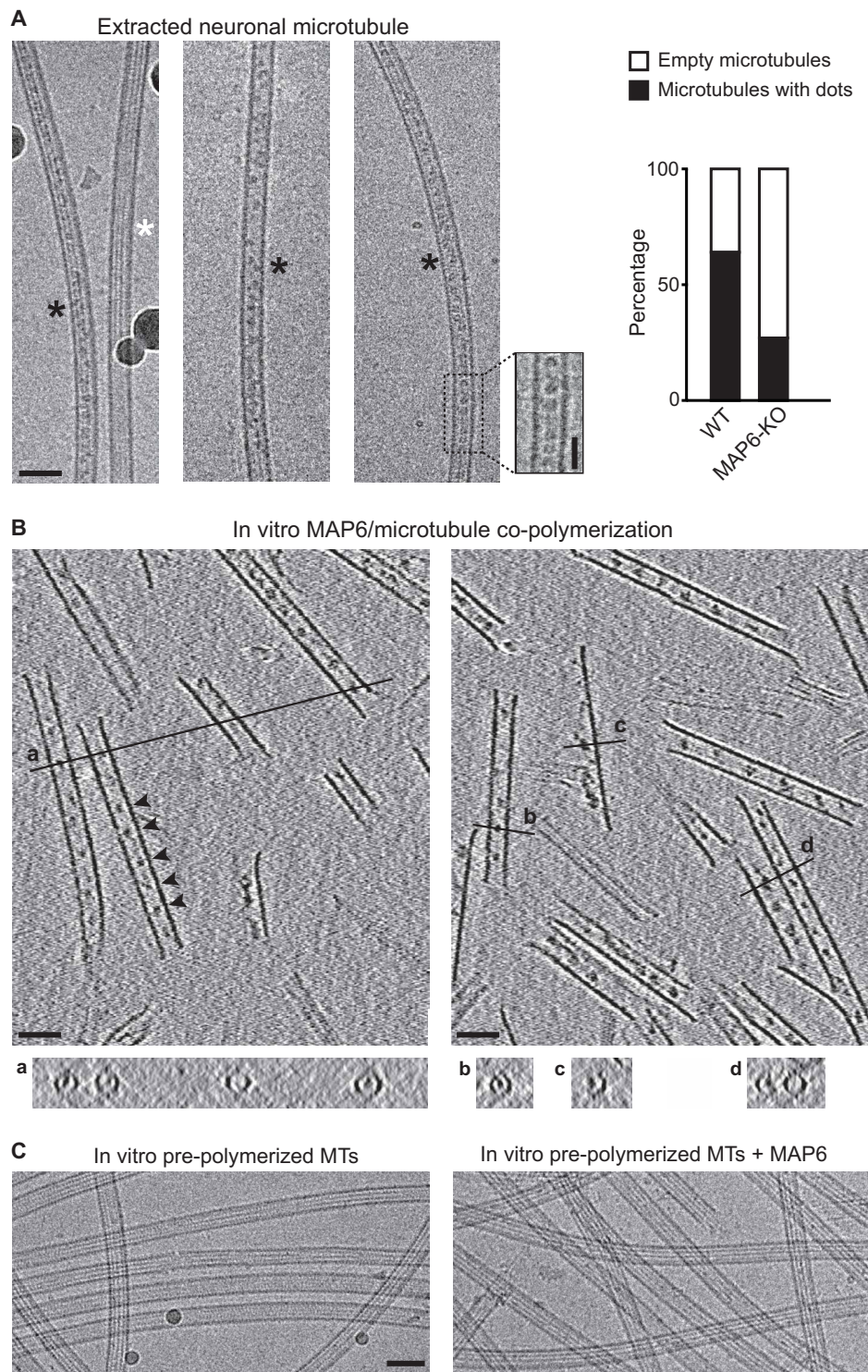


Fig. 1. MAP6 localizes inside microtubules. (A) Cryo-electron microscopy images showing the two types of microtubules extracted from primary cultured neurons of mouse embryos. Black and white stars indicate microtubules with and without intraluminal particles, respectively. Inset shows a high-magnification image of the area denoted by the dashed rectangle (a band-pass filter was applied and added to the original image to improve contrast). The percentages of microtubules with or without these particles in wild-type (WT) versus MAP6-KO neurons are indicated on the right. The total length of measured microtubules was 278 and 242 μm for wild-type and MAP6-KO conditions, respectively. Scale bars, 50 nm (horizontal) and 25 nm (vertical). (B) Main panels: Cryo-electron tomography of microtubules copolymerized in vitro with purified tubulin and MAP6 in the presence of GMPCPP. Arrowheads, microtubule inner particles. Bottom: (a to d) Transverse sections along the lines indicated in top panels showing localization of dots inside hollow tubes (a and b) or at the inner side of open protofilament sheets (c and d). (C) Cryo-electron microscopy images of in vitro pre-polymerized and taxol-stabilized microtubules (MTs), incubated with or without MAP6. Scale bars, 50 nm.

responsible for doublet microtubule stabilization (16). Could MAP6 be an inner protein for neuronal microtubules?

Because it would be difficult to answer this question in cells, we used *in vitro* reconstitution experiments to polymerize microtubules from purified tubulin in the presence of recombinant neuronal MAP6 (fig. S1A). Cryo-electron tomography revealed regularly spaced particles within microtubules copolymerized with MAP6 (Fig. 1B). Cross sections of the microtubules show that these particles are localized within the lumen and on the inner face of unclosed protofilament sheets at microtubule's growing end (Fig. 1B, a to d, and movie S1). These intraluminal particles have a mean diameter of 9 nm [9.27 ± 1.74 (SD), $n = 85$] and are spaced at ~ 31 -nm intervals [31.1 ± 6.7 (SD), $n = 189$]. When preformed taxol-stabilized microtubules were incubated with MAP6, no particles appeared within the microtubules (Fig. 1C), but MAP6-green fluorescent protein (GFP) did decorate the lattice exterior (fig. S1, B and C). This indicates that the intraluminal particles form only when MAP6 is present during co-polymerization.

MAP6 modulates microtubule dynamics

We next used total internal reflection fluorescence (TIRF) microscopy to analyze the influence of low concentrations of MAP6 on microtubule growth from stable seeds (Fig. 2A and fig. S2). MAP6 strongly inhibited microtubule depolymerization by reducing the shrinking rate and promoting rescue events (Fig. 2B). Unexpectedly, MAP6 also increased the frequency of catastrophes (Fig. 2B). This is unusual for a structural stabilizing MAP but would be expected for end-binding proteins that accumulate at the microtubule tips such as end-binding proteins (EBs) and members of the kinesin family (KIF2A, KIF18A, and KIF3C) (17–19). Thus, MAP6 exerts a strong stabilizing effect that likely involves binding along the lattice; at the same time, it destabilizes the microtubule ends. The combination of these two activities appears to produce slow-growing, largely stable microtubules with highly dynamic extremities.

MAP6 induces microtubule helical deformation

Besides influencing microtubule dynamics, MAP6 also altered the conformation of the growing microtubule. This effect, already visible at 30 nM MAP6, was quite notable at 150 to 200 nM (Fig. 2C). When observed by TIRF microscopy, microtubules grown in the presence of MAP6 took on the appearance of a dashed line instead of the continuous line visible in the control condition, because parts of the strand curve away from the illuminated field (~ 100 nm) at the bottom of the perfusion chamber (fig. S3A) (wide-field illumination is able to show the continuity of the strand). The orientation and the periodicity of the “dashes” compared to the overall direction of the microtubule indicate a left-handed, long-range helicity with a pitch of 5.5 ± 0.8 μm (SD, $n = 478$), which we confirmed using confocal microscopy with deconvolution (Airy scanning microscopy) at several focal illuminations along the z axis (Fig. 2D and movie S2). These curvatures cannot be explained by an increase in microtubule flexibility, because the overall growth of these three-dimensional (3D) helical microtubules remained linear for the duration of the experiment (movie S3). When MAP6 was added to preformed microtubules, only the newly growing sections were helical, while the preexisting ones remained linear (Fig. 2, E and F). These results indicate that, as for the formation of intraluminal particles, MAP6-dependent changes in microtubule structure require MAP6 to be present at the time of polymerization. This suggests that MAP6 acts at the tip of growing microtubules.

Intraluminal localization of MAP6 is required for microtubule helical deformation

The co-occurrence of tip destabilization, intraluminal particle formation, and microtubule conformational changes suggests that these events are linked. To see whether we could parse these events, we tested several MAP6 mutants with deletion of domains conserved among the neuronal isoforms of MAP6 family: the microtubule stabilizing Mn and Mc domains (MAP6 Δ Mn and MAP6 Δ Mc; fig. S4) and the N-terminal domain (MAP6 Δ 4–35; Fig. 3A) (20, 21). These domains are all required for microtubule curvature and microtubule inner particle formation (Fig. 3, B and D, and fig. S4). MAP6 Δ 4–35 was of particular interest, because it retains the known microtubule-binding domains (Fig. 3A) and accordingly bound to and stabilized microtubules to a similar degree as the full-length MAP6 by reducing shrinkage rates and increasing rescue events but failed to stimulate catastrophes (Fig. 3C). Overall, these data imply that the presence of MAP6 inside the lumen of growing microtubules is necessary for it to induce microtubule helicity.

MAP6 induces the formation of stable apertures in growing microtubules

Another consequence of the presence of MAP6 during microtubule polymerization is the apparition of numerous apertures in the lattice (Fig. 4, A and B). The fact that aperture frequency (~ 0.2 μm^{-1}) and size (~ 100 nm) did not change significantly over time (15 to 90 min; Fig. 4, C and D) indicates that MAP6-induced holes are not prone to efficient repair, such as that described for enzymatically or mechanically damaged microtubules (22, 23). MAP6 did not induce aperture formation in preformed taxol-stabilized microtubules (Fig. 4E), confirming that MAP6 must be present during microtubule polymerization to induce the mechanical stress that leads to aperture formation. Accordingly, the MAP6 Δ 4–35 mutant, which neither formed particles inside the lumen nor induced curvature, showed no more tendency to form apertures than control (Fig. 3E). It is worth noting that a cellular cryo-electron microscopy study recently reported similarly sized apertures within neuronal microtubules (24), which suggests that our results are relevant to the *in vivo* condition.

MAP6 induces microtubule bending: The frustrated core-shell model

How can we link the presence of MAP6 particles inside the lumen of growing microtubules with the formation of helical microtubules containing stable apertures? The induction of microtubule curvature by MAP6 can be explained by a frustrated core-shell model built on our previous tubulin bistability model (25, 26) based on two assumptions: (i) After GTP hydrolysis, the GDP-tubulin can exist as long or short tubulin states (Fig. 5A; see also Supplementary Text), and (ii) a cooperative (allosteric) interaction within a protofilament favors the switching of adjacent tubulins. In the absence of MAPs or external forces, following GTP hydrolysis, GDP-tubulins will predominantly switch to their short state and the microtubule is straight [Fig. 5B and (26)]. In the presence of MAP6, this picture changes drastically as large-scale coherent superhelices are formed. We propose that when tubulin and MAP6 are copolymerized, MAP6 forms an elastic network inside the microtubule lumen by binding to GTP-tubulin. The GDP-tubulin resulting from GTP hydrolysis tries to shorten, but the intraluminal MAP6 elastic network exerts an opposite effect favoring the long state (Fig. 5C). To solve this

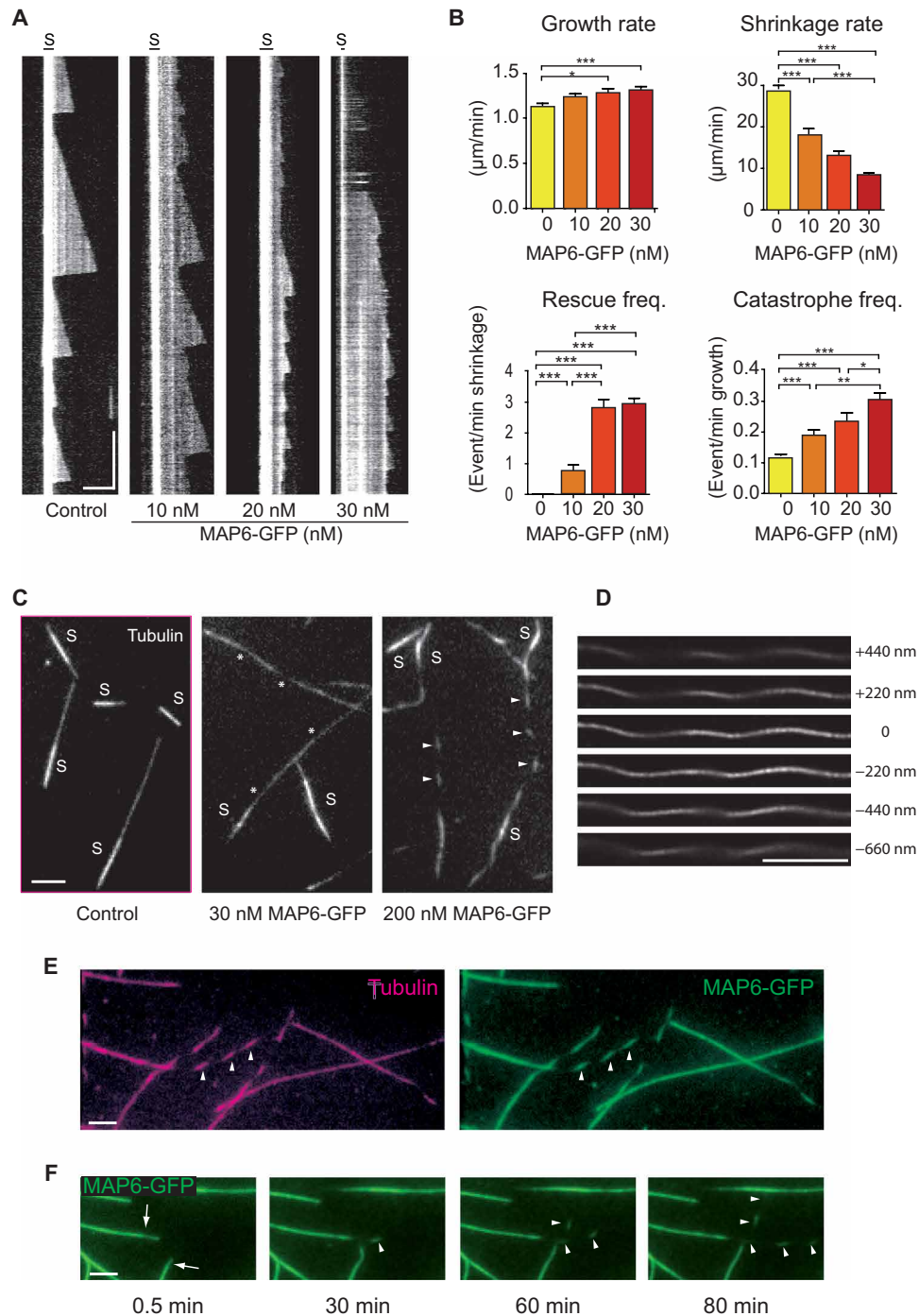


Fig. 2. MAP6 promotes the growth of stable, curved microtubules. (A) Kymographs show microtubules grown from GMPCPP seeds (S) in the presence of 10 μM tubulin and 0 (control), 10, 20, or 30 nM MAP6-GFP ($n = 93, 41, 38,$ and 40 microtubules, respectively). (B) Graphs show rates of growth and shrinkage and frequencies of rescue and catastrophe, extracted from kymographs presented in (A). (C) Pictures of microtubules grown as in (A) from GMPCPP seeds in the presence of 0 (control), 30, or 200 nM MAP6-GFP for 90 min. Note the modification of microtubule appearance, with increasing concentrations of MAP6, from a straight, uniform conformation (control, left), to a slightly curved shape with portions showing less fluorescence (*, middle), and finally to a dashed line appearance (arrowheads, right). (D) Microtubules grown in the presence of 200 nM MAP6-GFP and imaged using confocal Airyscan. Distance variations in the z axis are indicated to the right. (E) Microtubules first grown with 15 μM tubulin and then incubated with 10 μM tubulin and 150 nM MAP6-GFP for an additional 90 min (arrowheads point to areas of less fluorescence that create a dashed appearance). Magenta, tubulin; green, MAP6-GFP. (F) Time course of microtubule polymerization after addition of 150 nM MAP6-GFP. Preexisting microtubules are polymerized without MAP6-GFP (arrows), and dash-shaped microtubules are polymerized in the presence of MAP6-GFP (arrowheads). Note the rapid binding of MAP6-GFP to preexisting microtubules. Scale bars, 5 μm (horizontal) and 5 min (vertical). Bars, means; error bars, SEM. * $P < 0.05$; ** $P < 0.01$; *** $P < 0.001$, Kruskal-Wallis analysis of variance (ANOVA) followed by post hoc Dunn's multiple comparisons test.

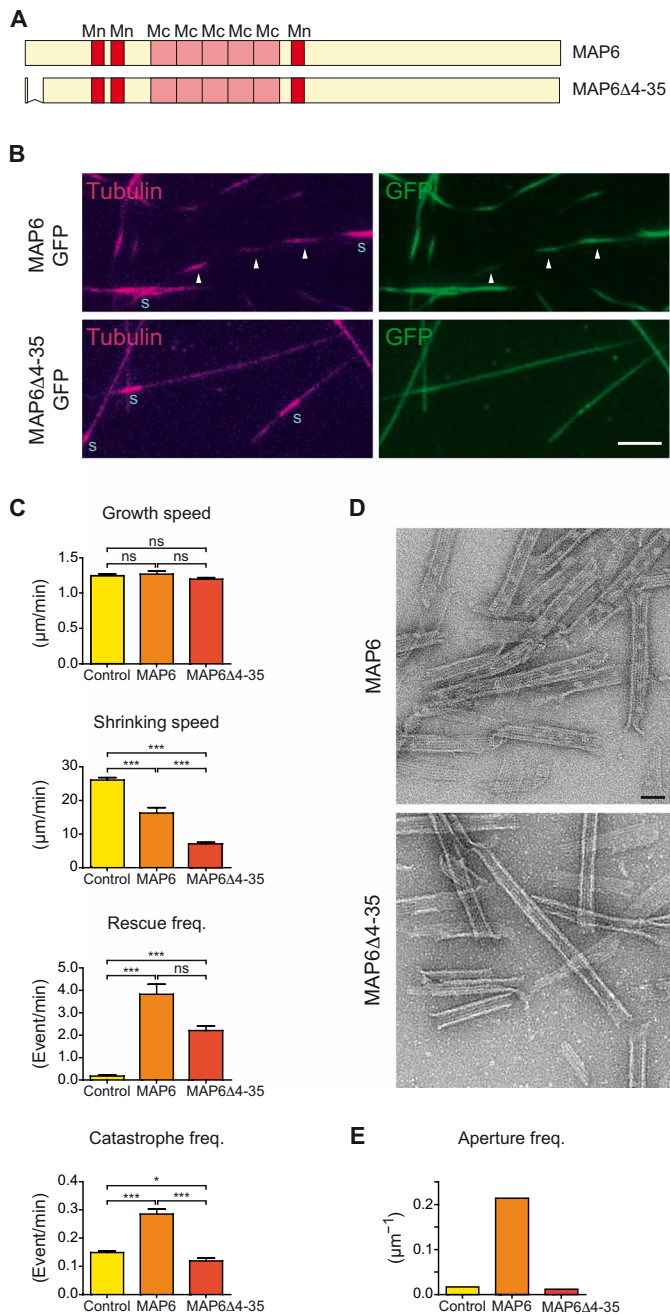


Fig. 3. MAP6Δ4-35 mutant stabilizes microtubules but does not lead to catastrophes, curvature, apertures, or particle densities within the lumen. (A) Scheme of MAP6 and MAP6Δ4-35 showing the temperature-sensitive (Mc) and temperature-insensitive (Mn) microtubule stabilization domains and the deletion present in the MAP6Δ4-35 mutant. (B) TIRF images of microtubules grown for 90 min from GMPCPP seeds in the presence of either 200 nM MAP6-GFP or MAP6Δ4-35-GFP. Arrowheads point to the dashed appearance of microtubules. Scale bar, 5 μm . (C) Dynamical parameters of microtubules polymerized in the absence or presence of either MAP6-GFP or MAP6Δ4-35-GFP ($n = 93, 29,$ and 43 microtubules, respectively). (D) Electron microscopy images of microtubules copolymerized with either MAP6-GFP or MAP6Δ4-35-GFP in the presence of GMPCPP and processed for negative staining. Scale bar, 50 nm. (E) Aperture frequency in microtubules copolymerized in the absence or presence of either MAP6-GFP or MAP6Δ4-35-GFP. * $P < 0.05$; *** $P < 0.001$, Kruskal-Wallis ANOVA followed by post hoc Dunn's multiple comparison. ns, not significant.

conflict and decrease the stored energy to a minimum, the lattice might adopt a frustrated conformation where, on one side of the microtubule lattice, a block of adjacent tubulin dimers adopts the short state conformation, while, on the opposite side, tubulin dimers stay in the long state conformation. This leads to a local bending in the direction of the short tubulin block. Once the curvature is established, the conformational switching of GDP-tubulin to the short state propagates via allosteric interaction along the protofilament axis and induces a continuous curvature of the microtubule, resulting in a global helical reshaping, a process reminiscent of the formation of polymorphic, helically coiled states of bacterial flagella (27, 28). As this spontaneous symmetry breaking mechanism is due to the coherent conformational switch of an entire block of protofilaments, the superhelical pitch is imposed by the intrinsic, lattice-imposed helicity of the protofilament along the microtubule axis (29, 30). This is in agreement with our data (Figs. 2 and 5D). Microtubules nucleated from guanylyl-(α, β)-methylene-diphosphonate (GMPCPP) microtubule seeds are likely to be composed of 14 protofilaments both because of the seeds (31) and the fact that MAP6 promotes the growth of 14-protofilament microtubules (fig. S5). The observation confirms that the superhelical shape of microtubules grown in the presence of MAP6 is left-handed, with a pitch of around 6 μm , in agreement with the intrinsic left-handed twisted protofilament structure observed in the 14-protofilament microtubules (without MAP) (32). This fact alone strongly supports the cooperativity assumption of our model.

We also measured the approximate width of the helix [around 700 nm (fig. S3B)] and calculated the average radius of curvature of helical microtubules (see Materials and Methods). The obtained value of 2.5 μm allows us to predict from the model a length difference of about 0.6% between the short and long state of GDP-tubulin (see Fig. 5D and Supplementary Text). MAP6Δ4-35 mutant that does not localize inside the microtubule wall fails to induce microtubule curvature (Fig. 5C).

Another consequence of the model is that the increased energy stored in the microtubule wall must be somehow released. It is possible that this extra stored energy destabilizes the microtubule lattice locally, leading to loss of specific dimers to relieve the mechanical stress; such a scenario could account for the increase in catastrophe frequency despite MAP6's potent stabilizing effect (Fig. 2) and the formation of apertures (Fig. 4).

What might be the functional relevance of helical microtubules with persistent holes and intraluminal densities in neurons? The heterogeneous distribution of neuronal MIPs that we and others find (14, 24) indicates that there are specialized functions for different kinds of stable microtubules. One possibility is that proteins inside microtubules and apertures in the microtubule lattice modify the accessibility of acetylation sites to αTAT1 (15, 33). By occupying greater width, a helical structure might influence the spatial organization of the microtubule network (e.g., by inhibiting microtubule co-alignment and bundling), help determine neurite or axonal width, or confer resistance to compressive loads such as might be encountered during development or regeneration (e.g., moving through a glial scar) (34). Given that MAP6 belongs to a family of four genes (MAP6, MAP6D1, FAM154A, and FAM154B) (21, 35), understanding the functions of these other proteins could help clarify the special roles of various microtubule types in neurons.

Luminal material has been known to exist within cellular microtubules for decades, but the identity and function of the particles have remained largely unknown (14, 24, 36). To our knowledge, the

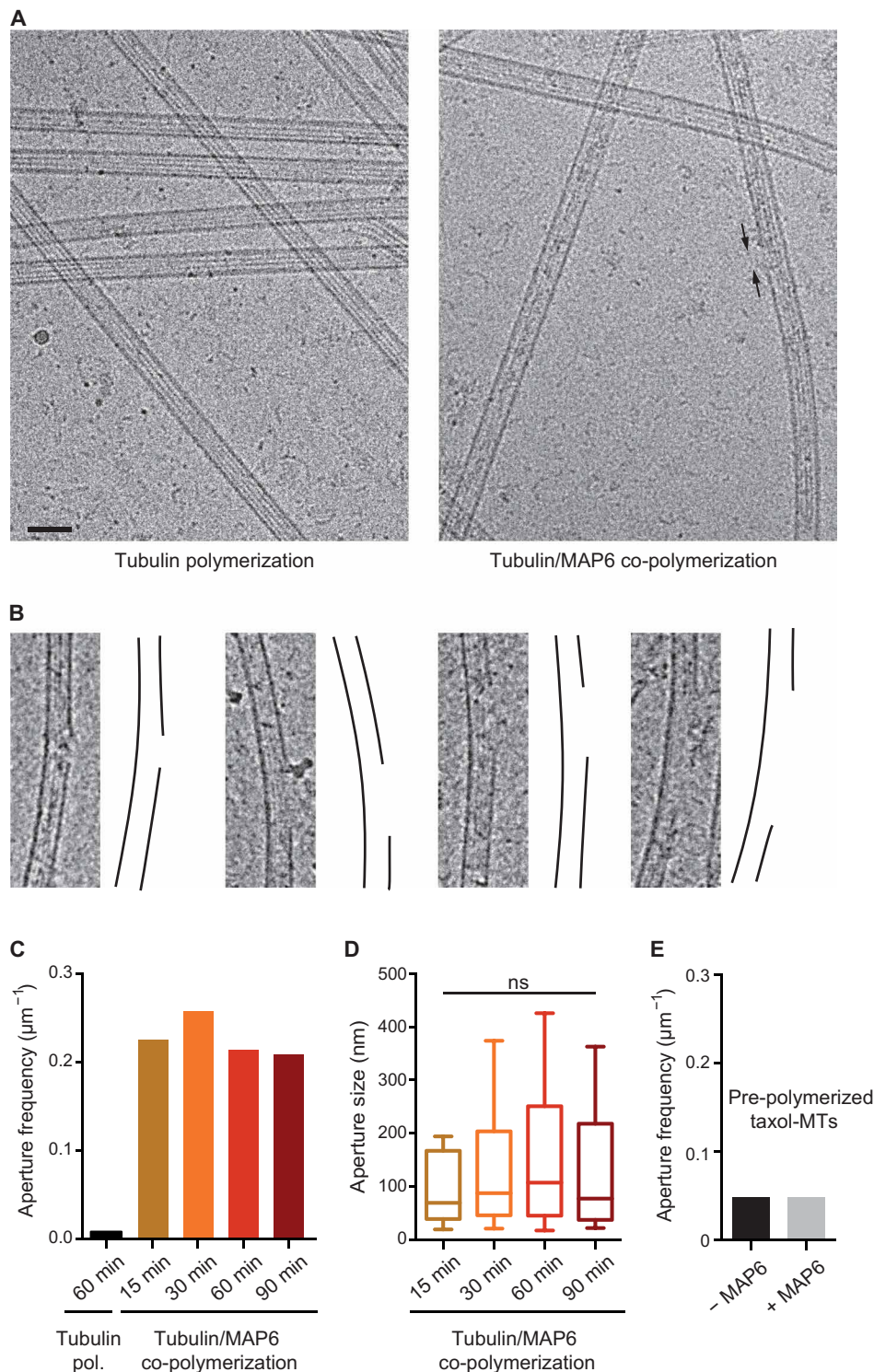


Fig. 4. MAP6 produces apertured microtubules. (A) Cryo-electron microscopy images of microtubules polymerized with tubulin alone (left) or in the presence of MAP6 (right). Arrows point to one aperture in the microtubule lattice. Scale bar, 50 nm. (B) Examples of apertures observed in microtubules polymerized with MAP6. In each case, the micrograph is on the left, and a drawing of the microtubule wall is on the right. To improve contrast, a band-pass filter was applied and added to original images. (C) Aperture frequency on microtubules polymerized with tubulin alone or in the presence of MAP6 at several polymerization times. The total length of measured microtubules was 370, 164, 291, 569, and 248 μm in the control (no MAP6) and at 15, 30, 60, and 90 min, respectively. (D) Distribution of aperture size in the presence of MAP6 at indicated polymerization times. Whiskers represent the 10th and 90th percentiles of the data. Bars within boxes represent the median. Kruskal-Wallis ANOVA followed by post hoc Dunn's multiple comparisons test; $n = 38, 75, 122,$ and 52 for assembly at 15, 30, 60, and 90 min, respectively. (E) Aperture frequency in preformed taxol-stabilized microtubules incubated without or with MAP6. The total length of measured microtubules was 319 and 237 μm without and with MAP6, respectively.

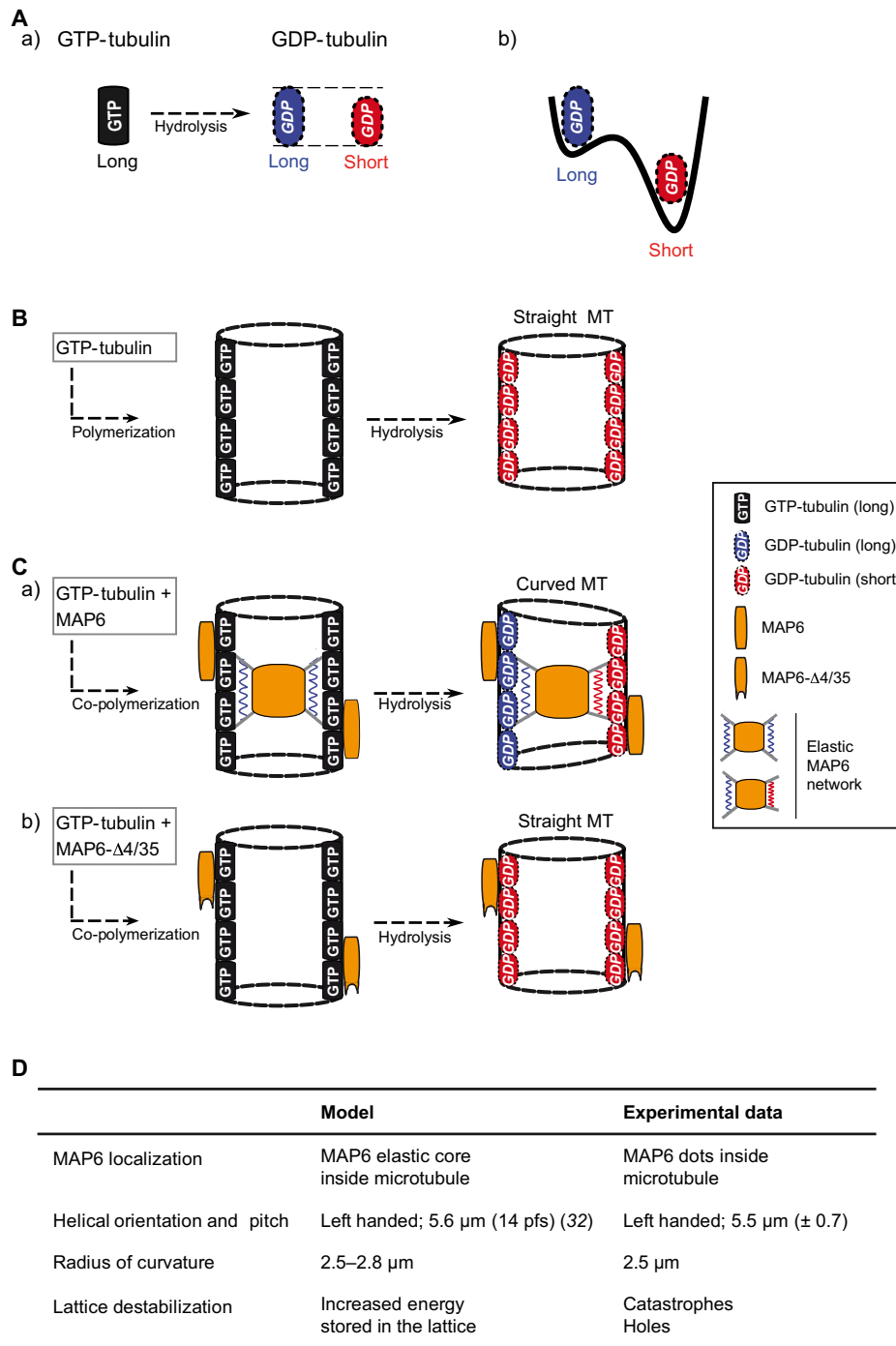


Fig. 5. MAP6 induces microtubule bending: The frustrated core-shell model. (A) After GTP hydrolysis, the GDP-bound tubulin protofilaments can exist in two distinct states (a), with slightly differing elongations (see Supplementary Text): a long tubulin state (blue) and a short tubulin state (red). (b) The short state of the GDP-tubulin is energetically favored with respect to the long one. (B) For microtubules polymerized with tubulin alone, GTP-tubulin is incorporated into the lattice in its long state. After GTP hydrolysis, the short GDP-tubulin state is energetically dominant. The microtubule shortens but stays straight. To allow visualization of the lumen, only two protofilaments, one on each side of the microtubule, are shown. (C) For microtubules copolymerized with tubulin and MAP6 (a), MAP6 binds to the nonhydrolyzed, long GTP-tubulin state and forms an elastic network inside the microtubule, stabilizing the initial (long) state at the time point of binding. After hydrolysis, the GDP-tubulin tends to shorten but enters into conflict with the force exerted by the intraluminal MAP6 network to maintain the tubulin long state. The resulting frustration is minimized by a symmetry-breaking mechanism [i.e., compact tubulin dimers (red) on one side of the cylinder and elongated tubulin dimers (blue) on the opposite side], leading to a curved ground state and in which areas of high local stress form holes or apertures (not shown in the scheme; Fig. 4). The observed radius of curvature of the superhelix, about 2.5 μm, is theoretically realized for a length difference of about 0.6% between the short and long state of GDP-tubulin (see Supplementary Text for more details). (b) MAP6Δ4-35 mutant only binds outside the microtubule where it stabilizes the lattice without inducing microtubule curvature. Note that MAP6 also binds on the microtubule external surface (a). (D) Model validation: The table shows the agreements between data predicted from the model with those experimentally obtained.

tubulin acetyl transferase α TAT1, which catalyzes tubulin acetylation in the lumen of microtubules, is the only protein so far thought to function inside microtubules—yet the evidence for α TAT1 localization within microtubules remains indirect (37). MAP6 would therefore be the first identified MIP in neurons. Further work will be needed to tease out the specific neuronal functions that require such a class of stable, helical microtubules.

MATERIALS AND METHODS

Preparation of tubulin

Tubulin was purified from bovine brain and labeled with ATTO-565 or ATTO-496 [ATTO-TEC GmbH, Germany (38)].

Recombinant protein expression

MAP6 with an N-terminal histidine-Tag was cloned either directly in pFastbac-Htb or in fusion with GFP and an additional histidine-Tag at the C termini. Bacmids and baculovirus were produced using DH10BAC and sf9 insect cells as indicated by the manufacturer (Thermo Fisher Scientific). Protein expression was carried out in High Five cells in suspension at 10^6 cells/ml for 48 hours at 27°C.

Purification of His-MAP6

Each population of 10^8 High Five cells was resuspended in 5 ml of lysis buffer [50 mM Hepes (pH 7.4), 400 mM NaCl, 0.5% Triton X-100, and 1 protease inhibitor tablet mini (Roche)] and centrifuged at 200,000g for 30 min at 4°C. Heat-stable proteins present in solution were recovered in the supernatant after incubation at 90°C for 15 min and centrifugation (200,000g for 30 min at 4°C). The soluble fraction was diluted three times with the dilution buffer [50 mM Hepes (pH 7.4) and 0.5% Triton X-100], passed through a 4-ml Q-Sepharose column, and loaded on a 5-ml SP Sepharose column. After washing with Q/SP column buffer [50 mM Hepes (pH 7.4), 150 mM NaCl, and 0.5% Triton X-100], bound proteins were eluted with five column volumes of elution buffer [50 mM Hepes (pH 7.4), 400 mM NaCl, and 0.05% Triton X-100]. Imidazole (2 mM) was then added, and the solution was loaded on a cobalt column (1 ml; Thermo Fisher Scientific). After washing with 10 mM imidazole in 50 mM Hepes (pH 7.4) and 400 mM NaCl, bound proteins were eluted by increasing the imidazole concentration up to 200 mM. The eluate volume was reduced to 200 μ l by concentration on Amicon Ultra 30K (Merck Millipore) and injected on a gel filtration column (Superdex 200 10/300; Thermo Fisher Scientific) in 20 mM Hepes (pH 7.4) and KCl 100 mM. Collected fractions containing the protein were pooled, concentrated as above on Amicon Ultra 30K, centrifuged at 200,000g for 10 min at 4°C, aliquoted, quick-frozen in liquid nitrogen, and stored at -80°C . Protein concentration was quantified by SDS-polyacrylamide gel electrophoresis (PAGE) and Coomassie blue staining against a bovine serum albumin (BSA) concentration ladder using ChemiDoc (Bio-Rad) scanning and ImageJ software.

Purification of His-MAP6-GFP-His, His-MAP6 Δ Mn-GFP-His, His-MAP6 Δ Mc-GFP-His, or His-MAP6- Δ 4-35-GFP-His protein

Each 10^8 High Five cell pellet was resuspended in 5 ml of lysis buffer A [50 mM Hepes (pH 7.4), 500 mM arginine, 1 mM EGTA/EDTA, and 1 protease inhibitor tablet mini (Roche)]. After centrifugation (150,000g for 30 min at 4°C), the supernatant was diluted 10 times in dilution buffer [50 mM Hepes (pH 7.4), 100 mM NaCl, 0.1% Triton X-100, and 1 mM EGTA/EDTA] and centrifuged again at 150,000g

for 30 min at 4°C. The supernatant was passed through a 4-ml Q-Sepharose and loaded on a 5-ml SP Sepharose. After washing with Q/SP column buffer [50 mM Hepes (pH 7.4), 150 mM NaCl, and 0.05% Triton X-100], bound proteins were eluted with a five-column volume of SP elution buffer [50 mM Hepes (pH 7.4), 400 mM NaCl, and 0.05% Triton]. Imidazole (6 mM) was then added, and the solution was loaded on a cobalt column (1 ml; Thermo Fisher Scientific). The cobalt column was first washed with 50 mM Hepes (pH 7.4) and 400 mM NaCl in the presence of 20 mM imidazole, and the bound proteins were further eluted in the presence of 200 mM imidazole. The proteins were further purified using Superdex-200 columns as described above for His-MAP6.

TIRF microscopy

Perfusion chambers were prepared with functionalized polyethylene glycol (PEG)-silane glass coverslips. Coverslips were first sonicated in acetone for 30 min, washed in acetone (30 min) and 96% ethanol (EtOH) (15 min), and rinsed with water. Coverslips were next treated with a 2% Hellmanex solution (Hellma) for 2 hours and rinsed in water. They were next sonicated in 1 M NaOH for 15 min, rinsed with water, further sonicated in 96% EtOH, and rinsed again with water. Coverslips were dried under clean air stream, treated with plasma, and incubated overnight at room temperature under gentle agitation in a 1 mg/ml solution of PEG-silane (30 kDa, Creative PEGWorks) or PEG-silane-biotin (3.5 kDa, Laysan Bio) in EtOH containing 0.02% HCl. Coverslips were next rinsed in 96% EtOH and water, air-dried, and stored at 4°C. Perfusion chambers were assembled between PEG-silane-coated and PEG-silane-biotin-coated coverslip using double adhesive tape face to form a flow chamber of around 5 μ l in volume.

Preparation of microtubule seeds

Microtubule seeds were obtained by polymerizing 10 μ M tubulin (50% of biotinylated tubulin and 50% of ATTO-565-labeled tubulin) in the presence of 1 mM GMPCPP in BRB80 buffer at 37°C for 1 hour. Microtubule seeds were then centrifuged for 5 min at 100,000g, resuspended in BRB80 with 1 mM GMPCPP, aliquoted, and stored in liquid nitrogen. For each experiment, one aliquot was thawed at 35°C and diluted (1:300 to 1:500) in BRB80 + 1% BSA.

Microtubule polymerization assay in TIRF microscopy

The flow chamber was successively perfused with neutravidin (25 μ g/ml; Pierce) in 1% BSA, Poly(L-lysine) (PLL)-g-PEG (2-kDa solution; 0.1 mg/ml; JenKem) in 10 mM Hepes (pH 7.4), 1% pluronic F127 in BRB80, and 1% BSA in BRB80 buffer and finally with the microtubule seed solution. Microtubule polymerization was initiated with 10 μ M tubulin (containing 10% of ATTO-565-labeled tubulin and 90% unlabeled tubulin) with the indicated concentration of MAP6 proteins in TIRF buffer {BRB80 plus 50 mM KCl, 4 mM dithiothreitol (DTT), 1% BSA, glucose (1 mg/ml), catalase (70 μ g/ml), glucose oxidase (600 μ g/ml), and 0.05% methylcellulose [1500 centipoise (cP)]}. Chambers were sealed with dental paste and visualized on an inverted microscope (Eclipse Ti, Nikon) equipped with an iLas TIRF system (Roper Scientific), a cooled charge-coupled device camera (EMCCD Evolve 512, Photometrics) with 512 \times 512-pixel imaging array (16 \times 16 μ m pixels), and a warm stage controller (LINKAM MC60), all under the control of MetaMorph software (version 7.7.5, Molecular Devices). Samples were excited with 491- and 561-nm lasers and observed using an Apochromat 60 \times or 100 \times oil-immersion objective (numerical aperture, 1.49). Time-lapse imaging

was performed at one frame per 5 s with a 100-ms exposure time during 45 to 90 min at 32°C.

Analysis of microtubule dynamics

Image analysis was performed in ImageJ software, with an in-house plugin for extracting the four parameters determining microtubule dynamics from the kymograph. Growth and shrinkage rates were calculated from the slopes corresponding to the microtubules' growing and shrinking phases, respectively. The frequencies of catastrophe and rescue events were calculated by dividing the number of events by the time spent in the growing or the shrinking phase, respectively. Graphs and statistical analysis were made using GraphPad Prism.

Wide-field TIRF and Airyscan imaging of microtubules

Microtubules were allowed to polymerize as described above, except that the perfusion chamber was not sealed but kept under wet atmosphere for 45 min. Free tubulin was removed by gentle perfusion with BRB containing 0.05% methylcellulose (1500 cP), and microtubules were fixed with 0.5% of glutaraldehyde in the same buffer for 5 min. Imaging buffer [BRB80, 0.1% methylcellulose (1500 cP), catalase (82 µg/ml), glucose oxidase (0.58 mg/ml), and glucose (1 mg/ml)] was then perfused, and flow chambers were sealed with paste. Imaging was done using TIRF microscopy as described above in TIRF or wide-field illumination or, for higher-resolution analysis, with a confocal LSM710/Airyscan (Zeiss) microscope.

Determination of the radius of curvature of helical microtubule

The radius of curvature (R_c) for the helical microtubule was calculated using the formula $R_c = r + p^2/4\pi^2r$, where r is the radius and p is the pitch of the helix. It yields a value of ~ 2.5 µm for a radius of 0.35 µm and a pitch of 5.5 µm.

MAP6-GFP interaction with taxol-stabilized microtubules

Microtubules were polymerized from 70 µM tubulin in BRB buffer plus 1 mM GTP for 30 min at 35°C. Taxol (100 µM) was then added, and the incubation was continued for additional 15 min. The polymerization mix was diluted to 15 µM tubulin and centrifuged at 200,000g for 10 min at 35°C. Microtubules were resuspended in one volume of binding buffer (BRB80 plus 50 mM KCl, 5 mM DTT, 0.05% Tween 20, and 10 µM taxol), and their concentration was quantified using a tubulin concentration ladder and analysis of the scanned Coomassie blue-stained SDS-PAGE gels with ImageJ software. Microtubules (200 nM) were incubated with increasing concentrations of MAP6-N-GFP (5 to 500 nM in triplicates) for 10 min at 35°C in 10 µl of binding buffer and centrifuged at 200,000g for 10 min at 35°C. The supernatants were discarded, the pellets were resuspended with 200 µl of 3 M urea in 100 mM tris-HCl (pH 8.0), and the quantities of MAP6-GFP co-sedimented with tubulin were quantified against a MAP6-GFP calibration curve using PHERAstar FS (BMG Labtech). Concentrations of bound MAP6-GFP were plotted as a function of the concentration of MAP6-GFP input. GraphPad Prism was used for curve fitting (one-site binding equation) and $K_{d,app}$ determination.

Extraction of neuronal microtubules for cryo-electron microscopy analysis

Mouse hippocampal neurons were prepared as previously described (21). In accordance with the policy of the Institut des Neurosciences of Grenoble (GIN) and the French legislation, experiments were done

in compliance with the European Community Council Directive of 24th November 1986 (86/609/EEC). The research involving animals was authorized by the Direction Départementale de la protection des populations—Préfecture de l'Isère-France and by the ethics committee of GIN number 004 accredited by the French Ministry for of Research. At 8 days of culture (8 days in vitro), they were rinsed with PEM buffer (80 mM Pipes, 2 mM EGTA, and 1 mM MgCl₂), permeabilized for 3 min at 37°C in PEM buffer supplemented with 10 µM taxol and 0.5% Triton X-100, and washed three times with PEM-taxol. Neurons were then scraped in PEM-taxol and centrifuged for 3 min at 40g, and the supernatants were immediately frozen.

Transmission electron microscopy and negative staining

Tubulin was polymerized at 3 µM in BRB80 buffer supplemented with 0.5 mM GMPCPP and 10% dimethyl sulfoxide (DMSO) in the absence or presence of 1 µM MAP6 or MAP-GFP for 40 min at 32°C. A 4-µl sample drop was applied to a glow-discharge copper carbon-coated grid, blotted, and stained with 2% uranyl acetate for 30 s. Grids were observed using a FEI Tecnai F20 200 kV FEG equipped with a 4K × 4K FEI Ceta CMOS (complementary metal-oxide semiconductor) camera (FEI Company Ltd.).

Cryo-electron microscopy and tomography

Vitreous ice-embedded microtubules were prepared under controlled temperature and humidity using the vitrification robot EM-GP2 (Leica). Tubulin (6 µM) was polymerized at 30°C in the presence of MAP6 (0.3 µM) in BRB80 buffer supplemented with 50 mM KCl and 1 mM GTP. Sample (4 µl) was applied onto holey carbon grids in the EM-GP2 chamber at various incubation times (15, 30, 60, and 90 min) followed by blotting and vitrification in liquid ethane. For control experiments, microtubules were polymerized from 60 µM tubulin in BRB80 buffer supplemented with 50 mM KCl and 1 mM GTP at 32°C for 60 min. For experiments using preformed microtubules, taxol-stabilized microtubules (1.5 µM) were incubated with MAP6 (0.3 µM) for 30 min at 32°C. For experiments using extracts, extracts containing microtubules were rapidly thawed before vitrification. Specimens were observed under low-dose conditions using a FEI Tecnai F20 equipped with a 4K × 4K FEI Ceta CMOS camera and operated at 200 kV. Image analysis was performed in ImageJ software.

For cryo-electron tomography, 10-nm gold nanoparticles coated with cationic BSA (Aurion Gold Tracers, 210111) were prepared in BRB80 as described previously (39) and used as fiducial markers for 3D reconstructions. Tubulin (6 µM) was polymerized in the presence of MAP6 (2 µM) in BRB80 buffer supplemented with 0.5 mM GMPCPP at 32°C during 40 min. Sample (4 µl) was mixed with 1 µl of fiducial markers and deposited onto a holey carbon-coated grid (Quantifoil, R 3.5/1) in the humid and temperature-controlled EM-GP2 chamber before blotting and vitrification. Specimens were observed on a FEI Tecnai F20 equipped with a 4K × 4K FEI Ceta CMOS camera and operated at 200 kV. Tomographic tilt series were acquired at a magnification of $\times 29,000$ between $\pm 60^\circ$ (2° increments) under low electron dose (1 to 2 $e/\text{Å}^2$) and at a defocus of -4 to -5 µm, using FEI tomography software. Tomograms were reconstructed using IMOD and binned by a factor of 2 (final pixel size of 0.70 nm).

SUPPLEMENTARY MATERIALS

Supplementary material for this article is available at <http://advances.sciencemag.org/cgi/content/full/6/14/eaaz4344/DC1>

[View/request a protocol for this paper from Bio-protocol.](#)

REFERENCES AND NOTES

- P. W. Baas, A. N. Rao, A. J. Matamoros, L. Leo, Stability properties of neuronal microtubules. *Cytoskeleton* **73**, 442–460 (2016).
- G. M. Alushin, G. C. Lander, E. H. Kellogg, R. Zhang, D. Baker, E. Nogales, High resolution microtubule structures reveal the structural transitions in $\alpha\beta$ -tubulin upon GTP hydrolysis. *Cell* **157**, 1117–1129 (2014).
- T. Mitchison, M. Kirschner, Dynamic instability of microtubule growth. *Nature* **312**, 237–242 (1984).
- R. P. Tas, L. C. Kapitein, Exploring cytoskeletal diversity in neurons. *Science* **361**, 231–232 (2018).
- C. Delphin, D. Bouvier, M. Seggio, E. Couriol, Y. Saoudi, E. Denarier, C. Bosc, O. Valiron, M. Bisbal, I. Arnal, A. Andrieux, MAP6-F is a temperature sensor that directly binds to and protects microtubules from cold-induced depolymerization. *J. Biol. Chem.* **287**, 35127–35138 (2012).
- D. Job, C. T. Rauch, R. L. Margolis, High concentrations of STOP protein induce a microtubule super-stable state. *Biochem. Biophys. Res. Commun.* **148**, 429–434 (1987).
- P. W. Baas, S. R. Heidemann, Microtubule reassembly from nucleating fragments during the regrowth of amputated neurites. *J. Cell Biol.* **103**, 917–927 (1986).
- L. Guillaud, C. Bosc, A. Fourest-Lieuvain, E. Denarier, F. Pirollet, L. Lafanèchère, D. Job, STOP proteins are responsible for the high degree of microtubule stabilization observed in neuronal cells. *J. Cell Biol.* **142**, 167–179 (1998).
- A. Andrieux, P. A. Salin, M. Vernet, P. Kujala, J. Baratier, S. Gory-Fauré, C. Bosc, H. Pointu, D. Proietto, A. Schweitzer, E. Denarier, J. Klumperman, D. Job, The suppression of brain cold-stable microtubules in mice induces synaptic defects associated with neuroleptic-sensitive behavioral disorders. *Genes Dev.* **16**, 2350–2364 (2002).
- J.-C. Deloulme, S. Gory-Fauré, F. Mauconduit, S. Chauvet, J. Jonckheere, B. Boulan, E. Mire, J. Xue, M. Jany, C. Maucler, A. A. Deparis, O. Montigon, A. Daoust, E. L. Barbier, C. Bosc, N. Deglon, J. Brocard, E. Denarier, I. Le Brun, K. Pernet-Gallay, I. Vilgrain, P. J. Robinson, H. Lahrech, F. Mann, A. Andrieux, Microtubule-associated protein 6 mediates neuronal connectivity through Semaphorin 3E-dependent signalling for axonal growth. *Nat. Commun.* **6**, 7246 (2015).
- U. Gimenez, B. Boulan, F. Mauconduit, F. Tauriel, M. Leclercq, E. Denarier, J. Brocard, S. Gory-Fauré, A. Andrieux, H. Lahrech, J. C. Deloulme, 3D imaging of the brain morphology and connectivity defects in a model of psychiatric disorders: MAP6-KO mice. *Sci. Rep.* **7**, 10308 (2017).
- A. Andrieux, P. Salin, A. Schweitzer, M. Bégou, B. Pachoud, P. Brun, S. Gory-Fauré, P. Kujala, M. F. Suaud-Chagny, G. Höfle, D. Job, Microtubule stabilizer ameliorates synaptic function and behavior in a mouse model for schizophrenia. *Biol. Psychiatry* **60**, 1224–1230 (2006).
- A. Daoust, S. Bohic, Y. Saoudi, C. Debacker, S. Gory-Fauré, A. Andrieux, E. L. Barbier, J.-C. Deloulme, Neuronal transport defects of the MAP6 KO mouse—a model of schizophrenia—and alleviation by Epothilone D treatment, as observed using MEMRI. *Neuroimage* **96**, 133–142 (2014).
- B. K. Garvalov, B. Zuber, C. Bouchet-Marquis, M. Kudryashev, M. Gruska, M. Beck, A. Leis, F. Frischknecht, F. Bradke, W. Baumeister, J. Dubochet, M. Cyrklaff, Luminal particles within cellular microtubules. *J. Cell Biol.* **174**, 759–765 (2006).
- E. Nogales, M. Whittaker, R. A. Milligan, K. H. Downing, High-resolution model of the microtubule. *Cell* **96**, 79–88 (1999).
- M. Ichikawa, K. H. Bui, Microtubule inner proteins: A meshwork of luminal proteins stabilizing the doublet microtubule. *Bioessays* **40**, 1700209 (2018).
- M. K. Gardner, M. Zanic, C. Gell, V. Bormuth, J. Howard, Depolymerizing kinesins Kip3 and MCAK shape cellular microtubule architecture by differential control of catastrophe. *Cell* **147**, 1092–1103 (2011).
- R. Mohan, E. A. Katrukha, H. Doodhi, I. Smal, E. Meijering, L. C. Kapitein, M. O. Steinmetz, A. Akhmanova, End-binding proteins sensitize microtubules to the action of microtubule-targeting agents. *Proc. Natl. Acad. Sci. U.S.A.* **110**, 8900–8905 (2013).
- S. Guzik-Lendrum, I. Rayment, S. P. Gilbert, Homodimeric kinesin-2 KIF3CC promotes microtubule dynamics. *Biophys. J.* **113**, 1845–1857 (2017).
- C. Bosc, R. Frank, E. Denarier, M. Ronjat, A. Schweitzer, J. Wehland, D. Job, Identification of novel bifunctional calmodulin-binding and microtubule-stabilizing motifs in STOP proteins. *J. Biol. Chem.* **276**, 30904–30913 (2001).
- S. Gory-Fauré, V. Windscheid, C. Bosc, L. Peris, D. Proietto, R. Franck, E. Denarier, D. Job, A. Andrieux, STOP-like protein 21 is a novel member of the STOP family, revealing a Golgi localization of STOP proteins. *J. Biol. Chem.* **281**, 28387–28396 (2006).
- L. Schaedel, K. John, J. Gaillard, M. V. Nachury, L. Blanchoin, M. Théry, Microtubules self-repair in response to mechanical stress. *Nat. Mater.* **14**, 1156–1163 (2015).
- A. Vemu, E. Szczesna, E. A. Zehr, J. O. Spector, N. Grigorieff, A. M. Deaconescu, A. Roll-Mecak, Severing enzymes amplify microtubule arrays through lattice GTP-tubulin incorporation. *Science* **361**, eaau1504 (2018).
- J. Atherton, M. Stouffer, F. Francis, C. A. Moores, Microtubule architecture in vitro and in cells revealed by cryo-electron tomography. *Acta Crystallogr. D Struct. Biol.* **74**, 572–584 (2018).
- H. Mohrbach, A. Johnner, I. M. Kulić, Cooperative lattice dynamics and anomalous fluctuations of microtubules. *Eur. Biophys. J.* **41**, 217–239 (2012).
- F. Ziebert, H. Mohrbach, I. M. Kulić, Why microtubules run in circles: Mechanical hysteresis of the tubulin lattice. *Phys. Rev. Lett.* **114**, 148101 (2015).
- S. Asakura, Polymerization of flagellin and polymorphism of flagella. *Adv. Biophys.* **1**, 99–155 (1970).
- C. R. Calladine, Construction of bacterial flagella. *Nature* **255**, 121–124 (1975).
- D. Chrétien, R. H. Wade, New data on the microtubule surface lattice. *Biol. Cell* **71**, 161–174 (1991).
- S. Ray, E. Meyhöfer, R. A. Milligan, J. Howard, Kinesin follows the microtubule's protofilament axis. *J. Cell Biol.* **121**, 1083–1093 (1993).
- A. A. Hyman, D. Chrétien, I. Arnal, R. H. Wade, Structural changes accompanying GTP hydrolysis in microtubules: Information from a slowly hydrolyzable analogue guanylyl-(α,β)-methylene-diphosphonate. *J. Cell Biol.* **128**, 117–125 (1995).
- R. H. Wade, D. Chrétien, Cryoelectron microscopy of microtubules. *J. Struct. Biol.* **110**, 1–27 (1993).
- V. Soppina, J. F. Herbstman, G. Skiniotis, K. J. Verhey, Luminal localization of α -tubulin K40 acetylation by cryo-EM analysis of fab-labeled microtubules. *PLoS ONE* **7**, e48204 (2012).
- C. Lazarus, M. Soheilypour, M. R. Mofrad, Torsional behavior of axonal microtubule bundles. *Biophys. J.* **109**, 231–239 (2015).
- D. Dacheux, B. Roger, C. Bosc, N. Landrein, E. Roche, L. Chansel, T. Trian, A. Andrieux, A. Papaxanthos-Roche, R. Marthan, D. R. Robinson, M. Bonhivers, Human FAM154A (SAXO1) is a microtubule-stabilizing protein specific to cilia and related structures. *J. Cell Sci.* **128**, 1294–1307 (2015).
- P. R. Burton, Luminal material in microtubules of frog olfactory axons: Structure and distribution. *J. Cell Biol.* **99**, 520–528 (1984).
- A. Szyk, A. M. Deaconescu, J. Spector, B. Goodman, M. L. Valenstein, N. E. Ziolkowska, V. Kormendi, N. Grigorieff, A. Roll-Mecak, Molecular basis for age-dependent microtubule acetylation by tubulin acetyltransferase. *Cell* **157**, 1405–1415 (2014).
- A. Hyman, D. Drechsel, D. Kellogg, S. Salser, K. Sawin, P. Steffen, L. Wordeman, T. Mitchison, Preparation of modified tubulins. *Methods Enzymol.* **196**, 478–485 (1991).
- F. M. Coquelle, S. Blestel, C. Heichette, I. Arnal, C. Kervran, D. Chrétien, Cryo-electron tomography of microtubules assembled in vitro from purified components. *Methods Mol. Biol.* **777**, 193–208 (2011).
- A. Nawrotek, M. Knossow, B. Gigant, The determinants that govern microtubule assembly from the atomic structure of GTP-tubulin. *J. Mol. Biol.* **412**, 35–42 (2011).
- M. Igaev, H. Grubmüller, Microtubule assembly governed by tubulin allosteric gain in flexibility and lattice induced fit. *eLife* **7**, e34353 (2018).
- A. Krebs, K. N. Goldie, A. Hoenger, Structural rearrangements in tubulin following microtubule formation. *EMBO Rep.* **6**, 227–232 (2005).
- P. Venier, A. C. Maggs, M.-F. Carlier, D. Pantaloni, Analysis of microtubule rigidity using hydrodynamic flow and thermal fluctuations. *J. Biol. Chem.* **269**, 13353–13360 (1994).
- I. Arnal, R. H. Wade, How does taxol stabilize microtubules? *Curr. Biol.* **5**, 900–908 (1995).
- E. H. Kellogg, N. M. A. Hejab, S. Howes, P. Northcote, J. H. Miller, J. F. Diaz, K. H. Downing, E. Nogales, Insights into the distinct mechanisms of action of taxane and non-taxane microtubule stabilizers from cryo-EM structures. *J. Mol. Biol.* **429**, 633–646 (2017).
- C. Elie-Caille, F. Severin, J. Helenius, J. Howard, D. J. Muller, A. A. Hyman, Straight GDP-tubulin protofilaments form in the presence of taxol. *Curr. Biol.* **17**, 1765–1770 (2007).
- L. A. Amos, W. B. Amos, The bending of sliding microtubules imaged by confocal light microscopy and negative stain electron microscopy. *J. Cell Sci. Suppl.* **14**, 95–101 (1991).
- R. Zhang, B. LaFrance, E. Nogales, Separating the effects of nucleotide and EB binding on microtubule structure. *Proc. Natl. Acad. Sci. U.S.A.* **115**, E6191–E6200 (2018).
- T. Shima, M. Morikawa, J. Kaneshiro, T. Kambara, S. Kamimura, T. Yagi, H. Iwamoto, S. Uemura, H. Shigematsu, M. Shirouzu, T. Ichimura, T. M. Watanabe, R. Nitta, Y. Okada, N. Hirokawa, Kinesin-binding-triggered conformation switching of microtubules contributes to polarized transport. *J. Cell Biol.* **217**, 4164–4183 (2018).
- L. Bouzar, M. M. Müller, R. Messina, B. Nöding, S. Köster, H. Mohrbach, I. M. Kulić, Helical superstructure of intermediate filaments. *Phys. Rev. Lett.* **122**, 098101 (2019).
- J. Howard, *Applied Mechanics Reviews* (Sinauer-Associates, 2001), vol. 55, chap. 3.

Acknowledgments: We thank L. Demacedo and A. Vinit for technical support in cell culture and protein biochemistry, E. Neumann for help with the electron microscope, and the zootechicians of the Grenoble Institute Neuroscience (GIN). **Funding:** This work was supported by INSERM, CEA, CNRS, Université Grenoble Alpes and by awards from the French Agence Nationale de la Recherche to A.A., I.A., and G.S. (2017-CE11-0026 MAMAs). This work was supported by grants from Agence Nationale de la Recherche ANR-15-IDEX-02 NeuroCoG in the framework of the "Investissements d'avenir" program. GIN is a member of the Grenoble Center of Excellence in Neurodegeneration (GREEN). The Photonic Imaging Center of Grenoble Institute Neuroscience (Univ. Grenoble Alpes—Inserm U1216) is part of the ISdV core facility

and certified by the IBISA label. This work used the EM facilities at the Grenoble Instruct-ERIC Center (ISBG; UMS 3518 CNRS CEA-UGA-EMBL) with support from the French Infrastructure for Integrated Structural Biology (FRISBI; ANR-10-INSB-05-02) and GRAL, a project of the University Grenoble Alpes graduate school (Ecoles Universitaires de Recherche) CBH-EUR-GS (ANR-17-EURE-0003) within the Grenoble Partnership for Structural Biology. The IBS Electron Microscope facility is supported by the Auvergne Rhône-Alpes Region, the Fonds Feder, the Fondation pour la Recherche Médicale, and GIS-IBISA. **Author contributions:** C.D. prepared recombinant proteins. C.D., C.C., and M.S. performed in vitro reconstitution experiments and analyzed data. J.D., I.A., and C.D. performed and analyzed cryo-electron microscopy, cryo-electron tomography, and negative staining experiments. J.D., M.B., and G.S. set up cryo-electron tomography acquisition. S.G.-F. performed neuronal cultures. E.D. performed image analysis. C.B. performed molecular biology. I.K. and H.M. performed and wrote theoretical modeling. C.D., I.A., A.A., and C.B. wrote the paper. **Competing interests:** The authors declare

that they have no competing interests. **Data and materials availability:** All data needed to evaluate the conclusions in the paper are present in the paper and/or the Supplementary Materials. Any additional datasets, analysis details, and material recipes are available upon request.

Submitted 9 September 2019

Accepted 9 January 2020

Published 1 April 2020

10.1126/sciadv.aaz4344








Citation: C. Cuveillier, J. Delaroche, M. Seggio, S. Gory-Fauré, C. Bosc, E. Denarier, M. Bacia, G. Schoehn, H. Mohrbach, I. Kulić, A. Andrieux, I. Arnal, C. Delphin, MAP6 is an intraluminal protein that induces neuronal microtubules to coil. *Sci. Adv.* **6**, eaaz4344 (2020).

ARTICLE

DOI: 10.1038/s41467-018-05869-z

OPEN

A key function for microtubule-associated-protein 6 in activity-dependent stabilisation of actin filaments in dendritic spines

Leticia Peris ¹, Mariano Bisbal ^{1,2}, José Martínez-Hernández ^{1,6}, Yasmina Saoudi¹, Julie Jonckheere¹, Marta Rolland¹, Muriel Sebastien ¹, Jacques Brocard¹, Eric Denarier ^{1,3}, Christophe Bosc ¹, Christophe Guerin^{4,5}, Sylvie Gory-Fauré¹, Jean Christophe Deloulme¹, Fabien Lanté¹, Isabelle Arnal¹, Alain Buisson¹, Yves Goldberg^{1,3}, Laurent Blanchoin^{4,5}, Christian Delphin¹ & Annie Andrieux ^{1,3}

Emerging evidence indicates that microtubule-associated proteins (MAPs) are implicated in synaptic function; in particular, mice deficient for MAP6 exhibit striking deficits in plasticity and cognition. How MAP6 connects to plasticity mechanisms is unclear. Here, we address the possible role of this protein in dendritic spines. We find that in MAP6-deficient cortical and hippocampal neurons, maintenance of mature spines is impaired, and can be restored by expressing a stretch of the MAP6 sequence called Mc modules. Mc modules directly bind actin filaments and mediate activity-dependent stabilisation of F-actin in dendritic spines, a key event of synaptic plasticity. In vitro, Mc modules enhance actin filament nucleation and promote the formation of stable, highly ordered filament bundles. Activity-induced phosphorylation of MAP6 likely controls its transfer to the spine cytoskeleton. These results provide a molecular explanation for the role of MAP6 in cognition, enlightening the connection between cytoskeletal dysfunction, synaptic impairment and neuropsychiatric illnesses.

¹GIN, Inserm 1216, Univ. Grenoble Alpes, 38000 Grenoble, France. ²Instituto de Investigación Médica Mercedes y Martín Ferreyra, INIMEC-CONICET-Universidad Nacional de Córdoba, 5016 Córdoba, Argentina. ³CEA, Inserm 1216, BIG-GPC, Univ. Grenoble Alpes, 38000 Grenoble, France.

⁴CytoMorpho Lab, UMR5168, Biosciences & Biotechnology Institute of Grenoble, CEA, CNRS, INRA, Univ. Grenoble-Alpes, 17 rue des Martyrs, 38054 Grenoble, France. ⁵CytoMorpho Lab, UMR51160, Institut Universitaire d'Hématologie, Hôpital Saint Louis, INSERM, CEA, Univ. Paris Diderot, 1 Avenue Claude Vellefaux, 75010 Paris, France. ⁶Present address: Ikerbasque, Department of Biochemistry and Molecular Biology, University of the Basque Country (UPV/EHU), Basque Foundation for Science, 48940 Leioa, Spain. These authors contributed equally: Leticia Peris, Mariano Bisbal. Correspondence and requests for materials should be addressed to L.P. (email: leticia.peris@univ-grenoble-alpes.fr) or to M.B. (email: mbisbal@immm.uncor.edu) or to A.A. (email: annie.andrieux@univ-grenoble-alpes.fr)

Dendritic spines, the neuronal membrane protrusions that form the post-synaptic part of most excitatory synapses in the adult mammalian brain, can display both striking structural flexibility and remarkable persistence. These features have long been known to depend on the spine actin cytoskeleton^{1,2}. Dendritic spines are rich in actin, and remodelling of spine actin networks is known to drive structural modifications associated with synaptic plasticity, such as the expansion of spine volume that accompanies activity-induced increases in synaptic efficacy^{3–5}. Spines contain different pools of actin filaments, displaying distinct dynamics, with sub-membrane foci of dynamic filaments likely providing the mechanical force needed for spine expansion, whereas the much more stable polymeric actin accumulated in the spine core seems to be required for stabilising large mature “memory” spines³. The molecular mechanisms that drive these dynamics remain incompletely defined. In addition to actin, the role of dendritic microtubules in plasticity events was also highlighted with the discovery of their transient entrance in spines during synaptic activity, in tight correlation with an increase in actin polymerisation and spine enlargement^{6–9}. Proteins associated with microtubule ends, such as EB3, interact with elements of the post-synaptic machinery, several of which are known to regulate actin dynamics^{6,10}; how such interactions contribute to spine plasticity remains unclear. The question arises whether other microtubule-associated factors might control aspects of the spine actin cytoskeleton.

The neuronal MAPs (microtubule associated proteins) including MAP1B, MAP2, Tau and MAP6 are attractive candidates in this regard. Long overlooked as mono-functional proteins controlling microtubule properties, MAPs have been recently shown to interact with actin^{11–16}. MAPs exist at synapses and MAP-deficient animals exhibit various synaptic defects^{17–21}. In particular, MAP6 KO (also known as STOP KO) mice display severe behavioural and cognitive deficits, associated with strong impairments in both short-term and long-term synaptic plasticity^{17,22}. MAP6 is known to bind and stabilise microtubules (MTs) through two types of MT-binding sequence elements: the so-called Mc modules (1 to 6 modules depending on species) that confer protection against MT disassembly at low temperature, and the Mn modules (3 modules) that convey resistance to both cold-induced and nocodazole-induced disassembly^{23,24}. Importantly, it was shown that CaMKII phosphorylation of MAP6 induced its relocalization from MTs toward actin-rich domains in neurons²⁵. MAP6 has been detected by immunostaining in synaptic compartments²⁵ and also found in several analyses of the post-synaptic proteome^{26–28}. Here, we investigate the possible participation of MAP6 in the regulation of the dendritic spine cytoskeleton. Using MAP6 KO mice, we show that MAP6 is involved in the formation and the maintenance of mature post-synaptic spines, and that this novel aspect of MAP6 function relies on the Mc modules. While at physiological temperature Mc modules are unable to bind microtubules²⁴, we find that they can bind actin filaments. Further, we show that, in dendritic spines, Mc modules mediate actin stabilisation in response to neuronal activation, a key event of synaptic plasticity. Finally, we study the interaction of Mc modules with actin, using purified proteins in a range of *in vitro* assays. We show that Mc modules do not affect the actin polymerisation rate but enhance filament nucleation, protect existing filaments against depolymerisation, act on filament conformation, and organise stable filament bundles in an ordered fashion. Altogether our findings indicate that MAP6 and the specific type of actin rearrangements it promotes are needed for proper maturation and plasticity-related modifications of excitatory synapses. These results also provide a molecular explanation for the crucial role of MAP6 in cognitive abilities.

Results

A role for MAP6 in spine maturation and maintenance. To visualise dendritic spines in MAP6-deficient neurons *in vivo*, MAP6 KO mice were cross-bred with *Thy1-eYFP-H* transgenic mice²⁹. Transgenic MAP6 KO offspring animals expressed yellow fluorescent protein in layer 5 cortical neurons, as did transgenic MAP6^{+/+} controls. Dendritic spine density and morphology were analysed in brain sections from these mice, using confocal microscopy (Fig. 1a). MAP6 KO neurons displayed significantly fewer dendritic spines than WT neurons (Fig. 1b; 1.18 ± 0.04 and 0.91 ± 0.04 spines/ μm for WT and MAP6 KO neurons, respectively). Similar results were obtained in cultured hippocampal MAP6 KO or WT neurons (Fig. 1d), and in WT neurons transfected with MAP6-targeting siRNAs³⁰ or scrambled control (Fig. 1g). MAP6 KO neurons exhibited a reduced density of dendritic spines (Fig. 1e; 1.15 ± 0.05 and 0.92 ± 0.05 spines/ μm , for WT and MAP6 KO neurons, respectively). MAP6 depletion by siRNA similarly resulted in a reduction of spines (Fig. 1h; 1.25 ± 0.04 and 0.91 ± 0.08 spines/ μm for control and MAP6 siRNAs, respectively).

Dendritic spines are often classified in three morphological types, corresponding to successive developmental stages: thin, stubby and mushroom-like spines³¹. We quantified the density of spine subtypes, in WT and MAP6 KO neurons *in vivo* (Fig. 1c). While no difference was found between genotypes in the number of thin spines, mushroom spines were significantly reduced in MAP6 KO neurons as compared to WT neurons (Fig. 1c; 0.38 ± 0.02 and 0.26 ± 0.02 spines/ μm for mushroom spines, in WT and MAP6 KO neurons, respectively). We performed the same quantitative analysis in cultured neurons (Fig. 1f–i). Similar to the *in vivo* data, the lack of MAP6 led to a decreased density of mushroom-like spines. We also observed a significant loss of stubby spines in MAP6 KO neurons *in vivo* (Fig. 1c; 0.31 ± 0.02 and 0.21 ± 0.01 spines/ μm in WT and MAP6 KO neurons, respectively); this latter was not reproduced in cultured KO neurons, perhaps due to differences in spine maturation conditions.

To determine whether the loss of spines correlated with changes in glutamatergic synaptic transmission, we performed whole-cell patch-clamp recordings of spontaneous miniature excitatory post-synaptic currents (mEPSCs) in cultured hippocampal neurons (Fig. 1j). In KO neurons, the mean mEPSCs amplitude was not significantly changed compared to WT neurons (Fig. 1k; 25.76 ± 0.79 and 23.84 ± 0.7 pA for WT and KO neurons, respectively). In contrast, the mean mEPSCs frequency recorded in KO neurons was strongly reduced compared to WT neurons (Fig. 1l; 1.25 ± 0.25 and 0.52 ± 0.17 Hz for WT and KO neurons, respectively). The reduction of mEPSCs frequency in KO neurons corroborates the reduction of spine density and is indicative of a perturbed glutamatergic neurotransmission.

Taken together, these results indicate that MAP6 has an important role in the formation and/or maintenance of mature dendritic spines.

MAP6 Mc modules mediate effects on dendritic spine density.

We next sought to determine which part of the MAP6 sequence was involved in spine formation and maintenance. Rescue experiments were carried out in KO neurons *in vitro*, using GFP-labelled MAP6 isoforms or deletion mutants (Fig. 2a) in combination with unfused mCherry as an outline marker. Spine density was measured using the mCherry image (Fig. 2b). Expression of either the MAP6-N-GFP or the MAP6-E-GFP isoform in MAP6 KO neurons resulted in an increase of spine density from 0.86 ± 0.06 to 1.07 ± 0.02 and 1.05 ± 0.03 spines/ μm , respectively, values

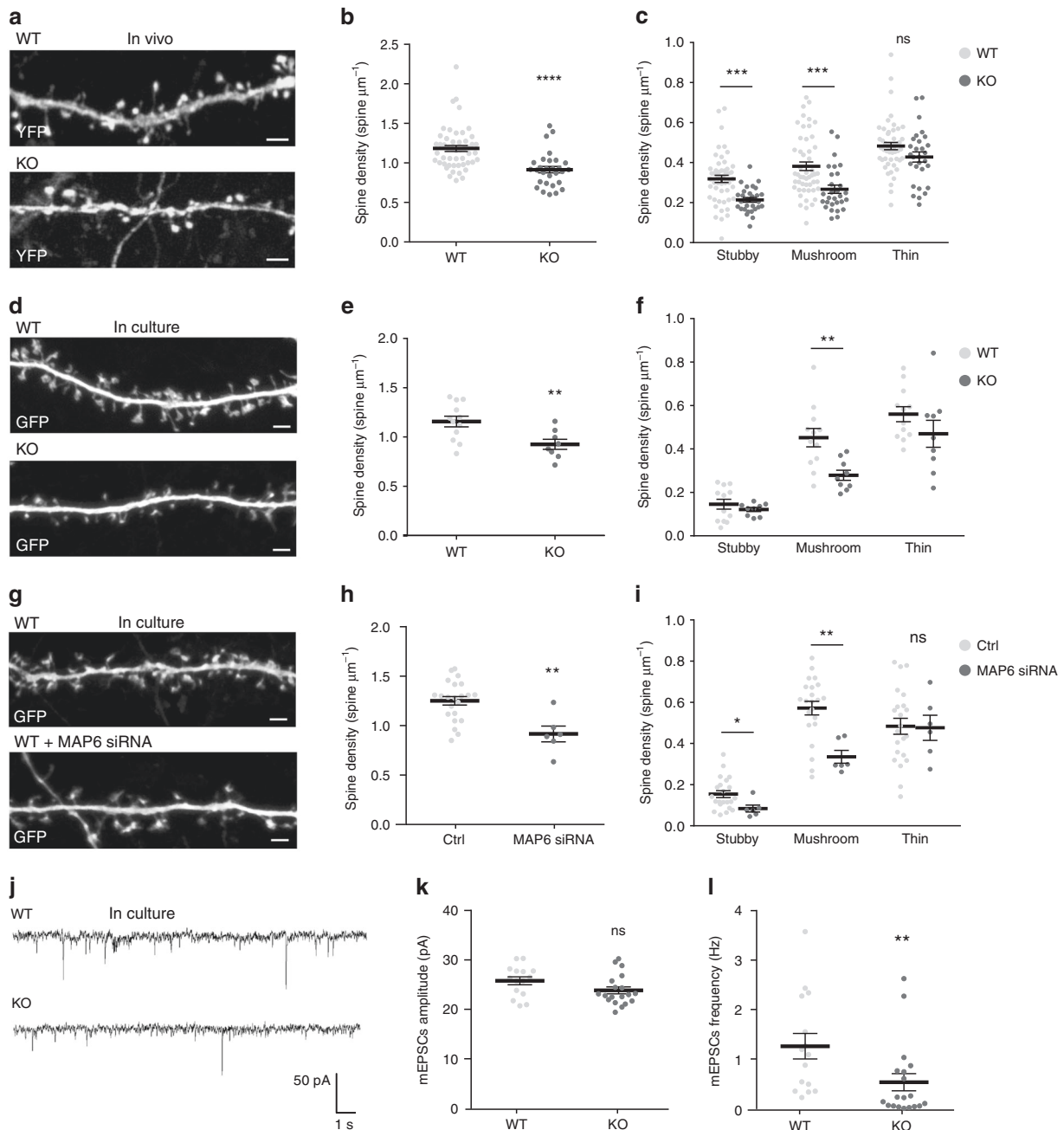
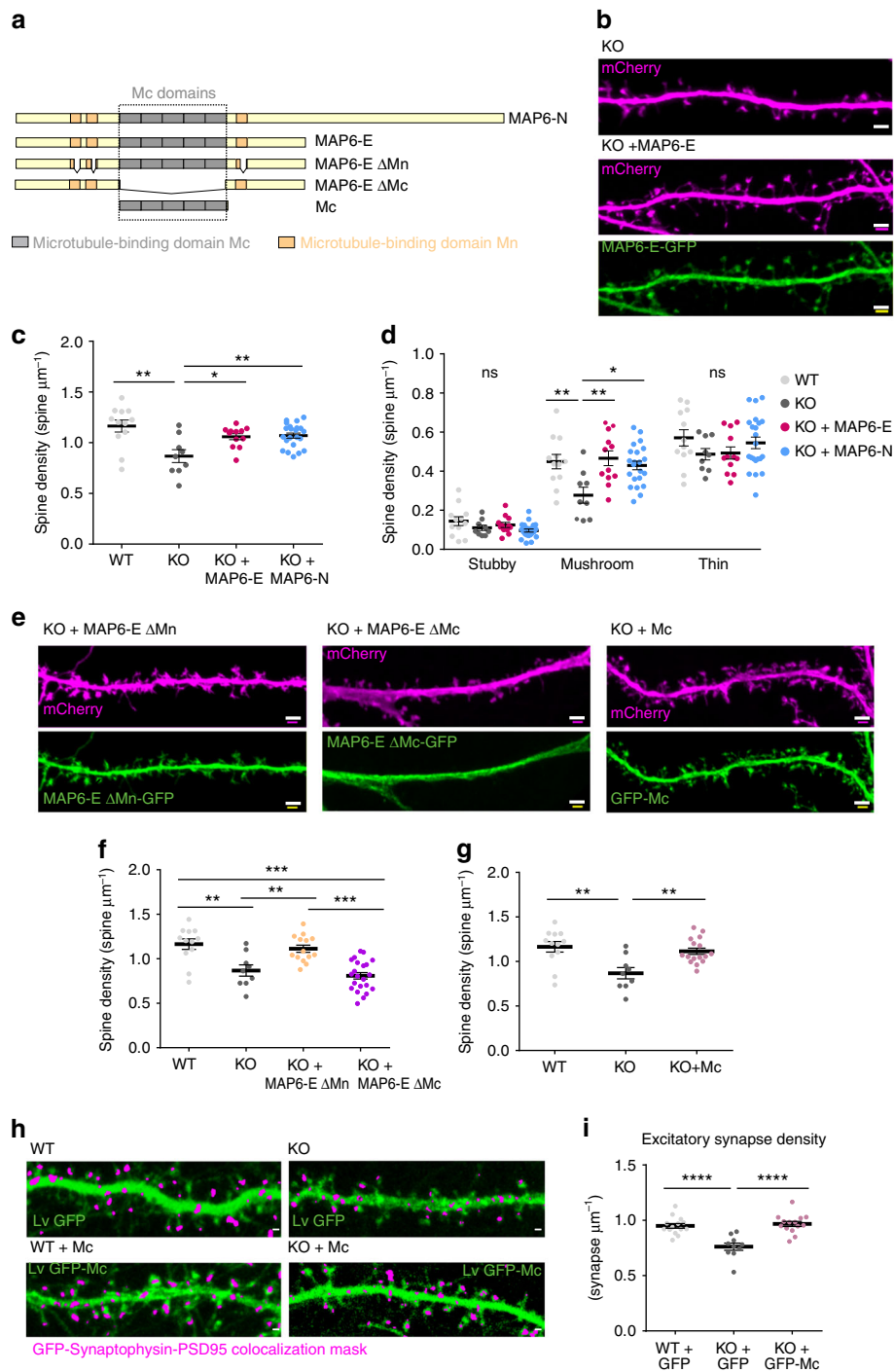


Fig. 1 MAP6 inhibition reduces dendritic spine density. **a** Confocal image showing representative examples of dendritic segments of layer 5 cortical neurons of WT and MAP6 KO *Thy1-eYFP-H* mice. Scale bar: 2 μm . **b, c** Graphs of dendritic spine density in apical secondary or tertiary dendrites. The total density (**b**), or that of each morphological spine type (**c**) in WT and MAP6 KO *Thy1-eYFP-H* neurons are represented as mean \pm SEM (ns: not significant, *** $p < 0.001$; Student's *t*-test), $n = 50$ neurons/ 4 WT animals and 29 neurons/ 4 KO animals. **d** Confocal image showing representative examples of dendritic segments of WT and MAP6 KO hippocampal neurons in culture at 18 DIV, transfected with GFP-expressing vector. Scale bar: 2 μm . **e, f** Graphs of total dendritic spine density (**e**) or density by shape type (**f**) in WT and MAP6 KO cultured neurons. Values are represented as mean \pm SEM (ns: not significant, *** $p < 0.001$ Student's *t*-test), $n = 12$ neurons/ 3 WT embryos and 9 neurons/ 3 KO embryos, respectively. **g** Confocal image showing representative examples of dendritic segments of 18 DIV cultured hippocampal WT neurons transfected with GFP-expressing vector and control siRNA or MAP6 siRNA. Scale bar: 2 μm . **h, i** Graphs of total dendritic spine density (**h**) or density by shape type (**i**) in neurons transfected with control or MAP6 siRNA. Values are represented as mean \pm SEM (ns: not significant, * $p < 0.05$; ** $p < 0.01$; Student's *t*-test), $n = 22$ neurons/ 4 embryos and 6 neurons/ 3 embryos from control and siRNA treated neurons, respectively. **j** Sample traces showing mEPSCs of WT and MAP6 KO 18 DIV cultured hippocampal neurons. **k, l** Graphs of the mean mEPSCs amplitude (**k**) and frequency (**l**) recorded in WT or MAP6 KO cultured neurons. Values are represented as mean \pm SEM (ns: not significant, ** $p < 0.01$; Student's *t*-test), $n = 15$ neurons/ 5 WT embryos and 19 neurons/ 3 KO embryos, respectively. For each experiment of cultured neurons, analysed neurons were pooled from at least three independent cultures



no longer significantly different from the density of 1.16 ± 0.06 spines/ μm , observed for WT neurons (Fig. 2b, c). Analysis of spine morphology indicated that both MAP6-E-GFP and MAP6-N-GFP restored a normal density of mushroom-like spines in MAP6 KO neurons (Fig. 2d). We then examined the ability of MAP6-E mutants devoid of microtubule-binding sequence modules to correct spine density defects. Figure 2a depicts the two types of MAP6 microtubule-binding modules, the Mn modules (orange) and the Mc modules in the central domain (grey). When transfected in MAP6 KO neurons, MAP6-E lacking Mn modules

(MAP6-E- ΔMn -GFP) was able to increase the spine density from 0.86 ± 0.06 to 1.11 ± 0.04 spines/ μm (Fig. 2e, f). In contrast, transfection of MAP6-E lacking Mc modules (MAP6-E- ΔMc -GFP) failed to significantly change the spine density (Fig. 2e, f). Conversely, expression of GFP fused to Mc modules alone (GFP-Mc) increased spine density up to values similar to those observed in WT neurons (Fig. 2e, g; 1.11 ± 0.04 and 1.16 ± 0.06 spines/ μm for rescued MAP6 KO neurons and WT neurons, respectively).

To determine whether changes in morphologically defined spines corresponded to synaptic alterations, we next used

Fig. 2 MAP6 Mc modules are important for dendritic spine maturation and maintenance. **a** Schematic representation of MAP6 domain structure and cDNA constructs used in this paper. **b** Confocal image showing representative examples of dendritic segments of MAP6 KO 18 DIV cultured hippocampal neurons transfected with mCherry-expressing vector alone or co-transfected with a MAP6-E construct. Scale bar: 2 μ m. **c, d** Graphs showing the quantification of dendritic spine density in WT neurons, MAP6 KO neurons and MAP6 KO neurons transfected with MAP6-E or MAP6-N constructs. Total spine density (**c**) or type-wise density (**d**) are represented as mean \pm SEM ($*p < 0.05$; $**p < 0.01$; one-way ANOVA and Tukey's post hoc test), $n = 12$ neurons/ 3 embryos, 9 neurons/ 3 embryos, 12 neurons/ 4 embryos and 22 neurons/ 5 embryos for WT, KO, KO + MAP6-E and KO + MAP6-N, respectively. **e-g** Rescue experiments in MAP6 KO neurons (**e**) Confocal image showing representative examples of dendritic segments of MAP6 KO 18 DIV cultured hippocampal neurons transfected with mCherry-expressing vector and MAP6-E Δ Mn-eGFP, MAP6-E Δ Mc-eGFP or eGFP-Mc domain constructs. Scale bar: 2 μ m. **f, g** Graphs of dendritic spine density in WT neurons, MAP6 KO neurons and after rescue of MAP6 KO neurons by MAP6-E Δ Mn or MAP6-E Δ Mc (**f**) or Mc modules (**g**). Data presented as mean \pm SEM ($**p < 0.01$, $***p < 0.001$; one-way ANOVA and Tukey's post hoc test), $n = 12$ neurons/ 3 embryos, 9 neurons/ 3 embryos, 14 neurons/ 4 embryos and 22 neurons/ 4 embryos neurons for WT, KO, KO + MAP6-E Δ Mn and KO + MAP6-E Δ Mc, respectively. **h** Representative images of dendrites of WT and MAP6 KO 18 DIV hippocampal neurons transduced with GFP or GFP-Mc lentivirus (green) and superposed with a magenta mask corresponding to pixels that simultaneously contain PSD-95 (post-synaptic), Synaptophysin (pre-synaptic) and GFP label. Scale bar, 2 μ m. **i** Graph showing the quantification of excitatory synapse density in dendrites of WT and MAP6 KO neurons transduced with GFP or GFP-Mc lentivirus. Data presented as mean \pm SEM. ($****p < 0.0001$ one-way ANOVA with Tukey's post hoc test), $n = 14$ neurons/ 3 embryos, 10 neurons/ 3 embryos and 14 neurons/ 3 embryos for WT + GFP, KO + GFP and KO + GFP-Mc, respectively. For each experiment, neurons were pooled from at least three independent cultures

immunological markers to label excitatory synapses³² in cultured neurons. Neurons were transduced with lentiviral vectors expressing GFP or Mc-GFP, fixed at DIV18, and stained for PSD-95/synaptophysin (a post-synaptic and a pre-synaptic marker, respectively). Fluorescent puncta containing both pre and post-synaptic markers were used to detect and count synapses formed on the dendrites of transduced cells, as shown in Fig. 2h. GFP-expressing WT neurons displayed 0.949 ± 0.020 synapses/ μ m (Fig. 2i), whereas GFP-expressing MAP6 KO neurons had 0.76 ± 0.030 synapses/ μ m (Fig. 2i), a value compatible with the presence of one synapse per dendritic spine. Thus, in MAP6 KO neurons, the reduced density of excitatory synapses is in tight correlation with the reduction of spine density. Expression of Mc modules (GFP-Mc) in MAP6 KO neurons rescued the number of synapses (Fig. 2h, i, 0.967 ± 0.022 synapses/ μ m) to values similar to those observed in WT neurons.

Altogether, these results demonstrate that Mc modules contribute to the growth and maintenance of dendritic spines and to the establishment of mature synapses.

A single Mc module ensures normal dendritic spine density. Human MAP6 only contains one Mc module, whereas Mc modules are present in five copies in rat MAP6³³ (R1 to R5, Supplementary Fig. 1A). We showed that rat R5, human MAP6-E or the human Mc module were able to correct the spine density deficit (Supplementary Fig. 1C-F). Thus, a single Mc module, as present in human MAP6, is sufficient to ensure dendritic spine maturation and maintenance.

Phosphorylation by CaMKII targets MAP6 to spines. To determine whether the effect of MAP6 on synapses requires it to enter spines, we took advantage of the physiological regulation of MAP6 targeting by CamKII²⁵. We showed that MAP6-E phosphorylation mutant (S/E mutant, Supplementary Fig. 1A, G-H) mimicking phosphorylated state was able to rescue spine density whereas MAP6-E phosphorylation mutant preventing phosphorylation (S/A mutant, Supplementary Fig. 1A, G-H) was not efficient. These results indicate that MAP6 transfer into the spines through phosphorylation by CamKII correlates with the effect of MAP6 on synapse maintenance.

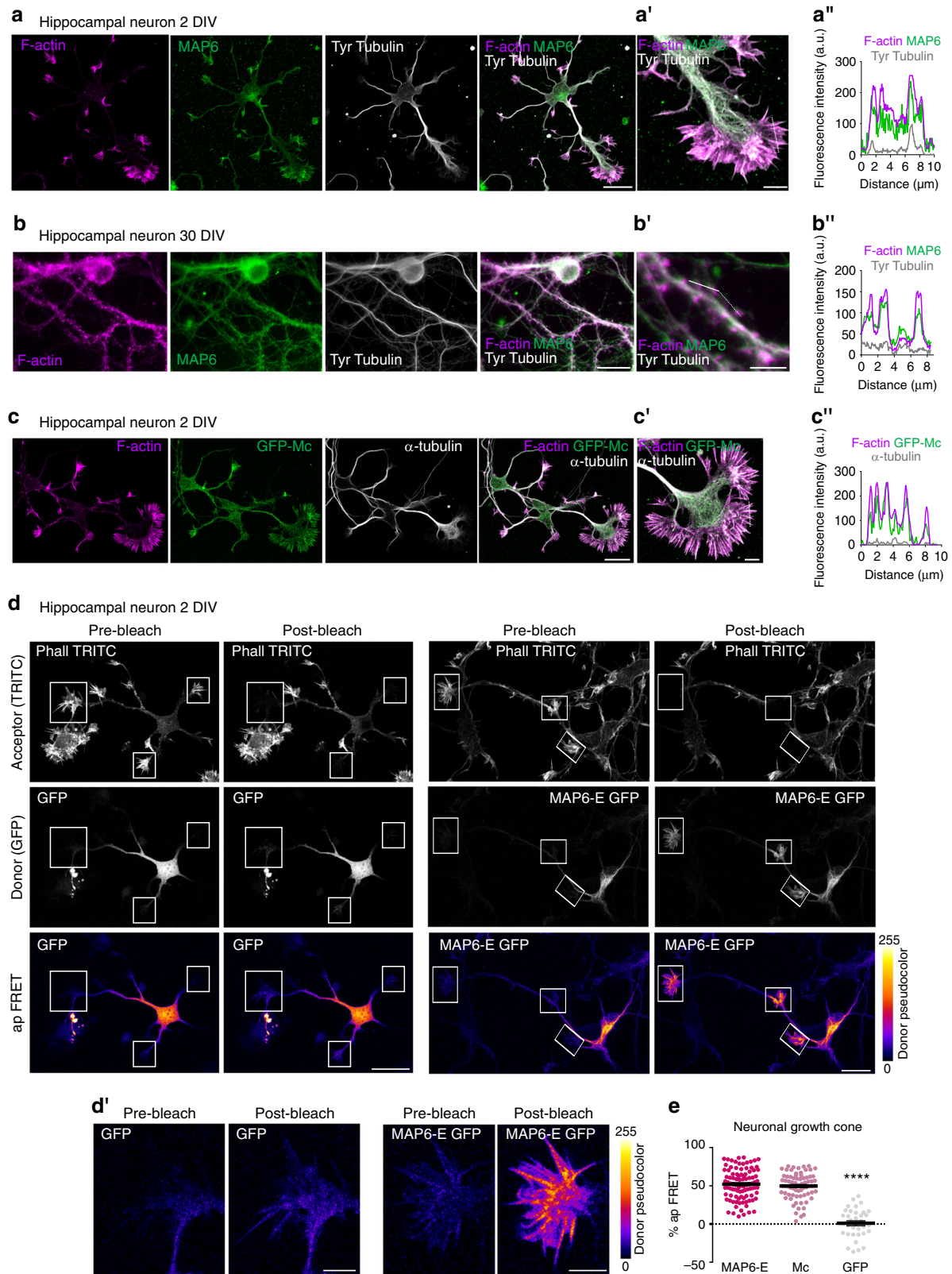
MAP6 Mc modules directly interact with actin. At physiological temperature, MAP6 interaction with microtubules relies on Mn domains (Fig. 2a), and Mc modules are not involved^{23,24}. We

thus wondered whether an interaction of the Mc modules with actin might occur, possibly accounting for the observed spine stabilisation. We analysed the comparative distribution of endogenous MAP6 and cytoskeletal elements in cultured hippocampal neurons at different stages of maturation. Endogenous MAP6 co-localised with microtubules throughout the cell, was especially enriched in axons, but also co-localised with actin in filopodia and lamellipodia within the growth cone (Fig. 3a, a', a''). After 30 days in culture, endogenous MAP6 continued to be present in cell body, axon and dendrites but also accumulated within dendritic spines (Fig. 3b, b', b''). To determine whether Mc modules could target the protein to actin-rich regions of the cell, we studied the localisation of a transiently expressed GFP-Mc fusion protein. The GFP-Mc polypeptide was found to co-localise with actin filaments both in mouse embryo fibroblasts (Supplementary Fig. 2) and in the growth cone of young neurons (Fig. 3c, c', c'').

To determine whether MAP6 directly interacted with actin filaments in neurons, we performed FRET (Förster Resonance Energy Transfer with Acceptor Bleaching) measurements using the acceptor photobleaching technique³⁴, with TRITC-phalloidin labelled actin filaments (as acceptor) and GFP or GFP-tagged MAP6 (as donor) (FRET-A; Fig. 3d, d'; Supplementary movie 1). We chose to analyse growth cones, where actin filaments are clearly visible. The fluorescence intensity of the donor MAP6-E-GFP within growth cone regions increased significantly after bleaching of the acceptor, revealing a FRET efficiency of $52 \pm 2\%$ (Fig. 3e). Similar experiments were performed with GFP-Mc modules, yielding a FRET efficiency of $49.6 \pm 2\%$ (Fig. 3e). As a control (Fig. 3d, d'), no transfer of fluorescence was observed between F-actin filaments and soluble GFP ($1.4 \pm 3\%$ of FRET, Fig. 3e). The FRET-AB technique did not allow us to obtain accurate measurements of FRET efficiency in dendritic spines.

Overall, these results show that endogenous MAP6 appears to be present very extensively throughout the neuron, including at actin-rich structures, where, as indicated by the acceptor photobleaching experiment, it can be in close proximity to F-actin.

MAP6 regulates actin dynamics in dendritic spines. The above results raise the possibility that MAP6 might participate in the regulation of actin dynamics in spines, which is crucially involved in spine remodelling and in synaptic plasticity events³⁵. In particular, long-term potentiation (LTP) is known to be accompanied by a rise of actin filaments, increased actin stabilisation and spine enlargement³⁶. To examine whether MAP6 contributes



to plasticity-related actin filament accumulation and spine expansion, we used neurons transfected with plasmids encoding GFP as a volume marker, together with the filamentous actin probe LifeAct-mCherry (Fig. 4a). The transfected neurons were subjected to synaptic activation, using a chemical protocol

mimicking LTP (cLTP, bicuculline and 4-Aminopyridine)²¹. Individual mushroom-like spines of live neurons were imaged before and after induction of cLTP (Fig. 4a). Consistent with previous publications^{4,37–39}, in WT neurons, cLTP resulted in a strong expansion of spine volume (Fig. 4b). By contrast, no

Fig. 3 The MAP6 Mc module directly interacts with the actin cytoskeleton. **a** Confocal image showing a representative cultured hippocampal neuron at 2 DIV, co-stained for actin filaments (phalloidin, magenta), endogenous MAP6 (green) and microtubules (grey). Scale bar: 20 μm . **a'** Higher magnification view of the axonal growth cone. Scale bar: 5 μm . **a''** Graph of the fluorescence intensity variations of actin filaments, MAP6 and microtubule staining along a line scan (white dotted line). **b** Confocal image showing a 30 DIV cultured hippocampal neuron stained as in **a**. Scale bar: 20 μm . **b'** Higher magnification view of a dendrite. Scale bar: 5 μm . **b''** Graph of the fluorescence intensity variations of actin filaments, endogenous MAP6 and microtubule staining along a line scan. **c** Confocal image showing a 2 DIV cultured hippocampal neuron transfected with GFP-Mc construct (green) and stained for actin filaments (magenta) and microtubule (grey). **c'** Higher magnification view of the axonal growth cone. Scale bar: 5 μm . **c''** Graph of the fluorescence intensity variations of actin filaments, GFP-Mc and microtubule staining along a line scan. **d** Acceptor Photobleaching FRET (ap FRET) analysis of 2 DIV cultured hippocampal neuron transfected with either GFP or MAP6-E GFP construct and stained for actin filaments (TRITC-phalloidin). Images were taken before (pre-) and after (post-) acceptor photobleaching for the acceptor (TRITC-phalloidin, upper images) and the donor (GFP or MAP6-E GFP, middle images). For better visualisation of the donor fluorescence intensity, a fire lookup table (LUT) was applied to pre- and post-bleach images, with colours corresponding to pixels from 0 (black-violet) to max intensity (yellow). The insert boxes show bleach regions of interest. Scale bar: 20 μm . **d'** Higher magnification view of the axonal growth cone before and after acceptor photobleaching. Scale bar: 5 μm . **e** Graphs showing the Acceptor Photobleaching FRET efficiency in neuronal growth cones of hippocampal neurons transfected with MAP6-E-GFP, GFP-Mc or GFP constructs. Data presented as mean \pm SEM (**** $p < 0.0001$; one-way ANOVA and Tukey's post hoc test), $n = 97, 72$ and 35 axonal growth cones from MAP6-E, Mc and GFP-expressing neurons of 8, 7 and 4 embryos respectively, from three independent cultures

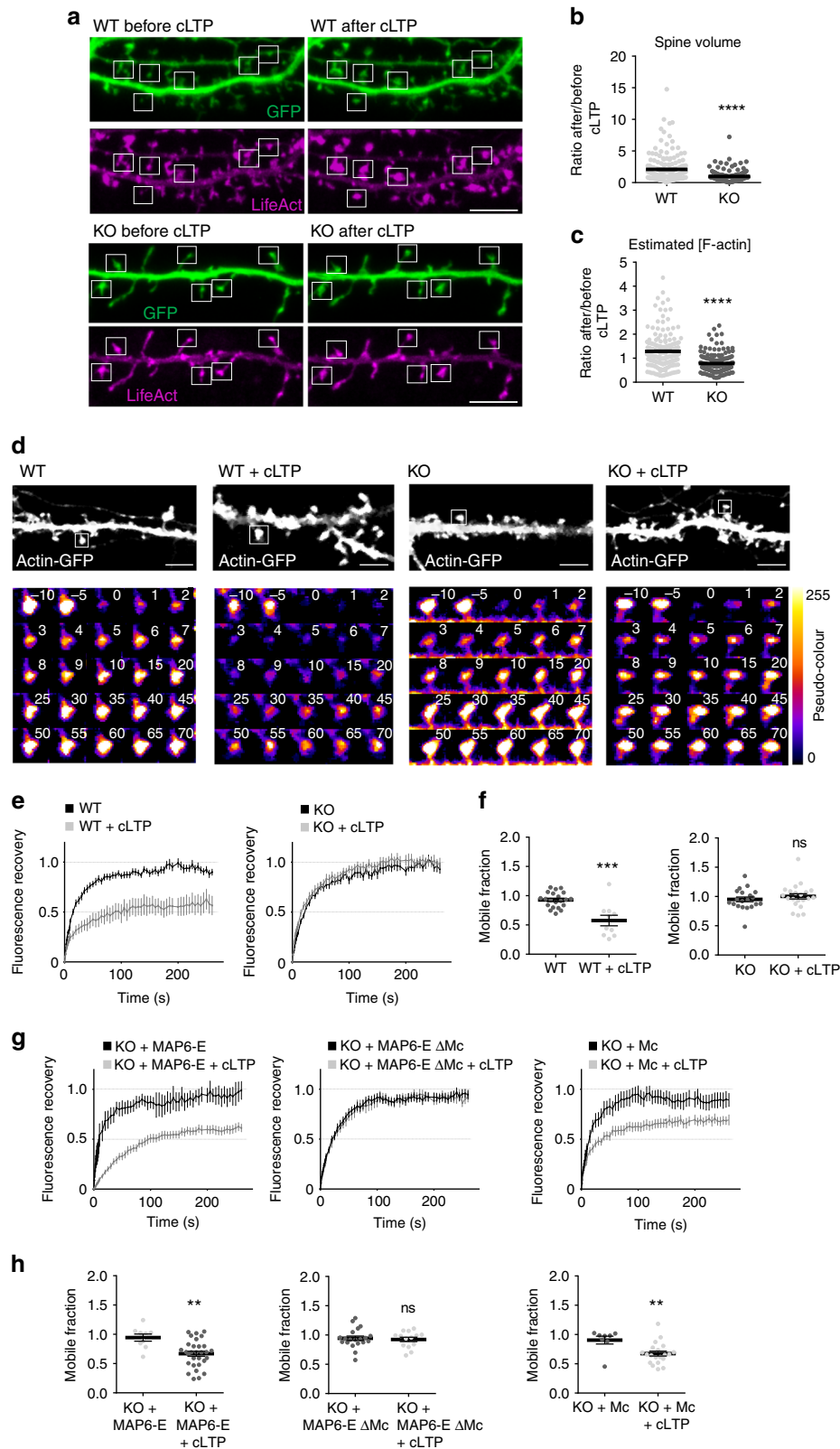
increase was detected in the spines of KO neurons (Fig. 4b). Further, in agreement with the results of Bosch et al.⁴, in WT spines, the concentration of actin filaments (estimated as the ratio of LifeAct vs. GFP) was $\sim 20\%$ higher following cLTP (Fig. 4c). Strikingly, no such change in actin concentration was detected in KO spines (Fig. 4c). Thus, MAP6 is required for the growth of the actin cytoskeleton that underlies spine expansion during activity-induced synaptic change. To determine whether MAP6 could regulate the polymerisation of spine actin, we compared the turnover rate of actin monomers in spines of MAP6 KO neurons and WT controls, by using fluorescence recovery after photobleaching (FRAP) of GFP-actin. Under our conditions, the mobile fraction of GFP-actin molecules calculated from the recovery kinetics corresponded to actin treadmilling in dynamic filaments, while the immobile fraction was composed of stable filaments³⁵. Hippocampal neurons cultured for 15 days in vitro were transfected with GFP-actin (Fig. 4d), 2 days later a specific spine was bleached and fluorescence recovery measured over time (Fig. 4d). In WT neurons, FRAP measurements yielded a classical average recovery curve with a characteristic recovery time of 40 s and almost full recovery of fluorescence (Fig. 4e, WT). Similar results were obtained for MAP6 KO neurons (Fig. 4e, KO) indicating similar actin dynamics in spines at resting state. Following cLTP, in WT neurons, FRAP measurements showed slower recovery of the mobile fraction and appearance of a significant immobile fraction, indicating as expected a diminished rate of actin turnover and an increased pool of stable actin filaments (Fig. 4e, WT + cLTP). In contrast, in MAP6 KO neurons, the cLTP protocol did not affect the recovery curve (Fig. 4e, KO + cLTP). Quantification, in WT neurons, of the dynamic GFP-actin in resting conditions or after cLTP clearly showed a reduction of the mobile fraction from $92.8 \pm 3\%$ to $57 \pm 9\%$ (Fig. 4f, 43% of immobile actin), whereas the mobile fraction was unchanged in MAP6 KO neurons (Fig. 4f, $95 \pm 4\%$ and $100.0 \pm 5\%$, in resting and activated conditions, respectively). These results indicate that the actin stabilisation triggered by chemical LTP requires MAP6.

We then determined the ability of full-size or truncated MAP6 to restore the actin stabilisation defects observed in spines (Fig. 4g, h). In neurons transfected with MAP6-E, cLTP-induced actin stabilisation was restored, as cLTP brought the mobile fraction down to $66.8 \pm 4\%$, very similar to $57\% \pm 9\%$ obtained in WT conditions (Fig. 4h) and significantly different from the $100 \pm 5\%$ found in MAP6 KO neurons (Fig. 4h). MAP6-E- Δ Mc was unable to allow actin stabilisation (Fig. 4g, h), whereas Mc was able to restore actin stabilisation, lowering the mobile fraction to $67.4 \pm 4\%$ (Fig. 4h). These results clearly

indicate that Mc modules stabilise actin in dendritic spines during plasticity events.

MAP6 Mc modules promote assembly of ordered actin bundles. We first assayed the in vitro binding of Mc modules to actin filaments using high-speed co-sedimentation assays. A significant fraction of Mc modules was found to associate with the actin pellet (Fig. 5a). Titration experiments showed that binding was saturable, with a K_d of 670 ± 106 nM and a B_{max} of 280 ± 13 nM for 500 nM actin (Fig. 5b).

To analyse in detail the interaction of Mc modules with actin filaments, we assayed in vitro the effect of purified Mc on a range of actin polymerisation parameters, including nucleation, elongation and bundling, known to be regulated by actin-binding proteins in spines^{1,5,36}. Actin nucleation was first assayed by following the polymerisation of pyrene-labelled actin over time. As shown in Fig. 5c, the initial lag corresponding to actin nucleation was shortened when actin was polymerised in the presence of Mc modules. Next, we investigated actin assembly by directly visualising actin polymerisation using total internal reflection fluorescence (TIRF) microscopy (Fig. 5d). After a 5 min assembly period, we measured the number of actin filaments present in the microscope field of view, in the presence or absence of Mc. Quantification showed that the total filament number was increased in the presence of Mc modules (Fig. 5e; total filament number: 66 ± 9.9 and 121.6 ± 15.5 ; for actin and actin + Mc modules, respectively). However, the elongation rate of polymerising filaments was not significantly changed by Mc (1.1 ± 0.02 and 1.1 ± 0.02 $\mu\text{m}/\text{min}$ for actin and actin + Mc, respectively). In contrast, we observed a dose-dependent induction of actin bundling by Mc modules, as indicated by the higher density of filaments, visualised by the orange to yellow pseudo-colour in Fig. 5f (fluorescence intensity ≥ 200 arbitrary units). Quantification indicated a higher percentage of actin bundling in the presence of Mc modules (Fig. 5g; $5.7 \pm 0.6\%$, $14.2 \pm 1.5\%$ and $19 \pm 2.5\%$ for 300 nM of actin alone, +150 and +300 nM Mc, respectively). To monitor the kinetics of Mc-induced actin bundle formation, we performed light-scattering assays during the polymerisation of actin monomers with or without Mc (Fig. 5h). In the presence of Mc, light scattering increased much more rapidly, indicating that Mc quickly bound and bundled newly forming actin filaments. Furthermore, the ability of Mc to bundle actin filaments was examined in a co-sedimentation assay (Fig. 5i). Complete actin polymerisation was checked by high-speed (HS) sedimentation (100,000 \times g, actin filaments in the pellet). At low-speed (LS) centrifugation (15,000 \times g), in the control condition, actin filaments were mainly present in the supernatant whereas,



in the presence of Mc, 4-time increase of actin was found in the pellet ($13 \pm 4.9\%$ and $58.5 \pm 3.9\%$ for actin alone and actin + Mc in the LS pellet). Finally, we analysed the impact of Mc modules on actin organisation using negative-staining electron microscopy. As shown Fig. 5j, in the presence of Mc modules, actin filaments formed bundles and appeared straightened as compared

to control conditions. Moreover Mc modules caused filaments to organise in single layered arrays, showing periodic striations spaced by 35.9 ± 1.2 nm (Fig. 5j, white arrowheads). These striations could also be seen in single filaments (spaced by 35.7 ± 1.1 nm) and were not observed in the absence of Mc. The period coincides with the helical pitch of actin (35.7 nm),

Fig. 4 MAP6 regulates the actin filaments stable pool in activated dendritic spines. **a** Representative confocal images of dendritic spines (boxes) of live cultured WT and KO hippocampal neurons at 18 DIV, co-transfected with GFP and LifeAct-RFP, before and after cLTP. Scale bar: 5 μ m. **b** Ratio of post- to pre-cLTP spine volumes. Data presented as mean \pm SEM. (*** p < 0.001; Mann-Whitney test). n = 172 and 169 spines from 10 WT and 10 KO neurons before and after cLTP, respectively. **c** Ratio of post- to pre-cLTP spine F-actin concentration. Data presented as mean \pm SEM. (*** p < 0.001; Mann-Whitney test). n = 186 spines/ 10 neurons/ 4 WT embryos and 185 spines/ 10 neurons/ 7 KO embryos before and after cLTP, respectively. **d** Representative examples of neurons at 16 DIV, transfected with actin-GFP before and after cLTP. A single spine (boxed) was photo-bleached and the time course of fluorescence recovery determined. Time series of fluorescence levels are shown in pseudo-colour for better visualisation, with colours corresponding to pixels from 0 (black-violet) to max intensity (yellow). Scale bar: 5 μ m. **e** Time course of actin-GFP fluorescence recovery in activated and non-activated neurons, averaged over experiments. Data presented as mean \pm SEM for each time point. **f** Mean value of mobile fractions derived by fitting individual curves to an exponential recovery model. Data presented as mean \pm SEM (ns: not significant, *** p < 0.001; Student's t -test), n = 21 spines/ 7 neurons/ 7 embryos, 10 spines/ 4 neurons/ 4 embryos, 20 spines/ 5 neurons/ 5 embryos and 21 spines/ 5 neurons/ 5 embryos from WT, WT + cLTP, KO and KO + cLTP neurons. **g** Time course of actin-GFP fluorescence recovery in activated and non-activated neurons transfected with actin-GFP and MAP6-E, MAP6-E Δ Mc or Mc modules, averaged over experiments. Data presented as mean \pm SEM for each time point. **h** Mean value of mobile fractions calculated as in **f**. Data presented as mean \pm SEM (ns: not significant, ** p < 0.01, Student's t -test), n = 9 spines/ 5 neurons/ 5 embryos, 30 spines/ 9 neurons/ 9 embryos, 20 spines/ 5 neurons/ 5 embryos, 14 spines/ 3 neurons/ 3 embryos, 8 spines/ 3 neurons/ 3 embryos and 20/ 4 neurons/ 4 embryos from KO + MAP6-E, KO + MAP6-E + cLTP, KO + MAP6-E Δ Mc, KO + MAP6-E Δ Mc + cLTP, KO + Mc and KO + Mc + cLTP neurons. For each experiment, neurons were pooled from two to four independent cultures

suggesting repeated association of Mc with a specific aspect of the filaments.

Altogether these *in vitro* results indicate that Mc modules regulate actin assembly and favour the formation of actin bundles.

MAP6 Mc modules stabilise actin filaments. To test whether Mc modules can stabilise actin filaments, we performed a dilution experiment. Filaments were polymerised from 2 μ M monomeric actin, next incubated alone or with 0.5 to 1 μ M of Mc modules and then the actin concentration was lowered by dilution to a final concentration of 0.1 μ M. After 20 min, the amount of remaining filaments was analysed using high-speed co-sedimentation assay, and compared to the initial amount of filaments (input) (Fig. 6a). As previously described⁴⁰, dilution of actin filaments led to depolymerisation (Fig. 6b) with only 38.61 \pm 2.43% of filaments resisting dissociation. In the presence of Mc modules, actin filaments were more resistant to depolymerisation (Fig. 6b; 52.3 \pm 1.6% and 54.7 \pm 1.8% for 0.5 and 1 μ M of Mc, respectively). To track depolymerisation over time, we performed similar dilution experiments with pyrene-labelled actin (Fig. 6c). Actin filaments showed a rapid decrease after buffer dilution (-25% of the initial fluorescence) whereas Mc-decorated actin filaments were more resistant (-11% of the initial fluorescence; Fig. 6c).

Taken together, these results indicate that Mc modules may stabilise actin filaments by preventing their depolymerisation.

Human Mc module bundles and stabilises actin filaments. Interestingly, we also showed that the hMc module was able to bundle actin filaments (Supplementary Fig. 3A–B) with periodic striations spaced by 36.02 \pm 1.138 nm and to protect actin filaments from depolymerisation (Supplementary Fig. 3C–D).

Discussion

It is well established that the maturation and plasticity of dendritic spines are strongly dependent on the complex, dynamic remodelling of the spine actin cytoskeleton. We show here that part of this remodelling is mediated by MAP6, a protein known to be indispensable for synaptic plasticity and for the normal development of brain circuits underlying aspects of cognition and behaviour. MAP6 KO and heterozygous mice exhibit cognitive defects, associated with strong impairments affecting both short and long-term synaptic plasticity, including defective LTP and LTD^{17,41}. Moreover, MAP6 deficits have been linked to autism⁴² in line with the involvement of spine pathology in human

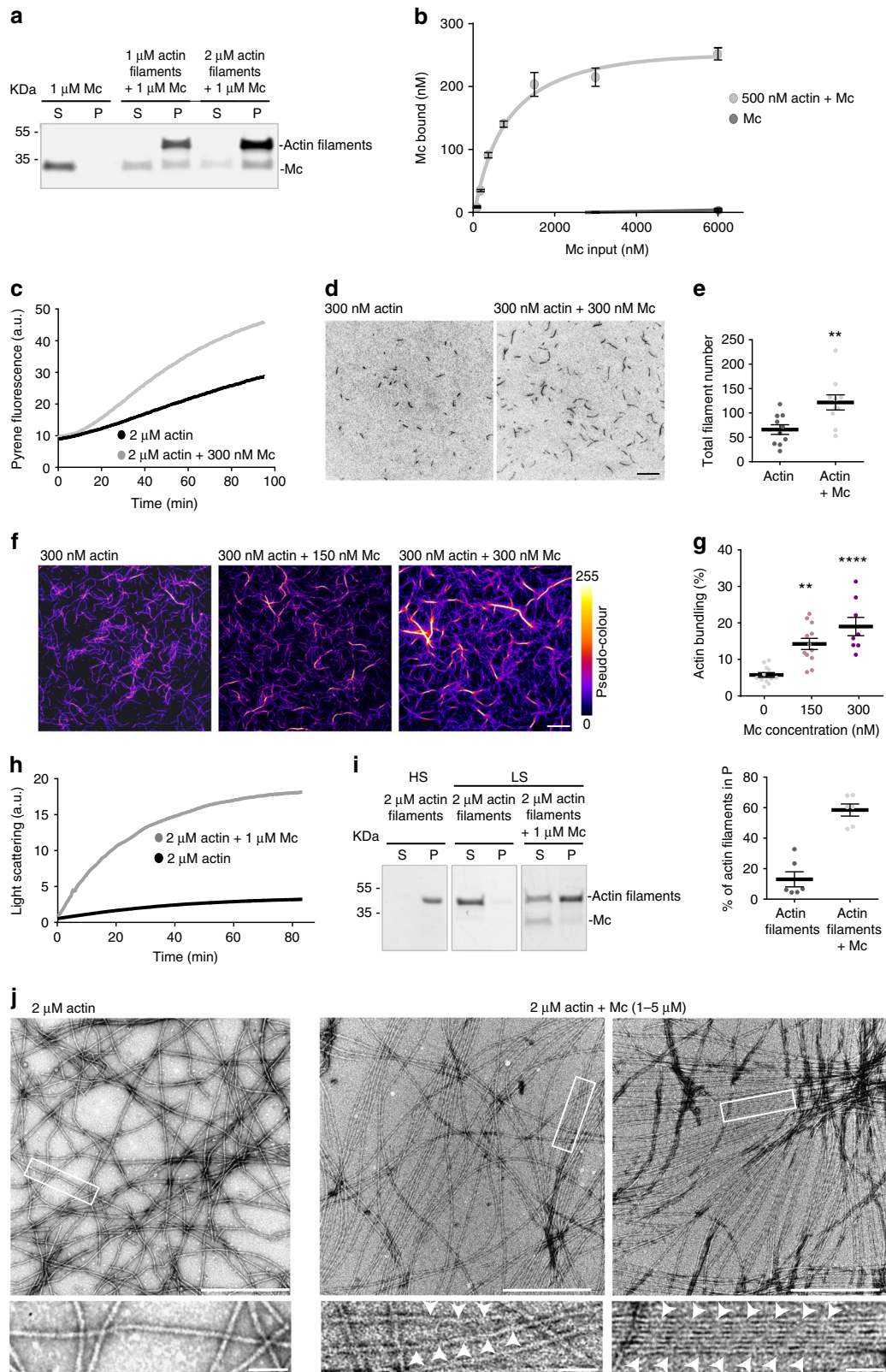
neuropsychiatric disease⁴³. MAP6 is known as a microtubule-associated protein that can also interact with actin depending on its phosphorylation state²⁵. In this work, using biochemical and microscopy approaches, we identify MAP6 as a novel regulator of actin filament dynamics and conformation, with implications for the mechanisms of synaptic homeostasis and plasticity.

MAP6 KO neurons, both *in vivo* as *in vitro*, displayed impairments in the morphological and functional maturation of post-synaptic compartments. The deficiency phenotype could be rescued by expressing different MAP6 isoforms. Remarkably, within the MAP6 sequence, the Mc modules were both necessary and sufficient to rescue dendritic spine density. This result cannot readily be explained by the known affinity of Mc modules for microtubules, as microtubule binding cannot occur at physiological temperature; instead, we find that Mc modules interact with actin filaments in a way consistent with direct regulation of the spine cytoskeleton.

Several results strengthen the idea that MAP6 binding to spine actin is instrumental to spine maintenance. In addition to microtubular localisation, full-size MAP6 as well as the isolated Mc domain are present in actin-rich regions of neurons, such as growth cones of young neurons or dendritic spines in mature cells. FRET assays supported the notion that, via the Mc modules, MAP6 closely interacts with actin filaments *in situ*. Using MAP6 phosphorylation mutants, localisation of the protein in the spine was shown to correlate with spine restoration. Functionally, FRAP measurements of spine actin dynamics revealed that MAP6 had a necessary role in the kinetic stabilisation of actin filaments that accompanies activity-induced synaptic change. Rescue experiments again showed that MAP6 depended on its Mc modules for regulating spine actin turnover; furthermore, Mc modules expressed on their own were able to restore actin stabilisation following cLTP in MAP6 KO neurons.

On the whole, these results indicate that MAP6 has an important part in the stabilisation of mature spine types (“mushroom-like” and “stubby” spines), *i.e.* those that transmit larger synaptic currents and encode long-lasting information⁴⁴. As the fraction of thin spines was not affected, MAP6 deficiency does not seem to result in a simple reversal of spine maturation. One explanation could be that the cytoskeletal structure promoted by MAP6 binding to actin is specifically required for maintaining mature spines.

The *in vitro* reconstitution of the Mc-actin interaction uncovered molecular properties that are consistent with the specific function of MAP6 in spine plasticity. We found, in our *in vitro* conditions, that purified Mc modules interact with actin filament with a K_d below the micromolar range and promote the formation of straight, stable, rigid actin bundles. Biophysical



modelling indicates that morphogenesis of the spine head can be quantitatively accounted for by a balance of forces, involving a combination of actin bundles pushing outward along the axis of the spine neck, and filaments that emerge from Arp2/3-nucleated branches and that exert isotropic radial pressure in the head⁴⁵.

Indeed, spines have been shown to harbour both a sub-membrane pool of actively polymerising filaments and a core population of stable actin filaments; the increase and stabilisation of core actin is a feature of LTP³. The action of MAP6 Mc modules on actin filament nucleation might be important during the initial

Fig. 5 Mc modules modify actin filament dynamics and organisation in vitro. **a** Mc modules co-sedimented without or with filamentous actin, analysed by SDS-PAGE and Coomassie blue staining (P: pellet, S: supernatant). **b** Concentration of Mc polypeptide bound to actin filaments (500 nM), plotted as a function of the total amount of Mc input. Data points represent mean \pm SEM, $n = 3$ for Mc alone and $n = 4$ for Mc + actin. **c** Representative graph showing the time course of polymerisation of pyrene-labelled actin (10%) in the absence or presence of Mc modules. **d** TIRF microscopy images of actin polymerised with or without Mc modules for 5 min. Scale bar: 10 μ m. **e** Quantification of the total filament number, obtained from **d** images. Data presented as mean \pm SEM. (** $p < 0.01$; Student's *t*-test). $n = 10$ independent experiments. **f** TIRF microscopy images of actin filaments polymerised in the absence or presence of Mc modules for 60 min. For better visualisation of actin bundles, a pseudo-colour lookup table (LUT) was applied. Fire LUT pixel intensity map show individual actin filaments in violet and actin bundles in red to yellow. Scale bar: 10 μ m. **g** Quantification of the percentage of bundled actin filaments related to total actin filaments network as a function of Mc modules concentration. Data presented as mean \pm SEM. (** $p < 0.01$, **** $p < 0.0001$; Kruskal–Wallis with Dunn's multiple comparison test). $n = 12$, 12 and 8 independent experiments for actin, actin + 150 nM Mc and actin + 300 nM Mc, respectively. **h** Representative time course of actin bundling in the absence or presence of Mc modules, monitored by light scattering at 400 nm (arbitrary units). **i** Actin filaments in high (100,000 \times g) and low-speed (15,000 \times g) co-sedimentation assays in the absence or presence of Mc modules (P: pellet, S: supernatant). Data presented as mean \pm SEM. (**** $p < 0.0001$; Student's *t*-test). $n = 6$ independent experiments. **j** Actin alone or in the presence of Mc modules visualised by negative staining and electron microscopy. Scale bar: 500 nm. Lower panels are higher magnifications of the insert in upper panels. Scale bar: 50 nm

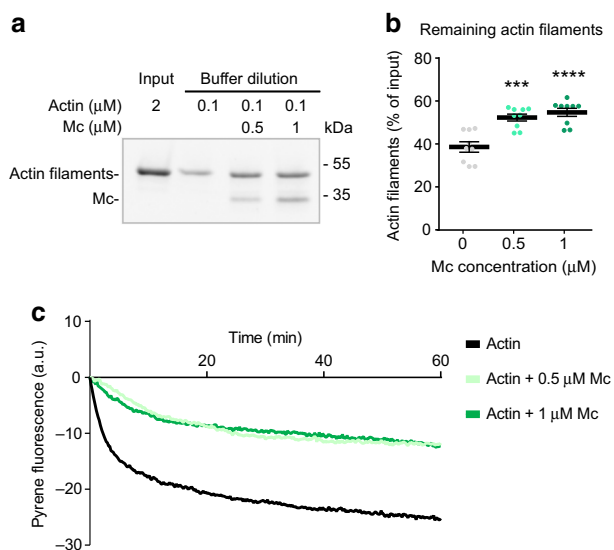


Fig. 6 Mc modules protect actin filaments from depolymerisation. **a** Actin depolymerisation induced by dilution of actin filaments alone or in the presence of Mc modules. After 20 min of incubation in a buffer containing 0.1 μ M actin (alone or with 0.5 μ M or 1 μ M Mc), samples were centrifuged at 100,000 \times g and pellets separated on SDS/PAGE and detected by Stain-Free system. **b** Quantification of the percentage of remaining actin filaments after buffer dilution. Data presented as mean \pm SEM. (**** $p < 0.001$, **** $p < 0.0001$, one-way ANOVA and Sidak's post hoc test), $n = 9$ gels from three independent experiments. **c** Mean time course of actin filaments and Mc-decorated actin filaments depolymerisation. After 1 h incubation of 40% pyrene-labelled actin filaments alone or in the presence of Mc modules, all samples were diluted to a final concentration of 0.1 μ M actin (alone or with 0.5 μ M or 1 μ M of Mc) and pyrene fluorescence (arbitrary unit) was measured over time

reorganisation of the actin cytoskeleton, whereas Mc-induced filament straightening and bundling could be necessary for the enlargement and maintenance of potentiated spines (mushroom-like forms).

Several other proteins, such as drebrin, spinophilin/neurabin, or CaMKII β , have been described as crucial for dendritic spine morphogenesis in association with their ability to bundle actin^{46–50}. However, the in vivo phenotype of MAP6 KO spines indicates that MAP6-induced actin arrangements carry specific properties, which are not conferred by other actin-binding proteins. The fact that the same MAP6 Mc module carries both nucleation-enhancing and bundling activities might allow MAP6 to promote the enlargement of the spine actin pool in a specific,

uniquely efficient fashion. Furthermore, at the ultrastructural level, both single and bundled actin filaments were seen to be strikingly straightened in the presence of the MAP6 Mc modules. The straightened fibres displayed regularly spaced striations, with a period of 35–36 nm, potentially corresponding to the helical pitch of bare actin filaments. This suggests that filaments cross-linked by Mc modules were aligned without torsion and in a highly ordered, extended conformation. The periodic striations seemingly correspond to a specific feature of MAP6-decorated actin filaments. Other MAPs such as tau and MAP2C, or the key neuronal actin-binding protein drebrin, were shown to induce assembly of actin filaments into rope-like structures or loose bundles, with no visible striations^{12,14,51,52}. Within the large group of actin-binding proteins, several members, including fimbrin, coronin, FRG-1 and p135^{ABP}, induce actin bundling without striations^{53–55}. In contrast, periodic striations similar to those seen here have been observed for fascin⁵⁶ and cortexillin⁵⁷ or septins⁵⁸. However, these latter proteins are either absent from dendritic spines or confined to their base and neck. Thus, MAP6 is the first MAP and the first protein present within dendritic spines able to induce actin bundling with periodic striations. One limitation of the present study is that the effect of Mc MAP6 on actin organisation could only be resolved in vitro, with isolated components, and we did not further test for interaction of Mc with other similar charge and mass; future work will need to further confirm the specificity of this interaction, and to address the challenge of imaging Mc-dependent actin ultrastructure in dendritic spines.

The extended conformation of Mc-bound filaments suggests that they are under tension. Such tension has been shown to decrease binding of the filament-severing protein, cofilin⁵⁹; hence MAP6 may conceivably protect a pool of spine actin against cofilin activity. Straight filaments induced by MAP6 might also increase the efficacy of myosin-mediated vesicular transport of lipid membrane and AMPA receptors into spines⁶⁰. Indeed, alteration of myosin isoforms resulted in impaired AMPAR trafficking, and, similar to MAP6 deficiency, in decreased frequency of miniature EPSCs and defective activity-induced synaptic change.

Under physiological conditions, the two main MAP6 isoforms in neurons, MAP6-N and MAP6-E, contain Mc modules but also Mn modules, which have strong microtubule binding affinity. Release of MAP6 from the dendritic microtubules is necessary for translocation into spines, and might be triggered by phosphorylation events occurring upon neuronal activation. We have previously shown that MAP6 was phosphorylated by CamKII, the major kinase in spines²⁵. Phosphorylation by CamKII-rendered MAP6 unable to associate with microtubules, while leaving actin-

binding unchanged (no change of binding following alkaline phosphate treatment)²⁵. Here, we correlated the translocation of MAP6 phosphorylation mutants from microtubules in the dendritic shaft to actin filaments in dendritic spines, with the ability of these mutants to restore spine density. The simplest explanation of our data is that the phosphorylation-defective MAP6 mutant (S to A) was retained on MTs and thus unable to translocate into spines and thereby to rescue the spine deficit in MAP6 KO neurons. Thus phosphorylation of MAP6 may mediate some of the effects of CamKII on structural plasticity.

Finally, beside its direct effects on actin filament dynamics and organisation, we cannot exclude that MAP6 also indirectly control spine actin via signalling events, such as activation of small GTPases. Indeed, MAP6 has been shown to directly interact with Rac1⁶¹, a GTPase known to induce strong cytoskeletal rearrangements. When present in dendritic spines and bound to actin, MAP6 might also regulate plasticity pathways by interacting with SH3 domain-containing proteins such as Intersectin or PI3K-kinase, through active PRD domains as reported in the case of Sema3E-dependant axonal guidance³⁰.

In summary, the present data provide evidence that MAP6 acts as a novel player in the regulation of actin cytoskeleton structure and dynamics, with important consequences for the maturation and maintenance of dendritic spines in hippocampal neurons. Reduced expression of MAP6 affects the density of dendritic spines and mature synapses *in vitro* and *in vivo*, and prevents the stabilisation of the spine actin cytoskeleton during plasticity events. The ability of MAP6 to regulate actin dynamics relies on its Mc modules, which we show are able to enhance actin filament nucleation, promote filament stabilisation and bundling, and induce the appearance of a specific, straightened filament conformation. Thus, these data shed new light on the mechanisms that might contribute to the cognitive impairments associated with MAP6 deficiency.

Methods

Animals. All experiments involving animals were conducted in accordance with the policy of the Institut des Neurosciences de Grenoble (GIN) and in compliance with the French legislation and European Union Directive of 22 September 2010 (2010/63/UE). The research involving animals was authorised by the Direction Départementale de la protection des populations - Préfecture de l'Isère - France and by the ethics committee of GIN n° 004 accredited by the French Ministry of Research. The homogeneous inbred 129SvPas/C57BL6, 129SvPas/C57BL6-Thy1-eYFP-H WT and MAP6 KO mice were generated as previously described⁶².

Plasmids and recombinant proteins. PCR amplification and cloning of cDNAs were performed with Phusion DNA polymerase (Thermo Scientific) and In-Fusion HD Cloning kit (Clontech), respectively. All constructs were verified by sequencing (Eurofins). A cDNA encoding human actin (GenBank accession number NM_001101) was PCR-amplified and inserted into the pEGFP-C1 vector. The plasmid encoding mCherry was from Clontech (pmCherry vector) and the actin filament marker LifeAct-RFP plasmid described in ref.²¹ A cDNA encoding rat MAP6-N (accession number NM_017204) was PCR-amplified and inserted into pEGFP-N1. Rat MAP6-N fragments aa 1–614 (MAP6-E) and aa 221–455 (Mc), rat MAP6-E deletions of aa 124–138 (replaced by Ala) + aa 162–171 + aa 481–495 (MAP6-E-ΔMn) and aa 225–450 (MAP6-E-ΔMc), rat MAP6-E point mutations S139A + S198A + T484 A + S537A (MAP6-E-4A) and S139E + S198E + T484E + S537E (MAP6-E-4E), according to the numbering of rat MAP6-N (NP_058900), were created by PCR and cloned into pEGFP-N1 (except into pEGFP-C1 for Mc). Rat MAP6-N fragments aa 359–451 (R4R5) and aa 404–451 (R5) according to the numbering of rat MAP6-N (NP_058900) was created by PCR and cloned into pEGFP-C1. DsRed2 cDNA was amplified by PCR from pDsRed2-C1 plasmid (Clontech) and inserted in place of GFP in the GFP fusions of the above described rat MAP6 fragments MAP6-E, Mc and MAP6-E ΔMn. A cDNA encoding human MAP6-E (accession number AB527183) was PCR-amplified and inserted into pEGFP-C1. Human MAP6-E fragment aa 224–280 (hMc), according to the numbering of human MAP6-E (AB527183) was created by PCR and cloned into pEGFP-N1. The lentiviral plasmid encoding eGFP was from Addgene (pWPXLd vector, kind gift from D. Trono). A cDNA encoding rat MAP6-N fragment aa 221–235 (5R), according to the numbering of rat MAP6-N (NP_058900), was created by PCR and cloned into pWPXLd.

Lentivirus production. Lentiviral particles encoding either GFP-Mc or unfused GFP were produced in our institute by co-transfection of the pWPXLd-based vector with the psPAX2 and pCMV-VSV-G helper plasmids (Addgene, Cambridge, MA) into HEK293T cells obtained from ATCC (ATCC-CRL-3216). Viral particles were collected by ultra-speed centrifugation.

Protein purification. The Mc domain was produced in insect cells and purified as already described²⁴. Human Mc synthetic peptide (hMc) was purchased from ThermoFisher Scientific, resuspended in BRB buffer (80 mM PIPES pH 6.75, 1 mM EGTA, 1 mM MgCl₂), aliquoted, frozen in liquid nitrogen and stored at –80 °C.

Cell culture, transfection and immunofluorescence. Hippocampi (E18.5) were digested in 0.25% trypsin in Hanks' balanced salt solution (HBSS, Invitrogen, France) at 37 °C for 15 min. After manual dissociation, cells were plated at a concentration of 5000–15,000 cells/cm² on poly-L-lysine-coated (1 mg/ml poly-L-lysine hydrobromide, Sigma Aldrich) coverslips for fixed samples, or on ibidi glass bottom 60 μDishes for live imaging. Neurons were incubated 2 h in DMEM-10% horse serum and then changed to MACS neuro medium (Miltenyl Biotec) with B-27 supplement (Invitrogen, France). Hippocampal neurons were incubated for 2, 16, 18 or 30 days *in vitro* (DIV) at 37 °C, 5% CO₂ in a humidified incubator. The neurons were transiently transfected with the cDNAs described above using Lipofectamine 3000 (Invitrogen) according to the manufacturer's instructions, and analysed 24 h later. For silencing experiments, efficient knockdown of MAP6 was obtained using previously described³⁰ Stealth RNAi siRNA1 and siRNA2 (Invitrogen). For immunocytochemistry, cells were fixed with 4% paraformaldehyde in 4% sucrose-containing PBS for 20 min and permeabilised with 0.2% Triton X-100/PBS for 5 min. Fixed cells were then incubated with primary antibodies for 3 h in 0.1% PBS/Tween and then with fluorophore-conjugated secondary antibodies for 1 h at room temperature. Primary antibodies were: rabbit polyclonal anti GFP (ThermoFisher Scientific. Cat# A-11122) diluted 1:1000, mouse monoclonal anti PSD-95 (clone K28/43, NeuroMab UC Davis/NIH NeuroMab Facility. Item # 75-028) diluted 1:500, rabbit polyclonal anti Synaptophysin (SYP (H-93), Santa Cruz Biotechnology, Inc. Cat# sc-9116) diluted 1:500, mouse monoclonal anti mCherry (Clontech Laboratories, Inc. Cat# 632543) diluted 1:1000, rabbit polyclonal antibody against MAP6 (Ab23N) diluted 1:250 and mouse monoclonal antibody against MAP6-N⁶³ (Ab 175) diluted 1:250, rat monoclonal anti Tyr-tubulin (YL1/2) diluted 1:1000 and mouse monoclonal antibody against alpha-tubulin⁶⁴ (clone α3A1) diluted 1:1000. Secondary antibodies were coupled to Alexa-488, to Cy3 or to Cy5 (Jackson Immuno-Research Laboratories). TRITC-Phalloidin (Sigma Aldrich, Inc. Cat# P1951) was used to label actin filaments. Fluorescent images were acquired with a Zeiss LSM 710 confocal microscope using a ×40 and ×63 oil-immersion objective (NA 1.25 and NA 1.4) and ZEN 2010 software (Carl Zeiss MicroImaging).

Imaging of dendritic spines. For fixed samples, images of dendritic segments of Thy1-eYFP-H mouse cortical neurons (serial sections of cortex) or 18 DIV transfected neurons visualised by soluble GFP or soluble mCherry fluorescence were obtained using a confocal laser scanning microscope (Zeiss, LSM 710). Serial optical sections (1024 × 1024 pixels) with pixel dimensions of 0.083 × 0.083 μm were collected at 200 nm intervals, using a ×63 oil-immersion objective (NA 1.4). The confocal stacks were then deconvolved with AutoDeblur. Dendritic spine analysis (spine counting and shape classification) was performed on the deconvolved stacks using Neuronstudio^{65,66}. All spine measurements were performed in 3D from the z-stacks. The linear density was calculated by dividing the total number of spines present on assayed dendritic segments by the total length of the segments. At least three dendritic regions of interest were analysed per cell from at least three independent cultures in each experimental condition.

For live imaging during chemical LTP, 17 DIV WT or MAP6 KO hippocampal neurons were co-transfected with GFP and LifeAct-RFP cDNAs using Lipofectamine 3000 and imaged 24 h later at 37 °C on a heated stage with 5% CO₂ (PeCon), using a confocal laser scanning microscope (Zeiss, LSM 710) and GaAsP detector (Zeiss Airyscan). Dendritic segments of neurons that simultaneously expressed GFP and LifeAct-RFP were selected to image ~30 spines per neuron at baseline state or 15 min after cLTP (50 μM bicuculline and 2.5 mM 4-Aminopyridine). Only modest bleaching was observed during the experiment. Cells showing signs of damage (pearling or blebbing) were discarded. Individual spines, identified using Neuronstudio^{65,67}, which were identifiable at initial and final time points were manually selected. Each dendritic spine volume before and after cLTP was quantified on the GFP stack using Neuronstudio and a ratio was calculated as follows: final volume (fi)/initial volume (iv) with iv as the volume before stimulation and fv as the volume 15 min after cLTP induction. To estimate F-actin concentration in dendritic spine, a region of interest (ROI) including the whole spine was placed at each previously identified dendritic spine on LifeAct-RFP and GFP stacks at baseline state or 15 min after cLTP induction. The fluorescence intensity (FI) of the Maximum Intensity z projection of the LifeAct-RFP and GFP stacks were measured for each spine, before and after cLTP. Individual spine F-actin concentration was estimated as follows: [FI LifeAct/FI GFP] after cLTP / [FI LifeAct/FI GFP] before cLTP.

Imaging of excitatory synapses. For immunodetection of excitatory synapses in transduced neurons, 1/100 of a hippocampal cell suspension was infected by 15 min incubation with GFP or GFP-Mc lentivirus (Lv) at a multiplicity of infection of 40. The infected population was then mixed with non-transduced cells and plated on poly-L-lysine-coated coverslips and incubated at 37 °C, 5% CO₂ in a humidified incubator. Neurons were fixed at 18 DIV and immunolabeled with GFP, PSD-95 and Synaptophysin antibodies. Fluorescent images were acquired with a Zeiss LSM 710 confocal microscope using a ×63 oil-immersion objective (NA 1.4) and ZEN 2010 software (Carl Zeiss MicroImaging). Images were enhanced for small structures with the LoG3D ImageJ plugin⁶⁸ using a 2 pixel radius, and thresholded to create a mask for: GFP (transfection and contour marker), Synaptophysin (pre-synaptic compartment) and PSD-95 (post-synaptic compartment). The mask corresponding to the overlap of the three markers was superposed to the GFP image. We manually counted the synaptic puncta present in dendritic spines or in the shaft and calculated their linear density. Mask creation and counting were done blind to the transduction condition.

Electrophysiological recordings in neuronal culture. Hippocampal neurons in culture were visualised in a chamber on an upright microscope with transmitted illumination and continuously perfused at 2 ml/min with oxygenated Artificial Cerebro-Spinal Fluid (ACSF in mM: 119 NaCl, 2.5 KCl, 1.25 NaH₂PO₄, 1.3 MgSO₄, 2.5 CaCl₂, 26 NaHCO₃, 0.001 tetrodotoxin, 0.05 bicuculline methiodide and 11 Glucose) at room temperature. Miniature excitatory post-synaptic currents (mEPSC) were recorded at a membrane potential of -60 mV with borosilicate glass pipettes of 4–5 MΩ resistance filled for whole-cell recordings (in mM: 117.5 CsMeSO₄, 15.5 CsCl, 10 TEACl, 8 NaCl, 10 HEPES, 0.25 EGTA, 4 MgATP, 0.3 NaGTP, pH 7.3). Signals were amplified with an EPC 10 Amplifier (HEKA Elektronik Dr. Schulze GmbH, Wiesenstrasse, Germany). Recordings were filtered at 1 kHz and sampled at 10 kHz using the Patchmaster Multi-channel data acquisition software (HEKA Elektronik Dr. Schulze GmbH, Wiesenstrasse, Germany).

Fluorescence resonance energy transfer-acceptor bleaching. Fluorescence resonance energy transfer with acceptor bleaching (FRET-AB)³⁴ was performed on 2 DIV or 18 DIV neurons transfected with GFP-tagged constructs (FRET donor) and stained for actin with TRITC-phalloidin (FRET acceptor). For photobleaching of the acceptor, ROIs corresponding to growth cones were exposed to five scans using the 561 nm laser line at 100% power on the LSM 710 confocal microscope. The whole neuron was imaged at lower power intensity with both the 488 and 561 nm lasers before and after the bleaching of acceptor. FRET efficiency was calculated as the relative increase of the fluorescence intensity of the donor after selective photobleaching of the acceptor, according to the formula $Efficiency = (F_{Donor\ post} - F_{Donor\ pre}) \times 100 / F_{Donor\ post}$. Control measurements were performed with the same imaging protocol in neurons that had not been stained with TRITC-phalloidin (donor alone), in non-transfected neurons labelled with TRITC-phalloidin-(acceptor alone), and by omitting the photobleaching step in transfected and labelled neurons.

Fluorescence recovery after photobleaching. FRAP experiments were performed in 16 DIV mouse hippocampal cultures transfected with GFP-actin cDNA using Lipofectamin 3000 (Lifetechnologies), as per manufacturer's instructions. FRAP was performed 24 h after transfection on GFP-actin expressing neurons at baseline state or 15 min after cLTP treatment. Images were acquired with an inverted Nikon Eclipse Ti C2 confocal microscope with a Nikon ×60 water objective with 1.33 numerical aperture. Only mature mushroom type spines were used for the experiments. A ROI including the whole spine was imaged 10 times before bleaching. GFP-actin was bleached at maximal laser power with the 405 nm laser line (five iterations, total bleach time of 0.66 s, fluorescence reduction of ~90%). The fluorescence recovery was measured by scanning the ROI with 488 nm laser light using the following protocol: 10 images at 1 frame/s before bleaching, 10 images at 1 frame/s after bleaching followed by 60 images at 1 frame/5 s for 300 s. Fluorescent signal analysis was performed with the Nikon software Nis. All the post-bleach values were divided by the values from the non bleached area of the cells and normalised to the first 10 pre-bleach values. The first post-bleach measurement was set to zero.

Raw fluorescence values were normalised by dividing by the values at each time point by the average value before bleaching. The analysis of the FRAP recovery data was performed with GraphPad Prism. For each FRAP assay, the plateau value (y_0), mobile fraction (A), first-order rate constant (k) and characteristic time (k^{-1}) were calculated by non-linear regression, fitting the data to a mono-exponential recovery model ($y = y_0 - A \cdot \exp(-k \cdot x)$). Goodness of fit was not improved when using a two-phase recovery model, therefore we retained the simpler monophasic curve. Mean plateau values were calculated from these individual fits. We checked the different groups of FRAP data for normality (Shapiro–Wilkes test) and variance homogeneity (Flinger test) and analysed them by one-way ANOVA, followed by post hoc pairwise t -tests. Diffusional entry of monomeric actin was not included in the model because in our hands it occurs with a time scale that is at least ~40-fold faster than polymerisation; any effect of diffusion is thus included in the value of the first recovery time point.

Pyrene actin polymerisation. 2 μM of 10% pyrene-labelled G-actin (actin monomers) was polymerised alone or in the presence of 300 nM of Mc modules, in buffer AP (Actin Polymerisation) containing 2 mM Tris, 10 mM imidazole pH 7.0, 0.2 mM ATP, 0.5 mM DTT, 0.1 mM CaCl₂, 50 mM KCl, 1 mM MgCl₂, 1 mM EGTA.

TIRF microscopy. Perfusion chambers were prepared with functionalised silane-PEG (Creative PEGwork) glass slides, as described previously¹¹. For actin polymerisation assays, the flow cell was incubated with PLL-g-PEG (2 kDa, 0.1 mg/ml in 10 mM Hepes, pH 7.4, Jenkem) and washed with 1% BSA in buffer AP. Actin growth was initiated by flowing 300 nM G-actin (containing 30% Alexa-488 labelled G-actin) alone or with 150–300 nM Mc modules in AP buffer containing 4 mM DTT, 1% BSA, 1 mg/ml glucose, 70 μg/ml catalase, 580 μg/ml glucose oxidase and 0.3% methylcellulose. Samples were visualised on an inverted microscope (Eclipse Ti, Nikon) equipped with an Ilas² TIRF system (Roper Scientific), a cooled charge-coupled device camera (EMCCD Evolve 512, Photometrics), a warm stage controller (LINKAM MC60), and controlled by MetaMorph software (version 7.7.5, Molecular Devices). Samples were excited with 491 nm laser light and time-lapse imaging (at 488 nm) was performed at 26 °C for actin polymerisation, during 45 min at 1 frame per 5 s with a 100-ms exposure time.

The elongation rate of actin filaments polymerisation with or without Mc modules was determined on kymographs using ImageJ software and a home-made plugin (KymoTool). Elongation of single actin filaments was derived from actin length measurements on image stacks. To analyse actin nucleation, 300 nM actin (labelled as above), alone or together with 300 nM Mc modules was incubated in AP buffer containing 4 mM DTT, 1% BSA, 1 mg/ml glucose, 70 μg/ml catalase, 580 μg/ml glucose oxidase and 0.3% methylcellulose in the perfusion chamber for 5 min at 26 °C and imaged. TIRF images were skeletonised and the number of filaments and the length of total actin network were measured. To analyse bundling activity, 300 nM actin alone or with 150 or 300 nM Mc modules was treated as before and images were taken after 45 min. TIRF images of actin filaments were enhanced using Feature detector⁶⁹ module of Icy⁷⁰. Actin network and bundles were segmented with Fiji⁷¹ using Otsu or Yen thresholding algorithms, respectively. The thresholded images were skeletonised and the total length of actin network or bundles was measured. The percentage of actin bundling was calculated by dividing the length of bundled actin by the total length of filamentous actin in the same field.

Light-scattering assay to measure bundling activity. A kinetic light-scattering assay was performed to determine the ability of Mc modules to form actin bundles during polymerisation. Light scattering by unlabelled 2 μM G-actin was monitored at 400 nm at a scattering angle of 90°. The change of light scattering was recorded after addition of 1 μM Mc modules.

High-speed and low-speed co-sedimentation assays. High- and low-speed co-sedimentation assays were used to examine actin polymerisation and actin bundling, respectively¹¹. All proteins were pre-clarified at 140,000×g before each experiment. 2 μM G-actin (actin monomers) was polymerised for 1 h at room temperature (RT) in AP (Actin Polymerisation) buffer containing 2 μM Phalloidin. To confirm the complete polymerisation of actin, samples were centrifuged for 15 min at 100,000×g (high-speed co-sedimentation assay: HS).

To measure the binding of Mc modules to actin filaments, various concentrations of polymerised actin were incubated with Mc modules in AP buffer for 1 h at room temperature. After HS sedimentation, Mc modules and actin present in the pellet or in the supernatant were analysed by SDS-PAGE and Coomassie blue staining (Supplementary Fig. 4). For titration analysis, co-sedimented Mc domains were quantified by western immunoblotting using anti-MAP6 antibody 23C⁶³ and chemiluminescent detection (ChemidocTMMP Imaging System, BioRad). Absolute protein amounts were determined by calibration with an Mc-domain concentration range, using ImageJ for image analysis. K_d and B_{max} values and their confidence interval were calculated with R by non-linear fitting of the data to the single-site binding isotherm, $B/B_{max} = (T - B)/(K_d + T - B)$, where T is the total (input) Mc concentration, B is the actin-bound Mc concentration, and B_{max} is the saturating concentration.

To analyse bundling activity, 1 μM Mc modules was added (or not) in the mixture after actin polymerisation and samples were centrifuged for 15 min at 15,000×g (low-speed co-sedimentation assay: LS). All supernatants and pellets were resolved by SDS-PAGE and detected by Stain-Free technology in the gel (Mini-PROTEAN[®] TGX Stain-Free[™], Biorad) (Supplementary Fig. 4). Protein bands were quantified from triplicate blots of independent experiments using ImageJ software (National Institutes of Health, Bethesda, MD).

Transmission electron microscopy. To analyse the effect of Mc modules on actin organisation, we performed negative staining electron microscopy in two sets of samples: in actin + Mc modules co-polymerisation and adding Mc modules after complete actin polymerisation. In co-polymerisation assays: 2 μM G-actin was incubated with 2 μM Phalloidin and 1 to 5 μM Mc modules in AP (Actin Polymerisation) buffer for 1 h at room temperature (RT).

In post-polymerisation assays: 2 μM G-actin was incubated with 2 μM Phalloidin in AP buffer for 1 h at RT. Then, Mc modules (1–5 μM) was added and incubated for 1 h at RT.

For negative staining, 1 μl of protein solution was loaded onto a carbon-mica interface. The carbon layer was floated on 2% uranyl acetate, recovered with a 400-mesh copper grid (Agar Scientific), air dried, and observed with a JEOL 1200EX transmission electron microscope at 80 kV. Images were acquired with a digital camera (Veleta, Olympus) at $\times 100,000$ magnification. Experiments were performed at the Electron Microscopy Facility of the Grenoble Institute of Neuroscience. To detect the periodic striations of Mc-decorated single and bundled filaments, a line was traced between the edges of each filament (outside or inside the bundle), staining intensity along the line was plotted, and the distances between successive intensity minima were measured. Each value corresponds to the mean distance between successive striations of the same filament. Images of independent experiments were analysed.

Actin depolymerisation by buffer dilution. To analyse actin depolymerisation, we first incubated 2 μM G-actin with 2 μM Phalloidin in AP buffer for 1 h at RT. Then, 0.5 to 1 μM of Mc modules was added and incubated for 1 h at RT. G-actin was diluted from 2 to 0.1 μM in AP buffer (alone or with 0.5 or 1 μM of Mc modules) for 20 min, centrifuged at 100,000 \times g and pellets were separated on SDS-PAGE and detected by Stain-Free technology in the gel (Mini-PROTEAN[®] TGX Stain-Free[™], Biorad). Protein bands were quantified from triplicate blots of independent experiments using ImageJ software (National Institutes of Health, Bethesda, MD). The remaining actin filaments were calculated as a percentage of the input. Kinetic depolymerisation of 2 μM of 40% pyrene-labelled actin, alone or in the presence of 0.5 or 1 μM of Mc modules, was monitored after dilution to 0.1 μM actin in AP buffer (alone or with 0.5 or 1 μM of Mc modules).

Statistical analysis. All data are presented as mean \pm SEM. Statistical significance of differences between conditions was calculated with Prism 5.0 (GraphPad Software), using tests as indicated in each figure.

Data availability. The datasets generated and/or analysed during the current study are available from the corresponding authors on request.

Received: 30 January 2018 Accepted: 27 July 2018

Published online: 17 September 2018

References

- Hotulainen, P. & Hoogenraad, C. C. Actin in dendritic spines: connecting dynamics to function. *J. Cell Biol.* **189**, 619–629 (2010).
- Dent, E. W. Of microtubules and memory: implications for microtubule dynamics in dendrites and spines. *Mol. Biol. Cell* **28**, 1–8 (2017).
- Honkura, N., Matsuzaki, M., Noguchi, J., Ellis-Davies, G. C. & Kasai, H. The subspine organization of actin fibers regulates the structure and plasticity of dendritic spines. *Neuron* **57**, 719–729 (2008).
- Bosch, M. et al. Structural and molecular remodeling of dendritic spine substructures during long-term potentiation. *Neuron* **82**, 444–459 (2014).
- Penzes, P. & Rafalovich, I. Regulation of the actin cytoskeleton in dendritic spines. *Adv. Exp. Med. Biol.* **970**, 81–95 (2012).
- Jaworski, J. et al. Dynamic microtubules regulate dendritic spine morphology and synaptic plasticity. *Neuron* **61**, 85–100 (2009).
- Merriam, E. B. et al. Dynamic microtubules promote synaptic NMDA receptor-dependent spine enlargement. *PLoS ONE* **6**, e27688 (2011).
- Hu, X., Viesselmann, C., Nam, S., Merriam, E. & Dent, E. W. Activity-dependent dynamic microtubule invasion of dendritic spines. *J. Neurosci.* **28**, 13094–13105 (2008).
- Kapitein, L. C. et al. NMDA receptor activation suppresses microtubule growth and spine entry. *J. Neurosci.* **31**, 8194–8209 (2011).
- Merriam, E. B. et al. Synaptic regulation of microtubule dynamics in dendritic spines by calcium, f-actin, and drebrin. *J. Neurosci.* **33**, 16471–16482 (2013).
- Elie, A. et al. Tau co-organizes dynamic microtubule and actin networks. *Sci. Rep.* **5**, 9964 (2015).
- He, H. J. et al. The proline-rich domain of tau plays a role in interactions with actin. *BMC Cell Biol.* **10**, 81 (2009).
- Yu, J. Z. & Rasenick, M. M. Tau associates with actin in differentiating PC12 cells. *FASEB J.* **20**, 1452–1461 (2006).
- Roger, B., Al-Bassam, J., Dehmelt, L., Milligan, R. A. & Halpain, S. MAP2c, but not tau, binds and bundles F-actin via its microtubule binding domain. *Curr. Biol.* **14**, 363–371 (2004).
- Villarroel-Campos, D. & Gonzalez-Billault, C. The MAP1B case: an old MAP that is new again. *Dev. Neurobiol.* **74**, 953–971 (2014).
- Bouquet, C., Ravaille-Veron, M., Propst, F. & Nothias, F. MAP1B coordinates microtubule and actin filament remodeling in adult mouse Schwann cell tips and DRG neuron growth cones. *Mol. Cell Neurosci.* **36**, 235–247 (2007).
- Andrieux, A. et al. The suppression of brain cold-stable microtubules in mice induces synaptic defects associated with neuroleptic-sensitive behavioral disorders. *Genes Dev.* **16**, 2350–2364 (2002).
- Kimura, T. et al. Microtubule-associated protein tau is essential for long-term depression in the hippocampus. *Philos. Trans. R. Soc. Lond. B. Biol. Sci.* **369**, 20130144 (2014).
- Mondragon-Rodriguez, S. et al. Interaction of endogenous tau protein with synaptic proteins is regulated by N-methyl-D-aspartate receptor-dependent tau phosphorylation. *J. Biol. Chem.* **287**, 32040–32053 (2012).
- Ittner, L. M. et al. Dendritic function of tau mediates amyloid-beta toxicity in Alzheimer's disease mouse models. *Cell* **142**, 387–397 (2010).
- Frandemich, M. L. et al. Activity-dependent tau protein translocation to excitatory synapse is disrupted by exposure to amyloid-Beta oligomers. *J. Neurosci.* **34**, 6084–6097 (2014).
- Delotterie, D. et al. Chronic administration of atypical antipsychotics improves behavioral and synaptic defects of STOP null mice. *Psychopharmacology* **208**, 131–141 (2010).
- Bosc, C. et al. Identification of novel bifunctional calmodulin-binding and microtubule-stabilizing motifs in STOP proteins. *J. Biol. Chem.* **276**, 30904–30913 (2001).
- Delphin, C. et al. MAP6-F is a temperature sensor that directly binds to and protects microtubules from cold-induced depolymerization. *J. Biol. Chem.* **287**, 35127–35138 (2012).
- Baratier, J. et al. Phosphorylation of microtubule-associated protein STOP by calmodulin kinase II. *J. Biol. Chem.* **281**, 19561–19569 (2006).
- Munton, R. P. et al. Qualitative and quantitative analyses of protein phosphorylation in naive and stimulated mouse synaptosomal preparations. *Mol. Cell Proteom.* **6**, 283–293 (2007).
- Cheng, D. et al. Relative and absolute quantification of postsynaptic density proteome isolated from rat forebrain and cerebellum. *Mol. Cell Proteom.* **5**, 1158–1170 (2006).
- Collins, M. O. et al. Molecular characterization and comparison of the components and multiprotein complexes in the postsynaptic proteome. *J. Neurochem.* **97**, 16–23 (2006).
- Feng, G. et al. Imaging neuronal subsets in transgenic mice expressing multiple spectral variants of GFP. *Neuron* **28**, 41–51 (2000).
- Deloulme, J. C. et al. Microtubule-associated protein 6 mediates neuronal connectivity through Semaphorin 3E-dependent signalling for axonal growth. *Nat. Commun.* **6**, 7246 (2015).
- Harris, K. M. & Weinberg, R. J. Ultrastructure of synapses in the mammalian brain. *Cold Spring Harbor Perspect. Biol.* **4**, a005686 (2012).
- Stamatakou, E., Marzo, A., Gibb, A. & Salinas, P. C. Activity-dependent spine morphogenesis: a role for the actin-capping protein Eps8. *J. Neurosci.* **33**, 2661–2670 (2013).
- Denarier, E. et al. Genomic structure and chromosomal mapping of the mouse STOP gene (Mtap6). *Biochem. Biophys. Res. Commun.* **243**, 791–796 (1998).
- Karpova, T. S. et al. Fluorescence resonance energy transfer from cyan to yellow fluorescent protein detected by acceptor photobleaching using confocal microscopy and a single laser. *J. Microsc.* **209**, 56–70 (2003).
- Star, E. N., Kwiatkowski, D. J. & Murthy, V. N. Rapid turnover of actin in dendritic spines and its regulation by activity. *Nat. Neurosci.* **5**, 239–246 (2002).
- Okamoto, K., Nagai, T., Miyawaki, A. & Hayashi, Y. Rapid and persistent modulation of actin dynamics regulates postsynaptic reorganization underlying bidirectional plasticity. *Nat. Neurosci.* **7**, 1104–1112 (2004).
- Matsuzaki, M., Honkura, N., Ellis-Davies, G. C. & Kasai, H. Structural basis of long-term potentiation in single dendritic spines. *Nature* **429**, 761–766 (2004).
- Park, M. et al. Plasticity-induced growth of dendritic spines by exocytic trafficking from recycling endosomes. *Neuron* **52**, 817–830 (2006).
- Meyer, D., Bonhoeffer, T. & Scheuss, V. Balance and stability of synaptic structures during synaptic plasticity. *Neuron* **82**, 430–443 (2014).
- Bryan, J. & Coluccio, L. M. Kinetic analysis of F-actin depolymerization in the presence of platelet gelsolin and gelsolin-actin complexes. *J. Cell Biol.* **101**, 1236–1244 (1985).
- Volle, J. et al. Reduced expression of STOP/MAP6 in mice leads to cognitive deficits. *Schizophr. Bull.* **39**, 969–978 (2013).
- Wei, H., Sun, S., Li, Y. & Yu, S. Reduced plasma levels of microtubule-associated STOP/MAP6 protein in autistic patients. *Psychiatry Res.* **245**, 116–118 (2016).
- Penzes, P., Cahill, M. E., Jones, K. A., VanLeeuwen, J. E. & Woolfrey, K. M. Dendritic spine pathology in neuropsychiatric disorders. *Nat. Neurosci.* **14**, 285–293 (2011).
- Kasai, H., Fukuda, M., Watanabe, S., Hayashi-Takagi, A. & Noguchi, J. Structural dynamics of dendritic spines in memory and cognition. *Trends Neurosci.* **33**, 121–129 (2010).

45. Miermans, C. A., Kusters, R. P., Hoogenraad, C. C. & Storm, C. Biophysical model of the role of actin remodeling on dendritic spine morphology. *PLoS ONE* **12**, e0170113 (2017).
46. Koganezawa, N., Hanamura, K., Sekino, Y. & Shirao, T. The role of drebrin in dendritic spines. *Mol. Cell Neurosci.* **84**, 85–92 (2017).
47. Ouimet, C. C., Katona, I., Allen, P., Freund, T. F. & Greengard, P. Cellular and subcellular distribution of spinophilin, a PP1 regulatory protein that bundles F-actin in dendritic spines. *J. Comp. Neurol.* **479**, 374–388 (2004).
48. Grossman, S. D., Hsieh-Wilson, L. C., Allen, P. B., Nairn, A. C. & Greengard, P. The actin-binding domain of spinophilin is necessary and sufficient for targeting to dendritic spines. *Neuromolecular. Med.* **2**, 61–69 (2002).
49. Okamoto, K., Narayanan, R., Lee, S. H., Murata, K. & Hayashi, Y. The role of CaMKII as an F-actin-bundling protein crucial for maintenance of dendritic spine structure. *Proc. Natl Acad. Sci. USA* **104**, 6418–6423 (2007).
50. Nakanishi, H. et al. Neurabin: a novel neural tissue-specific actin filament-binding protein involved in neurite formation. *J. Cell Biol.* **139**, 951–961 (1997).
51. Fulga, T. A. et al. Abnormal bundling and accumulation of F-actin mediates tau-induced neuronal degeneration in vivo. *Nat. Cell Biol.* **9**, 139–148 (2007).
52. Worth, D. C., Daly, C. N., Geraldo, S., Oozeer, F. & Gordon-Weeks, P. R. Drebrin contains a cryptic F-actin-bundling activity regulated by Cdk5 phosphorylation. *J. Cell Biol.* **202**, 793–806 (2013).
53. Goode, B. L. et al. Coronin promotes the rapid assembly and cross-linking of actin filaments and may link the actin and microtubule cytoskeletons in yeast. *J. Cell Biol.* **144**, 83–98 (1999).
54. Liu, Q., Jones, T. I., Tang, V. W., Briehner, W. M. & Jones, P. L. Facioscapulohumeral muscular dystrophy region gene-1 (FRG-1) is an actin-bundling protein associated with muscle-attachment sites. *J. Cell Sci.* **123**, 1116–1123 (2010).
55. Yokota, E. & Shimmen, Ki. T. T. Actin-bundling protein isolated from pollen tubes of lily. Biochemical and immunocytochemical characterization. *Plant Physiol.* **116**, 1421–1429 (1998).
56. Jansen, S. et al. Mechanism of actin filament bundling by fascin. *J. Biol. Chem.* **286**, 30087–30096 (2011).
57. Faix, J. et al. Cortexillins, major determinants of cell shape and size, are actin-bundling proteins with a parallel coiled-coil tail. *Cell* **86**, 631–642 (1996).
58. Xie, Y. et al. The GTP-binding protein Septin 7 is critical for dendrite branching and dendritic-spine morphology. *Curr. Biol.* **17**, 1746–1751 (2007).
59. Hayakawa, K., Tatsumi, H. & Sokabe, M. Actin filaments function as a tension sensor by tension-dependent binding of cofilin to the filament. *J. Cell Biol.* **195**, 721–727 (2011).
60. Kneussel, M. & Wagner, W. Myosin motors at neuronal synapses: drivers of membrane transport and actin dynamics. *Nat. Rev. Neurosci.* **14**, 233–247 (2013).
61. Capala, M. E. et al. Mitochondrial dysfunction in human leukemic stem/progenitor cells upon loss of RAC2. *PLoS ONE* **10**, e0128585 (2015).
62. Gimenez, U. et al. 3D imaging of the brain morphology and connectivity defects in a model of psychiatric disorders: MAP6-KO mice. *Sci. Rep.* **7**, 10308 (2017).
63. Galiano, M. R. et al. Astrocytes and oligodendrocytes express different STOP protein isoforms. *J. Neurosci. Res.* **78**, 329–337 (2004).
64. Peris, L. et al. Tubulin tyrosination is a major factor affecting the recruitment of CAP-Gly proteins at microtubule plus ends. *J. Cell Biol.* **174**, 839–849 (2006).
65. Rodriguez, A., Ehlenberger, D. B., Hof, P. R. & Wearne, S. L. Rayburst sampling, an algorithm for automated three-dimensional shape analysis from laser scanning microscopy images. *Nat. Protoc.* **1**, 2152–2161 (2006).
66. Rodriguez, A., Ehlenberger, D. B., Dickstein, D. L., Hof, P. R. & Wearne, S. L. Automated three-dimensional detection and shape classification of dendritic spines from fluorescence microscopy images. *PLoS ONE* **3**, e1997 (2008).
67. Rodriguez, A. D., Lear, M. J. & La Clair, J. J. Identification of the binding of scorpion to MreB via a bidirectional affinity protocol. *J. Am. Chem. Soc.* **130**, 7256–7258 (2008).
68. Sage, D., Neumann, F. R., Hediger, F., Gasser, S. M. & Unser, M. Automatic tracking of individual fluorescence particles: application to the study of chromosome dynamics. *IEEE Trans. Image Process.* **14**, 1372–1383 (2005).
69. Jacob, M. & Unser, M. Design of steerable filters for feature detection using canny-like criteria. *IEEE Trans. Pattern Anal. Mach. Intell.* **26**, 1007–1019 (2004).
70. de Chaumont, F. et al. Icy: an open bioimage informatics platform for extended reproducible research. *Nat. Methods* **9**, 690–696 (2012).
71. Schindelin, J. et al. Fiji: an open-source platform for biological-image analysis. *Nat. Methods* **9**, 676–682 (2012).

Acknowledgements

We are grateful to zootechnicians of the Grenoble Institute of Neurosciences, S. Andrieu, M. Lapiere, F. Mehr and F. Rimet for animal care. We thank N. Collomb, C. Corrao, F. Vossier and C. Paoli for technical assistance; T. Rush and M. Seggio for introducing L. P. to FRAP, TIRF microscopy; Ju Brocard and G. Falivelli for helping with virus production and Fondation Bettencourt Schueller for equipment. This work was supported by INSERM, CEA, Université Grenoble Alpes – Inserm U1216) which is part of the ISdV core facility and certified by the IBISA label. PhD stipends were from the French Ministry for Research and Higher Education for M.R., from AFM-Téléthon for M.S. and from Région Auvergne Rhones Alpes for J.J. M.B. was a recipient of the Roche Pharmaceutical RPF program (AA team and F Hoffmann-La Roche Ltd, Basel, Switzerland).

Author contributions

L.P., M.B. and A.A. conceived and designed the study. L.P. and M.B. performed the experiments, with contributions from J.M.-H., Y.S., J.J., M.S., J.B., E.D., C.B., S.G.-F., J.C.D. and C.D. C.G., I.A. and L.B. contributed to cell-free studies. F.L., M.R. and A.B. performed electrophysiological experiments. L.P., M.B., Y.G. and A.A. wrote the manuscript, with contribution from all co-authors.

Additional information

Supplementary Information accompanies this paper at <https://doi.org/10.1038/s41467-018-05869-z>.

Competing interests: The authors declare no competing interests.

Reprints and permission information is available online at <http://npg.nature.com/reprintsandpermissions/>

Publisher's note: Springer Nature remains neutral with regard to jurisdictional claims in published maps and institutional affiliations.



Open Access This article is licensed under a Creative Commons Attribution 4.0 International License, which permits use, sharing, adaptation, distribution and reproduction in any medium or format, as long as you give appropriate credit to the original author(s) and the source, provide a link to the Creative Commons license, and indicate if changes were made. The images or other third party material in this article are included in the article's Creative Commons license, unless indicated otherwise in a credit line to the material. If material is not included in the article's Creative Commons license and your intended use is not permitted by statutory regulation or exceeds the permitted use, you will need to obtain permission directly from the copyright holder. To view a copy of this license, visit <http://creativecommons.org/licenses/by/4.0/>.

© The Author(s) 2018

CYTOSKELETON

Vasohibins/SVBP are tubulin carboxypeptidases (TCPs) that regulate neuron differentiation

Chrystelle Aillaud,^{1,2} Christophe Bosc,^{1,2} Leticia Peris,^{1,2} Anouk Bosson,^{1,2} Pierre Heemeryck,^{1,2} Juliette Van Dijk,^{3,4} Julien Le Fricc,^{1,2} Benoit Boulan,^{1,2} Frédérique Vossier,^{1,2} Laura E. Sanman,⁵ Salahuddin Syed,⁵ Neri Amara,⁵ Yann Couté,⁶ Laurence Lafanechère,⁷ Eric Denarier,^{1,2,8} Christian Delphin,^{1,2} Laurent Pelletier,^{1,2} Sandrine Humbert,^{1,2} Matthew Bogyo,⁵ Annie Andrieux,^{1,2,8,*†} Krzysztof Rogowski,^{3,*†} Marie-Jo Moutin^{1,2,*}

Reversible detyrosination of α -tubulin is crucial to microtubule dynamics and functions, and defects have been implicated in cancer, brain disorganization, and cardiomyopathies. The identity of the tubulin tyrosine carboxypeptidase (TCP) responsible for detyrosination has remained unclear. We used chemical proteomics with a potent irreversible inhibitor to show that the major brain TCP is a complex of vasohibin-1 (VASH1) with the small vasohibin binding protein (SVBP). VASH1 and its homolog VASH2, when complexed with SVBP, exhibited robust and specific Tyr/Phe carboxypeptidase activity on microtubules. Knockdown of vasohibins or SVBP and/or inhibitor addition in cultured neurons reduced detyrosinated α -tubulin levels and caused severe differentiation defects. Furthermore, knockdown of vasohibins disrupted neuronal migration in developing mouse neocortex. Thus, vasohibin/SVBP complexes represent long-sought TCP enzymes.

Microtubules are cytoskeletal polymers of α/β tubulin dimers centrally involved in cell division, motility, and morphogenesis. In the detyrosination/tyrosination cycle of tubulin, the C-terminal tyrosine of α -tubulin is removed by an elusive peptidase [tyrosine carboxypeptidase (TCP)] and re-added by the tubulin tyrosine ligase (TTL) (1). This cycle, which is specific to α -tubulin and mostly conserved from chordates to mammals, has a vital role in vivo (2). Tubulin detyrosination and tyrosination of α -tubulin is an important regulatory signal for mitosis (3–5), neuronal physiology (6–8), and muscle mechanotransduction (9, 10). Consequently, abnormal tyrosination levels are associated with cell transformation and tumor aggressiveness (11, 12), neuronal disorganization (2), and heart failure and cardiomyopathies (10, 13). Although the detyrosination reaction was first described 40 years ago (14), the identity of TCP has remained unknown.

To enrich for TCP, we designed a three-step purification procedure using taxol-stabilized radiolabeled tyrosinated microtubules as a substrate to follow activity. A typical procedure gave a final purification factor of nearly 400-fold (Fig. 1A and fig. S1A). The last fraction (IV) was able to cleave the C-terminal tyrosine from tubulin incorporated in microtubules but not from EB1

(fig. S1B). EB1 is a protein that shares a similar C-terminal sequence with α -tubulin (–QEEY instead of –GEEY) and is generally not a substrate for TCP in physiological contexts (15).

To isolate the protein(s) responsible for TCP activity from fraction IV, we reasoned that an irreversible inhibitor could be used as in other chemical proteomic studies (16). We tested the sensitivity of brain TCP to various commercial protease inhibitors. The activity was inhibited by several serine/cysteine protease inhibitors [4-(2-aminoethyl)benzenesulfonyl fluoride hydrochloride (AEBSF), Tosyl-L-lysyl-chloromethyl ketone (TLCK), Tosyl phenylalanyl chloromethyl ketone (TPCK), E-64, and parthenolide] and by the thiol-reactive compound *N*-ethylmaleimide (Fig. 1B and fig. S2A). These results, in agreement with prior studies (17), strongly suggested that the catalytic activity of the putative TCP depends on a catalytic cysteine.

Although E-64 only showed modest inhibitory activity [median inhibitory concentration (IC_{50}) around 300 μ M] (Fig. 1B), it is an ideal starting point for inhibitor design because its reactive epoxide electrophile can display a peptide- or amino acid–mimicking native protein C terminus. Furthermore, parthenolide, which is widely used to down-regulate detyrosination levels in cells (4, 6, 9, 10), contains an epoxide func-

tion that is essential to its cellular effect (17). We thus synthesized three inhibitors—epoY, epoEY, and epoEEY—which contain the epoxide coupled to one, two, or three amino acids from the α -tubulin C terminus, respectively (fig. S2B). EpoY was the most potent inhibitor of the TCP activity (IC_{50} around 500 nM) (Fig. 1B). Alkyne-epoY, which retained a strong inhibitory potency (Fig. 1, B and C) and irreversibly inhibited the activity (fig. S2, C and D), was used to perform tetramethylrhodamine (TAMRA) labeling of fraction IV by means of click chemistry (Fig. 1D). This labeling showed specific modification of a small number of proteins (Fig. 1E). We then purified the inhibitor targets using agarose beads and, after on-beads trypsin digestion and quantitative mass spectrometry analyses of the resulting peptides from three independent experiments, we identified the protein vasohibin-1 (VASH1) as the most likely TCP candidate (Fig. 1D and tables S1 and S2). Peptides covering the almost full VASH1 sequence were detected (fig. S2E). Furthermore, recent bioinformatics data show that Vasohibin-1 and its homolog vasohibin-2 (VASH2) possess a noncanonical Cys-His-Ser catalytic triad and are members of the transglutaminase-like cysteine proteases family (Fig. 1F) (18).

Vasohibin proteins (41 to 42 kDa) have been extensively characterized as angiogenesis regulators but are poorly understood on a molecular level (19). Small vasohibin binding protein (SVBP) (Ccdc23) is a high-affinity binding partner of vasohibins that has a chaperone-like function (20). We examined the ability of VASH proteins to detyrosinate α -tubulin in cells in the absence or presence of SVBP. Expression of vasohibins alone in human embryonic kidney (HEK) 293T cells resulted in a slight increase of detyrosinated tubulin, whereas expression of either protein with SVBP resulted in a substantial increase in detyrosinated tubulin corresponding to a nearly complete loss of endogenous tyrosinated tubulin (Fig. 2A). Mutation of the putative catalytic cysteine on vasohibins [C179A for VASH1 and C158A for VASH2 (18)] abolished their capacity to produce detyrosinated tubulin. (Single-letter abbreviations for the amino acid residues are as follows: A, Ala; C, Cys; D, Asp; E, Glu; F, Phe; G, Gly; H, His; I, Ile; K, Lys; L, Leu; M, Met; N, Asn; P, Pro; Q, Gln; R, Arg; S, Ser; T, Thr; V, Val; W, Trp; and Y, Tyr. In the mutants, amino acids were substituted at certain locations; for example, C179A indicates that cysteine at position 179 was replaced by alanine.) Similarly, in mouse embryonic fibroblasts (MEFs), expression of the vasohibins with SVBP resulted in complete detyrosination of endogenous α -tubulin (Fig. 2B and fig. S3A).

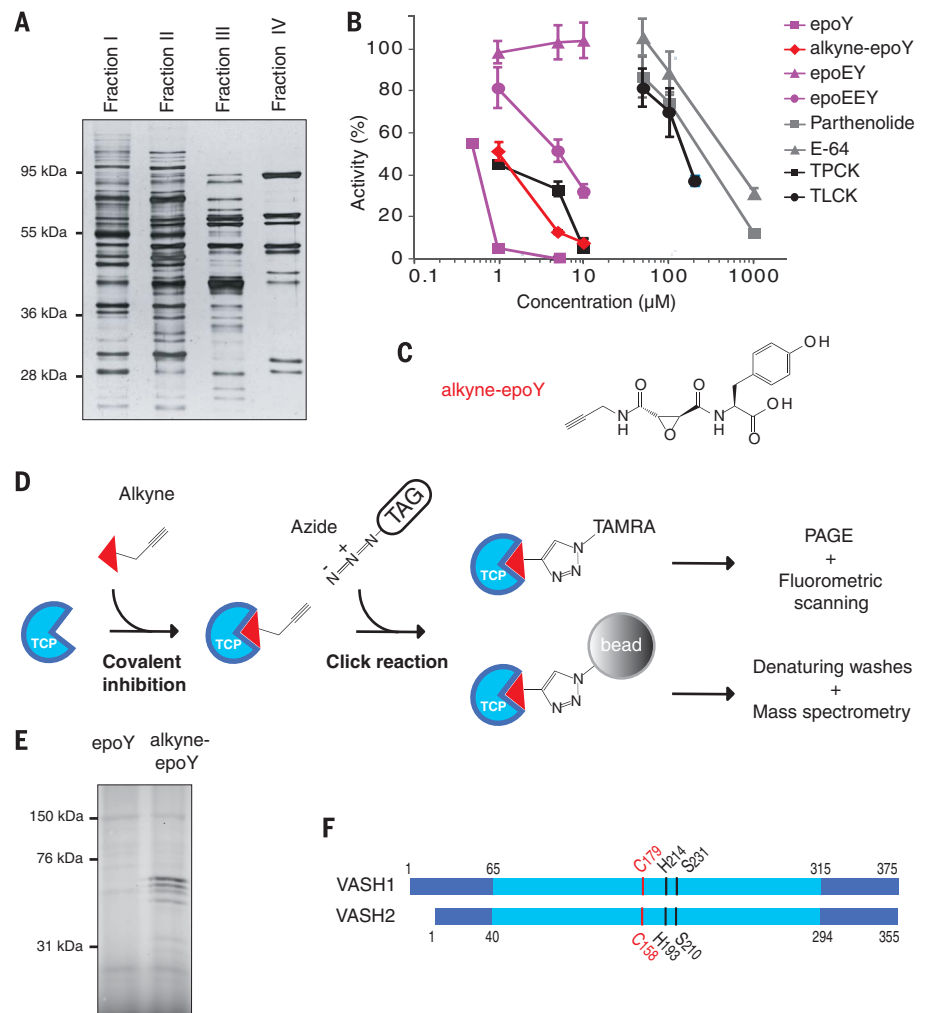
α -Tubulins are generally encoded with a C-terminal tyrosine preceded by two glutamates.

¹Grenoble Institut des Neurosciences (GIN), Université Grenoble Alpes, F-38000 Grenoble, France. ²Inserm, U1216, F-38000 Grenoble, France. ³Institut de Génétique Humaine (IGH), Université Montpellier, CNRS UMR9002, 34000 Montpellier, France. ⁴Centre de Recherche en Biochimie Macromoléculaire (CRBM), Université Montpellier, CNRS UMR5237, 34000 Montpellier, France. ⁵Department of Pathology, Stanford University School of Medicine, Stanford, CA 94305, USA. ⁶Institut de Biosciences et Biotechnologies de Grenoble (BIG)—Laboratoire Biologie à Grande Échelle, Université Grenoble Alpes, CEA, INSERM, F-38000 Grenoble, France. ⁷Team Regulation and Pharmacology of the Cytoskeleton, Institute for Advanced Biosciences, INSERM U 1209, CNRS UMR 5309, Université Grenoble Alpes, 38000 Grenoble, France. ⁸BIG—Physiopathologie du Cytosquelette, CEA, F-38000 Grenoble, France.

*Corresponding author. Email: moutinm@univ-grenoble-alpes.fr (M.-J.M.); annie.andrieux@univ-grenoble-alpes.fr (A.A.); krzysztof.rogowski@igh.cnrs.fr (K.R.) †These authors contributed equally to this work.

Fig. 1. Purification and identification of mouse brain TCP.

(A) SDS–polyacrylamide gel electrophoresis (silver staining) of the indicated fractions of TCP enrichment from mouse brain (1 μ g of proteins): ammonium sulfate precipitation step followed by two ion exchange columns stages (fig. S1A). **(B)** Fraction IV sensitivity to inhibitors. TPCK and TLCK are commercial serine/cysteine inhibitors containing either a Phe or a Lys residue. Fraction IV activity showed a 100-fold higher sensitivity to TPCK than to TLCK. E-64 is a natural product inhibitor of clan CA cysteine protease. EpoY, epoEY, and epoEEY are designed inhibitors containing an epoxide group coupled with Y, EY, or EEY amino acids, respectively. Alkyne-epoY is a clickable version of epoY. Results are expressed as percentage of enzyme activity (radioactivity assay) in the control with dimethyl sulfoxide (mean \pm SD, $n = 3$ to 6 assays). **(C)** Structure of alkyne-epoY. **(D)** Schematic representation of the last steps of TCP identification by using Cu-catalyze azide-alkyne cycloaddition (click reaction). **(E)** Labeling of putative TCP from fraction IV with TAMRA red-fluorescent dye by using alkyne-epoY (nonclickable epoY is used as control). **(F)** Schematic representation of mouse vasohibin-1 and vasohibin-2 [69% overall sequence homology; 77% for core domains (clear blue boxes)]. These putative transglutaminase-like cysteine peptidases contain an unconventional triad of catalytic residues (Cys, His, and Ser).



α 4-Tubulin lacks the C-terminal tyrosine, and α 8-tubulin contains a C-terminal phenylalanine residue. Phenylalanine can be incorporated in place of tyrosine in tubulin and be a possible cause of neuronal dysfunction (27). We tested the substrate specificity of the vasohibins by overexpressing α 1B- and α 8-tubulin together with VASH1 or VASH2 and SVBP in HEK293T cells. Both tubulin isotypes were cleaved by active vasohibins when expressed with SVBP (Fig. 2C and fig. S3B). Vasohibins were unable to cleave the C-terminal residue when tyrosine was mutated to alanine (Fig. 2C and fig. S3B), confirming the specificity of VASH proteins for C-terminal tyrosine and phenylalanine residues.

We overexpressed vasohibins in HEK293T cells in the absence or presence of SVBP and purified the resulting complexes using a cobalt resin. SVBP copurified with both vasohibins as expected from previous affinity measurements [dissociation constant (K_d) 30 to 90 nM] (20), and complex formation was not dependent on catalytic activity (fig. S4A). The two protein complexes efficiently catalyzed tubulin detyrosination, whereas complexes containing the catalytic dead versions of the vasohibins were unable to detyrosinate tubulin (Fig. 2D). Both complexes cleaved microtubules

more rapidly as compared with tubulin dimers (Fig. 2E and fig. S4B), which is consistent with the reported preference of brain TCP in *in vitro* experiments (1, 22, 23). Purified VASH1/SVBP complex was not able to cleave the C-terminal tyrosine from EB1, indicating its clear tubulin preference. Intriguingly, VASH2/SVBP complex was able to partially detyrosinate EB1 in the same conditions (Fig. 2F). In most cell types, including neuronal-derived cells, C-terminal tyrosine cleavage is restricted to tubulin (1, 15). EB1 can, however, be detyrosinated in specific endothelial and tumor cells (24), and this may be related to their VASH2 contents or defect in a regulatory mechanism.

To confirm the functional importance of vasohibins and their role in α -tubulin detyrosination, we assessed the phenotypic effects of knocking down expression of these proteins in differentiating neurons, where the detyrosination/tyrosination cycle is highly important for growth cone pathfinding and axon differentiation—that is, for neuron polarization (2, 7, 8). Although we were unable to detect vasohibins and SVBP by means of immunoblot in mouse neurons using commercial antibodies, we amplified their transcripts from RNA preparations of cultured hippo-

campal neurons as well as of adult and embryonic mouse brain tissues (Fig. 3A and figs. S5A and S6A). We transfected hippocampal neurons with plasmids expressing short hairpin RNAs (shRNAs) targeting either the vasohibins or SVBP (validated in figs. S5B and S6B) as well as control shRNAs. The levels of detyrosinated α -tubulin were decreased by almost 50% when the two vasohibins, or the SVBP, were down-regulated. Addition of inhibitor (alkyne-epoY) also largely reduced detyrosinated α -tubulin (Fig. 3, B and C). When added together with the shRNAs, levels of detyrosinated tubulin were decreased up to 75% (Fig. 3, B and C). The remaining pool of detyrosinated α -tubulin could be due to incomplete depletion of vasohibins activities or to the presence of α 4-tubulin, which genetically lacks the C-terminal tyrosine and remains in detyrosinated form in the brain (25). The occurrence of other detyrosinases can however not be excluded. Confocal images of neurons cultured 2 days *in vitro* (2DIV) confirmed a decrease in the levels of the native detyrosinated α -tubulin upon reduction of vasohibins expression or addition of inhibitor (Fig. 3D and fig. S5C). The remaining detyrosinated pools were specifically concentrated in the axon, whereas α -tubulin in the other neurites appeared

highly tyrosinated. Vasohibins down-regulation led to a clear delay in axonal differentiation (Fig. 3E). Tau and ankyrin G staining of neurons bearing an axon confirmed normal distribution, with Tau highly expressed in axon shaft at 3DIV and ankyrin G in the axon initial segment at 10DIV (fig. S7). Neurons 2DIV knocked down for vasohibins developed an increased number of neurites

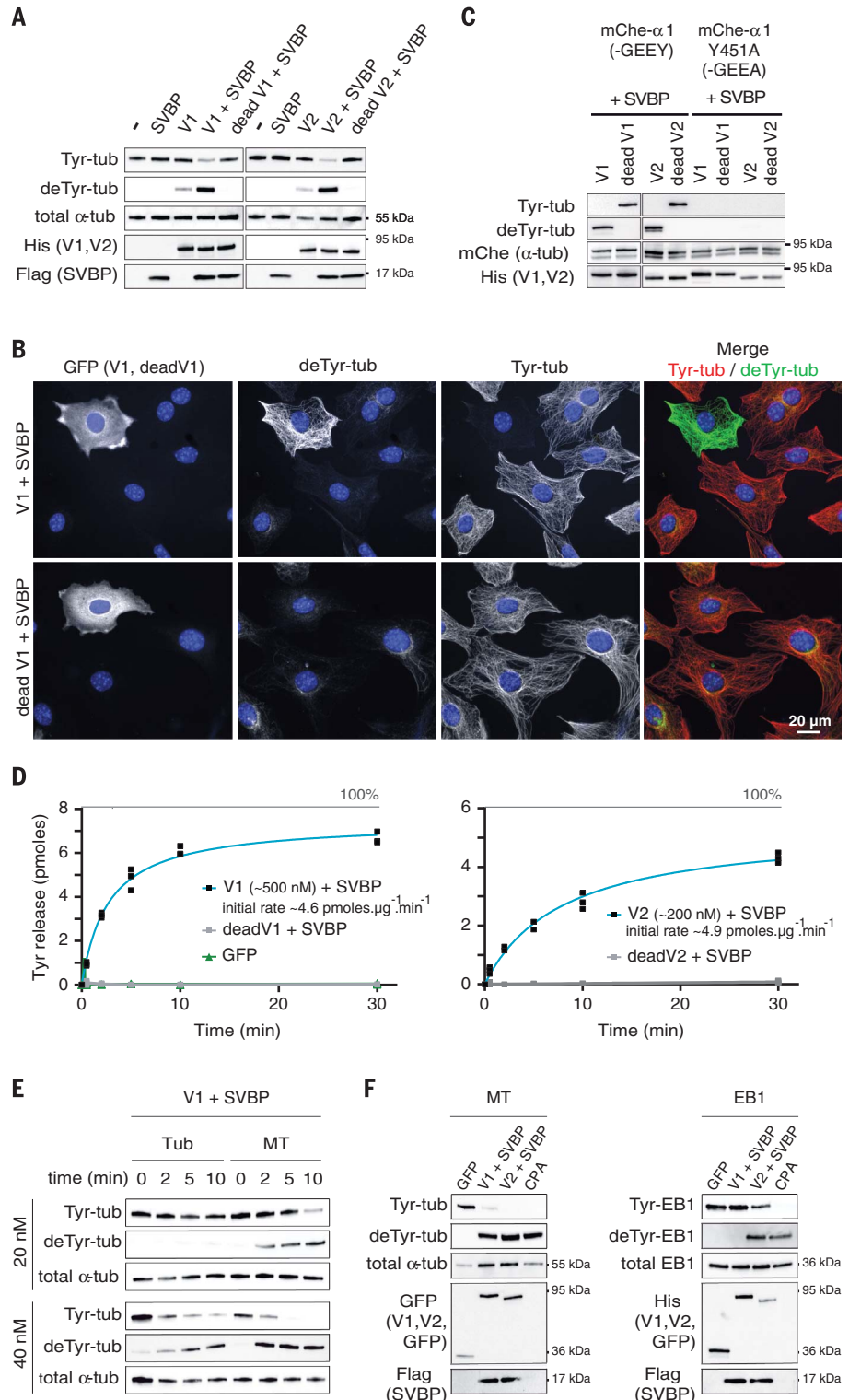
and branches with overall reduced axon length (Fig. 3F). A delay of axon differentiation and similar morphological anomalies were observed when down-regulating SVBP (fig. S6, D to F). Transfection of a plasmid allowing coexpression of shRNAs that target SVBP and a shRNA-resistant form of SVBP rescued α -tubulin detyrosination levels (fig. S6, A and C). Thus, contrary to the

premature axonal differentiation observed in the absence of the reverse enzyme TTL (2), we observed a clear delay of axon differentiation when down-regulating vasohibins or SVBP.

We next tested the functional importance of vasohibins in vivo in mouse brain and focused on the cerebral cortex, where the detyrosination/tyrosination cycle is critical for the neocortex

Fig. 2. Vasohibins associated to SVBP are potent tubulin tyrosine carboxypeptidases.

(A) Immunoblot of endogenous tubulin from HEK293T cells expressing each VASH (V1 and V2) or their dead versions in the absence or presence of exogenous SVBP coexpression. Antibodies specific to tyrosinated and detyrosinated tubulin were used to assess detyrosination. Antibodies to α -tubulin, His, and Flag respectively reveal amounts of tubulin, vasohibin, and SVBP. Nontransfected cells (-) show endogenous levels of tubulin modifications. **(B)** Immunofluorescence images of detyrosinated/tyrosinated α -tubulin pools from MEF cells expressing active or inactive VASH1, and SVBP. Vasohibins were probed with antibody to green fluorescent protein (GFP). **(C)** Immunoblot of protein extracts from HEK293T cells expressing mCherry- α 1B-tubulin, each VASH, and SVBP. Native or mutated versions of α 1B-tubulin, respectively ending with EEY or EEA, were used. Levels of detyrosinated/tyrosinated tubulin were measured as in (A). Antibody to mCherry demonstrates same amounts of exogenous α -tubulin. **(D)** Detyrosination activity of purified VASH/SVBP complexes assessed by using [¹⁴C]-tyrosinated taxol-stabilized microtubules (6 to 8 μ M) (triplicate assay). Active and catalytic dead versions of the vasohibins were coexpressed with SVBP in HEK293T cells and purified on cobalt resin (fig. S4A). A purified GFP-His construct was used as a control. Data points were fitted with a single exponential (blue line). The theoretical maximal tyrosine release is indicated by a 100% line. **(E)** Detyrosination activity of purified VASH1/SVBP complexes (20 or 40 nM) on brain microtubules or tubulin dimers (5 μ M) assessed by means of immunoblot. We controlled that tubulin was in dimeric or in assembled form (fig. S4C) and that the same amounts of enzymatic complexes were present (fig. S4D). **(F)** Detyrosination activity of purified VASH/SVBP complexes (600 nM) on brain microtubules or recombinant GFP-EB1 (5 μ M). Enzyme quantities are much higher than in Fig. 2E. Carboxypeptidase A (CPA) was used as positive control. Antibodies against tyrosinated and detyrosinated EB1 were characterized in (15).



Downloaded from https://www.science.org at INSERM on April 05, 2022

layer organization (2). During corticogenesis, neuronal migration relies in part on neuron polarization, which was highly dependent on vasohibins (Fig. 3, D and E) and SVBP (fig. S6, D and E). We electroporated embryonic day 14.5 (E14.5) embryos with the plasmids express-

ing shRNAs that target the vasohibins as well as control shRNA, and analyzed radial neuronal migration 4 days later. At E18.5, most neurons from control brains had reached the upper layer (bin 1), whereas when vasohibins were down-regulated, a significant fraction of neurons failed

to do so (Fig. 4, A and B). Thus, these enzymes have a crucial role in neuronal migration during brain cortex development.

TCP remained the crucial missing element of the α -tubulin detyrosination/tyrosination cycle for 40 years. We identified vasohibins as enzymatic

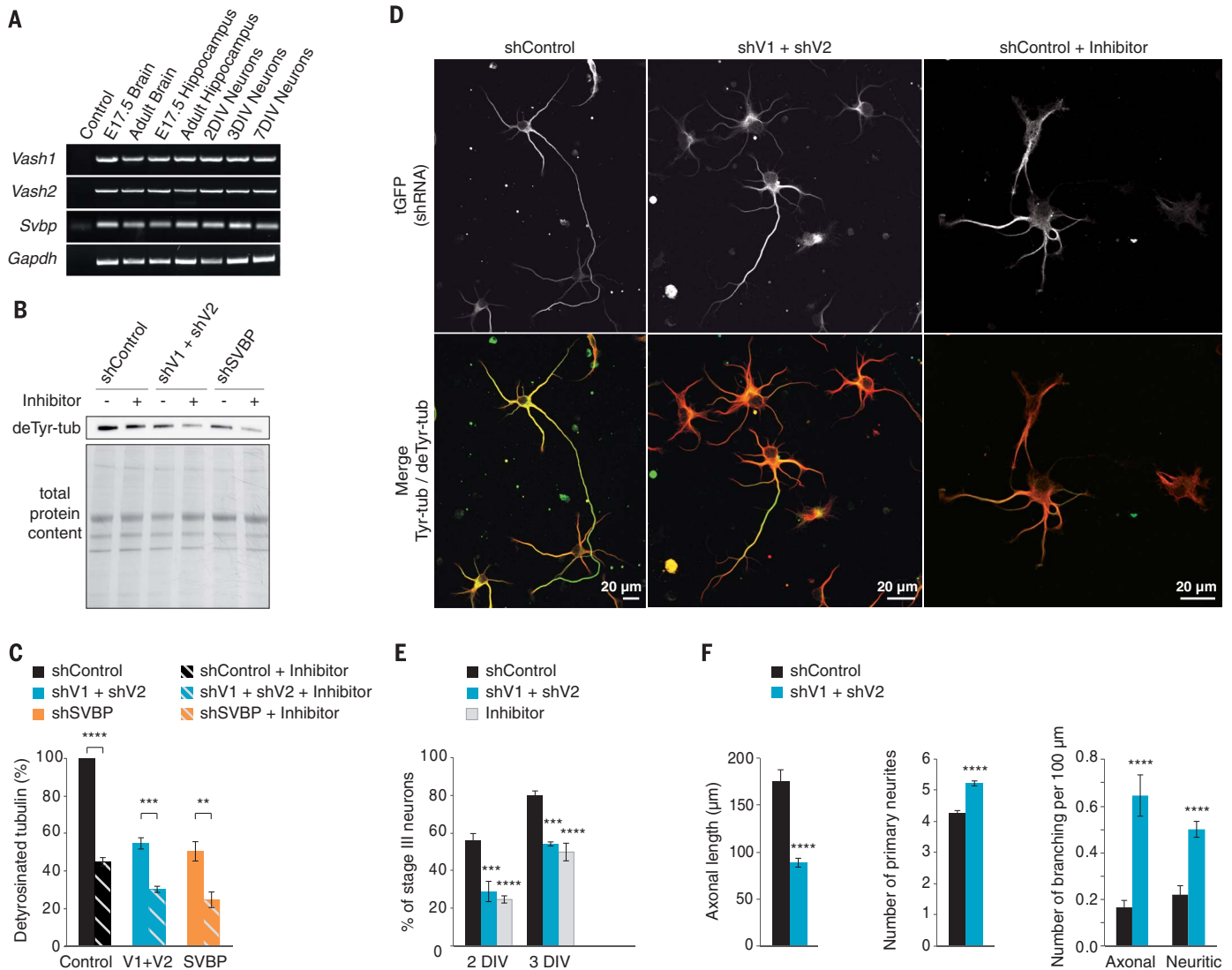


Fig. 3. Down-regulation of VASH1 and VASH2 affects neuronal differentiation.

(A) *Vash1*, *Vash2*, and *Svb* transcripts are found in brain tissues and hippocampal neurons. Reverse transcription polymerase chain reaction reactions of 45 cycles were performed, except for *Gapdh*, for which only 25 cycles were performed. (B) Immunoblot analysis of the effect of VASH1 and VASH2 (shV1+shV2) or SVBP (shSVBP) down-regulation with or without alkyne-epoY (inhibitor) on detyrosinated α -tubulin levels in neurons. Neurons were transfected by means of electroporation, with shRNAs associated to turboGFP (tGFP) cDNA just before plating and analyzed at 2DIV. Inhibitor (5 μ M) was added at 0DIV and at 1DIV. Results are from duplicate immunoblots of three independent neuronal cultures. (C) Quantification of immunoblots as in (B) (duplicate of four to eight independent neuronal cultures). Results are expressed as percentage of detyrosinated tubulin related to shControl (mean \pm SEM). Detyrosinated tubulin was significantly reduced in all conditions compared with shControl [one-way analysis of variance (ANOVA) with Sidak's multiple comparisons test]. Detyrosinated tubulin

was additionally reduced when shV1+shV2 and shSVBP transfected neurons were incubated with the inhibitor (Student's *t* test). (D to F) Effect of vasohibins down-regulation on neurite outgrowth and axonal differentiation. Neurons were transfected as in (B) and analyzed by means of immunostaining at 2DIV and 3DIV. (D) Tyrosinated and detyrosinated α -tubulin levels were imaged at 2DIV using the same antibodies as in Fig. 2A. Levels of shRNA were imaged by using an antibody to tGFP. The size of scale bars are different. (E) Stage III neurons (bearing an axon) were counted manually on immunofluorescence images [generated as in (C)] from 4 to 10 independent cultures, at 2DIV and 3DIV. Proportion of stage III neurons (an index of neuronal differentiation) is represented as mean \pm SEM (one-way ANOVA with Bonferroni multiple comparison test). (F) Morphometric analyses of at least 85 neurons (2DIV) by using AutoNeuriteJ macro (details are available in the supplementary materials, materials and methods) on immunofluorescence images generated as in (D) (mean \pm SEM, Mann-Whitney tests). In (C), (E), and (F): **P* < 0.05, ***P* < 0.01, ****P* < 0.001, *****P* < 0.0001.

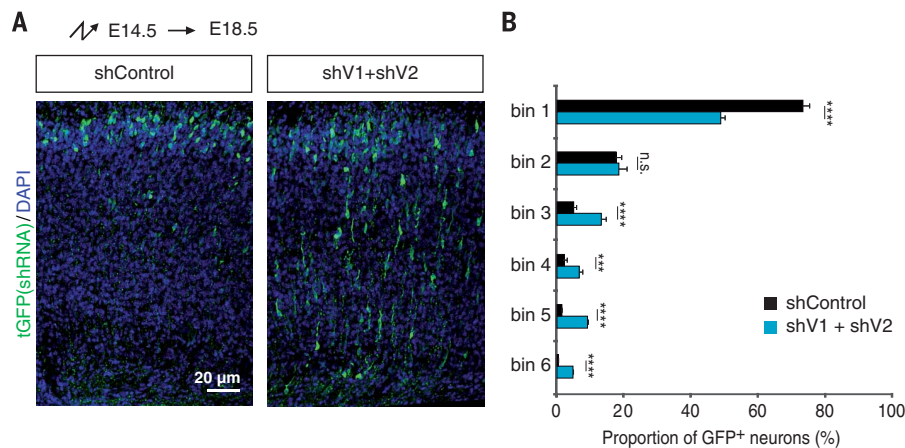


Fig. 4. Down-regulation of vasohibins affects radial migration of newborn cortical neurons.

(A) Cortical coronal sections of E18.5 mice embryos electroporated at E14.5 with indicated shRNAs. (B) Quantitative analysis showing the distribution of tGFP-positive neurons across the cortex divided into six bins of equal surface. Data are from five brains per condition, three slides per embryo (at least 260 GFP⁺-neurons per embryo), mean ± SEM. n.s., not significant; ****P* < 0.001, *****P* < 0.0001 (Mann-Whitney test).

proteins that perform the TCP function (fig. S8). The failure of prior attempts to identify TCPs most probably resulted from their association with SVBP for stability and activity, which could likely be lost during standard purification assays. In agreement with TCP functions, vasohibins are widely distributed in eukaryotes and have broad tissue expression, and vasohibin-1 (which is generally more expressed than vasohibin-2) is abundant in the brain, heart, and kidney [(18, 26, 27) and GTEx Portal, on www.gtexportal.org/home]. Additionally, we demonstrated their critical role in neuron and brain physiology.

REFERENCES AND NOTES

- H. S. Barra, C. A. Arce, C. E. Argaraña, *Mol. Neurobiol.* **2**, 133–153 (1988).
- C. Erck *et al.*, *Proc. Natl. Acad. Sci. U.S.A.* **102**, 7853–7858 (2005).

- A. C. Badin-Larçon *et al.*, *Proc. Natl. Acad. Sci. U.S.A.* **101**, 5577–5582 (2004).
- M. Barisic *et al.*, *Science* **348**, 799–803 (2015).
- L. Peris *et al.*, *J. Cell Biol.* **174**, 839–849 (2006).
- P. Gobrecht *et al.*, *J. Neurosci.* **36**, 3890–3902 (2016).
- Y. Konishi, M. Setou, *Nat. Neurosci.* **12**, 559–567 (2009).
- S. Marcos *et al.*, *PLOS ONE* **4**, e5405 (2009).
- J. P. Kerr *et al.*, *Nat. Commun.* **6**, 8526 (2015).
- P. Robison *et al.*, *Science* **352**, aaf0659 (2016).
- L. Lafanechère *et al.*, *J. Cell Sci.* **111**, 171–181 (1998).
- R. A. Whipple *et al.*, *Cancer Res.* **70**, 8127–8137 (2010).
- S. Belmadani, C. Poüs, R. Ventura-Clapier, R. Fischmeister, P. F. Méry, *Mol. Cell. Biochem.* **237**, 39–46 (2002).
- M. E. Hallak, J. A. Rodriguez, H. S. Barra, R. Caputto, *FEBS Lett.* **73**, 147–150 (1977).
- A. Bosson *et al.*, *PLOS ONE* **7**, e33490 (2012).
- M. A. Child *et al.*, *Nat. Chem. Biol.* **9**, 651–656 (2013).
- X. Fonrose *et al.*, *Cancer Res.* **67**, 3371–3378 (2007).
- L. Sanchez-Pulido, C. P. Ponting, *Bioinformatics* **32**, 1441–1445 (2016).
- Y. Sato, *J. Biochem.* **153**, 5–11 (2013).

- Y. Suzuki *et al.*, *J. Cell Sci.* **123**, 3094–3101 (2010).
- Y. Ditamo, Y. M. Dentesano, S. A. Purro, C. A. Arce, C. G. Bisig, *Sci. Rep.* **6**, 38140 (2016).
- G. G. Deanin, S. F. Preston, R. K. Hanson, M. W. Gordon, *Eur. J. Biochem.* **109**, 207–216 (1980).
- N. Kumar, M. Flavin, *J. Biol. Chem.* **256**, 7678–7686 (1981).
- A. Rovini *et al.*, *PLOS ONE* **8**, e65694 (2013).
- V. Redeker, *Methods Cell Biol.* **95**, 77–103 (2010).
- S. Nimmagadda *et al.*, *Dev. Dyn.* **236**, 1358–1362 (2007).
- T. Shibuya *et al.*, *Arterioscler. Thromb. Vasc. Biol.* **26**, 1051–1057 (2006).

ACKNOWLEDGMENTS

We dedicate this manuscript to Dr. Hector Barra, father of the deetyrosination/tyrosination cycle who passed away on 2 December 2016. We are grateful to D. Job who strongly supported initiation of the project and for his constant encouragement. We thank M. Comte, E. Martin, C. Corrao, and C. Paoli for technical assistance. We thank members of the Plateforme d'Imagerie Cellulaire du Grenoble Institut des Neurosciences for their help in cell imaging and zootechicians of the Grenoble Institut des Neurosciences for animal care. We thank M. Steinmetz for providing purified TTL and A. Beghin for initial development of AutoNeuriteJ macro. We thank the support of the discovery platform and informatics group at EDyP. This work was supported by INSERM, CEA, Université Grenoble Alpes, CNRS, and by La Ligue Contre le Cancer comités de l'Isère et de Savoie (to M.-J.M.), Association pour la Recherche sur le Cancer (grants SFI20111204053 to M.-J.M., DOC20120605000 to A.B., and 20151203348 to L.L.), Fondation pour la Recherche Médicale grant FDT20160435356 (to C.A.), Agence National de la Recherche grant ANR-13-JSV2-0002/TYRTUB (to K.R.), Institut National du Cancer grant 2016-165 (to LL) and the National Institutes of Health grant R01 EB005011 (to M.B.). Proteomic experiments were partly supported by the ProFi grant (ANR-10-INBS-08-01). An EU patent titled "Methods and pharmaceutical compositions for treating tubulin carboxypeptidases associated diseases" has been filed by Inserm and UGA (patent application no. EP17306476.7). Data described can be found in the main figures, supplementary materials, and table S2.

SUPPLEMENTARY MATERIALS

www.sciencemag.org/content/358/6369/1448/suppl/DC1
Materials and Methods
Supplementary Text
Figs. S1 to S7
Tables S1 and S2
References (28–37)

27 July 2017; accepted 3 November 2017
Published online 16 November 2017
10.1126/science.aao4165

Vasohibins/SVBP are tubulin carboxypeptidases (TCPs) that regulate neuron differentiation

Chrystelle AillaudChristophe BoscLeticia PerisAnouk BossonPierre HeemeryckJuliette Van DijkJulien Le FriecBenoit BoulanFrédérique VossierLaura E. SanmanSalahuddin SyedNeri AmaraYohann CoutéLaurence LafanechèreEric DenarierChristian DelphinLaurent PelletierSandrine HumbertMatthew BogyoAnnie AndrieuxKrzysztof RogowskiMarie-Jo Moutin

Science, 358 (6369), • DOI: 10.1126/science.aao4165

Tubulin carboxypeptidase identity revealed

Enzymes of the β -tubulin detyrosination/tyrosination cycle create landmarks on microtubules that are essential for their multiple cellular functions and are altered in disease. Tubulin carboxypeptidases (TCPs) responsible for detyrosination have remained elusive for 40 years (see the Perspective by Akhmanova and Maiato). Aillaud *et al.* identified vasohibins as enzymes that perform the TCP function and found that their small interacting partner SBVP was essential for their activity. Vasohibin/SVBP complexes were involved in neuron polarization and brain cortex development. The authors also developed an inhibitor targeting this family of enzymes. Using a completely different strategy, Nieuwenhuis *et al.* also showed that vasohibins can remove the C-terminal tyrosine of β -tubulin.

Science, this issue p. 1448, p. 1453; see also p. 1381

View the article online

<https://www.science.org/doi/10.1126/science.aao4165>

Permissions

<https://www.science.org/help/reprints-and-permissions>

Use of this article is subject to the [Terms of service](#)

Science (ISSN 1095-9203) is published by the American Association for the Advancement of Science, 1200 New York Avenue NW, Washington, DC 20005. The title *Science* is a registered trademark of AAAS.

Copyright © 2017 The Authors, some rights reserved; exclusive licensee American Association for the Advancement of Science. No claim to original U.S. Government Works

MAP6-F Is a Temperature Sensor That Directly Binds to and Protects Microtubules from Cold-induced Depolymerization*

Received for publication, July 5, 2012, and in revised form, August 6, 2012. Published, JBC Papers in Press, August 17, 2012, DOI 10.1074/jbc.M112.398339

Christian Delphin^{†1}, Denis Bouvier[§], Maxime Seggio[‡], Emilie Couriol[‡], Yasmina Saoudi[‡], Eric Denarier[‡], Christophe Bosc[‡], Odile Valiron[‡], Mariano Bisbal^{‡2}, Isabelle Arnal[¶], and Annie Andrieux[‡]

From [†]Team 1 Physiopathology of Cytoskeleton; Commissariat à l'Energie Atomique, Institut National de la Santé et de la Recherche Médicale, U836-GIN iRTSV-GPC, Site Santé La Tronche, BP170, 38042 Grenoble, Cedex 9, France, [§]the European Molecular Biology Laboratory, Grenoble Outstation, 6 rue Jules Horowitz, BP181, 38042 Grenoble Cedex 9, France, and [¶]Team 13 Dynamic and Structural Regulation of Cytoskeleton, Institut National de la Santé et de la Recherche Médicale, U836-GIN, Site Santé La Tronche, BP170, 38042 Grenoble, Cedex 9, France

Background: Microtubules are intrinsically cold-sensitive polymers, but cold-stable microtubules are observed in cells.

Results: Progressive temperature-dependent conformational change in MAP6-F coincides with its binding to microtubules and with its microtubule cold stabilization activity.

Conclusion: MAP6-F is a temperature sensor that protects microtubules from cold-induced depolymerization at temperatures ranging from 4 to 20 °C.

Significance: This work provides a better understanding of cellular microtubule stabilization under hypothermic stress.

Microtubules are dynamic structures that present the peculiar characteristic to be ice-cold labile *in vitro*. *In vivo*, microtubules are protected from ice-cold induced depolymerization by the widely expressed MAP6/STOP family of proteins. However, the mechanism by which MAP6 stabilizes microtubules at 4 °C has not been identified. Moreover, the microtubule cold sensitivity and therefore the needs for microtubule stabilization in the wide range of temperatures between 4 and 37 °C are unknown. This is of importance as body temperatures of animals can drop during hibernation or torpor covering a large range of temperatures. Here, we show that in the absence of MAP6, microtubules in cells below 20 °C rapidly depolymerize in a temperature-dependent manner whereas they are stabilized in the presence of MAP6. We further show that in cells, MAP6-F binding to and stabilization of microtubules is temperature-dependent and very dynamic, suggesting a direct effect of the temperature on the formation of microtubule/MAP6 complex. We also demonstrate using purified proteins that MAP6-F binds directly to microtubules through its Mc domain. This binding is temperature-dependent and coincides with progressive conformational changes of the Mc domain as revealed by circular dichroism. Thus, MAP6 might serve as a temperature sensor adapting its conformation according to the temperature to maintain the cellular microtubule network in organisms exposed to temperature decrease.

Microtubules are essential components of the cell cytoskeleton, being involved in cell division, cell migration and intracel-

lular trafficking. Microtubules result from the polymerization of tubulin dimers in protofilaments that associate through lateral contacts (for reviews see Refs. 1–4). Microtubules are dynamic structures alternating growing and shrinking phases ended by catastrophes and rescues, respectively. *In vitro*, microtubule dynamics are under the control of the tubulin concentration and numerous other physico-chemical parameters (5–8). Among them, temperature plays a crucial role as microtubules depolymerize upon a temperature shift from 37 to 4 °C. This could be due to the modification of different dynamics parameters especially the increase of catastrophe and the disappearance of rescue events at such temperatures (9, 10). In a cold environment ectothermic organisms express tubulin variants able to assemble at temperatures below 4 °C and to resist to cold-induced depolymerization (11). The amino acid substitutions affect residues located at sites implicated in tubulin lateral contact and are thought to increase interactions between protofilaments (12). Among endotherms that contain cold-sensitive microtubules, some may undergo a significant drop in their body temperature during natural events. Indeed, during hibernation or torpor, body temperature can decrease by several degrees down to temperatures close to 0 °C depending on the species (13, 14). In human, deep hypothermia can occur during accidental events or be medically provoked to preserve tissues. During such events, the maintenance of a minimal network of microtubules is thought to be required for basal cellular functions. It has been shown that the main proteins able to protect microtubules against cold-induced depolymerization are the microtubule-associated proteins MAP6³ (also called STOP for Stable Tubule Only Polypeptide) (15, 16). MAP6 belongs to a family of proteins encoded by a single gene (16, 17). They are restricted to vertebrates and expressed in several tissues including brain, heart, muscle, kidney, lung, and testis (18).

³The abbreviations used are: MAP, microtubule-associated protein; MEF, mouse embryonic fibroblasts; PIPES, piperazine-*N,N'*-bis(2-ethanesulfonic acid); EM, electron microscopy.

* This work was supported by INSERM, CEA, University Joseph Fourier, and French National Research Agency Awards 2010Blan120201 CBioS (to A. A.).

¹To whom correspondence should be addressed: Inserm U836, Equipe 1 Bâtiment Edmond J. Safra, Université Joseph Fourier, Site Santé à La Tronche, BP 170, 38042 GRENOBLE Cedex 9-France. Tel.: 33-456-520-539; Fax: 33-456-520-657; E-mail: christian.delphin@ujf-grenoble.fr.

²Recipient of the Roche Pharmaceutical RPF program (AA team and F Hoffmann-La Roche Ltd, Basel, Switzerland).

Microtubule Stabilization by MAP6

At the cellular level, MAP6 have been found in neurons, astrocytes, oligodendrocytes, fibroblasts, and pulmonary endothelium (16, 19–21). Depending on mouse strains, MAP6 isoforms contain a Mc domain composed of a 4 or 5 times tandemly repeated 46-residue motif. This Mc domain, when overexpressed in HeLa cells (that do not express any MAP6 variants), is able to stabilize microtubules against exposure to 4 °C (22).

In a previous study, it was shown that NIH/3T3 fibroblastic cells (16) mainly expressed the smallest MAP6-F isoform. In these cells, at 37 °C, microtubules are dynamic, non stable (as revealed by nocodazole sensitivity) (23) whereas they are stable at 4 °C. Concomitantly, MAP6-F relocates from the cytosol at 37 °C to the microtubule network upon chilling at 4 °C (16). These data suggest that microtubule stabilization by MAP6-F is dependent on the binding of MAP6-F to the microtubules. However, the cold sensitivity of cellular microtubules to temperatures between 37 and 4 °C and the effect of these temperatures on MAP6 binding to microtubules were unclear. Moreover, the exact mechanisms involved in the regulation of MAP6 interaction with microtubules under cold exposure have yet to be identified.

Here, we show that in the absence of MAP6, cellular microtubules depolymerize in a temperature-dependent manner as soon as the temperature decreases below 20 °C. In fibroblasts, which contain MAP6-F, microtubule cold resistance is directly correlated with a rapid and temperature-dependent interaction of MAP6-F with the microtubules. Using purified *in vitro* systems, we provide evidence that MAP6-F stabilizes microtubules via a direct interaction through its Mc domain. Furthermore, we found structural changes in the MAP6 Mc domain upon temperature modifications, indicating that MAP6 behaves as a “temperature-sensor” adapting its conformation to allow microtubule binding and preservation upon temperature drop.

EXPERIMENTAL PROCEDURES

Cell Culture—Mouse fibroblastic NIH/3T3 cells were grown at 37 °C in DMEM 4.5 g/liter glucose (Invitrogen) supplemented with 10% fetal bovine serum (Hyclone Laboratories Inc.), 50 units/ml of penicillin and 50 µg of streptomycin (Invitrogen). Human epithelial HeLa cells and mouse embryonic fibroblasts (MEF) prepared from either wild-type or MAP6-null mice as in Ref. 24, were maintained as for NIH/3T3 cells except that 1 g/liter glucose DMEM was used instead of 4.5 g/liter glucose DMEM.

Cell Cold Treatment and Permeabilization—For immunofluorescence analysis of cellular microtubule content, cells were plated 24 to 48 h before analysis on glass coverslips placed in B60 cell culture dishes. For analysis of time- and temperature-dependent effects on cellular microtubule content, coverslips were placed in culture medium complemented with 10 mM HEPES pH 7.4 in P24 culture dishes whose temperature was pre-equilibrated in water baths. For short incubation times of 1 min or less, incubations were done in PBS instead of culture medium. At the end of the indicated time, cells were washed with PBS at the incubation temperature and then permeabilized to wash out the soluble cell content through two 30 s incubations in OPT buffer (100 mM PIPES/KOH pH 6.75, 1 mM

MgCl₂, 1 mM EGTA, 10% glycerol, 0.5% Triton X-100) at the incubation temperature. Cells were then fixed in –20 °C methanol and processed for immunodetection. For immunofluorescence analysis of MAP6-dependent microtubule cold stability, NIH/3T3 cells on coverslips were treated as described above except that cells were permeabilized and washed (2 × 30 s) in PEMT buffer (OPT buffer without glycerol) at the incubation temperature and then dipped in 4 °C PEMT buffer for 10 min before methanol fixation.

Detection and Quantification of Cellular Microtubule Content by Immunofluorescence—Methanol-fixed cells were incubated for 30 min in PBST (PBS buffer plus 0.3% Tween 20) plus 5% (v/v) of normal goat serum (NGS). Mouse monoclonal anti-tubulin α3a1 antibody (24) (dilution 1/6,000) in PBST plus 1% NGS was then added and incubated for 1 h at room temperature. Coverslips were washed five times with PBST and then incubated for 45 min with Alexa488-coupled anti-mouse secondary antibody (Invitrogen). Coverslips were washed five times with PBST, once with PBS, incubated for 15 min with PBS containing 100 ng/ml of Hoechst 33258, briefly rinsed with PBS, ethanol dried, and mounted on glass slides using DAKO mounting medium. Images were acquired using Axioskop 50 (Carl Zeiss Micro Imaging) microscope and Metamorph (Universal Imaging Corp.) software. For microtubule quantification, at least 12 pictures of 30 to 50 cells were taken for each condition. The surface covered by microtubules was quantified using ImageJ software (25) and reported to the number of cells in each corresponding picture. Statistical analysis and graphs were made using Excel software (Microsoft).

Immunofluorescence Analysis of MAP6-F Association with the Microtubule Network—MEF cells grown on coverslips were placed in culture medium complemented with 10 mM HEPES pH 7.4 and either kept at 37 °C or incubated at 4 °C for 30 min. Cells were permeabilized in OPT buffer and fixed with 3.7% paraformaldehyde, 0.5% glutaraldehyde, and 0.1% Triton X-100 in PBS, followed by a treatment with 1 mg/ml NaBH₄ in PBS for 10 min. Tubulin was detected using α3A1 antibody (1/1,000) and MAP6-F with polyclonal 23C antibody (1/1,000). Images were recorded with an Axioskop 20 microscope (Carl Zeiss) (Leica) coupled with Coolnaps ES camera (Roper Scientific) driven by Metaview Software (Universal Imaging).

Video Microscopy Analysis of mCherry-MAP6-F Localization in HeLa Cells—pmCherry-C2 vector was obtained by replacing the EGFP sequence of pEGFP-C2 vector (Clontech) by the mCherry sequence from pmCherry-C1 (Clontech) using AgeI/BsrG1 cloning sites. mCherry-MAP6-F expression vector was then constructed by inserting MAP6-F cDNA from p16C-APa (16) into pmCherry-C2 vector using XhoI/KpnI cloning sites. HeLa cells transfected with pmCherry-MAP6-F using Amaxa technology (Lonza) were grown on coverslip for 24 h and then placed in a perfusion chamber at 37 °C. Cell culture medium was progressively cooled from 37 °C to 15 °C during the course of the experiment (15 min). Images were recorded every minute on a DMI6000 microscope (Leica) with an EMCCD Quantem camera (Roper Scientific) driven by MetaMorph Software (Universal Imaging).

Western Blot Analysis of MAP6-F Recruitment to Cellular Insoluble Material—For analysis of the temperature-dependent solubility of MAP6-F in NIH/3T3 cells, cells were grown in B35 cell culture dishes. The cell culture medium was renewed with the same medium supplemented with 10 mM HEPES pH 7.4, equilibrated at the temperature of the assay and the culture dishes were placed in a temperature-controlled water bath. For incubation times of 1 min or less, PBS was used instead of cell culture medium. Dishes were incubated in water bath at the temperature and for the time indicated. Dishes were rinsed with 1 ml of PBS at incubation temperature and permeabilized with 400 μ l of OPT at the incubation temperature. After 1 min, OPT medium was recovered and added to 100 μ l of 5 \times Laemmli buffer (soluble extract). Insoluble cell material was recovered in 500 μ l of 1 \times Laemmli buffer. Extracts were run on 12% SDS-PAGE and transferred onto nitrocellulose membranes. Membranes were blocked with 5% nonfat milk in TTBS (50 mM Tris-HCl, pH 7.4, 150 mM NaCl, 0.3% Tween 20). Membranes were probed in the same buffer with affinity-purified rabbit anti-MAP6 antibody 23C (dilution 1/5,000) or monoclonal anti-tubulin antibody α 3a1 (1/10,000). HRP-coupled secondary antibodies were incubated in TTBS and probed using Pierce ECL Substrate (ThermoScientific) and light sensitive film (Fischer Scientific).

Western Blot Analysis of MAP6 Expression in NIH/3T3, HeLa, MEF^{+/+}, and MEF^{-/-}—Cells grown on B30 cultures dishes were washed with PBS and lysed by addition of 400 μ l of Laemmli buffer. Extracts were normalized for the quantity of tubulin by semi-quantitative Western blot using α 3A1 antibody. MAP6 proteins expression was then analyzed by Western blot as described above using a mixture of both anti-MAP6 23N and 23C polyclonal antibodies at 1/5,000 dilution each.

MAP6-F and Mc Domain Expression and Purification—MAP6-F was cloned into pFAST-BAC HTb as previously reported (22). The Mc domain coding sequences were cloned into NcoI/XhoI cloning sites of pFAST-BAC HTb in frame with the His₆ tag. Recombinant baculoviruses were obtained and amplified in Sf9 insect cells (Invitrogen). Protein expressions were carried out in High Five insect cells grown in suspension in Express Five culture medium (Invitrogen). For His-tagged MAP6-F purification, 500 ml of infected High Five cell culture were spun down at 4 °C for 5 min at 125 \times g. Pellets were frozen and thawed in 50 ml of lysis buffer (20 mM PIPES-KOH pH 6.6, 150 mM KCl, 0.1% Triton X-100, 10% glycerol, 1 mM MgCl₂, 1 mM EGTA, 0.1 mM DTT, 50 μ g/ml AEBSE, 5 μ g/ml aprotinin, 10 μ g/ml leupeptin, 2.5 μ g/ml pepstatin, and 10 μ g/ml E64. Cells were lysed by passing three times through a 23-gauge needle and cell debris were pelleted by centrifugation for 30 min at 4 °C and 30,000 \times g. Supernatant was diluted with one volume of Q-Sepharose-adjusting buffer (100 mM HEPES pH 8.0, 50 mM KCl, 0.9% Triton X-100, 1 mM EGTA, 1 mM MgCl₂, 0.1 mM DTT plus protease inhibitors and centrifuged at 100,000 \times g. The supernatant was loaded onto a 25 ml Q-Sepharose column equilibrated in Q buffer (100 mM HEPES-KOH pH 8.0, 100 mM KCl, 0.5% Triton X-100, 1 mM EGTA, 1 mM MgCl₂, 0.1 mM DTT). Flow through and 25 ml wash with Q buffer were collected, mixed with 1 volume of Ni-Sepharose adjustment buffer (60 mM imidazole pH 8.0, 900 mM KCl, 0.5%

Triton X-100, 20% sucrose, 1 mM MgCl₂, 1 mM EGTA, and protease inhibitors) and incubated at 4 °C for 90 min with 1 ml of Ni-Sepharose beads previously equilibrated in Ni column buffer (50 mM HEPES-KOH pH 8.0, 500 mM KCl, 0.5% Triton X-100, 10% sucrose, 50 mM Imidazole, 0.1 mM DTT). Beads were spun down at 100 \times g for 5 min at 4 °C, washed twice with Ni-column buffer, and packed in a disposable plastic column. The column was further washed with Ni-column buffer, equilibrated in equilibration buffer (50 mM HEPES-KOH pH 8.0, 250 mM KCl, 0.1 mM DTT, 50 mM imidazole), and the protein was eluted with equilibration buffer containing 250 mM imidazole. Purified His-tagged MAP6-F was extensively dialyzed against PEM buffer, aliquoted, frozen in liquid nitrogen, and stored at -80 °C. Protein purity was analyzed on Coomassie Blue-stained SDS-PAGE. Quantification was made with ImageJ and Excel softwares from scanned gel using bovine serum albumin as standard. For His-Mc domain purification, a 50 ml culture of infected High Five cells was spun down and frozen as indicated above. Cells were lysed in 10 ml of buffer (20 mM HEPES pH 7.4, 300 mM NaCl, 0.5% Triton X-100, and protease inhibitors), and centrifuged at 30,000 \times g for 30 min at 4 °C. The supernatant was heated at 90 °C for 15 min, cooled on ice, and centrifuged again. The supernatant was adjusted to 2.5 mM of imidazole and loaded on a 1 ml cobalt column (Pierce) connected to Duo Flow apparatus (Bio-Rad) pre-equilibrated in buffer A (20 mM HEPES pH 7.4, 300 mM NaCl, 2.5 mM imidazole). Column was washed with 20 ml of Buffer A and the proteins were eluted using a 2.5 to 200 mM imidazole gradient. Fractions with the Mc domain were pooled, concentrated with Ultracel-10K (Millipore), loaded on a S200 gel-filtration column equilibrated in 2 \times BRB buffer (160 mM PIPES pH 6.75, 2 mM EGTA, 2 mM MgCl₂). Elution fractions were analyzed, diluted with one volume of water, reconcentrated with Ultracel-10K, aliquoted, frozen in liquid nitrogen, and stored at -80 °C. For circular dichroism experiments, the buffer containing the Mc domain was changed to 50 mM potassium phosphate buffer (pH 6.75) through repeated concentrations and dilution steps with Ultracel-10K.

In Vitro Analysis of the Mc Domain Binding to Taxol-stabilized Microtubules—Microtubules were polymerized from 50 μ M brain bovine PC-tubulin prepared as published (26). Tubulin was incubated for 20 min at 37 °C in PEM buffer (100 mM PIPES pH 6.75, 1 mM MgCl₂, 1 mM EGTA) supplemented with 1 mM of GTP. Mixture was further incubated at 37 °C for 10 min in the presence of Taxol (100 μ M) and then diluted to 2 μ M final concentration of tubulin. Five μ l of microtubule solution were incubated with 5 μ l of various concentrations of the Mc domain in PEM buffer plus 0.05% Tween 20 and 1 mM DTT. After 10 min at the indicated temperature, microtubules were sedimented through centrifugation at 100,000 \times g for 10 min at the incubation temperature. Pellets were recovered in 80 μ l of Laemmli buffer. Fifteen μ l of each fraction were loaded on a 12% SDS-PAGE gels. After migration, 2 gel bands were cut from each gel. The first at 45/60 kDa was Coomassie Blue stained to verify the even quantity of tubulin present in the assay. The second, at 30–45 kDa was transferred onto a single nitrocellulose membrane at 100 V for 1 h in transfer buffer containing 20% ethanol and 0.05% SDS. The Mc domain detection was

Microtubule Stabilization by MAP6

carried out as described for Western blot detection of MAP6-F except that pico-ECL kit (Pierce) was used, and the signal was recorded with Chemidoc apparatus (Bio-Rad). Signal intensities were quantified with ImageJ software, and the corresponding amount of protein present in the extract was determined by comparison with the ECL signal obtained with a ladder of given quantity of the protein using Excel software.

In Vitro Analysis of Microtubules Cold Stability—Microtubules were polymerized from 60 μM of bovin brain tubulin in PEM buffer plus 1 μM GTP at 37 °C for 30 min. Three μl of microtubule solution were mixed with 3 μl of PEM solution containing either 100 μM taxol or increasing concentration of purified MAP6-F or Mc domain and incubated on ice for 10 min. Five μl of the mix were loaded on 100 μl of a 30% sucrose cushion in PEM buffer, centrifuged at 100,000 $\times g$ for 30 min at 4 °C. The pellets were recovered in Laemmli buffer and analyzed by SDS-PAGE and Coomassie Blue staining.

Cryo-electron Microscopy Analysis of Microtubule Ends at 4 °C—Microtubules were grown from 80 μM of bovine brain tubulin in PEM-GTP buffer for 30 min at 37 °C. Microtubules were then diluted at 37 °C to 55 μM either with PEM buffer alone or supplemented with the Mc domain (5.5 μM final concentration). After 10 min at 37 °C, the mixes were incubated on ice for either 1 min in the control condition (rapid depolymerization) or for 20 min when microtubules were stabilized by the Mc domain. Five μl of chilled mixes were loaded onto holey carbon-coated grids, briefly blotted and plunged into liquid ethane using the vitrification robot Vitrobot MARK IV (FEI Co.). Specimens were observed with a Phillips CM200 using a Gatan G26 cryoholder. Images were recorded on Kodak SO163 films under low dose conditions at defocus in the range of 2 to 3 μm and at a magnification of $\times 27,500$. Micrographs were digitized with an Epson scanner at 1600 dpi.

Thermostability Analysis of MAP6-F—Forty μl of PEM buffer containing 1 μg of MAP6-F were either kept on ice or incubated for 30 min at 90 °C. Heated solutions were cooled down on ice and centrifuged at 100,000 $\times g$ for 15 min at 4 °C. Supernatants were recovered and mixed with 10 μl of 5 \times Laemmli buffer, while pellets were resuspended in 50 μl of Laemmli buffer. As control for the total amount of MAP6-F, 40 μl of non-centrifuged protein solution were treated as described for the supernatants. Protein solutions were analyzed by SDS-PAGE on 12% gel and Coomassie Blue staining.

Circular Dichroism Analysis—Circular dichroism spectra were recorded with a Jasco J-810 spectropolarimeter interfaced with a Peltier temperature control unit. The Mc domain concentration was 9 μM in 50 mM potassium phosphate buffer at pH 6.75. The path length of the cuvette was 1 mm. Thermal folding was followed by monitoring the CD signal at 220 nm and 208 nm while changing the temperature from 5 to 80 °C by 1 °C steps. The structural changes observed while varying the temperature was emphasized by subtracting the CD spectrum at 5 °C from the CD spectra obtained at given temperatures.

RESULTS

MAP6 Protects Microtubules against Temperature-dependent Depolymerization in Cells—Previous experiments have shown that in HeLa cells that do not express MAP6 proteins,

microtubules depolymerize when incubated on ice for a prolonged time (23). However, no data were available on the effect of moderate chilling conditions on microtubules. To assess the effect of intermediate drops in temperature on cellular microtubules, we incubated HeLa cells grown on coverslips at temperatures varying from 37 to 4 °C before rapid permeabilization and fixation (23). The remaining microtubules were observed and quantified (Fig. 1, A and B). The quantity of microtubules was constant for temperatures above 25 °C. This quantity then progressively decreased with lower temperatures to reach a very low level at 4 °C. Similar results were obtained with mouse embryonic fibroblasts derived from MAP6-null mice (MEF^{-/-}) (Fig. 1, A and C) albeit with stronger chilling effect on microtubules. In MEF^{-/-}, significant microtubule loss appeared below 25–20 °C with a rapid drop between 20 and 15 °C with only about 20% of microtubule left and a complete microtubule depolymerization below 10 °C (Fig. 1C).

On the contrary, in NIH/3T3 cells or MEF wild type (MEF^{+/+}) that express MAP6, microtubules were mostly resistant to cold-induced depolymerization (Fig. 1A). In NIH/3T3 cells, close to 80% of the total amount of microtubules was preserved at temperatures below 25 °C (Fig. 1B). In MEF^{+/+}, microtubule resistance to cold-induced depolymerization was not as strong as in NIH/3T3 cells, with 80% of remaining microtubules at 15 °C and 30% under 10 °C (Fig. 1C). This discrepancy between NIH/3T3 and MEF^{+/+} could be correlated with the difference of MAP6-F expression as revealed by Western blot analysis (Fig. 1D).

We then analyzed the kinetics of cold-induced microtubule depolymerization in HeLa cells that do not express MAP6 proteins at 4 °C and 15 °C (Fig. 1E). At 4 °C, microtubules depolymerized rapidly and completely in 2 min. At 15 °C, microtubule amount dropped by about 40% in a few minutes but remained stable thereafter. This suggested that, in cells, a decrease in temperature induces a change from an equilibrium state at 37 °C to a new one with a lower quantity of microtubules. Altogether, these experiments indicated that below 25–20 °C, cellular microtubules depolymerize rapidly in a temperature-dependent manner unless they are protected by the presence of MAP6.

MAP6-F Binding and Stabilization of Microtubules under Cold Exposure Are Dynamic and Temperature-dependent—To better understand the mechanisms involved in microtubule stabilization by MAP6 upon chilling, we intended to correlate the cold conditions required for microtubule depolymerization to those required for MAP6 binding to and stabilization of microtubules.

It was shown that upon chilling, MAP6-F of NIH/3T3 cells re-localized from the cytoplasm to the microtubule network (16). Cold-dependent association of MAP6-F with microtubules was also observed in MEF^{+/+} as revealed by immunofluorescence analysis (Fig. 2). Indeed, after cell permeabilization, MAP6-F was found associated with the microtubule network at 4 °C but not at 37 °C (upper panels). The low MAP6-F nuclear labeling visible at 37 °C correspond to background as observed in MEF^{-/-} (lower panels). In addition, temperature-dependent translocation of mCherry-MAP6-F from the cytoplasm to microtubules in HeLa cells was observed using live video

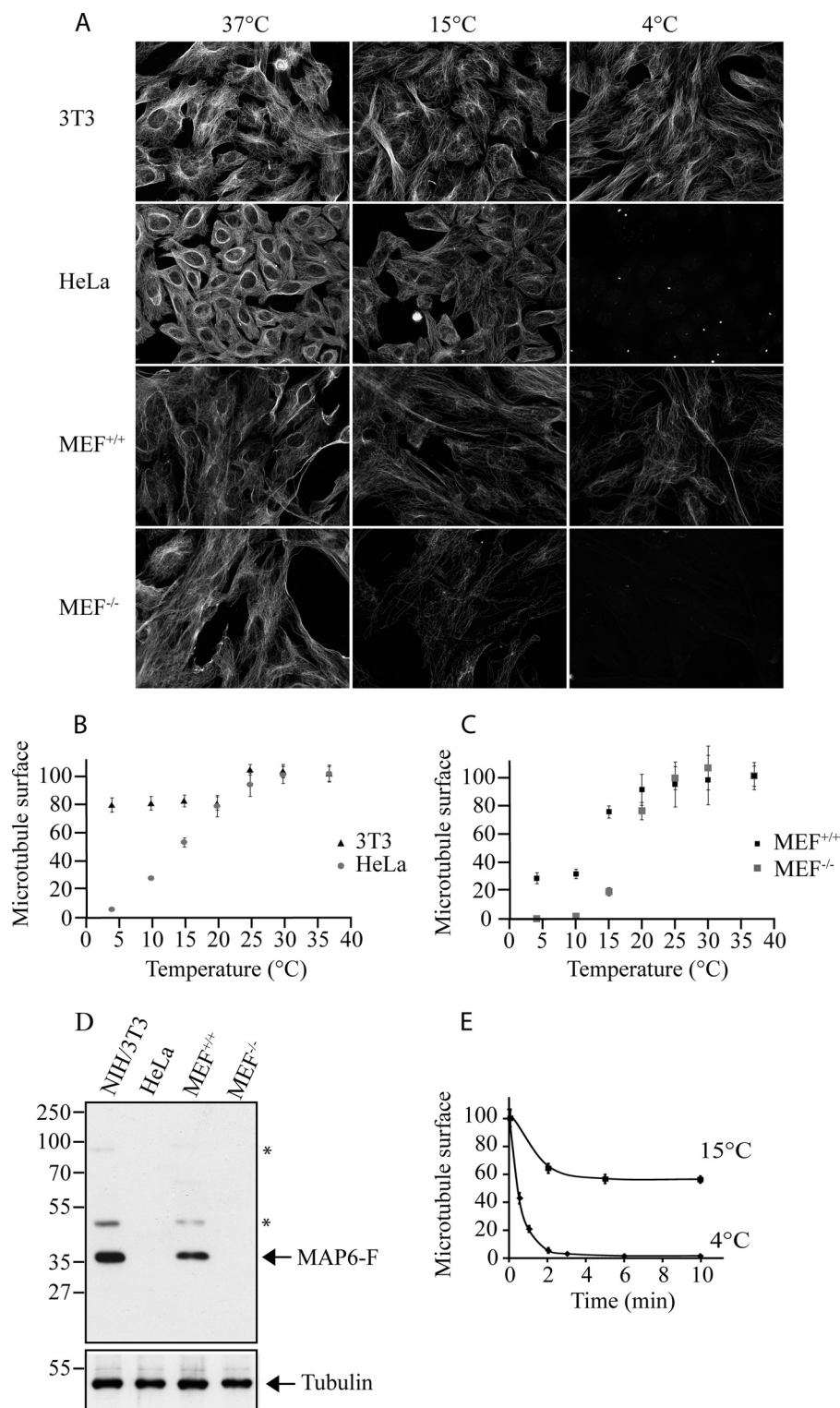


FIGURE 1. MAP6-F protects fibroblastic microtubules from temperature- and time-dependent cold-induced depolymerization. *A*, immunofluorescence analysis of microtubules of NIH/3T3 cells, HeLa cells, MEF^{+/+}, and MEF^{-/-} exposed to the indicated temperature. *B* and *C*, quantification of microtubule surface in immunofluorescence experiments as shown in *A* for each cell line (NIH/3T3 and HeLa in *B*, MEF^{+/+} and MEF^{-/-} in *C*). *D*, NIH/3T3, HeLa, MEF^{+/+} and MEF^{-/-} cell extracts were normalized for their content in tubulin and then analyzed for the expression of MAP6-F by Western blot. * indicates minor MAP6 isoforms (16, 19). *E*, quantification of microtubules remaining in HeLa cells after incubation for the indicated time at 4 or 15 °C. In *B*, *C*, and *E*, data represent mean \pm S.E. ($n \geq 12$) and are expressed as a percentage of the signal obtained without cold treatment (37 °C).

microscopy analysis (Fig. 3). Results revealed a progressive localization of the protein on microtubules during temperature shift from 37 to 15 °C.

To further characterize the association of MAP6-F with microtubules, we performed cell fractionation and analyzed MAP6-F presence in soluble *versus* insoluble fractions. In par-

Microtubule Stabilization by MAP6

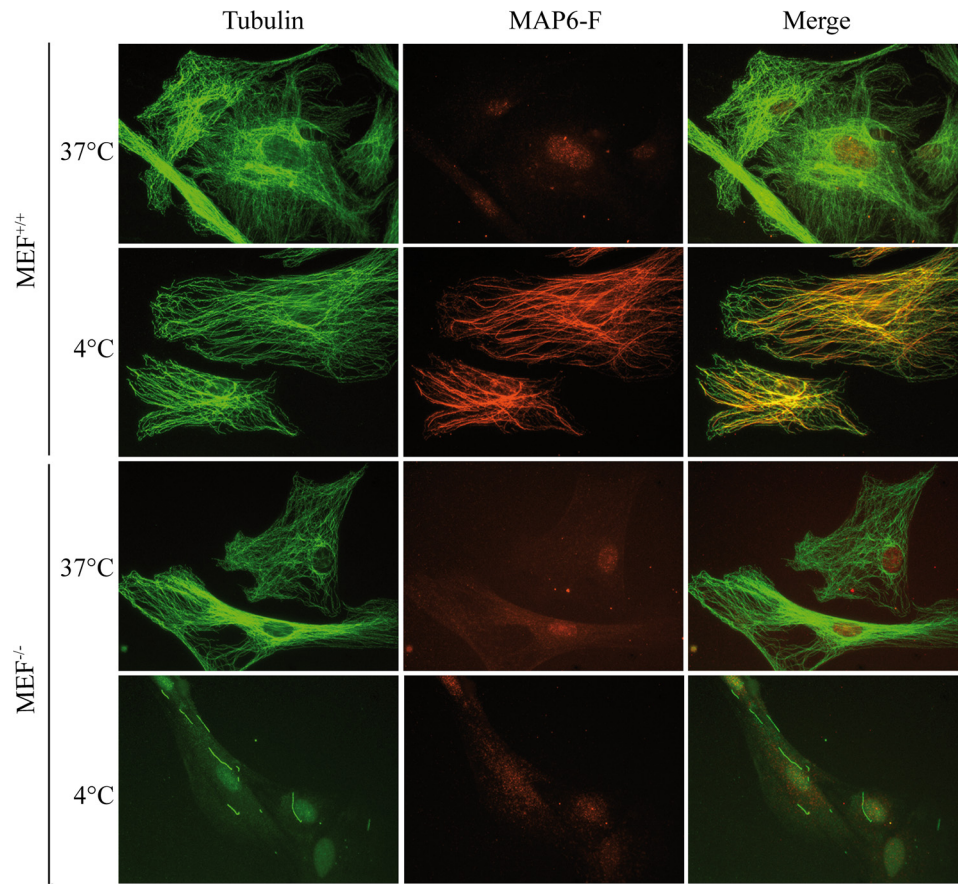


FIGURE 2. **Cold-induced association of MAP6-F with the microtubule network in MEF.** MEF^{+/+} or MEF^{-/-} were either kept at 37 °C or incubated at 4 °C for 30 min as indicated. Cells were then permeabilized with OPT at the incubation temperature, fixed, and processed for immunodetection of tubulin (green) or MAP6-F (red).

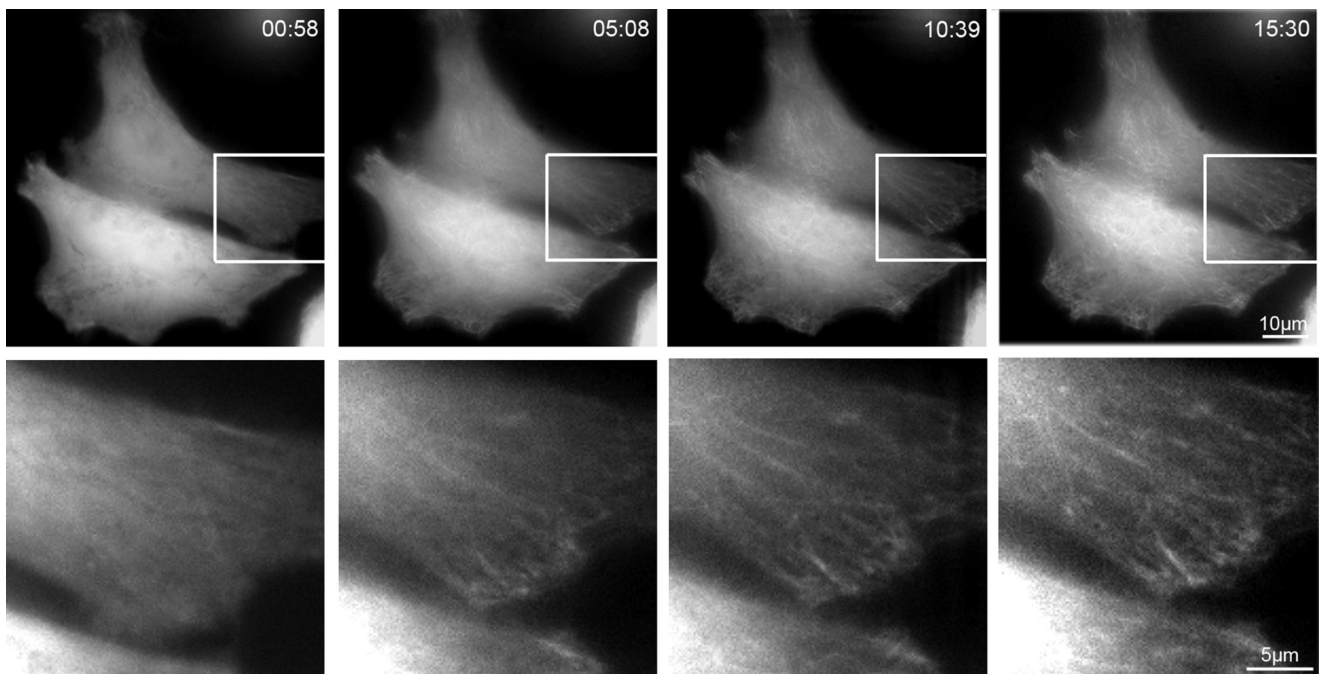


FIGURE 3. **Cooling cells from 37 to 15 °C induces a progressive accumulation of MAP6-F-mCherry on microtubule network in HeLa cells.** HeLa cells overexpressing MAP6-F fused to mCherry were placed in a perfusion chamber at 37 °C. Cell culture medium was progressively cooled from 37 to 15 °C during the course of the experiment (15 min:30 s). *Upper panels* are recorded images of MAP6-F-mCherry at the indicated time (min:s). *Lower panels* are enlargements (3×) of part of the images indicated by *white squares*.

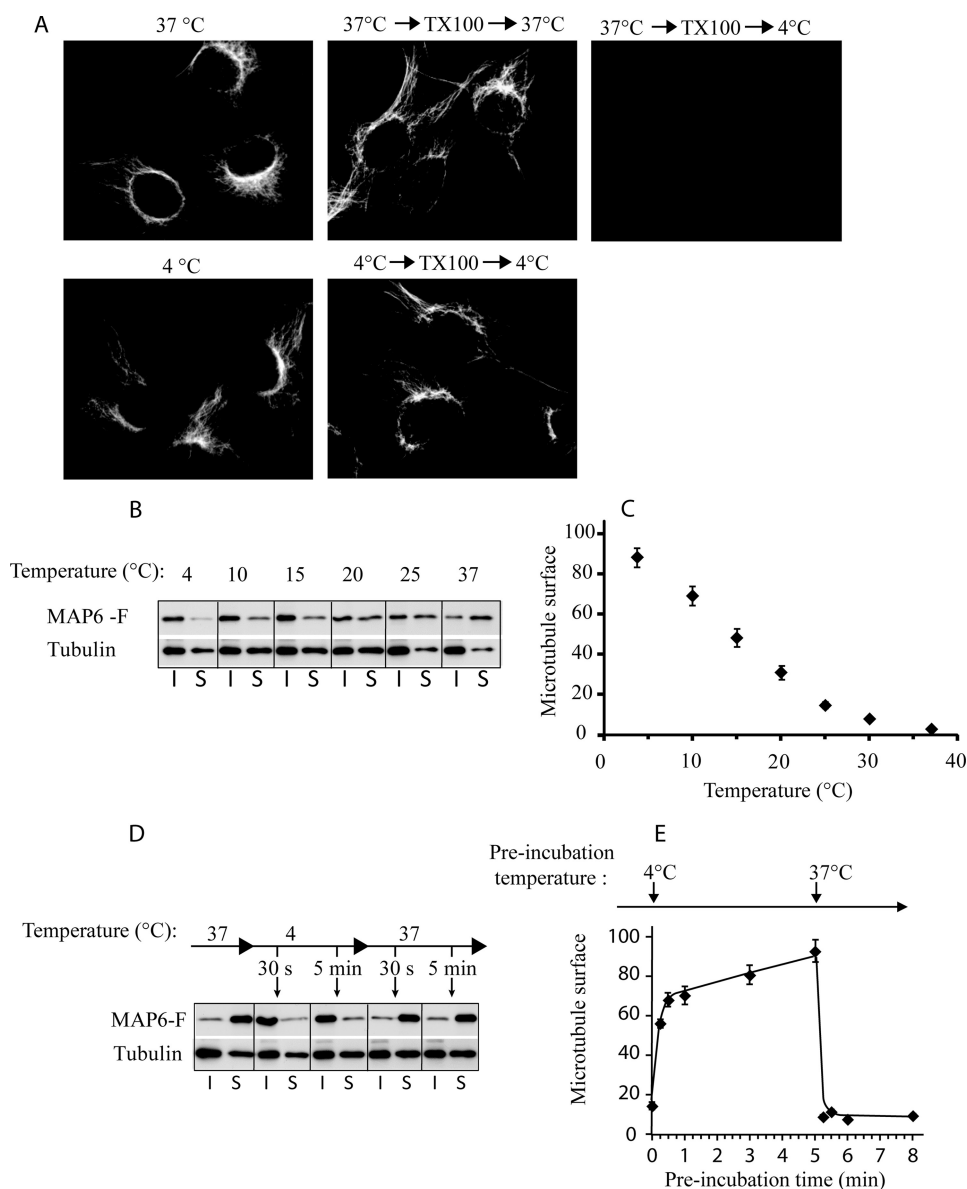


FIGURE 4. **MAP6-F association with microtubules and stabilization of microtubules are fast and temperature-dependent.** *A*, NIH/3T3 cells at 37 °C (*upper lane*) or incubated at 4 °C (*lower lane*), were permeabilized (TX100) and either directly fixed (*left*) or further incubated for 10 min at 37 °C (*upper middle*) or at 4 °C (*upper and lower right*) before microtubule immunodetection. *B*, Western blot analysis of MAP6-F present in soluble (S) or insoluble (I) fractions of NIH/3T3 cells exposed to the indicated temperature. *C*, quantification by immunofluorescence of the remaining microtubules in NIH/3T3 cells preincubated and permeabilized at the indicated temperature, and then further incubated at 4 °C. Data represent mean \pm S.E. ($n \geq 12$) and are expressed as a percentage of the signal obtained without cold treatment (37 °C). *D* and *E*, NIH/3T3 cells were treated as in *B* and *C*, respectively, except that the cell incubation and permeabilization temperatures were switched from 37 to 4 °C and then from 4 back to 37 °C. MAP6-F solubility (*D*) and subsequent microtubule cold stabilization at 4 °C (*E*) were analyzed at the indicated time course.

allel, we evaluated MAP6-F activity in NIH/3T3 cells by quantifying its microtubule cold-protecting effect. Indeed, since MAP6-F is not associated with the microtubules at 37 °C it is washed out upon cell permeabilization. Thus, when NIH/3T3 cells were incubated and permeabilized with a Triton X-100 containing buffer at 37 °C before cooling at 4 °C for additional 10 min, microtubules were not protected against cold and were lost (Fig. 4A, *upper right panel*). In contrast, when cells were first preincubated at 4 °C for 10 min to promote MAP6-F association with microtubules before permeabilization, microtubules stayed protected (Fig. 4A, *lower right panel*). The amount of remaining microtubules after preincubation of the cells under various temperature conditions before permeabilization

(at the same temperature) and subsequent incubation at 4 °C could then be quantified by immunodetection of tubulin. We thus analyzed under similar conditions the effect of pre-incubation temperatures varying from 4 to 37 °C on MAP6-F soluble/insoluble fractionation (Fig. 4B) and on microtubule cold stability (Fig. 4C). Results presented in Fig. 4B show a progressive increase in MAP6-F in the insoluble fraction and a decrease in the soluble fraction when the temperature decreased. Consistently, microtubule cold preservation increased progressively when the temperature decreased from 37 to 4 °C (Fig. 4C).

We next assessed in similar experiments, the kinetics of MAP6-F association with insoluble fraction and stabilization of

Microtubule Stabilization by MAP6

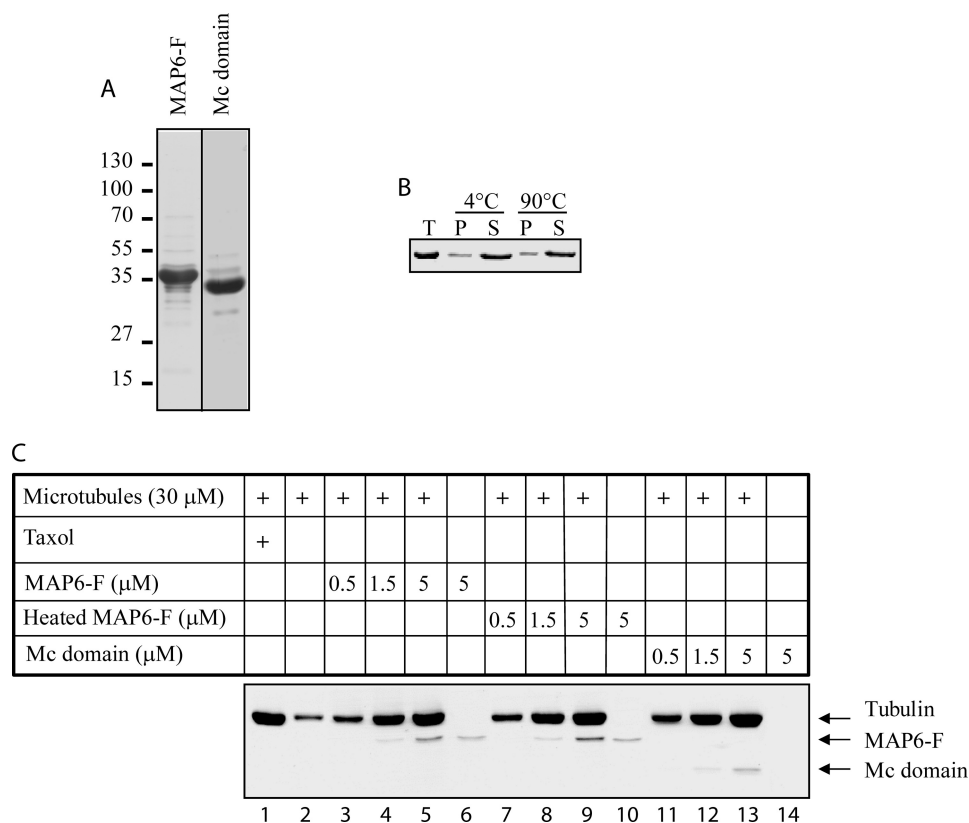


FIGURE 5. MAP6-F is a heat stable protein that stabilizes microtubules *in vitro* through interaction with its Mc domain. *A*, Coomassie Blue-stained SDS-PAGE gel of the purification products of MAP6-F and the Mc domain expressed as His-tagged proteins in insect cells. *B*, solubility analysis of purified MAP6-F at 4 °C or after heating for 30 min at 90 °C. Proteins in the 100,000 × *g* pellet (*P*) or supernatant (*S*) were analyzed in Coomassie Blue-stained SDS-PAGE gel. *T*: total. *C*, microtubule cold-stabilizing activity of MAP6-F, heated MAP6-F, and the Mc domain. Microtubules were grown from pure tubulin *in vitro*, mixed with either taxol (60 μM) or increasing concentration of MAP6-F, 90 °C-treated MAP6-F, or with the Mc repeat domain as indicated and then incubated on ice for 10 min. Cold-resistant microtubules were isolated by centrifugation, and the pellets were analyzed by SDS-PAGE and Coomassie Blue staining.

microtubules at 4 °C. As shown in Fig. 4*D*, an incubation at 4 °C as short as 30 s was sufficient for maximum MAP6-F association with the insoluble fraction and this association was reversible with apparently similar fast kinetics when cells were transferred back from 4 to 37 °C. As for the temperature-dependence experiment, induction of microtubule cold stabilization followed the localization of MAP6-F in the insoluble fraction (Fig. 4*E*). In addition, analysis of early time points showed that cold-induced stabilization of microtubules was mostly achieved within 15 s.

These results indicate that under cold exposure, MAP6-F interaction with microtubules is very fast and dynamic. This probably involves a direct effect of the temperature on one of the binding partners rather than a post-translational modification. Furthermore, the concomitant cold exposure conditions for microtubule depolymerization (Fig. 1) and MAP6-F association with microtubules (Fig. 4) suggested that microtubules and/or MAP6-F and/or other partners involved in the interaction might undergo temperature-dependent conformational changes.

MAP6-F Is a Heat-stable Protein That Protects Microtubules from Cold-induced Depolymerization through Direct Interaction via Its Mc Domain—To test whether MAP6-F by itself is capable of stabilizing microtubules and in which conditions, we carried out the purification of the MAP6-F protein as well as of its Mc domain that constitute two third of the molecule (189/

306 amino acids) and has been shown to specifically protect microtubules from cold when ectopically expressed in HeLa cells (22). Both polypeptides expressed in fusion with a His₆ tag using baculovirus-insect cells system were purified to purity close to 95% (Fig. 5*A*). During the course of the purification, we also observed that MAP6-F is a heat stable protein. Indeed, contrary to most proteins that denature and precipitate at temperatures above 50 °C, heating MAP6-F to 90 °C for 30 min did not lead to protein aggregation (Fig. 5*B*).

Using a microtubule sedimentation assay, we analyzed the capacity of purified MAP6-F to protect *in vitro* polymerized microtubules from cold-induced depolymerization. Fig. 5*C* shows that, as expected, microtubules grown at 37 °C were mostly lost when incubated at 4 °C alone (*lane 2*) as compared with the total amount of microtubules stabilized with taxol (*lane 1*). Addition of MAP6-F just before cooling at 4 °C protected microtubules from cold-induced depolymerization in a dose-dependent manner (*lanes 3–5*). The same held true when heated MAP6-F was used, confirming the heat stability of MAP6-F (*lanes 7–9*). The Mc domain was also used in this assay and presented the same ability as the full-length molecule for microtubule stabilization (*lanes 11–13*). It is interesting to note that the Mc domain was more soluble and did not sediment in the absence of microtubules (compare *lane 14* with *lanes 6* and *10*). Altogether, these results demonstrated for the first time that MAP6-F stabilizes microtubules exposed to cold via a

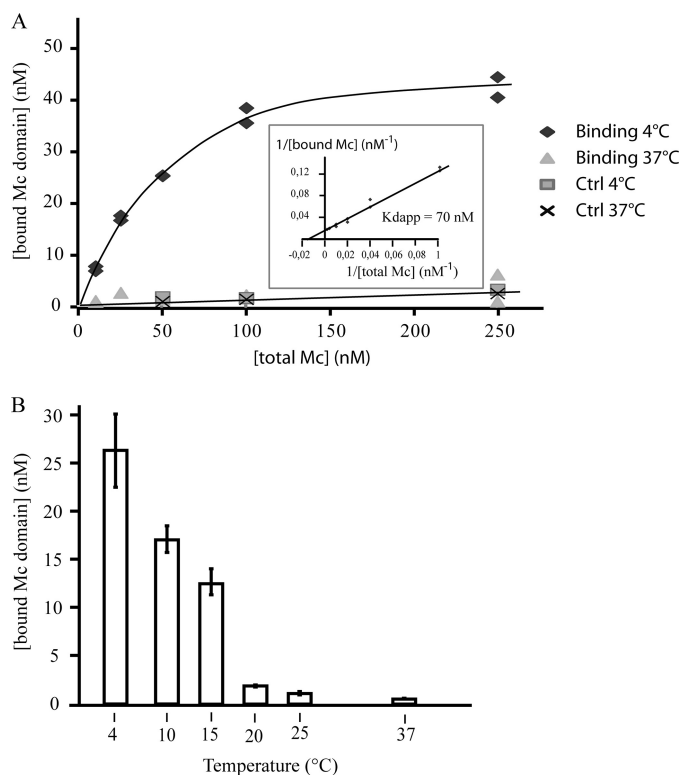


FIGURE 6. *In vitro* analysis of temperature-dependent binding of the MAP6 Mc domain with taxol-stabilized microtubules. *A*, microtubules were grown at 37 °C from 60 μM pure tubulin, stabilized with Taxol and diluted to 1 μM in the final binding reaction mix. The Mc domain was added at increasing concentrations and incubated at 4 or 37 °C for 10 min. Microtubules were isolated by centrifugation and the associated Mc domain was quantified by Western blot using Chemidoc apparatus, ImageJ, and Excel softwares. 4 and 37 °C controls (*Ctrl*) are the amount of the Mc domain pelleted in the absence of microtubules. *Insert*, Lineweaver-Burk plot analysis of the data shown in *A* gave 70 nM as the apparent dissociation constant (K_{dapp}) for the binding of the Mc domain to microtubules at 4 °C. *B*, the Mc domain (50 nM) binding to microtubules was analyzed as in *A* at the indicated temperatures. Data represent mean \pm S.E. ($n = 4$).

direct interaction. The Mc domain is able by itself to fully recapitulate this activity and is thus the main domain involved in this function.

Characterization of the Mc Domain Binding to Microtubules at 4 °C—To further characterize the effect of the temperature on MAP6-F interaction with microtubules, we performed a titration binding curve of the Mc domain to Taxol-stabilized microtubules. Results presented in Fig. 6*A* show that, at 4 °C, the Mc domain binding to 1 μM of microtubules was titratable with a binding stoichiometry of 1 mol of the Mc domain for 25 mol of tubulin dimer. The apparent affinity determined was 70 nM. On the contrary, at 37 °C, no specific interaction was detected (Fig. 6*A*). Using a Mc domain concentration close to the apparent dissociation constant (K_d), we analyzed the effect of various temperatures on the Mc domain interaction with microtubules in the same conditions. Results presented in Fig. 6*B* show that, as for MAP6-F association with and stabilization of microtubule in NIH/3T3 cells (Fig. 4, *B* and *C*), *in vitro* microtubule binding of the Mc domain progressively increases with the fall of temperature. The interaction started to be detectable at 25 °C, rapidly increased between 20 °C and 15 °C and then was further strengthened between 15 °C and 4 °C.

Circular Dichroism Analysis of Temperature-dependent Conformational Changes in the Mc Domain—To investigate whether the temperature-associated changes in the binding affinity between the Mc domain and microtubules could be associated to conformational changes in the Mc domain, we carried out circular dichroism experiments (Fig. 7). Absorption spectra from 190 to 250 nm, obtained at different temperatures (Fig. 7*A*), indicated that the Mc domain was essentially unstructured with mainly random coiled signal (negative absorption peak near 195 nm) (27). Nevertheless, with increasing temperatures, the intensity of the negative bands at 198 nm decreased and shifted to slightly higher wavelengths while absorption at 219 nm appeared. Moreover, the presence of an isodichroic point at 208 nm indicated a two conformational state system. To characterize this structure, subtraction spectra were drawn (Fig. 7*B*). The difference spectra showed the apparition with heating of negative bands at 219 nm and positive bands at 195 nm. This signal is characteristic of beta structures (28). Temperature-dependent Mc domain absorption spectra at 220 nm (Fig. 7*A*, *inset*) indicated that the conformational change between 5 and 80 °C was linear and reversible. Altogether these data indicated that the Mc domain which contains beta structures progressively unfolded upon chilling from 37 to 5 °C.

Structural Analysis of Microtubules Stabilized at 4 °C by the Mc Domain—To gain insight into the mechanisms by which MAP6-F protects microtubules from depolymerization under cold exposure, we used cryo-electron microscopy to analyze microtubules at 4 °C in the absence or in the presence of the Mc domain. Growing and shrinking microtubules assume various conformations at their extremities, including sheet-like extensions and blunt ends during polymerization and outwardly curled protofilaments in disassembling conditions (29, 30). As MAP6-F inhibits cold-induced microtubule disassembly, we wondered whether it could affect the global structure of microtubule ends. Microtubules were polymerized at 37 °C and then incubated at 4 °C with or without the Mc domain. In our conditions, we could not observe the Mc domain bound to the stabilized microtubules. The main observed differences concerned the structures of the microtubule ends that presented mostly curled depolymerizing protofilaments in the absence of the Mc domain and about 50% of blunt extremities in the presence of the Mc domain (Fig. 8). These data indicated that the Mc domain stabilized the extremities of microtubule exposed to cold. However, one would have expected a near to complete stabilization of microtubules without curled ends in the presence of the Mc domain. The remaining 50% of curled microtubule ends indicates that the microtubule stabilization is not complete and that the Mc domain might only dramatically slow down depolymerization and/or allow very slow dynamics at low temperatures.

DISCUSSION

MAP6 proteins have been shown to be essential for the stabilization of microtubules in cells at 4 °C. In fibroblastic cells, the main isoform, MAP6-F, was shown to relocalize from the cytoplasm to the microtubule network upon chilling to 4 °C. It has been suggested that the changes in MAP6-F binding to microtubules relied on temperature-induced changes in

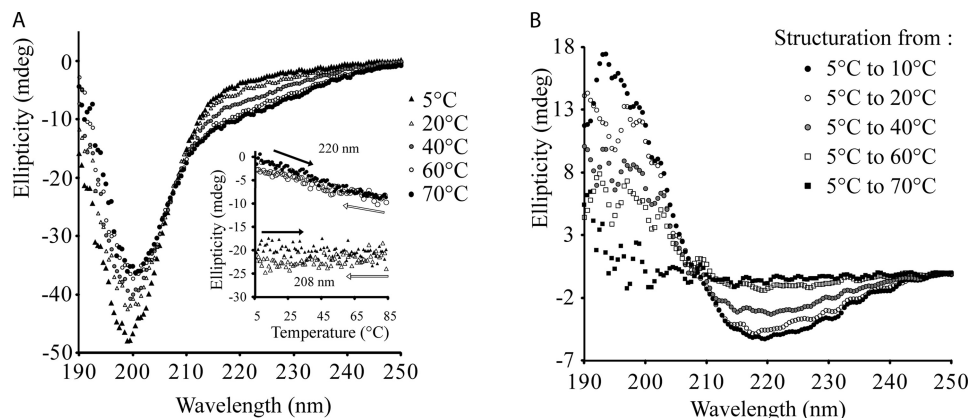


FIGURE 7. Temperature induces secondary structure changes in the Mc domain of MAP6. *A*, circular dichroism spectra at 5 °C showed a clear minimum for the spectrum at 198 nm, indicating a mostly random coiled structure. This minimum is shifted with increasing temperature toward higher wavelengths and a minimum at 219 nm appears. This indicates an increase in structuration. In the *inset*, the structuration has been monitored at 220 nm from 5 to 85 °C as indicated by the *black arrow*. The folding reversibility from 85 °C to 5 °C is indicated by the *open arrow*. The isodichroic point at 208 nm suggests a two-state system characterizing the secondary structure of the Mc domain. *B*, difference CD spectra from *A*. The subtraction of the CD spectrum at 5 °C from CD spectra at 10, 20, 40, and 70 °C gave the structure gain during the temperature titration. The spectra obtained correspond to β -sheet conformation.

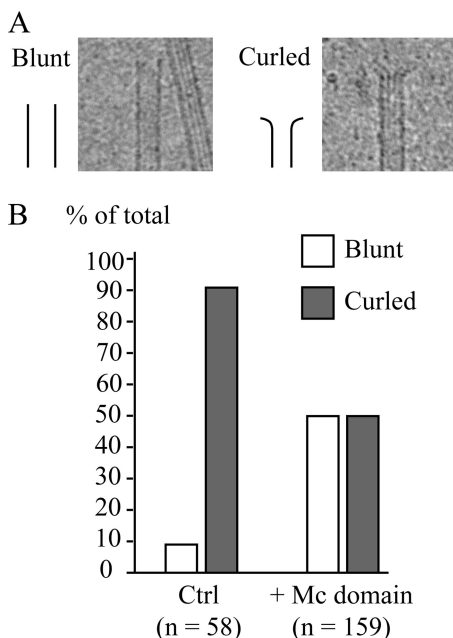


FIGURE 8. Microtubule cold-stabilization by the Mc domain is associated with an increase of blunt-ended microtubules. Microtubules were grown from 80 μ M of pure tubulin at 37 °C, mixed at a final concentration of 55 μ M with buffer alone (*Ctrl*) or with 5.5 μ M final of the Mc domain (*Mc*). After 10 min at 37 °C, microtubules were chilled on ice for 1 min to allow partial depolymerization of microtubules alone or for 20 min for the Mc domain-stabilized microtubules. Microtubules were loaded on grids, frozen in liquid ethane, and observed by cryo-electron microscopy. *A*, pictures and schematic representations of microtubule curled and blunt ends. *B*, quantitative analysis of the proportion of blunt *versus* curled ends in control condition or in the presence of the Mc domain.

MAP6-F post-translational modifications (16). We show here that under cold exposure, MAP6-F recruitment to microtubules and stabilization is highly dynamic, indicating a direct effect of the temperature on the interaction. *In vitro*, purified MAP6-F can directly interact with and stabilize microtubules against cold-induced depolymerization through its Mc domain. As observed *in vivo* for MAP6-F, *in vitro* binding of the Mc domain to microtubules is temperature-dependent. The binding was very low at 37 °C and increased significantly when the

temperature decreased below 20 °C to reach a high affinity ($K_{dapp} = 70$ nM) at 4 °C. Thus, *in vivo* and *in vitro*, the Mc domain of MAP6 recognizes and stabilizes microtubules as soon as the temperature drops under 20 °C.

What Is the Structural Element that Regulates the Interaction between Microtubules and the Mc Domain of MAP6?—Our results reveal that lowering of temperature is accompanied by the recruitment of MAP6-F on microtubules both in cells and *in vitro*. This suggests that MAP6-F adopts a cold-dependent conformation enabling its interaction with the polymers, and/or that MAP6-F recognizes a structural feature of microtubules depolymerizing under cold exposure. Our data provide strong evidence that variations in temperatures induce conformational changes of MAP6-F. MAP6-F exhibits beta structures at 37 °C and progressively unfolds as the temperature decreases, enabling its interaction with microtubules and their subsequent stabilization. MAP6-F binding to microtubules at low temperatures could also involve the recognition of a specific feature of cold-induced depolymerizing polymers. In particular, shrinking microtubules display curled protofilaments at their ends, but we did not observe any accumulation of MAP6-F at the extremity of disassembling microtubules, neither in cells (Figs. 2 and 3) nor in purified assays (Fig. 8), suggesting that specific recognition of the outwardly curled protofilaments by MAP6-F is an unlikely mechanism. MAP6-F might associate preferentially to a cold-sensitive lattice region, although little information is available on changes occurring at low temperatures within the microtubule wall. High-resolution structures of MAP6-F and MAP6-F/microtubule complexes will be required to visualize the Mc domain and its precise binding sites to the microtubule lattice.

How Does the Mc Domain of MAP6 Stabilize Microtubules at 4 °C?—As suggested above, under cold exposure, the Mc domain of MAP6 might bridge adjacent protofilaments. This, in turn, would decrease the catastrophe frequency thought to be involved in cold-induced microtubule depolymerization (9). Reinforcing lateral interactions has already been proposed to be a way of stabilizing microtubules in cold-living organisms (12). Such a mechanism is reminiscent of the doublecortin microtu-

bule stabilization mode at 37 °C (31). Doublecortin is an anti-catastrophe factor that stabilizes microtubules by linking adjacent protofilaments and counteracting their outward bending in depolymerizing microtubules (32). The analysis of the Mc domain effects on microtubule dynamics at low temperature should be very informative but such experiments which require a controlled cold environment are still technically challenging.

A Link Between the Mc Domain Structure and MAP6 Aggregation in Human Pathology?—During our *in vitro* studies we discovered that MAP6-F is a weakly structured molecule as revealed by its heat stability, a feature shared by other MAPs such as MAP1, MAP2, and Tau (33). The folding of MAP6-F into beta structures represents a peculiar behavior already reported for the Tau protein (34). These beta structures have been implicated in the formation of pathologic amyloid aggregates (35) and beta structures of MAP6 might be implicated in the aggregation of MAP6 in Lewis bodies during amyotrophic lateral sclerosis (36).

A Physiological Function for MAP6 Stabilization of Microtubules under Cold Exposure?—In HeLa cells, that do not express MAP6 proteins, microtubules depolymerized in a temperature-dependent manner as soon as the temperature decreased below 20 °C with virtually no microtubules left at 4 °C. On the contrary, in MAP6-containing NIH/3T3 cells, 80% of microtubules were preserved upon cold exposure from 20 to 4 °C. In more physiological conditions, MAP6 of MEF^{+/+} allowed to preserve about 80% of microtubules at 15 °C and 30% at temperatures below 10 °C. In animals, such low temperatures could be achieved during episodes of torpor or hibernation and MAP6 could be required to preserve a minimal level of microtubules in such challenging conditions. In this study we considered the whole Mc domain without analyzing the contribution of each individual repeat. However, one can speculate that the composition in repeats of the Mc domain would determine the strength of the cold response. Along this line, we found a relatively good correlation between the number of repeats (from 1 to 9) in the Mc domain of mammals and the ability of the animals to hibernate or to make torpor. For example, almost all genome-sequenced rodents (house mice, Norway rat, thirteen-lined ground squirrel) which exhibit MAP6 with 3 to 9 Mc repeats are able to hibernate/torpor, whereas the naked mole rat which exhibits only one repeat is very sensitive to cold exposure (main cause of lethality).

Also, in primates, only the lemurian branch which contains several Mc repeats (3 to 6 for small-eared galago and gray mouse lemur) can enter torpor whereas all other primates including human, Sumatran orangutan, chimpanzee, gorilla, Rhesus monkey, and Hamadryas baboon do not enter torpor and express MAP6 containing only one repeat. In human, MAP6 stabilization of microtubules can still be useful during accidental hypothermic episodes or even during perioperative hypothermia following anesthesia.

In conclusion, the Mc domain of MAP6 behaves as a sensor of temperature able to protect microtubules from temperature variations. How microtubule stabilization upon temperature reduction is involved and whether it is crucial to adapt cold-dependent cell responses such as metabolic changes are exciting questions.

Acknowledgments—We thank D. Job for helpful discussions on the work and to L. Aubry, J. Brocard, F. Costagliola, and J.C. Deloulme for critical reading of the manuscript. We are grateful to the Institute of Structural Biology Jean-Pierre Ebel (Grenoble, France) for the use of its EM facility.

REFERENCES

- Akhmanova, A., and Steinmetz, M. O. (2008) Tracking the ends: a dynamic protein network controls the fate of microtubule tips. *Nat. Rev. Mol. Cell Biol.* **9**, 309–322
- Howard, J., and Hyman, A. A. (2009) Growth, fluctuation and switching at microtubule plus ends. *Nat. Rev. Mol. Cell Biol.* **10**, 569–574
- Nogales, E., and Wang, H. W. (2006) Structural intermediates in microtubule assembly and disassembly: how and why? *Curr. Opin Cell Biol.* **18**, 179–184
- Wade, R. H. (2009) On and around microtubules: an overview. *Mol. Biotechnol.* **43**, 177–191
- Lee, J. C., and Timasheff, S. N. (1977) *In vitro* reconstitution of calf brain microtubules: effects of solution variables. *Biochemistry* **16**, 1754–1764
- Olmsted, J. B., and Borisy, G. G. (1975) Ionic and nucleotide requirements for microtubule polymerization *in vitro*. *Biochemistry* **14**, 2996–3005
- Regula, C. S., Pfeiffer, J. R., and Berlin, R. D. (1981) Microtubule assembly and disassembly at alkaline pH. *J. Cell Biol.* **89**, 45–53
- Schilstra, M. J., Bayley, P. M., and Martin, S. R. (1991) The effect of solution composition on microtubule dynamic instability. *Biochem. J.* **277**, 839–847
- Fyngenson, D. K., Braun, E., and Libchaber, A. (1994) Phase diagram of microtubules. *Phys. Rev. E. Stat. Phys. Plasmas Fluids Relat Interdiscip Topics* **50**, 1579–1588
- Modig, C., Wallin, M., and Olsson, P. E. (2000) Expression of cold-adapted β -tubulins confer cold-tolerance to human cellular microtubules. *Biochem. Biophys. Res. Commun.* **269**, 787–791
- Detrich, H. W., 3rd. (1997) Microtubule assembly in cold-adapted organisms: functional properties and structural adaptations of tubulins from antarctic fishes. *Comp. Biochem. Physiol. A. Physiol.* **118**, 501–513
- Detrich, H. W., 3rd, Parker, S. K., Williams, R. C., Jr., Nogales, E., and Downing, K. H. (2000) Cold adaptation of microtubule assembly and dynamics. Structural interpretation of primary sequence changes present in the α - and β -tubulins of Antarctic fishes. *J. Biol. Chem.* **275**, 37038–37047
- Geiser, F. (1988) Reduction of metabolism during hibernation and daily torpor in mammals and birds: temperature effect or physiological inhibition? *J. Comp. Physiol. B.* **158**, 25–37
- Heldmaier, G., Ortman, S., and Elvert, R. (2004) Natural hypometabolism during hibernation and daily torpor in mammals. *Respir. Physiol. Neurobiol.* **141**, 317–329
- Andrieux, A., Salin, P. A., Vernet, M., Kujala, P., Baratier, J., Gory-Fauré, S., Bosc, C., Pointu, H., Proietto, D., Schweitzer, A., Denarier, E., Klumperman, J., and Job, D. (2002) The suppression of brain cold-stable microtubules in mice induces synaptic defects associated with neuroleptic-sensitive behavioral disorders. *Genes Dev.* **16**, 2350–2364
- Denarier, E., Fourest-Lieuvin, A., Bosc, C., Pirollet, F., Chapel, A., Margolis, R. L., and Job, D. (1998) Nonneuronal isoforms of STOP protein are responsible for microtubule cold stability in mammalian fibroblasts. *Proc. Natl. Acad. Sci. U.S.A.* **95**, 6055–6060
- Bosc, C., Andrieux, A., and Job, D. (2003) STOP proteins. *Biochemistry* **42**, 12125–12132
- Aguezoul, M., Andrieux, A., and Denarier, E. (2003) Overlap of promoter and coding sequences in the mouse STOP gene (Mtap6). *Genomics* **81**, 623–627
- Galiano, M. R., Bosc, C., Schweitzer, A., Andrieux, A., Job, D., and Hallak, M. E. (2004) Astrocytes and oligodendrocytes express different STOP protein isoforms. *J. Neurosci. Res.* **78**, 329–337
- Guillaud, L., Bosc, C., Fourest-Lieuvin, A., Denarier, E., Pirollet, F., Lafanchère, L., and Job, D. (1998) STOP proteins are responsible for the high degree of microtubule stabilization observed in neuronal cells. *J. Cell Biol.* **142**, 167–179

Microtubule Stabilization by MAP6

21. Ochoa, C. D., Stevens, T., and Balczon, R. (2011) Cold exposure reveals two populations of microtubules in pulmonary endothelia. *Am. J. Physiol. Lung Cell Mol. Physiol.* **300**, L132–L138
22. Bosc, C., Frank, R., Denarier, E., Ronjat, M., Schweitzer, A., Wehland, J., and Job, D. (2001) Identification of novel bifunctional calmodulin-binding and microtubule-stabilizing motifs in STOP proteins. *J. Biol. Chem.* **276**, 30904–30913
23. Lieuvin, A., Labbé, J. C., Dorée, M., and Job, D. (1994) Intrinsic microtubule stability in interphase cells. *J. Cell Biol.* **124**, 985–996
24. Erck, C., Peris, L., Andrieux, A., Meissirel, C., Gruber, A. D., Vernet, M., Schweitzer, A., Saoudi, Y., Pointu, H., Bosc, C., Salin, P. A., Job, D., and Wehland, J. (2005) A vital role of tubulin-tyrosine-ligase for neuronal organization. *Proc. Natl. Acad. Sci. U.S.A.* **102**, 7853–7858
25. Schneider, C. A., Rasband, W. S., and Eliceiri, K. W. (2012) NIH Image to ImageJ: 25 years of image analysis. *Nat. Methods* **9**, 671–675
26. Paturle-Lafanechère, L., Eddé, B., Denoulet, P., Van Dorselaer, A., Mazarguil, H., Le Caer, J. P., Wehland, J., and Job, D. (1991) Characterization of a major brain tubulin variant which cannot be tyrosinated. *Biochemistry* **30**, 10523–10528
27. Venyaminov, S. Y., Baikalov, I. A., Shen, Z. M., Wu, C. S., and Yang, J. T. (1993) Circular dichroic analysis of denatured proteins: inclusion of denatured proteins in the reference set. *Anal. Biochem.* **214**, 17–24
28. Greenfield, N., and Fasman, G. D. (1969) Computed circular dichroism spectra for the evaluation of protein conformation. *Biochemistry* **8**, 4108–4116
29. Arnal, I., Karsenti, E., and Hyman, A. A. (2000) Structural transitions at microtubule ends correlate with their dynamic properties in *Xenopus* egg extracts. *J. Cell Biol.* **149**, 767–774
30. Chrétien, D., Fuller, S. D., and Karsenti, E. (1995) Structure of growing microtubule ends: two-dimensional sheets close into tubes at variable rates. *J. Cell Biol.* **129**, 1311–1328
31. Moores, C. A., Perderiset, M., Francis, F., Chelly, J., Houdusse, A., and Milligan, R. A. (2004) Mechanism of microtubule stabilization by doublecortin. *Mol. Cell* **14**, 833–839
32. Moores, C. A., Perderiset, M., Kappeler, C., Kain, S., Drummond, D., Perkins, S. J., Chelly, J., Cross, R., Houdusse, A., and Francis, F. (2006) Distinct roles of doublecortin modulating the microtubule cytoskeleton. *EMBO J.* **25**, 4448–4457
33. Vera, J. C., Rivas, C. I., and Maccioni, R. B. (1988) Heat-stable microtubule protein MAP-1 binds to microtubules and induces microtubule assembly. *FEBS Lett.* **232**, 159–162
34. von Bergen, M., Friedhoff, P., Biernat, J., Heberle, J., Mandelkow, E. M., and Mandelkow, E. (2000) Assembly of tau protein into Alzheimer paired helical filaments depends on a local sequence motif ((306)VQIVYK(311)) forming beta structure. *Proc. Natl. Acad. Sci. U.S.A.* **97**, 5129–5134
35. Mukrasch, M. D., Biernat, J., von Bergen, M., Griesinger, C., Mandelkow, E., and Zweckstetter, M. (2005) Sites of tau important for aggregation populate {beta}-structure and bind to microtubules and polyanions. *J. Biol. Chem.* **280**, 24978–24986
36. Letournel, F., Bocquet, A., Dubas, F., Barthelaix, A., and Eyer, J. (2003) Stable tubule only polypeptides (STOP) proteins co-aggregate with spherical neurofilaments in amyotrophic lateral sclerosis. *J. Neuropathol. Exp. Neurol.* **62**, 1211–1219

Identification of an AHNAK Binding Motif Specific for the Annexin2/S100A10 Tetramer*

Received for publication, July 10, 2006, and in revised form, September 7, 2006. Published, JBC Papers in Press, September 19, 2006, DOI 10.1074/jbc.M606545200

Sandrine De Seranno^{‡§¶}, Christelle Benaud^{‡§¶}, Nicole Assard^{‡§¶}, Sami Khediri^{‡§¶}, Volker Gerke^{||}, Jacques Baudier^{‡§¶}, and Christian Delphin^{‡§¶}

From [‡]INSERM, EM101–04 and the [§]Commissariat à l’Energie Atomique, DRDC/TS, Grenoble 38054, France, the [¶]Université Joseph Fourier, Grenoble 38041, France, and the ^{||}Institute of Medical Biochemistry, Center for Molecular Biology of Inflammation, University of Muenster, D-48149, Germany

The Annexin2 tetramer (A2t), which consists of two Annexin2 molecules bound to a S100A10 dimer, is implicated in membrane-trafficking events. Here, we showed using a yeast triple-hybrid experiment and *in vitro* binding assay that Annexin2 is required for strong binding of S100A10 to the C-terminal domain of the protein Ahnak. We also revealed that this effect involves only the Annexin2 N-terminal tail, which is implicated in S100A10/Annexin2 tetramerization. The minimal A2t binding motif (A2tBP1) in Ahnak was mapped to a 20-amino acid peptide, and this peptide is highly specific for A2t. We also identified a second A2t binding motif (A2tBP2) present in the N-terminal domain of Ahnak, which binds to A2t, albeit with less affinity. When overexpressed as an EGFP fusion protein in MDCK cells, A2tBPs cofractionate in a calcium-dependent manner and co-immunoprecipitate with S100A10 and Annexin2. In living cells, A2tBPs target EGFP to the cytoplasm as does Annexin2. In response to oxidative and mechanical stress, EGFP-A2tBPs relocate within minutes to the plasma membrane; a behavior shared with Annexin2-GFP. These results suggest that the A2t complex exists within the cytoplasm of resting living cells and that its localization at the plasma membrane relies on cellular signaling. Together, our data demonstrate that A2tBP1 is a specific A2t complex binding domain and may be a powerful tool to help elucidate A2t structure and cellular functions.

Annexin2 is a member of a multigene family of proteins widely expressed among multicellular organisms (1). It binds to negatively charged phospholipids in a calcium-dependent manner (2–4) and has been implicated in several membrane transport events such as endocytic and secretory pathways (5–14). Annexin2 is composed of a core domain of four 70-amino acid repeats and a short N-terminal tail of 30 residues

(2). The core domain is responsible for the calcium-dependent interaction with the membrane phospholipids (15–17). The very first twelve N-terminal residues form an amphipathic α -helix that constitutes the minimal binding domain for its partner, S100A10 (15, 18–20). S100A10 belongs to the large S100 family of EF-hand calcium-binding proteins. It has the peculiarity of having lost its calcium-sensing properties and is locked in a constitutively active conformation (21). Similar to other members of the family, S100A10 homodimerizes and was found inside the cell either as a homodimer or as a heterotetramer (A2t)³ in which each of the two S100A10 subunits interacts with one Annexin2 molecule (for reviews see Refs. 22 and 23). Binding partners have been identified for each component: Annexin2 was found to interact with F-actin, caveolin, and HIV1-Gag protein (24–26), and S100A10 was reported to interact with various cell surface receptors and ion channels such as TRPV5, TRPV6, Na_v1.8, TASK-1, and ASIC1 (27–32). Given the affinity of S100A10 for Annexin2 ($K_d < 3 \times 10^{-8}$, Ref. 19), it is generally assumed that it is indeed the A2t complex that interacts with the different substrates. However, in most cases whether both components contribute to the A2t ability to bind substrates has not been investigated. Furthermore, co-immunoprecipitation experiments failed to detect Annexin2 in association with the complex S100A10/TASK1 (30), suggesting that, at least for the S100A10 subunit, interaction with some targets occurs independently of the formation of the tetramer. Understanding the functions of the tetramer, as opposed to those of its two components, relies on the identification of substrates that specifically interact with the tetramer.

In a previous study, we have identified the giant protein Ahnak as a binding partner of A2t. In epithelial cells, A2t recruits Ahnak to cholesterol-rich microdomains of the plasma membrane. This recruitment appears to be essential for the establishment of the proper cytoarchitecture of polarized columnar epithelial cells (33). Ahnak is composed of an N-terminal 498-amino acid domain, a large central region of 4390 amino acids organized in 36 repeated units, and the C-terminal 1002 amino acids. We have shown that the S100A10 subunit mediates the interaction of A2t with the C-terminal domain of Ahnak (33).

* This study has been supported by Grant 5643 from the Association pour la Recherche sur le Cancer (ARC) (to C. D.) and Grant 11597 from the Association Française contre les Myopathies (AFM). The costs of publication of this article were defrayed in part by the payment of page charges. This article must therefore be hereby marked “advertisement” in accordance with 18 U.S.C. Section 1734 solely to indicate this fact.

¹ To whom correspondence may be addressed: INSERM EMI 0104 / TS-DRDC, CEA Grenoble, 17 rue des Martyrs, 38054 Grenoble Cedex 9, France. Tel.: 33-4-38-78-47-27; Fax: 33-4-38-78-50-58; E-mail: jbaudier@cea.fr.

² To whom correspondence may be addressed: INSERM EMI 0104 / TS-DRDC, CEA Grenoble, 17 rue des Martyrs, 38054 Grenoble Cedex 9, France. Tel.: 33-4-38-78-47-27; Fax: 33-4-38-78-50-58; E-mail: cdelphin@cea.fr.

³ The abbreviations used are: A2t, Annexin2 tetramer; A2tBP, A2t-binding peptide; GST, glutathione S-transferase; MDCK, Madin-Darby canine kidney; Tricine, N-[2-hydroxy-1,1-bis(hydroxymethyl)ethyl]glycine; DTT, dithiothreitol; mAb, monoclonal antibody; EGFP, enhanced green fluorescent protein.

In the present work, we have extended the molecular and functional characterization of the A2t/Ahnak interaction. We have shown that the C-terminal domain of Ahnak constitutes a highly specific substrate of A2t and does not bind significantly to S100A10 or Annexin2 individually. We have delineated the Annexin2 contribution in the A2t-Ahnak complex formation to its S100A10 binding site and have mapped down the A2t binding site in the Ahnak C-terminal domain to a 20-amino acid peptide (A2tBP1). We have shown that *in vitro* A2tBP1 binding to A2t is characterized by a high affinity and specificity. We have also demonstrated that EGFP-A2tBP1 expressed in MDCK cells co-fractionates and co-immunoprecipitates with S100A10 and Annexin2. Furthermore, we have shown, that through its specific binding, EGFP-A2tBP1 allows us to follow stress-induced relocalization of Annexin-2 in living cells. Thus, A2tBP1 is the first specific A2t complex binding motif, which might be a powerful tool to study the structure of A2t and to dissect functions strictly involving the complex A2t, not its individual subunits.

EXPERIMENTAL PROCEDURES

Cell Culture—MDCK epithelial cells were maintained in Dulbecco's modified Eagle's medium (Invitrogen, Carlsbad, CA), 10% fetal bovine serum (Sigma Aldrich), and 1% penicillin/streptomycin (Invitrogen). For metabolic labeling, cells were labeled in methionine-free MEM, 5% fetal calf serum supplemented with [³⁵S]Met/Cys mix (5 μ Ci/ml) for 4 days.

Production of MDCK Stable Transformants—Annexin2-EGFP plasmid was a generous gift from Dr. Moss. EGFP-A2tBP1 and 2 were obtained by subcloning of the BamHI/XbaI A2tBP fragments from the pGEX-KG vector to pEGFP-C1 vector. Plasmids were purified using the Qiagen kit and used for transformation of MDCK cells with FuGENE6 transfection reagent following the manufacturer's instructions (Roche Applied Science). Transfected cells were selected and maintained in culture medium containing 0.6 mg/ml of geneticin. Because aminoglycoside antibiotics have been shown to bind to and interfere with phospholipid-dependent cellular functions (34), geneticin was removed from the culture medium at least a week before the experiment was performed.

Cellular Fractionation and Immunoprecipitation—MDCK cells grown to confluence in 10-cm culture plates were washed with phosphate-buffered saline and collected in 0.5 ml of Buffer L (Tris-HCl 20 mM, pH 7.4, 150 mM NaCl, 1 mM DTT, 0.3% Triton X-100 plus 10 μ g of each protease inhibitor (AEBSE, leupeptin, aprotinin)) in the presence of 0.3 mM CaCl₂ or 1 mM EGTA. Cells were passed through a 26-gauge needle and centrifuged at 20,000 \times g for 30 min at 4 °C. Supernatants were removed (S), and pellets (P) were resuspended by sonication in one volume of Buffer L. For Western blot analysis, 20 μ l of each sample were separated by 11% Tris-Tricine polyacrylamide gel electrophoresis. After transfer to a nitrocellulose membrane, proteins were detected using anti-Annexin2 mAb, anti-S100A10 mAb (both Transduction Laboratories), and anti-EGFP pAb (AbCam, Paris, France). For immunoprecipitation, the calcium concentration of 100- μ l samples was adjusted to 0.3 mM and incubated with 1.5 μ g of anti-EGFP mAb (AbCam) for 1 h at 4 °C. 10 μ l of protein A-Sepharose were then added

and incubated at 4 °C for 1 h. Beads were spun down at 2000 \times g, washed three times with buffer L, and resuspended in 100 μ l of Laemmli buffer. Western blot analysis was carried out as described above.

Purification of S100A10 and Annexin2—Native A2t was purified from porcine intestine as previously described (35). S100A10 and Annexin2 were dissociated from the complex with 9 M urea. Each subunit was purified by gel filtration in 20 mM Tris-HCl, pH 7.4, 9 M urea, 100 mM NaCl, 2 mM DTT, 1 mM EGTA, 1 mM NaN₃ and stored in aliquots at -80 °C. Prior to the binding experiment, S100A10 and Annexin2 were renatured by dialyzing against 20 mM Tris-HCl, pH 7.4, 150 mM NaCl, 0.3% Triton X-100, and 1 mM DTT.

In Vitro Protein-Protein Interaction/GST Pull-down Assays—For production of GST fusion proteins, Ahnak C-ter cDNA was cloned into pGEX-KG (GE Health Care) as previously described (33). Shorter Ahnak fragments were obtained either by deleting Ahnak-Cter by restriction digestion, blunting, and re-ligation or by PCR cloning. Detailed cloning information for specific GST-Ahnak fragment expression is available upon request. Numbering of Ahnak residues is from the human Ahnak sequence (GenBank™ accession number NM001620). The constructs were introduced in *Escherichia coli* BL21(DE3)pLysS strain. Bacteria were grown to an A₆₀₀ of 0.6–0.8 and treated with 1 mM isopropyl-1-thio- β -D-galactopyranoside for 2–3 h to induce protein expression. All subsequent steps were carried out at 4 °C. Bacteria were lysed in buffer A (40 mM Tris-HCl, pH 7.4, 300 mM NaCl, 1 mM DTT) complemented with 1 mg/ml lysozyme, 1% Triton X-100, 5 mM EDTA, and protease inhibitors (AEBSE, leupeptin, aprotinin, pepstatin 10 μ g/ml each) through three cycles of freeze-thaw. The lysates were centrifuged at 30,000 \times g for 1 h, and the supernatants were incubated in batch with glutathione-Sepharose beads for 2 h. Beads were washed in batch three times with buffer A plus 1% Triton X-100 and 5 mM EDTA and then with ten bead volumes in column. The columns were equilibrated in buffer A, and the proteins were eluted in buffer A plus 30 mM glutathione. Fractions containing the proteins were pooled and extensively dialyzed against buffer A. Protein concentration was quantified on a Coomassie-stained acrylamide gel using bovine serum albumin as standard. Proteins in working aliquots were flash-frozen in liquid nitrogen and stored at -80 °C. For the GST pull-down assay, 2 μ g of recombinant protein were incubated for 1 h at 4 °C with 10 μ l of glutathione-Sepharose beads and then washed in buffer B (20 mM Tris-HCl, pH 7.4, 150 mM NaCl, 0.3% Triton X-100, 1 mM DTT, 300 μ M CaCl₂). GST pull-down assays were carried out either with different combinations of purified proteins (2.7 μ g of Annexin2, 0.8 μ g of S100A10, 2 μ g of native A2t, 5 μ g of Annexin2 (1–13) as indicated in the figure legends or with cellular extracts. For GST pull-down, cell extracts from confluent MDCK cells were prepared essentially as described for cell fractionation, and the supernatant of cells lysed in Buffer L in the presence of EGTA was used. After incubation for 1 h at 4 °C in a 300- μ l final volume of buffer B, the beads were spun down at 2000 \times g for 2 min, washed three times with 0.5 ml of buffer B, and boiled in SDS sample buffer. Proteins were separated on 11% Tris-

A2t-specific Binding Motif

Tricine acrylamide gel electrophoresis, transferred to nitrocellulose, and detected by Western blot using the ECL kit.

Surface Plasmon Resonance—Real-time binding experiments were performed on a BIAcore biosensor system (Pharmacia Biosensor AB, Uppsala, Sweden). All experiments were performed at 25 °C. Anti-GST antibodies in 10 mM sodium acetate (pH 3.5), were coupled directly through their amino groups to the sensor (CM5) surface activated by *N*-hydroxysuccinimide and *N*-ethyl-*N'*-(dimethylaminopropyl)carbodiimide according to the manufacturer's instructions. The remaining reactive groups were then inactivated with 1 mM ethanolamine. GST or GST-A2tBP1 binding to the antibodies, and interaction experiments with native purified A2t were done in running buffer containing 20 mM Hepes, pH 7.4, 150 mM NaCl, and 0.01% Triton X-100. Sensorgrams obtained with different concentrations of A2t (297, 595, and 1190 nM) were analyzed using the Kaleidagraph software. The association and dissociation curves were fitted with an equation model of one analyte (A2t) binding two heterogenous ligands (GST-A2tBP1). In Equation 1,

$$R = R_{eq1}(1 - e^{-k_{s1}(t - t_0)}) + R_{eq2}(1 - e^{-k_{s2}(t - t_0)}) \quad (\text{Eq. 1})$$

R is the response, subscript 1 and 2 refer to each of the two ligands, *t* is the time (s), $k_s = k_a C_n + k_d$ where *C_n* is the concentration of the analyte, and *R_{eq}* is the steady state response level. The correlation coefficient of the fitting, close to 1 (between 0.99485 and 0.99996) indicated the quality of the fitting. A simple explanation for this model with two ligands is that once A2t, which is a large complex (94 kDa), is bound to one of the two A2tBP1 sites on the dimer (because of GST dimerization, Ref. 36) of GST-A2tBP1, the steric constraint perturbs the binding of another A2t to the second GST-A2tBP1 site. This is in agreement with the binding stoichiometry found at steady state (up to 1.5 A2t per GST-A2tBP1 dimer at the higher concentration of the analyte tested (1.19 μM)). For the evaluation of the *K_d* of A2t with AtBP1, only the high affinity responses were considered.

Yeast Triple Hybrid—pLex-Ahnak-Cter and pAct2-S100A10 constructs were obtained as previously described (33). For expression of Annexin2 in yeast, a ΔlexA version of pEG202 vector was first obtained. For this purpose, the SphI-SphI fragment of pEG202 containing the lexA sequence was subcloned into a pGEMT vector, where the NotI-NotI fragment was previously deleted. The lexA sequence was then excised out by digesting with HindIII and EcoRI, blunting with Deep vent polymerase, and self-ligation. The ΔlexA SphI fragment was subcloned back into pEG202 at the SphI site. Annexin2 from pGEMTp36 (generous gift from Dr. Borsotto) was digested with and cloned into the NotI site of pEG202ΔlexA. Constructs in different combination as indicated in the figure legends were used to transform the AMR70 yeast strain. pAct2, pEG202ΔLexA, and pLex-lamin were used as control. Colonies were grown into the selective media (uracil-depleted YPD medium minus tryptophan (for pLex10), leucine (for pAct2), and histidine (for pEG202ΔlexA)). For β-galactosidase assays, the activity of three independent colonies from each transformation was measured in triplicate as previously described (37).

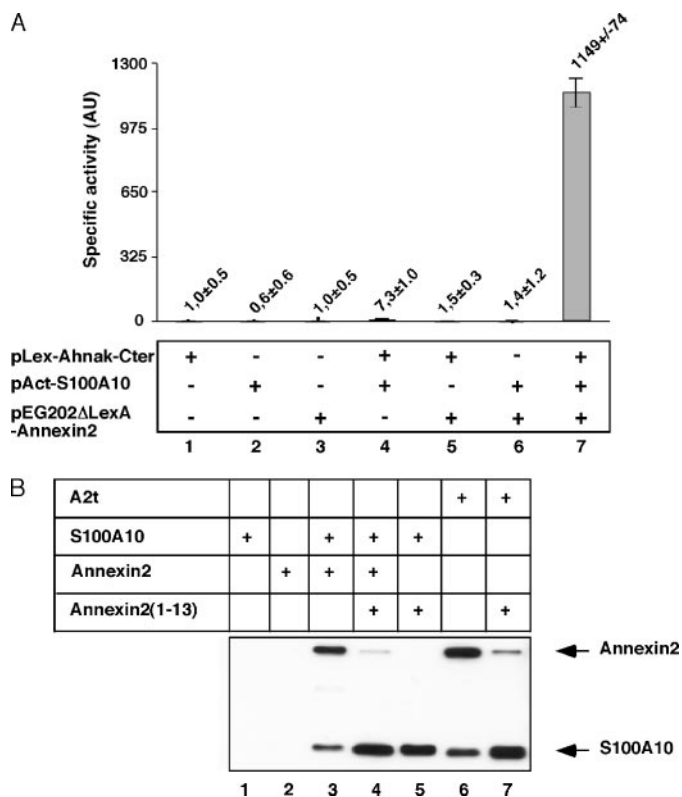


FIGURE 1. Tetramerization of S100A10 and Annexin2 is required for tight interaction with the Ahnak C-terminal domain. *A*, in yeast, the weak Ahnak-Cter/S100A10 interaction is drastically stimulated in the presence of Annexin2. Yeasts were co-transformed with pLex-Ahnak-Cter, pAct-S100A10, or/and pEG202ΔLexA-Annexin2 vectors as indicated. pLex-Lamin (lanes 2, 3, and 6), pAct (lanes 1, 3, and 5), and pEG202ΔLexA (lanes 1, 2, and 4) were used as negative control (–). The interactions were scored by β-galactosidase activity assays. Specific activities were obtained from three independent clones tested in triplicate (*n* = 9). *B*, Annexin2/S100A10 binding motif is involved in A2t/Ahnak C-ter interaction. Native A2t, isolated S100A10, Annexin2, and/or synthetic *N*-acetylated Annexin2 (1–13) peptide, were mixed as indicated with GST-Ahnak-Cter bound to glutathione-Sepharose. After washing, bound proteins were resolved by SDS-PAGE and detected by Western blot.

RESULTS

In a former study, we had shown that S100A10 mediates the interaction between A2t and the C-terminal domain of Ahnak (Ahnak C-ter) (33). However, the implication of Annexin2 in this interaction has not been investigated. To test whether Annexin2 is also involved in the interaction with Ahnak-Cter, we carried out yeast triple-hybrid experiments with the three components of the A2t-Ahnak complex. Because the N-terminal extremity of Annexin2 is crucial for its tetramerization with S100A10, we chose not to use it as a fusion protein. Instead, we expressed Annexin2 as a free molecule in addition to LexA-Ahnak-Cter and Gal4-S100A10 (33). By doing so, it was possible to analyze in yeast the effect of Annexin2 on Ahnak-Cter/S100A10 interaction. The interactions between Ahnak-Cter and S100A10 were then assessed in a quantitative manner through measurement of β-galactosidase activity. Results presented in Fig. 1*A* show that a subtle but detectable interaction is observed between S100A10 and Ahnak-Cter when they are expressed in the absence of Annexin2. However, when Annexin2 is co-expressed with LexA-Ahnak-Cter and Gal4-S100A10, the specific activity is dramatically increased by a fac-

tor of more than 150. No effect was seen when Annexin2 was expressed alone or solely with LexA-Ahnak-Cter or Gal4-S100A10. These results indicate that in eukaryotic cells, the presence of Annexin2 and thus, most likely, the formation of the tetramer, is required for efficient S100A10 interaction with Ahnak-Cter. In this complex, the interaction between S100A10 and Ahnak-Cter would be strengthened by Annexin2 through either direct interaction of Annexin2 with Ahnak-Cter or by modulation of the S100A10 affinity for Ahnak.

To investigate whether Annexin2 could directly interact with Ahnak-Cter and to further characterize the A2t interaction with Ahnak, we performed *in vitro* binding experiments. The C-terminal domain of Ahnak was produced as a GST-tagged protein and used in a pull-down assay. S100A10 and Annexin2 subunits isolated from pig intestine (see "Experimental Procedures") were added either individually or in combination in the binding assay. Under the conditions of the assay, no interaction of Ahnak with S100A10 nor with Annexin2 was detectable (Fig. 1B, lanes 1 and 2). As expected from the triple hybrid data, when S100A10 and Annexin2 are mixed together they readily bind to Ahnak-Cter (lane 3). To investigate whether the full-length Annexin2 protein or solely the S100A10 binding site on Annexin2 influences the binding of A2t to Ahnak, an *N*-acetylated Annexin2 peptide (amino acids 1–13) harboring the entire S100A10 binding site was tested in the assay (19). As shown in Fig. 1B (lane 5), the peptide mimicks the action of the full-length protein in allowing complex formation between S100A10 and Ahnak-Cter. We have verified the specificity of the peptide action through integration within A2t by testing its ability to compete with full-length Annexin2. When the peptide was added in the assay in the presence of S100A10 and in excess as compared with Annexin2, Annexin2 was displaced from the complex (Fig. 1B, upper lane 4) although S100A10 is still present (Fig. 1B, bottom lane 4). Noticeably, a stronger interaction of S100A10 with Ahnak-Cter was detected in the presence of Annexin2 peptide than in the presence of full-length Annexin2 (compare lanes 3 and 4). This observation suggests that in A2t, it is the S100A10 binding domain of Annexin2 that stimulates the interaction with Ahnak. However, because Annexin2 and S100A10 used in this experiment were subjected to a denaturation/renaturation protocol (see "Experimental Procedures"), we could not exclude the possibility of an artifact caused by improper refolding. We therefore performed the experiment with the native A2t complex. Here again, the Annexin2 peptide by dissociating the complex and replacing Annexin2, induces S100A10 binding to Ahnak (Fig. 1B, lanes 6 and 7). Altogether, these data indicate that, by binding to S100A10, Annexin2 creates conditions for a strong S100A10/Ahnak interaction. We can envision that this effect is due either to a change in the S100A10 conformation or to the formation of a binding platform at the interface between S100A10 and the Annexin2 N-terminal peptide.

To map the A2t binding domain on Ahnak-Cter, we compared the interaction of A2t with a series of GST-Ahnak-Cter deletion mutants by pull-down assays (Fig. 2A). Using this strategy, we mapped the A2t binding sequence in Ahnak-Cter to a 20-amino acid peptide comprising residues 5645–5673 (Fig. 2A). When further deletions of 5 or 9 residues from the N- or

C-terminal extremity, respectively, were made, the peptide lost its binding properties, indicating that these residues are crucial for the interaction. This 20-amino acid peptide that binds A2t will hereafter be referred to as A2tBP1 (for A2t Binding Peptide 1). GST pull-down assay, using cytoplasmic extracts of MDCK cells metabolically labeled with [³⁵S]methionine/cysteine, showed that A2tBP1 is equivalent to Ahnak-Cter for its ability to bind A2t (Fig. 2B, left panel, lanes 3 and 4). Annexin2 and S100A10 whose identity was assessed by Western blot bound specifically and to a similar extent to both GST fusion constructs (Fig. 2B, right panel). Furthermore, a synthetic A2tBP1 readily antagonized the interaction between GST-Ahnak-Cter and the A2t (Fig. 2C), confirming that A2tBP1 constitutes the entire A2t binding domain of GST-Ahnak-Cter. More importantly, Fig. 2B (left panel) indicates that Annexin2 and S100A10 are the major if not the only proteins pulled-down by GST-Ahnak-Cter and GST-A2tBP1. Using GST-A2tBP1 bound to a biosensor chip via anti-GST antibodies, we next analyzed the kinetics of binding of purified native A2t complex to GST-A2tBP1 (Fig. 2D). The sensorgram shows a fast binding and a slow release kinetics indicating a high affinity between GST-A2tBP1 and A2t. Indeed, the k_a and k_d derived from three different curves ranged from 5 to 16×10^4 (k_a) and 2.3 to 2.6×10^{-3} (k_d), which gives a K_d of $3(\pm 1.5) \times 10^{-8}$ (see "Experimental Procedures"). The high affinity of A2t binding to A2tBP1 with a k_d of 2.4×10^{-3} is consistent with the observation that, while the A2tBP1 synthetic peptide efficiently competed with Ahnak-Cter for binding to A2t (Fig. 2C), it only weakly displaced A2t from GST-Ahnak-Cter/A2t or GST-A2tBP1/A2t preformed complex (data not shown). To conclude, we have identified the minimal domain in the C-terminal domain of Ahnak that binds specifically and with a high affinity to the A2t complex.

To identify other A2t-specific binding partners, we searched in data banks for proteins containing motifs homologous to A2tBP1. Surprisingly, in addition to Ahnak A2tBP1 from other mammalian species, only two peptides both belonging to Ahnak molecules showed significant homology with A2tBP1. The A2tBP1 sequence is strictly conserved in the C-terminal domain of all mammalian Ahnak for which sequences are available, indicating that this sequence is probably necessary for the function of the molecule. The two other sequences homologous to A2tBP1 are located at two different sites within the N-terminal domain of Ahnak. In human Ahnak, the first peptide corresponding to residues 302–321 shows 65% identity/75% homology with the A2tBP1 peptide (Fig. 3A, upper lanes). Its conservation among mammalian species ranges from 65% identity (*Rattus versus Canis*) to 90% identity (human *versus Taurus*). The second peptide localized at position 426–447 of human Ahnak harbors 50% identity/65% homology with A2tBP1 (Fig. 3A, bottom lanes). Among mammalian Ahnak proteins, this domain is also well conserved when compared with the human sequence with 68% identity/78% homology to 81% identity/95% homology for the *Rattus* and the *Canis* sequences, respectively. These homologies with A2tBP1 and conservation during evolution prompted us to investigate by GST pull-down assays using MDCK cell extracts, whether

A2t-specific Binding Motif

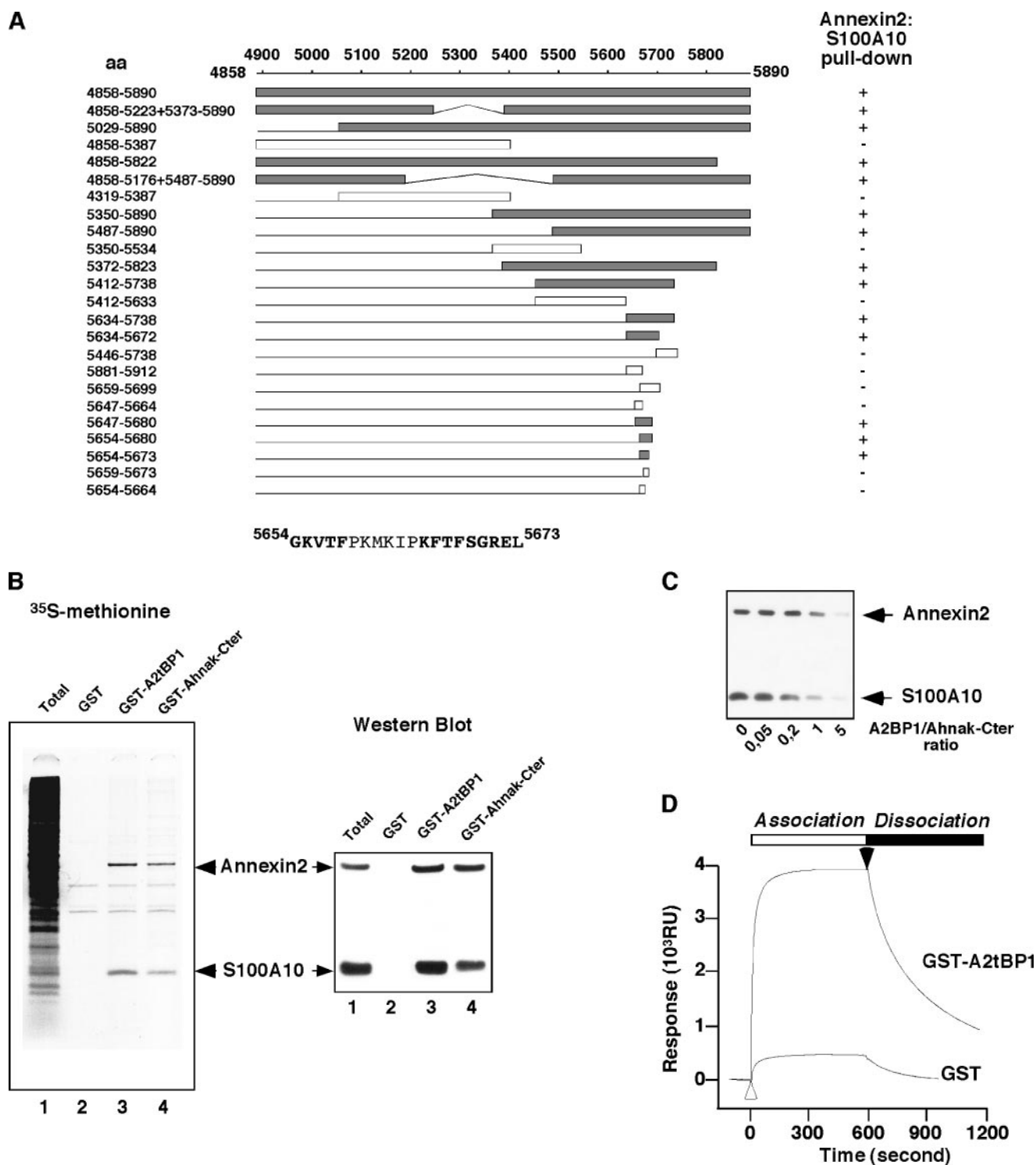


FIGURE 2. Identification of a 20-amino acid motif on Ahnak C-ter specific for S100A10/Annexin2 complex. *A*, mapping of a 20-amino acid motif from Ahnak C-ter that interacts with the A2t complex. GST-Ahnak C-terminal domain or deletion mutants (as indicated) were bound to glutathione-Sepharose and incubated with MDCK cell extract. After pull-down, and washing, bound Annexin2 and S100A10 proteins were resolved by SDS-PAGE and detected by Western blot. The presence of bound Annexin2 and S100A10 detected by Western blot is indicated on the right and by a gray box on the schematic representation of the Ahnak. Amino acid positions of the fragments within the Ahnak full-length sequence is indicated on the left. The sequence of the smallest fragment competent for Annexin2/S100A10 binding corresponding to Ahnak(5645–5673) is presented on the bottom. **Bold letters** indicate residues whose deletion impaired Annexin2/S100A10 binding. *B*, Annexin2 and S100A10 are specific Ahnak C-ter and A2tBP1 targets. [³⁵S]methionine/cysteine-labeled MDCK whole cell extracts (lane 1) were incubated with GST (lane 2) and GST-A2tBP1 (lane 3) or GST-Ahnak C-ter (lane 4) bound to glutathione-Sepharose. Interacting proteins were resolved on SDS-PAGE and detected by autoradiography (left panel) or Western blot using anti-Annexin2 and anti-S100A10 monoclonal antibodies (right panel). *C*, A2t binding strength of A2tBP1 is comparable to that of Ahnak C-ter. MDCK cell extracts were incubated with GST fusion Ahnak C-ter in the absence or in the presence of increasing A2tBP1 concentrations. Bound proteins were analyzed by Western blotting using anti-Annexin 2 and anti-S100A10 antibodies. The molar A2tBP1/Ahnak C-ter ratio is indicated. *D*, real-time surface plasmon resonance recording. The association curve (light box) of the sensorgrams were recorded after injection (light arrowhead) of A2t (595 nm) onto GST-A2tBP1 (upper curve) or GST (lower curve) immobilized on the sensor chip. After 10 min, A2t injection was stopped (dark arrowhead), and the dissociation curve was recorded (dark box).

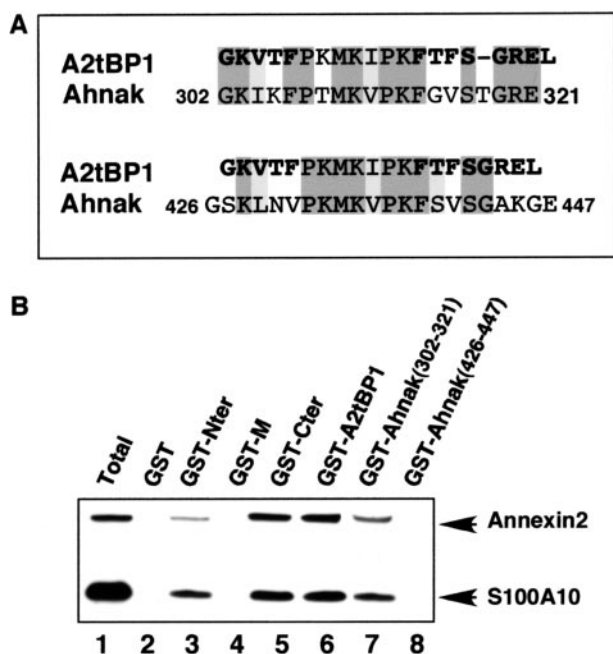


FIGURE 3. Identification of a second A2t binding motif in the Ahnak protein. A, comparison of A2tBP1 with Ahnak residues 302–321 (upper lanes) and 426–447 (bottom lanes). Dark gray and light gray indicate identical and homologue residues, respectively. B, GST-Ahnak N-terminal domain and GST-Ahnak residues 302–321 bind to S100A10 and Annexin2. GST alone (lane 2) or fused to the N terminus (lane 3), part of the median domain (M, lane 4), the C-terminal domain (lane 5), A2tBP1 (lane 6), Ahnak-(302–321) (lane 7), and Ahnak-(426–447) (lane 8) were used in the pull-down assay with MDCK cell extracts. Bound S100A10 and Annexin 2 were detected by Western blot.

these two peptide motifs could interact with A2t. As shown in Fig. 3B, the C-terminal domain and A2tBP1 interacted significantly with A2t in these assays (lanes 5 and 6; see also Fig. 1). The N-terminal domain containing the two putative binding sequences also interacted with A2t (lane 3) even though its affinity for A2t seemed lower than that of the C-terminal domain. The peptide corresponding to residues 302–321 of human Ahnak bound to A2t to a similar extent as the N-terminal domain from which it is derived (lane 7). In contrast, the peptide 426–447 of human Ahnak did not interact detectably with A2t (lane 8). GST alone and the median domain (M) of Ahnak containing 4 Ahnak internal repeats (38), used as controls, did not show any interaction with A2t. Taken together, these data indicate the existence, in Ahnak, of a second sequence closely related to A2tBP1 and capable of interacting with A2t, albeit with a slightly less avidity than A2tBP1. This A2t binding domain was called A2tBP2.

To confirm that in eukaryotic cells, A2tBPs interact with A2t, the peptide-coding sequences were cloned in-fusion with the EGFP gene, and stable transformants of MDCK cells were obtained. Because A2t has been shown to interact with the membranous fraction in a calcium-dependent manner, the cells were lysed either in the presence of calcium or in the presence of EGTA. Cellular debris including membranes were pelleted, and partitioning of A2t subunits and A2tBPs into the pellet and in the supernatant was analyzed by Western blot. Results presented in Fig. 4A show that as expected, Annexin2 and S100A10 are essentially present within the pelletable fraction in the pres-

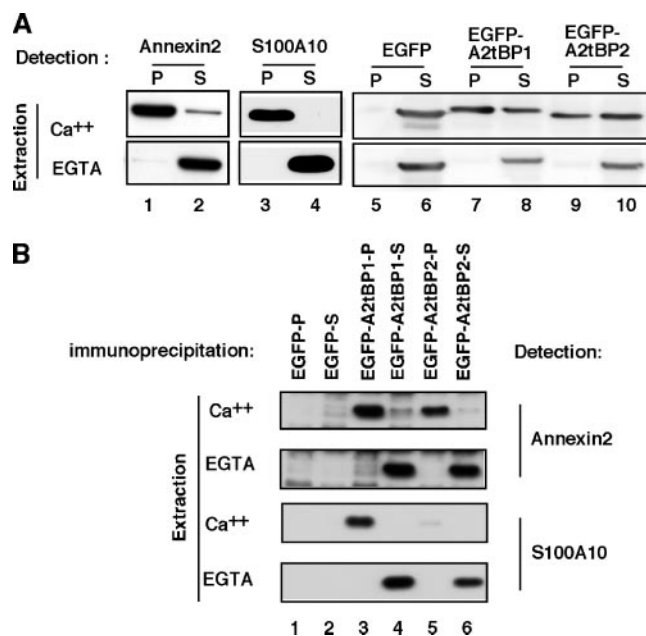


FIGURE 4. EGFP-A2tBP1 interacts with S100A10 and Annexin2 in MDCK cells. A, EGFP-A2tBP1 expressed in MDCK cells co-fractionate in a calcium-dependent manner with Annexin2 and S100A10. MDCK cells stably transformed with EGFP (lanes 1–6), EGFP-A2tBP1 (lanes 7 and 8), or EGFP-A2tBP2 (lanes 9 and 10) were lysed in the presence of 0.3 mM Ca^{2+} (upper panel) or 1 mM EGTA (lower panel). Lysates were spun down, and pellets (P) and supernatants (S) were analyzed by Western blot using anti-Annexin2 (lanes 1 and 2), anti-S100A10 (lanes 3 and 4), or anti-EGFP (lanes 5–10). B, EGFP-A2tBP1 co-immunoprecipitates with Annexin2 and S100A10. Calcium concentration of the pellets (lanes 1, 3, 5, and 7) and supernatants (lanes 2, 4, 6, and 8) from A were adjusted to 0.3 mM. EGFP (lanes 1 and 2), EGFP-A2tBP1 (lanes 3 and 4), and EGFP-A2tBP2 (lanes 5 and 6) were immunoprecipitated using anti-EGFP antibodies, and the presence of co-immunoprecipitated Annexin2 (two upper panels) and S100A10 (two bottom panels) was analyzed by Western blot.

ence of calcium (compare upper lanes 1 to 2 and 3 to 4). In contrast, in the presence of EGTA, both were found in the supernatant (lanes 2 and 4) and not in the pellet (lanes 1 and 3). When we analyzed the fractionation of EGFP fusion peptides, we observed that A2tBP1 and to a lesser extent A2tBP2 promote a calcium-dependent association of EGFP with the pelletable fraction. Whereas EGFP alone distributed into the supernatant fraction independently of the presence of calcium (lanes 5 and 6), A2tBP1 and 2 fused to EGFP were found in the pelletable fraction in the presence of calcium (compare bottom lanes 7 to 10). A2tBP2 showed a less prominent recruitment compared with EGFP-A2tBP1. These data indicate that calcium promotes a recruitment of Annexin2, S100A10, A2tBP1, and to a lesser extent A2tBP2 to insoluble cellular components. Because this effect has already been shown for A2t (39) and given the binding specificity and affinity of A2tBP1 for A2t, we can assume that in these experiments, A2tBPs fractionation is dependent on their interaction with A2t. We then carried out co-immunoprecipitation experiments to confirm the *in vivo* interaction of A2t with A2tBPs in MDCK cells (Fig. 4B). For this purpose, we used protein fractions obtained under the same (Ca^{2+} /EGTA) conditions as described above. Fig. 4B shows that Annexin2 and S100A10 present in the calcium pellet (Fig. 4A, lanes 1 and 3) or in the EGTA supernatant (Fig. 4A, lanes 2 and 4) co-immunoprecipitated with EGFP-A2tBP1 (Fig. 4B, lanes 7 and 8) and to a lesser extent with EGFP-A2tBP2 (Fig. 4B,

A2t-specific Binding Motif

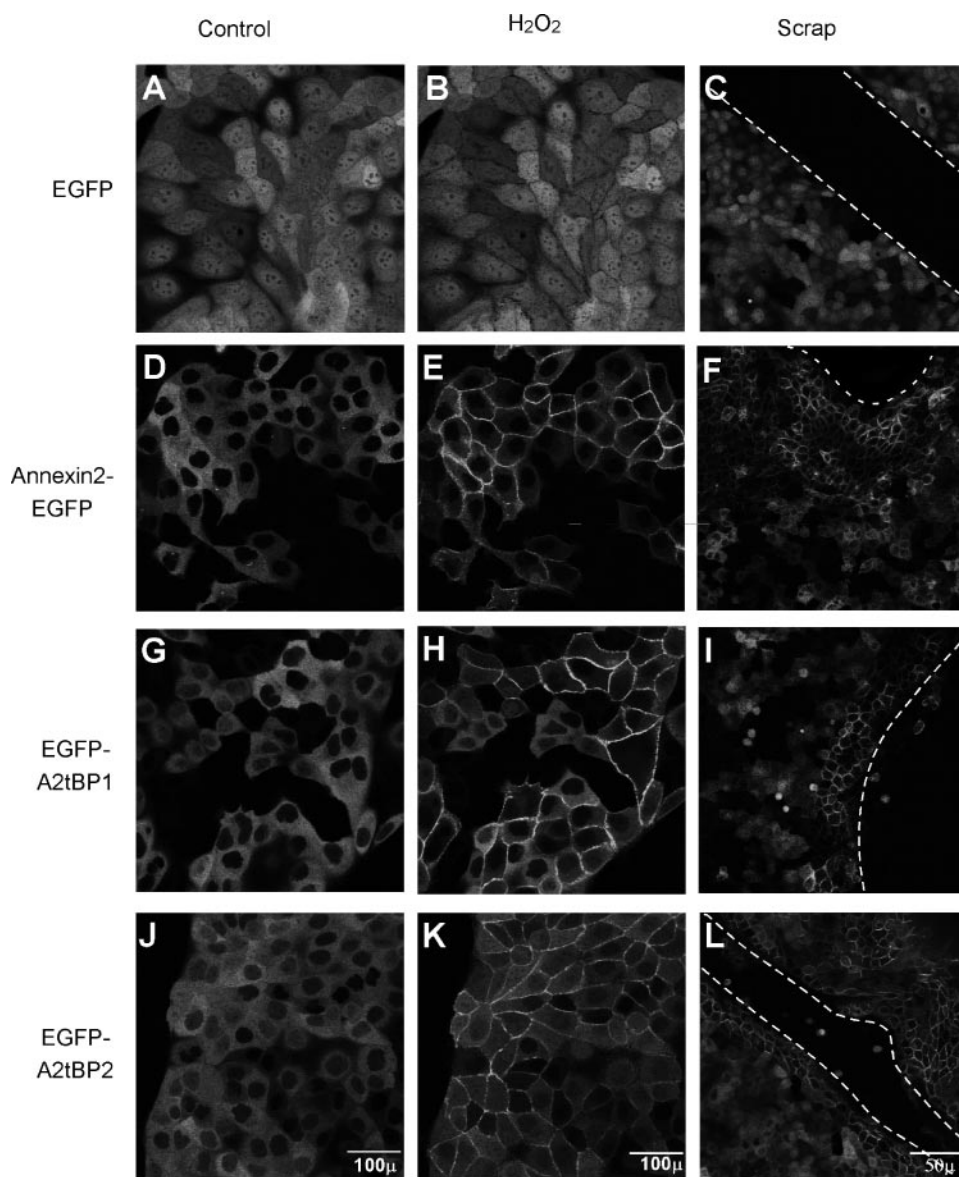


FIGURE 5. Annexin2 and A2tBP1 re-localize from the cytosol to the plasma membrane in response to cellular stress. MDCK cells stably transfected with EGFP, Annexin2-EGFP, EGFP-A2tBP1 and 2 as indicated were either treated with 1 mM H₂O₂ or scraped (*Scrap*) with a fine tip pastette (*dotted line*). EGFP fluorescence of living cells was recorded after 5 min with a confocal microscope. Scale bars indicated in the *bottom panels* are of 100 micrometers in control and H₂O₂ treatments and 50 micrometers for the scraping experiments.

lanes 9 and 10). As expected, Annexin2 and S100A10 were not found associated to immunoprecipitated EGFP (Fig. 4A, lane 6) present in the EGTA supernatant (Fig. 4B, lane 2). Together, these data indicate that in MDCK cells, overexpressed A2tBP1 is associated in a tight complex with A2t.

To test whether A2tBP1 could be used to trace A2t within cells, we carried out live fluorescence analysis of EGFP-A2tBPs and Annexin2-EGFP overexpressed in MDCK (Fig. 5). As previously described, EGFP alone was localized throughout the cells with an accumulation within the nucleus (*panel A*). When EGFP was fused to Annexin2, its localization became essentially cytoplasmic (*panel D*). A2tBPs also targeted EGFP to the cytoplasm (*panels G and J*) as expected if they were to interact in the cytoplasm with A2t. Annexin2 was shown to be relocalized in response to oxidative stress (40). We therefore tested whether

Annexin2-EGFP and EGFP-A2tBPs localization under our cellular conditions would change in response to H₂O₂ treatment. As shown in *panels E, H, and K*, H₂O₂ treatment led to a fast re-localization to the plasma membrane of Annexin2-EGFP and EGFP-A2tBP1 and 2, respectively. Localization changes were observable after 2 min of treatment (data not shown) and completed after 5 min. These modifications of intracellular localization were entirely reversible when transferring the cells back to fresh culture medium (data not shown). We notice that in agreement with its weaker interaction with A2t, A2tBP2 was less efficient than A2tBP1 in targeting EGFP to the cytoplasm in resting cells (compare *panels G and J*) and to the plasma membrane of H₂O₂-treated cells (compare *panels H and K*). The contrast in EGFP fluorescence between the nucleus and the cytoplasm under both conditions and between the cytoplasm and the plasma membrane in treated cells is stronger with EGFP-A2tBP1 than with EGFP-A2tBP2. We also tested the response of the EGFP fusion proteins to a mechanical stress induced by wounding of a cell monolayer. Here again, Annexin2-EGFP, EGFP-A2tBP1, and EGFP-A2tBP2 within the cells close to the wound re-localized to the plasma membrane during the few minutes required for the observation (*panels F, I, and L*, respectively). Neither H₂O₂ nor wounding had any effect on GFP cellular distribution. It is interesting to note that

these relocalization events are detectable only in living cells since after fixation and immunodetection, EGFP-A2tBP1, Annexin2-EGFP, and endogenous Annexin2 are essentially detected at the plasma membrane in resting cells (data not shown). Together, these data indicate that EGFP-A2tBP1 expressed in MDCK follows the Annexin2-EGFP localization. Given our previous data indicating that A2tBP1 binding is specific for A2t, we can assume that EGFP-A2tBP1 localization is dependent on and reflects the endogenous A2t localization.

DISCUSSION

In this article, we have shown that efficient S100A10 interaction with Ahnak requires its tetramerization with Annexin2. The fact that the Annexin2 contribution localizes to the first 13 amino acids of Annexin2 corresponding to its S100A10 binding

site suggests that it might act by changing the conformation of S100A10 and thereby increasing S100A10 affinity for Ahnak. The crystal structure of the S100A10 dimer alone or in complex with the Annexin2 binding site has been solved (20). S100A10, as the other members of the S100 proteins, is composed of two EF-hand motifs linked by a flexible loop. In the S100A10 dimer, the flexible loop (L2) of each subunit adopts a different conformation leading to an asymmetric structure. In the complex, the two S100A10 molecules adopt the same conformation in which the flexible loops form short stretch of α -helices implicated in part in binding to the Annexin2 peptide. Such a conformational change could explain the increase in the interaction of the Annexin2 peptide-S100A10 complex with Ahnak. However, when bound to S100A10, the Annexin2 peptide is exposed to the surface of the complex. We thus cannot exclude that it may form together with S100A10 a platform in which each subunit would participate to Ahnak binding. A2t formed with full-length Annexin2 is less efficient in binding Ahnak than the Annexin2 peptide-S100A10 complex. One can speculate that this difference is caused by steric constraint for the formation of the A2t/Ahnak-Cter complex providing a way for A2t to modulate its binding with its targets through a change in Annexin2 conformation. Crystallographic studies would be useful to reveal the real nature of A2t binding to its targets. Co-crystallization of S100A10 with full-length Annexin2 has not been achieved to date. This might be because of the flexibility between the N-terminal S100A10 binding region and the core domain. In this regard, A2tBP1 might be a powerful tool for a co-crystallization assay with A2t.

A2tBP1 was identified in this report as a twenty amino acid peptide in AhnakC-ter that mediates the interaction with A2t. A2tBP1 is the first binding motif specific for the tetramer characterized to date. This peptide is 100% conserved among different mammalian Ahnak species, indicating that it is likely to be involved in key functions. Because the only cellular binding partners detected for A2tBP1 are the A2t subunits, we propose that Ahnak binding to A2t is required for crucial cellular functions probably including the targeting of Ahnak to cholesterol-rich membrane domains and the establishment of cell polarity (33). Surprisingly, the only two motifs found in data banks as homologs of A2tBP1 are in the Ahnak molecule itself. No homology was found when comparing A2tBP1 to known S100A10 or Annexin2 targets (data not shown) suggesting that they probably do not share the same mode of interaction with A2t. Among the two A2tBP1 homologous peptides that are localized in the N-terminal domain of Ahnak, only one, named A2tBP2 interacts *in vitro* with A2t, albeit with a lower apparent binding affinity for A2t than A2tBP1. Unfortunately, sequence comparison could not clearly point out specific residues of A2tBP1 conserved in A2tBP2 and absent from the third non-A2t-interacting homologue (data not shown). Identification of A2tBP1 residues involved in the interaction with A2t will require mutagenesis or structural investigations.

We have shown that A2tBP1 binds specifically and with high affinity to the A2t complex but not to the individual S100A10 or Annexin2 subunits. A2t was the only detectable A2tBP1 cellular binding partner in GST pull-down assays

using metabolically labeled cell extracts. In addition, EGFP-A2tBP1 co-fractionated in a calcium-dependent manner and co-immunoprecipitated with S100A10 and Annexin2. These data suggest that EGFP-A2tBP1 could be used to follow A2t localization in living cells. Indeed, EGFP-A2tBP1 localization is identical to that of Annexin2-EGFP in resting cells and changes with the same dynamics as Annexin2-EGFP upon cellular stress. Given our previous data, we can reasonably assume that it is the interaction of A2tBP1 with endogenous A2t that is responsible for EGFP-A2tBP1 localization in cells. This statement is strengthened by the observation that A2tBP2, which has a reduced binding affinity to A2t, is also less efficient in targeting EGFP to sites of Annexin2 localization.

Because, A2t is thought to be involved in membrane trafficking/remodeling and is likely to associate with various cellular components including small organelles (5–9,41), the identification of its cellular location is of major importance to study its mechanisms of action. Carrying out live imaging experiments will be required to study dynamic events in which endogenous A2t takes part and to avoid artifacts caused by immunodetection techniques. We believe that EGFP-A2tBP1 might constitute a critical tool to dissect functions strictly involving the complex and not the individual subunits. In this respect, our live experiments strongly suggest that A2t complex exists in the cytoplasm of resting cells and that its plasma membrane localization relies on cellular signaling.

The subunit of A2t, which is implicated in membrane binding, may depend on the cellular context. It has been shown in chromaffin cells that p11 is constitutively expressed at the subplasmalemmal region of the cell and that Annexin2 plasma membrane localization relies on nicotinic activation and calcium rise (42). In huvec, S100A10 is required for cell surface translocation of Annexin2 upon temperature stress (43). In contrast, in living HepG2 cells, Annexin2 is the subunit that mediates A2t complex binding to the plasma membrane (44).

Several mechanisms can be envisioned to participate in the stress-induced A2t targeting to the plasma membrane. On the one hand, because A2t interaction with the membrane is calcium-dependent and because both H₂O₂ treatment (45) and cellular wounding (46) can induce a rapid increase of intracellular calcium, one can speculate that the observed membrane localization of A2t is caused by transient calcium increase. On the other hand, oxidation treatment as well as wounding (47) may induce alteration of some membrane lipids such as peroxidation (48) that would promote binding of A2t. Alternatively, stress-induced A2t membrane localization could involve direct modification of Annexin2 such as tyrosine phosphorylation (43).

Acknowledgments—We thank Drs. Zhuxiang Nie and Takashi Hashimoto for the pC-DY plasmid, Dr. Marc Borsotto for the pGEMTp36 plasmid, and Dr. Stephen Moss for the Annexin2-EGFP plasmid. We are indebted to Dr. Gerard Klein for the analysis of real-time plasmon resonance data. We gratefully acknowledge Dr. Jean-Christophe Deloulme and Dr. Laurence Aubry for critical analysis of the manuscript.

REFERENCES

- Gerke, V., Creutz, C. E., and Moss, S. E. (2005) *Nat. Rev. Mol. Cell. Biol.* **6**, 449–461
- Raynal, P., and Pollard, H. B. (1994) *Biochim. Biophys. Acta* **1197**, 63–93
- Gerke, V., and Moss, S. E. (1997) *Biochim. Biophys. Acta* **1357**, 129–154
- Swairjo, M. A., and Seaton, B. A. (1994) *Annu. Rev. Biophys. Biomol. Struct.* **23**, 193–213
- Emans, N., Gorvel, J. P., Walter, C., Gerke, V., Kellner, R., Griffiths, G., and Gruenberg, J. (1993) *J. Cell Biol.* **120**, 1357–1369
- Harder, T., Kellner, R., Parton, R. G., and Gruenberg, J. (1997) *Mol. Biol. Cell* **8**, 533–545
- Jost, M., Zeuschner, D., Seemann, J., Weber, K., and Gerke, V. (1997) *J. Cell Sci.* **110**, 221–228
- Diakonova, M., Gerke, V., Ernst, J., Liautard, J. P., van der Vusse, G., and Griffiths, G. (1997) *J. Cell Sci.* **110**, 1199–1213
- Merrifield, C. J., Rescher, U., Almers, W., Proust, J., Gerke, V., Sechi, A. S., and Moss, S. E. (2001) *Curr. Biol.* **11**, 1136–1141
- Ali, S. M., Geisow, M. J., and Burgoyne, R. D. (1989) *Nature* **340**, 313–315
- Sarafian, T., Pradel, L. A., Henry, J. P., Aunis, D., and Bader, M. F. (1991) *J. Cell Biol.* **114**, 1135–1147
- Harder, T., and Gerke, V. (1993) *J. Cell Biol.* **123**, 1119–1132
- Knop, M., Aareskjold, E., Bode, G., and Gerke, V. (2004) *EMBO J.* **23**, 2982–2992
- Mayorga, L. S., Beron, W., Sarrouf, M. N., Colombo, M. I., Creutz, C., and Stahl, P. D. (1994) *J. Biol. Chem.* **269**, 30927–30934
- Glennay, J. (1986) *J. Biol. Chem.* **261**, 7247–7252
- Glennay, J. R., Jr., Tack, B., and Powell, M. A. (1987) *J. Cell Biol.* **104**, 503–511
- Powell, M. A., and Glennay, J. R. (1987) *Biochem. J.* **247**, 321–328
- Becker, T., Weber, K., and Johnsson, N. (1990) *EMBO J.* **9**, 4207–4213
- Johnsson, N., Marriott, G., and Weber, K. (1988) *EMBO J.* **7**, 2435–2442
- Rety, S., Sopkova, J., Renouard, M., Osterloh, D., Gerke, V., Tabaries, S., Russo-Marie, F., and Lewit-Bentley, A. (1999) *Nat. Struct. Biol.* **6**, 89–95
- Gerke, V., and Weber, K. (1985) *EMBO J.* **4**, 2917–2920
- Gerke, V., and Moss, S. E. (2002) *Physiol. Rev.* **82**, 331–371
- Santamaria-Kisiel, L., Rintala-Dempsey, A. C., and Shaw, G. S. (2006) *Biochem. J.* **396**, 201–214
- Jones, P. G., Moore, G. J., and Waisman, D. M. (1992) *J. Biol. Chem.* **267**, 13993–13997
- Ryzhova, E. V., Vos, R. M., Albright, A. V., Harrist, A. V., Harvey, T., and Gonzalez-Scarano, F. (2006) *J. Virol.* **80**, 2694–2704
- Smart, E. J., De Rose, R. A., and Farber, S. A. (2004) *Proc. Natl. Acad. Sci. U. S. A.* **101**, 3450–3455
- Nilius, B., Gerke, V., Prenen, J., Szucs, G., Heinke, S., Weber, K., and Droogmans, G. (1996) *J. Biol. Chem.* **271**, 30631–30636
- Okuse, K., Malik-Hall, M., Baker, M. D., Poon, W. Y., Kong, H., Chao, M. V., and Wood, J. N. (2002) *Nature* **417**, 653–656
- van de Graaf, S. F., Hoenderop, J. G., Gkika, D., Lamers, D., Prenen, J., Rescher, U., Gerke, V., Staub, O., Nilius, B., and Bindels, R. J. (2003) *EMBO J.* **22**, 1478–1487
- Girard, C., Tinel, N., Terrenoire, C., Romey, G., Lazdunski, M., and Borsoffo, M. (2002) *EMBO J.* **21**, 4439–4448
- Poon, W. Y., Malik-Hall, M., Wood, J. N., and Okuse, K. (2004) *FEBS Lett.* **558**, 114–118
- Donier, E., Rugiero, F., Okuse, K., and Wood, J. N. (2005) *J. Biol. Chem.* **280**, 38666–38672
- Benaud, C., Gentil, B. J., Assard, N., Court, M., Garin, J., Delphin, C., and Baudier, J. (2004) *J. Cell Biol.* **164**, 133–144
- Jones, A. T., and Wessling-Resnick, M. (1998) *J. Biol. Chem.* **273**, 25301–25309
- Gerke, V., and Weber, K. (1985) *J. Biol. Chem.* **260**, 1688–1695
- Mikhailenko, I., Krylov, D., Argraves, K. M., Roberts, D. D., Liau, G., and Strickland, D. K. (1997) *J. Biol. Chem.* **272**, 6784–6791
- Deloulme, J. C., Assard, N., Mbele, G. O., Mangin, C., Kuwano, R., and Baudier, J. (2000) *J. Biol. Chem.* **275**, 35302–35310
- Gentil, B. J., Delphin, C., Mbele, G. O., Deloulme, J. C., Ferro, M., Garin, J., and Baudier, J. (2001) *J. Biol. Chem.* **276**, 23253–23261
- Liu, L., Tao, J. Q., and Zimmerman, U. J. (1997) *Cell Signal* **9**, 299–304
- Matsuda, D., Nakayama, Y., Horimoto, S., Kuga, T., Ikeda, K., Kasahara, K., and Yamaguchi, N. (2006) *Exp. Cell Res.* **312**, 1205–1217
- Eberhard, D. A., Karns, L. R., VandenBerg, S. R., and Creutz, C. E. (2001) *J. Cell Sci.* **114**, 3155–3166
- Chasserot-Golaz, S., Vitale, N., Sagot, I., Delouche, B., Dirrig, S., Pradel, L. A., Henry, J. P., Aunis, D., and Bader, M. F. (1996) *J. Cell Biol.* **133**, 1217–1236
- Deora, A. B., Kreitzer, G., Jacovina, A. T., and Hajjar, K. A. (2004) *J. Biol. Chem.* **279**, 43411–43418
- Zobiack, N., Gerke, V., and Rescher, U. (2001) *FEBS Lett.* **500**, 137–140
- Burlando, B., and Viarengo, A. (2005) *Cell Calcium* **38**, 507–513
- Hinman, L. E., Beilman, G. J., Groehler, K. E., and Sammak, P. J. (1997) *Am. J. Physiol.* **273**, L1242–L1248
- Moldovan, L., Moldovan, N. I., Sohn, R. H., Parikh, S. A., and Goldschmidt-Clermont, P. J. (2000) *Circ. Res.* **86**, 549–557
- Spiteller, G. (2006) *Free Radic. Biol. Med.* **41**, 362–387

Specific AHNAK Expression in Brain Endothelial Cells With Barrier Properties

BENOÎT J. GENTIL,¹ CHRISTELLE BENAUD,¹ CHRISTIAN DELPHIN,¹ CHANTAL REMY,³
VINCENT BEREZOWSKI,⁴ ROMÉO CECHELLI,⁴ OLIVIER FERAUD,²
DANIEL VITTE,² AND JACQUES BAUDIER^{1*}

¹Laboratoire de Transduction du Signal INSERM EMI-0104, Grenoble, France

²Laboratoire du Développement et Vieillesse de l'endothélium EMI-0219,
DRDC CEA-Grenoble, Grenoble, France

³Laboratoire de Résonance Magnétique Nucléaire Bioclinique,
INSERM U438 La Tronche, France

⁴Laboratoire mixte Université d'Artois-Institut Pasteur de Lille (EA 2465),
Faculté des Sciences Jean Perrin, Lens, France

The blood–brain barrier (BBB) is essential for maintaining brain homeostasis and low permeability. Because disruption of the BBB may contribute to many brain disorders, they are of considerable interests in the identification of the molecular mechanisms of BBB development and integrity. We here report that the giant protein AHNAK is expressed at the plasma membrane of endothelial cells (ECs) forming specific blood–tissue barriers, but is absent from the endothelium of capillaries characterized by extensive molecular exchanges between blood and extracellular fluid. In the brain, AHNAK is widely distributed in ECs with BBB properties, where it co-localizes with the tight junction protein ZO-1. AHNAK is absent from the permeable brain ECs of the choroid plexus and is down-regulated in permeable angiogenic ECs of brain tumors. In the choroid plexus, AHNAK accumulates at the tight junctions of the choroid epithelial cells that form the blood–cerebrospinal fluid (CSF) barrier. In EC cultures, the regulation of AHNAK expression and its localization corresponds to general criteria of a protein involved in barrier organization. AHNAK is up-regulated by angiotensin-1 (Ang-1), a morphogenic factor that regulates brain EC permeability. In bovine cerebral ECs co-cultured with glial cells, AHNAK relocates from the cytosol to the plasma membrane when endothelial cells acquire BBB properties. Our results identify AHNAK as a protein marker of endothelial cells with barrier properties. *J. Cell. Physiol.* 203: 362–371, 2005.

© 2004 Wiley-Liss, Inc.

The giant phosphoprotein AHNAK (also called desmoyokin; Mr 700 kDa) was first identified in two independent studies as a component of desmosomal attachment plaques in stratified skin epithelium (Hieda and Tsukita, 1989; Hashimoto et al., 1993) and as a gene whose transcription is repressed in neoplastic neuroblasts, in comparison to differentiated derivatives of the neuroectodermal lineage (Shtivelman et al., 1992). More recently in rodent fibroblasts, the transcription of AHNAK was found to be subject to a strong down-regulation by transforming Ras alleles (Zuber et al., 2000). AHNAK has also been found associated with a new type of vesicles called “enlargosomes.” Enlargosome have been proposed to participate in cell membrane differentiation and repair (Borgonovo et al., 2002). In epithelial cell model, the protein AHNAK relocates from the cytosol to the cytosolic surface of the plasma membrane during the formation of cell–cell contacts and the development of epithelial polarity (Sussman et al., 2001). This targeting is reversible and regulated by Ca²⁺-dependent cell–cell adhesion (Benaud et al., 2004). At the plasma membrane AHNAK associates as a multimeric complex with actin (Hohaus et al., 2002) and the annexin 2/S100A10 complex (Benaud et al., 2004). In epithelial cells, the preferential association of AHNAK with lipid raft domains of the plasma membrane suggests that AHNAK could be implicated in regulation of signaling pathways that are compartmentalized within these microdomains (Benaud et al., 2004). Several others putative interacting proteins for AHNAK have been identified in vitro, including PLCgamma (Sekiya et al., 1999), the beta subunit of cardiac L-type calcium channels (Haase et al., 1999), and the brain specific

calcium- and zinc-binding protein S100B abundantly expressed in the perivascular processes of astrocytic dendrites (Gentil et al., 2001).

One approach to further delineate the biological functions of AHNAK is to analyze its expression and localization in tissues. In adult mouse, AHNAK is expressed at the plasma membrane of most muscular cells including cardiomyocytes, skeletal muscle cells, smooth muscle cells, fibromyocytes, and myoepithelial cells. AHNAK is also highly expressed at the plasma membrane of epithelia that define body compartments and form physical barriers where passive diffusion is limited (Hashimoto et al., 1995; Benaud et al., 2004). We here show that AHNAK is also specifically expressed in ECs with specific blood–tissue barriers properties, but is absent from the endothelium of capillaries characterized by extensive molecular exchanges between blood and extracellular fluid. We also show that, in embryonic stem (ES) cell-derived endothelial cells, AHNAK expression and

Benoît J. Gentil and Christelle Benaud contributed equally to this study.

Contract grant sponsor: Association pour la Recherche contre le Cancer.

*Correspondence to: Jacques Baudier, TS/INSERM EMI 0104/DRDC, CEA Grenoble, 17 rue des Martyrs, 38054 Grenoble Cedex 9, France. E-mail: jbaudier@cea.fr

Received 27 May 2004; Accepted 2 September 2004

DOI: 10.1002/jcp.20232

membrane localization is stimulated by angiopoietin-1 (Ang-1). Ang-1 is considered as a key molecule responsible for astrocyte-mediated brain vascular remodeling that regulates brain endothelial cell permeability (Acker et al., 2001; Uemura et al., 2002; Lee et al., 2003). Moreover, in an in vitro EC blood-brain barrier model consisting of ECs co-cultured with glial cells, the targeting of AHNAK to the endothelial cells plasma membrane strictly correlates with the development of barrier properties. Collectively, our data suggest that AHNAK is a protein linked to the establishment of cell barrier properties.

MATERIALS AND METHODS

Antibodies

Primary antibodies directed against von Willebrand Factor were from DAKO (Carpinteria, CA), rat anti ZO-1 clone 6A1 was from Biogenesis (Poole, UK), rat anti-PECAM is a hybridoma supernatant from clone MEC13-3 (Vecchi et al., 1994), FITC-conjugated anti-mouse PECAM was from Pharmingen (San Diego, CA). Rabbit polyclonal anti-human occludin and rabbit polyclonal anti-human zonula occludens (ZO-1) were from Zymed Laboratories, Inc. (San Francisco, CA). The affinity purified rabbit polyclonal anti KIS-AHNAK antibodies were developed in our laboratory (Benaud et al., 2004). Alexa 488 anti-rat and anti-mouse secondary antibodies were from Molecular Probes (Leiden, The Netherlands). Cyanin 3 and cyanin 5 anti-rat and anti-rabbit secondary antibodies were from Jackson ImmunoResearch Laboratories (West Grove, PA).

Immunoblot

For whole tissues, brain cortex and cerebellum were removed from adult mouse, minced, and quickly frozen with liquid nitrogen. Tissues were homogenized with a glass homogenizer in SDS-sample buffer. For ES cell extracts, undifferentiated ES cells (day 0) and ES-derived embryoid bodies (EBs) at day 3, 4, 5, 6, 7, 10, 12 after the induction of differentiation were lysed in SDS-sample buffer. Extracts were then heated at 90°C for 3 min in denaturation buffer (2% SDS, 25 mM Tris-HCl, pH 6.8, 10% glycerol, 0.1% bromophenol blue, 1 mM EDTA). Proteins were separated on 5% SDS-PAGE and immunoblotting were carried out with affinity-purified KIS antibody.

Immunofluorescence and electron microscopy

Mouse and rat tissues were frozen in isopentane at -80°C and cut in 10 µm cryostat sections. Slides were fixed with 4% paraformaldehyde for 30 min before permeabilization for 5 min with 0.5% Triton X-100 in TBS. Whole choroid plexus were dissected from mouse brain in phosphate buffer saline (PBS) and fixed in methanol at -20°C for 5 min. After extensive wash and goat serum blocking, primary antibodies were incubated overnight at 4°C at the following dilutions: KIS-AHNAK 0.3 µg/ml; PECAM 1:5; ZO-1 1:500. Slides were then incubated with secondary antibodies for 1 h and nuclear counterstaining was performed with HOECHST 33258 (1 µg/ml). Double immunofluorescence analysis was performed using confocal microscopy (Leica TCS-SP2) and fluorescence microscopy (Zeiss Axiovert 200M). Images were directly captured, saved, and transferred to Adobe Photoshop® 5.5.

Cryostat sections (10 µm) from EBs or frozen brain embedded into Tissue-tek OCT compound (Sakura Finetek, Zoeterwoude, The Netherlands) were collected onto polylysine coated glass slides. Collagen gels containing EBs were transferred onto glass slides, then dehydrated in seconds using nylon linen and absorbent filter cards and conserved at -80°C. For electron microscopy, we used the ABC system from DAKO. Briefly, 200 µm thin floating slides were neutralized for endogenous peroxidase with 3% H₂O₂, followed by 0.5% sodium azide in TBS for 10 min. KIS-AHNAK antibody was then used as described above. After incubation with a biotinylated secondary antibody and extensive washes, an avidin/biotin-horse raddish peroxidase complex was used. The immunoreaction was revealed using diaminobenzidine (DAB). Immunoreaction without the primary antibody was used as control. After per-

oxidase staining, slides were fixed with 0.5% osmium tetroxide and dehydrated for epon infiltration and embedding. Then, 300 nm sections were counterstained with 5% uranyl acetate and observed on a JEOL 1200 EX II electron microscope at 80 kV.

Tumor models

Tumors were induced in male Wistar rats by stereotactic injection of 10⁴ 9L glioma cells, 3 mm under the dura, into the striatum. Animal care and all experiments performed on the animals are conformed to the guidelines of the French Government (Decree Number 87-848, October 19, 1987, Licenses 006722 and A38071). Brain of rats were removed 10 days after cell implantation and freezeed in isopentane at -80°C for cryostat section. Ten micrometers coronal sections of the brain were immunostained with anti-AHNAK or anti-PECAM antibodies.

Primary differentiation of ES cells

CJ7-ES cells were grown as previously described (Vittet et al., 1997). ES cells were initiated to differentiate in Iscove's medium containing glutamax (IMDM, Invitrogen, Groningen, The Netherlands) supplemented with 1% methylcellulose (StemCell Technologies, Inc., Vancouver, Canada), 15% fetal calf serum (Biocrom, Berlin, Germany), 450 µM monothio-glycerol, 10 µg ml⁻¹ insulin (Roche Diagnostics, Meylan, France), 50 U ml⁻¹ penicillin, and 50 µg ml⁻¹ streptomycin. To improve differentiation into the endothelial lineage, ES cell differentiation was performed in the presence of a growth factor (GFs) cocktail containing 50 ng ml⁻¹ human vascular endothelial growth factor (VEGF; Peprotech, Rocky Hill, NJ), 100 ng/ml human basic fibroblast growth factor (FGF2; Peprotech), 2 U ml⁻¹ mouse erythropoietin (EPO; Roche Diagnostics), and 10 ng ml⁻¹ murine interleukin 6 (IL6; Peprotech), as described previously (Vittet et al., 1997). ES cells (1.25 × 10³ cells ml⁻¹) were seeded in a final volume of 2 ml in 35 mm bacterial grade Petri dishes (Greiner, Nürtingen, Germany).

Embryoid body maturation into type I collagen gels

For secondary culture into collagen gel, EBs were collected after 11 days of differentiation by dilution of the semi-solid methylcellulose medium with IMDM Glutamax. After centrifugation (200g, 5 min) and two further washes, EBs were suspended in IMDM Glutamax and mixed with a collagen culture medium at a final concentration of 50 EBs ml⁻¹. Final composition of freshly prepared collagen-based culture medium was as described (Feraud et al., 2001). IMDM containing 1.25 mg ml⁻¹ rat tail collagen, type I (Becton Dickinson, Bedford, MA), 15% fetal calf serum (Biocrom), 450 µM monothio-glycerol, 10 µg ml⁻¹ insulin, 50 U ml⁻¹ penicillin, and 50 µg ml⁻¹ streptomycin. After thorough mixing of EBs into collagen-based medium, 1.2 ml were dispensed into 35 mm bacterial petri dishes. Cultures were performed in the presence of the GFs/angiogenic factor cocktail that was shown to induce sprouting angiogenesis from the initial EB cord-like vascular structures (Feraud et al., 2001) not supplemented or supplemented with recombinant angiopoietin 1 (0.5 µg ml⁻¹) obtained from R&D Systems (Ref: 923-AN-025).

Co-Culture of bovine brain capillary endothelial cells (BCEC) and at glial cells

BCEC were isolated from bovine brain cortex according to Meresse et al. (1989). A pure endothelial cell population with no pericyte contamination is obtained. The cells were cultured in Dulbecco's modified Eagle medium (DMEM) supplemented with 10% (vol/vol) heat-inactivated calf serum and 10% (vol/vol) horse serum (Hyclone Laboratories, Logan, UT), 2 mM glutamine, 50 µg/ml gentamycin and basic fibroblast growth factor (bFGF, 1 ng/ml, added every other day).

Primary cultures of mixed glial cells were prepared from newborn rat cerebral cortex. After removing the meninges, the brain tissue was forced gently through a nylon sieve as described by Booher and Sensenbrenner (1972). Glial cells were then plated on 6-multiwell dishes (Nunc, Roskilde, Denmark) at a concentration of 1.2 × 10⁵ cells/ml in 2 ml of DMEM supplemented with 10% (vol/vol) fetal calf serum (Hyclone

Laboratories). The medium was changed twice a week. The glial cells consist of 60% astrocytes, plus oligodendrocytes, and microglial cells.

After stabilization of the glial cells, collagen-coated filters were set in the 6-well dishes and BCECs were plated on the upper side of the filters. Co-cultures are left for 12 days (5 days after confluence) to acquire all characteristics of the BBB (Cecchelli et al., 1999). In the no co-cultured condition, BCECs were grown on filters without glial cells for 12 days.

Transendothelial transport studies

On the day of the experiments, Ringer-HEPES (150 mM NaCl, 5.2 mM KCl, 2.2 mM CaCl₂, 0.2 mM MgCl₂, 6 mM NaHCO₃, 2.8 mM glucose, 5 mM HEPES) was added to the lower compartments of a 6-well plate (2.5 ml per well). Filters (triplicates per condition) were then transferred into the first wells of the six-well plate containing Ringer, and Ringer containing 0.1 μ Ci [¹⁴C]sucrose (Amersham Biosciences, Buckinghamshire, England, UK) at 37°C was placed in the upper compartments. At different times after addition of sucrose (15, 30, 45, 60 min), filters were transferred to another 6-well plate to minimize the possible passage from the lower to the upper compartment. Incubations were performed on a rocking platform at 37°C. The samples were taken from a lower and upper compartment for estimation of radioactivity in a liquid scintillation counter (Tri Carb 2100, Packard Instrument Company, Meriden, CT). Permeability calculations were performed as described by Siflinger-Birnboim et al. (1987). To obtain a concentration-independent transport parameter, the clearance principle was used. The increment in cleared volume between successive sampling events was calculated by dividing the amount of solute transport during the interval by the donor chamber concentration. The total cleared volume at each time point was calculated by summing the incremental cleared volumes up to the given time point: Clearance (μ l) = Cl (μ l) = X/Cd, where X was the amount of solute in the receptor chamber and Cd was the donor chamber concentration at each time-point. During the 60 min experiment, the clearance volume increased (linearly) with time. The average volume cleared was plotted versus time, and the slope estimated by linear regression analysis. The slope of the clearance curves for the culture was denoted PS_t, where PS was the permeability \times surface area product (in microliter per min). The slope of the clearance curve with the control filter coated only with collagen was denoted PS_f. The PS value for the endothelial monolayer (PS_e) was calculated from: $1/PS_e = 1/PS_t - 1/PS_f$. The PS values were divided by the surface area of the porous membrane to generate the endothelial permeability coefficient (P_e, in cm per min).

RESULTS

Blood vessels of the adult mouse brain express AHNAK

Western blot analysis of total adult mouse brain extracts with affinity purified polyclonal antibodies raised against KIS-AHNAK peptide (Gentil et al., 2003) can be seen on Figure 1. A single protein band migrating at a size corresponding to AHNAK protein is detected. To specify the cell type expressing AHNAK, we performed an immunohistological study of the adult mouse brain parenchyma. AHNAK decorates the entire brain vasculature (Fig. 2). The specificity of the immunostaining given by KIS-AHNAK antibody reported in this study was confirmed by several criteria. AHNAK immunostaining totally disappears when antibodies are preincubated with KIS-AHNAK peptide. The AHNAK immunostaining pattern given by KIS-AHNAK antibody in adult brain was identical to that revealed by an affinity purified polyclonal antibody raised against the C-terminus of AHNAK (aa5630–5643) or by a rabbit polyclonal antibody raised against the central part of mouse desmoyokin developed in Hashimoto's group (Hashimoto et al., 1993) (data not shown). Double

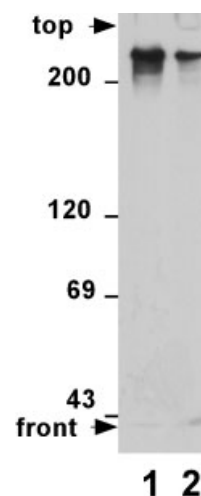


Fig. 1. AHNAK is expressed in adult mouse brain. Western blot analysis shows that AHNAK is present in cerebral cortex (lane 1) and cerebellum (lane 2). The position of the molecular weight standards is indicated in the left margin.

labeling with AHNAK and the platelet-endothelial cell adhesion molecule-1 (PECAM) reveals AHNAK immunoreactivity in vascular endothelium of capillaries (parts A and B), intermediate brain vessels (part C) and small arterioles (part D). AHNAK immunoreactivity also unsheathes endothelial cells, indicating that the protein is also present in mural pericytes and smooth muscle cells that surround brain ECs. In transverse section of intermediate brain vessels and small arterioles, AHNAK immunostaining appears concentrated at the ECs junctions. Double labeling of AHNAK and the tight junction associated ZO1 protein in frozen brain slices fixed with methanol, reveals a striking co-localization of AHNAK with ZO1 in capillaries and in intermediate brain vessels (Fig. 2E,F). Electron microscopy observations confirmed the presence of AHNAK in ECs and pericytes of brain capillaries (Fig. 2G). AHNAK immunoreactivity accumulates at the inner and outer membranes of the endothelial cells. The capillary endothelium is supported by a thin basement membrane that is totally devoid of AHNAK immunostaining. The electron micrograph also reveals an AHNAK positive pericyte that embraces the capillary. The external lamina (equivalent to basement membrane) around the pericyte is devoid of AHNAK immunoreactivity.

AHNAK is not expressed by the fenestrated capillaries of the brain choroid plexus, but accumulates at the tight junctions of the choroid epithelial cells

Within the brain, the choroid plexus is a vascular structure arising from the wall of the ventricles and responsible for the production of cerebrospinal fluid (CSF). It is composed of a network of small capillaries which arise from small afferent arterioles that lie in between two layers of choroid epithelial cells. The tortuous small diameter capillaries are fenestrated allowing the free movement of small molecules. The blood-CSF barrier is assumed by the adjacent choroid epithelial cells that unsheath the vascular structures. The epithelial cells form tight junctions preventing most macromolecule from effectively passing into the CSF from the blood (Brightman, 1968). Double labeling with PECAM and AHNAK on choroid plexus whole mounts shows that only afferent arterioles, but not small

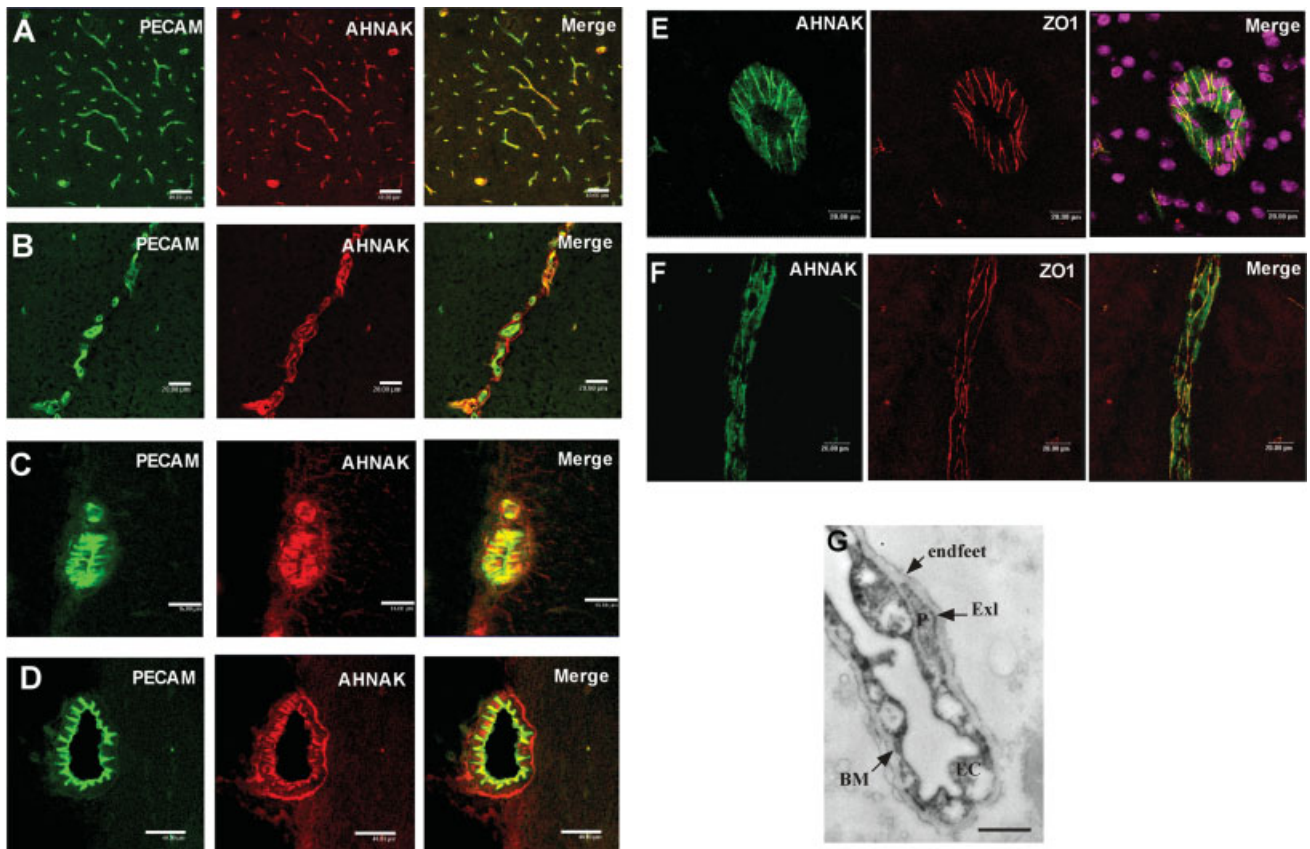


Fig. 2. AHNAK is localized in capillaries of adult mouse brain. **A–D**: Confocal laser scanning microscopy analysis of AHNAK and PECAM immunoreactivities in parenchymal brain capillaries (A, scale bar: 40 μ m; B, scale bar: 20 μ m), in intermediate size vessels (C, scale bar: 16 μ m), and small arteriole-venule (D, scale bar: 40 μ m). Right parts: Merged image of AHNAK and PECAM immunostaining. **E–F**: AHNAK co-localizes with ZO-1 at the tight junction of brain endothelial cells. Double immunostaining for AHNAK (green) and ZO-1 (red) reveals the co-localization of AHNAK and ZO-1 at the tight

junctions of the brain endothelial cells in a transversal (E) and longitudinal section (F). Scale bar: 20 μ m. **G**: Analysis of AHNAK localization in a brain capillary by electron microscopy. Immunoreaction deposits show that AHNAK is localized in the cytoplasm and at the plasma membrane of an endothelial cell (EC). An AHNAK positive pericyte (P) and a smooth abluminal deposit of AHNAK immunoreaction in the astrocyte endfeet are also observed. The basal membrane (BM) and the external lamina (Exl) located between the endothelium and the astrocyte endfeet are devoid of AHNAK. Scale bar: 1 μ m.

diameter capillaries, are characterized by high AHNAK immunoreactivity (Fig. 3A,B). AHNAK antibodies also stain choroid epithelial cells. Single confocal image acquired thru the x-y axis of the endothelial cells layer and reconstitution of x-z sections (part B) clearly shows that tortuous capillary-sized vessels are not immunostained with AHNAK antibodies. The x-z image also shows that, AHNAK immunoreactivity is concentrated at the most apical part of the lateral membranes of the choroid epithelial cells on both sides of the capillary network. In choroid epithelial cells, significant AHNAK immunoreactivity is also present in a punctuate patterns suggestive of a vesicular localization (parts A and B).

In mouse choroid epithelial cells, ZO-1 is exclusively localized at tight junctions (Wolburg et al., 2001). Double labeling of AHNAK and ZO1 reveals that AHNAK co-localize with ZO-1 at the tight junction of the choroid epithelial cells (Fig. 3C,E). There is also a striking co-localization of both antigens at the tight junctions of endothelial cells of afferent arterial (Fig. 3D). As expected, endothelial cells of the tortuous fenestrated capillaries show a severe down-regulation of both AHNAK and ZO-1 immunoreactivities. All together, these observations suggest that regulation of AHNAK expression may be a crucial determinant of the permeability properties of brain endothelial and epithelial cells.

AHNAK expression in brain endothelial cells is down-regulated during tumor angiogenesis

To confirm a link between AHNAK expression and the differentiated structural organization of the brain blood vessels characterized by endothelial barrier properties, we have analyzed AHNAK immunoreactivity in ECs of brain tumors vasculature. Loss of the endothelial barrier phenotypes is a major event characterizing brain tumor angiogenic ECs (Vick and Bigner, 1972). Experimental brain tumors were generated by intracranial injection of rat glial 9L cells into the left hemisphere of a rat brain. Double-labeled fluorescence immunostaining of AHNAK and PECAM analyzed by confocal laser microscopy was used to evaluate AHNAK protein expression in capillary ECs in the control brain parenchyma of the right hemisphere (Fig. 4A) and in the tumor xenograft within the left hemisphere (Fig. 4B). Results show that AHNAK immunoreactivity strongly decreases in angiogenic ECs of the tumor vasculature. No overlap of AHNAK and PECAM immunostaining is observed in longitudinal, or in transverse sections of tumor capillaries as revealed by the total absence of yellow pixels. The absence of AHNAK labeling in tumor ECs results in appearance of a “black ghost” in the middle of AHNAK positive glial tumor cells. Note also that the abundant cytoplasmic AHNAK immunoreactivity in tumor glial cells contrasts with the restricted

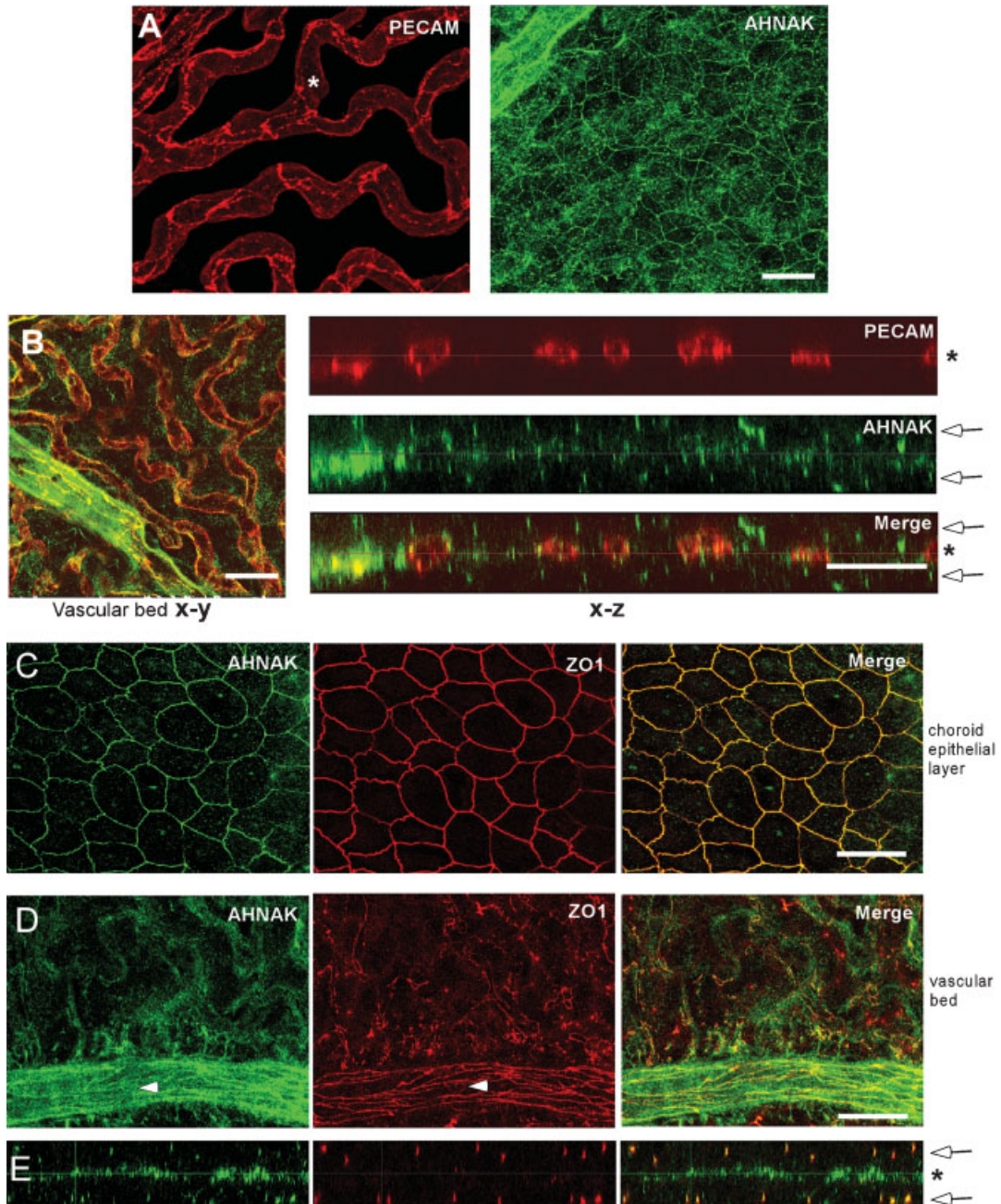


Fig. 3. AHNAK is not expressed by the fenestrated capillaries of the brain choroid plexus, but is present at the tight junction of the choroid epithelial cells that form to the blood–cerebrospinal fluid barrier. **A–B:** Choroid plexus whole mount double immunolabelled for PECAM (red) and AHNAK (green) reveals that AHNAK is not expressed by the fenestrated capillaries. Part A: Tri-dimensional merged stacking of confocal laser scanning x-y axis sections of PECAM (red) and AHNAK (green) immunoreactivities taken through the whole plexus. Part B: Confocal microscopy image of a single x-y section focused on the vascular structure of the choroid plexus, and vertical reconstitution (x-z axis) of the merged PECAM and AHNAK immunoreactivities. The

star indicates the capillaries vascular bed and the arrows point to the plexus choroid epithelial cells. **C–E:** Choroid plexus whole mount double immunolabelled for AHNAK (green) and ZO-1 (red) reveals the co-localization of AHNAK and ZO-1 at the tight junctions of large vessels (D, arrow head) and of the choroid epithelial cells that contribute to the blood-cerebrospinal fluid barrier. Part C: Confocal microscopy image of x-y axis section focused on the apical membrane of the choroid epithelial cells. Part D: Confocal microscopy image of x-y axis section focused on the vascular structure of the choroid plexus. Part E: x-z axis reconstitution showing two layers of epithelial cells (arrows) on each side of the vascular bed (star). Scale bars: 20 μ m.

AHNAK localization to the perivascular processes of the normal astrocytes.

AHNAK is not expressed in peripheral capillaries characterized by extensive molecular exchanges between blood and extracellular medium

We confirmed in peripheral tissues a direct relationship between AHNAK expression in endothelial cells and the permeability properties of the blood vessels

(Fig. 5). In renal corpuscles, the fenestrated endothelium of the kidney glomeruli, which allows the blood plasma to be filtered, is devoid of AHNAK immunoreactivity (part A). The network of capillaries that surrounds the tubules of the renal cortex and which reabsorbs molecules from the glomerular filtrates back into the general circulation is also not immunostained by AHNAK antibodies. In contrast, ECs of the afferent and efferent arterioles of the renal corpuscule (part A),

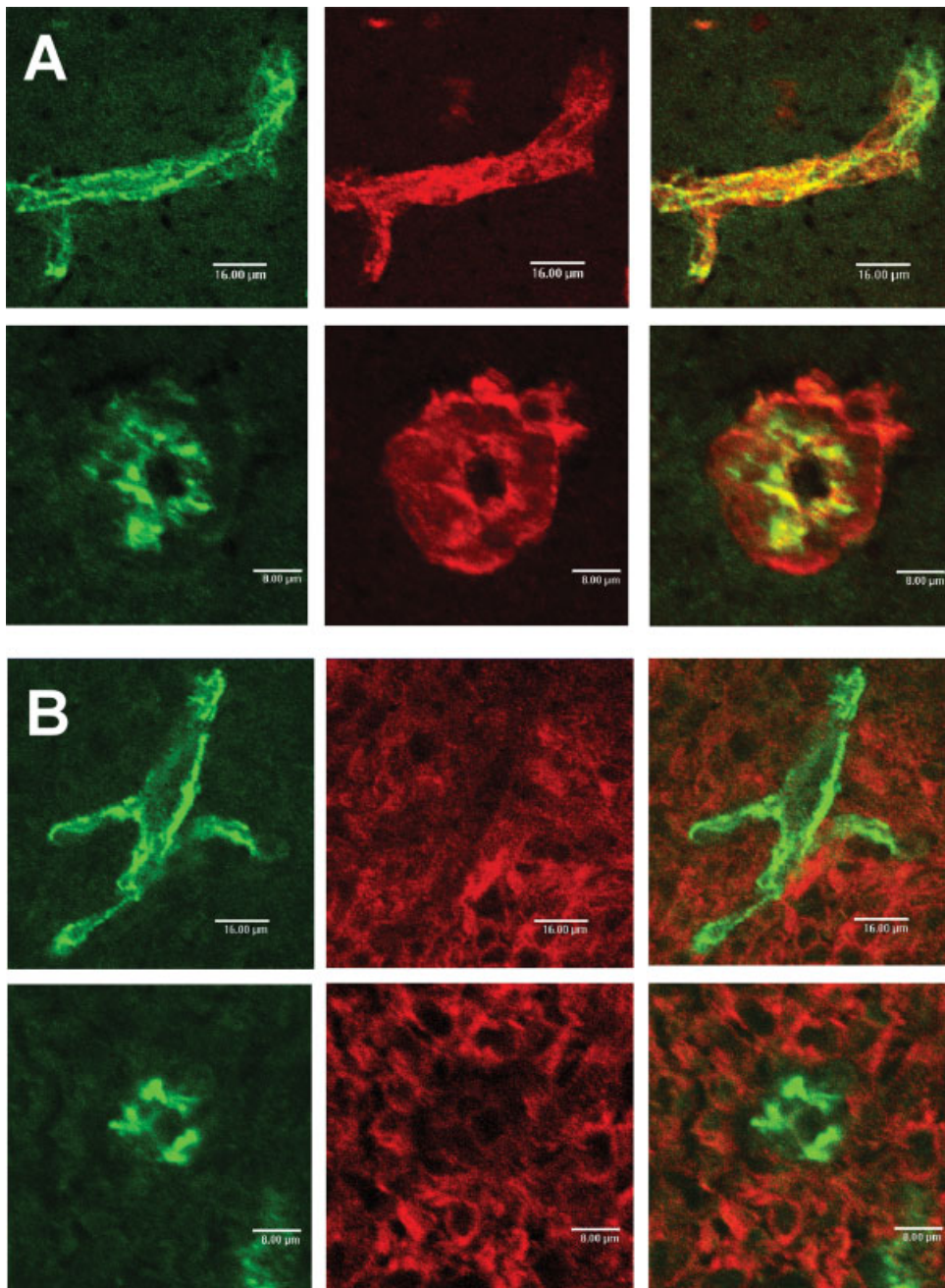


Fig. 4. AHNAK is down-regulated in tumor blood vessels. **A–B:** Comparison by confocal laser scanning microscopy of AHNAK (red) and PECAM (green) immunolabelling in control and in experimental tumor xenografts. **A:** Vessels of normal brain tissue present a classical pattern of AHNAK immunostaining, which overlaps to some extent

with that of PECAM. **B:** Vessels in the tumor are devoid of AHNAK immunoreactivity. In **A** and **B**, vessels are shown both in longitudinal (upper part, scale bar: 16 μ m) and cross section (lower part, scale bar: 8 μ m). Right parts: Merged image of AHNAK and PECAM immunostaining.

and of the cortical radial artery surrounded by single layer of AHNAK positive muscle cells (part B), do express AHNAK. In the liver, AHNAK protein is absent from the hepatic sinusoid cells through which blood percolates (part C). This contrasts with the presence of AHNAK in the hepatic portal vein and the hepatic artery (Gentil et al., 2003). Similarly, the continuous capillaries of the lung that surround the alveoli and are involved in gaseous exchanges are also devoid of AHNAK immunoreactivity, whereas AHNAK is expressed in less specialized lung endothelium (data not shown).

Angiopoietin 1 up-regulates AHNAK expression in endothelial cells derived from ES cells

ES cell in vitro differentiation provides a powerful model system for studies of vascular development. Primitive ECs can be obtained from ES cells. Upon leukemia inhibitory factor (LIF) removal, ES cells spontaneously differentiate into complex EBs, which contain derivatives from the three primitive germ layers, including ECs (Yamashita et al., 2000; Feraud et al., 2001). Western blot analysis of ES cell extracts shows that AHNAK expression rapidly increases upon differ-

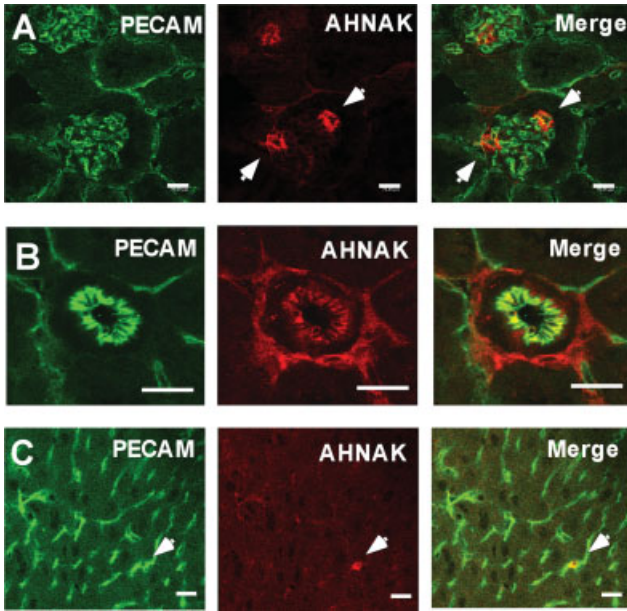


Fig. 5. The endothelium of vessels which present high level of filtration and permeability between the blood and tissue parenchyma are devoid of AHNAK. Confocal laser scanning micrographs of double immunolabelling for AHNAK (red) and PECAM (green) in kidney and liver. **A–B:** In kidney, ECs of the glomerulus and of the vasa recta capillaries are not immunostained by AHNAK antibodies, whereas AHNAK is expressed by ECs of the glomerulus afferent and efferent arterioles (part A, arrow heads) and of the cortical arteriole (part B). **C:** In liver, AHNAK antibody do not immunostain sinusoid ECs, but stain an interlobular veinule (arrow head). Right parts: Merged images of AHNAK and PECAM immunostaining. Scale bars: 20 μ m.

entiation (Fig. 6A). However, double labeling with AHNAK and PECAM antibodies revealed that ES-derived ECs neither expressed AHNAK during EB development (Fig. 6B,C) nor when EBs were replated in type I collagen gels, a three-dimensional culture system recapitulating angiogenesis (Fig. 6D,E, parts a–e). AHNAK positive cells develop in close association with PECAM positive cells. Further characterization of these cells showed that they correspond to smooth muscle cells, as they are immunostained by the smooth muscle cell marker α -smooth muscle actin (SMA) (data not shown). Expression of ZO-1 protein was not detected in ECs at this stage, indicating that ECs have not yet formed complete cell–cell junctions (Fig. 6E, part c).

A growing body of evidences indicates that angiopoietin 1 (Ang-1) is a key factor involved in maturation of ECs underlying the organization of the blood vessels and their impermeability *in vitro* and *in vivo* (Thurston et al., 1999; Acker et al., 2001; Uemura et al., 2002; Lee et al., 2003). ES cells do express the Ang-1 receptor, Tie2 (Feraud et al., 2001; Baudino et al., 2002). Treatment of ES-derived ECs grown in collagen gels with recombinant Ang-1 induced the formation of larger ECs sprouts (Fig. 6E, parts f–j). Ang-1 also strongly increased the expression of ZO-1 in ECs (part h) that correlated with the appearance and recruitment of AHNAK to the cell–cell contacts (part i, j). These observations indicate that functional maturation of ECs revealed by formation of tight junctions appears to be of prime importance in specifying AHNAK expression and membrane targeting in ECs.

Blood–brain barrier formation controls targeting of AHNAK to the endothelial cells plasma membrane

In the brain, ECs are subjected to regulation by a variety of extracellular and cytoplasmic signaling systems that contribute to their differentiation and to the establishment and maintenance of barrier properties (Lee et al., 2003). Astrocyte–endothelial cell interactions are essential to the formation of the EC blood–brain barrier (BBB) (Janzer and Raff, 1987). To confirm a role for AHNAK during brain ECs differentiation and BBB formation, we have analyzed AHNAK localization in an *in vitro* BBB model consisting of primary BCEC co-cultured with glial cells (Cecchelli et al., 1999). BCEC were grown on microporous membrane coated with collagen alone or in co-culture with glial cells. Co-culture with glial cells induces formation of BBB highlighted by the decrease in permeability of the BCECs monolayer for 14 C-sucrose (Fig. 7A). Remarkably, BBB formation did not affect the total level of AHNAK protein (Fig. 7B), but resulted in a progressive relocation of AHNAK from a punctate cytoplasmic to a cell–cell contacts staining (Fig. 7C, parts e,f). Such relocation during the glial cells induced formation of BBB in the ECs is highly specific to AHNAK. The tight junction associated proteins occludin (parts a,b) and ZO-1 (parts c,d), which are particularly important in regulating functional BBB organization (Rubin and Staddon, 1999), are present at the intercellular contacts between BCECs both in the absence and in the presence of glial cells.

DISCUSSION

Previous immunohistochemical analysis of the AHNAK protein in mouse tissues has revealed a striking localization of the protein in most lining epithelia that form physical barriers to define body compartments and protect the body from the external environment (Gentil et al., 2003). We here report that AHNAK is also expressed in endothelial cells in vessels characterized by blood–tissues barrier properties. Remarkably, AHNAK is absent from endothelia that allow passive molecular exchanges between blood and extracellular fluid, including the fenestrated endothelium of choroid plexus, the kidney glomeruli, the hepatic sinusoids and the continuous capillaries of the lung that surround the alveoli (not shown). These observations point out for a possible role of AHNAK in regulation of ECs properties.

In the brain, the specialized permeability characteristics of ECs, referred to as the BBB, depend on the expression of high levels of junction proteins and on the targeting of specific membrane transporting protein and receptors capable of shuttling macromolecules into the brain or back into the blood (Rubin and Staddon, 1999; Schinkel, 2001; Pardridge, 2003). These processes are thought to depend on ECs response to inducing factors found in their immediate environment (Rubin and Staddon, 1999). A first step towards deciphering a possible implication of AHNAK in the BBB would then be to demonstrate that AHNAK is down-regulated in brain ECs that have lost BBB properties. Regulation of AHNAK expression and localization in ECs by brain-derived factors represents a second crucial issue for investigation. We addressed these issues by comparing AHNAK expression in normal brain ECs and in tumor brain ECs, and by investigating the regulation of AHNAK expression and localization in ECs by brain-derived factors that promote endothelial cell maturation and barrier properties.

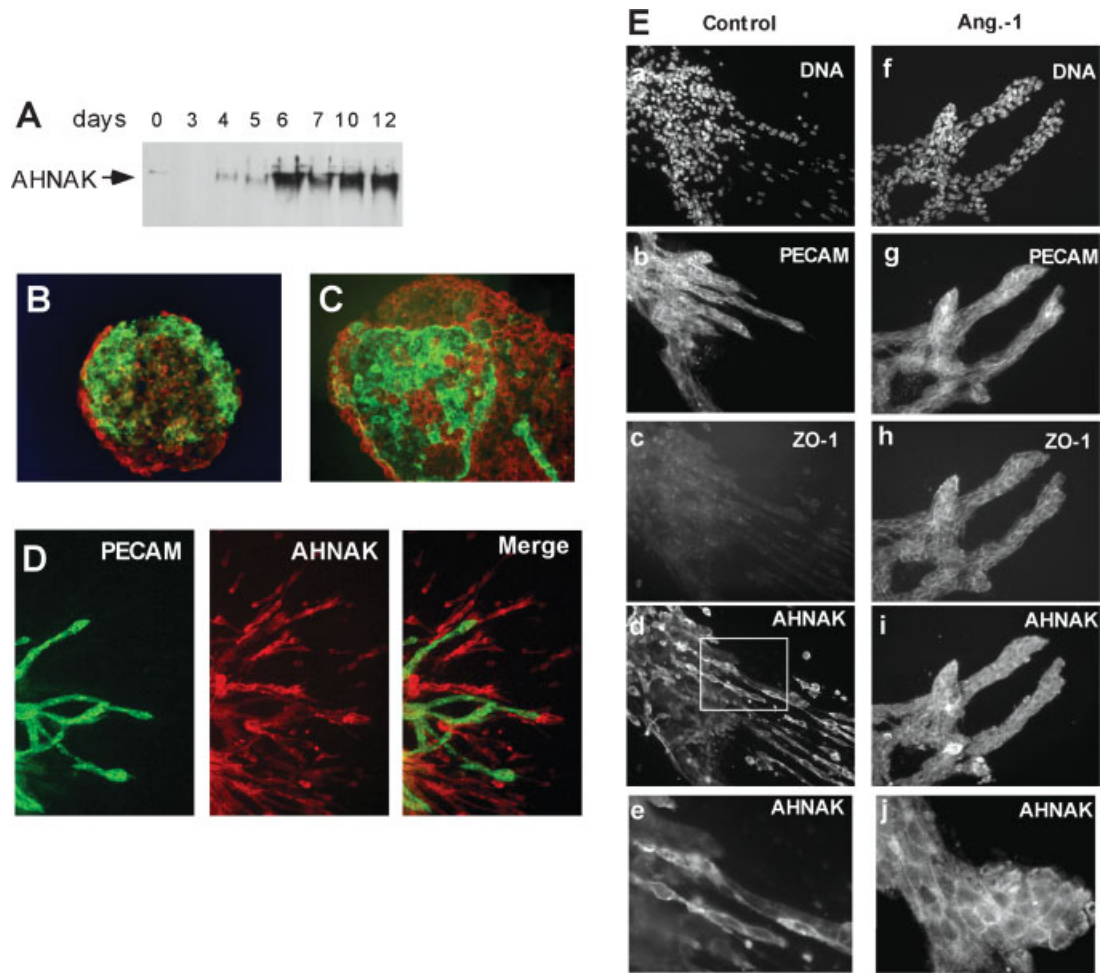


Fig. 6. Induction of AHNAK by angiopoietin 1 in ES cell-derived ECs. **A:** Whole cell extracts of undifferentiated ES cells (day 0) and of EBs at days 3, 4, 5, 6, 7, 10, 12 after the induction of vascular differentiation analyzed by Western blot for AHNAK expression. **B–C:** Double immunofluorescence analysis of AHNAK (red) and PECAM (green) in 7-day-old EBs (B) and 12-day-old EBs (C). **D:** Double immunofluorescence analysis of AHNAK (red) and PECAM (green) in 11-day-old EBs after 3 days of secondary culture in collagen gel. In the right part

is the merged image of AHNAK and PECAM immunostaining. **E:** Eleven-day-old EBs were grown for 3 days in collagen gel in the absence (Control, a–e) or in the presence of Ang-1 (Ang-1, f–j) as indicated. Cells were triple immunolabelled with mouse FITC-conjugated PECAM antibody (PECAM, b and g), rat-anti ZO-1 (ZO-1, c and h), and rabbit-anti AHNAK (AHNAK, d, e, i, and j) antibodies. e and j correspond to higher magnification images. DNA was stained with HOECHST 33258 (DNA, a and f).

In glial tumors, the structural organization of the capillary ECs is severely impaired compared to normal tissue. Tumor vasculature is characterized by an increase in vessel wall thickness with open endothelial gaps and fenestration. These structural abnormalities form the basis for the loss of BBB function in these tumors. We have shown that down-regulation of AHNAK characterizes brain ECs of vascularized xenografted glial brain tumors. One other prominent characteristic of brain tumor capillaries is the absence of astrocyte endfeet and pericytes that normally cover most of the capillary's basal surface. Pericytes and astrocytes secrete factors that have a profound influence on the morphogenetic events underlying the organization of the vessel and their permeability (Ramsauer et al., 2002). Among these is Ang-1 (Lee et al., 2003). We have shown that Ang-1 is a strong inducer of AHNAK expression in ES-derived ECs. The formation of larger EC sprouts by Ang-1 was accompanied by the accumulation of AHNAK immunoreactivity to the plasma membrane. In ES-derived ECs, membrane localization of AHNAK also correlates with formation of intercellular tight junctions between ECs. These observations identify AHNAK as a protein that might directly partici-

pate to Ang-1-dependent EC membrane remodelling. Similarly, in an in vitro model of BBB consisting of a coculture of BCECs and glial cells, membrane localization of AHNAK in BCECs is induced by glial cells and strictly correlates with the development of EC barrier properties suggesting that AHNAK may directly participate to elaboration of the BBB. The function of AHNAK in brain barrier properties is not restricted to ECs, but might also apply to epithelial cells. In the brain choroid plexus, AHNAK is expressed at low levels in fenestrated endothelial cells, but accumulates at the tight junctions of the choroid epithelial cells that form the blood–CSF barrier.

The BBB is established both by a lack of passive paracellular permeability and by the limitation and high regulation of transcellular fluxes. To understand the molecular mechanisms by which AHNAK may function in the regulation of brain endothelial cell properties, several attempts were made to down-regulate AHNAK expression in ECs using AHNAK specific RNAi (Benaud et al., 2004), but we found ECs highly resistant to transfection. However, we have observed that the down-regulation of AHNAK expression in the epithelial polarized MDCK cells does not significantly affect the

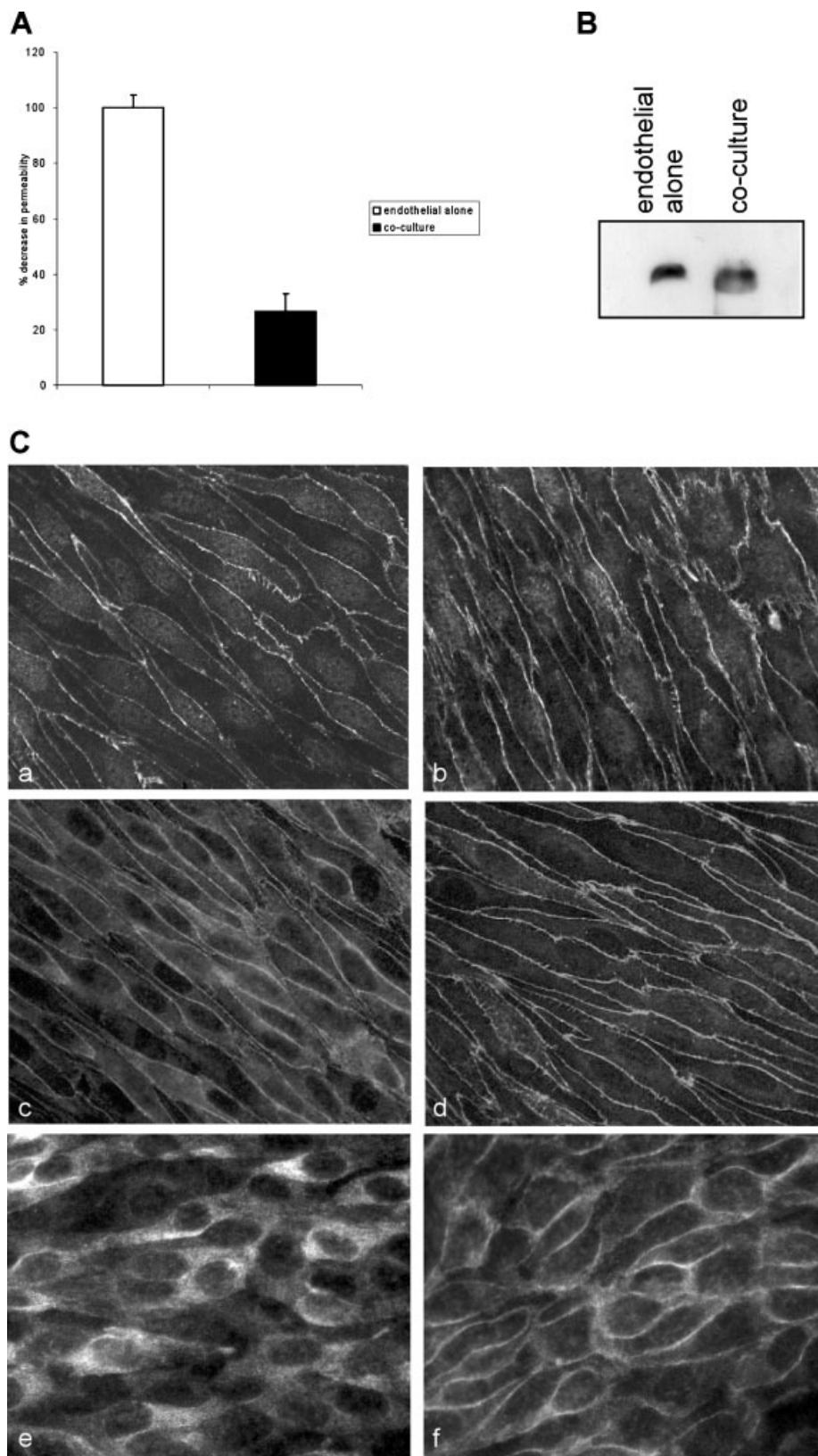


Fig. 7. Relocalization of AHNAK in primary cerebral capillary endothelial cells with the acquisition of barrier property. **A:** Mean \pm SD percentage decrease of BCEC monolayer permeability to [14 C]-sucrose after co-culture with glial cells for 12 days. The 100% control value (EC cultured alone for 12 days) represents a Pe of $0,79 \times 10^{-3}$ cm/min for [14 C]-sucrose (n = 3 EC monolayers/condition) from four independent

experiments. **B:** Whole cell extracts of endothelial cells cultivated alone or in co-culture with glial cells were analyzed by western blotting for AHNAK levels. **C:** Immunofluorescent localization of Occludin (a, b), ZO-1 (c, d), and AHNAK (e, f) in BCECs cultured for 12 days alone (a, c, e) or with glial cells (b, d, f).

rate of paracellular diffusion of fluorescein isothiocyanate (FITC)-dextran (molecular mass 10,000) (data not shown), suggesting that AHNAK may not be implicated at the level of the paracellular permeability. We, therefore, more likely envision a role for AHNAK during BBB formation in association with cell membrane remodelling and the control of transcellular fluxes. Transcellular fluxes cross the BBB are regulated by membrane transporting proteins and receptors expressed at the apical membrane of ECs (Rubin and Staddon, 1999; Schinkel, 2001; Partridge, 2003). Indirect immunofluorescence analysis in both epithelial and endothelial cells revealed that AHNAK accumulates at the lateral membrane, but is also found within vesicle-like structure in the cytoplasm. In MDCK cells, AHNAK shuttles between the cytoplasm to cholesterol-rich plasma membrane domains in association with the annexin2/S100A10 complex during the formation of cell-cell contacts and the development of epithelial polarity (Benaud et al., 2004). Recently, the annexin 2/S100A10 complex has been identified in MDCK cells as a component of vesicular carriers responsible for targeting of membrane proteins to the raft-containing apical membrane of the polarized cells (Jacob et al., 2004). The possibility that AHNAK cooperates with the annexin2/S100A10 in organizing the routing of these vesicles and the recruitment of specific barrier-associated proteins or transporters to the apical membrane of epithelial and endothelial cells has now to be considered.

Alternatively, one can also envision a role for AHNAK in preserving the integrity of EC barrier properties. Most tissues, in which AHNAK is expressed, including the vascular endothelium, receive considerable levels of mechanical stress (Gentil et al., 2001). These stresses often result in tears in the plasma membrane, and survival requires that the cell rapidly repair or reseal the disruption (McNeil and Steinhardt, 2003). AHNAK has been found associated with a new population of Ca^{2+} -regulated vesicles capable of fast exocytosis called enlargosome (Borgonovo et al., 2002). AHNAK was also found to appear on the surface of cells after membrane disruptions were induced, suggesting that the enlargosomes may play a role in membrane remodeling and repair. Further studies on the role of AHNAK in prevention of disruption and repair of EC plasma membrane are required.

ACKNOWLEDGMENTS

We thank Dr. LaMarre for helpful discussions and critical reading of the article, Dr. Paintrand and Dr. Hachimi for their help with electron microscopy analysis, Dr. D. Grunwald and Dr. Deloulme for help with confocal microscopy (imaging core facility, DRDC, CEA Grenoble), Dr. Hashimoto for anti-desmoyokin/AHNAK antibody DY. Miss Farion for technical assistance. This work was supported by grant from the Association pour la Recherche contre le Cancer (CD) and by a fellowship from la Ligue Nationale contre le Cancer (BG).

LITERATURE CITED

Acker T, Beck H, Plate KH. 2001. Cell type specific expression of vascular endothelial growth factor and angiopoietin-1 and-2 suggests an important role of astrocytes in cerebellar vascularization. *Mech Dev* 108(1-2): 45-57.

Baudino TA, McKay C, Pendeville-Samain H, Nilsson JA, Maclean KH, White EL, Davis AC, Ihle JN, Cleveland JL. 2002. c-Myc is essential for vasculogenesis and angiogenesis during development and tumor progression. *Genes Dev* 16(19):2530-2543.

Benaud C, Gentil BJ, Assard N, Court M, Garin J, Delphin C, Baudier J. 2004. AHNAK interaction with the annexin 2/S100A10 complex regulates cell membrane cytoarchitecture. *J Cell Biol* 164(1):133-144.

Booher J, Sensenbrenner M. 1972. Growth and cultivation of dissociated neurons and glial cells from embryonic chick, rat, and human brain in flask cultures. *Neurobiology* 2(3):97-105.

Borgonovo B, Cocucci E, Racchetti G, Podini P, Bachi A, Meldolesi J. 2002. Regulated exocytosis: A novel, widely expressed system. *Nat Cell Biol* 4(12): 955-962.

Brightman MW. 1968. The intracerebral movement of proteins injected into blood and cerebrospinal fluid of mice. *Prog Brain Res* 29:19-40.

Cecchelli R, Dehouck B, Descamps L, Fenart L, Buee-Scherrer VV, Duhem C, Lundquist S, Rentfel M, Torpier G, Dehouck MP. 1999. In vitro model for evaluating drug transport across the blood-brain barrier. *Adv Drug Deliv Rev* 36(2-3):165-178.

Feraud O, Cao Y, Vittet D. 2001. Embryonic stem cell-derived embryoid bodies development in collagen gels recapitulates sprouting angiogenesis. *Lab Invest* 81(12):1669-1681.

Gentil BJ, Delphin C, Mbele GO, Deloulme JC, Ferro M, Garin J, Baudier J. 2001. The giant protein AHNAK is a specific target for the calcium- and zinc-binding S100B protein: Potential implications for Ca^{2+} homeostasis regulation by S100B. *J Biol Chem* 276(26):23253-23261.

Gentil BJ, Delphin C, Benaud C, Baudier J. 2003. Expression of the giant protein AHNAK (Desmoyokin) in muscle and lining epithelial cells. *J Histochem Cytochem* 51(3):339-348.

Haase H, Podzuweit T, Lutsch G, Hohaus A, Kostka S, Lindschau C, Kott M, Kraft R, Morano I. 1999. Signaling from beta-adrenoreceptor to L-type calcium channel: Identification of a novel cardiac protein kinase A target possessing similarities to AHNAK. *FASEB J* 13(15):2161-2172.

Hashimoto T, Amagai M, Parry DA, Dixon TW, Tsukita S, Miki K, Sakai K, Inokuchi Y, Kudoh J, et al. 1993. Desmoyokin, a 680 kDa keratinocyte plasma membrane-associated protein, is homologous to the protein encoded by human gene AHNAK. *J Cell Sci* 105(Pt 2):275-286.

Hashimoto T, Gamou S, Shimizu N, Kitajima Y, Nishikawa T. 1995. Regulation of translocation of the desmoyokin/AHNAK protein to the plasma membrane in keratinocytes by protein kinase C. *Exp Cell Res* 217(2):258-266.

Hieda Y, Tsukita S. 1989. A new high molecular mass protein showing unique localization in desmosomal plaque. *J Cell Biol* 109(4 Pt 1):1511-1518.

Hohaus A, Person V, Behlke J, Schaper J, Morano I, Haase H. 2002. The carboxyl-terminal region of ahnak provides a link between cardiac L-type Ca^{2+} channels and the actin-based cytoskeleton. *FASEB J* 16(10):1205-1216.

Jacob R, Heine M, Eikemeyer J, Frerker N, Zimmer KP, Rescher U, Gerke V, Naim HY. 2004. Annexin II is required for apical transport in polarized epithelial cells. *J Biol Chem* 279(5):3680-3684.

Janzer RC, Raff MC. 1987. Astrocytes induce blood-brain barrier properties in endothelial cells. *Nature* 325(6101):253-257.

Lee SW, Kim WJ, Choi YK, Song HS, Son MJ, Gelman IH, Kim YJ, Kim KW. 2003. SSeCKs regulates angiogenesis and tight junction formation in blood-brain barrier. *Nat Med* 9(7):900-906.

McNeil PL, Steinhardt RA. 2003. Plasma membrane disruption: Repair, prevention, adaptation. *Annu Rev Cell Dev Biol* 19:697-731.

Meresse S, Dehouck MP, Delorme P, Bensaid M, Tauber JP, Delbart C, Fruchart JC, Cecchelli R. 1989. Bovine brain endothelial cells express tight junctions and monoamine oxidase activity in long-term culture. *J Neurochem* 53(5):1363-1371.

Partridge WM. 2003. Blood-brain barrier genomics and the use of endogenous transporters to cause drug penetration into the brain. *Curr Opin Drug Discov Devel* 6(5):683-691.

Ramsauer M, Krause D, Dermietzel R. 2002. Angiogenesis of the blood-brain barrier in vitro and the function of cerebral pericytes. *FASEB J* 16(10):1274-1276.

Rubin LL, Staddon JM. 1999. The cell biology of the blood-brain barrier. *Annu Rev Neurosci* 22:11-28.

Schinkel AH. 2001. The roles of P-glycoprotein and MRP1 in the blood-brain and blood-cerebrospinal fluid barriers. *Adv Exp Med Biol* 500:365-372.

Sekiya F, Bae YS, Jhon DY, Hwang SC, Rhee SG. 1999. AHNAK, a protein that binds and activates phospholipase C-gamma1 in the presence of arachidonic acid. *J Biol Chem* 274(20):13900-13907.

Shtivelman E, Cohen FE, Bishop JM. 1992. A human gene (AHNAK) encoding an unusually large protein with a 1.2-microns polyionic rod structure. *Proc Natl Acad Sci USA* 89(12):5472-5476.

Siflinger-Birnboim A, Del Vecchio PJ, Cooper JA, Blumenstock FA, Shepard JM, Malik AB. 1987. Molecular sieving characteristics of the cultured endothelial monolayer. *J Cell Physiol* 132(1):111-117.

Sussman J, Stokoe D, Ossina N, Shtivelman E. 2001. Protein kinase B phosphorylates AHNAK and regulates its subcellular localization. *J Cell Biol* 154(5):1019-1030.

Thurston G, Suri C, Smith K, McClain J, Sato TN, Yancopoulos GD, McDonald DM. 1999. Leakage-resistant blood vessels in mice transgenically overexpressing angiopoietin-1. *Science* 286(5449):2511-2514.

Uemura A, Ogawa M, Hirashima M, Fujiwara T, Koyama S, Takagi H, Honda Y, Wiegand SJ, Yancopoulos GD, Nishikawa S. 2002. Recombinant angiopoietin-1 restores higher-order architecture of growing blood vessels in mice in the absence of mural cells. *J Clin Invest* 110(11):1619-1628.

Vecchi A, Garlanda C, Lampugnani MG, Resnati M, Matteucci C, Stoppacciaro A, Schnurch H, Risau W, Roco L, Mantovani A, et al. 1994. Monoclonal antibodies specific for endothelial cells of mouse blood vessels. Their application in the identification of adult and embryonic endothelium. *Eur J Cell Biol* 63(2):247-254.

Vick NA, Bigner DD. 1972. Microvascular abnormalities in virally-induced canine brain tumors. Structural bases for altered blood-brain barrier function. *J Neurol Sci* 17(1):29-39.

Vittet D, Buchou T, Schweitzer A, Dejager E, Huber P. 1997. Targeted null-mutation in the vascular endothelial-cadherin gene impairs the organization of vascular-like structures in embryoid bodies. *Proc Natl Acad Sci USA* 94(12): 6273-6278.

Wolburg H, Wolburg-Buchholz K, Liebner S, Engelhardt B. 2001. Claudin-1, claudin-2 and claudin-11 are present in tight junctions of choroid plexus epithelium of the mouse. *Neurosci Lett* 307(2):77-80.

Yamashita J, Itoh H, Hirashima M, Ogawa M, Nishikawa S, Yurugi T, Naito M, Nakao K. 2000. Flk1-positive cells derived from embryonic stem cells serve as vascular progenitors. *Nature* 408(6808):92-96.

Zuber J, Tchernitsa OI, Hinzmann B, Schmitz AC, Grips M, Hellriegel M, Sers C, Rosenthal A, Schafer R. 2000. A genome-wide survey of RAS transformation targets. *Nat Genet* 24(2):144-152.

AHNAK interaction with the annexin 2/S100A10 complex regulates cell membrane cytoarchitecture

Christelle Benaud,¹ Benoît J. Gentil,¹ Nicole Assard,¹ Magalie Court,² Jerome Garin,² Christian Delphin,¹ and Jacques Baudier¹

¹Laboratoire de Transduction du Signal, INSERM EMI-0104, DRDC-TS, and ²Laboratoire de Chimie des Proteines, INSERM ERM-0201, DRDC-CP, CEA-Grenoble, 38054 Grenoble Cedex 9, France

Remodelling of the plasma membrane cytoarchitecture is crucial for the regulation of epithelial cell adhesion and permeability. In Madin-Darby canine kidney cells, the protein AHNAK relocates from the cytosol to the cytosolic surface of the plasma membrane during the formation of cell–cell contacts and the development of epithelial polarity. This targeting is reversible and regulated by Ca²⁺-dependent cell–cell adhesion. At the plasma membrane, AHNAK associates as a multimeric complex with actin and the annexin 2/S100A10 complex. The S100A10 subunit serves to mediate the interaction between annexin 2

and the COOH-terminal regulatory domain of AHNAK. Down-regulation of both annexin 2 and S100A10 using an annexin 2–specific small interfering RNA inhibits the association of AHNAK with plasma membrane. In Madin-Darby canine kidney cells, down-regulation of AHNAK using AHNAK-specific small interfering RNA prevents cortical actin cytoskeleton reorganization required to support cell height. We propose that the interaction of AHNAK with the annexin 2/S100A10 regulates cortical actin cytoskeleton organization and cell membrane cytoarchitecture.

Introduction

AHNAK was first identified as a gene whose transcription is repressed in cell lines of neuroblastoma and some other tumors (Shtivelman et al., 1992). More recently, transcription of AHNAK was found to be subject to strong down-regulation by transforming Ras alleles in rodent fibroblasts (Zuber et al., 2000). AHNAK is a protein of an exceptionally large size (700 kD) that is encoded by an intronless gene located on human chromosome 11q12–13 (Shtivelman and Bishop, 1993; Kudoh et al., 1995). The deduced amino acid sequence of human AHNAK predicts a protein of 5,643 amino acids that can be divided into three main structural regions: the NH₂-terminal 251 amino acids, a large central region of 4,390 amino acids composed of the 128-aa unit repeated 26 times, and the COOH-terminal 1,002 amino acids. The recurrent 7-aa motif present within the AHNAK repeats, P-[ED]-[AVIL]-[ED]-L-[KR]-G, has striking similarities with repeated domains found in two other repeat-containing proteins, the giant sea urchin vesicle-associated protein (600 kD; Barton et al., 1992) and L-periaxin (147 kD; Dytrych et

al., 1998). Several putative regulatory elements are clustered within the COOH terminus, including several NLSs (Nie et al., 2000), a leucine zipper (Shtivelman and Bishop, 1993), and several potential phosphorylation sites for PKB, PKC, and CKII (Sussman et al., 2001). The exact biological function of AHNAK is unknown, although several putative interacting proteins have been identified. In vitro, AHNAK fragments bind and activate PLC γ in the presence of arachidonic acid (Sekiya et al., 1999). AHNAK is also a major target protein for the calcium- and zinc-binding protein S100B (Gentil et al., 2001). In cardiomyocytes, AHNAK associates with the β subunit of cardiac L-type calcium channels at the plasma membrane, and is phosphorylated by PKA in response to adreno receptor stimulation (Haase et al., 1999). In vitro, the COOH-terminal AHNAK region (aa 5262–5643) binds to G-actin and cosediments with F-actin. A possible role for AHNAK in the maintenance of the structural and functional organization of the subsarcolemmal cytoarchitecture has been proposed (Hohaus et al., 2002). More recently, AHNAK immunoreactivity has been found within the lumen of specific vesicles called “enlargosomes,” and is redistributed to the external surface of the plasma membrane in response to large increases in Ca²⁺. Enlargosomes have been proposed to par-

The online version of this article includes supplemental material.

Address correspondence to Jacques Baudier, INSERM EMI-0104, DRDC-TS, CEA-Grenoble, 17 rue des Martyrs, 38054 Grenoble Cedex 9, France. Tel.: (33) 4-38-78-43 28. Fax: (33) 4-38-78-50-58. email: jbaudier@cea.fr

Key words: actin; calcium; cytoskeleton; cell adhesion; S100B

Abbreviation used in this paper: siRNA, small interfering RNA.

ticipate in cell membrane differentiation and repair (Borgonovo et al., 2002). A nuclear localization of AHNAK has also been reported (Shtivelman and Bishop, 1993; Sussman et al., 2001). During early mouse embryonic development, AHNAK is abundantly expressed in mesenchymal and epithelial cells at the major sites of morphogenesis, where it is essentially localized at the plasma membrane (Kingsley et al., 2001; Downs et al., 2002). In adult mice, AHNAK has a restricted tissue distribution. It is expressed at the plasmalemma of elastic tissues submitted to contracting and stretching forces and/or tissues forming in physical barriers that define body compartments. AHNAK is expressed in all muscular cells including cardiomyocytes, skeletal muscle cells, smooth muscle cells, fibrocytes, and myoepithelial cells (Haase et al., 1999; Gentil et al., 2003). AHNAK is also highly expressed at the plasma membrane of lining epithelial cells (Hieda and Tsukita, 1989; Hashimoto et al., 1993; Gentil et al., 2003), but is absent from epithelia with secretory or absorptive functions (Gentil et al., 2003). The exact mechanisms by which AHNAK is localized to the plasma membranes remain to be investigated, especially because AHNAK does not possess a transmembrane domain. In the present work, we have developed cellular and molecular analyses to elucidate the function of AHNAK at the plasma membrane, and to identify proteins interacting with AHNAK in this cellular compartment. First, we show that at the plasma membrane, AHNAK interacts with the annexin 2/S100A10 complex, which regulates AHNAK plasma membrane localization. We also demonstrate that down-regulation of AHNAK affects the cell membrane cytoarchitecture of epithelial cells, and we propose a role of AHNAK in controlling the physical and mechanical properties of cell-peripheral membranes. Our results provide significant insights into the molecular mechanisms by which annexin 2 regulates cell membrane organization (Babiychuk et al., 2002; Gerke and Moss, 2002).

Results

AHNAK is redistributed at the cytosolic surface of the plasma membrane in confluent MDCK cells

In canine epithelial MDCK cells, AHNAK redistributes from the cytoplasm to a cortical/plasma membrane localization as cell density increases and as cells establish cell-cell contacts (Sussman et al., 2001; Fig. 1 A). This redistribution of AHNAK follows the reorganization of the actin cytoskeleton into cortical actin (Fig. 1 A). Three different AHNAK antibodies, the affinity-purified AHNAK-KIS pAb directed against the repeated central domain of AHNAK, the affinity-purified AHNAK-CQL pAb directed against the extreme COOH terminus (Gentil et al., 2003), and the anti-AHNAK (desmoyokin) antibody (DY) (Hashimoto et al., 1993) gave a similar immunostaining pattern. A recent work has shown that in secretory cell models, AHNAK can be localized within the lumen of specific vesicles called enlargosomes and is redistributed to the external surface of the plasma membrane in response to large increases in Ca^{2+} (Borgonovo et al., 2002). Therefore, we evaluated in confluent MDCK cells on which side of the plasma membrane AHNAK is distributed, and whether AHNAK is present in

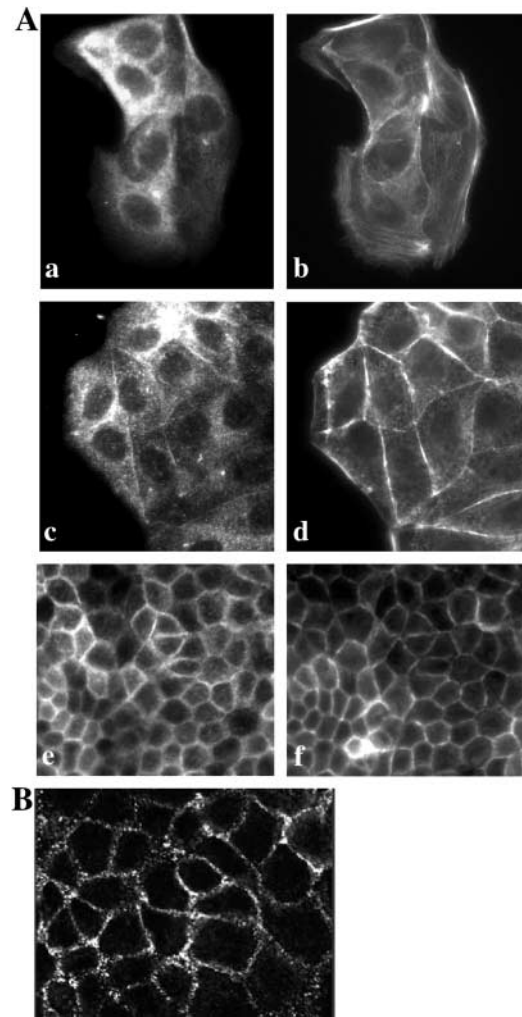


Figure 1. Density-dependent localization of AHNAK to the cytoplasmic face of the MDCK cell plasma membrane. (A) Redistribution of AHNAK and actin during confluence mediated cell-cell contact and polarization. MDCK cells were cultured on glass coverslips for 2 (a and b), 24 (c and d) or 96 h (e and f), and stained with anti-AHNAK-KIS antibody (a, c, and e) and F-actin visualized with phalloidin (b, d, and f). (B) Confocal immunofluorescence with polyclonal anti-AHNAK-KIS antibody of streptolysin O-permeabilized confluent MDCK cells reveals a positive signal at the cytoplasmic surface of the plasma membrane.

the lumen of cortical vesicles or in the cytoplasm. To resolve this issue, we compared the immunostaining obtained with our affinity-purified anti-AHNAK-KIS antibody in detergent-permeabilized cells, in streptolysin O-permeabilized cells, and in nonpermeabilized live confluent MDCK cells. In nonpermeabilized cells, no surface AHNAK immunolabeling was detected (unpublished data). When the plasma membrane of live cells was permeabilized with streptolysin O, a condition in which only cytoplasmic and not the vesicle luminal proteins are accessible to the antibodies, the plasma membrane was labeled (Fig. 1 B). An identical result was obtained with the anti-AHNAK (desmoyokin) antibody (DY) previously shown to recognize the membrane-bound protein in epithelial cells (Hashimoto et al., 1993, 1995; unpublished data). Even though we cannot exclude the possibility that a population of AHNAK is present in enlargosomes,

these results clearly indicate that in our epithelial cell model, AHNAK is predominantly a cytosolic protein localized at the intracellular face of plasma membrane.

Membrane-bound AHNAK interacts with the annexin 2/S100A10 complex

To gain further insight into AHNAK function at the plasma membrane, we sought to identify proteins interacting with AHNAK using coimmunoprecipitation coupled to mass spectrometry analysis. For convenient peptide sequence identification using human databases, we used human epithelial MCF-7 cells, which predominantly express AHNAK at the plasma membrane. Confluent MCF-7 cells were treated with the membrane-permeable cross-linker dithiobis succinimidyl propionate, and AHNAK was immunoprecipitated with anti-AHNAK-CQL antibodies. Proteins present within the AHNAK immunoprecipitate were reduced, separated by SDS-PAGE, and identified by mass spectrometry. One major protein recovered within AHNAK immunoprecipitate was identified as annexin 2 (Fig. S1, available at <http://www.jcb.org/cgi/content/full/jcb.200307098/DC1>). The interaction between AHNAK and annexin 2 was confirmed both by coimmunoprecipitation in absence of cross-linking with two independent antibodies directed against AHNAK and immunodetection, and by a pull-down approach using recombinant AHNAK fragments linked to the GST tag (Fig. 2 A). The COOH-terminal fragment of AHNAK (Cter; aa 4642–5643), but neither a central fragment of AHNAK (M1; aa 820–1330) nor the GST tag alone, interacted with annexin 2. The interaction of annexin 2 with AHNAK is specific because other annexin family members, annexin IV and annexin VI, are not recovered in the AHNAK immunoprecipitates or in the pull-down experiments.

At the plasma membrane, annexin 2 can form a tetrameric complex with the S100A10 subunit (Harder and Gerke, 1993), a protein that belongs to the S100 family of EF hand-type Ca^{2+} -binding proteins (Schafer and Heizmann, 1996). In contrast to other S100 proteins, S100A10 has lost the ability to bind Ca^{2+} (Gerke and Weber, 1985). Therefore, we examined whether S100A10 associates with annexin 2 when complexed to AHNAK. In both MCF-7 and MDCK cells, S100A10 is recovered together with annexin 2 in AHNAK immunoprecipitates (Fig. 2 B). The interaction of the annexin 2/S100A10 complex with AHNAK-Cter domain was confirmed in pull-down assays (Fig. 2 C). In MDCK cells metabolically labeled with [^{35}S]methionine/cysteine, two major proteins migrating with a molecular mass corresponding to annexin 2 and S100A10 bound specifically to the AHNAK-Cter domain (Fig. 2 C, left). The identity of these bands as annexin 2 and S100A10 was confirmed by Western blot analysis (Fig. 2 C, right). The interaction occurred in EDTA/EGTA-containing buffer, indicating that the interaction between AHNAK and annexin 2/S100A10 is Ca^{2+} independent.

To evaluate the contribution of S100A10 in the annexin 2/S100A10/AHNAK interaction, we examined the effect of the S100B protein on that interaction. Previously, we have shown that S100B, another member of the S100 family, interacts with AHNAK-Cter in a strict calcium-dependent manner (Gentil et al., 2001). Because striking structural

similarities exist between S100A10 and Ca^{2+} -bound S100B (McClintock et al., 2002), we examined whether S100B can displace annexin 2/S100A10. First, we controlled that the interaction between the annexin 2/S100A10 complex and GST-AHNAK-Cter occurs in the presence of Ca^{2+} . Next, we observed that in the presence of Ca^{2+} , but not in EGTA (unpublished data), addition of recombinant S100B to the cell extracts fully antagonizes the binding of the annexin 2/S100A10 complex in a dose-dependent and competitive manner (Fig. 2 D). These data suggest that the annexin 2/S100A10- and S100B-binding domains on AHNAK-Cter overlap, and that S100A10 mediates the interaction between AHNAK and annexin 2.

The direct interaction of S100A10 with AHNAK was confirmed *in vitro*. When expressed in rabbit reticulocyte, S100A10 protein binds to and is pulled down by the recombinant GST-COOH-terminal domain of AHNAK (Fig. 2 E). No binding of rabbit reticulocyte that expressed annexin 2 could be detected (unpublished data). The direct interaction of S100A10 with AHNAK was also confirmed in yeast two-hybrid experiments. A human heart cDNA library was screened using the extreme COOH-terminal domain of AHNAK (CterC; aa 5124–5643) as a bait. 15 colonies were obtained out of 2×10^6 primary yeast transformants. The interaction specificity was retested after the mating assays on YC-UWLH medium and X-gal filter tests. Out of the 15 library plasmids retested, only two interacted specifically with CterC. The remaining plasmids gave a positive result with lamin and were considered as false positive. The nucleotide sequence of the two positive clones revealed that they correspond to S100A10. The specificity of interaction between S100A10 and CterC is illustrated in Fig. 2 F. Only CterC is competent for interaction with S100A10, and not CterN (aa 4642–5124), CterdLZ (aa 4642–4826), or lamin. Our double-hybrid experiment also reveals that S100B is capable of heterodimerizing with S100A10 in a yeast two-hybrid system (Fig. 2 F). Heterodimerization of S100B with other S100 proteins, such as S100A1, S100A6, and S100A11, has been observed previously (Deloulme et al., 2000). In contrast to the results obtained with S100A10, no interaction between S100B and AHNAK peptides could be detected in the yeast two-hybrid system (unpublished data). This is likely attributable to the limitation of yeast two-hybrid analysis to calcium-independent interactions (Deloulme et al., 2003).

AHNAK and the annexin 2/S100A10 complex are recruited to the sites of early cell–cell contacts

Confocal scanning immunofluorescence analyses of confluent epithelial MDCK cells reveal that AHNAK and annexin 2 colocalize all over the plasma membrane, including the sites of cell–cell contacts (Fig. 3 A). An identical pattern of distribution was observed for S100A10 (unpublished data). We had observed that AHNAK was recruited to the plasma membrane as cell confluence increased and as cells polarized (Fig. 1 A, e). The polarized phenotype of these cells was confirmed by the reorganization of the actin cytoskeleton (Fig. S2, available at <http://www.jcb.org/cgi/content/full/jcb.200307098/DC1>) and the apicolateral polarization of the tight junction marker ZO-1 (unpublished data). In po-

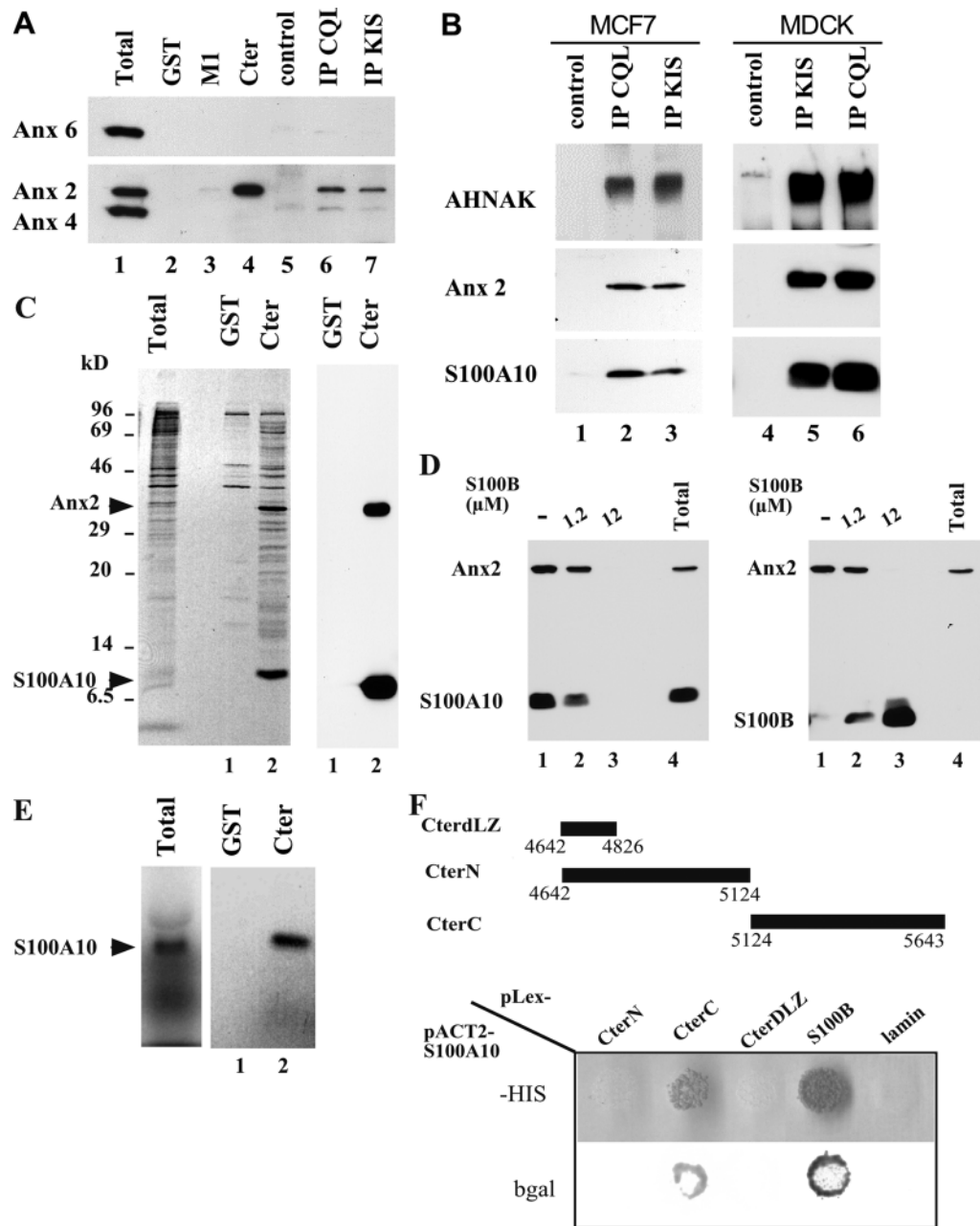


Figure 2. Interaction of the annexin 2/S100A10 complex with AHNAK. (A) MCF-7 cell extracts were incubated with glutathione-Sepharose (lanes 2–4) or protein A-Sepharose (lanes 5–7) in the presence of recombinant GST alone (lane 2), recombinant GST fused to AHNAK central repeat domain M1 (lane 3), recombinant GST fused to AHNAK COOH-terminal domain (lane 4), anti-AHNAK-CQL antibody (lane 6), or anti-AHNAK-KIS antibody (lane 7). Bound proteins were analyzed by Western blotting with anti-annexin 2, -4, and -6 antibodies. Lane 1 is total cell extract. (B) MCF-7 or MDCK cell extracts were incubated with control protein A-Sepharose beads (lanes 1 and 4), or with anti-AHNAK-CQL (lanes 2 and 6) or anti-AHNAK-KIS (lanes 3 and 5) antibodies. Coimmunoprecipitated proteins were analyzed by Western blotting with anti-AHNAK-KIS, anti-annexin 2, and anti-S100A10 antibodies. (C) S100A10 and annexin 2 are the major proteins that interact with the AHNAK Cter domain. [³⁵S]Methionine/cysteine labeled MDCK whole-cell extracts (total; left) were incubated with GST (lane 1) and GST fusion AHNAK-Cter (lane 2) in EGTA/EDTA-containing buffer. Bound proteins were resolved on SDS-PAGE and were detected either by autoradiography (left) or blotted on nitrocellulose membrane and detected with mixed anti-annexin 2 and anti-S100A10 mAbs (right). (D) S100B antagonizes annexin 2/S100A10 binding to the AHNAK Cter domain. U87 cell extracts were incubated with GST fusion AHNAK-Cter in the absence (lane 1) or in the presence (lanes 2 and 3) of increasing S100B concentrations in Ca²⁺/Zn²⁺-containing buffer. Bound proteins were analyzed by Western blotting using anti-annexin 2 and anti-S100A10 antibodies (left), or with anti-annexin 2 and anti-S100B antibodies (right). Lane 4 is total cell extract. (E) [³⁵S]Methionine/cysteine-labeled S100A10 was produced in rabbit reticulocyte (total), and the translation reaction was incubated with glutathione-Sepharose in the presence of recombinant GST (lane 1) or recombinant GST fused to the AHNAK COOH-terminal domain (lane 2) in Ca²⁺/Zn²⁺-containing buffer. Bound proteins were resolved on SDS-PAGE and detected by autoradiography. (F) S100A10 specifically interacts with AHNAK CterC and S100B in the yeast two-hybrid system. Top: diagram of the various AHNAK COOH-terminal fragments used. Yeast were cotransfected with S100A10 pACT2 vector and different baits corresponding to AHNAK Cter deletion mutants, S100B, and lamin cloned into the pLEX vector as indicated. The interactions were scored by the growth of transfected yeast on YC-UWLH medium lacking histidine (HIS) and confirmed by β-galactosidase activity assay (bgal).

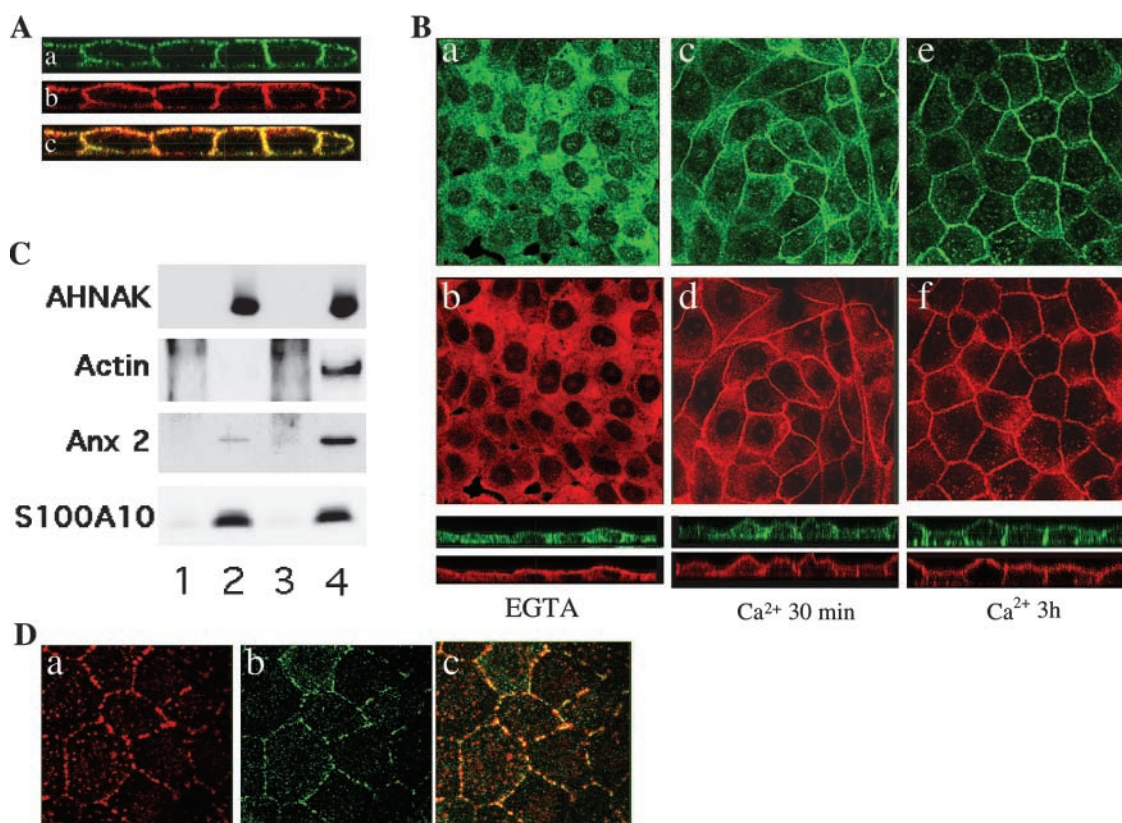


Figure 3. AHNAK colocalizes with the annexin 2/S100A10 complex at the plasma membrane in MDCK cells. (A) Confocal microscopy analysis (x-z axis) of the distribution in confluent MDCK cells of AHNAK (a), annexin 2 (b), and merge image (c). (B) Disruption of calcium-dependent cell–cell contacts causes the dissociation of AHNAK and annexin 2/S100A10 from the plasma membrane. Confluent MDCK cells were incubated in medium containing 5 mM EGTA supplemented with 1 mM MgCl₂ for 30 min at 37°C (a and b), and were then shifted to calcium-containing medium for 30 min (c and d) or 3 h (e and f). Cultures were double immunolabeled for AHNAK (a, c, and e) and S100A10 (b, d, and f). Single-plane confocal microscopy (x-y axis) and x-z section (bottom) images are shown. (C) Confluent MDCK cells incubated with EGTA-MgCl₂ medium for 30 min (lanes 1–2), then shifted back to Ca²⁺-containing medium for 3 h (lanes 3 and 4), were cross-linked with dithiobis succinimidyl propionate. Whole-cell lysates were incubated with protein A–Sepharose beads (lanes 1 and 3) or anti-AHNAK–CQL antibody cross-linked onto Sepharose beads (lanes 2 and 4). Immunoprecipitated proteins were reduced and analyzed by Western blot with anti-AHNAK–CQL, anti-actin, mouse monoclonal anti-annexin 2, and anti-S100A10 antibodies. (D) Confocal immunofluorescence of actin stained with phalloidin (a) and AHNAK (b) in MDCK cells treated with 1 μg/ml cytochalasin D for 1 h (c) is the merged image.

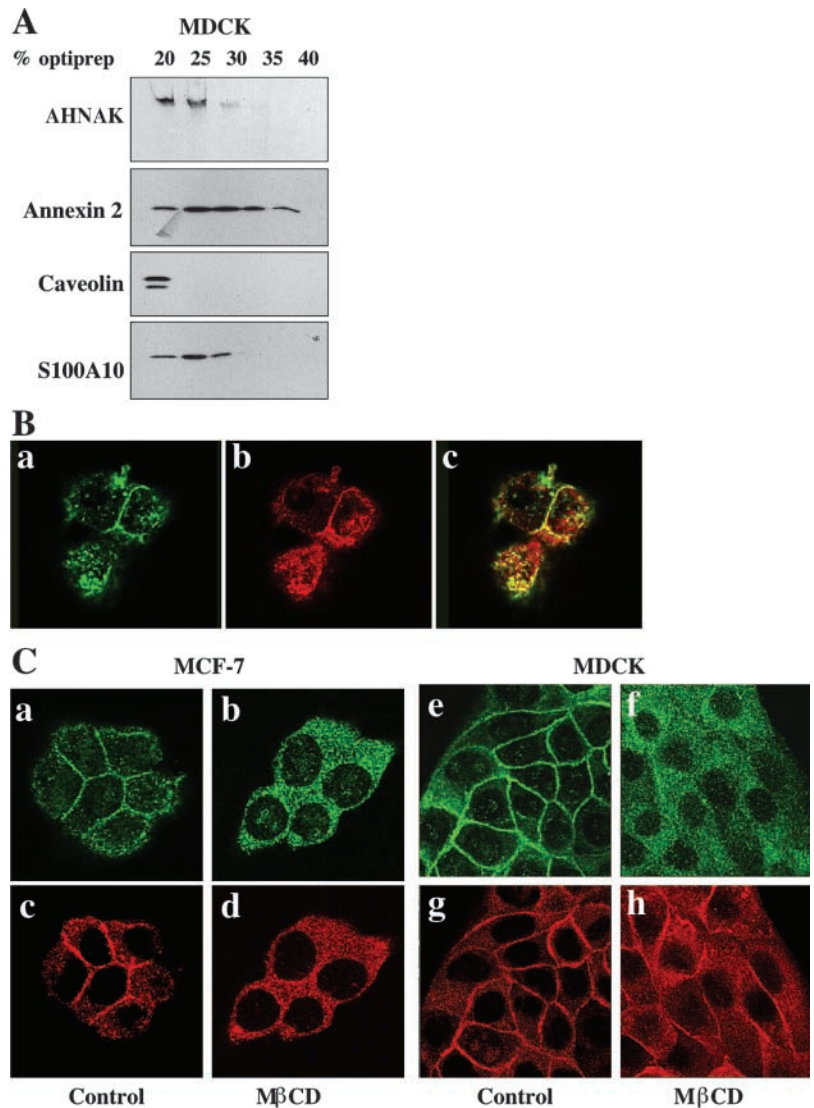
larized epithelial cells, cell–cell contacts initiate plasma membrane remodelling and the development of cell polarity (Drubin and Nelson, 1996). Therefore, we tested the role of the formation of cell–cell contacts in recruiting AHNAK to the plasma membrane. Lowering the Ca²⁺ concentration in the culture medium of an MDCK monolayer interferes with the stability of intercellular contacts (Grindstaff et al., 1998). Treatment of confluent MDCK cells with low Ca²⁺ medium resulted in the redistribution of AHNAK and of the annexin 2/S100A10 complex from cell contacts to the cytoplasm, and correlated with a more flattened morphology of the cells (Fig. 3 B, a and b). This membrane dissociation of AHNAK and of the annexin 2/S100A10 complex was reversible (Fig. 3 B, c–f). When cell–cell contacts were allowed to reform by readdition of calcium into the culture medium, AHNAK and the annexin 2/S100A10 complex were recruited to the sites of cell–cell contacts with a similar kinetic of relocation and distribution pattern. Within 30 min of calcium addition, AHNAK and S100A10 started to relocate to the newly forming cell–cell contacts (Fig. 3 B, c and d), and to strongly accumulate there after 3 h, as cell acquired a more cuboidal

epithelial morphology (Fig. 3 B, e and f). Coimmunoprecipitation experiments on cross-linked MDCK cells during the calcium switch experiment revealed that AHNAK forms a multimeric complex containing actin and annexin 2/S100A10, and that this association is strictly dependent on the localization of AHNAK at the plasma membrane (Fig. 3 C, lane 4). Upon membrane dissociation of AHNAK, only S100A10, and to a lesser extent annexin 2, are recovered within the AHNAK immunoprecipitates (lane 2).

The interaction of the membrane-bound form of AHNAK with the cortical actin cytoskeleton was confirmed by indirect immunofluorescence analysis of MDCK cells treated with cytochalasin D, which disrupts the integrity of the actin cytoskeleton (Fig. 3 D). As a consequence of its effect on actin, cytochalasin D treatment will also reversibly disrupt the organization of actin-associated membrane protein. In addition to the modification in the actin pattern, cytochalasin D treatment dramatically altered AHNAK distribution. At the apicolateral plasma membrane, AHNAK and actin precisely colocalized in a series of aggregates around the cell border, supporting the association of AHNAK with

Figure 4. AHNAK and annexin 2/S100A10 associate with cholesterol-rich membranes.

(A) AHNAK and annexin 2/S100A10 cofractionate to the lipid raft fractions. MDCK cells were lysed in buffer containing 1% Triton X-100 on ice, and flotation fractionation was performed in a 5–40% OptiPrep™ gradient. Fractions were analyzed by Western blotting using antibodies against AHNAK, annexin 2, and S100A10. Caveolin-1 was used as a marker of lipid raft-containing fraction. (B) Confocal microscopy analysis of FITC-cholera toxin β chain (a) and AHNAK (b) colocalization in MDCK cells. (c) Merged image. (C) Specific release of membrane-bound AHNAK by sequestration of membrane cholesterol. Confocal microscopy analysis of AHNAK (a, b, e, and f) and annexin 2 (HH7; c, d, g, and h) in MCF-7 (a–d) and MDCK (e–h) cells not treated (a, c, e, and g) or incubated with 3.8 mM of methyl- β -cyclodextrin (M β CD) for 15 min (b and d) or 1 h (f and h) at 37°C before fixation.



actin. Together, these data indicate that calcium-dependent cell–cell adhesion provides a signal for initiating the localized recruitment of AHNAK and annexin 2/S100A10 to sites of cell–cell contacts, where they form a stable protein complex with cortical actin cytoskeleton.

The annexin 2/S100A10/AHNAK complexes colocalize to intercellular junctions in a cholesterol-dependent mechanism

In addition to the Ca^{2+} -dependent association of annexin 2 with phospholipids, annexin 2 can also associate with the plasma membrane lipid raft microdomains in a cholesterol-dependent manner (Oliferenko et al., 1999; Babiychuk and Draeger, 2000; Babiychuk et al., 2002). Several laboratories have reported that annexin 2 may link lipid rafts with the cortical cytoskeleton (Oliferenko et al., 1999), and that annexin 2 recruits signaling proteins to intercellular junctions in a cholesterol-dependent manner (Hansen et al., 2002). To test a possible association of AHNAK with the annexin 2/S100A10 complex within lipid rafts, we performed flotation experiments in OptiPrep™ gradients in the presence of cold Triton X-100 (Fig. 4 A). In

this gradient, the detergent-insoluble lipid rafts will float at the interphase between the 0 and 20% OptiPrep™ layers. In MDCK cells, a significant amount of AHNAK partitioned with annexin 2 and S100A10 into the lipid raft fraction together with caveolin-1, a known cholesterol-binding protein (Fig. 4 A). Not all the annexin 2 cosedimented with AHNAK, suggesting that only a portion of the annexin 2/S100A10 complex interacts with AHNAK and associates with the lipid rafts. We confirmed the association of AHNAK with lipid rafts in whole cells by colocalization of AHNAK with the FITC-labeled β subunit of cholera toxin, which specifically binds the lipid raft ganglioside GM1 (Harder et al., 1998). Confocal laser scanning microscopy of MCF-7 cells showed an extensive overlap of AHNAK staining with the FITC-labeled cholera toxin β chain at the plasma membrane, including intercellular junctions (Fig. 4 B). Furthermore, depletion of plasma membrane cholesterol in MDCK and MCF-7 cells with methyl- β -cyclodextrin released a population of annexin 2 from the plasma membrane and totally abolished the junctional membrane localization of AHNAK, causing their redistribution to the cell cytoplasm (Fig. 4 C).

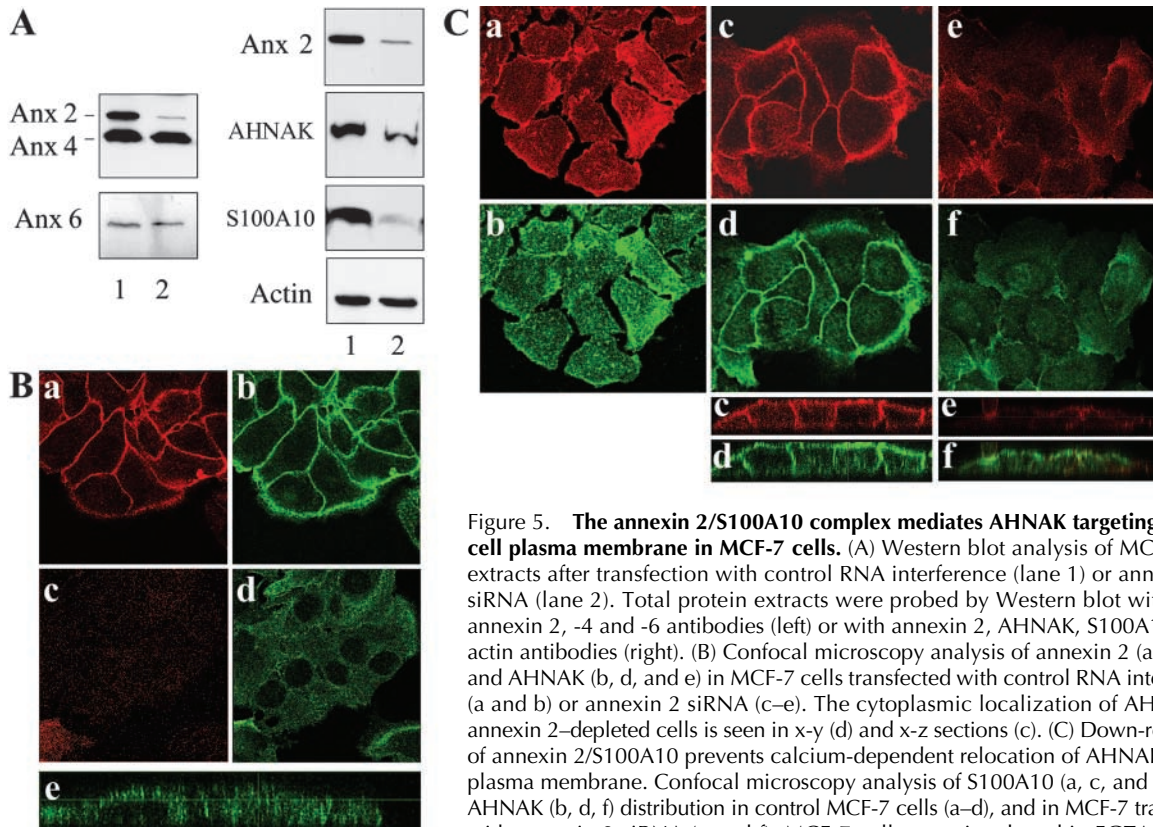


Figure 5. The annexin 2/S100A10 complex mediates AHNAK targeting to the cell plasma membrane in MCF-7 cells. (A) Western blot analysis of MCF-7 cell extracts after transfection with control RNA interference (lane 1) or annexin 2 siRNA (lane 2). Total protein extracts were probed by Western blot with anti-annexin 2, -4 and -6 antibodies (left) or with annexin 2, AHNAK, S100A10, and actin antibodies (right). (B) Confocal microscopy analysis of annexin 2 (a and c) and AHNAK (b, d, and e) in MCF-7 cells transfected with control RNA interference (a and b) or annexin 2 siRNA (c–e). The cytoplasmic localization of AHNAK in annexin 2-depleted cells is seen in x-y (d) and x-z sections (c). (C) Down-regulation of annexin 2/S100A10 prevents calcium-dependent relocation of AHNAK to the plasma membrane. Confocal microscopy analysis of S100A10 (a, c, and e) and AHNAK (b, d, f) distribution in control MCF-7 cells (a–d), and in MCF-7 transfected with annexin 2 siRNA (e and f). MCF-7 cells were incubated in EGTA-MgCl₂ medium for 30 min (a and b), then shifted to Ca²⁺-containing medium for 3 h (c–f). Both x-y and x-z sections are shown.

Annexin 2/S100A10 down-regulation in MCF-7 cells interferes with membrane localization of AHNAK and cell height

To evaluate whether the annexin 2/S100A10 complex cooperates with AHNAK functions at the plasma membrane, we first analyzed the incidence of annexin 2 down-regulation on AHNAK subcellular localization. A small interfering RNA (siRNA) duplex was designed against the human annexin 2 cDNA sequence. This siRNA does not function in down-regulating canine annexin 2 in MDCK cells, but is highly efficient in human epithelial MCF-7 cells (Fig. 5 A). Transfection of MCF-7 cells with annexin 2 siRNA significantly abrogated the expression of annexin 2, but did not affect the levels of related annexins expressed in MCF-7, annexin 4, and annexin 6. The down-regulation of annexin 2 in MCF-7 cells induced a drastic concomitant down-regulation of S100A10. This was likely the result of both transcriptional and post-translational regulations of the S100A10 level by annexin 2, a previously described well-known phenomenon (Puisieux et al., 1996; Van de Graaf et al., 2003). A decrease in AHNAK levels was also observed in transfected cells. This effect of annexin 2 RNA interference on AHNAK levels was specific because the total level of actin was not affected, and the transfection with a nonspecific siRNA did not alter the levels of AHNAK (unpublished data). Consistent with the Western blot data, the membrane-associated AHNAK immunoreactivity dropped in annexin 2-depleted MCF-7 cells, and the remaining AHNAK signal appeared diffuse within the cytoplasm (Fig. 5 B). The interdependence that exists between the

expression of annexin 2/S100A10 and the recruitment of AHNAK at the plasma membrane was confirmed in Ca²⁺ switch experiments (Fig. 5 C). As observed with MDCK cells (Fig. 3 B), disruption of calcium-dependent cell–cell contacts causes a reversible dissociation of AHNAK and of the annexin 2/S100A10 complex from the plasma membrane in MCF-7 cells (Fig. 5 C, a–d). However, in cells depleted with annexin 2/S100A10, AHNAK could not be re-recruited to the plasma membrane upon Ca²⁺-mediated cell–cell adhesion, and cells retained a flattened morphology (Fig. 5 C, e and f).

Confocal microscopy analysis of actin distribution visualized with fluorescent phalloidin in control and annexin 2/S100A10-depleted cells confirmed the change in the morphology of cells with low annexin 2/S100A10 content (Fig. 6 A). The overall height of annexin 2/S100A10-depleted MCF-7 cells is decreased, with most of the actin-associated fluorescence found in the more basal focal planes. Similar changes in cell morphology and actin-associated fluorescence were also observed in MCF-7 cells depleted for AHNAK after transfection with AHNAK siRNA (Fig. 6 B; see following paragraph). Together, these data suggest that the membrane-associated annexin 2/S100A10 complex is essential to the recruitment of AHNAK at the plasma membrane, and that the annexin 2/S100A10/AHNAK complexes regulate actin-dependent cytoarchitecture.

AHNAK regulates the actin cytoskeleton scaffold of epithelial cells

To confirm the function of AHNAK in the regulation of cortical actin organization, we have down-regulated AH-

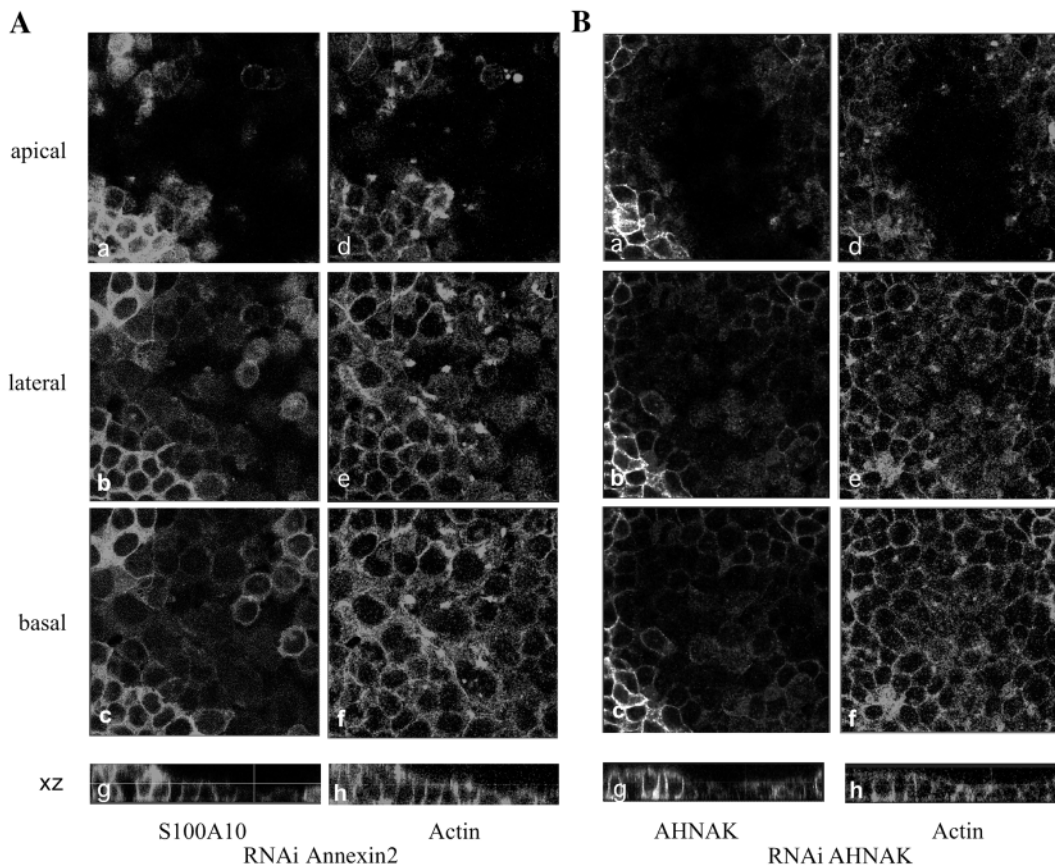


Figure 6. Effect of the invalidation of AHNAK and annexin 2 on cell height. Confocal images of MCF-7 cells transfected either with annexin 2 (A) or AHNAK (B) RNA interference. Apical (a and d), lateral (b and e), basal (c and f), and x-y sections and x-z merged sections (g and h) double immunostained for actin (A and B; d-f and h) and S100A10 (A; a-c and g) or AHNAK (B; a-c and g) reveals a similar collapse in cell height in both annexin 2- and AHNAK-invalidated cells. In A and B, x-y and x-z sections are from independent experiments.

NAK levels in MDCK cells, which rearrange their cytoskeleton in a highly structured manner as they polarize concomitantly with AHNAK recruitment to the plasma membrane (Fig. 1). An siRNA designed against the highly conserved repeated central domains of AHNAK efficiently and specifically down-regulates AHNAK levels in MDCK cells (Fig. 7 A; Fig. S3, available at <http://www.jcb.org/cgi/content/full/jcb.200307098/DC1>). We examined the effect of AHNAK siRNA on F-actin cytoskeleton rearrangement by confocal microscopy (Fig. 7, B–D). The extent of AHNAK down-regulation varied among transfected cells. Cells depleted for AHNAK were characterized by a marked disorganization of their actin cytoskeleton, visualized with fluorescent phalloidin. Unlike AHNAK-expressing cells, which rearranged their actin cytoskeleton into a lateral cortical belt and an apical actin network, cells devoid of AHNAK were unable to form an apicolateral cortical actin network, and F-actin could only be detected in the basal confocal plane (Fig. 7 B). AHNAK-negative cells retained a flattened morphology (Fig. 7 C). This decrease in cell height results in the void observed in the higher lateral and apical focal planes (Fig. 7 B, e and f). Note also that many AHNAK-negative cells at high density were dislodged from the cell monolayer and acquired rounded morphology (Fig. 7 B, arrows). This probably reflects an incapacity of invalidated cells to sustain density pressure because we did not observe a loss of adhesion of

AHNAK-negative cells at low density (unpublished data). Although down-regulation of AHNAK has a drastic effect on actin cytoskeleton organization at the apicolateral plasma membrane that acts to support cell height, it has only a subtle effect on the basal actin organization. Cells invalidated for AHNAK only displayed more punctuate actin stress fibers on their basal side, compared with control cells (Fig. 7 D). Note also that in AHNAK-depleted cells, the annexin 2/S100A10 complex remains localized at the plasma membrane (unpublished data). This observation indicates that annexin 2/S100A10 is not sufficient to regulate actin cytoskeleton organization that acts to support cell height, and argues for a direct cooperation with AHNAK. Together, our data suggest that AHNAK regulates cortical actin cytoskeleton organization.

Discussion

In epithelial cells, AHNAK is predominantly a cytosolic protein localized at the plasma membrane intracellular face. A faint AHNAK immunoreactivity within the cell nuclei was observed in cells submitted to a Ca^{2+} switch (Fig. 5 C), but was never observed in other cell culture conditions. The apparent exclusive cytoplasmic localization of AHNAK in MDCK cells contrasts with the results of Shivelman's group, who reported nuclear localization of AHNAK in

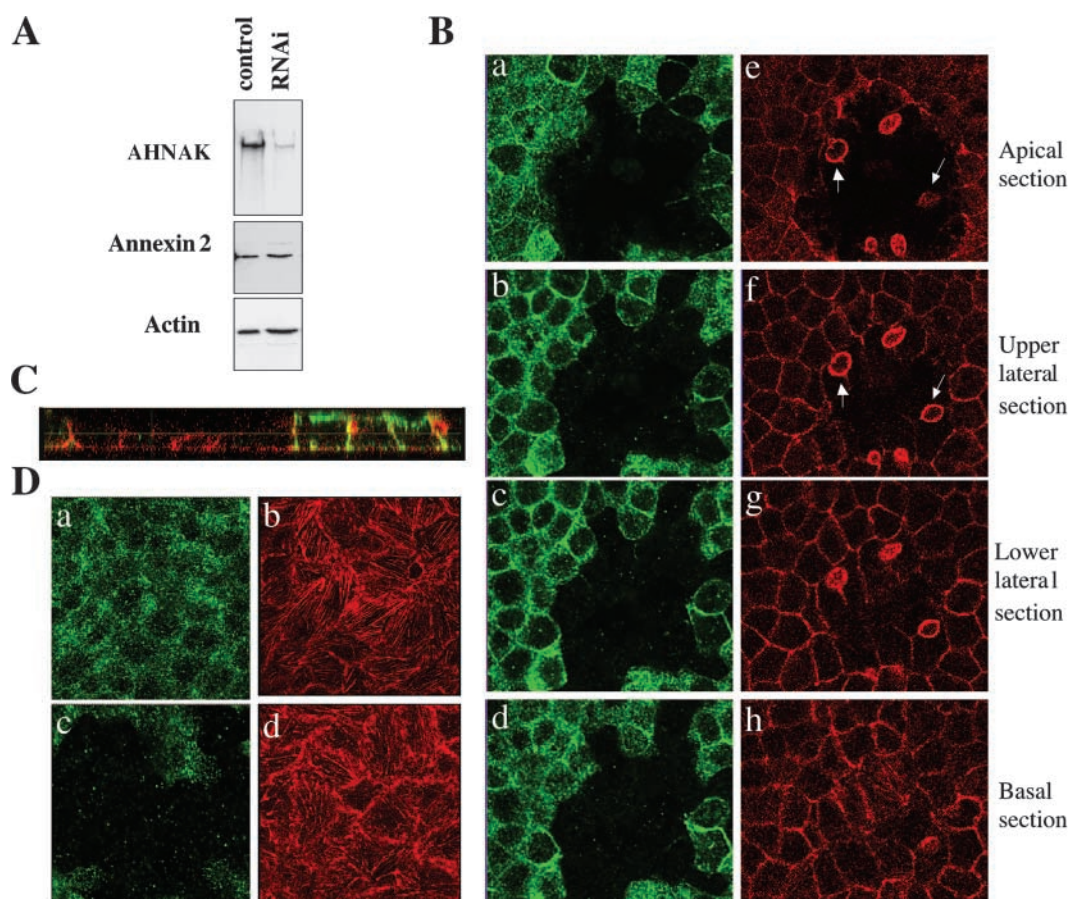


Figure 7. AHNAK regulates actin-based cell membrane cytoarchitecture. (A) Down-regulation of AHNAK by siRNA in MDCK cells. Total cell lysates of cells treated with AHNAK RNA interference or control RNA interference were analyzed by Western blot for AHNAK, annexin 2, and actin levels. (B) Effect of AHNAK siRNA on actin organization. MDCK cells transfected with AHNAK RNA interference were stained for AHNAK (a–d) and F-actin (e–h) with phalloidin. Confocal x-y sections at the apical (a and e), upper lateral (b and f), lower lateral (c and g), and basal (d and h) levels of the cells show that cells devoid of AHNAK are unable to form an apicolateral cortical actin network, leaving a black void in the higher apicolateral planes. Rounded AHNAK-negative cells can be seen within the monolayer (arrows). (C) Confocal microscopy x-z merged sections of AHNAK (green) and actin (red) staining reveals that cells invalidated for AHNAK retains a flattened morphology. (D) The effect of AHNAK siRNA on basal actin stress fibers. Basal confocal microscopy section shows that cells invalidated for AHNAK (c and d) displayed disorganized actin stress fibers on their basal side, compared with control cells (a and b).

sparse MDCK cell cultures (Sussman et al., 2001). Several possible explanations could be envisioned to explain the apparent discrepancies in subcellular AHNAK localization in MDCK cells. Some discrepancies can arise from the well-known heterogeneities in specific cell lines or clones in the various laboratories. Differences in epitope accessibility might also have to be considered. AHNAK nuclear immunoreactivity has only been reported with one antibody, FEN (Shtivelman and Bishop, 1993; Sussman et al., 2001). Because a recent work has pointed out that FEN cross reacts with a nuclear protein that is not recognized by two other AHNAK-specific antibodies (Borgonovo et al., 2002), we suggest that when located within the cell nuclei, AHNAK may adopt a conformation that could only be revealed by a specific antibody such as FEN.

In cultured epithelial cells, AHNAK targeting to the plasma membrane is reversible and triggered by Ca^{2+} -dependent cell adhesion. Disruption of E-cadherin-mediated cell-cell contacts by low extracellular Ca^{2+} results in the dissociation of AHNAK from the plasma membrane. After readdition of Ca^{2+} , AHNAK is rapidly re-recruited to the

plasma membrane at the sites of newly formed cell-cell contacts. In contrast to the tight junction-associated protein ZO-1, AHNAK immunoreactivity will progressively become more widely distributed all over the plasma membrane (unpublished data). In fully polarized MDCK cells, AHNAK immunoreactivity decorates the entire basal, lateral, and apical cell membranes. Such distribution of AHNAK suggests that AHNAK is not a junctional protein. Down-regulation of AHNAK levels in MDCK cells using AHNAK-specific siRNA prevents cortical actin cytoskeleton reorganization. These observations suggest a more general function for AHNAK in organizing cell cytoarchitecture at the plasma membrane.

To gain further insight into the molecular mechanisms of AHNAK function at the plasma membrane, we have searched for AHNAK partners at the plasma membrane. We have identified the annexin 2/S100A10 complex as a major AHNAK-binding protein in epithelial cells. Annexin 2 (also called calpactin I heavy chain, p36) is a member of the annexin family of Ca^{2+} - and phospholipid-binding proteins, which has been implicated in membrane trafficking and organization (for review see Gerke and Moss, 2002). Annexin

2 has been proposed to play a role in the organization of cholesterol-rich membrane microdomains (Oliferenko et al., 1999), the connection of lipid rafts with the underlying actin cytoskeleton (Harder et al., 1997; Gerke and Moss, 2002), and in cholesterol-mediated adherent junction formations (Harder et al., 1997; Corvera et al., 2000). Within cells, annexin 2 can occur either as a monomer or as a heterotetrameric complex coupled with S100A10 (also called calpactin I light chain, p11). The heterotetrameric annexin 2/S100A10 complex is the predominant form of annexin 2 present at the plasma membrane in epithelial cells (Harder and Gerke, 1993). The interaction between AHNAK and annexin 2/S100A10 occurs within the COOH-terminal domain of AHNAK. The direct interaction of S100A10 with the extreme COOH-terminal domain of AHNAK observed *in vitro* and in yeast two-hybrid experiments strongly suggests that S100A10 mediates the interaction between AHNAK and annexin 2. The physical interaction between AHNAK and the annexin 2/S100A10 complex in the cell is supported by several observations. First, a strict correlation exists between accumulation of AHNAK and the annexin 2/S100A10 complex to the plasma membrane during both confluence-mediated (Hansen et al., 2002; Fig. 1 A) and Ca^{2+} -dependent cell–cell adhesion (Fig. 3). Second, at the plasma membrane, AHNAK colocalizes with the annexin/S100A10 complex, and a significant amount of proteins associate with membrane rafts in a cholesterol-dependent manner (Fig. 4). Third, annexin 2 depletion by siRNA promotes AHNAK release to the cytoplasm (Fig. 5, B and C). The annexin/S100A10 dependence for AHNAK membrane localization strongly suggests that annexin 2/S100A10 contributes to the recruitment and stabilization of AHNAK at the plasma membrane. Two recent reports have pointed out a role for S100A10 in targeting channel proteins to the plasma membrane (Girard et al., 2002; Van de Graaf et al., 2003). A more general function for the annexin 2/S100A10 in the routing of proteins to the plasma membrane must now be considered.

Membrane-bound AHNAK not only interacts with annexin 2/S100A10, but also is part of a complex containing actin (Fig. 3, C and D). This observation is consistent with a recent paper describing physical interaction between AHNAK and F-actin and G-actin (Hohaus et al., 2002), and strongly suggests that AHNAK and annexin 2/S100A10 are part of a submembranous complex that interacts physically with the cortical actin cytoskeleton. Annexin 2/S100A10- and AHNAK-depleted MCF-7 cells both display decreased cell height. A similar and more drastic effect is observed in polarized epithelial MDCK cells, which retain a mesenchymal morphology upon AHNAK depletion (Fig. 7). Down-regulation of AHNAK prevents the apicolateral actin cytoskeleton reorganization required to support cell height. We propose that AHNAK and the annexin 2/S100A10 complex are involved in the regulation of the actin cytoskeleton organization at the lateral plasma membrane, and thus could be implicated in plasma membrane remodelling and in the establishment of specialized intercellular interaction. Such a role for AHNAK is consistent with its specific expression in most lining epithelium and in endothelial cells of impermeable brain capillaries and peripheral blood vessels, and con-

versely with its absence in the highly permeable fenestrated endothelium of the kidney glomeruli, the hepatic sinusoid, and the continuous capillaries of lung (Gentil et al., 2003). In adult tissues, AHNAK is also abundantly expressed at the plasma membrane of smooth muscle cells (Gentil et al., 2003). In smooth muscle cells, annexin 2 is thought to function as a cross-linker of lipid rafts with the underlying actin cytoskeleton to regulate sarcolemmal tension (Babiychuk and Draeger, 2000; Babiychuk et al., 2002). In these cells, AHNAK may cooperate with annexin 2 in the coordination of cytoskeletal and membrane rearrangements—a coordination that provides structural support of the membrane to respond to and control stretching forces (Babiychuk and Draeger, 2000; Babiychuk et al., 2002). A similar role for AHNAK has already been suggested in cardiac muscle (Hohaus et al., 2002). Although our paper highlights a structural role of AHNAK, the association of AHNAK with lipid rafts also opens the possibility that AHNAK could be implicated in regulation of signaling pathways that are compartmentalized within these microdomains (Simons and Toomre, 2000; Zajchowski and Robbins, 2002).

Materials and methods

Cell culture

U87 glioblastomas, MCF-7, and MDCK epithelial cells were maintained in DME (Life Technology), 10% FBS (Sigma-Aldrich), and 1% penicillin/streptomycin.

For calcium switch experiments, cells were incubated for 30 min with DME supplemented with 5 mM EGTA and 1 mM MgCl_2 to lower extracellular Ca^{2+} concentration and to perturb strict Ca^{2+} -dependent cell–cell adhesion, but to maintain Mg^{2+} -dependent cell–matrix adhesion. Cell–cell contacts were allowed to reform for the indicated times by returning cells to complete medium.

Reagents and antibodies

The pAbs directed against AHNAK, KIS, and CQL have been described previously (Gentil et al., 2003). Anti-annexin 2 mAb HH7 was a gift from V. Gerke (University of Münster, Münster, Germany). Anti-annexin 2, anti-annexin 2 light chain (S100A10), anti-annexin IV, anti-annexin VI, and anti-caveolin-1 mAbs were purchased from Transduction Laboratories. Texas red–phalloidin was purchased from Molecular Probes, Inc., and anti-actin mAb was purchased from Sigma-Aldrich. FITC-labeled cholera toxin B subunit and the cholesterol chelator methyl- β -cyclodextrin were purchased from Sigma-Aldrich.

In vitro protein–protein interaction assay/GST pull-down

GST-AHNAK-Cter and GST-AHNAK-M1 proteins (Gentil et al., 2001) were produced in the *Escherichia coli* AD494(DE3)pLysS strain (Novagen) and purified by glutathione-Sepharose affinity chromatography. For metabolic labeling, cells were labeled in methionine-free MEM and 5% FCS supplemented with 50 $\mu\text{Ci/ml}$ [^{35}S]methionine/cysteine mix for 12 h. For binding assays, cells were lysed at 4°C in TTBS buffer (40 mM Tris-HCl, pH 7.5, 150 mM NaCl, and 0.3% Triton X-100) plus protease inhibitors (leupeptin, aprotinin, pepstatin, and AEBSF; 10 $\mu\text{g/ml}$ each), and were centrifuged for 10 min. Cell lysates were precleared by incubation for 10 min with 50 μl GST-Sepharose. 500- μl aliquots of precleared supernatant were supplemented with either 5 mM EDTA/5 mM EGTA or with 0.3 mM CaCl_2 /10 μM ZnSO_4 and mixed with 10 μg purified GST fusion proteins plus 30 μl affinity GST-Sepharose beads equilibrated in the same buffers. After mixing for 15 min at 4°C, the beads were spun down and the supernatant was removed. The beads were washed three times with 1 ml binding buffers. At the last wash, beads were transferred to new tubes and boiled in SDS sample buffer.

Mass spectrometric analysis and protein identification

Proteins recovered within AHNAK immunoprecipitates were excised from Coomassie blue–stained gels and washed with 50% acetonitrile. Gel pieces were dried in a vacuum centrifuge and rehydrated in 20 μl of 25

mM NH_4HCO_3 containing 0.5 μg trypsin (sequencing grade; Promega). After 4 h incubation at 37°C, a 0.5- μl aliquot was removed for MALDI-TOF analysis and spotted onto the MALDI sample probe on top of a dried 0.5- μl mixture of 4:3 saturated α -cyano-4-hydroxy-trans-cinnamic acid in acetone/10 mg/ml nitrocellulose in acetone/isopropanol 1:1. Samples were rinsed by placing a 5- μl volume of 0.1% TFA on the matrix surface after the analyte solution had dried completely. After 2 min, the liquid was blown off by pressurized air. MALDI mass spectra of peptide mixtures were obtained using a mass spectrometer (Bruker Biflex; Bruker-Franzen Analytik). Internal calibration was applied to each spectrum using trypsin autodigestion peptides (MH+ 842.50, MH+ 1045.55, and MH+ 2211.11). Protein identification was confirmed by tandem mass spectrometry experiments as described previously (Gentil et al., 2001).

Double hybrid

For plasmid constructions, fusion proteins with LexA DNA-binding domain (LexADB1) were constructed in pLex10. For the pLex-AHNAK Cter construct, BamHI-EcoRI AHNAK fragment (aa 4642–5643) from pDY-C (Nishimoto) was subcloned into pcDNA3.1. The insert was then excised with BamHI and XhoI digestion and cloned into BamHI-Sall sites of pLex10. pLex-CterN was obtained by deleting AHNAK pstI–pstI fragment from pLex-AHNAK Cter. To obtain the pLex-AHNAK-CterC construct, pstI–pstI AHNAK fragment (aa 5124–5643) of pLex-AHNAK Cter was subcloned into the pstI site of plex10. For the pLex-Cter-LZ construct, the pLex-CterN plasmid was deleted by Sall–PstI digestion, blunted with Deep vent polymerase, and self ligated. pLexS100B was obtained by amplification of human S100B cDNA using primers containing Smal and pstI sites immediately flanking the start and the stop codon, respectively, and cloning of the PCR product into Smal–pstI sites of pLex10.

Large-scale yeast transformations using the human heart Matchmaker™ cDNA library constructed in pACT2T plasmid (CLONTECH Laboratories, Inc.) and two-hybrid screens were performed using an L40 yeast strain essentially as described previously (Deloulme et al., 2000). Primary transformants were analyzed on YC-UWLH medium plates. Growing clones were then tested for β -galactosidase expression (Deloulme et al., 2000). Library plasmids expressing LEU2 from positive transformants were selected using HB101 *E. coli*, which requires leucine supplementation for growth. cDNAs were retested in a mating assay against the original bait construct and pLexA-lamin as a control using the AMR70 yeast strain as described below. The interactions were also tested by yeast mating essentially as described previously (Deloulme et al., 2000).

Immunoprecipitation and Western blotting

For total cell lysates and coimmunoprecipitation, cells were washed in PBS and lysed on ice in lysis buffer (50 mM Tris, pH 8.0, 150 mM NaCl, 0.05% deoxycholic acid, 1% Triton X-100, 10% glycerol, 2 mM EDTA/EGTA, and protease inhibitor cocktail). Lysates were passed through a 26G needle and centrifuged for 10 min at 2,500 rpm in a tabletop centrifuge. Supernatants were either quantified with the BCA protein micro assay (Pierce Chemical Co.) and boiled in 1× DTT Laemmli buffer (total cell lysates), or incubated with either anti-AHNAK-KIS antibody together with protein A–Sepharose (Amersham Biosciences), anti-AHNAK-CQL antibody cross-linked onto Sepharose beads, or with protein A–Sepharose alone, for 1 h rotating at 4°C. The immunoprecipitates were washed three times in lysis buffer, and the beads boiled in 1× Laemmli with 20 mM DTT. Proteins were separated by SDS-PAGE using 5, 8, or 14% polyacrylamide concentrations to resolve AHNAK, actin, or annexin 2/S100A10, respectively. Proteins were blotted onto nitrocellulose membranes.

For cross-linking experiments, cells were washed in PBS, incubated for 5 min with 0.5 mM dithiobis succinimidyl propionate (Pierce Chemical Co.) in PBS, and washed twice in 50 mM glycine in PBS before cell lysis and AHNAK immunoprecipitation. Immunoprecipitated proteins were reduced by boiling for 5 min in 1× Laemmli buffer containing 5% β -mercaptoethanol, and were analyzed by Western blot.

RNA interference

21-nt siRNA duplexes targeting the 5'-AAGAUCUCCAUGCCUGAUGUG-3' mRNA sequence in the repeated domains of *ahnak*, and the 5'-AAGUGCAUAUGGGUCUGUCA-3' mRNA sequence corresponding to the NH₂-terminal domain of human *annexin 2* were purchased from Dharmacon. The sequence used was submitted to a BLAST search to ensure targeting specificity. The specificity of AHNAK and annexin 2 down-regulation was further checked by Western blotting analysis. MCF-7 or MDCK cells plated at low density ($3 \times 10^4/\text{cm}^2$) were transfected with 20 nM of either annexin 2 or AHNAK siRNA duplex, or scrambled siRNA using Oli-

gofectamine™ (Life Technologies) on two consecutive days, and maintained for a total of 4 d in DME 10% serum.

Immunofluorescence

Cells were either fixed in 4% PFA for 10 min at RT, followed by a permeabilization with 0.1% Triton X-100 for 10 min or with 70% methanol at –20°C for 10 min. Cells were then washed in TBS and incubated with the primary antibody in TBS containing 3% goat serum overnight at 4°C. After TBS washes, cells were then incubated for 1 h at RT with the secondary antibody in TBS goat serum, and phalloidin when required. The secondary antibodies coupled with Alexa® 488 were purchased from Molecular Probes, Inc., and those coupled with Cy3 and Cy5 were purchased from Jackson ImmunoResearch Laboratories. After the final washes, cells were mounted in fluorescence mounting medium (DakoCytomation) and analyzed with a fluorescent microscope (Axiovert 200M; Carl Zeiss MicroImaging, Inc.) or a confocal microscope (TCS-SP2; Leica).

For plasma membrane permeabilization, cells were treated with 0.5 U streptolysin O (Sigma-Aldrich) in 0.1% BSA-PBS at 4°C and transferred at 37°C for 5 min. Cells were then washed with PBS and incubated with the primary antibody diluted in PBS/5% goat serum for 30 min at 4°C. After PBS washes, cells were fixed with 4% PFA and processed as above.

Cholera toxin labeling of GM1

MCF-7 cells were incubated with 0.5 $\mu\text{g}/\text{ml}$ FITC-labeled cholera toxin β chain in DME for 4 min at 37°C. Cells were then washed twice with DME, fixed with 4% PFA for 10 min at RT, and permeabilized with 0.1% Triton X-100 for 10 min at RT. Cells were then analyzed by immunofluorescence for AHNAK and S100A10.

Flotation gradients

For the isolation of lipid rafts, cells grown in 100-mm tissue culture dishes were washed and scraped in PBS, pelleted, and lysed on ice for 30 min in 100 μl Triton X-100 lysis buffer (400 mM Tris, pH 7.5, 150 mM NaCl, 1 mM DTT, 1% Triton X-100, and protease inhibitor cocktail). After a 10-min spin at 2,500 rpm at 4°C, the supernatant was mixed with 200 μl of a 60% OptiPrep™ (Axis-Shield) solution to obtain a 40% final solution, and transferred to centrifuge tubes. The sample was overlaid with 270 μl of a 35, 30, 25, 20, and 5% solution of OptiPrep™ in Triton lysis buffer. The gradient was centrifuged in an ultracentrifuge (Optima TL; Beckman Coulter) at 45,000 rpm for 4 h at 4°C in a rotor (TLS-55; Beckman Coulter). The fractions were collected and analyzed by Western blotting.

Online supplemental material

Fig. S1 shows a Coomassie blue stain of the proteins coimmunoprecipitated with AHNAK. Fig. S2 shows the rearrangement of the actin cytoskeleton in polarized MDCK cells. Fig. S3 shows the specific down-regulation of AHNAK protein by immunofluorescence in MDCK cells treated with AHNAK siRNA. The online supplemental material is available at <http://www.jcb.org/cgi/content/full/jcb.200307098/DC1>.

We thank Dr. Deloulme for his help with yeast two-hybrid experiments; Dr. D. Grunwald for his help with confocal microscopy (Imaging Core Facility, DRDC, CEA-Grenoble); Dr. Nie and Dr. Hashimoto (Kurume University, Kurume, Japan) for pC-DY plasmid and anti-desmoyokin/AHNAK antibody DY, Dr. Gerke for HH7 antibody, and Dr. Lamarre for critical reading of the manuscript.

This work was supported by grant from the Association pour la Recherche contre le Cancer (ARC 5643 to C. Delphin) and by a fellowship from la Ligue Nationale contre le Cancer (to B.J. Gentil).

Submitted: 15 July 2003

Accepted: 20 November 2003

References

- Babiychuk, E.B., and A. Draeger. 2000. Annexins in cell membrane dynamics. Ca²⁺-regulated association of lipid microdomains. *J. Cell Biol.* 150:1113–1124.
- Babiychuk, E.B., K. Monastyrskaya, F.C. Burkhard, S. Wray, and A. Draeger. 2002. Modulating signaling events in smooth muscle: cleavage of annexin 2 abolishes its binding to lipid rafts. *FASEB J.* 16:1177–1184.
- Barton, N.R., E.M. Bonder, D.J. Fishkind, R.H. Warren, and M.M. Pratt. 1992. A novel vesicle-associated protein (VAP-1) in sea urchin eggs containing multiple RNA-binding consensus sequences. *J. Cell Sci.* 103:797–809.
- Borgonovo, B., E. Cocucci, G. Racchetti, P. Podini, A. Bachi, and J. Meldolesi.

2002. Regulated exocytosis: a novel, widely expressed system. *Nat. Cell Biol.* 4:955–962.
- Corvera, S., C. DiBonaventura, and H.S. Shpetner. 2000. Cell confluence-dependent remodeling of endothelial membranes mediated by cholesterol. *J. Biol. Chem.* 275:31414–31421.
- Deloulme, J.C., N. Assard, G.O. Mbele, C. Mangin, R. Kuwano, and J. Baudier. 2000. S100A6 and S100A11 are specific targets of the calcium- and zinc-binding S100B protein in vivo. *J. Biol. Chem.* 275:35302–35310.
- Deloulme, J.C., B.J. Gentil, and J. Baudier. 2003. Monitoring of S100 homodimerization and heterodimeric interactions by the yeast two-hybrid system. *Microsc. Res. Tech.* 60:560–568.
- Downs, K.M., J. McHugh, A.J. Copp, and E. Shtivelman. 2002. Multiple developmental roles of Ahnak are suggested by localization to sites of placentation and neural plate fusion in the mouse conceptus. *Gene Expr. Patterns.* 2:27–34.
- Drubin, D.G., and W.J. Nelson. 1996. Origins of cell polarity. *Cell.* 84:335–344.
- Dytrych, L., D.L. Sherman, C.S. Gillespie, and P.J. Brophy. 1998. Two PDZ domain proteins encoded by the murine periaxin gene are the result of alternative intron retention and are differentially targeted in Schwann cells. *J. Biol. Chem.* 273:5794–5800.
- Gentil, B.J., C. Delphin, G.O. Mbele, J.C. Deloulme, M. Ferro, J. Garin, and J. Baudier. 2001. The giant protein AHNAK is a specific target for the calcium- and zinc-binding S100B protein: potential implications for Ca²⁺ homeostasis regulation by S100B. *J. Biol. Chem.* 276:23253–23261.
- Gentil, B.J., C. Delphin, C. Benaud, and J. Baudier. 2003. Expression of the giant protein AHNAK (desmoyokin) in muscle and lining epithelial cells. *J. Histochem. Cytochem.* 51:339–348.
- Gerke, V., and K. Weber. 1985. The regulatory chain in the p36-kd substrate complex of viral tyrosine-specific protein kinases is related in sequence to the S-100 protein of glial cells. *EMBO J.* 4:2917–2920.
- Gerke, V., and S.E. Moss. 2002. Annexins: from structure to function. *Physiol. Rev.* 82:331–371.
- Girard, C., N. Tinel, C. Terrenoire, G. Romey, M. Lazdunski, and M. Borsotto. 2002. p11, an annexin II subunit, an auxiliary protein associated with the background K⁺ channel, TASK-1. *EMBO J.* 21:4439–4448.
- Grindstaff, K.K., C. Yeaman, N. Anandasabapathy, S.C. Hsu, E. Rodriguez-Boulan, R.H. Scheller, and W.J. Nelson. 1998. Sec6/8 complex is recruited to cell-cell contacts and specifies transport vesicle delivery to the basal-lateral membrane in epithelial cells. *Cell.* 93:731–740.
- Haase, H., T. Podzuweit, G. Lutsch, A. Hohaus, S. Kostka, C. Lindschau, M. Kott, R. Kraft, and I. Morano. 1999. Signaling from β -adrenoceptor to L-type calcium channel: identification of a novel cardiac protein kinase A target possessing similarities to AHNAK. *FASEB J.* 13:2161–2172.
- Hansen, M.D., J.S. Ehrlich, and W.J. Nelson. 2002. Molecular mechanism for orienting membrane and actin dynamics to nascent cell-cell contacts in epithelial cells. *J. Biol. Chem.* 277:45371–45376.
- Harder, T., and V. Gerke. 1993. The subcellular distribution of early endosomes is affected by the annexin IIp11(2) complex. *J. Cell Biol.* 123:1119–1132.
- Harder, T., R. Kellner, R.G. Parton, and J. Gruenberg. 1997. Specific release of membrane-bound annexin II and cortical cytoskeletal elements by sequestration of membrane cholesterol. *Mol. Biol. Cell.* 8:533–545.
- Harder, T., P. Scheiffle, P. Verkade, and K. Simon. 1998. Lipid domain structure of the plasma membrane revealed by patching of membrane components. *J. Cell Biol.* 141:929–942.
- Hashimoto, T., M. Amagai, D.A. Parry, T.W. Dixon, S. Tsukita, K. Miki, K. Sakai, Y. Inokuchi, J. Kudoh, N. Shimizu, and T. Nishikawa. 1993. Desmoyokin, a 680 kDa keratinocyte plasma membrane-associated protein, is homologous to the protein encoded by human gene AHNAK. *J. Cell Sci.* 105:275–286.
- Hashimoto, T., S. Gamou, N. Shimizu, Y. Kitajima, and T. Nishikawa. 1995. Regulation of translocation of the desmoyokin/AHNAK protein to the plasma membrane in keratinocytes by protein kinase C. *Exp. Cell Res.* 217:258–266.
- Hieda, Y., and S. Tsukita. 1989. A new high molecular mass protein showing unique localization in desmosomal plaque. *J. Cell Biol.* 109:1511–1518.
- Hohaus, A., V. Person, J. Behlke, J. Schaper, I. Morano, and H. Haase. 2002. The carboxyl-terminal region of ahnak provides a link between cardiac L-type Ca²⁺ channels and the actin-based cytoskeleton. *FASEB J.* 16:1205–1216.
- Kingsley, P.D., K.E. McGrath, K.M. Maltby, A.D. Koniski, R. Ramchandran, and J. Palis. 2001. Subtractive hybridization reveals tissue-specific expression of ahnak during embryonic development. *Dev. Growth Differ.* 43:133–143.
- Kudoh, J., Y. Wang, S. Minoshima, T. Hashimoto, M. Amagai, T. Nishikawa, E. Shtivelman, J.M. Bishop, and N. Shimizu. 1995. Localization of the human AHNAK/desmoyokin gene (AHNAK) to chromosome band 11q12 by somatic cell hybrid analysis and fluorescence in situ hybridization. *Cytogenet. Cell Genet.* 70:218–220.
- McClintock, K.A., L.J. Van Eldik, and G.S. Shaw. 2002. The C-terminus and linker region of S100B exert dual control on protein-protein interactions with TRTK-12. *Biochemistry.* 41:5421–5428.
- Nie, Z., W. Ning, M. Amagai, and T. Hashimoto. 2000. C-Terminus of desmoyokin/AHNAK protein is responsible for its translocation between the nucleus and cytoplasm. *J. Invest. Dermatol.* 114:1044–1049.
- Oliferenko, S., K. Paiha, T. Harder, V. Gerke, C. Schwarzler, H. Schwarz, H. Beug, U. Gunthert, and L.A. Huber. 1999. Analysis of CD44-containing lipid rafts: Recruitment of annexin II and stabilization by the actin cytoskeleton. *J. Cell Biol.* 146:843–854.
- Puisieux, A., J. Ji, and M. Ozturk. 1996. Annexin II up-regulates cellular levels of p11 protein by a post-translational mechanisms. *Biochem. J.* 313:51–55.
- Schafer, B.W., and C.W. Heizmann. 1996. The S100 family of EF-hand calcium-binding proteins: functions and pathology. *Trends Biochem. Sci.* 21:134–140.
- Sekiya, F., Y.S. Bae, D.Y. Jhon, S.C. Hwang, and S.G. Rhee. 1999. AHNAK, a protein that binds and activates phospholipase C- γ 1 in the presence of arachidonic acid. *J. Biol. Chem.* 274:13900–13907.
- Shtivelman, E., and J.M. Bishop. 1993. The human gene AHNAK encodes a large phosphoprotein located primarily in the nucleus. *J. Cell Biol.* 120:625–630.
- Shtivelman, E., F.E. Cohen, and J.M. Bishop. 1992. A human gene (AHNAK) encoding an unusually large protein with a 1.2- μ m polyionic rod structure. *Proc. Natl. Acad. Sci. USA.* 89:5472–5476.
- Simons, K., and D. Toomre. 2000. Lipid rafts and signal transduction. *Nat. Rev. Mol. Cell Biol.* 1:31–39.
- Sussman, J., D. Stokoe, N. Ossina, and E. Shtivelman. 2001. Protein kinase B phosphorylates AHNAK and regulates its subcellular localization. *J. Cell Biol.* 154:1019–1030.
- Van de Graaf, S.F., J.G. Hoenderop, D. Gkika, D. Lamers, J. Prenen, U. Rescher, V. Gerke, O. Staub, B. Nilius, and R.J. Bindels. 2003. Functional expression of the epithelial Ca²⁺ channels (TRPV5 and TRPV6) requires association of the S100A10-annexin 2 complex. *EMBO J.* 22:1478–1487.
- Zajchowski, L.D., and S.M. Robbins. 2002. Lipid rafts and little caves. Compartmentalized signalling in membrane microdomains. *Eur. J. Biochem.* 269:737–752.
- Zuber, J., O.I. Tchernitsa, B. Hinzmann, A.C. Schmitz, M. Grips, M. Hellriegel, C. Sers, A. Rosenthal, and R. Schafer. 2000. A genome-wide survey of RAS transformation targets. *Nat. Genet.* 24:144–152.

ARTICLE

Expression of the Giant Protein AHNAK (Desmoyokin) in Muscle and Lining Epithelial Cells

Benoit J. Gentil, Christian Delphin, Christelle Benaud, and Jacques Baudier

Laboratoire de Transduction du Signal INSERM EMI-0104, Grenoble, France

SUMMARY Here we report a detailed analysis of the expression and localization of the giant protein AHNAK in adult mouse tissues. We show that AHNAK is widely expressed in muscle cells, including cardiomyocytes, smooth muscle cells, skeletal muscle, myoepithelium, and myofibroblasts. AHNAK is also specifically expressed in epithelial cells of most lining epithelium, but is absent in epithelium with more specialized secretory or absorptive functions. In all adult tissues, the main localization of AHNAK is at the plasma membrane. A role for AHNAK in the specific organization and the structural support of the plasma membrane common to muscle and lining epithelium is discussed.

(*J Histochem Cytochem* 51:339–348, 2003)

KEY WORDS

muscle
AHNAK
epithelium
tissue localization

THE GIANT PROTEIN AHNAK has been identified by Shtivelman et al. (1992) as a gene whose transcription is repressed in cell lines derived from neuroblastomas and other tumors. Hieda and Tsukita (1989) identified the mouse homologue of AHNAK (desmoyokin) as a plasma membrane-associated protein localized to the desmosomal attachment plaques in stratified epithelium. AHNAK is unusual in the sense that it is a very large protein of approximately 700 kD whose gene is composed of a single exon located on human chromosome 11q12 (Kudoh et al. 1995). Moreover, AHNAK is characterized by a large internal domain (4300 amino acids) composed of highly conserved repeated elements, most of which are 128 amino acids in length. This internal domain is flanked by a short NH₂ terminus and a COOH terminus of 1000 amino acids. The COOH terminus of AHNAK contains nuclear localization sequences and a nuclear export signal (Shtivelman et al. 1992; Sussman et al. 2001). In various cell lines, including NIH 3T3 fibroblasts, MDCK cells, and HeLa cells, AHNAK is located principally (but not exclusively) in the nucleus and is phos-

phorylated on serine and threonine residues (Shtivelman and Bishop 1993). PKB phosphorylation of AHNAK prevents its nuclear accumulation in HeLa and MDCK cells (Sussman et al. 2001). In contrast, in tissues such as skin and heart, AHNAK has an exclusive plasma membrane localization (Hashimoto et al. 1993; Haase et al. 1999). The targeting of AHNAK to the plasma membrane is dependent on PKC activation in epithelial DJM-1 cells (Hashimoto et al. 1995) and is regulated by cell density in human MDCK cells (Sussman et al. 2001). The cellular functions of AHNAK are unknown, but several studies have implicated AHNAK in signal transduction pathways. In vitro, AHNAK binds and activates PLC γ in the presence of arachidonic acid (Sekiya et al. 1999). In cardiomyocytes, AHNAK associates with the β -subunit of cardiac L-type calcium channels and is phosphorylated by PKA in response to adrenoceptor stimulation (Haase et al. 1999). Moreover, we have shown that AHNAK interacts with the EF-hand calcium and zinc binding S100B protein (Gentil et al. 2001), which is abundantly expressed in the central nervous system, skin, and muscle (Boni et al. 1997; Shrestha et al. 1998). Although studies on the cellular and sub-cellular localization of AHNAK in cultured cell lines are available in the literature, its tissue localization has been poorly investigated. Recently, a study on the expression of AHNAK in embryonic tissues revealed a tissue-specific expression of AHNAK (Kingsley et al.

Correspondence to: Jacques Baudier, Departement Reponse et Dynamique Cellulaires, TS EMI 0104, DRDC, CEA Grenoble, 17 rue des Martyrs, 38054 Grenoble Cedex 9, France. E-mail: jbaudier@cea.fr

Received for publication July 25, 2002; accepted October 9, 2002 (2A5867).

2001). At E8.5, AHNAK is expressed in extraembryonic tissue, in migratory mesenchymal cells, in mesenchymal cells lining the branchial artery, and in nasal epithelia and skin. In these cells, AHNAK immunoreactivity was essentially found associated with plasma membrane and cytoplasm. In adult mammals, the expression and function of AHNAK have not yet been investigated. In this study we investigated AHNAK expression in adult mouse tissues.

Materials and Methods

Antibodies and Controls

Rabbit polyclonal antibodies were made against AHNAK using two different epitopes. The first, KIS (CKISMPDVLHLKGPK), was chosen according to the strategy of Shtivelman and Bishop (1993). The second epitope, CQL (CQLPEVELSVSTKKE), is localized in the C-terminus of the protein (aa 5630–5643). The KIS-AHNAK and CQL-AHNAK antibodies used throughout our study are affinity-purified. Antibodies were purified from immunized rabbit sera by affinity chromatography using KIS or CQL peptide crosslinked to Sepharose beads. The purity of the immunoglobulins was controlled by SDS-PAGE in the absence and in the presence of a reducing agent. The purified antibodies were stored in PBS and 50% glycerol at a concentration of 0.15 mg/ml. The specificity of the antibodies was tested in Western blotting on HeLa cell extracts and on the recombinant AHNAK protein. To control for antibody specificity, the KIS-AHNAK antibody and the CQL-AHNAK antibody were incubated with the corresponding KIS or CQL peptides before primary immunoreaction. No immunoreaction was detected using this method. For immunocytochemistry, the specificity of immunostaining was controlled by preincubation of the affinity-purified KIS-AHNAK antibody with the KIS peptide. For double immunofluorescence experiments, we used a monoclonal anti-PECAM, MEC13.3, from Sigma (St Louis, MO). Cyan3 and Alexa 488 antibodies used as second antibody were provided by Molecular Probes (Eugene, OR).

Immunoblotting

In adult mouse, specimens from kidney, heart, thymus, esophagus, pancreas, liver, and lung were removed. These specimens were cut into small pieces and quickly frozen with liquid nitrogen until used. Specimens were homogenized with a glass homogenizer and were then heated at 90°C for 3 min in denaturation buffer composed of 2% SDS, 25 mM Tris-HCl, pH 6.8, 10% glycerol, 0.1% bromophenol blue, 1M EDTA. Proteins were electrophoretically resolved by one-dimensional SDS-PAGE (6% polyacrylamide), the gel was then equilibrated in transfer buffer containing 0.03% SDS and proteins were transferred onto nitrocellulose membrane. The membrane was first incubated with CQL-AHNAK antibody (1:100 dilution) in TBS containing 0.3% Tween-20 (TTBS) at 4°C for 16 hr. After washing, the membrane was incubated with a 1:10,000 dilution of horseradish peroxidase secondary antibody and the immune complex was revealed by chemiluminescence. Nitrocellulose membrane was then stripped in TTBS with 1% SDS and 0.1% sodium

azide, and then reprobbed with the KIS-AHNAK antibody (1:1000 dilution).

Immunocytochemistry

Tissues were screened for AHNAK localization using a tissue array produced by ResGen Co. (Invitrogen; Carlsbad, CA). We used paraffin-embedded tissue spots representing several mouse organs: adrenal, brain, heart, large intestine, small intestine, renal cortex, renal medulla, liver, lung, lymph node, skeletal muscle, pancreas, salivary gland, skin, spleen, stomach, thymus, prostate, testis, ovary, uterus, breast, and esophagus. Paraffin was removed and immunohistochemistry was then performed using the DAKO ABC horseradish peroxidase system (DAKO; Carpinteria, CA). After endogenous peroxidase inactivation with H₂O₂ 3% and sodium azide 0.05%, followed by extensive washing, tissues were blocked in 5% normal goat serum in TBS for 30 min and incubated with the KIS-AHNAK antibody at 1:100 dilution in TBS plus 2% normal goat serum overnight at 4°C. After rinsing with TBS, tissues were incubated with a biotinylated goat anti-rabbit Ig (DAKO) diluted 1:100 in TBS plus 5% normal goat serum for 30 min at room temperature. After extensive washing with TBS, the slide was incubated with the horseradish peroxidase complex according to the manufacturer's recommendations. The chromogen used was AEC+ (DAKO). Slides were counterstained with hematoxylin. For indirect immunofluorescence localization of AHNAK, mouse testis, brain, and liver were frozen in isopentane at -80°C and cut in 10- μ m sections. Slides were fixed with 4% paraformaldehyde for 30 min and washed abundantly before permeabilization for 5 min with 0.5% Triton X-100 in TBS. After extensive washing and blocking with goat serum, primary antibodies were incubated overnight at 4°C at the following dilutions: KIS-AHNAK 1:100; PECAM 1:5. Slides were then incubated with secondary antibody for 1 hr and nuclear counterstaining was performed with Hoechst 33258 (1 μ g/ml). Double immunofluorescence analysis was performed using confocal microscopy (Leica TCS-SP2) or fluorescence microscopy (Zeiss Axiovert 200M). Images were directly captured, saved, and transferred to Adobe Photoshop 5.5.

Results

Immunoblotting Analysis and Tissue Distribution of AHNAK

Extracts from various mouse tissues were analyzed for AHNAK expression by immunoblotting using affinity-purified antibodies raised against the CQL and the KIS peptides (Figure 1). To normalize for total protein content of the tissue preparations, the extracts were also analyzed for α -tubulin content (Figure 1A). Both the CQL and the KIS antibody reacted strongly with a major protein band that migrated with the expected molecular weight for AHNAK, confirming the specificity of our antibodies (Figure 1B). A high level of expression of AHNAK was observed in heart, lung and esophagus, whereas kidney, pancreas, and liver expressed only moderate levels of AHNAK. AHNAK

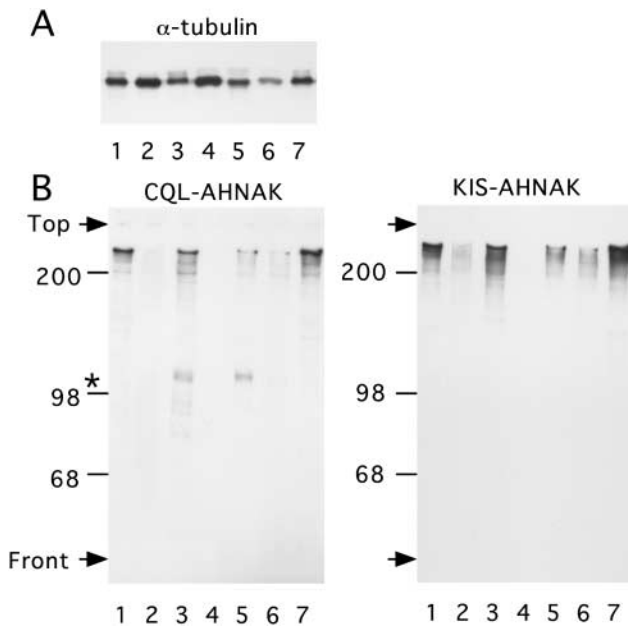


Figure 1 Immunoblotting analysis of AHNAK content in mouse organs or tissues. Tissue extracts were analyzed by Western blotting using α -tubulin (A), CQL, or KIS (B) antibody. Lane 1, heart; Lane 2, liver; Lane 3, lung; Lane 4, thymus; Lane 5, kidney; Lane 6, pancreas; Lane 7, esophagus. Asterisk indicates a 100-kD band that may correspond to a proteolytic fragment of the C-terminus of AHNAK.

immunoreactivity was absent in the thymus. CQL and KIS antibodies also reacted with lower molecular weight protein bands. These protein bands are present only in tissue extracts that express the full-length AHNAK protein and may therefore represent proteolytic products of AHNAK. In support of that assumption, we found that AHNAK is highly sensitive to metal-dependent proteases. When tissues are lysed in the absence of the metal chelators EDTA and EGTA, the full-length AHNAK immunoreactivity decreases, with a concomitant increase in the lower molecular weight protein bands recognized by both the AHNAK KIS and CQL antibodies (data not shown). A band of approximately 100 kD was also detected with the CQL antibody but not with the KIS antibody. This band might correspond to a C-terminal AHNAK proteolytic fragment. The affinity-purified KIS antibody was next used for immunoperoxidase and indirect immunofluorescence analysis of AHNAK immunoreactivity in mouse tissues (Figures 2–5).

AHNAK Localization in Muscle Cells

Immunohistochemical analysis of AHNAK immunoreactivity in different tissues revealed a specific localization of AHNAK in muscle cells (Figure 2). As previously reported by Haase et al. (1999), heart sections clearly show a plasma membrane localization of

AHNAK in cardiomyocytes (Figure 2A). Figure 2B shows a muscle section incubated with affinity-purified KIS antibody that was preincubated with the KIS peptide and counterstained with biotinylated horseradish peroxidase. In this control, AHNAK staining was completely abolished, confirming our biochemical analysis that the KIS antibody used in our study is specific for AHNAK protein. AHNAK expression is not restricted to cardiomyocytes, but appears to be a general feature of the different muscular cell types. As observed in cardiomyocytes, in the skeletal myocytes forming the striated skeletal muscle fiber, AHNAK immunoreactivity also accumulated at the plasma membrane (Figure 2C). In the small intestine, AHNAK antibodies decorated the layers of smooth muscle cells of the tunica underlining the epithelium (Figure 2D). Both the longitudinal and the circular layer of smooth muscle cells showed strong AHNAK immunoreactivity. A cross-section of the circular layer clearly showed that AHNAK is localized at the plasma membrane. This pattern of AHNAK immunoreactivity in smooth muscle cells was also observed on the muscularis propria of the body of the stomach, which also consists of an inner circular and outer longitudinal layer (data not shown). Other structures composed of smooth muscle cells found in various tissue also express AHNAK (Figure 2E and 2F). In the ovary, theca cells showed strong plasma membrane AHNAK immunoreactivity (Figure 2E). Theca cells, which are important for steroid secretion, also have muscle characteristics (Motta and Familiari 1981; Self et al. 1988). At ovulation, these cells by their contraction may be capable of squeezing the follicular wall or may favor follicle collapse and subsequent involution during atresia. Smooth muscle cells that compose the tunica media and ensheath large blood vessels in various tissue were also stained with AHNAK antibodies. In testis, smooth muscle cells surrounding small and large arteries were AHNAK-positive (Figure 2F). AHNAK was also expressed by PECAM-positive endothelial cells, as revealed by yellow pixels in merged confocal double-labeled fluorescent image (Figure 2F). We also observed apparently higher AHNAK immunoreactivity in endothelial cells of small arterioles than in large arteries. Slender smooth muscle-like cells surrounding seminiferous tubules also expressed AHNAK (Figure 2F). These cells are responsible for the production of collagen and elastin fibers present in the lamina propria, while their contractile activity helps the movement of spermatogonia along the tubule.

AHNAK Localization in Lining Epithelium

In the stratified epithelium of the skin, AHNAK was expressed at the plasma membrane of keratinocytes of the stratum basale and the stratum spinosum (Figure

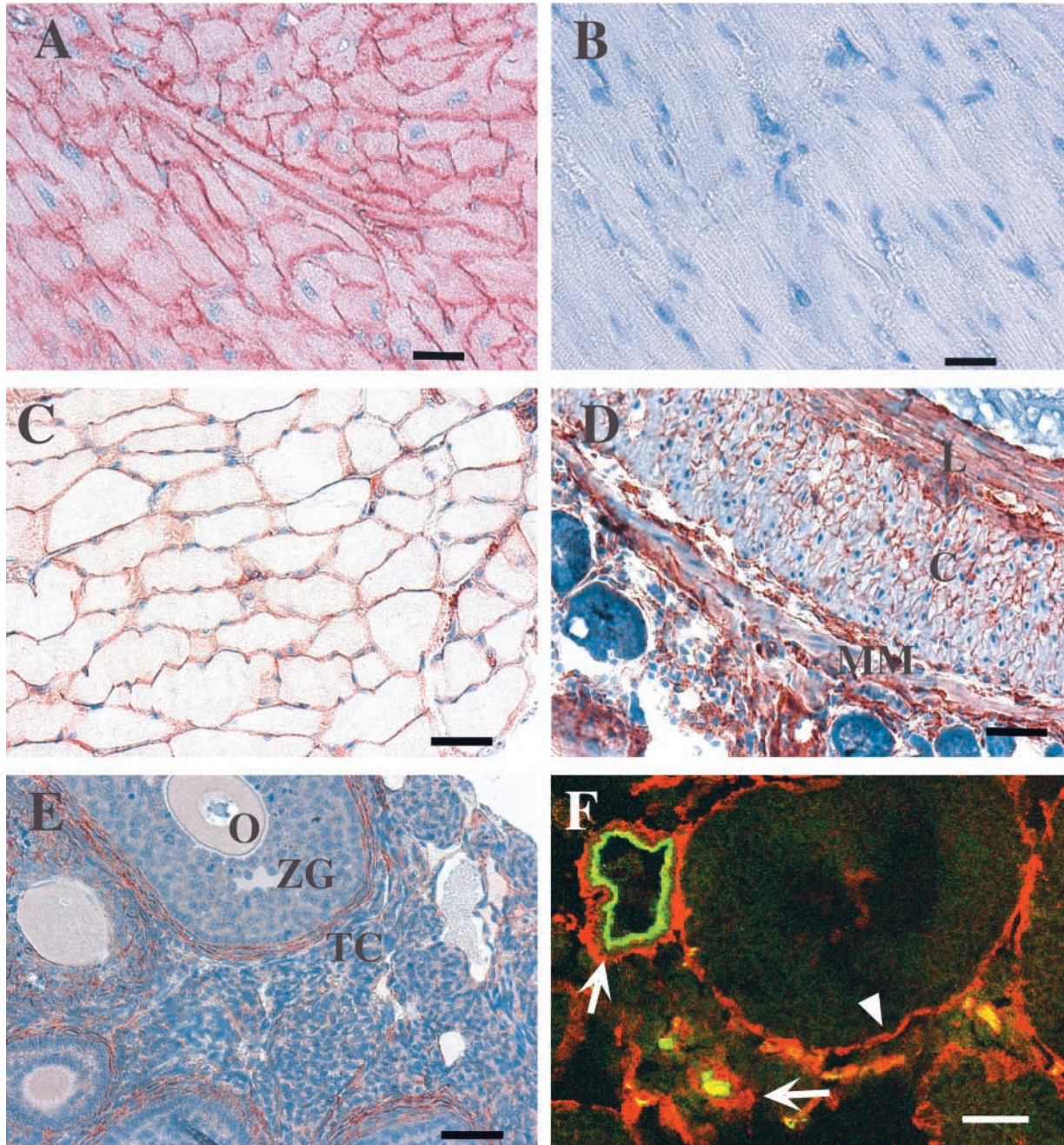
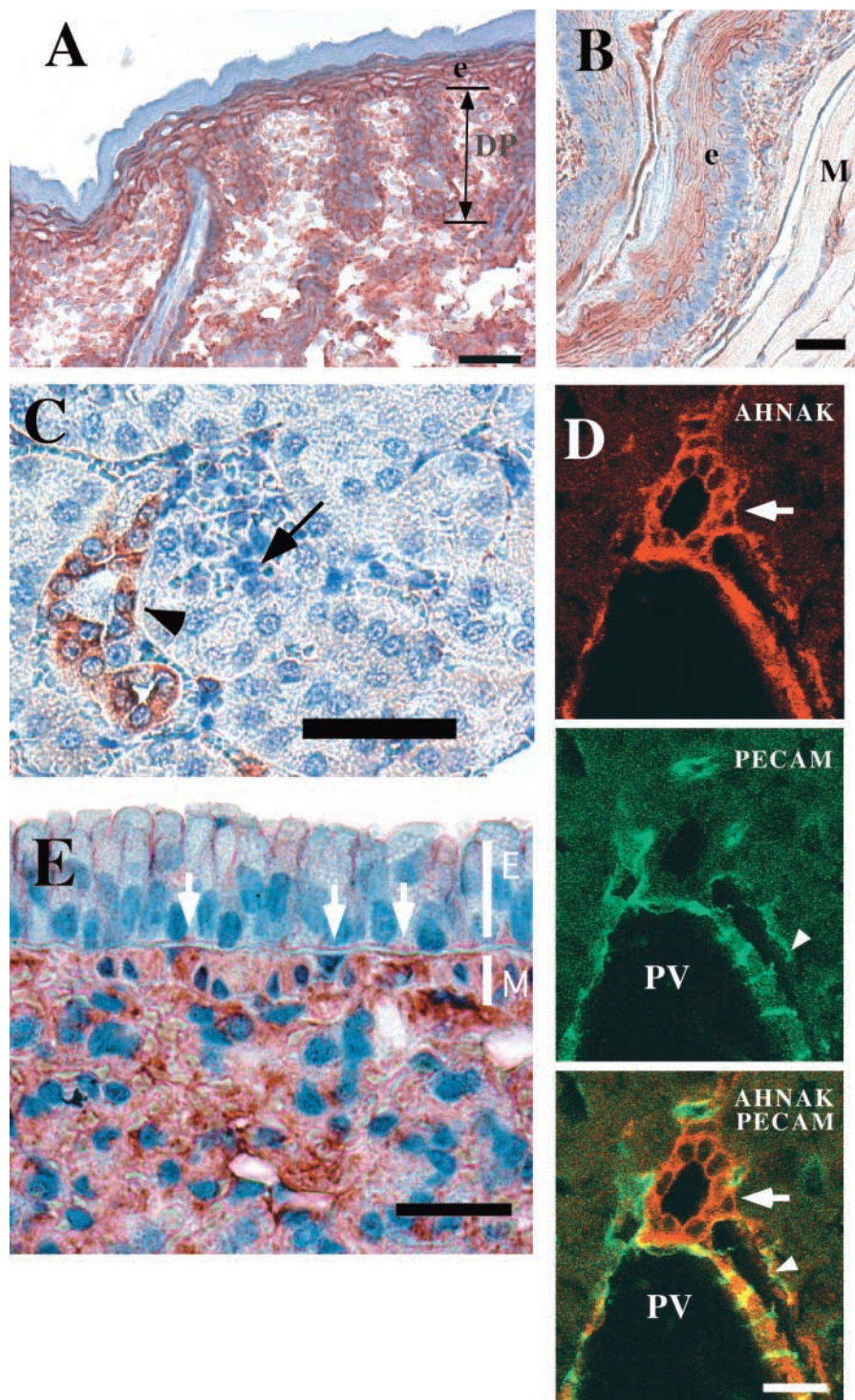


Figure 2 AHNAK localization in muscle tissue. (A) Heart section showing strong AHNAK immunoreactivity at the cardiomyocyte plasma membrane. (B) The specificity of AHNAK immunostaining of heart section was controlled by preincubation of the affinity-purified KIS-AHNAK antibody with KIS peptide. Bars = 20 μ m. (C) Section of skeletal muscle shows strong membrane localization of AHNAK in the myofiber. (D) The mucosae of the gastrointestinal duct (here the small intestine) is surrounded by a layer of smooth muscle cells, the outer longitudinal (L), the central circular layer (C), and the muscularis mucosae (MM) bordering the mucosae are AHNAK-positive. Note in the circular layer of smooth muscle cells the membranous localization of AHNAK. (E) In the ovarian follicle, an oocyte (O) is seen with the surrounding zona granulosa (ZG) and the theca layer (TC). The layer of theca cells is AHNAK-positive. (F) Double immunofluorescence analysis of AHNAK (red) and PECAM (green) in a seminiferous tubule of testis cut in transverse section. The myoid cells forming a thin layer surrounding the tubule (arrow head), the smooth muscle cells surrounding a small arteriole and an artery (arrows), and the endothelial cells are AHNAK-positive. Bars = 50 μ m.

3A). AHNAK staining was not observed in the cornified layer. AHNAK is also expressed in cells of papillary dermis and in some cells of the hair follicle (Figure 3A).

In the upper part of the digestive tract, i.e., the esophagus, AHNAK was found in the stratified squamous epithelium, which in rodents may be keratinized (Figure 3B). Here again, AHNAK immunoreactivity

Figure 3 AHNAK localization in lining epithelium. (A) Skin section. The stratified squamous keratinizing epithelium, but not the cornified layer of the epidermis (e), is AHNAK-positive. The junction between the epidermis and the dermis is characterized by downward folds of the epidermis called rete ridges, which interdigitate with upward projections of the dermis called dermal papillae (DP). Some cells of the dermis and a small layer of cells in the hair follicle complex are AHNAK-positive. (B) The lumen of the esophagus is lined by a thick AHNAK-positive protective stratified squamous epithelium (e) which, in this specimen, is keratinized. The underlying lamina propria is relatively condensed and the underlying muscularis mucosae is barely visible. Note the presence of skeletal muscle (M) in the muscularis, supporting the idea that the specimen is derived from the upper part of the esophagus. Bars = 50 μ m. (C) Kidney section. AHNAK staining is located in an epithelium that may correspond to the collecting tubule (arrowhead). This renal specimen contains a glomerulus (arrow) which is not AHNAK labeled. Bar = 20 μ m. (D) Liver section. Double immunofluorescence analysis of AHNAK (red) and PECAM (green) by confocal microscopy focuses on a typical portal tract containing a terminal branch of the hepatic portal vein (PV), an arteriole (arrowhead), and the bile ductule (arrow). Bar = 50 μ m. (E) In lung, dense immunoreaction deposit is observed in a bronchiole at the apical plasma membrane of epithelial cells and in contact with the basement membrane (white arrow). The underlayer smooth muscle (M) and the lung parenchyma cells are heavily immunostained. Bar = 20 μ m.



was concentrated mainly at the plasma membrane. As shown in Figure 3B, AHNAK was also present in the muscle cells of the striated muscularis layer. In kidney, AHNAK immunocytochemistry showed that AHNAK was localized in a special type of epithelium of the urinary system that lines the collecting ducts, ducts of Bellini, and the pelvicalyceal system (Figure 3D; and data not

shown). This transitional epithelium, called urothelium, is present along the conducting passages of the urinary system and protects the organism from acid and hypertonic urine. In liver, AHNAK immunoreactivity was confined to the portal tract. Figure 3E focuses on a typical portal tract containing three main structures. The largest is a terminal branch of the he-

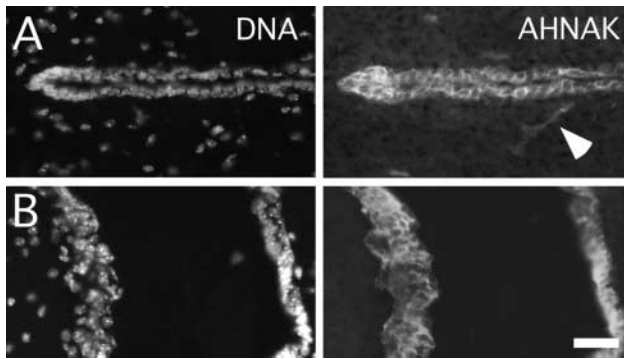


Figure 4 AHNAK is localized in the ventricular wall of adult brain. Double immunofluorescence analysis of AHNAK and HOECHST (DNA) labeling in the third ventricle (A) and the fourth ventricle (B) shows that AHNAK is localized in the ependymal cells that border the ventricles. AHNAK is also present in the brain parenchymal capillaries (arrowhead). Bar = 20 μ m.

patric portal vein (PV), which has a thin wall lined by endothelial cells labeled with PECAM antibody. These endothelial cells were AHNAK-positive. Smaller-diameter vessels are arterioles, which show lower AHNAK immunostaining. Finally, the bile collecting duct, lined by simple columnar epithelium, was strongly immunostained with AHNAK antibody. In these lining epithelial cells, AHNAK was concentrated at the plasma membrane. There was no AHNAK immunostaining of the liver hepatocytes. Immunohistochemistry with the lung (Figure 3E) confirmed the Western blotting analysis, showing that a high level of AHNAK protein is present in lung (Figure 1, Lane 3). AHNAK was highly expressed in parenchymal cells (epithelium of alveoli) and in the smooth muscle layer surrounding the bronchiolar epithelium. Faint AHNAK immunoreactivity was also present in pseudostratified bronchial epithelium. The labeled epithelial cells were mainly ciliated cells characterized by large nuclei. Their soma was weakly immunostained but concentrated immunoreaction deposit was observed at the apical plasma membrane and in contact with the basement membrane (white arrow).

We also found AHNAK immunoreactivity associated with the plasma membrane of several other lining epithelia, such as the stratified epithelium of the tunica albuginea of the testis (data not shown), and also in the epithelial cells lining the ventricles of the central nervous system (Figure 4). In the adult mouse brain, AHNAK immunoreactivity was abundant in epithelial cells that bordered all the ventricles, including the lateral ventricles (not shown), the third ventricle (Figure 4A), and the fourth ventricle (Figure 4B). There was no apparent AHNAK immunostaining of neuronal and glial cell soma. Brain capillary endothelial cells were also immunostained (see Figure 4A).

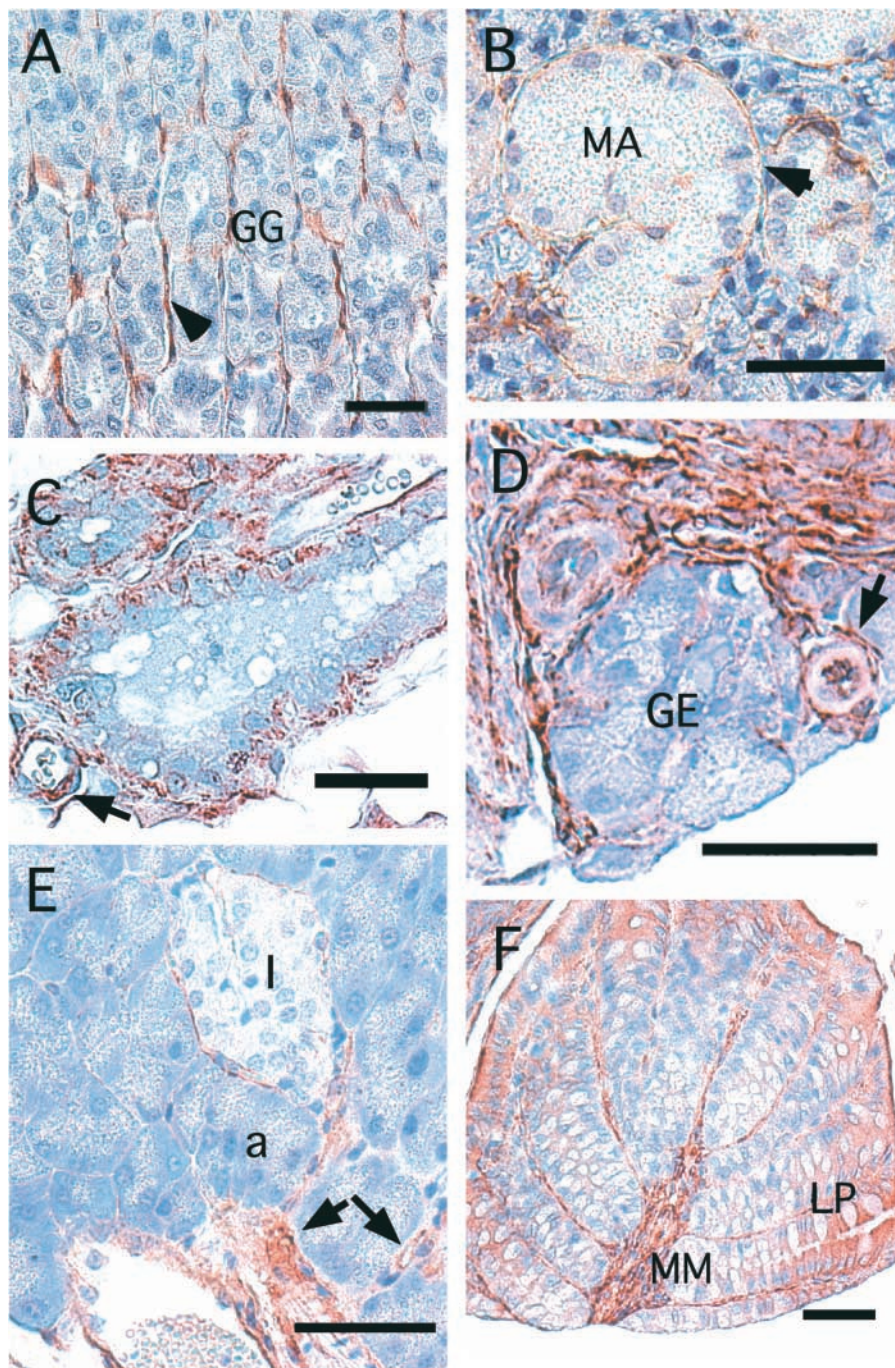
In contrast to muscle cells, not all epithelial cells

synthesize AHNAK. As shown in Figure 5A, the different secretory epithelial cells that constitute the stomach mucosa, including mucus-secreting cells, acid-secreting cells, and pepsin-secreting cells, were not AHNAK-immunoreactive. AHNAK staining appeared as a thin strand between the gastric gland, which corresponds to the muscularis mucosae that extends from the base of a gastric gland, to the lumen, whose contraction expels gastric secretion into the stomach lumen. The absence of AHNAK in secretory epithelium was confirmed in the salivary gland (Figure 5B), the mammary gland (Figure 5C), and the prostate gland (Figure 5D). In the salivary gland, the epithelium of serous acini, with nuclei flattened against the basement membrane, and the epithelium of mucous acini were not AHNAK-immunoreactive. The thin AHNAK immunoreactivity surrounding serous acini corresponds to the processes of contractile myoepithelial cells. In mammary glands, myoepithelial cells surrounding the gland and endothelial cells of capillaries were also labeled by the AHNAK antibody (Figure 5C). The prostate glandular epithelium was not positive for AHNAK, whereas the supporting tissue, which contains numerous smooth muscle cells and capillaries, was labeled by the AHNAK antibody (Figure 5D). Figure 5E shows the immunolabeling of AHNAK in the pancreas, a large gland composed of glandular epithelium with exocrine and endocrine functions. The endocrine tissue formed by the islets of Langerhans was not stained, nor were the glandular acini, which constitute the exocrine part of the pancreas. Only the endothelial cells of the capillaries were immunolabeled. AHNAK immunostaining was also not observed in epithelium with absorptive functions, such as the epithelium of the small intestine (data not shown; see also Figure 2D) and the absorptive epithelium lining the colon, which also has protective functions (Figure 5F). The mucosa of the colon, formed of straight tubular glands consisting of cells specialized for water absorption and of mucus-secreting goblet cells, was devoid of AHNAK immunoreactivity. However, significant cytoplasmic immunoreactivity was present in the cells of the luminal portion of the epithelium. These cells, which are derived from precursor cells present in the basal portion of the epithelium, are more mature and are subjected to the stretching forces of the luminal content. The muscularis mucosae, which extends into the lamina propria between the folds of the gland, also expressed AHNAK.

Discussion

Table 1 summarizes the tissue distribution and the cellular localization of AHNAK in mouse tissues. The protein AHNAK is a hallmark of muscular and muscle-like cells with contractile properties organized in

Figure 5 AHNAK localization is restricted to lining epithelium. (A) The mucosae of the stomach is thrown into prominent folds consisting of gastric glands (GG). AHNAK is observed in a thin strand that lies immediately beneath the base of the gastric glands and extends from the base of the glands in the lamina propria between the glands (arrowhead). This strand corresponds to the muscularis mucosae and supporting tissue (lamina propria and blood vessels). (B) Salivary glands are composed of mucous acini (MA) and serous acini. Both are embraced by processes of contractile cells called myoepithelial cells (arrowhead) which, on contraction, force the secretion from the acinar lumen into the duct system. (C) In the alveolar duct of the breast, myoepithelial cells surrounding the ductal lining cells are AHNAK-positive, whereas cuboidal epithelial cells are not immunostained. (D) The prostate glandular epithelium (GE) is AHNAK-negative, whereas the supporting tissue, which contains many smooth muscle cells, is AHNAK-positive. (E) The exocrine pancreas, which forms the bulk of the gland, is composed of glandular acini (a), whereas the endocrine tissue of the pancreas forms the islets of Langerhans (I) scattered throughout the exocrine tissue. In this organ, AHNAK immunoreactivity is restricted to vessels (arrows). (F) The simple tubular glands (LP) of the colon extend from lumen into the muscularis mucosae (MM). Lamina propria, composed of supporting tissue and a thin strand of muscularis mucosae, is AHNAK-positive. Note also the cytoplasmic AHNAK immunoreactivity in luminal enterocytes. Arrows in C–E point to blood vessels. Bars = 50 μ m.



contractile tissue or scattered in the tissue as fibrocytes or myoepithelial cells. AHNAK is also specifically expressed in epithelial cells of the skin, the esophagus, the tunica albuginea of the testis, the bile ducts, and the brain ventricles. In contrast to muscle cells, not all epithelial cells express AHNAK. We did not find significant AHNAK immunoreactivity in the glandular epithelium of the mammary gland, the salivary gland, the stomach, the prostate, or the exocrine

and endocrine pancreas, all of which have secretory functions. We were also unable to detect AHNAK in the absorptive epithelium of the proximal part of the nephron and of the intestine. In addition to muscle cells and lining epithelial cells, AHNAK is also present in endothelial cells of several capillary and blood vessels (see Figures 2F, 3D, 4A, and 5C–5E). However, in fenestrated endothelium of the kidney glomeruli (Figure 3C), the hepatic sinusoid (data not shown), and

Table 1 Tissue and cell localization of AHNAK

Tissue and organ	AHNAK-positive structure or cell type	Type of epithelium in the organ	AHNAK in epithelium
Epidermis	Keratinocytes	Lining	++
Esophagus	Stratified epithelium of mucosae, muscular layer (smooth muscle and skeletal muscle)	Lining	++
Liver	Bile duct epithelium	Lining	++
Brain	Ependymal cells	Lining	++
Testis	Tunica albuginea, myofibroblasts	Lining	++
Prostate	Supporting tissue (smooth muscle cells)	Secretory	-
Breast	Myoepithelial cells	Secretory	-
Salivary gland	Myoepithelial cells	Secretory	-
Small intestine	Smooth muscle layers	Secretory	-
Stomach	Muscularis mucosae, smooth muscle layers	Secretory	-
Adrenal	Negative	Secretory	-
Pancreas	Negative	Secretory	-
Heart	Cardiomyocytes		
Skeletal muscle	Muscle fiber, myocytes		
Uterus	Myometrium		
Ovary	Theca cells		
Kidney	Epithelium of collecting tubule, duct of Bellini, pelvicalyceal system	Lining/absorptive	++/-
Large intestine	Smooth muscle layers	Absorptive and protective	+
Lung	Epithelium of bronchiole, epithelium of alveoli (pneumocytes), ^a smooth muscle	Lining/secretory Lining	+ ++
Spleen	Negative		
Thymus	Negative		
Lymph node	Negative		
Blood vessels	Endothelium and smooth muscle cells		

^aConfirmed in human lung.

the continuous capillaries of lung (data not shown), AHNAK immunoreactivity was below the detection limit. This suggests that the level of AHNAK expression in endothelial cells might depend on the blood vessel properties.

In adult tissue, the main subcellular localization of AHNAK is at the plasma membrane. Cytoplasmic staining was also observed in fibroblast or certain epithelial cells, such as those in the colon (Figure 5F). Exclusive membrane location of AHNAK has also been recently reported in rat cardiomyocytes by Hohaus et al. (2002), using two region-specific AHNAK antibodies raised against either amino-terminal or carboxyl-terminal epitopes. These findings contrast with the predominant nuclear localization of AHNAK observed in cultured cell lines of nonepithelial origin (Shtivelman and Bishop 1993). However, recent data reported that in MDCK cells derived from canine kidney epithelium, membrane targeting of AHNAK is regulated by cell density and the formation of cell-cell contacts (Sussman et al. 2001). The authors proposed that the plasma membrane-anchored AHNAK may be involved in the growth arrest of normal epithelial cells (Sussman et al. 2001). In adult mouse tissues, AHNAK-expressing cells are terminally differentiated cells and therefore do not proliferate. This status

might account for the predominant membrane localization of AHNAK in most adult tissues. Alternatively, recent studies indicate that AHNAK may be proteolytically cleaved in vivo (Skoldberg et al. 2002) and that AHNAK fragments may have functional roles intracellularly (Sekiya et al. 1999). It is therefore possible that, in cell culture, cytoplasmic AHNAK is more susceptible to proteolysis, and that AHNAK proteolysis could contribute to the apparent nuclear localization of the protein. In normal keratinocytes, endogenous full-length AHNAK accumulates at the cell membrane, but the transfected C-terminus of AHNAK accumulates within the cell nuclei (Nie et al. 2000).

The predominant cellular expression of AHNAK in muscles and in lining epithelium that we report in this study might help to elucidate the membrane function of this giant protein. First, it allows restriction of the search for AHNAK function to essentially two specialized cell types. Moreover, several structural and functional features are shared between muscle and lining epithelium. These tissues are subjected to stretching force and have elastic properties. For example, the epithelium of the esophagus is subjected to the stretching force of the bolus, and muscle cells to stretching forces during the contraction-relaxation cycles. This implies that common cellular organizations are involved in

both tissues to respond and control the stretching forces. The first is the cell–cell interactions necessary for maintaining tissue integrity. Several molecular structures are known to participate in cell–cell interactions, such as desmosomes, tight junctions, and adherens junctions. Although initially AHNAK was co-purified with the desmosomal component during cell fractionation of keratinocytes (Hieda and Tsukita 1989), and therefore was named desmoyokin, later studies clearly demonstrated that AHNAK (desmoyokin) is not directly associated with desmosomes (Masunaga et al. 1995). We have investigated the possible association of AHNAK with tight junctions in endothelial cells of brain capillary and ependymal cells (data not shown). Double immunofluorescence labeling and confocal microscopy analysis for AHNAK and the tight junction-associated protein ZO1 revealed a distinct localization of the two proteins (unpublished data). Finally, the observation that AHNAK can migrate from the cytoplasm to the plasma membrane in cell culture without any effect on cell–cell adhesion (Hashimoto et al. 1995) does not support a direct role for AHNAK in cell–cell interactions. We envision that AHNAK may be more likely associated with the structural support of the membrane during changes in membrane shape, the reinforcement of the cortical framework, and signaling pathways. It is significant that AHNAK shares structural similarity and subcellular localization with two other giant proteins abundantly expressed in muscle cells, titin and dystrophin. Both of these giant proteins lie close beneath the plasma membrane (Shimada et al. 1993; Mussini et al. 1995). Dystrophin is part of a multimeric protein complex that links actin on the inside of the cells to extracellular matrix protein through transmembrane proteins (Samitt and Bonilla 1990; Wakayama et al. 1993; Norwood et al. 2000). Titin is a giant muscle protein. Its size and location within the sarcomere structure suggests that it plays an important role in the mechanism of muscle elasticity (Freiburg et al. 2000). It will be very interesting to investigate if AHNAK may also act as a scaffold protein, recruiting and maintaining the organization of cytoskeletal proteins at the plasma membrane. This will obviously require the identification and characterization of AHNAK-associated proteins at the plasma membrane. Two membrane-associated signaling pathways regulated by AHNAK have already been characterized. In the cardiomyocyte, AHNAK modulates membrane-bound L-type calcium channel activity (Haase et al. 1999). Intriguingly, organization of the cortical actin network has been implicated in modulation of voltage-gated ion channel activity (Maguire et al. 1998), and in vitro interaction between the carboxyl-terminal region of AHNAK and actin has recently been described (Hohaus et al. 2002). Peptides from the central domain of

AHNAK also bind and activate PLC γ in the presence of arachidonic acid (Sekiya et al. 1999). The activation of this enzyme mediates several cellular responses, including cytoskeletal rearrangements that lead to protection of the plasma membrane in response to mechanical stress (Ryan et al. 2000; Ruwhof et al. 2001). Finally, taking into account that AHNAK is an abundant muscular protein with possible important functions associated with structural support of the plasma membrane, it will be now of primary interest to investigate if its function is altered in muscular dystrophies that are characterized by cell membrane defects.

Acknowledgments

Supported in part by a grant from Association pour la Recherche contre le Cancer (Christian Delphin) and a Ligue Nationale contre le Cancer fellowship (Benoit Gentil).

We thank Dr Peoc'h for valuable advice and Dr La Marre Jonathan for critical reading of the manuscript.

Literature Cited

- Boni R, Burg G, Doguoglu A, Ilg EC, Schafer BW, Muller B, Heizmann CW (1997) Immunohistochemical localization of the Ca²⁺ binding S100 proteins in normal human skin and melanocytic lesions. *Br J Dermatol* 137:39–43
- Freiburg A, Trombitas K, Hell W, Cazorla O, Fougerousse F, Centner T, Kolmerer B, et al. (2000) Series of exon-skipping events in the elastic spring region of titin as the structural basis for myofibrillar elastic diversity. *Circ Res* 86:1114–1121
- Gentil BJ, Delphin C, Mbele GO, Deloulme JC, Ferro M, Garin J, Baudier J (2001) The giant protein AHNAK is a specific target for the calcium- and zinc-binding S100B protein: potential implications for Ca²⁺ homeostasis regulation by S100B. *J Biol Chem* 276:23253–23261
- Haase H, Podzuweit T, Lutsch G, Hohaus A, Kostka S, Lindschau C, Kott M, et al. (1999) Signaling from beta-adrenoceptor to L-type calcium channel: identification of a novel cardiac protein kinase A target possessing similarities to AHNAK. *FASEB J* 13:2161–2172
- Hashimoto T, Amagai M, Parry DA, Dixon TW, Tsukita S, Miki K, Sakai K, et al. (1993) Desmoyokin, a 680 kDa keratinocyte plasma membrane-associated protein, is homologous to the protein encoded by human gene AHNAK. *J Cell Sci* 105:275–286
- Hashimoto T, Gamou S, Shimizu N, Kitajima Y, Nishikawa T (1995) Regulation of translocation of the desmoyokin/AHNAK protein to the plasma membrane in keratinocytes by protein kinase C. *Exp Cell Res* 217:258–266
- Hieda Y, Tsukita S (1989) A new high molecular mass protein showing unique localization in desmosomal plaque. *J Cell Biol* 109:1511–1518
- Hohaus A, Person V, Behlke J, Schaper J, Morano I, Haase H (2002) The carboxyl-terminal region of ahnak provides a link between cardiac L-type Ca²⁺ channels and the actin-based cytoskeleton. *FASEB J* 16:1205–1216
- Kingsley PD, McGrath KE, Maltby KM, Koniski AD, Ramchandran R, Palis J (2001) Subtractive hybridization reveals tissue-specific expression of ahnak during embryonic development. *Dev Growth Differ* 43:133–143
- Kudoh J, Wang Y, Minoshima S, Hashimoto T, Amagai M, Nishikawa T, Shtivelman E, et al. (1995) Localization of the human AHNAK/desmoyokin gene (AHNAK) to chromosome band 11q12 by somatic cell hybrid analysis and fluorescence in situ hybridization. *Cytogenet Cell Genet* 70:218–220

- Maguire G, Connaughton V, Prat AG, Jackson GR Jr, Cantiello HF (1998) Actin cytoskeleton regulates ion channel activity in retinal neurons. *Neuroreport* 9:665–670
- Masunaga T, Shimizu H, Ishiko A, Fujiwara T, Hashimoto T, Nishikawa T (1995) Desmoyokin/AHNAK protein localizes to the non-desmosomal keratinocyte cell surface of human epidermis. *J Invest Dermatol* 104:941–945
- Motta PM, Familiari G (1981) Occurrence of a contractile tissue in the theca externa of atretic follicles in the mouse ovary. *Acta Anat (Basel)* 109:103–114
- Mussini I, Sogos V, Della Barbera M, Ennas MG, Gremo F (1995) Immunolocalisation of dystrophin in the immature human neurons and muscles. *Ital J Anat Embryol* 100:155–163
- Nie Z, Ning W, Amagai M, Hashimoto T (2000) C-Terminus of desmoyokin/AHNAK protein is responsible for its translocation between the nucleus and cytoplasm. *J Invest Dermatol* 114:1044–1049
- Norwood FL, Sutherland-Smith AJ, Keep NH, Kendrick-Jones J (2000) The structure of the N-terminal actin-binding domain of human dystrophin and how mutations in this domain may cause Duchenne or Becker muscular dystrophy. *Structure Fold Des* 8:481–491
- Ruwhof C, van Wamel JT, Noordzij LA, Aydin S, Harper JC, van der Laarse A (2001) Mechanical stress stimulates phospholipase C activity and intracellular calcium ion levels in neonatal rat cardiomyocytes. *Cell Calcium* 29:73–83
- Ryan MJ, Gross KW, Hajduczuk G (2000) Calcium-dependent activation of phospholipase C by mechanical distension in renin-expressing As4.1 cells. *Am J Physiol* 279:E823–829
- Samitt CE, Bonilla E (1990) Immunocytochemical study of dystrophin at the myotendinous junction. *Muscle Nerve* 13:493–500
- Sekiya F, Bae YS, Jhon DY, Hwang SC, Rhee SG (1999) AHNAK, a protein that binds and activates phospholipase C-gamma1 in the presence of arachidonic acid. *J Biol Chem* 274:13900–13907
- Self DA, Schroeder PC, Gown AM (1988) Hamster thecal cells express muscle characteristics. *Biol Reprod* 39:119–130
- Shimada Y, Arisuta F, Sonoda M, Shiozaki M, Maruyama K (1993) Distribution of connectin (titin) and transverse tubules at myotendinous junctions. *Scann Microsc* 7:157–163
- Shrestha P, Muramatsu Y, Kudiken W, Mori M, Takai Y, Ilg EC, Schafer BW, et al. (1998) Localization of Ca(2+)-binding S100 proteins in epithelial tumours of the skin. *Virchows Arch* 432:53–59
- Shtivelman E, Bishop JM (1993) The human gene AHNAK encodes a large phosphoprotein located primarily in the nucleus. *J Cell Biol* 120:625–630
- Shtivelman E, Cohen FE, Bishop JM (1992) A human gene (AHNAK) encoding an unusually large protein with a 1.2-microns polyionic rod structure. *Proc Natl Acad Sci USA* 89:5472–5476
- Skoldberg F, Ronnblom L, Thornemo M, Lindahl A, Bird PI, Rorsman F, Kampe O, et al. (2002) Identification of AHNAK as a novel autoantigen in systemic lupus erythematosus. *Biochem Biophys Res Commun* 291:951–958
- Sussman J, Stokoe D, Ossina N, Shtivelman E (2001) Protein kinase B phosphorylates AHNAK and regulates its subcellular localization. *J Cell Biol* 154:1019–1030
- Wakayama Y, Shibuya S, Jimi T, Takeda A, Oniki H (1993) Size and localization of dystrophin molecule: immunoelectron microscopic and freeze etching studies of muscle plasma membranes of murine skeletal myofibers. *Acta Neuropathol (Berl)* 86:567–577

The Zinc- and Calcium-binding S100B Interacts and Co-localizes with IQGAP1 during Dynamic Rearrangement of Cell Membranes*

Received for publication, May 30, 2002, and in revised form, October 8, 2002
Published, JBC Papers in Press, October 10, 2002, DOI 10.1074/jbc.M205363200

Gaelh Ouengue Mbele‡, Jean Christophe Deloulme‡, Benoît Jean Gentil‡, Christian Delphin‡, Myriam Ferro§, Jérôme Garin§, Miyoko Takahashi¶, and Jacques Baudier‡||

From the ‡Département Réponse et Différenciation Cellulaires du Commissariat à l'Energie Atomique (CEA), INSERM EMI-0104 DRDC-TS, §Laboratoire de Chimie des Protéines DRDC-CP, CEA, Grenoble 38054, France and ¶Syn-X Pharma, Inc., 6354 Viscount Rd., Mississauga, Ontario L4V 1H4, Canada

The Zn²⁺- and Ca²⁺-binding S100B protein is implicated in multiple intracellular and extracellular regulatory events. In glial cells, a relationship exists between cytoplasmic S100B accumulation and cell morphological changes. We have identified the IQGAP1 protein as the major cytoplasmic S100B target protein in different rat and human glial cell lines in the presence of Zn²⁺ and Ca²⁺. Zn²⁺ binding to S100B is sufficient to promote interaction with IQGAP1. IQ motifs on IQGAP1 represent the minimal interaction sites for S100B. We also provide evidence that, in human astrocytoma cell lines, S100B co-localizes with IQGAP1 at the polarized leading edge and areas of membrane ruffling and that both proteins relocate in a Ca²⁺-dependent manner within newly formed vesicle-like structures. Our data identify IQGAP1 as a potential target protein of S100B during processes of dynamic rearrangement of cell membrane morphology. They also reveal an additional cellular function for IQGAP1 associated with Zn²⁺/Ca²⁺-dependent relocation of S100B.

S100B is a member of the S100 family of proteins containing two EF-hand-type calcium-binding domains (1). This protein interacts not only with Ca²⁺ but also with Zn²⁺ ions, binding Zn²⁺ ions with an affinity in the nanomolar range (2). The capacity of S100B to bind and release Zn²⁺ suggests that Zn²⁺ may not only play a structural role but might also be involved, together with Ca²⁺, in concerted regulation of S100B function. The S100B protein is naturally highly expressed in the vertebrate nervous system, where it is present in astrocytes and Schwann cells (3). In the adult central nervous system, the S100B protein is present in the nuclei and cytoplasm of astrocytes and accumulates in the astrocytic dendrites in the perivascular processes (4). Studies in different laboratories suggest a variety of intracellular regulations by S100B, including negative cell growth regulation (5), cell structure (6), and calcium homeostasis (7). The S100B protein is also secreted from astrocytes and has extracellular functions (8). Extracellular S100B acts as a modulator of neuronal synaptic plasticity (9). Although nanomolar quantities have beneficial neurotrophic effects on nerve cells, high levels of this protein have been implicated in glia activation and could contribute to the devel-

opment of brain pathology as observed in Down's syndrome and Alzheimer's disease (10). The recent observation that S100B triggers activation of the pro-inflammatory cell surface receptor for advanced glycation end products has shed more light on its extracellular function (11). In cultured human astrocytoma U87 cells, S100B secretion is dependent on relocation of S100B toward vesicle-like structures at the periphery of the cells and is regulated by Ca²⁺ and Zn²⁺ (12). S100B can also be secreted into the bloodstream and cerebrospinal fluid and is a biochemical marker of brain damage or dysfunction in acute and chronic diseases (13, 14). A relationship between S100B accumulation in the astrocytic end-feet and morphological changes of astrocytes in the perivascular regions has been reported previously (15). These changes may be related to the release of S100B into the blood stream (15). Consistent with dynamic regulation of astrocyte cell shape by S100B, antisense inhibition of S100B production in cultured rat glial C6 cells is correlated with alterations in cellular morphology (6). The mechanisms of regulation of astrocyte cell morphology by S100B and its secretion pathway remain unclear. By analogy with other EF-hand Ca²⁺-binding proteins, such as calmodulin, one might suppose that the biological activity of S100B is related to Ca²⁺/Zn²⁺-dependent interaction with target proteins. In this study, we identify IQGAP1 protein as the first S100B target protein identified to date whose interaction with S100B is regulated by Zn²⁺ and Ca²⁺. IQGAP1 is also the major specific cytoplasmic S100B target protein present in both rat glial C6 and human U373 or U87 astrocytoma cell lines. We also provide evidence that cytoplasmic S100B specifically binds to a sub-population of IQGAP1 molecules that localize at the polarized leading edge and areas of membrane ruffling and that both S100B and IQGAP1 proteins are relocated in a Ca²⁺-dependent manner within vesicle-like structures. The interaction of S100B with IQGAP1 may have important implications for understanding the roles played by S100B in processes of dynamic rearrangement of cell membranes and in the mechanisms of Zn²⁺/Ca²⁺-dependent relocation and secretion of S100B.

MATERIALS AND METHODS

Cell Cultures and ³⁵SMet/Cys Labeling—Human astrocytoma U-373MG, U-87MG cells, rat glioma C6 cells, mammary carcinoma MCF7 cells, and NIH 3T3 fibroblasts were cultured in Dulbecco's modified Eagle's medium with Glutamax (Invitrogen) supplemented with 10% fetal calf serum (Invitrogen). Cells were labeled in methionine-free minimal essential medium, 5% fetal calf serum supplemented with ³⁵SMet/Cys mix (50 μCi/ml) for 6 h.

Transfection Experiments—U-373MG, U-87MG, NIH 3T3, and MCF7 cells were transfected with the pcDNA-Neo containing the wild-type or C-terminal deleted S100B cDNA (17) using FuGENE™ 6 reagent transfection according to manufacturer's protocol. For stably transfected S100B-MCF7 cell lines, cells were incubated, 48 h after

* This work was supported by grants from the Association pour la Recherche sur le Cancer and la Ligue Nationale Contre le Cancer. The costs of publication of this article were defrayed in part by the payment of page charges. This article must therefore be hereby marked "advertisement" in accordance with 18 U.S.C. Section 1734 solely to indicate this fact.

|| To whom correspondence should be addressed. Tel.: 33-438-78-43-28; Fax: 33-438-78-58-89; E-mail: jbaudier@cea.fr.

transfection, in complete medium supplemented with 500 $\mu\text{g ml}^{-1}$ neomycin (G418), and neomycin-resistant S100B-MCF7 clones were selected.

S100- and CaM-Sepharose Beads—S100B and CaM¹ were purified from bovine brain to homogeneity (16). S100B- and CaM-Sepharose were prepared by reaction of bovine brain S100B and CaM with CnBr-Sepharose in 20 mM HEPES, pH 7.8, 0.5 mM CaCl₂. Both S100B- and CaM-Sepharose contained 2 mg of protein per milliliter of beads. The purification protocols for human S100A1, S100A6, S100B, and S100A11 recombinant proteins have been described previously (17). Recombinant human S100B, S100A1, S100A6, and S100A11 were coupled to CnBr-Sepharose (1 mg of protein per milliliter of beads) as described above.

Primary Antibodies—Monoclonal anti- β -tubulin antibody was a gift from Drs L. Paturle and D. Job (Laboratoire du cytosquelette, CEN-Grenoble). Polyclonal rabbit anti-S100B antibodies (Z0311 and A5110) were from Dako. Purified S100B monoclonal antibody S16 was previously described (18). Monoclonal anti-calmodulin (C-7055) and monoclonal anti-S100A6 antibody (S5046) were from Sigma. The monoclonal mouse anti-calmodulin (05-173) and the monoclonal mouse anti-IQGAP1 AF4 (05-504) antibodies were from Upstate Biotechnology. IQGAP1 AF4 antibody was used for immunoprecipitation experiments. The mouse monoclonal anti-IQGAP1 (mAb IgG1, I53820) antibody was from Transduction Laboratories and used at 1:2000 in Western blot analysis. Polyclonal rabbit anti-IQGAP1 antibody was a gift from Dr. J. Erickson (Cornell University, Ithaca, NY) and was used at 1:2000 for immunofluorescence. Mouse monoclonal anti β -catenin antibody was from Transduction Laboratories (C19220). Polyclonal rabbit anti-Cdc42 antibody was from Santa Cruz Biotechnology (SC-87). MyoD monoclonal antibody 5.8A was from H. Weintraub (Seattle, WA).

Western Blot Analysis—S100B protein was resolved with SDS-Tris-Tricine-11%-PAGE (17). β -tubulin, β -catenin, and IQGAP1 were analyzed using Laemmli SDS-PAGE. The proteins were transferred to nitrocellulose membrane and incubated with the primary antibodies. Proteins were visualized using an ECL kit (PerkinElmer Life Sciences).

Plasmid Constructions—The following constructs were used for *in vitro* translation using the TnT T7 Quick system (Promega): (i) pCAN-myc-IQGAP1 containing a cDNA encoding IQGAP1 was a gift from J. Erickson (Cornell University, Ithaca, NY); (ii) the pcDNA vector containing a cDNA coding for the IQGAP1-N terminus (amino acids 1–863) was generated by digesting pCAN-myc-IQGAP1 with *Bam*HI and subcloning the *Bam*HI-*Bam*HI fragment into a *Bam*HI site in pcDNA3.1(+) (Invitrogen); (iii) the pcDNA containing a cDNA coding for the IQGAP1-IQ domains (amino acids 740–869) was generated by digesting the pcDNA/N-ter with *Stu*I and *Bam*HI and subcloning the *Stu*I/*Bam*HI fragment into the *Eco*RV/*Bam*HI sites in pcDNA3.1(–) (Invitrogen); (iv) the pcDNA/CHD-IQ was obtained by digesting pcDNA/N-ter with *Stu*I and by religating the vector; (v) the pcDNA/IR-IQ (amino acids 232–740) was obtained by digesting pcDNA/N-ter with *Stu*I and *Bam*HI. Then the *Stu*I/*Stu*I and *Stu*I/*Bam*HI fragments were subcloned into *Eco*RV/*Bam*HI sites in pcDNA3.1(–).

Mass Spectrometric Analysis and Protein Identification—The 170-kDa protein that binds to S100B-Sepharose in the absence of calcium was excised from Coomassie Blue-stained gels and washed with 50% acetonitrile. Gel pieces were dried in a vacuum centrifuge and rehydrated in 20 μl of 25 mM NH₄HCO₃ containing 0.5 μg of trypsin (Promega, sequencing grade). After 4-h incubation at 37 °C, a 0.5- μl aliquot was removed for MALDI-TOF analysis and spotted onto the MALDI sample probe on top of a dried 0.5- μl mixture of 4:3 saturated α -cyano-4-hydroxy-*trans*-cinnamic acid in acetone/10 mg/ml nitrocellulose in acetone/isopropanol 1:1. Samples were rinsed by placing a 5- μl volume of 0.1% trifluoroacetic acid on the matrix surface after the analyte solution had dried completely. After 2 min, the liquid was blown off by pressurized air. MALDI mass spectra of peptide mixtures were obtained using a Bruker Biflex mass spectrometer (Bruker-Franzen Analytik, Bremen, Germany). Internal calibration was applied to each spectrum using trypsin autodigestion peptides (MH⁺ 842.50, MH⁺ 1045.55, MH⁺ 2211.11). Protein identification was confirmed by tandem mass spectrometry experiments. After in-gel tryptic digestion, the gel pieces were extracted with 5% formic acid solution and then with

acetonitrile. The extracts were combined with the original digest, and the sample was evaporated to dryness in a vacuum centrifuge. The residues were dissolved in 0.1% formic acid and desalted using a Zip Tip (Millipore). Elution of the peptides was performed with 5–10 μl of 50% acetonitrile/0.1% formic acid solution. The peptide solution was introduced into a glass capillary (Protana) for nanoelectrospray ionization. Tandem mass spectrometry experiments were carried out on a quadrupole time-of-flight hybrid mass spectrometer (Micromass, Altrincham, UK) to obtain sequence information. Collision-induced dissociation of selected precursor ions was performed using argon as the collision gas and collision energies of 40–60 eV. Protein identification was achieved using both MALDI peptide mass fingerprints and MS/MS sequence information. Mass spectrometric data were compared with known sequences using the programs MS-Fit and MS-Edman located at the University of California San Francisco (available at prospector.ucsf.edu). Tandem mass spectrometry sequencing of three different peptides (LGLAPQIQDLYGK, LEGVLAEVAQHYYQDTLIR, and FPD-AGEDELK) confirmed the strict identity of the 170-kDa protein with IQGAP1. These peptides are not found in other human protein sequences, including IQGAP2 and the putative IQGAP3 sequence.

Cell Extracts—For binding assays and co-immunoprecipitation experiments, cells were lysed at 4 °C in TTBS buffer (40 mM Tris-HCl, pH 7.5, 150 mM NaCl, 0.3% Triton X-100) plus protease inhibitors (leupeptin, aprotinin, pepstatin, and 4-(2-aminoethyl)benzenesulfonyl fluoride hydrochloride, 10 $\mu\text{g/ml}$ each) and centrifuged for 10 min. Cell lysates were precleared by incubation for 10 min with 50 μl of protein A-Sepharose.

S100B and CaM Binding Assays—500- μl aliquots of precleared supernatant were supplemented with either 5 mM EDTA/5 mM EGTA, or with 20 μM ZnSO₄, or with 0.3 mM CaCl₂/10 μM ZnSO₄ and mixed with 20 μl of affinity beads equilibrated in the same buffers. After mixing at 4 °C for 15 min, the beads were spun down and the supernatant was removed. The beads were washed three times with 1 ml of binding buffers. At the last wash, beads were transferred to new Eppendorf tubes and boiled in SDS-sample buffer. For binding assays using recombinant IQGAP1 or IQGAP1 domains, 20 μl of reaction lysates were diluted in 500 μl of TTBS and processed as described for cell extracts.

Co-immunoprecipitation Analysis—500- μl aliquots of pre-cleared supernatant were mixed with 40 μM GTP γ S (Sigma) plus 5 mM MgCl₂, if needed, and with either 5 mM EDTA/5 mM EGTA or 0.3 mM CaCl₂/10 μM ZnSO₄ and mixed with the appropriate antibodies (5 μg) plus 20 μl of protein A- or protein G-Sepharose equilibrated in the same buffers. After mixing at 4 °C for 50 min, the beads were centrifuged briefly (5 s, 13,000 rpm), and the supernatant was removed. The beads were washed three times with 1 ml of appropriate incubation buffers. At the last wash, beads were transferred to new microcentrifuge tubes and boiled in SDS-sample buffer containing 5 mM EGTA and 5 mM EDTA.

Immunofluorescence Analysis—cells grown on permanox slides from Nunc, Inc. were fixed for 30 min with 4% paraformaldehyde in HBS (10 mM HEPES, pH 7.4, 130 mM NaCl, 15 mM KCl, 5 mM MgCl₂) and permeabilized for 5 min with TBS (30 mM Tris-HCl, pH 7.4, 150 mM NaCl) containing 0.2% Triton X-100 plus 1 mM CaCl₂. After washing with TBS/1 mM CaCl₂, cells were incubated for 30 min in TBS/1 mM CaCl₂ containing 10% normal goat serum and then incubated with primary antibodies for 90 min in the same buffer containing 5% normal goat serum. The cells were then washed with TBS/1 mM CaCl₂ and incubated for 1 h with the appropriate secondary antibodies conjugated with cyanin3 (Jackson ImmunoResearch Laboratories) or with Alexa488 (Molecular Probes, Inc., Eugene, OR) in the same buffer as described for the primary antibodies. After washing with TBS/1 mM CaCl₂, cells were incubated in a solution of Hoechst 33258 (2 $\mu\text{g/ml}$) for 5 min and placed under coverslips. Preparations were analyzed with a Zeiss fluorescence microscope (Axiovert 200M) or a Leica confocal microscope (TCS-SP2).

RESULTS

S100B Overexpression Correlates with Changes in U373 Cell Morphology—In the transformed human astrocytoma U373 cell line, the expression of S100B is up-regulated in post-confluent cells (Fig. 1). Up-regulation of S100B is specific, because it is not observed with β -tubulin, calmodulin (CaM), and IQGAP1.

Indirect immunofluorescence analysis of post-confluent U373 cells, double-stained with polyclonal rabbit anti-human S100B (red) and mouse monoclonal anti-S100A6 (green), reveals heterogeneity in S100B staining among cells (Fig. 2A).

¹ The abbreviations used are: CaM, calmodulin; Tricine, N-[2-hydroxy-1,1-bis(hydroxymethyl)ethyl]glycine; MALDI-TOF, matrix-assisted laser desorption ionization time-of-flight; MS/MS, tandem mass spectrometry; GTP γ S, guanosine 5'-3-O-(thio)triphosphate; GFP, green fluorescent protein.

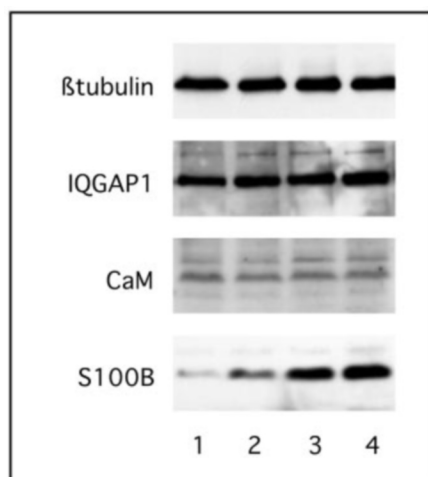


FIG. 1. Western blot analysis for β -tubulin, IQGAP1 calmodulin, and S100B expression in astrogloma U373 MG cells. Total protein (25 μ g) from exponentially growing U373 MG cells (lane 1) and from cells left post-confluent for 1 day (lane 2), 3 days (lane 3), and 4 days (lane 4) were immunoblotted using specific antibodies directed against β -tubulin, IQGAP1, calmodulin (CaM) (Sigma), and S100B as indicated.

Although all cells are uniformly immunostained with S100A6 antibodies (Fig. 2B), considerable variation in S100B immunostaining characterized post-confluent U373 cells. In post-confluent culture, the strongest S100B-positive cells had grown on top of the cell layer. These cells are characterized by intense cytoplasmic S100B immunoreactivity and have adopted a less flattened morphology with long processes. Confocal microscopy analysis of S100B immunostaining in confluent and post-confluent U373 cells confirmed a relationship between S100B overexpression and change in cell shape (Fig. 2, C and D). In these experiments, cells were double-labeled with S100B polyclonal antibodies (red) and IQGAP1 monoclonal antibody (green). U373 cells that enter confluence have a flattened morphology. In these cells, the weak S100B immunoreactivity is mostly nuclear and IQGAP1 accumulates at the cell periphery (Fig. 2C). In post-confluent culture, cells characterized by intense cytoplasmic S100B immunoreactivity have adopted a less flattened morphology with long processes (Fig. 2D). Overlapping of the S100B and IQGAP1 stainings (white pixels) reveals that some of the S100B colocalizes with IQGAP1 at the cytoplasmic membrane and within processes. The correlation between cytoplasmic S100B overexpression with changes in cell shape is consistent with previous studies that showed that selective inhibition of S100B production by antisense strategies in rat glioma C6 cells resulted in a more flattened cellular morphology (6). In rat C6 glioma cells, S100B is also up-regulated in post-confluent cells, and its up-regulation correlates with drastic cell morphological changes (data not shown).

IQGAP1 Is the Major Specific S100B Binding Protein in the Glial C6 and U373 Cells—In an attempt to identify specific S100B target proteins that could mediate the effect of S100B on cell morphology, we compared proteins in astrocytoma U373 and glial C6 cell extracts that bind to S100B-Sepharose beads. A major S100B-binding protein that migrated with an apparent molecular mass of 170 kDa was identified in both cell lines (Fig. 3A). The 170-kDa protein binds to S100B-Sepharose beads in EGTA/EDTA- and $\text{Ca}^{2+}/\text{Zn}^{2+}$ -containing buffer. The 170-kDa human protein from U373 MG cells was further characterized by mass spectrometry. Protein identification was achieved using both MALDI peptide mass fingerprints and MS/MS sequence information (see “Materials and Methods”). Results revealed that it corresponds to human IQGAP1. IQ-

GAP1 is a widely expressed protein that acts as a scaffold in recruiting and maintaining the organization of cytoskeletal proteins at the plasma membrane (19–27). The other high molecular weight $\text{Ca}^{2+}/\text{Zn}^{2+}$ -dependent S100B-binding protein present in glial C6 cells, but not in U373 cell extract, has been previously identified as AHNAK (28). The binding of IQGAP1 to S100B is specific, because it is not observed with S100A6 (Fig. 3B, lanes 5 and 6), and S100A11 (Fig. 3C, lanes 3 and 7), two other S100 species expressed in U373 cells (17). S100A1, the closest S100B homologue that is not expressed in U373 cells (17), also binds IQGAP1 (Fig. 3B, lanes 3 and 4). IQGAP1 in U373 cell extract also binds to calmodulin-Sepharose beads (Fig. 3C, lanes 4 and 8).

IQGAP1 Co-immunoprecipitates with S100B from U373 Cell Extract—A physical interaction between S100B with IQGAP1 was confirmed by co-immunoprecipitation of a S100B/IQGAP1 complex from confluent U373 cell extract (Fig. 4). In a first set of experiments, S100B was immunoprecipitated with S16 monoclonal S100B antibody that recognizes an epitope located within the N terminus of S100B (18). The presence of IQGAP1 in the S100B immunoprecipitate was revealed with anti-IQGAP1 polyclonal antibodies. A small but detectable amount of IQGAP1 is found in the S100B immunoprecipitates in EDTA/EGTA buffer (Fig. 4A, lane 4). The amount of IQGAP1 immunoprecipitated with S100B monoclonal antibody increased substantially in buffer containing $\text{Ca}^{2+}/\text{Zn}^{2+}$ (Fig. 4A, lane 5). The co-immunoprecipitation of IQGAP1 with S100B is specific, because it is not observed with control anti-MyoD antibodies (Fig. 4A, lanes 2 and 3). The $\text{Ca}^{2+}/\text{Zn}^{2+}$ requirement for the interaction between soluble S100B and IQGAP1 contrasts with the apparent divalent ion-independent interaction observed with S100B cross-linked to Sepharose beads (see below).

In a second set of experiments, IQGAP1 was immunoprecipitated with anti-IQGAP1 AF4 monoclonal antibody (Fig. 4B). S100B is found associated with IQGAP1 immunoprecipitates when using $\text{Ca}^{2+}/\text{Zn}^{2+}$ -containing buffer. Cdc42 and β -catenin, two other IQGAP1 target proteins (22–24) are also found associated with IQGAP1 immunoprecipitates in both EGTA/EDTA and $\text{Ca}^{2+}/\text{Zn}^{2+}$ buffer. Several laboratories have also shown intracellular interactions between CaM and IQGAP1 (19–20, 26, 29). In Fig. 4C, we compared the association of calmodulin (CaM) and S100B with immunoprecipitate IQGAP1 out of exponentially growing and post-confluent U373 cells in EGTA/EDTA- and $\text{Ca}^{2+}/\text{Zn}^{2+}$ -containing buffer. CaM and S100B that co-immunoprecipitated with IQGAP1 were sequentially revealed using the same nitrocellulose transfer membrane. CaM co-immunoprecipitates with IQGAP1 in all conditions tested, whereas S100B only co-immunoprecipitates with IQGAP1 from post-confluent cell extracts in buffer containing $\text{Ca}^{2+}/\text{Zn}^{2+}$ (compare lanes 2 and 3). It is noteworthy that, although other laboratories reported that Ca^{2+} enhances the interaction between CaM and IQGAP1 (26, 29–30), we found more CaM immunoreactivity associated with IQGAP1 in U373 cell extracts containing EGTA and EDTA (compare lanes 2 and 3 or lanes 5 and 6). This unexpected observation cannot solely be explained by a competition with S100B, because it is also observed with sub-confluent culture characterized by low S100B expression.

Zn^{2+} -dependent Interaction between S100B and IQGAP1—In a pull-down assay using S100B cross-linked onto Sepharose beads, the S100B/IQGAP1 interaction can be detected independently of the presence of EGTA/EDTA or $\text{Ca}^{2+}/\text{Zn}^{2+}$ in binding buffer (Fig. 3). In contrast, co-immunoprecipitation experiments with endogenous cellular proteins revealed that IQGAP1/S100B interaction is markedly strengthened when Ca^{2+} and Zn^{2+} are included in binding buffer (Fig. 4).

FIG. 2. Localization of S100B in post-confluent astrogloma U373 MG cells. A and B, post-confluent U373 MG cells (day 3) were fixed and double-stained with polyclonal rabbit anti-human S100B (A) (red) and mouse monoclonal anti-S100A6 (B) (green). C and D, confocal microscopy analysis of confluent (C) and post-confluent (day 3) (D) U373 MG cells double-stained with polyclonal anti-S100B (red) or with monoclonal anti-IQGAP1 (green). Overlapping red and green pixels are shown in white.

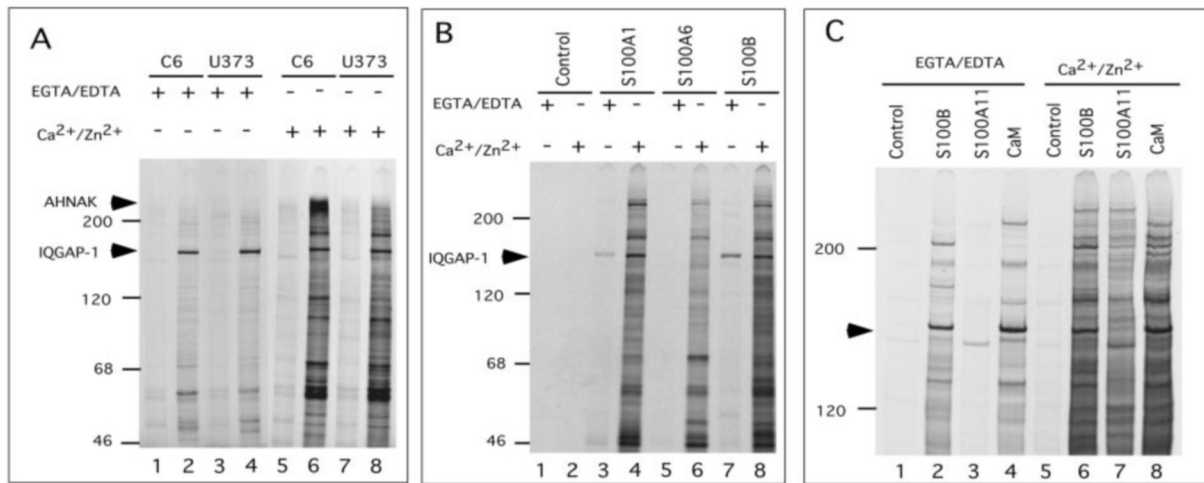
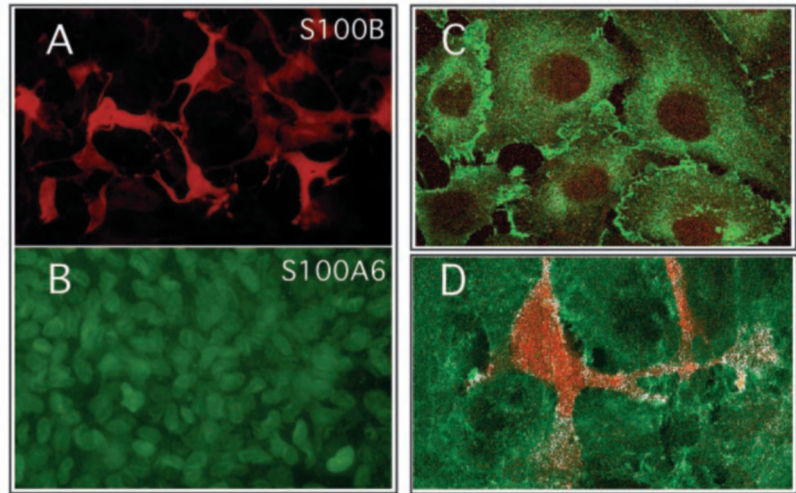


FIG. 3. Identification of S100B-binding proteins in rat glioma C6 cells and astrogloma U373 MG cells. A, comparison of [³⁵S]methionine-labeled proteins in rat glioma C6 cells (lanes 1–2 and 5–6) and in U373 MG cells (lanes 3–4 and 7–8) that interact with control Sepharose beads (lanes 1, 3, 5, and 7) or with S100B-Sepharose (lanes 2, 4, 6, and 8) in the absence (lanes 1–4) or in the presence of calcium (lanes 5–8). B, comparison of [³⁵S]methionine-labeled proteins in U373 MG cell extracts that interact with control Sepharose beads (lanes 1–2), S100A1-Sepharose (lanes 3–4), S100A6-Sepharose (lanes 5–6), and S100B-Sepharose (lanes 7–8) in the absence (lanes 1, 3, 5, and 7) or in the presence of calcium (lanes 2, 4, 6, and 8). C, comparison of [³⁵S]methionine-labeled proteins in U373 MG cell extracts that interact with control Sepharose beads (lanes 1 and 5), S100B-Sepharose (lanes 2 and 6), S100A11-Sepharose (lanes 3 and 7), and CaM-Sepharose (lanes 4 and 8) in the absence (lanes 1–4) or in the presence of calcium (lanes 5–8). In A–C, the bound proteins were resolved on 5% SDS-PAGE. In C, the bound proteins were resolved on 5% SDS-PAGE and autoradiographed. In panel C, proteins with low molecular weight were left to run out of the gel. Values at left indicate molecular size in kDa of protein standards. Arrowheads indicate the position of IQGAP1 and of the giant protein AHNAK.

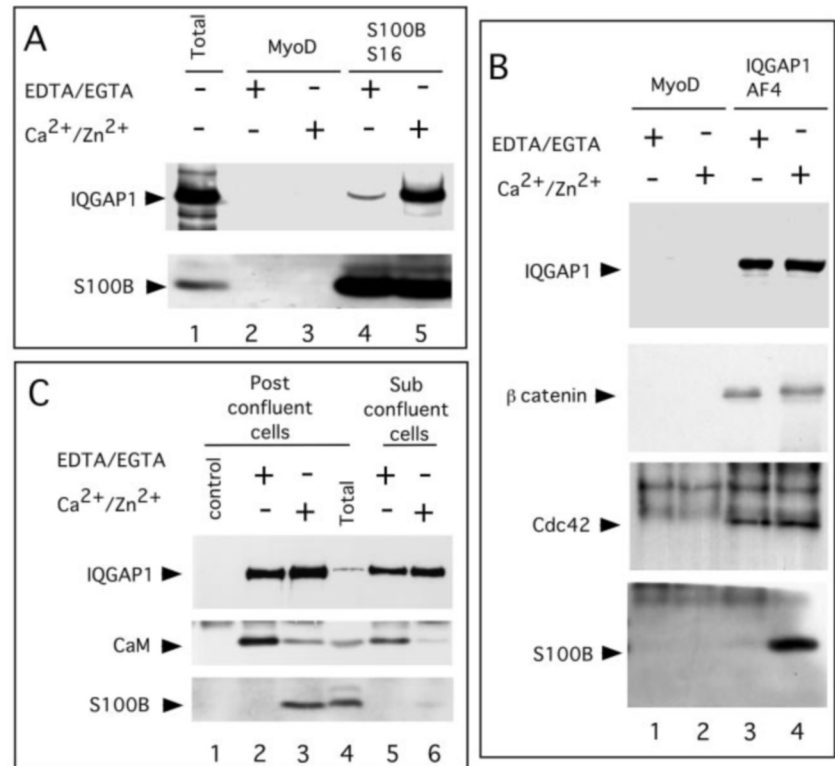
One factor that might explain this apparent discrepancy is the high S100B protein concentration used in the pull-down assay (1.5–3 μM) compared with the soluble S100B in cell extracts. To evaluate the effect of S100B concentration on complex formation with IQGAP1, we performed co-immunoprecipitation analysis using MCF7 cells extracts (which do not express the S100B protein) supplemented with increasing concentrations of recombinant human S100B (Fig. 5A). Results confirm that the S100B/IQGAP1 interaction is regulated by divalent ions and that high concentrations of S100B are not sufficient to promote ion-independent interactions.

Previous studies from our laboratory have shown that chemical modifications within the S100B molecule may have profound effects on the protein quaternary and tertiary structures (2, 31). We thus investigated the possibility that cross-linking of S100B onto Sepharose beads modifies S100B conformation as to favor interaction with IQGAP1. To test this, we compared the interaction of recombinant IQGAP1 produced in rabbit reticulocytes with the equal amount of soluble S100B, by means of co-immunoprecipitation, and S100B cross-linked onto

Sepharose beads by pull-down assays. As shown in Fig. 5B, S100B cross-linked onto Sepharose beads, but not soluble S100B, interacts with *in vitro* translated IQGAP1 in EGTA/EDTA-containing buffer (compare lanes 3 and 7). We next evaluated the contribution of individual divalent ions, Zn^{2+} and Ca^{2+} , to the S100B/IQGAP1 interaction. In the co-immunoprecipitation and pull-down assays, addition of Zn^{2+} (10 μM) to binding buffer stimulates interaction between S100B and IQGAP1 (lanes 4 and 8). Further addition of Ca^{2+} repeatedly enhanced that interaction (lanes 5 and 9). Quantitative evaluation of the radioactivity associated with S100B-Sepharose beads in different buffer conditions is shown in Fig. 5C. Together, these data suggest that, when cross-linked onto Sepharose beads, S100B adopts a conformation that favors its interaction with IQGAP1. This conformational state is probably very similar to that induced upon Zn^{2+} binding. They also suggest that Ca^{2+} might also strengthen the S100B/IQGAP1 interaction.

Zn^{2+} -dependent interaction of S100B with IQGAP1 was also observed with cellular proteins (Fig. 5D). NIH-3T3 cells were

FIG. 4. Co-immunoprecipitation of IQGAP1/S100B in U373 MG cell lysates. *A*, post-confluent (day 4) U373 MG cell extracts in buffer containing 5 mM EDTA and 5 mM EGTA (*lanes 2 and 4*) or 0.3 mM CaCl_2 and 10 μM ZnSO_4 (*lanes 3 and 5*) were immunoprecipitated with control anti MyoD antibody (*lanes 2 and 3*) or monoclonal anti-S100B S16 antibody (*lanes 4 and 5*). In *lane 1* is total cell extract used for immunoprecipitation. *B*, confluent U373 MG cell extracts supplemented with 40 μM $\text{GTP}\gamma\text{S}$ and with 5 mM EDTA and 5 mM EGTA (*lanes 1 and 3*) or with 0.3 mM CaCl_2 and 10 μM ZnSO_4 (*lanes 2 and 4*) were immunoprecipitated with control anti-MyoD antibody (*lanes 1-2*) or monoclonal anti-IQGAP1 AF4 antibody (*lanes 3-4*). *C*, cell extracts obtained from post-confluent (day 4) (*lanes 1-4*) and sub-confluent (*lanes 5-6*) U373 MG cells were immunoprecipitated with control MyoD antibody (*lane 1*), or monoclonal anti-IQGAP1 AF4 antibody (*lanes 2-3 and 5-6*). *Lane 4* is total cell extract from post-confluent cells used for immunoprecipitation. In *A*, *B*, and *C*, protein complexes were resolved by SDS-PAGE, transferred to nitrocellulose membranes, and probed with monoclonal anti-IQGAP1, monoclonal anti- β -catenin, polyclonal anti-Cdc42, monoclonal anti-CaM (Upstate Biotechnology), and polyclonal anti-S100B antibodies. Immune complexes were visualized using an ECL kit.



transfected with S100B expression plasmid and S100B/IQGAP1 complex formation analyzed by co-immunoprecipitation with S16 monoclonal antibody in different buffer conditions. When transfected cells are lysed in binding buffer containing 20 μM EGTA, the S100B/IQGAP1 interaction is almost undetectable (*lane 1*). If cell extract containing 20 μM EGTA is supplemented with Zn^{2+} (40 μM), binding of IQGAP1 to S100B is rescued (*lane 2*). Addition of Ca^{2+} (300 μM) or Zn^{2+} plus Ca^{2+} to EGTA containing cell extract also rescues S100B/IQGAP1 interaction (*lanes 3 and 4*). As observed with *in vitro* translated ^{35}S -labeled IQGAP1 (Fig. 5, *B* and *C*), a slight but significant increase in IQGAP1 immunoreactivity is found associated with S100B immunoprecipitates in buffer containing Ca^{2+} . That stimulation was more clearly seen with lower exposure of the Western blot membrane to ECL film. All together these data suggest that, in solution, the S100B/IQGAP1 interaction requires either Zn^{2+} or Ca^{2+} ions and that Zn^{2+} is sufficient to promote that interaction. IQGAP1 is thus the first S100B target protein identified whose interaction with S100B is mediated by Zn^{2+} -dependent conformational change on S100B.

Mechanism of Zn^{2+} -dependent Interaction of S100B with IQGAP1—To further confirm the essential role of Zn^{2+} -dependent conformational change on S100B for interaction with IQGAP1, we next compared the mechanism of interaction of S100B with IQGAP1 and with a strict calcium-dependent target protein, AHNAK (28). We first studied the interactions of the wild-type S100B and of a C-terminal deleted mutant S100B (S100B Δ Ct) with IQGAP1 and AHNAK. We used S100B Δ Ct because the C terminus domain of S100B is required for interactions between S100B and strict Ca^{2+} -dependent target protein (32, 33). NIH 3T3 cells were transfected with expression vectors encoding S100B or S100B Δ Ct, and complex formation was assayed by co-immunoprecipitation using the N-terminal S100B monoclonal antibody S16 (Fig. 6A). Although we repeatedly observed a much lower expression of S100B Δ Ct compared with wild-type S100B, both wild-type S100B and mutant S100B Δ Ct co-immunoprecipitate with IQGAP1 from cell ly-

167
sates in $\text{Zn}^{2+}/\text{Ca}^{2+}$ -containing buffer (*lanes 6 and 9*). Deletion of the C terminus of S100B specifically abrogated $\text{Zn}^{2+}/\text{Ca}^{2+}$ -dependent interaction of S100B with AHNAK (compare *lanes 6 and 9*). These results suggest that the C terminus of S100B is not implicated in Zn^{2+} -dependent interaction of S100B with IQGAP1. We next compared the contribution of individual divalent ions, Zn^{2+} and Ca^{2+} , to the S100B Δ Ct/IQGAP1 interaction (Fig. 6B). When transfected NIH 3T3 cells are lysed in binding buffer containing 20 μM EGTA, the S100B Δ Ct/IQGAP1 interaction is almost undetectable (*lane 2*). If cell extract containing 20 μM EGTA is supplemented with Zn^{2+} (40 μM) (*lane 3*) or Zn^{2+} plus Ca^{2+} (*lane 5*), binding of IQGAP1 to S100B Δ Ct is rescued. However, in contrast to the full-length S100B (Fig. 5D, *lane 3*), addition of Ca^{2+} (300 μM) alone also stimulates S100B Δ Ct/IQGAP1 interaction, but to a much lower extent than Zn^{2+} or Zn^{2+} plus Ca^{2+} (Fig. 6B, *lane 4*). All together these data confirm that, in solution, Zn^{2+} is sufficient to promote the S100B/IQGAP1 interaction and that Ca^{2+} binding to S100B might contribute to strengthen the interaction via the C terminus of S100B.

Mapping the Minimal Interaction Domain for S100B on IQGAP1—To investigate which domains of IQGAP1 are responsible for S100B binding, the full-length protein and the indicated mutants of IQGAP1 were produced in rabbit reticulocytes (Fig. 7A), and their interaction with S100B- and CaM-Sepharose beads compared (Fig. 7B), as described under “Materials and Methods.” There is no difference between the full-length IQGAP1 and the N-terminal domain of IQGAP1 in binding S100B and CaM beads. All fusion proteins containing the IQ domain (IQ, CHD-IQ, and IR-IQ) also bind to S100B and CaM in the presence of EGTA/EDTA. These findings suggest that IQ motifs are essential for interactions between S100B and IQGAP1. They are also consistent with previous data showing that the high affinity CaM binding region on IQGAP1 corresponds to its IQ domains (29).

To confirm that S100B and the CaM-binding domain on IQGAP1 overlap and to investigate if S100B competes with

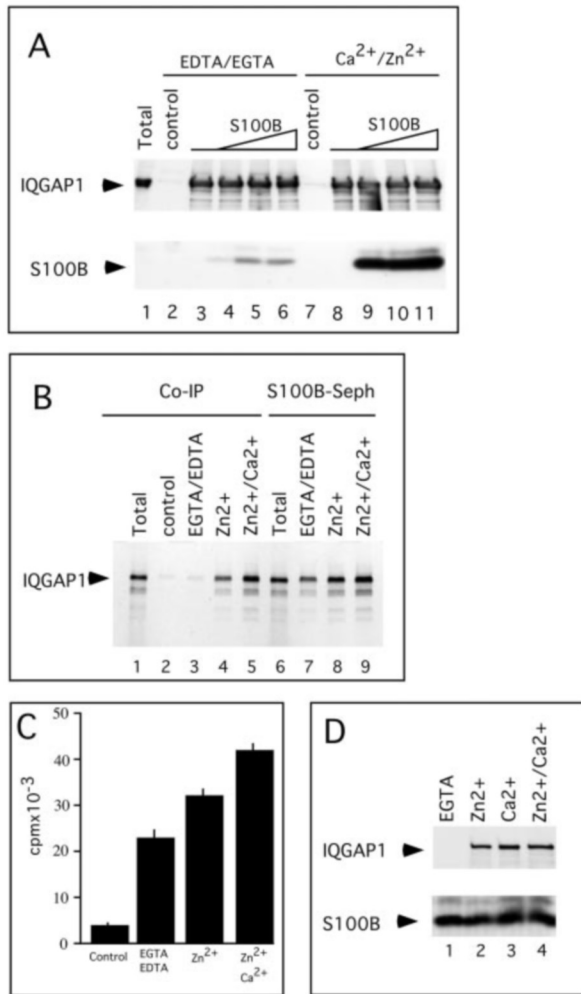


FIG. 5. Zn^{2+} -dependent interaction between S100B and IQGAP1. A, MCF7 cell extracts in buffer containing 5 mM EDTA and 5 mM EGTA (lanes 2–6) or 0.3 mM CaCl_2 and 10 μM ZnSO_4 (lanes 7–11) were not supplemented (lanes 2–3 and 7–8) or supplemented with purified human recombinant S100B at concentrations of 1 μM (lanes 4 and 9), 2 μM (lanes 5 and 10), and 4 μM (lanes 6–11) prior to immunoprecipitation with control anti MyoD antibody (lanes 2 and 7) or monoclonal anti-IQGAP1 AF4 antibody (lanes 3–6 and 8–11). Lane 1 is total cell extract used for immunoprecipitation. Protein complexes were resolved by SDS-PAGE, transferred to nitrocellulose membranes, and probed with monoclonal anti-IQGAP1 or with polyclonal anti-S100B antibodies. Immune complexes were visualized using an ECL kit. B, [^{35}S]methionine-labeled recombinant IQGAP1 produced in rabbit reticulocyte was mixed with soluble purified recombinant S100B (2 μM), then S100B was immunoprecipitated with monoclonal anti-S100B S16 antibody (1 μg) (lanes 3–5) or with S100B-Sepharose beads (2 μM) (lanes 7–9) in buffer containing 5 mM EDTA and 5 mM EGTA (lanes 3 and 7), 10 μM ZnSO_4 (lanes 4 and 8), or 0.3 mM CaCl_2 and 10 μM ZnSO_4 (lanes 5 and 9). Protein complexes were resolved by SDS-PAGE and autoradiography. Lanes 1 and 6 correspond to total reticulocyte lysate. Lane 2 is immunoprecipitation with control anti MyoD antibody. C, quantitative analysis of the radioactivity associated with S100B-Sepharose beads as shown in B. Results are the average of one typical experiment done in triplicate. Lane C corresponds to S100A11-Sepharose beads used as control. D, mouse NIH 3T3 cells were transfected with S100B pcDNA, and S100B was immunoprecipitated with monoclonal S16 antibody in buffer containing 20 μM EGTA (lane 1), 20 μM EGTA plus 40 μM ZnSO_4 (lane 2), 20 μM EGTA plus 0.3 mM CaCl_2 (lane 3), or 20 μM EGTA plus 40 μM ZnSO_4 and 0.3 mM CaCl_2 (lane 4). Protein complexes were resolved by SDS-PAGE, transferred to nitrocellulose membranes, and probed with monoclonal anti-IQGAP1 or with polyclonal anti-S100B antibodies. Immune complexes were visualized using an ECL kit.

CaM for binding with IQGAP1, we next performed competition assays. Purified S100B was mixed with ^{35}S -labeled recombinant IQGAP1 together with CaM-Sepharose beads. The

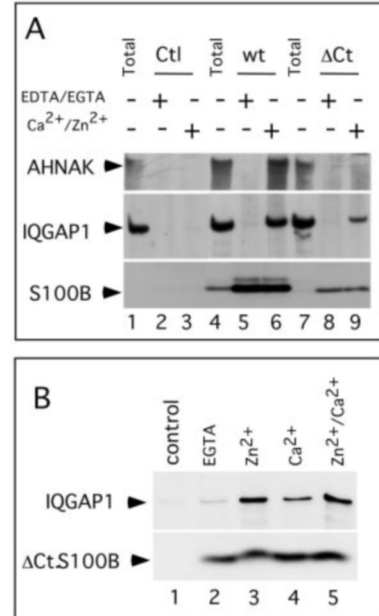
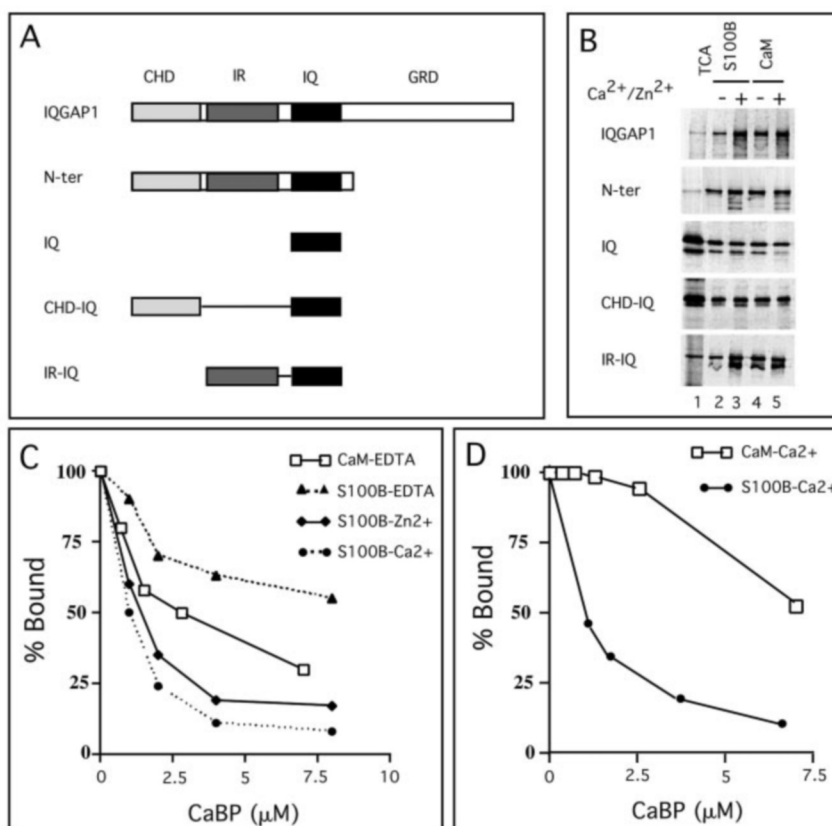


FIG. 6. Mechanism of Zn^{2+} -dependent interaction of S100B with IQGAP1. A, NIH 3T3 fibroblasts were transfected with empty (control) plasmid (lanes 1–3), or with wild-type (wt) S100B (lanes 4–6) or mutant (ΔCt) S100B (ΔCt) (lanes 7–9) plasmids for 36 h by the calcium phosphate method. Cell extracts were immunoprecipitated using the monoclonal anti-S100B S16 antibody (lanes 2–3, 5–6, and 8–9). Immunoprecipitations were performed in the absence (lanes 2, 5, and 8) or in the presence (lanes 3, 6, and 9) of $\text{Ca}^{2+}/\text{Zn}^{2+}$. Lanes 1, 4, and 7 are total cell extracts used for immunoprecipitation. B, NIH 3T3 cells were transfected with control plasmid (lane 1) or with S100B ΔCt plasmid (lanes 2–5) as in A. S100B ΔCt was immunoprecipitated with monoclonal S16 antibody in buffer containing 20 μM EGTA (lanes 1 and 2), 20 μM EGTA plus 40 μM ZnSO_4 (lane 3), 20 μM EGTA plus 0.3 mM CaCl_2 (lane 4), or 20 μM EGTA plus 40 μM ZnSO_4 and 0.3 mM CaCl_2 (lane 5). In A and B, protein complexes were resolved by SDS-PAGE, transferred to nitrocellulose membrane, and probed with monoclonal anti-IQGAP1, polyclonal anti-AHNAK, and polyclonal rabbit anti-S100B. Immune complexes were visualized by an ECL kit.

amount of IQGAP1 bound to calmodulin, in the presence of various concentrations of divalent ions and of S100B, was quantified by measuring the radioactivity associated with the CaM-beads pellet (Fig. 7C). In the absence of divalent ion, S100B interfered with the association of IQGAP1 with CaM only at high concentration. In the presence of Zn^{2+} , or Zn^{2+} plus Ca^{2+} , S100B produced a dose-dependent inhibition of binding of IQGAP1 to CaM. The S100B concentration-dependent inhibition curves show that, in the presence of Zn^{2+} , or Zn^{2+} plus Ca^{2+} , half inhibition occurs with a S100B concentration below the estimated CaM-Sepharose concentration in the assay (1.8 μM), suggesting that, in its Zn^{2+} - or $\text{Ca}^{2+}/\text{Zn}^{2+}$ -bound conformations S100B may have higher affinity for IQGAP1 than CaM. As expected, when purified bovine brain CaM was used in competition with CaM-Sepharose, in the presence of Ca^{2+} and Zn^{2+} , for binding IQGAP1, the inhibition curve is shifted to a higher competitor protein concentration (Fig. 7C). Inversely, when the purified competitor proteins, CaM and S100B, were mixed with ^{35}S -labeled recombinant IQGAP1 together with S100B-Sepharose beads, CaM antagonized IQGAP1 binding to S100B-Sepharose at a much higher concentration than S100B (Fig. 7D) confirming that in its $\text{Ca}^{2+}/\text{Zn}^{2+}$ -bound conformations S100B has a higher affinity for *in vitro* translated IQGAP1 than has CaM.

S100B Co-localizes with IQGAP1 at Ruffling Membranes but Not at Sites of Cell-Cell Contact in U373 Cells—The specificity of interaction between S100B and IQGAP1 in U373 cells was then investigated at the cellular level by indirect double im-

FIG. 7. Mapping of the S100B-binding domains on IQGAP1. A, domain diagram of IQGAP1. IQGAP1 has a variety of domains, including a calponin homologous domain (CHD), six internal repeats (IR) of yet unknown function, four IQ repeats, and a Ras GAP-related domain (GRD). B, *in vitro* translated IQGAP1 and different N-terminal domains as indicated were tested for interaction with S100B-Sepharose (lanes 2–3) or CaM-Sepharose (lanes 4–5) in buffer supplemented with 5 mM EDTA/EGTA (lanes 2 and 4) or 0.3 mM Ca^{2+} plus 10 μM Zn^{2+} (lanes 3 and 5). Lane 1 corresponds to total reticulocyte lysate that has been precipitated by 20% trichloric acid (TCA). C and D, S100B and CaM compete with CaM-Sepharose for binding with IQGAP1. C, binding of [^{35}S]methionine-labeled recombinant IQGAP1 to CaM-Sepharose beads (1.8 μM) was analyzed in the presence of increasing bovine brain S100B (\blacktriangle , \blacklozenge , and \bullet) or CaM (\square) concentrations in buffer containing 5 mM EDTA and 5 mM EGTA (\blacktriangle), 10 μM ZnSO_4 (\blacklozenge), or 0.3 mM CaCl_2 and 10 μM ZnSO_4 (\bullet and \square). D, binding of [^{35}S]methionine-labeled recombinant IQGAP1 to S100B-Sepharose beads (1.3 μM) was analyzed in the presence of increasing bovine brain S100B (\bullet) or CaM (\square) concentrations in buffer containing or 0.3 mM CaCl_2 and 10 μM ZnSO_4 (\bullet and \square). In C and D, results are representative of two experiments in duplicate.



munofluorescence studies (Fig. 8). In sub-confluent U373 MG cells, S100B expression is down-regulated (Fig. 1) and is hardly detectable with the monoclonal S16 anti S100B antibody. Sparse U373 cells were transfected with the S100B cDNA and the sub-cellular localization of both ectopically expressed S100B and IQGAP1 were evaluated with anti S100B monoclonal antibody and rabbit anti-IQGAP1 antibody (Fig. 8). The majority of ectopically expressed S100B protein translocates and accumulates within cell nuclei. Nevertheless, a substantial amount of S100B remains specifically sequestered within the cytoplasm. In the cytoplasm, S100B accumulates and co-localizes with IQGAP1 in a region that resembles the polarized leading edge and area of membrane ruffling (Fig. 8A, see *arrow*). Membrane ruffles were characterized by intense staining with fluorescein isothiocyanate-phalloidin (not shown). Several groups have shown previously in different cell models that IQGAP1 accumulates at the polarized leading edge and areas of membrane ruffling (27, 34). At the polarized leading edge, IQGAP1 forms a tripartite complex with CLIP-170 and Rac1/Cdc42 to regulate linkage of microtubules to the cortical region (27). In transfected U373 cells, S100B immunoreactivity is totally excluded at the sites of cell-cell contacts where IQGAP1 also localizes (Fig. 8B, see *arrowheads*). At the cell-cell junctions, IQGAP1 may associate with Cdc42 or β -catenin for regulation of cadherin-based cell adhesion (22–25).

S100B and IQGAP1 Relocate in a Ca^{2+} -dependent Manner within Secretion-associated Vesicle-like Structures in Human Astrocytoma U87 Cells—Relocation of S100B from the perinuclear area toward the periphery of the cell in the form of vesicle-like structures in response to intracellular Ca^{2+} increase has been recently reported in the human astrocytoma U87 cell line transfected with S100B-GFP fusion protein (12). In this cell model, Ca^{2+} -dependent relocation of S100B-GFP has been linked to the S100B secretion pathway (12). To evaluate whether IQGAP1 could be implicated in the S100B-secre-

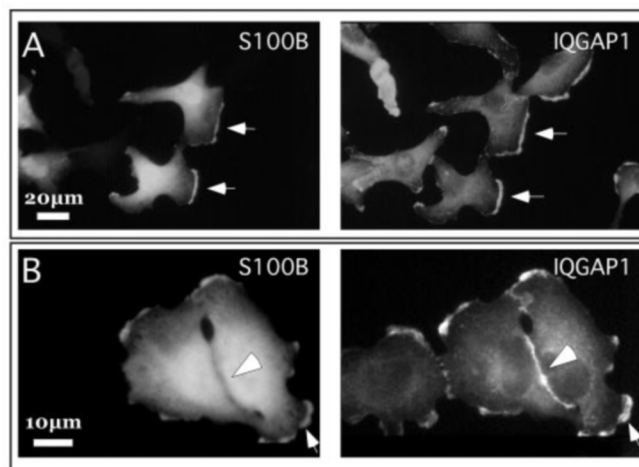


FIG. 8. Cytoplasmic S100B protein co-localizes with IQGAP1 protein at membrane ruffling but not at sites of cell-cell contact in U373 MG cells. Sparse U373 MG cells transfected with the S100B expression plasmid were fixed and double-stained with monoclonal anti-S100B and polyclonal anti-IQGAP1 as indicated. In sub-confluent U373 MG cells, S100B expression is down-regulated and is hardly detectable with the monoclonal S16 anti-S100B antibody. Only transfected cells with S100B plasmid are strongly immunostained. *Arrows* show co-localization of S100B with IQGAP1 in the region that resembles the polarized leading edge and area of membrane ruffling. *Arrowheads* point to the site of cell-cell contact where IQGAP1 but not S100B also localizes.

tion pathway, we studied the effect of intracellular Ca^{2+} increase on S100B and IQGAP1 localization in U87 cells. U87 cells were transiently transfected with the S100B cDNA and the sub-cellular localization of S100B, and IQGAP1 were evaluated by immunocytochemistry (Fig. 9). In U87 cells grown in normal medium, ectopically expressed S100B protein localizes

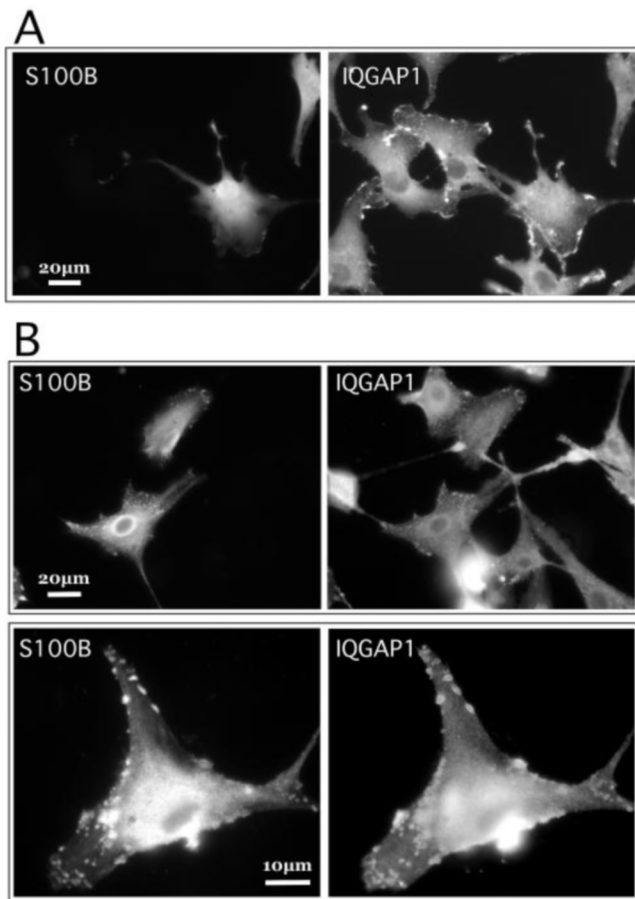


FIG. 9. Ca^{2+} -dependent relocation of S100B and IQGAP1 within secretion associated vesicle-like structure in U87 cells. Transiently transfected U87 cells with S100B-pcDNA were incubated 5 min in complete medium plus Me_2SO (A) or $5 \mu\text{M}$ ionomycin in Me_2SO (B). Cells were fixed and double-stained with polyclonal anti-S100B or with monoclonal anti-IQGAP1 as indicated.

to membrane ruffling, the perinuclear area, and within the cell nuclei (Fig. 9A). Ionomycin stimulation of U87 cells induces rapid relocation of S100B within vesicle-like structures that have the appearance of membrane blebs (Fig. 9B). As previously noticed (12), these vesicle-like structures are often located toward the periphery of the cells. When considering IQGAP1 in non-stimulated U87 cells, IQGAP1 is diffusely located within the cytoplasm and accumulates at membrane ruffling (Fig. 9A). Increase in the intracellular Ca^{2+} concentration causes relocation of IQGAP1 to the newly formed membrane blebs where it co-localizes with S100B (Fig. 9B). IQGAP1 relocation did not depend on the expression levels of S100B, because it is also observed in non-transfected cells.

Ca^{2+} Regulates Both Relocation and Stable Association of S100B and IQGAP1 with Membrane Vesicles in MCF7 Cells—As observed in most epithelial cells, in MCF7 human breast epithelial cells, IQGAP1 accumulates at the cell-cell junction (Ref. 24 and Fig. 10A). With MCF7 cells stably transfected with the S100B gene (S100B-MCF7) and grown in complete culture medium, IQGAP1 remains concentrated at the cell-cell junction, whereas the ectopically expressed S100B protein accumulates within the cell nuclei (Fig. 10A). When S100B-MCF7 cells are cultured in serum-free medium, intracellular calcium elevation mediated by calcium ionophore ionomycin produced a rapid relocation of both S100B and IQGAP1 within the cell cytoplasm (Fig. 10B). When ionomycin-containing medium was replaced by fresh complete medium, both S100B and IQGAP1 relocated to the cell nuclei and the cell-cell

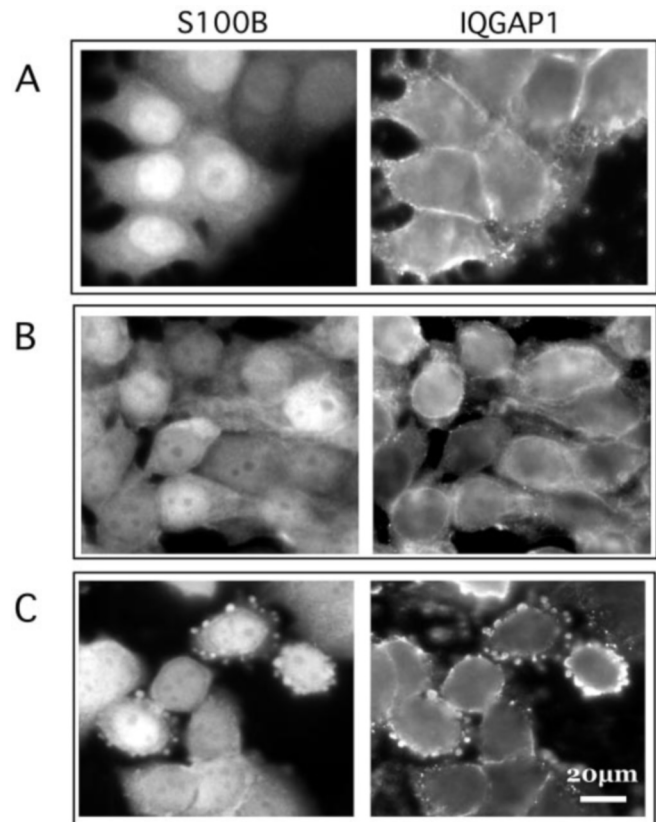


FIG. 10. Ca^{2+} regulates relocation of S100B and IQGAP1 in MCF7 cells. A, stably transfected MCF7 cells with S100B-pcDNA were grown in complete medium. B, S100B-MCF7 cells were left 20 h in serum-free medium and stimulated 5 min with $5 \mu\text{M}$ ionomycin prior to fixation. C, S100B-MCF7 cells were treated as in B. After 5 min culture medium was changed to fresh complete medium and cells were left 1 h prior to fixation. In A, B, and C, cells were double-stained with polyclonal anti-S100B or with monoclonal anti-IQGAP1 as indicated.

junctions, respectively, indicating that Ca^{2+} -dependent translocation is reversible. However, in many S100B-MCF7 cells, a co-localization of S100B and IQGAP1 persisted within newly formed membrane blebs located toward the periphery of the cells (Fig. 10C).

DISCUSSION

Characterization of the Molecular Interaction between S100B and IQGAP1—In solution, S100B associates as a non-covalent dimer. In its dimeric form, S100B interacts not only with Ca^{2+} but also with Zn^{2+} ions (2). S100B binds Zn^{2+} ions with affinity in the nanomolar range (2). In contrast, the S100B dimer affinity for calcium is rather weak compared with other EF-hand calcium-binding proteins and is not within the range of physiological intracellular calcium concentrations (2). In the presence of Zn^{2+} , or upon alkylation of Zn^{2+} ligand Cys84, the S100B adopts a “ Ca^{2+} -bound-like” conformation (2, 31). That conformation is associated with destabilization of the quaternary protein structure, exposure of the calcium-binding sites to solvent, and increased apparent Ca^{2+} affinity compatible with local intracellular calcium concentration (2, 31). The capacity of S100B to bind and release Zn^{2+} without denaturation suggests that Zn^{2+} may not only play a structural role but might be involved, together with Ca^{2+} , in concerted regulation of S100B interaction with target proteins. In this study, we identified for the first time a Zn^{2+} -dependent S100B target protein, IQGAP1. Zn^{2+} -bound S100B co-immunoprecipitates with IQGAP1 present in cell extract or expressed in rabbit reticulocyte. In contrast to immunoprecipitation assay, pull-down assay using

S100B cross-linked onto Sepharose beads revealed that the S100B/IQGAP1 interaction can also be detected in the presence of EGTA/EDTA in binding buffer. We have shown that these discrepancies probably result from differences in conformation between the soluble S100B and the S100B cross-linked onto Sepharose beads (Fig. 5B). This was further confirmed by competition experiments using CaM-Sepharose. Only in its Zn^{2+} - or Zn^{2+}/Ca^{2+} -bound conformations is S100B capable of substantially antagonizing the binding of recombinant IQGAP1 to CaM-Sepharose beads (Fig. 7C). The mainly CaM-binding domains on IQGAP1 correspond to IQGAP1-IQ motifs (29). It is therefore likely that Zn^{2+} -dependent interactions of S100B with IQGAP1 also require IQGAP1-IQ motifs. This was confirmed by mapping the Ca^{2+} -independent S100B-binding domain on IQGAP1 using a pull-down assay (Fig. 7, A and B). The IQ motif was initially identified in brain-specific protein kinase C substrates neuromodulin (GAP43) and neurogranin as part of Ca^{2+} -independent CaM binding and protein kinase C phosphorylation site domain (35, 36). IQ motifs have since been identified as binding sites for CaM in a variety of proteins (37). We provide here evidence that the IQ motifs are not specific to CaM and can also be targeted by Zn^{2+} -bound S100B. The Zn^{2+} -dependent interaction of S100B with IQGAP1 is unique among the S100B-target proteins so far identified. With conventional S100B target proteins, Zn^{2+} does not promote direct interaction but modulate S100B Ca^{2+} affinity (28). Although Zn^{2+} binding to S100B is sufficient to promote interaction of S100B with IQGAP1, quantitative comparison of binding of full length recombinant IQGAP1 to S100B revealed that addition of Ca^{2+} to the binding buffer significantly potentiates the interaction between the two proteins (Fig 5B). A similar effect of Ca^{2+} was reported for CaM/IQGAP1 interaction (26, 30). It has been proposed that differences in CaM binding to IQGAP1 in the absence and in the presence of Ca^{2+} is attributable to difference between IQ motifs, some of which bind Ca^{2+} -CaM, and others bind Ca^{2+} -free CaM (26, 30). Because Zn^{2+} -bound S100B prevents the binding of IQGAP1 to Ca^{2+} -free CaM, it is possible that, in its Zn^{2+} -bound conformation, S100B interacts with some of the IQ motifs that are capable of binding CaM in the absence of Ca^{2+} . When complexed to Ca^{2+} , the S100B would then be able to utilize the four IQ motifs to further strengthen its interaction with IQGAP1. It is also possible that other domains on IQGAP1 could confer Ca^{2+} sensitivity to the S100B/IQGAP1 interaction. A striking amino acid sequence conservation exists between the IQGAP1-5 repeat motif (⁵⁴¹INEALDEGDAQ⁵⁵⁰) and the Ca^{2+} -dependent S100B-binding domain on p53 (³⁴⁴LNEALELKDAQ³⁵³) (38). The S100B-binding domain present on p53 is a tetramerization domain that is also implicated in the interaction of p53 with other regulatory proteins (39). Further studies should explore if the interaction of S100B with IQGAP1 could regulate IQGAP1 interactions with partner proteins through its repeat motifs.

IQGAP1 as a Mediator of S100B-induced Regulation of Cell Shape and S100B Secretion Pathway—In post-confluent human glioma U373 MG, the strongest S100B immunoreactivity is found associated with cells that are characterized by a less flattened morphology and long processes (Fig. 2). In these cells, a co-localization of S100B and IQGAP1 is evident at plasma membrane and within growing processes. Transient transfection of S100B in sub-confluent U373 MG cells confirmed that cytoplasmic S100B specifically co-localizes with IQGAP1 at the plasma membrane but not at sites of cell-cell junction (Fig. 8). Many studies have implicated IQGAP1 as a scaffold to recruit and localize protein complexes involved in actin and microtubule-based cellular functions at the plasma membrane (19, 20, 27, 34). Interaction of Ca^{2+}/Zn^{2+} -S100B with IQGAP1 could

therefore, regulate IQGAP1 scaffold function at the plasma membrane in response to incoming signals linked to the reorganization of the actin and microtubule cytoskeleton. This hypothesis is consistent with previous studies showing that selective inhibition of S100B expression by antisense strategies in rat glioma C6 cells resulted in a more flattened cellular morphology and a more organized actin stress fiber staining pattern with less membrane ruffling (6). It is noteworthy that IQGAP1 can also bind to S100A1 (Fig. 3B). S100A1, the closest S100B homologue, is also a potential regulator of cell cytoskeleton and cell morphology (41).

In this study, we have also provided evidence that the interaction between S100B and IQGAP1 might also occur within vesicle-like structures that also have the appearance of membrane blebs in the human astrocytoma U87 and MCF7 cells. In U87 cells, both S100B and IQGAP1 translocate and co-localize within vesicle-like structures in response to increased intracellular calcium. The Ca^{2+} -dependent translocation of S100B in U87 has been studied in detail elsewhere (12). It has been proposed that these vesicle-like structures, which correspond to cytoplasmic extensions that form and disappear dynamically, are implicated in Ca^{2+} -dependent S100B secretion process (12). In U87 cells not stimulated with ionomycin, these vesicle-like structures were rarely immunostained with IQGAP1 antibodies, suggesting that Ca^{2+} regulates targeting of IQGAP1 to these structures. The mechanism that controls Ca^{2+} -dependent IQGAP1 relocation is independent of S100B, because it is also observed in cells that do not express S100B. Ca^{2+} -dependent translocation of S100B and IQGAP1 within structures having the appearance of membrane blebs was confirmed with stably transfected S100B-MCF7 cells (Fig. 10). In stably transfected S100B-MCF7, IQGAP1 is naturally targeted to the cell-cell junctions and S100B accumulates predominantly within the cell nuclei. Serum deprivation coupled to intracellular calcium elevation mediated by ionomycin induces a relocation of both S100B and IQGAP1 within the cell cytoplasm. This process is maximal within 5 min, supporting the idea that it depends on calcium fluxes. When ionomycin-containing medium is replaced by fresh complete medium, the majority of S100B and IQGAP1 has a tendency to relocate to nuclei and to cell-cell junctions, respectively, indicating that Ca^{2+} -dependent translocation is reversible. However, in many S100B-MCF7 cells, a co-localization of S100B and IQGAP1 persisted within membrane blebs located toward the periphery of the cells. Hence, Ca^{2+} is required for both S100B and IQGAP1 relocation and their subsequent stable association with newly formed membrane structures. Taking into account the high affinity interaction between S100B and IQGAP1, we propose that IQGAP1 might be implicated in recruiting S100B to secretory vesicular structures and might be involved in the Ca^{2+} -dependent S100B secretion pathway. The observed Ca^{2+} -dependent association of IQGAP1 with vesicle-like structure is new and might reveal an additional cellular function for the protein. Whether or not IQGAP1 directly participates in stabilization, turnover, and dynamics of these vesicle-like structures has yet to be evaluated. It is significant that functional disruption of Iqg1p, a yeast homologue of the mammalian IQGAPs, has been directly implicated in vesicle accumulation at the growing bud, suggesting a possible involvement of yeast Iqg1p in secretion or some aspect of vesicle trafficking (40).

The interaction between cytoplasmic S100B and IQGAP1 might also have important implications for understanding the relationship between overexpression of cytoplasmic S100B and the development of a more aggressive cell phenotype during brain tumor progression. In astroglial brain tumors, progression from low grade (astrocytoma) into faster growing, more

dysplastic and invasive high grade tumors (glioblastomas), correlates with increased expression of cytoplasmic S100B (42). Although a causal relationship between S100B concentration and malignancy has not been demonstrated, it is hypothesized that increased concentration of S100B may contribute to neoplastic transformation. In these brain tumor cells, overexpressed S100B could interfere with the regulatory function of IQGAP1 during processes of dynamic rearrangement of cell-cell adhesion (23, 24) to favor cell motility and metastasis.

Acknowledgments—We thank Dr. J. Erickson for helpful discussion and the generous gift of IQGAP1 cDNAs and IQGAP1 antibodies, N. Assard for technical assistance, Mbélé T. and Mbélé A. for encouragements, and Drs. J. LaMarre and C. Benaud for the critical reading and comments on the manuscript.

REFERENCES

- Schäfer, B. W., and C. Heizmann. (1996). *Trends Biochem. Sci.* **21**, 134–140
- Baudier, J., Glasser, N., and Gérard, D. (1986) *J. Biol. Chem.* **261**, 8192–8203
- Haglid, K. G., Hamberger, A., Hansson, H. A., Hyden, H., Persson, L., Ronnback, L. (1975) *Nature* **258**, 748–749
- Rickmann, M., and Wolff, J. R. (1995) *Histochemistry* **103**, 135–145
- Scotto, C., Delphin, C., Deloulme, J. C., and Baudier, J. (1999) *Mol. Cell. Biol.* **19**, 7168–7180
- Selinfreund, R. H., Barger, S. W., Welsh, M. J., and Van Eldik, L. J. (1990) *J. Cell Biol.* **111**, 2021–2028
- Xiong, Z., O'Hanlon, D., Becker, L. E., Roder, J., MacDonald, J. F., and Marks, A. (2000) *Exp. Cell Res.* **257**, 281–289
- Donato, R. (2001) *Int. J. Biochem. Cell Biol.* **33**, 637–668
- Nishiyama, H., Knopfel, T., Endo, S., and Itohara, S. (2002) *Proc. Natl. Acad. Sci. U. S. A.* **99**, 4037–4042
- Griffin, W. S., Stanley, L. C., Ling, C., White, L., MacLeod, V., Perrot, L. J., White, C. L., and Araoz, C. (1989) *Proc. Natl. Acad. Sci. U. S. A.* **86**, 7611–7615
- Hofmann, M. A., Drury, S., Fu, C., Qu, W., Taguchi, A., Lu, Y., Avila, C., Kambham, N., Bierhaus, A., Nawroth, P., Neurath, M. F., Slattery, T., Beach, D., McClary, J., Nagashima, M., Morser, J., Stern, D., and Schmidt, A. M. (1999) *Cell* **97**, 889–901
- Davey, G. E., Murmann, P., and Heizmann, C. W. (2001) *J. Biol. Chem.* **276**, 30819–30826
- Peskind, E. R., Griffin, W. S., Akama, K. T., Raskind, M. A., and Van Eldik, L. J. (2001) *Neurochem. Int.* **39**, 409–413
- Portela, L. V., Brenol, J. C., Walz, R., Bianchin, M., Tort, A. B., Canabarro, U. P., Beheregaray, S., Marasca, J. A., Xavier, R. M., Neto, E. C., Goncalves, C. A., and Souza, D. O. (2002) *Clin. Diagn. Lab. Immunol.* **9**, 164–166
- Abdul-Khaliq, H., Schubert, S., Stoltenburg-Didinger, G., Troitzsch, D., Bottcher, W., Hubler, M., Meissler, M., Grosse-Siestrop, C., Alexi-Meskishvili, V., Hetzer, R., and Lange, P. E. (2000) *Clin. Chem. Lab. Med.* **38**, 1169–1172
- Baudier, J., Mochly-Rosen, D., Newton, A., Lee, S. H., Koshland, D. E., Jr., and Cole, R. D. (1987) *Biochemistry* **26**, 2886–2893
- Deloulme, J. C., Assard, N., Ouengue Mbele, G., Mangin, C., Kuwano, R., and Baudier, J. (2000) *J. Biol. Chem.* **275**, 35302–35310
- Takahashi, M., Chamczuk, A., Hong, Y., and Jackowski, G. (1999) *Clin. Chem.* **45**, 1307–1311
- Bashour, A. M., Fullerton, A. T., Hart, M. J., and Bloom, G. S. (1997) *J. Cell Biol.* **137**, 1555–1566
- Erickson, J. W., Cerione, R. A., and Hart, M. J. (1997) *J. Biol. Chem.* **272**, 24443–24447
- Fukata, M., Kuroda, S., Fujii, K., Nakamura, T., Shoji, I., Matsuura, Y., Okawa, K., Iwamatsu, A., Kikuchi, A., and Kaibuchi, K. (1997) *J. Biol. Chem.* **272**, 29579–29583
- Fukata, M., Kuroda, S., Nakagawa, M., Kawajiri, A., Itoh, N., Shoji, I., Matsuura, Y., Yonehara, S., Fujisawa, H., Kikuchi, A., and Kaibuchi, K. (1999) *J. Biol. Chem.* **274**, 26044–26050
- Fukata, M., Nakagawa, M., Itoh, N., Kawajiri, A., Yamaga, M., Kuroda, S., Kaibuchi, K. (2001) *Mol. Cell. Biol.* **21**, 2165–2183
- Kuroda, S., Fukata, M., Nakagawa, M., Fujii, K., Nakamura, T., Ookubo, T., Izawa, I., Nagase, T., Nomura, N., Tani, H., Shoji, I., Matsuura, Y., Yonehara, S., and Kaibuchi, K. (1998) *Science* **281**, 832–835
- Li, Z., Kim, S. H., Higgins, J. M., Brenner, M. B., and Sacks, D. B. (1999) *J. Biol. Chem.* **274**, 37885–37892
- Mateer, S. C., McDaniel, A. E., Nicolas, V., Habermacher, G. M., Lin, M. J., Cromer, D. A., King, M. E., and Bloom, G. S. (2002) *J. Biol. Chem.* **277**, 12324–12333
- Fukata, M., Watanabe, T., Noritake, J., Nakagawa, M., Yamaga, M., Kuroda, S., Matsuura, Y., Iwamatsu, A., Perez, F., and Kaibuchi, K. (2002) *Cell* **109**, 873–885
- Gentil, B., Delphin, C., Ouengue Mbele, G., Deloulme, J. C., Ferro, M., Garin, J., and Baudier, J. (2001) *J. Biol. Chem.* **276**, 23253–23261
- Ho, Y. D., Joyal, J. L., Li, Z., and Sacks, D. B. (1999) *J. Biol. Chem.* **274**, 464–470
- Joyal, J. L., Annan, R. S., Ho, Y. D., Huddleston, M. E., Carr, S. A., Hart, M. J., and Sacks, D. B. (1997) *J. Biol. Chem.* **272**, 15419–15425
- Baudier, J., Glasser, N., and Duportail, G. (1986) *Biochemistry* **25**, 6934–6941
- Rustandi, R. R., Baldisseri, D. M., Drohat, A. C., and Weber, D. J. (1999) *Protein Sci.* **8**, 1743–1751
- McClintock, K. A., Van Eldik, L. J., and Shaw, G. S. (2002) *Biochemistry* **41**, 5421–5428
- Hart, M. J., Callow, M. G., Souza, B., and Polakis, P. (1996) *EMBO J.* **15**, 2997–3005
- Alexander, K. A., Wakim, B. T., Doyle, G. S., Walsh, K. A., and Storm, D. R. (1998) *J. Biol. Chem.* **263**, 7544–7549
- Baudier, J., Deloulme, J. C., Van Dorsselaer, A., Black, D., and Matthes, H. W. (1991) *J. Biol. Chem.* **266**, 229–237
- Chakravarthy, B., Morley, P., and Whitfield, J. (1999) *Trends Neurosci.* **22**, 12–16
- Delphin, C., Ronjat, M., Deloulme, J. C., Garin, G., Debussche, L., Higashimoto, Y., Sakaguchi, K., and Baudier, J. (1999) *J. Biol. Chem.* **274**, 10539–10544
- Stommel, J. M., Marchenko, N. D., Jimenez, G. S., Moll, U. M., Hope, T. J., and Wahl, G. M. (1999) *EMBO J.* **18**, 1660–1672
- Osman, M. A., and Cerione, R. A. (1998) *J. Cell Biol.* **142**, 443–455
- Zimmer, D. B., Cornwall, E. H., Reynolds, P. D., and Donald, C. M. (1998) *J. Biol. Chem.* **273**, 4705–4711
- Van Eldik, L. J., Jensen, R. A., Ehrenfried, B. A., and Whetsell, W. O. (1986) *J. Histochem. Cytochem.* **34**, 977–982

The Giant Protein AHNAK Is a Specific Target for the Calcium- and Zinc-binding S100B Protein

POTENTIAL IMPLICATIONS FOR Ca^{2+} HOMEOSTASIS REGULATION BY S100B*

Received for publication, November 26, 2000, and in revised form, April 18, 2001
Published, JBC Papers in Press, April 18, 2001, DOI 10.1074/jbc.M010655200

Benoit J. Gentil‡, Christian Delphin‡, Gaëlh Ouengue Mbele‡, Jean Christophe Deloulme‡, Myriam Ferro§, Jérôme Garin§, and Jacques Baudier‡¶

From the ‡Département de Biologie Moléculaire et Structurale du Commissariat à l'Énergie Atomique, INSERM EPI-0104 and §Laboratoire de Chimie des Protéines DBMS-CP, CEN-G, 38054 Grenoble, France

Transformation of rat embryo fibroblast clone 6 cells by ras and temperature-sensitive p53val¹³⁵ is reverted by ectopic expression of the calcium- and zinc-binding protein S100B. In an attempt to define the molecular basis of the S100B action, we have identified the giant phosphoprotein

AHNAK as the major and most specific Ca^{2+} -dependent S100B target protein in rat embryo fibroblast cells. We next characterized AHNAK as a major Ca^{2+} -dependent S100B target protein in the rat glial C6 and human U-87MG astrocytoma cell lines. AHNAK binds to S100B-Sepharose beads and is also recovered in anti-S100B immunoprecipitates in a strict Ca^{2+} - and Zn^{2+} -dependent manner. Using truncated AHNAK fragments, we demonstrated that the domains of AHNAK responsible for interaction with S100B correspond to repeated motifs that characterize the AHNAK molecule. These motifs show no binding to calmodulin or to S100A6 and S100A11. We also provide evidence that the binding of 2 Zn^{2+} equivalents/mol S100B enhances Ca^{2+} -dependent S100B-AHNAK interaction and that the effect of Zn^{2+} relies on Zn^{2+} -dependent regulation of S100B affinity for Ca^{2+} . Taking into consideration that AHNAK is a protein implicated in calcium flux regulation, we propose that the S100B-AHNAK interaction may participate in the S100B-mediated regulation of cellular Ca^{2+} homeostasis.

Calcium is a ubiquitous second messenger that regulates many cellular functions including cell growth, differentiation, and apoptosis (1, 2). EF-hand calcium-binding proteins, such as calmodulin, troponin C, parvalbumin, and S100, are implicated in calcium transduction pathways (3). These proteins bind Ca^{2+} through their EF-hand motifs, and in their Ca^{2+} -bound conformation they interact with secondary effector proteins. S100 proteins constitute one of the largest subfamilies of EF-hand proteins (4). To date, 17 different proteins have been assigned to the S100 protein family. The S100 proteins are small proteins (10 kDa) that are generally expressed in tissue- and cell-specific manners. They show different degrees of ho-

mology, ranging from 25% to 55% identity at the amino acid level. *In vivo*, the S100 proteins associate as noncovalent homodimers but may also heterodimerize with other individual S100 species (5–8). Some S100 protein members including S100B, S100A1, S100A3, S100A6, S100A7, and S100A11 are not only calcium-binding proteins but also bind Zn^{2+} ions (9). The interaction of S100B protein with Zn^{2+} may be important in its biological function. Unlike Ca^{2+} binding, Zn^{2+} binding to S100B has a minimal effect on the conformation of the overall protein structure but profoundly increases affinity for calcium (10). An important question related to Zn^{2+} binding to S100 proteins in general is how Zn^{2+} regulates the functions of S100.

S100B is abundant in the brain, where it localizes to astrocytes. This protein has attracted much interest over the past few years because, like other proteins implicated in neurodegeneration (*e.g.* β -amyloid and superoxide dismutase), its gene is located on chromosome 21, which is trisomic in Down's syndrome (11). Overexpression of S100B in the brain of patients with Down's syndrome or Alzheimer's disease (12, 13) and in the brains of patients with AIDS (14) has led to the hypothesis that S100B plays a contributory role in several neuropathologies associated with these diseases. Outside the central nervous system, expression of S100B protein is increased in many tumors (15). In cardiomyocytes, S100B synthesis is induced in response to hypoxia (16) and acts as a negative modulator of the hypertrophic response after myocardial infarction (17). S100B null mice are viable and exhibit no behavioral abnormalities up to 12 month of age (18). On the other hand, astrocytes derived from S100B null mice show abnormal calcium elevation in response to agents that normally induce a transient Ca^{2+} increase (18). These results suggest that S100B plays a role in the maintenance of Ca^{2+} homeostasis within cells. The identification of *in vivo* S100B target proteins is essential for determination of the exact contribution of the S100B-dependent signaling pathways to cellular functions. Several putative S100B target proteins have already been characterized, including cytoplasmic cytoskeletal-associated proteins (19–21); enzymes such as nuclear kinase Ndr (22), retinal membrane-bound guanylate cyclase (23), and fructose 1,6-bisphosphate-aldolase (24); and transcription factors (25, 26). Most of these putative target proteins are also able to interact with the other S100 species and/or calmodulin.

We show here that a major and specific target protein for S100B is the giant phosphoprotein AHNAK. AHNAK/des-moyokin (molecular mass, 700 kDa) is a protein originally identified by Shtivelman *et al.* (27) and Shtivelman and Bishop (28) as a nuclear phosphoprotein repressed in cell lines derived from human neuroblastomas and in several other types of tumors. Subsequently, Hashimoto *et al.* (29) described

* This work was supported by Association pour la Recherche sur le Cancer Grant 5643 and a grant from the Ligue Nationale Contre le Cancer. The costs of publication of this article were defrayed in part by the payment of page charges. This article must therefore be hereby marked "advertisement" in accordance with 18 U.S.C. Section 1734 solely to indicate this fact.

¶ To whom correspondence should be addressed: Département de Biologie Moléculaire et Structurale, EPI-0104, Centre d'Étude Nucléaire de Grenoble, 17 rue des Martyrs, 38054 Grenoble Cedex 9, France. Tel: 33-4-38-78-43-28; Fax: 33-4-38-78-58-89; E-mail: jbaudier@cea.fr.

AHNAK/desmoyokin as a desmosomal plaque protein in epithelial tissues. In epithelial cells, AHNAK/desmoyokin is present mainly in the cytoplasm when cells are kept in low Ca^{2+} medium but translocates to the plasma membrane after an increase in extracellular Ca^{2+} concentration or protein kinase C activation (30). More recently, AHNAK has been found in cardiomyocytes associated with L-type calcium channels. In these cells, AHNAK may play a role in cardiac calcium signaling by modulating L-type calcium channels in response to β -adrenergic stimulation (31). A recent report also identified AHNAK as a protein that binds and activates phospholipase C- γ 1 in the presence of arachidonic acid to generate inositol trisphosphate and diacylglycerol, two second messengers that control intracellular calcium flux (32). A possible role for AHNAK in S100B-mediated regulation of cell calcium homeostasis is discussed.

MATERIALS AND METHODS

Cell Cultures—REF¹ cells (clone 6) (44) were grown in RPMI 1640-Glutamax (Life Technologies, Inc.) supplemented with 5% fetal calf serum (Life Technologies, Inc.) at 37.5 °C. Glial C6 cells, U87-MG, U373-MG, and HeLa cells were grown in Dulbecco's modified Eagle's medium-Glutamax (Life Technologies, Inc.) supplemented with 10% fetal calf serum (Life Technologies, Inc.) at 37.5 °C.

Antibodies—Purified S100B monoclonal antibody S16 was a generous gift from Dr. M. Takahashi (Skye PharmaTech Inc.). S100B polyclonal antibodies were from DAKO. KIS/AHNAK polyclonal antibodies (28) were obtained from Dr. E. Shtivelman (University of California San Francisco, San Francisco, CA). p53-specific monoclonal antibody PAb421 was purified from hybridoma supernatants by protein A-agarose chromatography. Anti-tubulin was a gift from Dr. L. Paturle and D. Job (CEA-Grenoble). Myc epitope-specific monoclonal antibody 9e10 and MyoD monoclonal antibody 5.8A were from H. Weintraub (Fred Utchinson Cancer Research Center, Seattle, WA).

S100B- and CaM-Sepharose Beads—S100B and CaM were purified from bovine brain to homogeneity (10). S100B- and CaM-Sepharose were prepared by reaction of bovine brain S100B and CaM with CnBr-Sepharose in 20 mM HEPES, pH 7.8, and 0.5 mM CaCl_2 . Both S100B- and CaM-Sepharose contained 2 mg protein/ml beads. Recombinant human S100B, S100A1, S100A6, and S100A11 were coupled to CnBr-Sepharose (1 mg protein/ml beads) as described above.

Bacterial Expression Plasmids—The bacterial expression plasmid for the production of His-tagged M2-DY (AHNAK amino acids 2589–3059) was constructed by cloning an *EcoRV/HindIII* fragment from Z83 (27) into *EcoRV/HindIII* sites of pet32b (Novagen). For His-tagged M3-DY (AHNAK amino acids 3730–4188) expression in *Escherichia coli*, the corresponding *SspI* DNA fragment from Z80 (27) was cloned into *EcoRV* site of pet32a (Novagen). His-tagged U1-DY (AHNAK amino acids 3730–3878) and His-tagged U2-DY (AHNAK amino acids 3730–3972) expression plasmids were obtained by deleting the carboxyl-terminal part of the AHNAK fragment of M3-DY. M3-DY expression vector was digested by *BspMI/XhoI* or *AatII/XhoI* for the production of U1-DY or U2-DY expression vector, respectively, blunted, and then self-ligated.

Recombinant Protein Expression and Purification—Recombinant protein expression was carried out in *E. coli* strain AD494(DE3)pLYsS (Novagen). Bacteria were grown to $A_{600} = 0.6$ in 100 ml of Luria-Bertani broth medium supplemented with 15 $\mu\text{g/ml}$ kanamycin, 34 $\mu\text{g/ml}$ chloramphenicol, 40 $\mu\text{g/ml}$ leucine, and 50 $\mu\text{g/ml}$ carbemycin. Protein expression was induced with 1 mM isopropyl-1-thio- β -D-galactopyranoside for 2 h. Bacteria were harvested and resuspended in 2 ml of lysis buffer (30 mM Tris-HCl, pH 7.4, 150 mM NaCl, 0.3% Triton X-100, 1 mM β -mercaptoethanol, 1 mg/ml lysozyme, and 2 $\mu\text{g/ml}$ of each protease inhibitor (leupeptin, aprotinin, pepstatin, and AEBSEF)). After one freeze/thaw cycle, bacterial lysates were cleared (100,000 $\times g$ for 20 min) and kept on ice or stored at -20 °C. His-tagged M3-DY, U2-DY, and U1-DY were purified by Ni^{3+} affinity chromatography.

S100B- and CaM-binding Assays—For binding assays using recombinant AHNAK fragments expressed in rabbit reticulocytes (TNTquick; Promega), 20 μl of reaction lysates were diluted in 500 μl of TTBS supplemented with either 5 mM EDTA and 5 mM EGTA or 0.3 mM CaCl_2

and 10 μM ZnSO_4 and mixed with 20 μl of affinity beads equilibrated in the same buffers. After mixing at 4 °C for 10 min, the beads were spun down, and the supernatant was removed. The beads were washed three times with the binding buffers and boiled in SDS-sample buffer. For binding assays using recombinant AHNAK fragments expressed in bacteria, soluble extracts (50 μl) were diluted in 500 μl of TTBS supplemented with either 5 mM EDTA and 5 mM EGTA or 0.3 mM CaCl_2 and 10 μM ZnSO_4 and treated as described above. For binding assays using crude cell extracts, cells were first labeled in methionine-free minimum Eagle's medium, 10% fetal calf serum, supplemented with [³⁵S]methionine/[³⁵S]cysteine mix (50 $\mu\text{Ci/ml}$) for 8 h. Cells were lysed in TTBS buffer supplemented with protease inhibitors (leupeptin, aprotinin, pepstatin, AEBSEF, *N*-acetyl-Leu-Leu-norleucinal, and *N*-acetyl-Leu-Leu-methioninal; 10 $\mu\text{g/ml}$ each) and centrifuged for 10 min at 14,000 $\times g$. The lysates were precleared by incubation for 10 min with 50 μl of protein A-Sepharose. Aliquots (500 μl) of precleared supernatant were mixed with 500 μl of TTBS supplemented with either 5 mM EDTA and 5 mM EGTA or 0.3 mM CaCl_2 and 10 μM ZnSO_4 and mixed with 20 μl of affinity beads equilibrated in the same buffers. After mixing at 4 °C for 10 min, the beads were spun down, and the supernatant was removed. The beads were washed three times with the binding buffers. At the last wash, the beads were transferred to new Eppendorf tubes and boiled in SDS-sample buffer.

Co-immunoprecipitations—For co-immunoprecipitation of AHNAK and S100B, NIH-3T3 cells in 100-mm dishes were first transfected with control plasmid or S100B plasmid (4 μg) using FuGENE™ reagent (12 μl) as recommended by the manufacturer (Roche). Cells were lysed after 36 h. For co-immunoprecipitation of p53 and AHNAK, confluent REF cells were labeled in methionine-free minimum Eagle's medium, 5% fetal calf serum, supplemented with [³⁵S]methionine/[³⁵S]cysteine mix (100 $\mu\text{Ci/ml}$) for 6 h. NIH-3T3 and REF cells were lysed in TTBS buffer supplemented with protease inhibitors (leupeptin, aprotinin, pepstatin, AEBSEF, *N*-acetyl-Leu-Leu-norleucinal, and *N*-acetyl-Leu-Leu-methioninal; 10 $\mu\text{g/ml}$ each). The lysates were precleared by a 10-min centrifugation at 14,000 $\times g$, and the supernatant was further incubated for 15 min with 50 μl of protein A-Sepharose. Aliquots (500 μl) of precleared supernatant were mixed with 500 μl of TTBS supplemented with either 5 mM EDTA and 5 mM EGTA or 0.3 mM CaCl_2 and 10 μM ZnSO_4 and mixed with appropriate antibodies (5 μg) plus 20 μl of protein A-Sepharose equilibrated in the same buffers. After mixing at 4 °C for 15 min, the beads were centrifuged briefly (5 s, 13,000 rpm), and the supernatant was removed. The beads were washed three times with the binding buffers. At the last wash, the beads were transferred to new Eppendorf tubes and boiled in SDS-sample buffer.

Mass Spectrometric Analysis and Protein Identification—The protein bands were excised from Coomassie Blue-stained gels and washed with 50% acetonitrile. Gel pieces were dried in a vacuum centrifuge and reswollen in 20 μl of 25 mM NH_4HCO_3 containing 0.5 μg of trypsin (sequencing grade; Promega). After 4 h of incubation at 37 °C, a 0.5 μl aliquot was removed for MALDI time of flight analysis and spotted onto the MALDI sample probe on top of a dried, 0.5 μl mixture of 4:3 saturated α -cyano-4-hydroxy-*trans*-cinnamic acid in acetone/10 mg/ml nitrocellulose in acetone/isopropanol 1:1. Samples were rinsed by placing a 5 μl volume of 0.1% trifluoroacetic acid on the matrix surface after the analyte solution had dried completely. After 2 min, the liquid was blown off by pressurized air. MALDI mass spectra of peptide mixtures were obtained using a Bruker Biflex mass spectrometer (Bruker-Franzen Analytik, Bremen, Germany). Internal calibration was applied to each spectrum using trypsin autodigestion peptides (MH+ 842.50, MH+ 1045.55, and MH+ 2211.11). Protein identification was confirmed by tandem mass spectrometry experiments. After in-gel tryptic digestion, the gel pieces were extracted with 5% formic acid solution and then extracted with acetonitrile. The extracts were combined with the original digest, and the sample was evaporated to dryness in a vacuum centrifuge. The residues were dissolved in 0.1% formic acid and desalted using a Zip Tip (Millipore). Elution of the peptides was performed with 5–10 μl of 50% acetonitrile/0.1% formic acid solution. The peptide solution was introduced into a glass capillary (Protana) for nano-electrospray ionization. Tandem mass spectrometry experiments were carried out on a quadrupole time of flight hybrid mass spectrometer (Micromass, Altrincham, United Kingdom) to obtain sequence information. Collision-induced dissociation of selected precursor ions was performed using argon as the collision gas and with collision energies of 40–60 eV. Protein identification was achieved using both MALDI peptide mass fingerprints and tandem mass spectrometry sequence information. Mass spectrometric data were compared with known sequences using the programs MS-Fit and MS-Edman from the University of California San Francisco.

¹ The abbreviations used are: REF, rat embryo fibroblast; CaM, calmodulin; TTBS, 40 mM Tris-HCl, pH 7.5, 150 mM NaCl, and 0.3% Triton X-100; MALDI, matrix-assisted laser desorption ionization; PAGE, polyacrylamide gel electrophoresis.

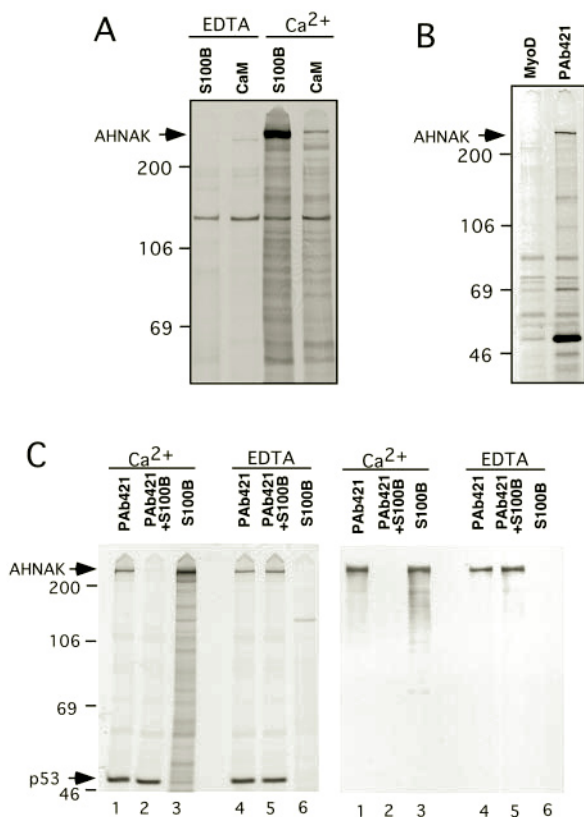


FIG. 1. AHNAK in REF clone 6 cells interacts with S100B. *A*, comparison of [³⁵S]methionine-labeled proteins in REF cell extracts that interact with S100B-Sepharose (*S100B*) or CaM-Sepharose (*CaM*) beads in the absence (*EDTA*) or presence of calcium (*Ca*²⁺). The bound proteins were resolved on 5% SDS-PAGE without stacking gel and autoradiographed. *B*, analysis of [³⁵S]methionine-labeled proteins in REF cell extracts that co-precipitate with p53val¹³⁵. Cell extracts were immunoprecipitated with either MyoD monoclonal antibody 5.8A or p53-specific monoclonal antibody PAb421 as indicated. Immunoprecipitates were resolved by 7.5% SDS-PAGE and autoradiographed. *C*, S100B prevents co-precipitation of AHNAK with p53val¹³⁵. *Left panel*, [³⁵S]methionine-labeled proteins in REF cell extracts were incubated with p53 monoclonal antibody PAb421 coupled to Sepharose in the absence (*lanes 1 and 4*) or presence of 5 μM purified S100B (*lanes 2 and 5*). Identical extracts were incubated with S100B-Sepharose in the presence (*lanes 3*) or absence of calcium (*lanes 6*). The bound proteins were electrophoresed on 7.5% SDS-PAGE gels and autoradiographed. *Right panel*, REF cell extracts were treated as described for the *left panel*. Proteins were electrophoresed on 5% SDS-PAGE and detected by Western blot analysis using KIS/AHNAK antibodies.

Real-time Surface Plasmon Resonance Recording—Real-time binding experiments were performed on a BIAcore biosensor system (Pharmacia Biosensor AB, Uppsala, Sweden). All experiments were performed at 25 °C. AHNAK peptides in 10 mM sodium acetate, pH 3.5, were coupled directly through their amino groups to the sensor surface activated by *N*-hydroxy-succinimide and *N*-ethyl-*N'*-(dimethylamino)propyl)carbodiimide according to the manufacturer's instructions. The remaining reactive groups were then inactivated with 1 mM ethanolamine. For control experiments, the sensor surface was treated as described above in the absence of peptide or coupled to His-tagged importin α1. All interaction experiments were done using a running buffer containing 20 mM Tris-HCl, pH 7.5, and 150 mM NaCl in the absence or presence of CaCl₂ as indicated. Between injections, the sensor chip was washed with a buffer containing 20 mM Tris-HCl, pH 7.5, 120 mM NaCl, and 2 mM EDTA and equilibrated with the appropriate running buffer. For Zn²⁺-dependent binding experiments, the S100B protein was incubated with ZnSO₄ before injection on the sensor chip. Sensorgrams were analyzed using the BIAevaluation 3.0 program (Pharmacia Biosensor AB).

RESULTS

Identification of the Giant Protein AHNAK as a Target Protein for S100B in Fibroblastic Cell Lines—Ectopic expression of

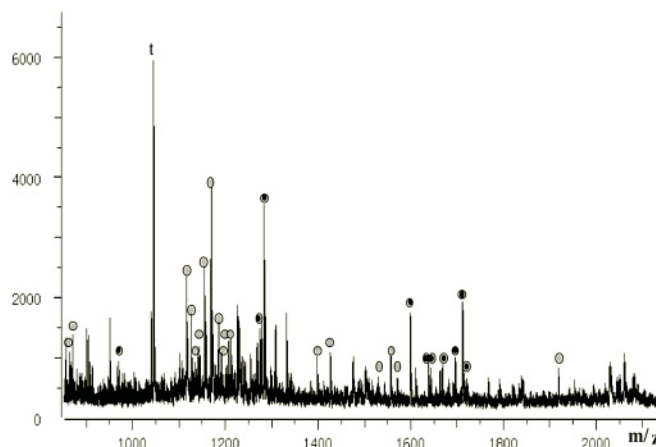


FIG. 2. Identification of AHNAK by mass spectrometry. Nano-electrospray mass spectral analysis was performed on the high molecular weight specific S100B target protein isolated from human HeLa cells as described under "Materials and Methods." Positive-ion mass spectrum of the tryptic peptide mixture obtained from in-gel digestion and microcolumn desalting is shown. The molecular weight of peptide ions indicated with *gray-filled circles* matched tryptic peptides from AHNAK. Peptides indicated with *black-filled circles* were sequenced by tandem mass spectrometry and found to match tryptic peptides from AHNAK. *t*, tryptic peptide from trypsin.

the calcium- and zinc-binding S100B protein in mouse embryo fibroblasts and REFs expressing the temperature-sensitive p53val¹³⁵ mutant cooperates with Ca²⁺ to promote nuclear accumulation of the wild-type p53val¹³⁵ conformational species and rescue wild-type p53 functions at the nonpermissive temperature (33, 34). To begin to characterize the mechanism behind this effect, we chose to characterize Ca²⁺-dependent S100B target proteins in REF clone 6 cells. REF cells were metabolically labeled with [³⁵S]methionine, after which protein extracts were incubated with S100-Sepharose beads in the absence or presence of Ca²⁺/Zn²⁺. To control for specificity of protein interactions, the pattern of protein binding was compared with that of CaM-Sepharose (Fig. 1*A*). The most abundant and specific calcium-dependent S100B target protein in REF cells is a large protein heavily labeled with [³⁵S]methionine that migrates at the top of the gel (Fig. 1*A*).

The corresponding human protein from HeLa cell extract was next isolated by Ca²⁺-dependent interaction with S100B-Sepharose beads and further characterized by mass spectrometry. Protein identification was achieved using both MALDI peptide mass fingerprints and tandem mass spectrometry sequence information (Fig. 2). Results revealed that the large molecular mass protein corresponds to the human protein AHNAK (27).

A physical Ca²⁺-dependent interaction between S100B and AHNAK was also demonstrated by exploiting the observation that AHNAK co-immunoprecipitates with the anti-p53 monoclonal antibody PAb421 from clone 6 cell extracts (Fig. 1*B* and Fig. 1*C*, *lanes 1 and 4*). AHNAK is not precipitated by the control monoclonal anti-MyoD antibody, showing that AHNAK co-immunoprecipitation with PAb421 is specific (Fig. 1*B*). If clone 6 cell extracts are supplemented with purified S100B (5 μM) before immunoprecipitation with PAb421, S100B prevents co-precipitation of AHNAK only when calcium is present (Fig. 1*C*, compare *lanes 1 and 2*). In the absence of calcium, AHNAK is unable to interact with S100B (*lanes 6*), and S100B does not dissociate AHNAK from PAb421 immunoprecipitates (Fig. 1*C*, compare *lanes 4 and 5*). S100B does not antagonize p53val¹³⁵ immunoprecipitation by PAb421 (Fig. 1*C*, compare *lanes 1 and 4* with *lanes 2 and 5*), confirming that the dissociation of AHNAK from PAb421 immunoprecipitate results from direct interaction between S100B and AHNAK.

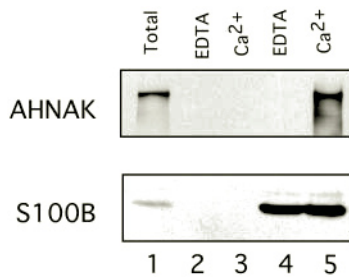


FIG. 3. Co-immunoprecipitation of AHNAK with S100B. NIH-3T3 cells were transfected with an expression plasmid containing the S100B gene (*lanes 1, 4, and 5*) or empty vector alone (*lanes 2 and 3*). After 36 h, cells were lysed in detergent-containing buffer and incubated with protein A-Sepharose and S100B monoclonal antibody S16 in the absence (*lanes 2 and 4*) or presence of calcium (*lanes 3 and 5*). Immunoprecipitates were either electrophoresed on 5% SDS-PAGE and analyzed for AHNAK by Western blot or electrophoresed on 11% SDS-Tricine PAGE followed by Western blot analysis for S100B. *Lane 1* corresponds to total extract of NIH-3T3 cells transfected with the S100B gene.

Finally, we confirmed a strict Ca^{2+} -dependent interaction between S100B and AHNAK by co-immunoprecipitation (Fig. 3). NIH-3T3 cells were transfected with an expression vector containing S100B cDNA, and complex formation was assayed by co-immunoprecipitation. AHNAK co-immunoprecipitates with S100B from cell lysates containing Ca^{2+} and Zn^{2+} (Fig. 3, *lane 5*) but not in the presence of EGTA/EDTA (Fig. 3, *lane 4*). The co-immunoprecipitation of AHNAK with S100B was specific because it was not observed in cells transfected with empty vector (Fig. 3, *lanes 2 and 3*).

Characterization of AHNAK as a Major Calcium-dependent S100B Target in Glial Cells—In humans, the S100B protein is abundant in glial cells. We therefore evaluated the presence of AHNAK in two human astrocytoma cell lines (U373-MG and U87-MG) (Fig. 4A) and one rat glioma cell line (C6) (Fig. 4B). Western blot analysis of crude cell extracts revealed that only human U-87-MG cells (Fig. 4A, *lane 1*) and rat C6 cells (Fig. 4B, *lane 1*) show strong AHNAK immunoreactivity. AHNAK was absent in the human astrocytoma cell line U-373-MG (Fig. 4A, *lane 2*; see also Fig. 5A). Western blot analysis (Fig. 4B) as well as affinity batch interaction studies using [^{35}S]methionine-labeled cells (Fig. 5) confirmed the strict calcium-dependent interaction of the AHNAK protein in U-87-MG cells and glial C6 cells with S100B-Sepharose beads. Note, here again, that most of the proteins that bound to S100B-Sepharose also bound to CaM-Sepharose and that AHNAK is the only protein that specifically bound to S100B-Sepharose beads in a strict $\text{Ca}^{2+}/\text{Zn}^{2+}$ -dependent manner (Fig. 5B, *lanes 3 and 4*).

Identification of the S100B-binding Region of AHNAK—A three-domain structure was predicted for AHNAK in which the amino- and carboxyl-terminal ends of the protein flank a large internal domain (Fig. 6A). The internal domain is composed of 30 repeated motifs, each of which is 128 residues long (27). The 128-residue motifs are, on average, ~80% identical to each other with respect to amino acid sequence. The 128-residue repeat is characterized by underlying heptad repeats that are also found in the first portion of the carboxyl terminus. To investigate which domains of AHNAK are responsible for specific binding to S100B, the amino terminus (residues 1–251, N-DY), four complete repeating units of the central domain (residues 820–1330, M1-DY), and the carboxyl-terminal 1002 amino acids (C-DY) tagged with a Myc epitope were translated *in vitro* using rabbit reticulocyte lysates. The interaction of the Myc-tagged AHNAK domains with anti-Myc and with S100B- or CaM-Sepharose was evaluated. The amino terminus was

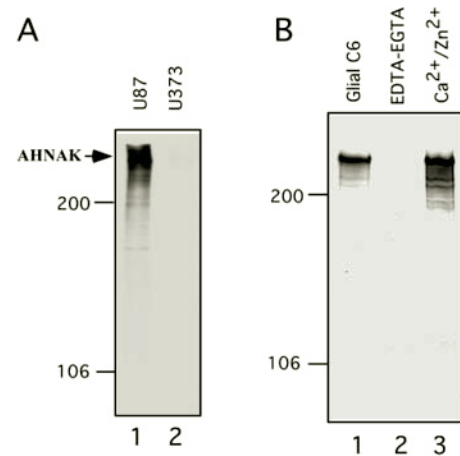


FIG. 4. AHNAK is present in glial cells. A, AHNAK is present in the human astrocytoma cell line U87-MG (*lane 1*) but not in U373-MG cells (*lane 2*). Cell extracts were analyzed by Western blot using KIS/AHNAK polyclonal antibodies. B, characterization of AHNAK as a calcium-dependent target for S100B in rat glial C6 cells. Proteins from total glial C6 extract (*lane 1*) and proteins that bound to S100B-Sepharose in the absence (*lane 2*) or presence of calcium (*lane 3*) were analyzed by Western blot using KIS/AHNAK polyclonal antibodies.

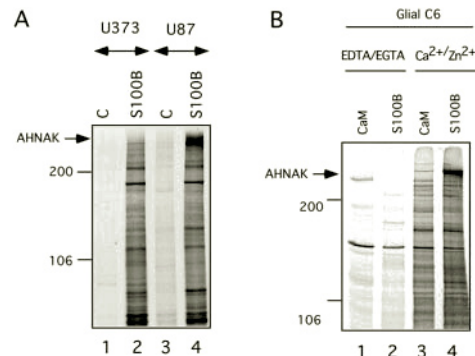


FIG. 5. AHNAK is a major and specific calcium-dependent target for S100B in glial cell lines C6 and U87-MG. A, comparison of soluble proteins in human astrocytoma U373-MG (*lanes 1 and 2*) and U87-MG cells (*lanes 3 and 4*) that bound to Sepharose (*lanes 1 and 3*) or to S100B-Sepharose (*lanes 2 and 4*) in the presence of calcium. B, comparison of soluble proteins in glial C6 extract that interact with CaM-Sepharose (*lanes 1 and 3*) or S100B-Sepharose (*lanes 2 and 4*) in the absence (*lanes 1 and 2*) or presence of calcium (*lanes 3 and 4*). In A and B, cells were metabolically labeled with [^{35}S]methionine for 8 h before lysis. Cell extracts (1 ml) were incubated with 20 μl of either Sepharose or Sepharose coupled to CaM or S100B in the absence or presence of calcium. The bound proteins were electrophoresed on 5% SDS-PAGE and visualized by autoradiography.

unable to bind to S100B- or CaM-Sepharose (Fig. 6B). The carboxyl terminus was found to bind to S100B-Sepharose and, to a much lesser extent, to CaM-Sepharose in a strictly $\text{Ca}^{2+}/\text{Zn}^{2+}$ -dependent manner (Fig. 6C). The M1-DY domain showed absolutely no binding to CaM-Sepharose but interacted strongly with the S100B-Sepharose in a $\text{Ca}^{2+}/\text{Zn}^{2+}$ -dependent manner (Fig. 6C). The specificity of the interaction of S100B with the M1-DY domain was confirmed by comparison with three other S100 proteins, S100A1, S100A6, and S100A11 (Fig. 6D). Only S100A1-Sepharose showed a faint Ca^{2+} -dependent interaction with M1-DY, albeit with a much lower avidity than S100B.

To confirm the contribution of the AHNAK repeat units to S100B binding, we next analyzed the interaction of two bacterial recombinant fusion AHNAK domains containing different repeating units from the central domain (M2-DY and M3-DY, see Fig. 6A) with S100B- and CaM-Sepharose. Both M2-DY and

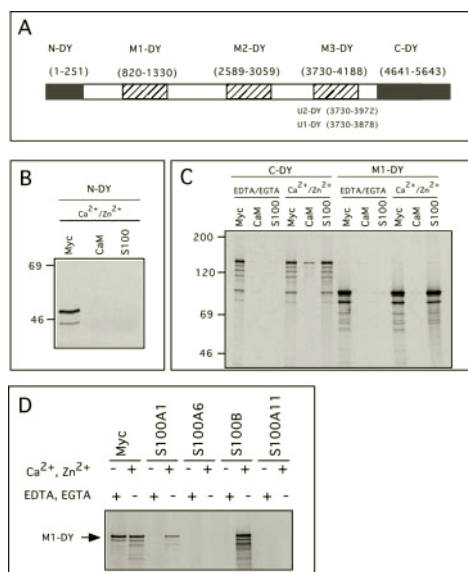


FIG. 6. Identification of the S100B-binding domain of AHNAK. A, schematic diagram of AHNAK showing the amino terminus (N-DY), central repeating units (M1-DY, M2-DY, and M3-DY), and carboxyl terminus (C-DY) AHNAK fragments used in this study. Numbers refer to the amino acid sequence of AHNAK domains. B and C, different Myc-tagged AHNAK domains corresponding to N-DY (B) and C-DY and M1-DY (C) were translated with rabbit reticulocytes. Equal amounts of the translation reaction (20 μ l) were immunoprecipitated with monoclonal antibody against Myc-tag (Myc) or incubated with 20 μ l of bovine brain CaM-Sepharose (CaM) or S100B-Sepharose (S100) in 1 ml of buffer supplemented with 5 mM EDTA/EGTA (EDTA/EGTA) or 0.2 mM Ca^{2+} + 10 μ M Zn^{2+} ($\text{Ca}^{2+}/\text{Zn}^{2+}$) as indicated. Bound proteins were electrophoresed on 8% SDS-PAGE gels and visualized by autoradiography. D, comparison between human recombinant S100-Sepharose proteins (1 mg/ml Sepharose) in binding Myc-tagged M1-DY domain translated in rabbit reticulocyte lysates. Incubation buffer contained 5 mM EDTA/EGTA or 0.2 mM Ca^{2+} + 10 μ M Zn^{2+} as indicated.

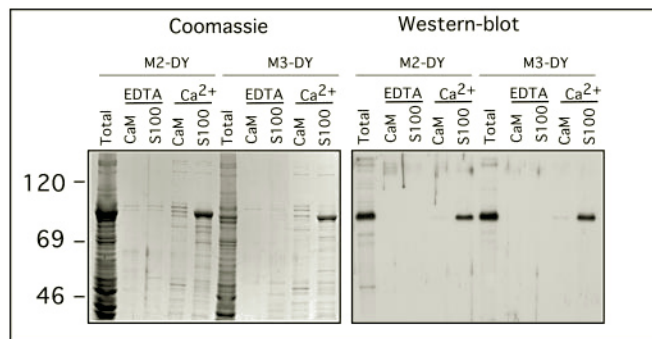


FIG. 7. Binding of M2-DY and M3-DY to S100B. AHNAK domains corresponding to M2-DY and M3-DY were expressed as recombinant proteins in bacteria. Calcium-dependent binding of the soluble bacterial proteins (Total) to CaM-Sepharose (CaM) or S100B-Sepharose (S100) was compared. Proteins were electrophoresed on 8% SDS-PAGE gels and revealed either by Coomassie Blue staining (left panel) or by Western blot analysis using KIS/AHNAK antibodies (right panel).

M3-DY specifically bound to S100B in a calcium-dependent manner but did not bind to CaM (Fig. 7).

S100B Binding to AHNAK Repeated Units—The interaction between S100B and AHNAK repeat units was next analyzed using surface plasmon resonance detection. His-tagged recombinant AHNAK peptides comprising three-repeat units (M3-DY, residues 3730–4188), two repeat units (U2-DY, residues 3730–3972), and one repeat unit (U1-DY, residues 3730–3878) were purified to homogeneity (Fig. 8A, inset) and separately coupled to the biosensor chip. Note that purified U1-DY shows two protein bands in SDS-PAGE. These two protein bands are recognized by KIS/AHNAK antibodies (data not shown). The

lower band is most likely a proteolytic product of the full-length U1-DY.

Fig. 8A shows a typical sensorgram representing the real-time interaction between purified $\text{Ca}^{2+}/\text{Zn}^{2+}$ -bound S100B and M3-DY peptide. In these experiments, S100B was injected onto the biosensor chip with 2 Zn^{2+} equivalents/mol S100B monomer and 0.1 mM CaCl_2 , and the sensor chip was then washed with Ca^{2+} -containing buffer in the absence of Zn^{2+} . The $\text{Ca}^{2+}/\text{Zn}^{2+}$ -dependent interaction of S100B with M3-DY is completely reversed by the addition of EDTA to the buffer. The reversibility of the interaction allows recycling of the biosensor chip with EDTA-containing buffer and permits a dose-dependent titration of the interaction with the same biosensor chip.

Fig. 8B shows the kinetics of the interaction between S100B at different concentrations with U2-DY peptide. The specificity of the interaction of S100B with U2-DY peptide is also assessed by comparison with bovine brain CaM and human recombinant S100A1, S100A6, and S100A11 (Fig. 8B, inset). Neither CaM, S100A1, S100A6, nor S100A11 showed interaction with the AHNAK peptide-coated sensor chip.

As shown in the inset in Fig. 8C, purified U1-DY peptides bind to S100B-Sepharose beads in a strict $\text{Ca}^{2+}/\text{Zn}^{2+}$ -dependent manner. Fig. 8C shows the kinetics of the interaction between S100B at different concentrations with U1-DY peptides. The best fit of the curve obtained with one repeat unit and 250 nM S100B was obtained with a 1:1 binding model and an estimated K_d of 50 nM. Taken together, these data indicate that one AHNAK repeat is sufficient for S100B binding.

Ca^{2+} and Zn^{2+} Dependence of S100B Binding to AHNAK Repeated Units—We next investigated the respective contributions of Zn^{2+} and Ca^{2+} to the S100B-AHNAK interaction. To begin, we studied the effect of Zn^{2+} alone on S100B binding to U2-DY peptide (Fig. 9A). In those experiments, S100B was incubated with 2 Zn^{2+} equivalents/mol S100B monomer before injection onto the biosensor chip. There was no binding of Zn^{2+} -S100B to AHNAK peptide in Ca^{2+} -free buffer. We confirmed this observation by analyzing the interaction of ^{35}S -labeled Myc-tagged M1-DY AHNAK domains with S100B-Sepharose beads (Fig. 9B). Zn^{2+} alone does not promote M1-DY binding to S100B-Sepharose. We next studied the effect of Zn^{2+} on Ca^{2+} -dependent binding of S100B to AHNAK peptides. In the absence of Zn^{2+} , only a faint interaction between S100B and U2-DY peptide coupled to the biosensor chip was observed at 100 μ M CaCl_2 (Fig. 9A). Calcium titration of the interaction between Myc-tagged M1-DY AHNAK domains and S100B-Sepharose beads confirmed that 100 μ M CaCl_2 is not sufficient for maximum interaction (Fig. 9B). If S100B is incubated with 2 Zn^{2+} equivalents/mol S100B monomer before injection onto the biosensor chip, the intensity of the interaction signal between S100B and the U2-DY peptide increases (Fig. 9A). In the presence of Zn^{2+} , calcium titration of the interaction between Myc-tagged M1-DY AHNAK domains and S100B-Sepharose beads is shifted to lower concentrations, with maximum binding at 50 μ M CaCl_2 (Fig. 9B). Such a shift is compatible with the positive effect of Zn^{2+} on S100B affinity for calcium (10) and is in agreement with previous determinations of the *in vitro* binding affinity of S100B for Ca^{2+} under the same experimental conditions (10). The effect of Zn^{2+} on Ca^{2+} -dependent interaction of S100B with U2-DY peptide is maximal with the addition of 2 Zn^{2+} equivalents/mol S100B and is decreased at higher Zn^{2+} :S100B molar ratios (Fig. 9C). This observation is consistent with previous reports showing that binding of 2 Zn^{2+} equivalents/mol S100B has the pronounced effect of increasing calcium affinity in S100B, whereas this effect is reversed at higher molar ratios (10).

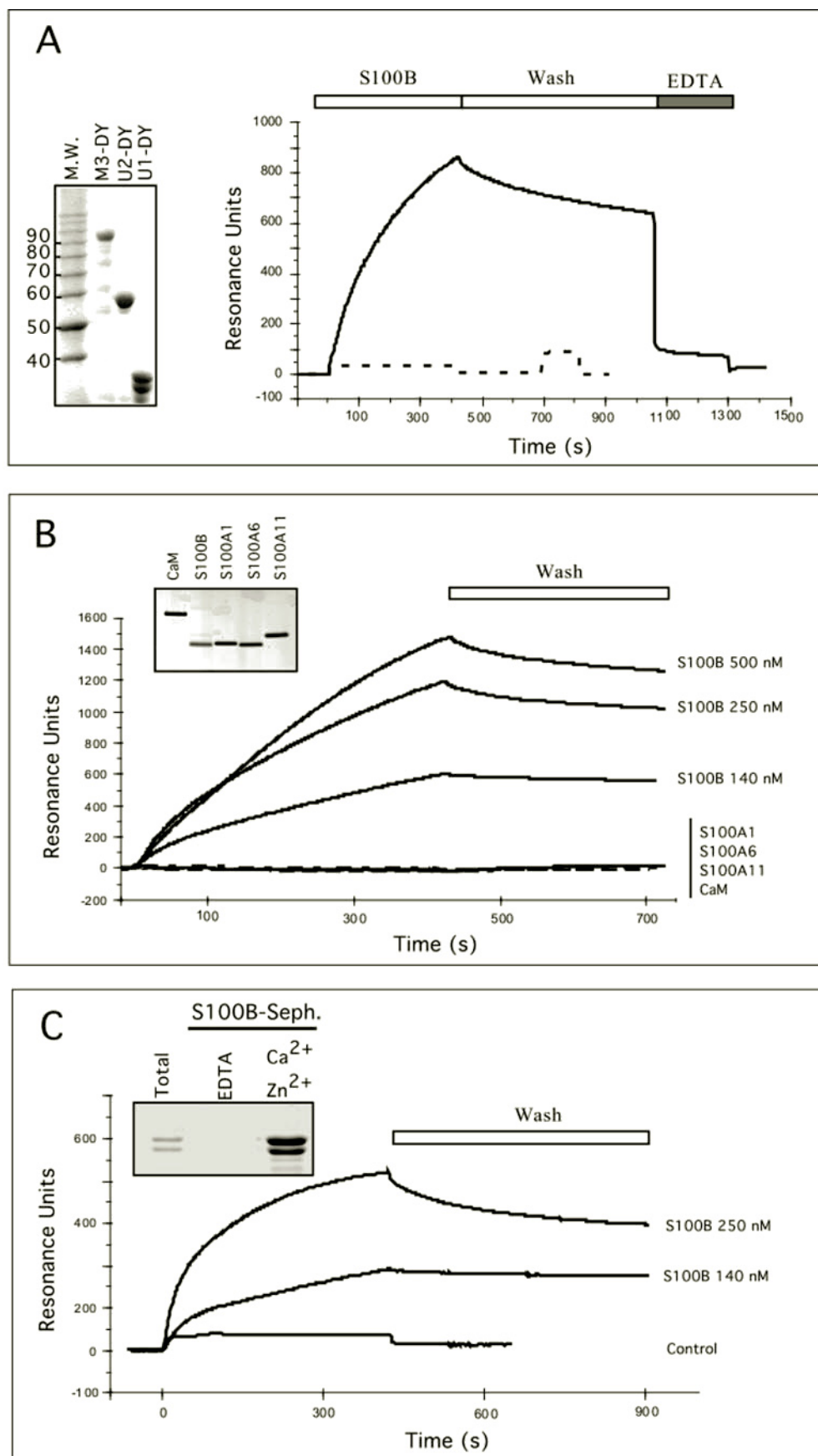


FIG. 8. Characterization of the interaction of purified S100B with AHNAK peptides using surface plasmon resonance detection. A, His-tagged M3-DY peptide and His-tagged importin $\alpha 1$ (dashed line), which was used as a control, were covalently immobilized on the sensor surface as described under "Materials and Methods." Running buffer contains 20 mM Tris-HCl, pH 7.5, 150 mM NaCl, and 0.1 mM CaCl_2 . Recombinant human S100B (140 nM) in the presence of 280 nM ZnSO_4 was injected (solid line). At the end of the injection, the sensor surface was washed with running buffer and then washed with a buffer containing 2 mM EDTA. Inset shows SDS-PAGE and Coomassie Blue staining of the

DISCUSSION

Identification of *in vivo* S100B target proteins represents a first step toward understanding the exact contribution of the S100B protein to calcium-dependent signaling pathways. In this study, we have presented data that suggest that the giant protein AHNAK is a specific calcium-dependent S100B target. AHNAK is the major protein that binds to S100B-Sepharose beads from REF clone 6 cell extracts and from two different astrocyte cell lines. A specific $\text{Ca}^{2+}/\text{Zn}^{2+}$ -dependent interaction of AHNAK with S100B was confirmed by co-immunoprecipitation (Fig. 3). An overlapping specificity of S100B and CaM for interaction with target proteins, peptides, and drugs is often observed (19, 22, 35). Hence, most of the proteins in crude cell extracts that bind S100B-Sepharose beads also bind to CaM. AHNAK is the only protein identified to date that demonstrates a strict $\text{Ca}^{2+}/\text{Zn}^{2+}$ -dependent interaction with S100B and absolutely no binding to CaM (Figs. 1A and 5B). That specificity of interaction has been confirmed using different AHNAK peptide domains. The same specificity of the S100B-AHNAK interaction was further confirmed with the finding that other S100 molecules do not bind AHNAK under similar conditions (Figs. 6D and 8B). S100B may thus represent a specific AHNAK regulator protein.

AHNAK is a protein of an unusually large size. The interaction of small EF-hand calcium binding proteins with giant proteins has a precedent in the literature. Two giant protein kinases, titin (3000 kDa) and twitchin (750 kDa), interact with Ca^{2+} -CaM and $\text{Ca}^{2+}/\text{Zn}^{2+}$ -S100A1, respectively (36). However, no kinase domain is predicted based on AHNAK structure. Another distinctive feature of the AHNAK protein is the repeated 128-residue motifs that characterize the middle portion and the carboxyl-terminal domain of the protein (27). Inspection of the 128-residue repeat revealed an underlying heptad repeat with the motif $\psi\pm\psi P\pm\psi\pm$, where ψ is a hydrophobic residue, \pm is a hydrophilic residue, and P is proline (27). Internal domain peptide (M1-DY, M2-DY, and M3-DY) and the carboxyl-terminal end (C-DY) of the protein display similar specific calcium-dependent binding to S100B (Figs. 6C and 7). It is thus likely that the repeated units represent structural elements involved in S100B binding. The interaction between S100B and AHNAK repeat units was confirmed using surface plasmon resonance detection (Fig. 8). The experiments shown in Fig. 8C indicate that one repeat unit is sufficient for binding S100B. Although CaM and other S100 proteins species are unable to interact with the internal domain peptides of AHNAK (M1-DY, M2-DY and M3-DY), a faint interaction of the carboxyl terminus of AHNAK (C-DY) with CaM is nevertheless observed (Fig. 6C). The extreme carboxyl terminus of AHNAK is characterized by a high proportion of basic and hydrophobic amino acids, with the potential to form an amphipathic α -helix. These features are generally found in other S100- and CaM-binding peptides (22) and are likely responsible for the faint binding of CaM.

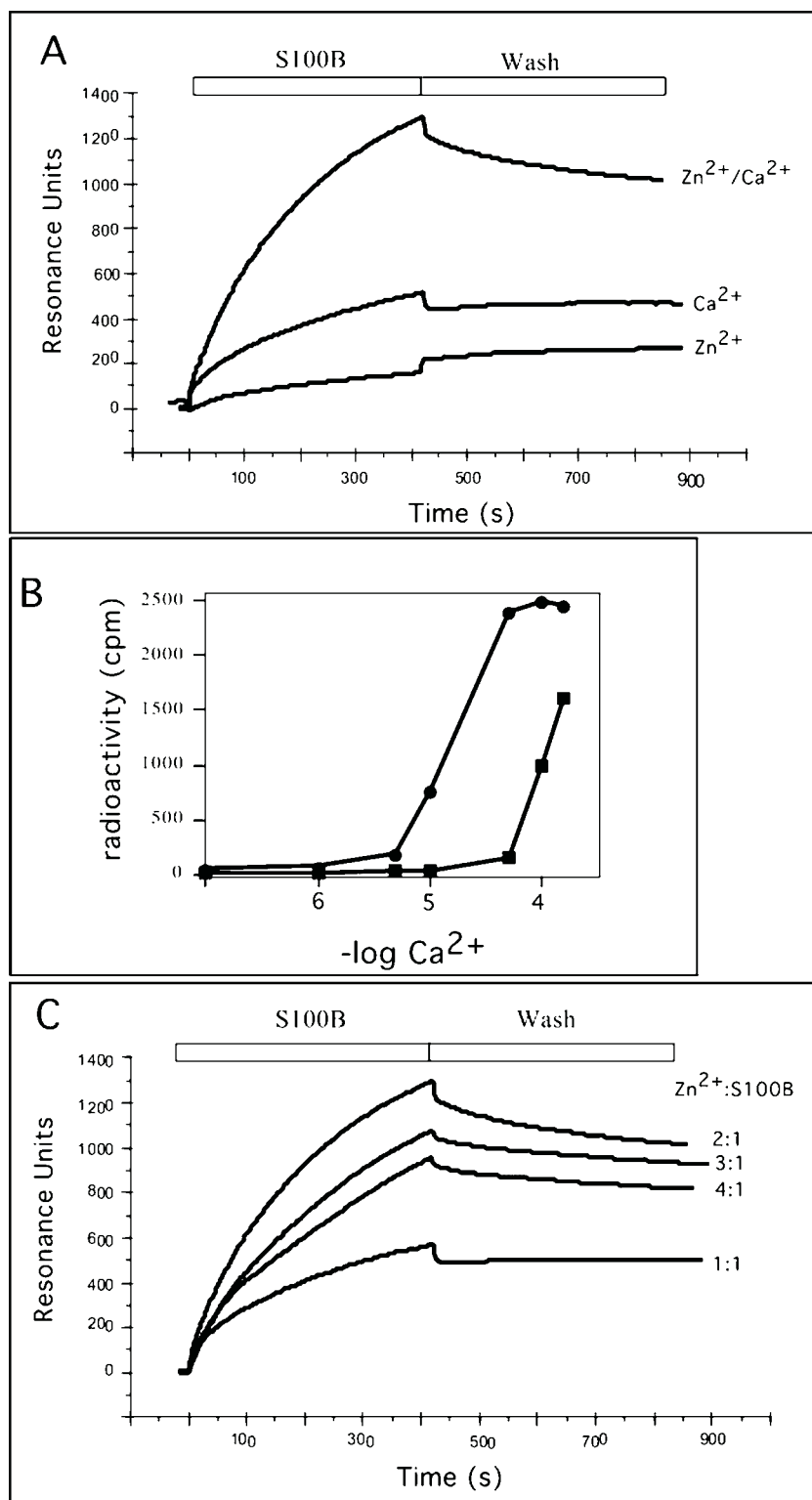
The highly specific interaction of AHNAK repeat units with S100B provided a model target protein to evaluate the respective role of Ca^{2+} and Zn^{2+} binding to S100B. Previous studies

using synthetic peptides corresponding to a calcium-sensitive epitope (TRTK-12) for S100B recognition revealed that although Zn^{2+} increases apparent peptide affinity for Ca^{2+} -S100B, Zn^{2+} is not directly implicated in binding of the target (37). In line with these observations, we found that Zn^{2+} binding alone to S100B is unable to promote AHNAK peptide binding. However, the binding of two Zn^{2+} equivalents to S100B enhances Ca^{2+} -dependent interactions (Fig. 9). In solution, S100B dimer is capable of binding up to 8 Zn^{2+} . The Zn^{2+} binding sites are not equivalent with respect to their affinity and associated conformational changes. Saturation of the two highest affinity Zn^{2+} -binding sites (K_d , 10–100 nM) has no significant effect on the overall S100B protein structure but produces drastic changes in Ca^{2+} binding affinity of site II β (10). In contrast, saturation of the lower affinity Zn^{2+} -binding sites on S100B produces drastic conformational changes, antagonizes calcium binding, and favors protein aggregation and precipitation. Thus, we consider it more likely that only the two high-affinity Zn^{2+} -binding sites on S100B may have regulatory functions. The three-dimensional structures of S100B and the related S100A7 predict that the highest affinity Zn^{2+} -binding site includes residues His⁸⁵ and His⁹⁰ (38, 39). These residues are located within the carboxyl-terminal domain that is essential for regulating Ca^{2+} binding to site II β (40). It is likely that Zn^{2+} binding to His⁸⁵ and His⁹⁰ induces subtle changes in the carboxyl-terminal region of S100B that increase accessibility of the EF-hand Ca^{2+} binding loop II to solvent (40). The increased affinity of Zn^{2+} -bound S100B for Ca^{2+} is illustrated by the shift to low calcium concentration of the Ca^{2+} titration curve for the interaction between Myc-tagged M1-DY AHNAK domains and S100B-Sepharose in the presence of Zn^{2+} (Fig. 9B). The Ca^{2+} titration curve in the presence of Zn^{2+} is in agreement with the binding affinity between S100B and Ca^{2+} determined under the same experimental condition (10). The effect of Zn^{2+} on the S100B-AHNAK interaction is maximal with the addition of 2 Zn^{2+} equivalents/mol S100B and decreased at higher Zn^{2+} :S100B molar ratios (Fig. 9C), confirming the regulatory role of the highest affinity sites. We therefore propose that Zn^{2+} regulates the function of S100B by binding and thereby regulating Ca^{2+} -dependent interactions of S100B with target molecules.

AHNAK/desmoyokin was first identified as a neuroblast differentiation-associated nuclear phosphoprotein (27). AHNAK was localized primarily (but not exclusively) to the nucleus of HeLa cells and neuroblastoma cells (28). In contrast with the predominant nuclear localization of human AHNAK protein in nonepithelial cells, the protein is found mainly at the plasma membrane in epithelial cells and is abundant within the cytoplasm of melanoma cells (29–30). Recently, Nie *et al.* (41) reported that a fragment consisting of the carboxyl-terminal 1002 amino acids of AHNAK (C-DY) accumulates in the nucleus of COS-7 cells, whereas N-DY and M-DY fragments remain cytoplasmic. The carboxyl-terminal region of AHNAK contains several putative nuclear localization signals (27). It is also characterized by the presence of a typical consensus leucine zipper sequence L-X(6)-L-X(6)-L-X(6)-L (residues 5012–5034) found in many gene-regulatory proteins (42). These

purified His-tagged M3-DY, U2-DY, and U1-DY AHNAK peptides used in A, B, and C. B, concentration dependence of the interaction of S100B with U2-DY peptide. Increasing concentrations of 2 Zn^{2+} -bound S100B as indicated were injected in running buffer on the sensor surface coated with U2-DY peptide. The interaction of S100B (140 nM) with U2-DY immobilized on the sensor chip surface is compared with S100A1, S100A6, S100A11, and calmodulin (140 nM each). Running buffer contains 20 mM Tris-HCl, pH 7.5, 150 mM NaCl, and 0.1 mM CaCl_2 . The different sensorgrams shown here were obtained on the same sensor surface. *Inset* shows SDS-PAGE and Coomassie Blue staining of the purified human recombinant S100B, S100A1, S100A6, S100A11, and bovine brain calmodulin used in these studies. C, interaction of S100B with U1-DY peptide. U1-DY peptide was covalently immobilized on the sensor surface. S100B/ Zn^{2+} (1:2 molar ratio), at the indicated concentration, was injected onto the sensor chip in running buffer containing 0.1 mM Ca^{2+} . After injection, the sensor chip was washed with calcium-containing running buffer. His-tagged importin α 1 covalently immobilized on the sensor surface was used as a control. The *inset* shows binding of U1-DY AHNAK peptides (*Total*) to S100B-Sepharose beads in $\text{Ca}^{2+}/\text{Zn}^{2+}$ -containing buffer ($\text{Ca}^{2+}/\text{Zn}^{2+}$) and in EDTA/EGTA-containing buffer (*EDTA*).

FIG. 9. Zn²⁺ regulates S100B binding to AHNAK peptides. *A*, Ca²⁺- and Zn²⁺-dependent interaction of S100B with U2-DY peptide. Recombinant human S100B (140 nM) in the presence of Ca²⁺ (0.1 mM) or Zn²⁺ (280 nM) or a mixture of Ca²⁺ and Zn²⁺ (0.1 mM Ca²⁺ and 280 nM Zn²⁺), as indicated, was injected on U2-DY peptide immobilized on the sensor chip surface. At the end of the injection, the sensor surface was washed with running buffer (20 mM Tris-HCl, pH 7.5, 150 mM NaCl, and 0.1 mM CaCl₂). *B*, Ca²⁺ titration of the interaction of ³⁵S-labeled M1-DY domain expressed in rabbit reticulocyte with S100B-Sepharose. Interactions were studied in binding buffer in the absence (■) or presence of 10 μM ZnSO₄ (●). *C*, Zn²⁺ titration of the interaction between S100B with U2-DY peptide. Recombinant human S100B (140 nM) in the presence of various Zn²⁺:S100B molar ratios, as indicated, was injected on U2-DY peptide immobilized on the sensor chip surface. At the end of the injection, sensor surface was washed with running buffer (20 mM Tris-HCl, pH 7.5, 150 mM NaCl, and 0.1 mM CaCl₂).



structural features suggest that the carboxyl-terminal region of AHNAK could have specialized nuclear functions. The dual intracellular location of AHNAK suggests the involvement of AHNAK in signal transduction pathways between the plasma membrane and the cell nucleus. A major feature of AHNAK is the repetitive heptad structure found in multiple copies within the large internal domain and the carboxyl terminus. The architectural arrangement of these repeat units in the full-length protein probably provides a scaffolding function that allows the assembly of multiprotein complexes. The strict calcium dependence of the interaction between S100B and repeat

units on AHNAK indicates that AHNAK is probably not a S100B anchor protein but most likely a protein subjected to regulation by calcium and S100B. In the cytoplasm, a possible function for S100B could be to regulate AHNAK interaction with other cellular proteins. Such a model is supported by the observation that S100B is capable of preventing co-immunoprecipitation of AHNAK with the p53val¹³⁵ in REF⁶ clone 6 cell extracts (Fig. 1). In REF clone 6 cells, p53val¹³⁵ is sequestered in the cytoplasm by an as yet unidentified short-lived protein (43). Within the cytoplasm, p53val¹³⁵ cooperates with ras for cell transformation (44). AHNAK could be part of a cytoplasmic

scaffold protein complex involved in p53val¹³⁵ cytoplasmic sequestration. In support of this, we have found that in REF cells, AHNAK is a short-lived cytoplasmic protein and that cycloheximide-mediated p53val¹³⁵ nuclear accumulation (43) correlates with AHNAK protein degradation (data not shown). Alternatively, the interaction of AHNAK with p53val¹³⁵ could be associated with the transforming activity of this p53 mutant protein (45). Dissociation of protein complexes involving p53val¹³⁵ and AHNAK by S100B might explain the effect of S100B on both reversion of the transformed phenotype of clone 6 cells (33) and the nuclear accumulation of the p53val¹³⁵ protein (34). The exact functional relationship between AHNAK and p53 proteins is under investigation.

The interaction of S100B with AHNAK might also open new opportunities for understanding the role played by S100B in the regulation of Ca²⁺ homeostasis within cells. Astrocytes derived from S100B null mice exhibit enhanced Ca²⁺ flux in response to depolarization or caffeine, suggesting that S100B plays a role in the maintenance of Ca²⁺ homeostasis in astrocytes through regulation of intracellular calcium flux (18). AHNAK has recently been found to be associated with a protein complex containing the β 2 subunit of L-type calcium channel (31). S100B may thus represent a regulator protein for AHNAK L-type calcium channel interaction in astrocytes. It is also significant that S100B is up-regulated in rat and human cardiomyocytes after ischemic injury and acts as a negative modulator of the adrenergic-mediated hypertrophic response (16–17). In cardiomyocytes, AHNAK is thought to play a role in cardiac adrenergic signal transduction (31). S100B-dependent regulation of AHNAK in the adrenergic-mediated hypertrophic response should clearly now be investigated. S100B might also represent a possible regulator protein for other functions of AHNAK within cells. AHNAK has recently been characterized as a protein that binds and activates phospholipase C- γ . The repeated motifs on AHNAK are directly implicated in phospholipase C- γ activation (32). Activation of phospholipase C- γ by repeated AHNAK motifs triggers inositol 1,4,5-trisphosphate synthesis. Inositol 1,4,5-trisphosphate, through binding to its receptors, is directly implicated in Ca²⁺ release from intracellular calcium stores. Hence, through interaction with L-type calcium channels or phospholipase C- γ , AHNAK appears to be a protein that may play a key regulator function in calcium homeostasis regulation. We propose that S100B represents one AHNAK regulatory protein and that AHNAK regulation by S100B might provide a clue for understanding Ca²⁺ homeostasis regulation by S100B (18).

Acknowledgments—We thank Dr T. Hashimoto and Z. Nie for supplying Myc-tagged N-DY, M1-DY, and C-DY plasmids and for communicating their results before publication, Dr. E. Shtivelman for supplying KIS/AHNAK antibodies and AHNAK cDNA, Dr. M. Takahashi for providing us with monoclonal anti-S100B antibodies, Dr. H. Wientraub for MyoD antibody, and Dr. J. Lammarr for critical reading of the manuscript.

REFERENCES

- Dolmetsch, R. E., Lewis, R. S., Goodnow, C. C., and Healy, J. I. (1997) *Nature* **286**, 855–858
- McConkey, D. J., and Orrenius, S. (1994) *Trends Cell Biol.* **4**, 370–375
- Nakayama, S., and Kretsinger, R. H. (1994) *Annu. Rev. Biophys. Biomol. Struct.* **23**, 473–507
- Schäfer, B. W., and Heizmann, C. (1996) *Trends Biochem. Sci.* **21**, 134–140
- Tarabykina, S., Kriajevska, M., Scott, D. J., Hill, T. J., Lafitte, D., Derrick, P. J., Dodson, G. G., Lukanidin, E., and Bronstein, I. (2000) *FEBS Lett.* **475**, 187–191
- Wang, G., Rudland, P. S., White, M. R., and Barraclough, R. (2000) *J. Biol. Chem.* **275**, 11141–11146
- Yang, Q., O'Hanlon, D., Heizmann, C. W., and Marks, A. (1999) *Exp. Cell Res.* **246**, 501–509
- Deloulme, J. C., Assard, N., Ouengue Mbele, G., Mangin, C., Kuwano, R., and Baudier, J. (2000) *J. Biol. Chem.* **275**, 35302–35310
- Schäfer, B. W., Fritschy, J. M., Murmann, P., Troxler, H., Durussel, I., Heizmann, C. W., and Cox, J. A. (2000) *J. Biol. Chem.* **275**, 30623–30630
- Baudier, J., Glasser, N., and Gérard, D. (1986) *J. Biol. Chem.* **261**, 8192–8203
- Allore, R., O'Hanlon, D., Price, R., Neilson, K., Willard, H. F., Cox, D. R., Marks, A., and Dunn, R. J. (1988) *Science* **239**, 1311–1313
- Griffin, W. S. T., Stanley, L. C., Ling, C., White, L., MacLeod, V., Perrot, L. J., White, C. L., and Araoz, C. (1989) *Proc. Natl. Acad. Sci. U. S. A.* **86**, 7611–7615
- Sheng, J. G., Mrak, R. E., and Griffin, W. S. T. (1994) *J. Neurosci. Res.* **39**, 398–404
- Stanley, L. C., Mrak, R. E., Woody, R. C., Perrot, L. J., Zhang, S., Marshak, D. R., Nelson, S. J., and Griffin, W. S. (1994) *J. Neuropathol. Exp. Neurol.* **53**, 231–238
- Cochran, A. J., Lu, H. F., Li, P. X., Saxton, R., and Wen, D. R. (1983) *Melanoma Res.* **3**, 325–330
- Tsoporis, J. N., Marks, A., Kahn, H. J., Butany, J., Liu, P. P., O'Hanlon, D., and Parker, T. G. (1997) *J. Biol. Chem.* **272**, 31915–31921
- Tsoporis, J. N., Marks, A., Kahn, H. J., Butany, J., Liu, P. P., O'Hanlon, D., and Parker, T. G. (1998) *J. Clin. Invest.* **102**, 1609–1616
- Xiong, Z., O'Hanlon, D., Becker, L. E., Roder, J., MacDonald, J. F., and Marks, A. (2000) *Exp. Cell Res.* **257**, 281–289
- Baudier, J., and Cole, R. D. (1988) *J. Biol. Chem.* **263**, 5876–5883
- Fujii, T., Mashino, K., Andoh, H., Satoh, T., and Kondo, Y. (1990) *J. Biochem. (Tokyo)* **107**, 133–137
- Ivanenkov, V. V., Jamieson, G. A., Gruenstein, E., and Dimlich, R. V. W. (1995) *J. Biol. Chem.* **270**, 14651–14658
- Millward, T. A., Heizmann, C. W., Schäfer, B. W., and Hemmings, B. A. (1998) *EMBO J.* **17**, 5913–5922
- Zimmer, D. B., and Van Eldik, L. J. (1986) *J. Biol. Chem.* **261**, 11424–11428
- Pozdnyakov, N., Goraczniak, R., Margulis, A., Duda, T., Sharma, R. K., Yoshida, A., and Sitaramayya, A. (1997) *Biochemistry* **36**, 14159–14166
- Baudier, J., Bergeret, E., Bertacchi, N., Weintraub, H., Gagnon, J., and Garin, J. (1995) *Biochemistry* **34**, 7834–7846
- Delphin, C., Ronjat, M., Deloulme, J. C., Garin, G., Debussche, L., Higashimoto, Y., Sakaguchi, K., and Baudier, J. (1999) *J. Biol. Chem.* **274**, 10539–10544
- Shtivelman, E., Cohen, F. E., and Bishop, M. J. (1992) *Proc. Natl. Acad. Sci. U. S. A.* **89**, 5472–5476
- Shtivelman, E., and Bishop, M. J. (1993) *J. Cell Biol.* **120**, 625–630
- Hashimoto, T., Amagai, M., Parry, D. A., Dixon, T. W., Tsukita, S., Tsukita, S., Miki, K., Sakai, K., Inokuchi, Y., Kudoh, J., Shimizu, N., and Nishikawa, T. (1993) *J. Cell Sci.* **105**, 275–286
- Hashimoto, T., Gamou, S., Shimizu, N., Kitajima, Y., and Nishikawa, T. (1995) *Exp. Cell Res.* **217**, 258–266
- Haase, H., Podzuweit, T., Lutsch, G., Hohaus, A., Kostka, S., Lindschau, C., Kott, M., Kraft, R., and Morano, I. (1999) *FASEB J.* **13**, 2161–2172
- Sekiya, F., Bae, Y. S., Jhon, D. Y., Hwang, S. C., and Rhee, S. G. (1999) *J. Biol. Chem.* **274**, 13900–13907
- Scotto, C., Deloulme, J. C., Rousseau, D., Chambaz, E., and Baudier, J. (1998) *Mol. Cell. Biol.* **18**, 4272–4281
- Scotto, C., Delphin, C., Deloulme, J. C., and Baudier, J. (1999) *Mol. Cell. Biol.* **19**, 7168–7180
- Marshak, D. R., Watterson, D. M., and Van Eldik, L. J. (1981) *Proc. Natl. Acad. Sci. U. S. A.* **11**, 6793–6797
- Heierhorst, J., Mann, R. J., and Kemp, B. E. (1997) *Eur. J. Biochem.* **249**, 127–133
- Barber, K. R., McClintock, K. A., Jamieson, G. A., Dimlich, R. V. W., and Shaw, G. S. (1999) *J. Biol. Chem.* **274**, 1502–1508
- Mäler, L., Potts, B. C. M., and Chazin, W. J. (1999) *J. Biomol. NMR* **13**, 233–247
- Brodersen, D. E., Nyborg, J., and Kjeldgaard, M. (1999) *Biochemistry* **38**, 1695–1704
- Baudier, J., Glasser, N., and Duportail, G. (1986) *Biochemistry* **25**, 6934–6941
- Nie, Z., Ning, W., Amagai, M., and Hashimoto, T. (2000) *J. Invest. Dermatol.* **114**, 1044–1049
- Busch, S. J., and Sassone-Corsi, P. (1990) *Trends Genet.* **6**, 36–40
- Gannon, J. V., and Lane, D. P. (1991) *Nature* **349**, 802–805
- Michalovitz, D., Halevy, O., and Oren, M. (1990) *Cell* **62**, 671–680
- Shaulian, E., Zauberman, A., Ginsberg, D., and Oren, M. (1992) *Mol. Cell. Biol.* **12**, 5581–5592

Calcium-dependent Interaction of S100B with the C-terminal Domain of the Tumor Suppressor p53*

(Received for publication, November 24, 1998, and in revised form, January 14, 1999)

Christian Delphin[‡], Michel Ronjat[§], Jean Christophe Deloulme[‡], G erome Garin[¶],
Laurent Debussche^{||}, Yuichiro Higashimoto^{**}, Kazuyasu Sakaguchi^{**}, and Jacques Baudier[‡] ^{‡‡}

From the [‡]D epartement de Biologie Mol culaire et Structurale du Commissariat   Energie Atomique, INSERM Unit  244, the [¶]Laboratoire de Chimie des Prot ines, and the [§]Laboratoire Canaux Ioniques et Signalization, Centre d' Etudes Nucl aire-Grenoble, 38054 Grenoble, France, the ^{||}Rh ne-Poulenc Rorer, Centre de Recherche de Vitry-Alfortville, 13 quai Jules Guesde, 94403 Vitry sur Seine Cedex, France, and the ^{**}Laboratory of Cell Biology, National Institutes of Health, Bethesda, Maryland 20892

***In vitro*, the S100B protein interacts with baculovirus recombinant p53 protein and protects p53 from thermal denaturation. This effect is isoform-specific and is not observed with S100A1, S100A6, or calmodulin. Using truncated p53 proteins in the N-terminal (p53^{1–320}) and C-terminal (p53^{73–393}) domains, we localized the S100B-binding region to the C-terminal region of p53. We have confirmed a calcium-dependent interaction of the S100B with a synthetic peptide corresponding to the C-terminal region of p53 (residues 319–393 in human p53) using plasmon resonance experiments on a BIAcore system. In the presence of calcium, the equilibrium affinity of the S100B for the C-terminal region of p53 immobilized on the sensor chip was 24 ± 10 nM. To narrow down the region within p53 involved in S100B binding, two synthetic peptides, O1^{357–381} (residues 357–381 in mouse p53) and YF-O2^{320–346} (residues 320–346 in mouse p53), covering the C-terminal region of p53 were compared for their interaction with purified S100B. Only YF-O2 peptide interacts with S100B with high affinity. The YF-O2 motif is a critical determinant for the thermostability of p53 and also corresponds to a domain responsible for cytoplasmic sequestration of p53. Our results may explain the rescue of nuclear wild type p53 activities by S100B in fibroblast cell lines expressing the temperature-sensitive p53val135 mutant at the nonpermissive temperature.**

The S100 family is one of the largest subfamily of calcium-binding proteins that are thought to play roles in mediating calcium signals during cell growth, differentiation, and motility (reviewed in Ref. 1). These proteins are characterized by highly conserved helix-loop-helix calcium-binding domains, known as EF-hand motifs. The S100B is found in astroglial cells in the central nervous system but also in a number of tissues outside the nervous system, including adipose tissue, testis, skin, and lymphocytes (2). In cultured cells, synthesis of S100B is tightly regulated and is maximum in the G₁ phase of the cell cycle (3–5). The S100B protein is a noncovalent homodimer formed by the association of two S100-β subunits (6, 7). Calcium bind-

ing induces conformational changes in the protein structure (8–10), destabilizing the S100B quaternary structure and allowing interaction with target proteins (7–12). For example, the Ca²⁺-dependent binding of S100B to microtubules (13), GFAP (14), Ndr protein kinase (15), and p53 (16) has been demonstrated. The identification of S100B target proteins is essential to better understand the mechanisms underlying S100B functions. Like calmodulin, S100B is likely to regulate multiple target proteins.

The tumor suppressor p53 protein (17) is a putative intracellular target for the S100B protein. *In vitro*, S100B binds to p53 and inhibits p53 aggregation and phosphorylation by PKC (16).¹ S100B also binds to a peptide derived from the extreme C-terminal end of p53 (12, 18). A functional interaction between S100B and p53 was recently demonstrated in p53-negative mouse embryo fibroblasts by sequential transfection with the S100B and temperature-sensitive p53val135 genes (5). In mouse embryo fibroblast cells expressing a low level of p53val135, S100B cooperates with calcium in triggering p53val135-dependent cell growth arrest and death at the nonpermissive temperature (37.5 °C). Activation of wild type p53 functions by S100B correlated with nuclear accumulation of p53val135 under a wild type conformation. S100B modulation of p53val135 functions was confirmed in the rat embryo fibroblast (REF) cell line clone 6, which is transformed by oncogenic Ha-ras and overexpression of p53val135 (19). Ectopic expression of S100B in clone 6 cells reverts transformed phenotypes and restores wild type p53 activities at 37.5 °C (5). We have hypothesized that S100B could either inactivate the mutant p53val135 species and/or favor folding of the p53val135 under a wild type conformation (5).

The functional activity of the p53val135 mutant is associated with its conformational flexibility (20). At the nonpermissive temperature (37.5 °C), the temperature-sensitive p53val135 mutant folds into an inactive mutant conformational form, detectable by the monoclonal antibody PAb240. At the permissive temperature, the p53val135 protein adopts a wild type conformation detectable by the monoclonal antibody PAb246 and is functionally active (*i.e.* able to specifically bind DNA and to activate transcription). The conformational flexibility that characterizes the temperature-sensitive p53val135 mutant is not unique to this mutation and could be representative of the conformational flexibility that also characterizes wild type p53 (20, 21). *In vivo*, conformational shift between the wild type and mutant conformations (recognized by the monoclonal antibodies PAb246 and PAb240, respectively) has been observed during embryonic differentiation of embryonic stem cells (22). *In*

* This work was supported by grants from the Association pour la Recherche sur le Cancer and La Ligue Nationale Contre le Cancer (to J. B.). The costs of publication of this article were defrayed in part by the payment of page charges. This article must therefore be hereby marked "advertisement" in accordance with 18 U.S.C. Section 1734 solely to indicate this fact.

^{‡‡} To whom correspondence should be addressed: INSERM Unit  244, DBMS-BRCE, CEA-Grenoble, 17 rue des Martyrs, 38054 Grenoble Cedex 9, France. Tel.: 33-476-88-43-28; Fax: 33-476-88-51-00; E-mail: jbaudier@cea.fr.

¹ The abbreviation used is: PKC, protein kinase C.

in vitro, wild type conformation of *Escherichia coli* expressed recombinant p53 can be allosterically regulated for stabilization by two regulatory sites found within the N and C termini of the molecule to which ligands may bind (23). A major challenge now is to characterize the domain on p53 associated with conformational shift and to identify the cellular co-factors that may govern the conformational switch controlling p53 activity (20).

In this report, we show that the S100B protein interacts with baculovirus recombinant p53 and protects p53 from thermal denaturation. We also identify a high affinity S100B-binding domain within p53 called YF-O2 (residues 320–346 in mouse p53). This domain constitutes a critical determinant for the stability and oligomerization status of p53 (24–26). It corresponds to the minimal region of the C terminus that confers thermal instability to p53 (25) and also corresponds to a domain responsible for cytoplasmic sequestration of p53 (27).

MATERIALS AND METHODS

Peptides—The p53^{319–393} peptide was synthesized as described previously (28). The peptide was dissolved in 20 mM HEPES-NaOH, pH 7.5, at the concentration of 98 μ M. Other peptides were synthesized by the solid phase method, using Fmoc (fluorenylmethoxycarbonyl) chemistry on an Applied Biosystems 430A peptide synthesizer. The O1 peptide, which encompasses the PKC phosphorylation site domain, corresponds to residues 357–381 within mouse p53: RAHSSYLKTKKGQSTSRHKTKMVKK. The peptide was dissolved in 20 mM Tris-HCl, pH 7.5, at the concentration of 100–200 μ M. YF-O2 peptide has the following sequence: YFTLKIRGRKRFEMFRELNEALELKD and corresponds to residues 321–346 within mouse p53. W-O2 peptide is a mutated version of YF-O2, and Tyr³²¹ and Phe³²² were both substituted with Trp residues. YF-O2 and W-O2 peptides were dissolved in 10 mM HEPES-HCl, pH 2.5, at the concentration of 200–400 μ M. Peptide stock solutions were stored at -20°C .

Proteins—S100B, S100A1, and calmodulin were purified from bovine brain (10). Recombinant Human p53 was expressed in SF9 cells and purified to homogeneity by S100B affinity chromatography as described previously (16). To express truncated human p53, corresponding cDNA fragments were generated from full-length human p53 by polymerase chain reaction (oligonucleotide sequences available upon request). After verification of DNA sequences, c-DNA fragments were inserted into pBlueBac III vector (Invitrogen). Expression in insect cells and interaction with S100B-Sepharose column were as described (16).

Electrophoretic Mobility Shift Assays—The method used was identical to that previously published (29). To study the effect of S100B and other related calcium-binding proteins on p53 DNA binding activity, purified p53 was first incubated in the presence or in the absence of calcium-binding proteins for 15 min at 30°C in 20 mM Tris-HCl buffer, pH 7.5, 110 mM KCl, 5 mM dithiothreitol, and 1 mM CaCl₂. The proteins were then mixed with 1 ng of labeled DNA, further incubated at 4°C for 10 min prior to electrophoresis onto a 5% nondenaturing polyacrylamide gel, and run in buffer containing 10 mM Hepes, 10 mM Tris, pH 8.0, and 0.5 mM CaCl₂.

Real Time Surface Plasmon Resonance Recording—Real time binding experiments were performed on a BIAcore biosensor system (Pharmacia Biosensor AB, Uppsala, Sweden). All experiments were performed at 25°C . p53^{319–393} peptide (35 μ l of 1 μ M peptide in 10 mM sodium acetate, pH 3.5) was directly coupled through its amino groups to the sensor surface activated by *N*-hydroxy-succinimide and *N*-ethyl-*N'*-(dimethylaminopropyl)carbodiimide according to the manufacturer's instructions. The remaining reactive groups were then inactivated with 1 mM ethanolamine. For control experiments, sensor surface was treated as above in the absence of peptide. All interaction experiments were done using a running buffer containing 20 mM Tris-HCl, pH 7.5, 120 mM NaCl, 1 mM CaCl₂. Between injections, the sensor chip was washed with a buffer containing 20 mM Tris-HCl, pH 7.5, 120 mM NaCl, 2 mM EDTA. Sensorgrams were analyzed using BIAevaluation 3.0 program (Pharmacia Biosensor AB) and kinetic constants were obtained by fittings curves to a single-site binding model ($A + B = AB$).

Protein Kinase C Activity Assay and PKC Inhibitor Assay—The PKC assays were performed as described previously (30). To analyze the effect of S100B and other calcium-binding proteins on the inhibitor capacity of YF-O2 or W-O2 peptides, the following procedure was used. 10 μ l of diluted inhibitor peptides in H₂O (1:4000–1:50 dilution of stock solution) were mixed in Eppendorf tubes with increasing concentration

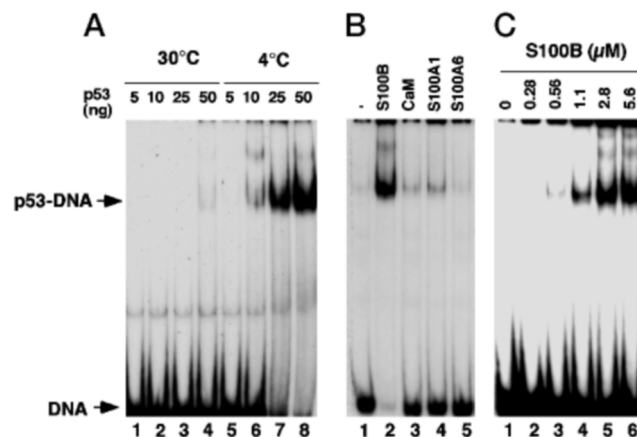


FIG. 1. The effect of S100B on thermal denaturation of p53. A, effect of temperature on DNA binding activity of p53. Increasing amounts of murine p53 as indicated were incubated for 15 min at 30°C (lanes 1–4) or at 4°C (lanes 5–8). The proteins were then mixed with 1 ng of labeled DNA and further incubated at 4°C for 10 min prior to electrophoresis. B, S100B counteracts the temperature-dependent inhibition of p53-DNA binding. p53 (0.1 μ g) was incubated for 15 min at 30°C in the absence (lane 1) or in the presence of 1 μ M of S100B (lane 2), calmodulin (lane 3), S100A1 (lane 4), or S100A6 (lane 5). The proteins were then mixed with 1 ng of labeled DNA and further incubated at 4°C for 10 min prior to electrophoresis. C, S100B titration of maximal stabilization of the DNA binding activity of p53 at 30°C . 1 μ M p53 was first incubated for 15 min at 30°C in the absence (lane 1) or in the presence of increasing amount of S100B (lanes 2–6) as indicated. The proteins were mixed with 1 ng of labeled DNA and 20 ng of unlabeled DNA.

of calcium-binding proteins in 30 μ l of 50 mM Tris-HCl buffer, pH 8.0, 0.5 mM CaCl₂. 10 μ l of PKC was subsequently added to each tube to reach a final concentration of 3 nM, and the protein mixture was vortex-mixed. The phosphorylation reaction was immediately initiated by the addition of 20 μ l of a mixture containing O1 peptide used as substrate at 8 μ M final concentration plus MgCl₂, phosphatidylserine, dioleoylglycerol, and [γ -³²P]ATP at final concentrations used in standard PKC assay (30).

Native Gel Electrophoresis—Gels containing 13% acrylamide, 0.375 M Tris-HCl, pH 8.3, and 0.5 mM CaCl₂ or 1 mM EGTA were prepared without stacking gel. W-O2 peptide and S100B were incubated in 40 mM Tris-HCl, pH 8.0, 0.2 M NaCl, 5 mM dithiothreitol, 15% glycerol, and 0.5 mM CaCl₂ or 1 mM EGTA for 5 min on ice prior to electrophoresis. The gels were run at 20 mA. The electrode buffer consisted of 25 mM Tris, 192 mM glycine, and 0.5 mM CaCl₂ or 1 mM EGTA. The gels were stained with Coomassie Blue.

Fluorescence Measurements—The fluorescence measurements were performed with a Perkin-Elmer spectrofluorometer in 25 mM Tris-HCl, pH 7.5, 0.12 M NaCl containing either 0.1 mM CaCl₂ or 2 mM EGTA. For titration experiments, excitation was at 280 nm, and emission was monitored at 340 nm.

RESULTS

S100B Protects p53 from Thermal Denaturation—Heating baculovirus recombinant p53 at 30°C for 15 min leads to self-aggregation (16) and permanent loss of DNA binding activity (Fig. 1A; see also Ref. 23). S100B protein, which prevents p53 from temperature-dependent aggregation (16), counteracts the temperature-dependent inhibition of p53 DNA binding activity (Fig. 1B, lanes 1 and 2). The S100B effect is specific because calmodulin, S100A1 and S100A6 have no effect (Fig. 1B, lanes 3–5). The dose response experiment shown in Fig. 1C reveals that the S100B concentrations required to protect the DNA binding activity of p53 from thermal inhibition are similar to those required to protect p53 from temperature-dependent aggregation (16). S100B was only able to activate p53 for DNA binding if preincubated with p53 at 30°C . S100B was not able to activate p53 for DNA binding when incubated at 4°C , and it did not reactivate DNA binding activity of denatured p53 (data not shown). Thus the effect of S100B is limited to protection of

p53 from thermal denaturation. In that respect, S100B behaves differently from PAb421. PAb421 binds to the extreme C terminus of p53 to activate p53 DNA binding but does not protect p53 from thermal denaturation (23).

Mapping of the Minimal S100B-binding Domain on p53—Recombinant human p53 (p53^{1–393}) expressed in SF9 cells accumulates in the cytoplasm and in the nuclei of infected cells. Both cytoplasmic and nuclear recombinant human p53 bind to S100B-Sepharose column in the presence of calcium and are eluted with buffer containing EGTA (Fig. 2A). We next compared the binding to S100B-Sepharose of human p53 fragments that lacks the C-terminal (p53^{1–320}) (Fig. 2B) or N-terminal (p53^{73–393}) domain (Fig. 2C). p53^{1–320} that lacks nuclear localization signals (31) accumulates within the cytoplasm of infected cells, whereas p53^{73–393} is predominantly present within the cell nuclei. Cell extracts enriched with each of these p53 fragments were loaded onto a S100B-Sepharose column, and the calcium-dependent binding of the p53 fragments to the column was analyzed by SDS-polyacrylamide gel electrophoresis, followed by Western blot analysis using monoclonal antibodies directed against N-terminal or C-terminal epitopes (Fig. 2, B and C). p53^{1–320} that lacks the C-terminal domain does not bind to S100B and was recovered in the flow-through fractions (Fig. 2B). Only p53^{73–393} efficiently binds to the S100B column in the presence of calcium and is eluted with buffer containing EGTA (Fig. 2C). Hence, the

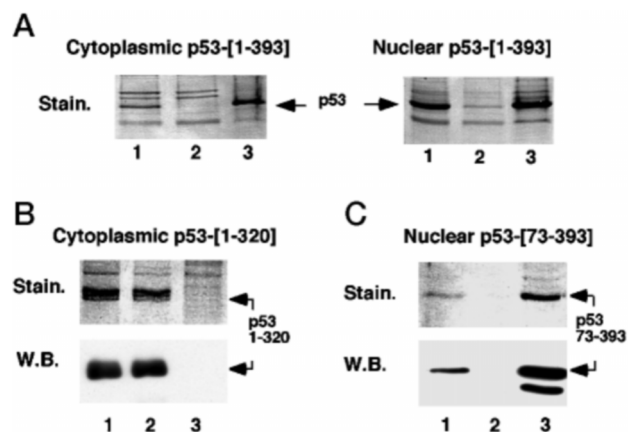


FIG. 2. **The interaction of p53 with S100B-Sepharose.** Insect cells were infected with different recombinant baculoviruses expressing full-length human p53 (1–393) (A) or truncated p53, p53 (1–320) (B), or p53 (73–393) (C). Cell extracts were loaded onto S100B-Sepharose columns (1 × 0.5 cm). Columns were washed with 10 column volumes of buffer containing 0.5 mM CaCl₂, and bound proteins were eluted with buffer containing 4 mM EGTA. Proteins in the loading samples (lanes 1), in column flow-through fractions (lanes 2), and in fractions eluted with EGTA (lanes 3) were subjected to 11% SDS-polyacrylamide gel electrophoresis. Gels were either Coomassie Blue-stained (Stain.) or transferred to nitrocellulose membranes, and the proteins were revealed by Western blot (W.B.) using monoclonal antibodies DO1 (B) or PAb421 (C).

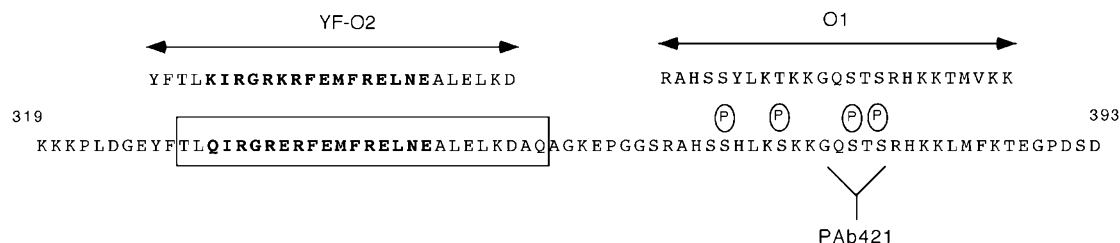


FIG. 3. **The C-terminal region of p53.** Amino acid sequence of the C-terminal region of human p53 involved in binding to S100B protein. This region is sufficient to transform primary fibroblasts in cooperation with *ras*. The minimal domain required for cell transformation is in bold (44). The oligomerization (28) and cytoplasmic sequestration domain is boxed (27). The putative PKC phosphorylation sites and PAb421 epitope are indicated (30). The mouse YF-O2 and O1 peptide sequences used in this study are also presented.

S100B-binding region is localized to the C-terminal region of the p53 protein (residues 320–393) (Fig. 3).

The molecular interaction between S100B and the C-terminal region of p53 was then analyzed using surface plasmon resonance detection (Fig. 4). A synthetic peptide corresponding to human p53^{319–393} was coupled to the biosensor chip through amino functions. Fig. 4A shows a typical sensorgram representing the real time interaction between purified Ca²⁺-bound S100B and the p53^{319–393} peptide. The S100B-p53^{319–393} interaction is strictly dependent on the presence of Ca²⁺ and completely reversed by addition of EDTA (Fig. 4A). We controlled that there is absolutely no interaction of S100B with a biosensor chip with no peptide immobilized and neutralized with ethanolamine (Fig. 4A). The reversibility of the S100B-p53^{319–393} interaction allows recycling the biosensor chip with EDTA containing buffer and to perform a dose-dependent titration of the interaction utilizing the same biosensor chip (Fig. 4B). At low S100B concentrations (10–100 nM) the kinetics of interactions could be fitted with a single interaction site model and an apparent equilibrium affinity of S100B for p53^{319–393} of 25 ± 10 nM. At higher S100B concentrations (100–900 nM), kinetics of interaction could barely be fitted with a single site model may be due to titration of lower affinity sites (see “Discussion”). The specificity of the high affinity Ca²⁺-dependent interaction between p53^{319–393} and S100B was confirmed by comparison with two other related EF-hand calcium-binding proteins, S100A1 and calmodulin (Fig. 4C, inset). Neither S100A1 nor calmodulin was able to interact with the p53^{319–393}-coated sensorship (Fig. 4C).

Molecular Mapping of the High Affinity S100B-binding Site on p53—To define in further detail the high affinity S100B-binding region within p53^{319–393}, two synthetic peptides corresponding to putative S100B-binding sites within the C-terminal domain of p53 were synthesized and assessed for their capacity to interact with purified S100B (Fig. 3).

The first peptide called O1^{357–381} (residues 357–381 in mouse p53) shows similarities with the S100B and calmodulin-binding domain of the MARCKS protein (16). Like its cognate peptide on MARCKS, O1 peptide is phosphorylated by PKC *in vitro* on multiple sites (30). Because binding of S100B to p53 inhibits p53 phosphorylation by PKC (16), we analyzed the effect of S100B on PKC-mediated phosphorylation of O1. As shown in Fig. 5, addition of S100B (O1^{357–381}:S100B molar ratio 0.5) had no effect on the phosphorylation of O1^{357–381} by PKC. On the contrary, monoclonal antibody PAb421 that binds to O1^{357–381} inhibited phosphorylation by PKC. PAb242, which does not bind to O1^{357–381}, had no effect on its phosphorylation. These results suggest that the high affinity S100-binding domain within p53 is distinct from O1^{357–381}. In further support of that conclusion, O1 peptide at the concentration of 1 μM did not antagonize S100B binding to the p53^{319–393}-coated sensorship (not shown).

The second peptide, YF-O2^{320–346} (residues 320–346 in

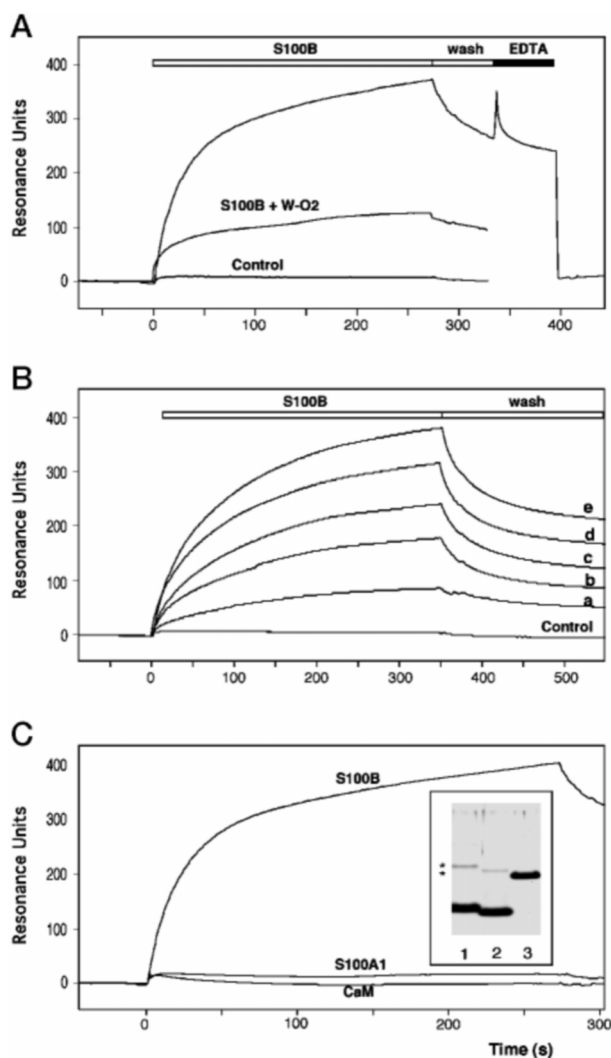


FIG. 4. Characterization of the interaction of purified S100B with p53³¹⁹⁻³⁹³ using surface plasmon resonance detection. p53³¹⁹⁻³⁹³ peptide was covalently immobilized on the sensor surface as described under "Materials and Methods." Running buffer contains 20 mM Tris-HCl, pH 7.5, 120 mM NaCl, 1 mM CaCl₂. The different sensorgrams shown here have been obtained on the same sensor surface except for the control. Three different sensor surfaces coated with p53³¹⁹⁻³⁹³ peptide gave similar results with respect to their interaction with the different proteins. **A**, S100B (90 nM in running buffer) was injected. At the end of injection, the sensor surface was washed with running buffer and then with a buffer containing 2 mM EDTA. Because of the high resonance signal induced by EDTA, the dissociation of S100B is only visible after the end of the injection of the EDTA buffer. S100B (90 nM in running buffer) was preincubated with WF-O2 peptide (1 μM) prior to injection (S100B-W-O2). Control corresponds to the injection of S100B on a sensor surface treated in the absence of p53³¹⁹⁻³⁹³ peptide. **B**, concentration dependence interaction of S100B with p53³¹⁹⁻³⁹³. Increasing concentration of S100B was injected in running buffer on the sensor surface coated with 11.25 nM (a), 30 nM (b), 45 nM (c), 60 nM (d), or 90 nM (e) of p53³¹⁹⁻³⁹³ peptide. Control is as in A. **C**, the interaction of S100B (90 nM) with p53³¹⁹⁻³⁹³ immobilized on the sensor chip surface is compared with S100A1 (90 nM) and calmodulin (90 nM). Insert shows SDS-polyacrylamide gel electrophoresis and Coomassie Blue staining of the purified bovine brain S100A1 (lane 1), S100B (lane 2), and calmodulin (lane 3) used in that study. The asterisks indicate position of covalent S100A1 and S100B dimers.

mouse p53) have sequence, structural, and functional homologies with the basic helix I domain on myogenic basic helix-loop-helix proteins, which is also capable of interacting with S100A1 or calmodulin (30, 32-34). We next analyzed the interaction of S100B with the YF-O2³²⁰⁻³⁴⁶ peptide and its tryptophan derivative, W-O2. In a competition assay, W-O2 is capable of

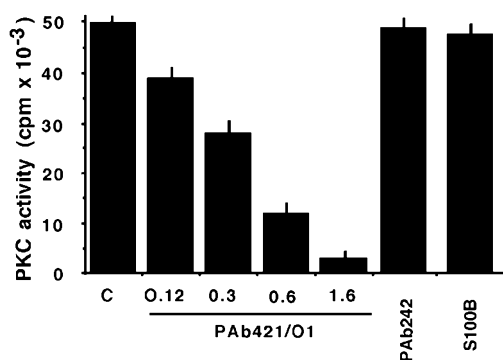


FIG. 5. PAb421 but not S100B inhibits O1 phosphorylation by PKC. O1 (2 μM) phosphorylation by PKC was studied in the presence of increasing amounts of monoclonal antibodies PAb421 (molar ratio as indicated), PAb242 (molar ratio of 2), and of S100B (4 μM).

antagonizing S100B binding to the p53³¹⁹⁻³⁹³-coated sensorship (Fig. 4A). A physical interaction of S100B with W-O2 peptide was then demonstrated by fluorescence spectroscopy, taking advantage of the fact that the S100B protein has no Trp residue (Fig. 6, A and B). Incubation of S100B with W-O2 in the presence of 0.1 mM CaCl₂ resulted in a 25% decrease in Trp fluorescence of the W-O2 peptide with a shift of the maximum emission from 345 to 340 nm (Fig. 6A). We next performed a dose-dependent titration of the fluorescence intensity changes of the W-O2 peptide at concentrations (1 μM and 2 μM) far above the apparent *K_d* determined with surface plasmon resonance. Maximum change in Trp fluorescence intensity was observed at a molar ratio of 0.5 mol S100B/mol W-O2, suggesting a stoichiometric binding of one β subunit of S100B protein/W-O2 peptide molecule (Fig. 6B). In the presence of EGTA, significant decrease in Trp fluorescence intensity can also be observed (Fig. 6B). These changes are probably representative of low affinity and nonspecific interactions. Native gel electrophoresis was also used to monitor complex formation between S100B and W-O2 (Fig. 6C). Using that method, low affinity Ca²⁺-independent interaction could not be detected. Only high affinity Ca²⁺-dependent complex formation between S100B and W-O2 was observed, as indicated by an upward shift of the S100B band. Note that in the presence of Ca²⁺, the change in electrophoretic mobility of S100B is due to conformational changes induced upon Ca²⁺ binding (32).

YF-O2³²⁰⁻³⁴⁶ corresponds to a putative PKC-binding domain on p53. The YF-O2³²⁰⁻³⁴⁶ peptide binds to the catalytic site of calcium-dependent PKC (PKC α, β, and γ) with affinity in the 50-100 nM range and inhibits kinase activities (30). As previously reported, the interaction of YF-O2³²⁰⁻³⁴⁶ with PKC results in a total inhibition of O1³⁵⁷⁻³⁸¹ peptide phosphorylation (Fig. 7A). The tryptophan derivative W-O2 was as potent as YF-O2³²⁰⁻³⁴⁶ in inhibiting O1³⁵⁷⁻³⁸¹ peptide phosphorylation (Fig. 7A). In the presence of S100B, inhibition of O1³⁵⁷⁻³⁸¹ peptide phosphorylation is abrogated, suggesting that S100B competes with PKC for binding on YF-O2 and W-O2 peptides (Fig. 7A). As expected, the half-maximum effect of S100B was dependent on the W-O2 peptide concentrations used in the assay (Fig. 7B). In all conditions, the maximum were reached for 0.5 mol S100B added per mol peptide, confirming a stoichiometric binding of one S100-β subunit per W-O2 or YF-O2 peptide molecule. Calmodulin or S100A6 counteracted W-O2- and YF-O2-dependent inhibition of PKC activity only at high concentrations (Fig. 7A). It has been proposed that YF-O2 domain might serve to target PKC on p53 and that it could be an important potency determinant in p53 phosphorylation by PKC (30). The ability of S100B to prevent YF-O2-PKC interac-

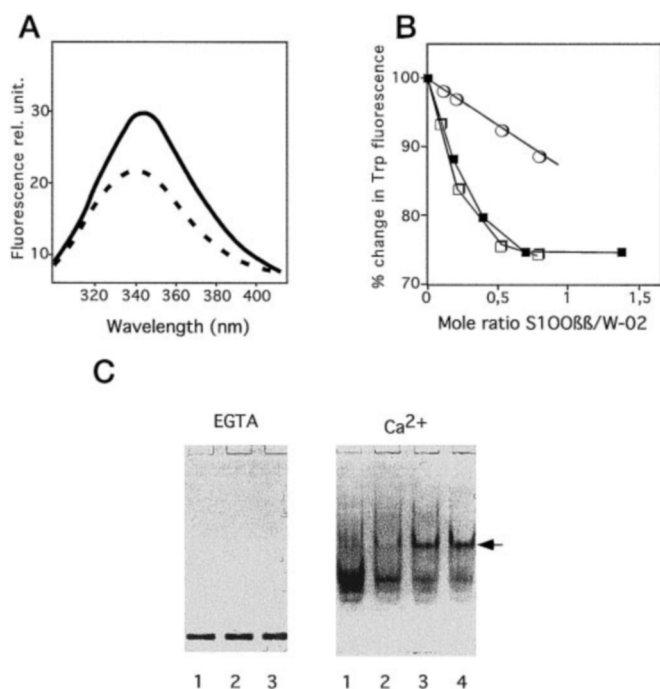


FIG. 6. S100B interacts with tryptophan-YF-O2 peptide derivative (W-O2). A, Trp fluorescence spectra of W-O2 ($1 \mu\text{M}$) in 25 mM Tris-HCl, pH 7.5, 0.12 M NaCl, 0.1 mM CaCl_2 in the absence (solid line) or in the presence (dashed line) of S100B ($1.4 \mu\text{M}$). B, titration of the percentage change in Trp fluorescence of W-O2 at the concentration of $1 \mu\text{M}$ (■) or $2 \mu\text{M}$ (□, ○) as a function of S100B($\beta\beta$)/W-O2 molar ratio in the presence of 0.1 mM CaCl_2 (■, □) or 2 mM EGTA (○). C, migration in native 13% polyacrylamide gel electrophoresis plus either 1 mM EGTA or 0.5 mM CaCl_2 , as indicated of S100B alone (lanes 1) or mixed with W-O2 at molar ratio of 0.5 (lanes 2), 1 (lanes 3), and 2 (lane 4). The arrowhead on the right points to S100 β -W-O2 complex.

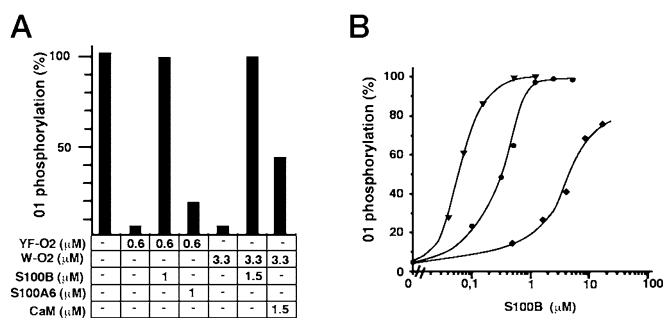


FIG. 7. S100B counteracts YF-O2 and W-O2 inhibition of PKC activity. A, inhibition of PKC activity by YF-O2 and W-O2 and release of this inhibition by S100B, S100A6, and calmodulin. PKC activity was measured using O1 peptide as substrate. B, titration curves of S100B-dependent release of PKC in the presence of $0.6 \mu\text{M}$ (▼), $3.3 \mu\text{M}$ (●), or $26 \mu\text{M}$ (◆) of W-O2 peptide.

tion might explain the inhibitory effect of S100B on full-length p53 phosphorylation by PKC (16).

DISCUSSION

In the first part of this study, we have confirmed that baculovirus recombinant wild type p53 is highly sensitive to thermal denaturation (16). Temperature-dependent denaturation of p53 is linked to protein aggregation (16) and compromised DNA binding activity of p53 (Fig. 2A). The interaction of S100B with recombinant wild type p53 protects p53 from thermal denaturation (16; Fig. 2, B and C). Secondly, we have confirmed a specific and strict calcium-dependent interaction of the S100B with a synthetic peptide derived from the C-terminal region of p53 (residues 319–393 in human p53) by plasmon resonance measurement experiments. We have also identified

the YF-O2 peptide as part of a high affinity S100B-binding site within the C-terminal region of p53. Structural studies have shown that the YF-O2 sequence is a critical domain for p53 thermostability (24, 25). It is likely that interaction of S100B with YF-O2 peptide on p53 is directly responsible for the increased resistance of p53 to thermal denaturation. Like S100B, the *E. coli* heat shock protein DnaK has been shown to bind to the C terminus of p53 and protect p53 from thermal denaturation (23, 26). S100B is the first mammalian protein to share this property with DnaK.

The YF-O2 peptide on p53 is involved in the dimerization and in subsequent tetramerization of p53 dimers (28, 35–37). The K_d value found for the tetramer-monomer transition of the C-terminal domain of p53 was determined to be $1\text{--}10 \mu\text{M}$ (28, 35). Because of the high K_d value, it has been proposed that in normal, undamaged cells, when the cytoplasmic p53 concentration is very low, p53 may be largely monomeric (35). However in its monomeric state, the p53 molecule is thermodynamically unstable relative to the tetramer (24, 25). The high equilibrium affinity of the S100B for the C-terminal domain immobilized on the sensor chip (K_d $24 \pm 10 \text{ nM}$) suggests that S100B could transiently interact with cytoplasmic p53 monomer to stabilize the p53 in a native conformation prior to nuclear translocation. Once p53 has translocated to the cell nuclei, it may be stabilized through its interactions with DNA targets as a tetramer. The idea that S100B could be involved in conformational modulation and stabilization of p53 monomer into a native (wild type) conformation is supported by *in vivo* observations (5). In mouse embryo fibroblast cells expressing low levels of the temperature-sensitive p53val135 mutant, S100B cooperates with calcium in stabilization and activation of the wild type p53val135 conformational species at the nonpermissive temperature ($37.5 \text{ }^\circ\text{C}$) (5). The YF-O2 sequence on p53 also corresponds to a “cytoplasmic sequestration domain” (27). Hence, one can envision that in response to intracellular calcium elevation, S100B could also dissociate the interaction between p53 and cytoplasmic anchoring proteins to favor p53 nuclear translocation. It is noteworthy that in mouse embryo fibroblast cells expressing S100B and the p53val135, calcium-mediated stabilization of the p53val135 under a wild type conformation is also associated with wild type p53val135 nuclear accumulation (5). The involvement of calcium signaling and S100B in activation of wild type p53 probably not only concern the p53val135 mutant but could be of more general occurrence. Intracellular calcium elevation is induced in physiological stimulation known to activate p53 functions, including cell contact (38) and hypoxia associated with tumor formation (39, 40). S100B, which is normally expressed at low levels in proliferating glial cells or in peripheral tissues, is also strongly induced by such stimulations. For examples, in C6 glial cells, S100B synthesis correlates with G_1 phase growth arrest at confluence (5). In cardiac myocytes, S100B is induced in response to hypoxia (41). This last observation also suggests that overexpression of S100B generally observed in brain tumors and peripheral tumors (42, 43) could be linked to hypoxia during tumor formation (39). It is tempting to speculate that in normal cells and also in tumor cells S100B induction could also be associated with p53 activation.

Finally, the high affinity S100B-binding domain within p53 that we identified also corresponds to the minimal transforming domain on mutant p53 (Ref. 44 and Fig. 3). Overexpression of the transforming C-terminal p53 mini-protein harboring YF-O2 domain cooperates with the *ras* oncogene in cell transformation in the absence of endogenous wild type p53 (45). This suggests that YF-O2-mediated transformation operates via stable interaction and inactivation of p53 target proteins. Be-

cause ectopic expression of S100B in a REF cell line overexpressing *ras* and the p53^{val135} is able to revert transformed phenotypes of the cells, it would be worth investigating whether S100B could also dissociate interactions between YF-O2 and target proteins.

The K_d value found for the interaction between S100B and the p53^{319–393} peptide (24 nM) is in the same range as that reported for the interaction between the S100A1 and the basic helix-loop-helix peptide of MyoD (20 nM) (32–34). A conserved amino acid sequence exists within the YF-O2 sequence of p53 (344^{LNEALELK}351) that is implicated in S100B binding and the helix I motif within myogenic transcription factor MyoD (124^{VNEAFETLK}132) involved in S100A1 binding. These two motifs are involved in the regulation of p53 and MyoD cellular localization (27, 46). The identification of a putative S100 target consensus motif within p53 and MyoD with functional homologies suggests that regulation of nuclear translocation of transcription factors associated with negative cell growth regulation may be a general feature of S100 proteins function. It is interesting to note that interaction of S100B and S100A1 with an other nuclear protein, the Ndr protein kinase, has recently been characterized (15). It would be interesting to study the possible contribution of S100 proteins in Ndr protein kinase nuclear translocation. Despite the strong amino acid sequence homology between the YF-O2 sequence on p53 and the helix I motif on MyoD, the interaction between p53^{319–393} peptide and S100B is isoform-specific (Fig. 4C). Such specificity suggests that in addition to the consensus sequence, other amino acids adjacent to that motif could be responsible for the specificity of interaction between S100B and p53. Weber's group (12, 18) recently reported that S100B binds to a basic peptide derived from the extreme C-terminal basic tail of human p53 (residues 367–388), which corresponds to the O1 peptide. The high dissociation constant for this interaction ($K_d = 20 \mu\text{M}$) (12, 18) would explain why we have not been able to detect interaction of this peptide with S100B (Fig. 5). In our experimental conditions, the low S100B concentration used (4 μM) was probably not sufficient to reveal low affinity interaction. It is nevertheless possible that O1 domain contribute to strengthen the interaction of S100B dimer with the full-length C-terminal region of p53. The possible implication of O1 in S100B binding to p53^{319–393} peptide may explain why analysis of the kinetics of interactions between S100B and p53^{319–393} immobilized on the sensor chip cannot be analyzed with a single interaction site model at high S100B concentration. Although O1 peptide is not involved in p53 dimerization and tetramerization (24, 28, 35, 36), this domain is nevertheless required for formation of higher oligomeric aggregates (37) and is engaged in transient interchain interaction with another domain within the protein tetramer (35, 47). It is likely that, in addition to its effect on wild type p53 stabilization, S100B could also affect an important protein interaction at the C-terminal domain involving O1 domain.

Acknowledgment—We thank Dr. Kuznicki for providing us with S100A6.

REFERENCES

- Schäfer, B. W., and Heizmann C. (1996) *Trends Biochem. Sci.* **21**, 134–140
- Takahashi, K., Isobe, T., Ohtsuki, Y., Sonobe, H., Takeda, I., and Akagi, T. (1984) *Am. J. Pathol.* **116**, 497–503
- Fan, K. (1982) *Brain Res.* **237**, 498–503
- Marks, A., Petsche, D., O'Hanlon, D., Kwong, P. C., Stead, R., Dunn, R., Baumal, R., and Liao, S.-K. (1990) *Exp. Cell Res.* **187**, 59–64
- Scotto, C., Deloulme, J. C., Rousseau, D., Chambaz, E., and Baudier, J. (1998) *Mol. Cell. Biol.* **18**, 4272–4281
- Drohat, A., Nenortas, E., Beckett, D., and Weber, D. J. (1997) *Protein Sci.* **6**, 1577–1582
- Kilby, P. M., Van Eldik, L. J., and Roberts, G. C. (1996) *Structure* **4**, 1041–1052
- Baudier, J., Glasser, N., and Gerard, D. (1986) *J. Biol. Chem.* **261**, 8192–8203
- Smith, P., and Shaw, G. S. (1998) *Structure* **6**, 211–222
- Baudier, J., and Gerard, D. (1986) *J. Biol. Chem.* **261**, 8204–8212
- Ivanenkov, V., Jamieson, G. A., Gruenstein, E., and Dimlich, R. V. W. (1995) *J. Biol. Chem.* **270**, 14651–14658
- Rustandi, R. R., Drohat, A. C., Baldissieri, D. M., Wilder, P. T., and Weber, D. J. (1998) *Biochemistry* **37**, 1951–1960
- Baudier, J., Briving, C., Deinum, J., Haglid, K., Sörskog, L., and Wallin, M. (1982) *FEBS Lett.* **147**, 165–167
- Bianchi, R., Giambanco, I., and Donato, R. (1993) *J. Biol. Chem.* **268**, 12669–12674
- Millward, T. A., Heizmann, C. W., Schäfer, B. W., and Hemmings, B. A. (1998) *EMBO J.* **17**, 5913–5922
- Baudier, J., Delphin, C., Grunwald, D., Khochbin, S., and Lawrence, J. J. (1992) *Proc. Natl. Acad. Sci. U. S. A.* **89**, 11627–11631
- Levine, A. J., Momand, J., and Finlay, C. A. (1991) *Nature* **351**, 453–456
- Wilder, P. T., Rustandi, R. R., Drohat, A. C., and Weber, D. J. (1998) *Protein Sci.* **7**, 794–798
- Michalovitz, D., Halevy, O., and Oren, M. (1990) *Cell* **62**, 671–680
- Milner, J. (1995) *Trends Biochem. Sci.* **20**, 49–51
- Milner, J., and Medcalf, E. A. (1991) *Cell* **65**, 765–774
- Sabapathy, K., Klemm, M., Jaenisch, R., and Wagner, E. F. (1997) *EMBO J.* **16**, 6217–6229
- Hansen, S., Hupp, T. R., and Lane, D. P. (1996) *J. Biol. Chem.* **271**, 3917–3924
- Johnson, C. R., Morin, P. E., Arrowsmith, C. H., and Freire, E. (1995) *Biochemistry* **34**, 5309–5316
- Mateu, M. G., and Fersht, A. (1998) *EMBO J.* **17**, 2748–2758
- Hansen, S., Midgley, C. A., Lane, D. P., Freemann, B. C., Morimoto, R., and Hupp, T. R. (1996) *J. Biol. Chem.* **271**, 30922–30928
- Liang, S. H., Hong, D., and Clarke, M. F. (1998) *J. Biol. Chem.* **273**, 19817–19821
- Sakamoto, H., Lewis, M. S., Kodama, H., Appella, E., and Sakaguchi, K. (1994) *Proc. Natl. Acad. Sci. U. S. A.* **91**, 8974–8978
- Delphin, C., Cahen, P., Lawrence, J. J., and Baudier, J. (1994) *Eur. J. Biochem.* **223**, 683–692
- Delphin, C., Huang, K. P., Scotto, C., Chapel, A., Vincon, M., Chambaz, E., Garin, J., and Baudier, J. (1997) *Eur. J. Biochem.* **245**, 684–692
- Shaulsky, G., Goldfinger, N., Ben-Ze'ev, A., and Rotter, V. (1990) *Mol. Cell. Biol.* **10**, 6565–6577
- Baudier, J., Bergeret, E., Bertacchi, N., Weintraub, H., Gagnon, J., and Garin, J. (1995) *Biochemistry* **34**, 7834–7846
- Hermann, S., Saarikettu, J., Onions, J., Hughes, K., and Grundström, T. (1998) *Cell Calcium* **23**, 135–142
- Onions, J., Hermann, S., and Grundström, T. (1997) *J. Biol. Chem.* **272**, 23930–23937
- Sakaguchi, K., Sakamoto, H., Lewis, M. S., Anderson, C. W., Erickson, J. W., Appella, E., and Xie, D. (1997) *Biochemistry* **36**, 10117–10124
- Clore, M. G., Omichinski, J. G., Sakaguchi, K., Zambrano, N., Sakamoto, H., Appella, E., and Gronenborn, A. M. (1994) *Science* **265**, 386–391
- Sturzbecher, H. W., Brain, R., Addison, C., Rugbe, K., Remm, M., Grimaldi, M., Keenan, E., and Jenkins, J. R. (1992) *Oncogene* **7**, 1513–1523
- Yahanda, A. M., Bruner, J. M., Donehower, L. A., and Morrison, R. S. (1995) *Mol. Cell. Biol.* **15**, 4249–4259
- Kinzler, K., and Vogelstein, B. (1996) *Nature* **379**, 19–20
- Graeber, T. G., Osmanian, C., Jacks, T., Housman, D. E., Koch, C. J., Lowe, S. W., and Giaccia, A. J. (1996) *Nature* **379**, 88–91
- Tsoporis, J. N., Marks, A., Kahn, H. J., Butany, J., Liu, P. P., O'Hanlon, D., and Parker, T. G. (1997) *J. Biol. Chem.* **272**, 31915–31921
- Nakajima, T., Watanabe, S., Sato, Y., Kameya, T., Hirota, T., and Shimosato, Y. (1982) *Am. J. Surg. Pathol.* **6**, 715–727
- Van Eldik, L. J., Jensen, R. A., Ehrenfried, B. A., and Whetsell, W. O. (1986) *J. Histochem. Cytochem.* **34**, 977–982
- Shaulian, E., Zauberman, A., Ginsberg, D., and Oren, M. (1992) *Mol. Cell. Biol.* **12**, 5581–5592
- Shaulian, E., Haviv, I., Shaul, Y., and Oren, M. (1995) *Oncogene* **10**, 671–680
- Vandromme, M., Cavadore, J. C., Bonniou, A., Froeschlé, A., Lamb, N., and Fernandez, A. (1995) *Proc. Natl. Acad. Sci. U. S. A.* **92**, 4646–4650
- Hupp, T. R., Sparks, A., and Lane, D. P. (1995) *Cell* **83**, 237–245

Concerted Regulation of Wild-Type p53 Nuclear Accumulation and Activation by S100B and Calcium-Dependent Protein Kinase C

CHRISTIAN SCOTTO, CHRISTIAN DELPHIN, JEAN CHRISTOPHE DELOULME,
AND JACQUES BAUDIER*

*Département de Biologie Moléculaire et Structurale du CEA, DBMS-BRCE INSERM Unité 244,
38054 Grenoble Cedex 9, France*

Received 9 February 1999/Returned for modification 18 March 1999/Accepted 10 June 1999

The calcium ionophore ionomycin cooperates with the S100B protein to rescue a p53-dependent G₁ checkpoint control in S100B-expressing mouse embryo fibroblasts and rat embryo fibroblasts (REF cells) which express the temperature-sensitive p53Val135 mutant (C. Scotto, J. C. Deloulme, D. Rousseau, E. Chambaz, and J. Baudier, *Mol. Cell. Biol.* 18:4272–4281, 1998). We investigated in this study the contributions of S100B and calcium-dependent PKC (cPKC) signalling pathways to the activation of wild-type p53. We first confirmed that S100B expression in mouse embryo fibroblasts enhanced specific nuclear accumulation of wild-type p53. We next demonstrated that wild-type p53 nuclear translocation and accumulation is dependent on cPKC activity. Mutation of the five putative cPKC phosphorylation sites on murine p53 into alanine or aspartic residues had no significant effect on p53 nuclear localization, suggesting that the cPKC effect on p53 nuclear translocation is indirect. A concerted regulation by S100B and cPKC of wild-type p53 nuclear translocation and activation was confirmed with REF cells expressing S100B (S100B-REF cells) overexpressing the temperature-sensitive p53Val135 mutant. Stimulation of S100B-REF cells with the PKC activator phorbol ester phorbol myristate acetate (PMA) promoted specific nuclear translocation of the wild-type p53Val135 species in cells positioned in early G₁ phase of the cell cycle. PMA also substituted for ionomycin in the mediating of p53-dependent G₁ arrest at the nonpermissive temperature (37.5°C). PMA-dependent growth arrest was linked to the cell apoptosis response to UV irradiation. In contrast, growth arrest mediated by a temperature shift to 32°C protected S100B-REF cells from apoptosis. Our results suggest a model in which calcium signalling, linked with cPKC activation, cooperates with S100B to promote wild-type p53 nuclear translocation in early G₁ phase and activation of a p53-dependent G₁ checkpoint control.

The tumor suppressor p53 protein has been implicated in cell differentiation (1, 50), cell contact inhibition of growth (65), protection of the cell from the acquisition of genomic abnormalities (32, 33), and cell senescence (53). The mechanisms by which p53 carries out these functions seem to be related to its ability to induce G₁ or G₂/M cell cycle arrest and/or apoptosis. In some systems, p53-dependent growth arrest may inhibit apoptosis and favor viable cell cycle arrest (46, 49). The diversity of cellular responses to p53 activation indicates that the outcome of p53 activation depends on other signalling pathways upstream and downstream to p53 activation (2, 27). The extremely short half-life of the p53 protein in normal cells suggests that multiple, transient, and probably interdependent control processes regulate cellular p53 at the levels of its synthesis, cytoplasmic anchorage, nuclear translocation, nuclear activities, and degradation. Conformational modulation of p53 between wild-type and mutant-like conformations has also recently emerged as a possible mechanism for regulation of p53 functions (50). Activation of p53 functions following an appropriate stimulus generally initiates a rapid and substantial increase in the total p53 level, achieved at least in part by the stabilization of the normally rapidly degraded wild-type p53 protein in the cell nuclei. On the other hand, stabilization of p53 protein in the absence of stimulus is always

a hallmark of loss of function which can occur after gene mutation or interaction with viral oncoprotein (reviewed in reference 7). In tumor cells harboring wild-type and mutant p53 alleles, mutant p53 accumulates in the cell nuclei and acts as a negative dominant fashion and abolishes the functions of the wild-type protein. There is thus considerable interest in understanding the intracellular signalling pathways and mechanisms responsible for conformational stabilization and selective nuclear accumulation of the wild-type p53 conformational species versus those of mutant p53 molecules. We have previously shown that the calcium- and zinc-binding S100B protein (3) can be implicated in activation of wild-type p53 functions (52). The S100B protein is found in astroglial cells in the central nervous system but also in a number of tissues outside the nervous system (42, 43). The synthesis of S100B is tightly regulated. Many cellular stimulations known to activate p53, such as cell contact (65), hypoxia (20), and UV irradiation (56), are also able to stimulate S100B expression (51, 52, 59, 60). In the central nervous system, both S100B and p53 are up regulated in neurodegenerative diseases and might synergize in mechanisms of cell death (9, 26, 52, 54). A functional interaction between S100B and p53 in negative cell growth regulation and cell death was recently demonstrated in p53-negative (p53^{-/-}) mouse embryo fibroblasts (MEF cells) by sequential transfection with the *S100B* and temperature-sensitive (ts) *p53val135* genes and in the rat embryo fibroblast (REF) cell line clone 6, which is transformed by oncogenic *Ha-ras* and overexpression of p53Val135 (52). Ectopic expression of S100B in clone 6 cells (S100B-REF cells) reverts transformed

* Corresponding author. Mailing address: Département de Biologie Moléculaire et Structurale, INSERM Unité 244, DBMS-BRCE, CEN-G, 17 rue des Martyrs, 38054 Grenoble Cedex 9, France. Phone: (33) 76 88 43 28. Fax: (33) 76 88 51 00. E-mail: jbaudier@cea.fr.

phenotypes characterized by the rescue of cell density-dependent inhibition of growth (52) and of a G_2/M checkpoint in response to double-strand DNA breaks (unpublished data). Moreover, ionomycin stimulation of S100B-MEF and S100B-REF cells was able to rescue a p53-dependent G_1 checkpoint control (52). Intracellular calcium elevation mediated by ionomycin not only activates calcium-binding proteins but also contributes to the activation of calcium-dependent protein kinase C (cPKC) isozymes (44, 45). An interdependence is thought to exist between S100B and cPKC-dependent signalling pathways (5, 10, 60). Hence, cPKC activation might also account for the effect of ionomycin on activation of a G_1 checkpoint in S100B-MEF and S100B-REF cells. PKC is a family of calcium/diacylglycerol-dependent serine/threonine kinases which play a central role in signal transduction and have been widely implicated in control of cell growth, differentiation, transformation, and apoptosis. The 11 known PKC isoenzymes are classified into three groups: the conventional cPKCs (isoforms α , β , and γ), the novel calcium-independent PKCs (nPKCs; δ , ϵ , and μ), and the atypical PKCs (λ and ζ) (reviewed in reference 23). Initial interest in PKC stemmed from its identification as the major cellular receptor for tumor-promoting phorbol esters (phorbol myristate acetate [PMA]), which act by binding to the diacylglycerol-binding site on the enzymes and subsequently promoting their activation (45). Bryostatin, a macrocyclic lactone with a structure significantly different from that of phorbol ester, was also found to bind and activate PKCs (28). PKC activation can lead to disordered growth, cell transformation, and inhibition of apoptosis (36). On the other hand, PKC activation can also promote cell growth inhibition and induction of apoptosis (18, 39, 66, 67). A key to understanding these diverse responses may be that individual PKC isoenzymes play specific and specialized roles in cell signalling. It is also likely that the genetic background of the cells under investigation and the contribution of other intracellular signalling pathways have a profound effect on the response of the cells to PKC activation. Finally, it is not known whether the long-term effects of PKC activators are due to activation or depletion of PKCs. Because of the importance of PKC isoenzymes in major cellular functions, they have been considered potential targets for therapeutic intervention (23). An important issue is now to characterize the PKC isoenzyme-specific functions and their relationships with other signalling pathways.

We have investigated the contributions of S100B and cPKC signalling pathways to the activation of the wild-type p53. We show that cPKC activation cooperates with S100B in regulating wild-type p53 nuclear translocation and accumulation in early G_1 phase of the cell cycle. Moreover, we provide evidence that cPKC-mediated nuclear translocation of the wild-type p53 in early G_1 is linked with activation of a p53-dependent G_1 checkpoint control.

MATERIALS AND METHODS

Cell cultures. REF (clone 6) (40) and S100B-REF cells (clones 6 β and 9 β) (52) cells were grown in RPMI-Glutamax (Gibco) supplemented with 5% fetal calf serum (FCS; Seromed) at 37.5°C. Hygromycin-resistant MEF cells not expressing S100B (clone C) and S100B-MEF cells not expressing (clone J- β) or expressing (clone J β 2p53) p53Val135 (52) were grown in Dulbecco modified Eagle medium (DMEM)-Glutamax (Gibco) supplemented with 10% FCS (Gibco).

Plasmids and antibodies. A plasmid encoding mouse wild-type p53 was constructed by inserting full-length p53 cDNA into pUTSV1 (Eurogentech, Seraing, Belgium) under the control of the enhancer and promoter from simian virus 40 (SV40). p53-Ala and p53-Asp mutants were made by PCR using oligonucleotides CGGAATCCAGTCAGTCTGAGTCAGGCCCACTTCTTGACCATGCTTTTATATGGCGGGCAGCAGCCTGGCCCTTCTTGCCCTTCAGGTAGCTGGCGTGAGCCCTGCTGTCTCC and CGGAATCCAGTCAGTCTGAGTCAGGCCCACTTCTTGACCATGCTTTTATATGGCGGGTATCATC

CTGGCCCTTCTTGCTCTCAGGTAGCTGTCGTGAGCCCTGCTGTCTCC, respectively. The fidelity of PCR synthesis was confirmed by sequencing plasmid constructs. Further details regarding the cloning are available upon request.

The green fluorescent protein (GFP) expression plasmid pEGFP-N1 was purchased from Clontech. The luciferase expression plasmid PGL3-control, encoding luciferase under the control of the SV40 enhancer and promoter, was from Promega. p53-specific monoclonal antibodies PAb240, PAb246, PAb242, and PAb421 were purified from hybridoma supernatants by protein A-agarose chromatography. Affinity-purified polyclonal rabbit anti-p21 and anti-p27 antibodies were from Santa Cruz Biotechnology. Anti-Rb (clone PMG3-245) was from Pharmingen. Anti-PKC α and rat brain extracts used as controls were from Transduction Laboratory. Anti- β -tubulin was a gift from L. Paturle and D. Job.

Transfections. MEF cells and S100B-MEF cells grown in DMEM-Glutamax supplemented with 10% FCS in 60-mm-diameter dishes at 37.5°C were transiently transfected with Fugene-6 (Boehringer); 1 to 4 μ g of wild-type p53 plasmid was cotransfected with 0.5 μ g of pEGFP-N1 or PGL3-control in the presence of 12 μ l of Fugene-6 as recommended by the manufacturer. Cells were harvested 36 h after transfection. We found that 30 to 50% of cells were efficiently transfected in these experimental conditions.

Protein concentration and Western blot analysis. Cells were lysed in radioimmunoprecipitation assay (RIPA) buffer, and protein concentration was estimated by the bicinchoninic acid method (Pierce), using bovine serum albumin as a standard. Western blot analysis used cell extracts in RIPA buffer mixed with an equal volume of 1% sodium dodecyl sulfate (SDS) containing 20% glycerol, 50 mM dithiothreitol (DTT), and a trace of bromophenol blue. Samples were boiled, and 50 μ g of protein was loaded on SDS-containing 12% (p21, p27, tubulin, and Mdm2) or 7.5% (Rb) polyacrylamide gels. Proteins were transferred to nylon membrane.

Flow cytometry. Cell cycle and cell sorting analysis by flow cytometry was performed on a FACStar+ (Becton Dickinson). For cell cycle parameter analysis, cells were collected in phosphate-buffered saline (PBS), rapidly vortexed with 0.2% Triton X-100, and fixed with 4% formaldehyde. DNA was stained with Hoechst 33258 (2 μ g/ml) just prior to flow cytometry analysis.

Mitotic detachment. Cells were grown at 37.5°C to 80% confluence. The plates were gently shaken for 5 s. The media containing mitotic cells were pooled and centrifuged at low speed. Cell pellets were resuspended in culture medium. This procedure yielded populations that consisted of early G_1 and mitotic cells (37). Mitotic cells were seeded on polylysine (0.1 mg/ml)-coated Permax slides from Nunc, Inc.

Immunofluorescence cell staining. Cells were fixed with 4% paraformaldehyde for 30 min and permeabilized for 3 min with 0.2% Triton X-100. After washing with PBS, cells were incubated at 4°C overnight in PBS containing 5% goat serum with either purified wild-type specific monoclonal antibody PAb246 or purified mutant specific monoclonal antibody PAb240 (1 μ g/ml). The cells were then washed five times with PBS and incubated for 1 h with fluorescein isothiocyanate or cyanin 3-conjugated secondary antibodies. Coverslips were mounted in Aquamount and observed on a Bio-Rad confocal microscope or a Zeiss Axioplan microscope ($\times 40$) equipped with an exposure command system MC80; 400 ASA color slides were used.

Nuclear extracts. Nuclear extracts were prepared as previously described (11), with minor modifications. S100B-REF cells (clone 6 β) were grown to 80% confluence in 100-mm-diameter dishes and labeled in methionine-free medium supplemented with [35 S]Met-Cys mix (50 μ Ci/ml) for 3 h. Cells were or were not stimulated with PMA, washed once with PBS, and frozen by putting the culture dishes on a layer of liquid nitrogen. Cells were immediately thawed in 1 ml of buffer A (20 mM Tris-HCl [pH 7.6], 0.2% Triton X-100, 12% sucrose, 2 mM EGTA, 1 mM Pefabloc, 10 μ g of aprotinin/ml, 10 μ g of leupeptin/ml, 1 μ M microcystin, 1 mM vanadate, 1 mM NaF). Nuclei were pelleted by low-speed centrifugation and lysed in 200 μ l of buffer B (10 mM Tris-HCl [pH 7.5], 0.5 M NaCl, 1 mM Pefabloc, 10 μ g of aprotinin/ml, 10 μ g of leupeptin/ml, 1 μ M microcystin, 1 mM vanadate, 1 mM NaF). After centrifugation at 200,000 $\times g$ for 20 min to remove DNA, the supernatant (200 μ l) was diluted in 600 μ l of buffer C (20 mM Tris-HCl [pH 7.4], 5 mM MgCl $_2$, 5% glycerol, 0.5% NP-40, 1 mM Pefabloc, 10 μ g of aprotinin/ml, 10 μ g of leupeptin/ml, 1 μ M microcystin, 1 mM vanadate, 1 mM NaF). Diluted nuclear extracts were then centrifuged for 15 min at 20,000 $\times g$. The supernatants were used either for immunoprecipitation or for DNA-binding studies.

S100B-MEF cells were labeled with [35 S]Met-Cys mix (100 μ Ci/ml) for 5 h. Nuclear extracts were prepared as described above except that the freezing step was omitted.

Immunoprecipitation. Nuclear extracts were incubated with purified p53 monoclonal antibodies (5 μ g/ml) and protein G-agarose for 30 min. The immunoprecipitates were washed three times with 1 ml of buffer C. [35 S]-labeled immunoprecipitated proteins were resuspended in 1% SDS-10 mM DTT and analyzed on SDS-12% polyacrylamide gels.

DNA-binding studies. A biotinylated double-stranded oligonucleotide corresponding to the sequence 5'-biotin-TTTTTTTCAGGAATTCGATAGGCATGTCTAGGCATGTCTATCAAGCTTATCGAT-3' was synthesized; it comprises the consensus binding site for p53 (16). Nuclear extracts were incubated for 30 min with biotin-DNA probe (0.6 μ g/ml), salmon sperm DNA (20 μ g/ml), and streptavidin-agarose. The streptavidin-agarose was then washed three times with 1 ml of buffer C. [35 S]-labeled proteins bound to biotin-target DNA were

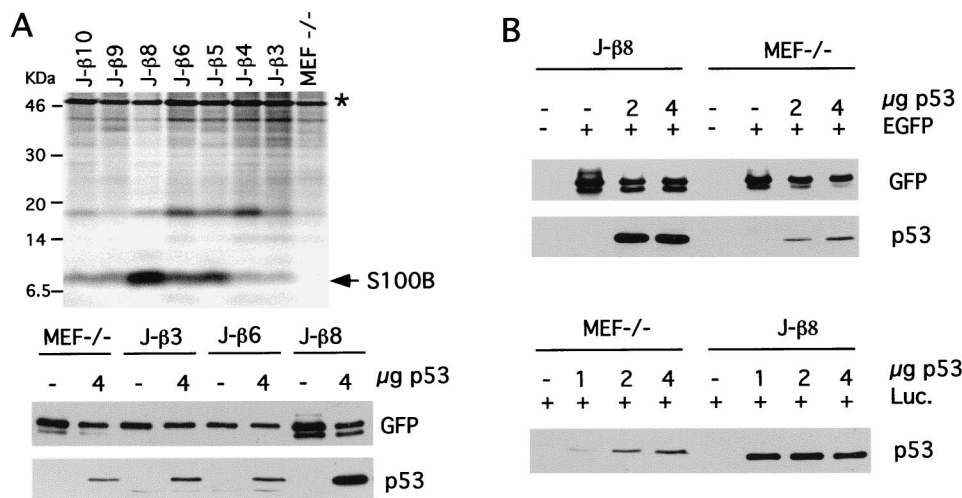


FIG. 1. S100B stabilizes wild-type p53. (A) The upper panel shows a comparison of S100B contents in MEF^{-/-} cells and J-β subclones selected by limiting dilution. Cells were metabolically labeled with [³⁵S]Met-Cys mix, and S100B was immunoprecipitated with rabbit polyclonal anti-S100B antibody as previously described (52). The asterisk indicates nonspecific binding. The lower panel shows levels of p53 in MEF^{-/-} cells and J-β3, J-β6, and J-β8 subclones following transient transfection as determined by Western blotting. Transfection efficiencies were determined by analysis of GFP expression. (B) Levels of p53 in S100B-MEF (clone J-β8) cells and MEF^{-/-} cells in transient transfection assays using different p53 plasmid concentrations. Upper panel, transfection efficiencies determined by Western blot analysis of GFP expression in parallel with that of p53; lower panel, transfection efficiencies determined by analyzing luciferase activities for each cell line, using a plasmid encoding luciferase (Luc.) under the control of the SV40 enhancer and promoter. Note that p53 expression in S100B-producing J-β8 cells resulted in cell growth arrest with a high incidence of cell death and decrease in luciferase activities. Hence, loading samples for Western blot analysis of p53 were adjusted to equal luciferase activities determined in the absence of p53 plasmids.

resuspended in 1% SDS–10 mM DTT and analyzed on SDS–12% polyacrylamide gels.

RESULTS

Contribution of S100B to wild-type p53 accumulation. To investigate the contribution of S100B to wild-type p53 accumulation, we used hygromycin-resistant p53^{-/-}MEF cells either expressing or not expressing S100B (52). After a few passages in culture, p53^{-/-}MEF cells stably transfected with the *S100B* gene drastically lost S100B expression, suggesting that S100B synthesis is detrimental for cell growth. S100B-producing clone J-β cells (52) were therefore subcloned by limiting dilution, and seven subclones were selected and analyzed for S100B production. Only one clone (J-β8) still expressed a significant amount of S100B (Fig. 1A, upper panel). Other selected clones were characterized by drastic down regulation of S100B synthesis. We next compared p53 levels in MEF cells not expressing (MEF^{-/-}) or expressing different S100B levels (clone J-β3, J-β6, and J-β8 cells). Cells were transfected with a plasmid encoding wild-type murine p53 under the control of the SV40 enhancer and promoter, which allow low protein expression. Transfection efficiencies were evaluated with a plasmid encoding enhanced GFP (EGFP) under the control of cytomegalovirus (CMV) promoter. Stronger accumulation of p53 was observed in S100B-producing J-β8 cells than in parental MEF cells or clone J-β3 and clone J-β6 cells that down regulated S100B expression (Fig. 1A, lower panel). This observation was confirmed with experiments utilizing different p53 plasmid concentrations and transfection efficiencies evaluated either with the plasmid encoding EGFP under the control of CMV promoter (Fig. 1B, upper panel) or a plasmid encoding luciferase under the control of the enhancer and promoter from SV40 (Fig. 1B, lower panel). We controlled so that S100B has no effect on CMV and SV40 promoters.

The S100B-dependent accumulation of p53 in MEF cells is reminiscent of that observed with the ts p53Val135 mutant (52). Expression of S100B in MEF cells cooperates with the calcium ionophore ionomycin to induce specific accumulation of the wild-type p53Val135 conformational species and to rescue wild-type p53 functions at the nonpermissive temperature 37.5°C (52). At 37.5°C, a significant amount of the p53Val135 can be folded under a wild-type conformation (37). Hence, one cannot exclude the possibility that ionomycin activates such a minor wild-type p53 population independently of S100B. To investigate whether S100B contributes to the nuclear accumulation and activation of p53Val135 under a wild-type conformation, we reproduced the experiment at 39°C, a temperature far above the nonpermissive temperature. Ionomycin stimulation produced a drastic accumulation of the p53Val135 protein (Fig. 2A). Accumulation of p53Val135 correlated with accumulation of the cells in the G₁ phase of the cell cycle (Fig. 2C). Both immunoprecipitation (Fig. 2B) and indirect immunofluorescence analysis (Fig. 2D) revealed that at 39°C, ionomycin caused specific nuclear accumulation of p53Val135 with a wild-type conformation (PAb246⁺), resulting in high wild-type/mutant ratios in the cell nuclei. Note that in control S100B-MEF cells grown at 39°C, the level of wild-type p53Val135 was below the detection limit (Fig. 2D). Note also that in control cells, the PAb240 immunoreactivity accumulated in the cell nuclei. Only a small number of cells with small rounded nuclei showed cytoplasmic staining; these cells were most likely in early G₁ phase of the cell cycle (see also Fig. 4).

Shifting S100B-MEF cells to the permissive temperature (32°C) had no significant effect on p53Val135 accumulation and cell cycle parameters (Fig. 2A and C). These observations confirm that calcium signalling and S100B are linked to specific activation of wild-type p53. They also suggest that temperature-dependent conformational shift at 32°C is not sufficient to activate wild-type p53Val135 function when the protein is present at a low concentration.

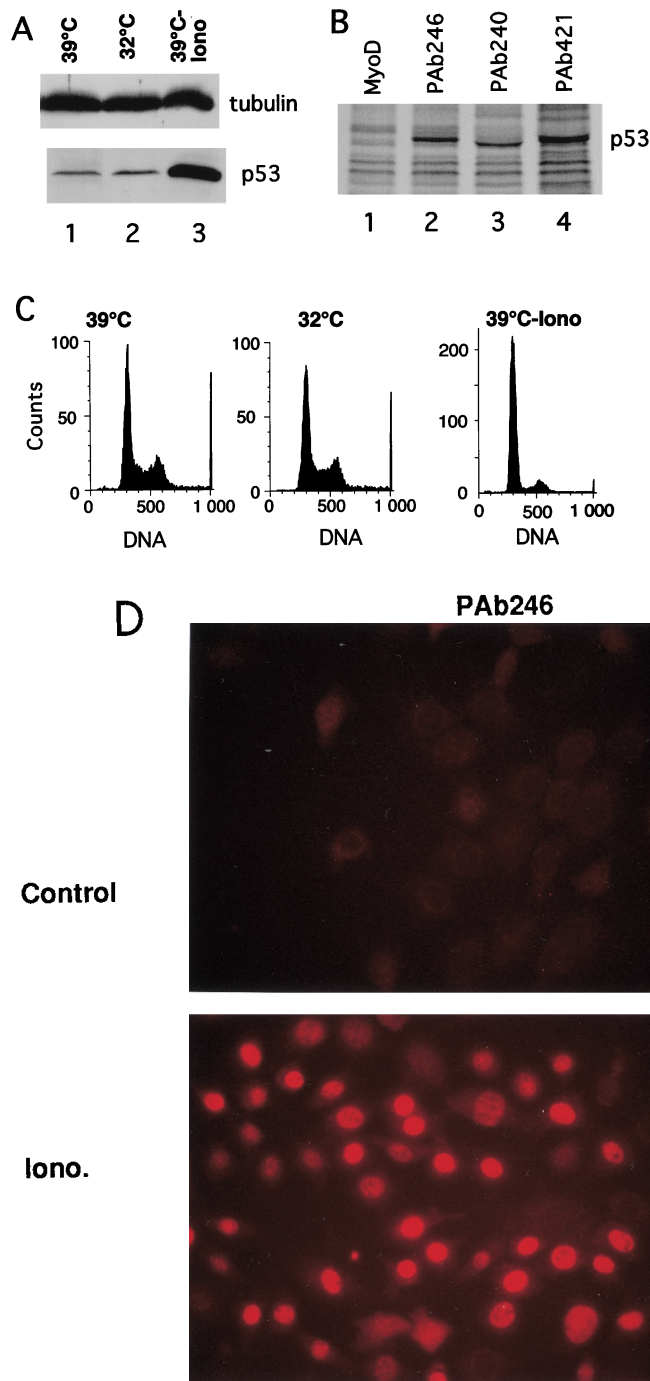


FIG. 2. Ionomycin stimulation, but not permissive temperature, promotes specific activation of wild-type p53 in S100B-MEF cells. (A) Comparison of p53Val135 contents in clone J-β2p53 cells grown at 39°C (lane 1), kept at 32°C for 22 h (lane 2), or stimulated with ionomycin (Iono) for 22 h at 39°C (lane 3). (B) Ionomycin stimulation promotes nuclear accumulation of the wild-type p53Val135 species in S100B-MEF cells grown at 39°C. Clone J-β2p53 cells grown at 39°C were stimulated for 12 h with 1 μM ionomycin prior to labeling with [³⁵S]Met-Cys mix (100 μCi/ml) for 5 h. Nuclear extracts were prepared, and ³⁵S-labeled p53Val135 was immunoprecipitated with anti-MyoD immunoglobulin G used as a control (lane 1), the wild-type-specific PAb246 (lane 2), the mutant-specific PAb240 (lane 3), or the pan-specific PAb421 (lane 4). (C) Flow cytometry analysis of the DNA content of clone J-β2p53 cells grown at 39°C (39°C), shifted to 32°C for 24 h (32°C), or grown at 39°C and stimulated with ionomycin for 36 h (39°C-Iono). (D) Immunofluorescence analysis of PAb246 and PAb240 immunoreactivities in subconfluent clone J-β2p53 cells grown at 39°C not stimulated (control) or stimulated with 1 μM ionomycin (Iono.) for 20 h.

cPKC activation mediates nuclear translocation and accumulation of the wild-type p53 in S100B-MEF cells. Previous studies pointed to a possible role of PKC in the regulation of p53 nuclear translocation (11). In vitro, p53 is a cPKC substrate that is phosphorylated on at least five serine and threonine residues (4, 12). To investigate a possible contribution of direct p53 phosphorylation by cPKC on p53 nuclear translocation, the five putative cPKC phosphorylation sites on wild-type murine p53 (Ser360, Thr365, Ser370, Ser372, and Thr377) were mutated to either an Ala residue to prevent phosphorylation or an Asp residue to mimic phosphorylation. The accu-

mulations and subcellular localizations of the p53 mutants were compared in transient transfection assays using S100B-MEF cells. Mutations had no significant effect on p53 nuclear accumulation (Fig. 3). However, incubation of S100B-MEF cells with the cPKC-specific inhibitor Gö6976 (38) prevented nuclear accumulation of both wild-type p53 and the p53-Asp mutant (Fig. 3). Together, these observations suggest that cPKC indirectly regulates wild-type p53 nuclear translocation (see also Discussion).

The contribution of cPKC activity to wild-type p53 nuclear translocation in S100B-MEF cells was also shown with S100B-

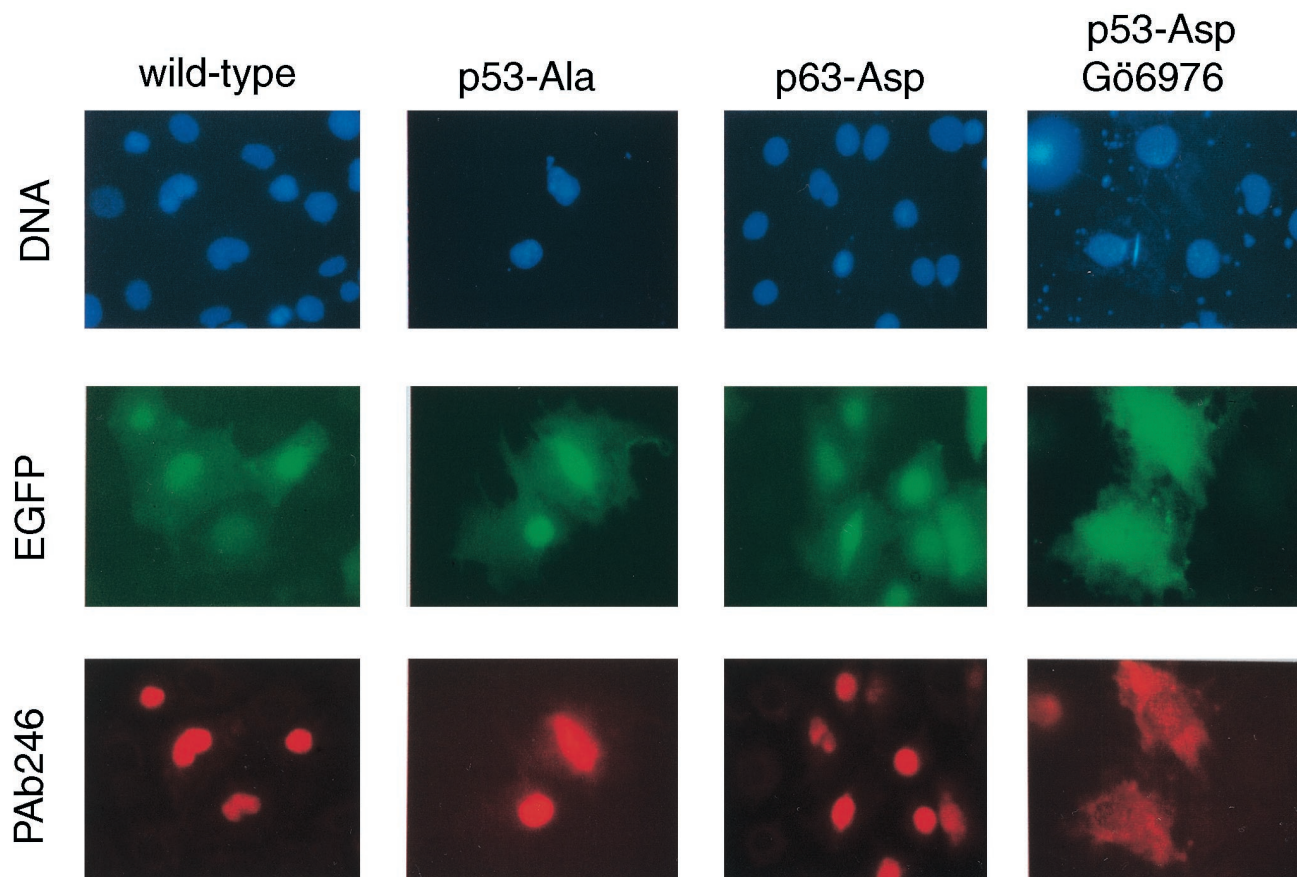


FIG. 3. Nuclear translocation of p53 is down regulated by Gö6976, a specific cPKC inhibitor. S100B-MEF clone J- β 8 cells were cotransfected with EGFP and plasmids encoding wild-type p53, mutant p53-Ala, or mutant p53-Asp as indicated. After 12 h, cells culture medium was changed to medium without or with 1 μ M Gö6976 as indicated. After 20 h cells were fixed. Immunofluorescence of PAb246 immunoreactivity was analyzed in parallel with DNA staining with Hoechst 33258 and EGFP autofluorescence.

MEF cells stably expressing the ts p53Val135 mutant. With these cells, incubation with Gö6976 drastically decreased ionomycin-mediated p53 accumulation (Fig. 4A) and totally inhibited ionomycin-mediated wild-type p53Val135 nuclear translocation (Fig. 4B). The strong correlation that exists between nuclear translocation and accumulation indicates that nuclear localization contributes to wild-type p53 stabilization.

cPKC activation promotes nuclear translocation of the wild-type p53Val135 conformational species in S100B-REF cells in early G₁. S100B-REF cells are derived from transformed REF cells expressing oncogenic Ha-*ras* and overexpressing p53Val135 (clone 6 cells) (40) transfected with the *S100B* gene (52). The amount of p53Val135 in S100B-REF cells is about 500-fold higher than the amount in S100B-MEF cells, and overexpression of p53Val135 in S100B-REF cells results in the presence of a significant amount of wild-type p53Val135 conformational species at the nonpermissive temperature (52). The loss of growth-suppressive function of the wild-type p53Val135 species in exponentially growing S100B-REF cells at 37.5°C is probably due to nuclear exclusion of the wild-type p53Val135 conformational species during the early G₁ phase of the cell cycle (11, 37) through interaction with a cytoplasmic anchor protein (20). To confirm a role for cPKC in regulation of wild-type p53 nuclear translocation, we analyzed the effect of PMA stimulation on the subcellular localization of the p53Val135 protein in S100B-REF cells synchronized in early G₁ by mitotic detachment (Fig. 5). PMA stimulation resulted

in a rapid nuclear translocation of the wild-type p53Val135 conformational species (PAb246⁺), whereas the mutant species (PAb240⁺) remained cytoplasmic. Such conformational specificity was restricted to cells in early G₁. As the cells progressed through the cell cycle, the mutant p53Val135 conformational species also translocated to the nucleus (not shown; see also references 11 and 37). Immunoprecipitation studies with ³⁵S-labeled nuclear extracts confirmed that PMA stimulation of S100B-REF cells produced rapid nuclear translocation of the wild-type p53Val135 species, with a maximum effect after 5 min of stimulation (Fig. 6A, lanes 1 and 2; Fig. 6B). PMA stimulation was also linked with p53 DNA binding activation. The DNA binding activity of the nuclear p53Val135 was tested in a DNA-binding assay based on the interaction of ³⁵S-labeled p53 with a biotinylated consensus p53 (p53-CON) target DNA (Fig. 6A, lanes 3 and 4; and Fig. 6C). The specificity of the interaction between p53 and the biotinylated target DNA was demonstrated by competition with nonbiotinylated p53-CON target DNA (Fig. 6A, lanes 3 and 4). PMA stimulation induced a rapid increase in ³⁵S-labeled p53Val135 which bound to biotinylated p53-CON target DNA (Fig. 6C, lanes 1 to 3). Depletion of the wild-type p53Val135 species from nuclear extracts by immunoprecipitation with PAb246 suppressed the PMA-dependent increase in DNA binding activity (Fig. 6C, lanes 4 and 5).

Dynamic nuclear translocation of the wild-type p53 mediated by PMA stimulation was followed by long-term cytosstatic

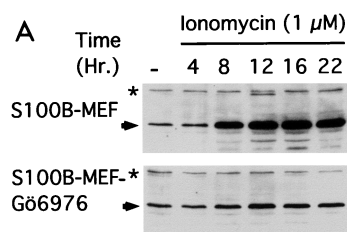
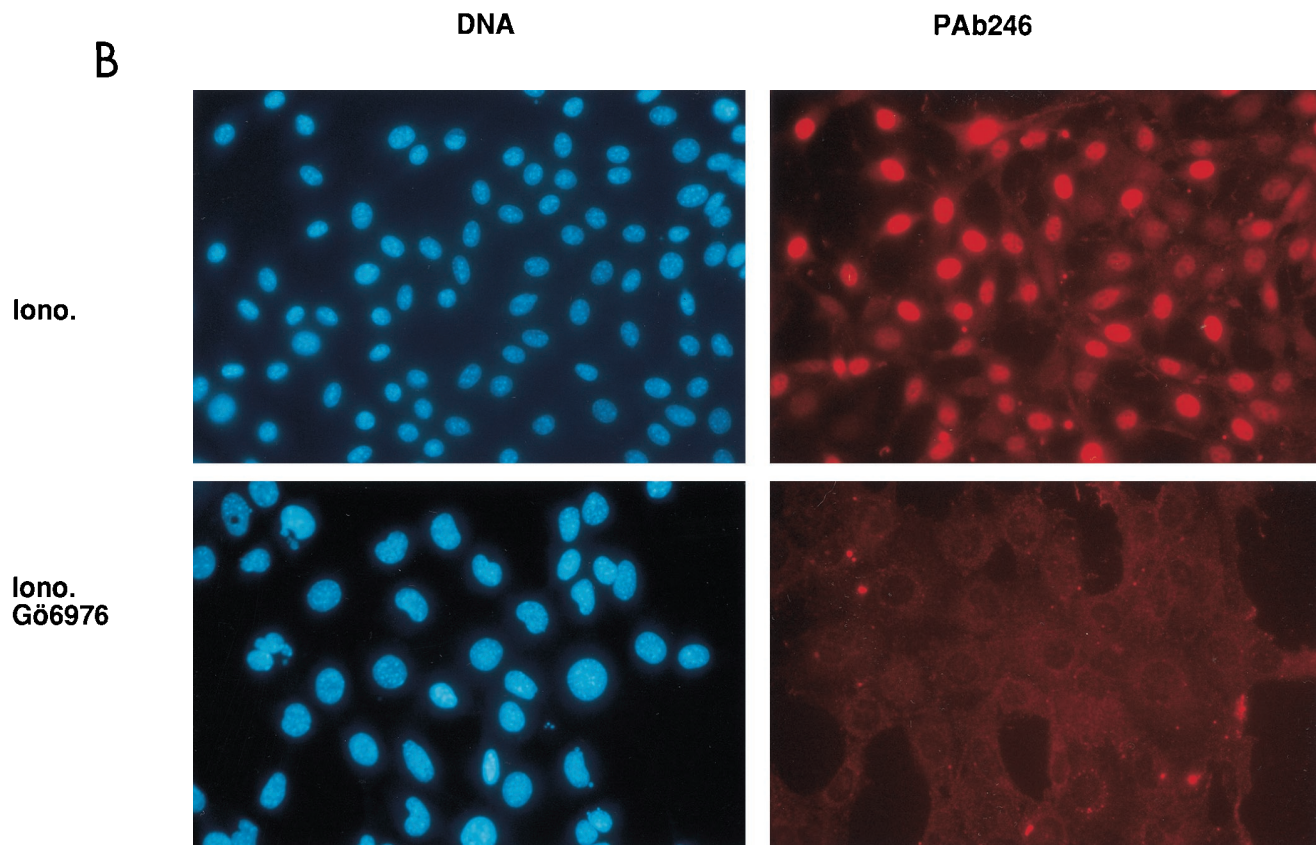


FIG. 4. Down regulation of cPKC by Gö6976 counteracts nuclear accumulation of the wild-type p53Val135 conformational species in S100B-MEF cells. (A) Western blot analysis of p53Val135 protein accumulation in clone J-β2p53 cells stimulated with 1 μM ionomycin in the absence (S100B-MEF) or in the presence of 1 μM Gö6976 (S100B-MEF-Gö6976). p53 was detected by a mixture of monoclonal antibodies PAb421 and PAb240. The asterisk indicates a cross-reacting protein that serves as internal loading control. (B) Microscopic analysis of PAb246 immunoreactivities in S100B-MEF clone J-β2p53 cells grown at 37.5°C and stimulated for 18 h with 1 μM ionomycin in the absence (Iono.) or in the presence (Iono. Gö6976) of 1 μM Gö6976. Left panels show DNA staining with Hoechst 33258.



effects. With parental REF cells, not expressing S100B, single stimulation with PMA (5 to 50 nM) decreased the rate of DNA synthesis by 50% (Fig. 7A), but cell cycle parameters were not significantly modified (Fig. 7B). With S100B-REF cells, single stimulation with 5 nM PMA induced a total inhibition of DNA synthesis (Fig. 7A). Fluorescence-activated cell sorting analysis showed that this inhibition corresponds to a G₁ phase growth arrest (Fig. 7B).

PMA-dependent growth arrest of S100B-REF cells was phenotypically indistinguishable from ionomycin-mediated G₁ arrest (52). The arrest was characterized by induction of the p21^{WAF1} cyclin-dependent kinase inhibitor protein but not the p27 inhibitor protein, and with dephosphorylation of the Rb protein (Fig. 7C). Time course analysis of Rb phosphorylation status revealed a biphasic dephosphorylation of Rb protein, with a first maximum effect between 2 and 3 h poststimulation, when the cell cycle parameters were not yet affected by the treatment. A trivial explanation for this phenomenon is that PMA activates a phosphatase which dephosphorylates Rb. Alternatively, it is also possible that PMA mediates p53-dependent transactivation of a phosphatase, like Wip1 (17), which

dephosphorylates Rb protein independently of the position of the cells within the cell cycle.

PMA stimulation of S100B-REF cells was also accompanied by increased expression of B99 (Fig. 7D), another cellular protein that is induced by wild-type p53 activity in REF cells (61). In NIH 3T3 cells, B99 is selectively induced in G₂/M phase of the cell cycle when p53 is activated (61). As expected, PMA-dependent B99 induction in S100B-REF cells correlates with progression of the cells from S to G₂/M phase, and B99 synthesis decreases when cells accumulate in G₁ phase. It is noteworthy that in contrast to PMA-mediated G₁ arrest, B99 synthesis was sustained in S100B-REF cells growth arrested at 32°C (Fig. 7D; compare lanes 7 and 8), suggesting that temperature shift-mediated growth arrest is distinct from PMA-dependent G₁ arrest (see also below and Discussion).

PMA-mediated G₁ arrest of S100B-REF cells was totally abolished by the cPKC-specific inhibitor Gö6976 (Fig. 8A and B), suggesting that the PMA effect is mediated via activation of a cPKC isoform. The implication of cPKC isoforms in the long-term cytostatic effect of PMA was confirmed by the use of bryostatin, a structurally distinct PKC activator. In many sys-

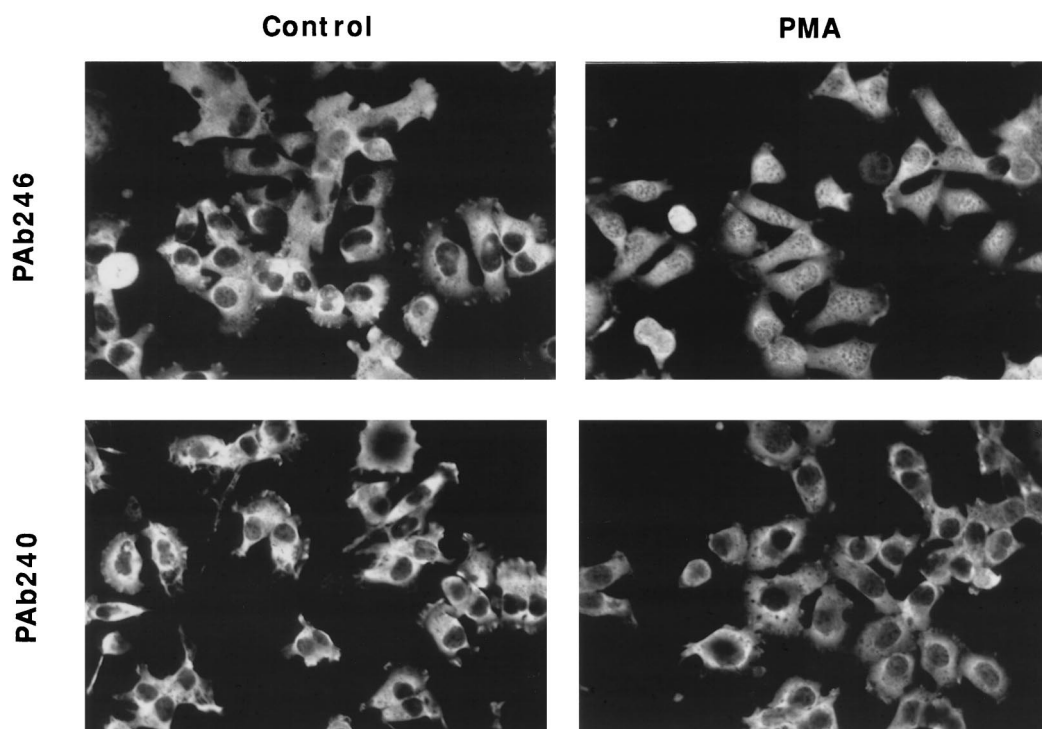


FIG. 5. Effect of PMA on cellular localization of wild-type and mutant p53Val135 in S100B-REF cells synchronized in the early G₁ phase of the cell cycle. Shown are the results of confocal microscope analysis of PAb246 and PAb240 immunoreactivities in clone 6 β cells synchronized by mitotic detachment and grown for 1 h on polylysine-coated coverslips allowing cells to pass through mitosis. Cells were either untreated (control) or stimulated with 8 nM PMA for 5 min (PMA).

tems, bryostatins induce only a subset of the responses to PMA and blocks those which it does not induce (22, 28, 57). The mechanisms by which bryostatins and PMA induce divergent long-term responses are linked with differential activation and down regulation of PKC isoforms (22, 57). With S100B-REF cells, bryostatins induced only partial inhibition of DNA synthesis at low concentrations (0.5 to 5 nM) (Fig. 8C) and antagonized the long-term cytostatic effect of PMA at higher concentrations (5 to 20 nM) (Fig. 8C). The divergent long-term responses of the cells to PMA or bryostatins stimulation correlated with specific down regulation of the calcium-dependent PKC α and PKC γ isoforms by bryostatins but not by PMA (Fig. 8D). In contrast to cPKC, the nPKC ϵ was down regulated by both PMA and bryostatins (Fig. 8D).

cPKC-dependent G₁ arrest but not permissive temperature restores full G₁ checkpoint control in S100B-REF cells. Parental REF cells showed only moderate apoptosis upon UV irradiation (52), and apoptosis was not significantly increased if cells were stimulated with PMA prior to UV irradiation (Fig. 9A). Exponentially growing S100B-REF cells are also insensitive to UV irradiation (52) but showed full apoptotic response if they were first arrested in G₁ upon PMA stimulation (Fig. 9B). Internucleosomal DNA cleavage in apoptotic cells was confirmed by agarose gel electrophoresis (Fig. 9C, lanes 1 to 3). Apoptosis of S100B-REF cells was rapid and maximal 24 h after UV irradiation if PMA was removed from the culture media after irradiation (Fig. 9B). It is important to note that if irradiated cells were left in the presence of PMA, the kinetics of apoptosis were considerably retarded, indicating that cell cycle progression is probably required for this apoptosis. Apoptosis still occurred when the transcriptional inhibitor actinomycin D was added 1 h before UV irradiation and maintained after irradiation (Fig. 9C, lane 4). We controlled so that the

cells treated with actinomycin D alone did not undergo apoptosis upon UV irradiation (not shown). p53Val135-dependent apoptosis in the absence of de novo transcription and translation in response to UV irradiation has also been observed in immortalized somatotrophic progenitor cells expressing p53Val135 (8). We also compared the apoptotic responses to UV irradiation of S100B-REF cells whose growth was arrested by shifting the temperature to 32°C and which were or were not stimulated with PMA (Fig. 9D). No apoptosis was observed in cells growth arrested at 32°C. Moreover, apoptosis could not be restored if the growth-arrested cells at 32°C were subsequently stimulated with PMA. At 32°C, apoptosis could be observed only when S100B-REF cells were first growth arrested with PMA prior to UV irradiation (Fig. 9D; Fig. 9C, lanes 5 and 6). Together these data confirm that S100B and PMA act in concert to specifically rescue a p53 apoptosis pathway in REF cells. They also show that temperature shift-mediated G₁ arrest at 32°C protects cells from UV-mediated apoptosis and is more likely associated with enhanced cell survival (see also Discussion).

DISCUSSION

The first observation reported in this study is the synchronized and concerted regulation of wild-type p53 nuclear translocation, accumulation, and activation by S100B and cPKC. A direct implication of S100B in wild-type p53 activation was first suggested by the fact that MEF cells expressing S100B tolerate only very low expression levels of the p53Val135 protein (52). Inversely, REF cells expressing a very high level of p53Val135 tolerate only low S100B expression levels (52). Moreover, calcium-dependent accumulation and activation of the wild-type p53Val135 functions in MEF and REF cells is strictly condi-

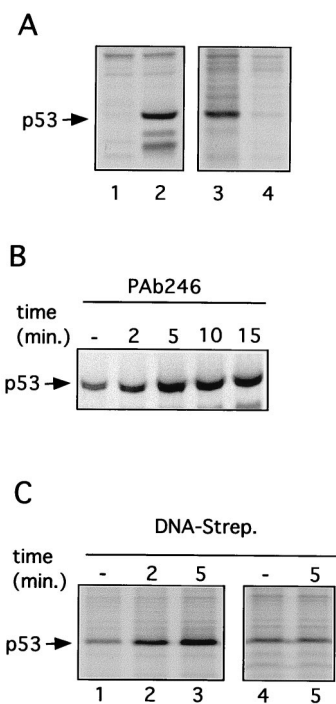


FIG. 6. PMA stimulates nuclear translocation and DNA binding of wild-type p53Val135 in S100B-REF cells. (A) Interaction of wild-type p53 with biotinylated p53-CON target DNA. Clone 6 β cell nuclear extracts were prepared, and ³⁵S-labeled p53 was immunoprecipitated with anti-MyoD immunoglobulin G used as a control (lane 1) or wild-type-specific PAb246 (lane 2). Nuclear extracts were also incubated with streptavidin-agarose and biotinylated p53-CON DNA target in the absence (lane 3) or presence (lane 4) of 20 μ g of nonbiotinylated p53-CON DNA used as a specific competitor. (B) PMA stimulates wild-type p53 (PAb246⁺) nuclear translocation. Clone 6 β cells were not stimulated (-) or were stimulated with 15 nM PMA for 2, 5, 10, and 15 min as indicated. Wild-type p53 was immunoprecipitated with PAb246. (C) PMA stimulates wild-type p53 binding to biotinylated target DNA. Clone 6 β cells were not stimulated (-) or stimulated with 15 nM PMA for 2 or 5 min as indicated. Lanes 1 to 3, nuclear extracts were incubated with biotinylated p53-CON DNA target and streptavidin (Strep.)-agarose. Lanes 4 and 5, nuclear extracts were first incubated with PAb246 and protein G-agarose; the remaining supernatants were then incubated with biotinylated p53-DNA target and streptavidin-agarose. Arrows indicate positions of ³⁵S-labeled p53 which bound to PAb246 or to a biotinylated DNA probe that was visualized by gel electrophoresis and autoradiography.

tioned by the presence of S100B (52). Although S100B expression in p53^{-/-}MEF cells was found to be sufficient for the accumulation of wild-type p53 in transient transfection assays (Fig. 1), in stable transfected MEF clones expressing both S100B and a low level of the ts p53Val135 mutant, ionomycin stimulation was required to promote nuclear accumulation of p53Val135 under a wild-type conformation (Fig. 2). These apparent discrepancies for calcium requirement in mediating S100B-dependent wild-type p53 accumulation are not clearly understood. It could be that in transient transfection assays, cellular stress associated with transfection conditions causes changes in intracellular calcium homeostasis similar to that produced by the calcium ionophore. It is also possible that calcium binding to S100B is not absolutely required for S100B to function in regulating wild-type p53. Other ions such as Zn²⁺, which bind to S100B with much higher affinity (K_D , 10 nM) and which induce Ca²⁺-like conformational changes (3), could also be implicated in regulating S100B functions. Strict calcium-dependent regulation of the wild-type p53Val135 in S100B-MEF cells could also be due to the heat sensitivity of this peculiar p53 mutant and its low expression level. In vitro, S100B interacts in a calcium-dependent manner with the C-

terminal regulatory domain of p53 (K_D , 20 \pm 10 nM) so as to protect p53 from thermal denaturation (13). The high-affinity and specific S100B-binding site on the C-terminal domain of p53 overlaps the multifunctional domain on p53 implicated in stabilization against Mdm2-directed degradation (29) and cytoplasmic anchorage (34) and is a critical determinant for the thermostability of p53 (13). Hence, in its calcium-bound state S100B could transiently interact with the p53Val135 to favor its nuclear translocation and subsequent accumulation. A correlation has also been observed between expression of S100A4 with enhanced levels of p53 in melanoma cells (55). Moreover, S100A2, which is 55% homologous to S100B, is a putative transcriptional target for p53 (58). This raises the possibility that p53 activation is a property shared by other S100 proteins. Finally, like calmodulin, S100B is likely to regulate multiple target proteins. Hence, other potential effector proteins of S100B, including cytoskeletal proteins and cytoskeleton-associated kinases (41) or other signalling pathways, may additionally synergize with S100B in p53 activation. The complexity of the calcium- and S100B-dependent regulation of wild-type p53 is further illustrated with the finding that cPKC is also implicated in the transduction of the calcium signal linked with p53 nuclear translocation, accumulation, and activation in the G₁ phase of the cell cycle. In the case of S100B-MEF cells expressing the ts p53Val135 mutant, the cPKC inhibitor Gö6967 inhibited nuclear translocation of the wild-type p53Val135 conformational species and severely decreased p53 accumulation mediated by ionomycin (Fig. 4). This finding indicates that wild-type p53 degradation is probably linked with cytoplasmic sequestration and that nuclear localization contributes to p53 stabilization. Cytoplasmic sequestration and degradation of wild-type p53 would allow cells to maintain a low level of p53 in the absence of p53 activation signals. Activation of cPKC by ionomycin or PMA could either induce phosphorylation of the cytoplasmic p53 or induce phosphorylation of cytoplasmic anchoring proteins (19). To resolve these issues, we performed studies to evaluate the phosphorylation status of the nuclear wild-type p53 in S100B-REF cells before and after PMA stimulation. The results showed that short-term (5-min) PMA stimulation enhanced nuclear accumulation of wild-type p53Val135 without affecting the phosphorylation status of the nuclear protein (data not shown). Moreover, mutations within the five putative PKC phosphorylation sites on murine wild-type p53 were found to have no significant effect on the nuclear translocation of the protein in transient transfection assays (Fig. 3A), suggesting that cPKC activity on p53 nuclear translocation is indirect. We consider that it is more likely that cPKC activity affects the phosphorylation status of cytoplasmic anchoring proteins (19) or of proteins implicated in p53 nuclear transport. It is noteworthy that the high-affinity S100B-binding domain within p53 (13) corresponds to a cytoplasmic sequestration domain on p53 (34). Hence, S100B might cooperate with cPKC by modulating interactions between p53 and cytoplasmic anchoring proteins to favor p53 nuclear translocation. Whether or not direct cPKC phosphorylation of p53 regulates other functions of p53 is also under investigation. In support of a more general role for calcium signalling in the regulation of p53 nuclear translocation in the G₁ phase of the cell cycle, a correlation can be established between the inhibition of nuclear translocation of p53 in G₁ phase by the anti-apoptotic protein Bcl2 (6, 48) and the capacity of Bcl2 to negatively regulate free intracellular calcium elevation by modulation of mitochondria and endoplasmic reticulum calcium pumps (30, 31, 63). The S100B and calcium-dependent activation of wild-type p53 which we have observed in MEF and REF cells could also be of more general occurrence. Many cellular

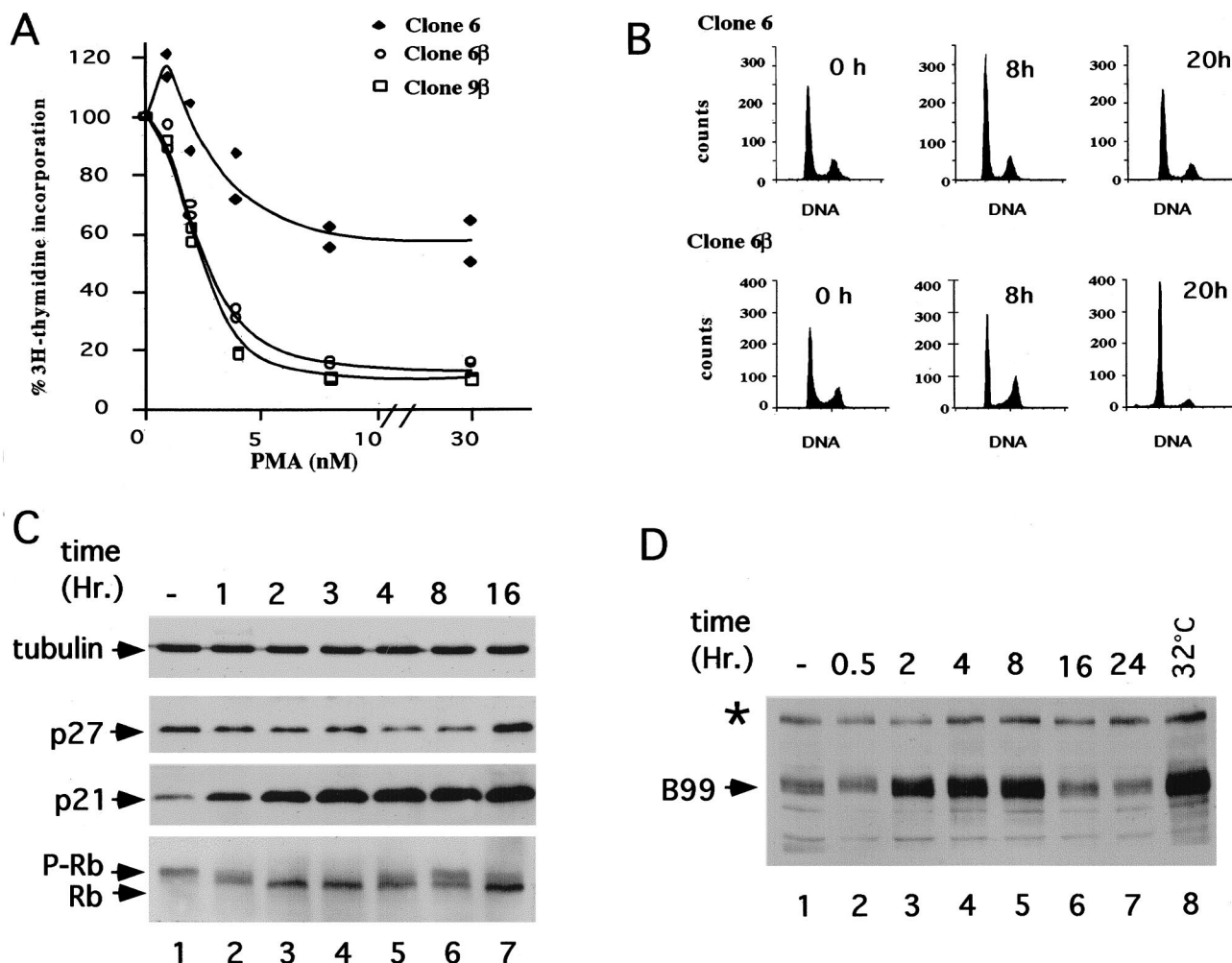


FIG. 7. PMA induces G_1 phase growth arrest of S100B-REF cells. (A) Effect of PMA concentration on the rate of DNA synthesis of clone 6 (\blacklozenge), clone 6 β (\circ), and clone 9 β (\square) cells grown at 37.5°C. Subconfluent cells were treated for 20 h with a single dose of PMA as indicated, and [3 H]thymidine uptake was measured during the last 2 h. (B) Flow cytometry analysis of the DNA content of clone 6 and clone 6 β cells stimulated with 8 nM PMA for 8 and 20 h as indicated. (C) Effect of PMA on cell cycle regulatory proteins in S100B-REF cells. Shown is a time course of p21 protein induction and Rb dephosphorylation in clone 6 β after PMA stimulation. Cells grown at 37.5°C were not stimulated (lane 1) or stimulated with 8 nM PMA for 1 h (lane 2), 2 h (lane 3), 3 h (lane 4), 4 h (lane 5), 8 h (lane 6), and 16 h (lane 7). Total cell extracts were analyzed by Western blotting using anti- β -tubulin, anti-p27, anti-p21, and anti-Rb antibodies as indicated. (D) Time course of B99 protein induction in clone 6 β cells after PMA stimulation (lanes 1 to 7) and comparison with growth-arrested cells at 32°C (lane 8). The asterisk indicates a cross-reacting protein that serves as internal loading control.

stimulations known to activate p53, such as cell contact (65), hypoxia (20), and UV irradiation (57), are also able to stimulate S100B expression (51, 52, 59, 60). Moreover, like p53, S100B has been implicated in cell differentiation, cellular senescence (21, 64), neurodegenerative disorders (26, 54), and negative tumor growth (24, 25). It is likely that in both normal cells and tumor cells, in neurodegenerative diseases and senescence, S100B induction could be associated with p53 nuclear translocation and activation.

The second major observation reported in this study is that cPKC-mediated p53 nuclear translocation rescues apoptotic response in S100B-REF cells at both permissive (37.5°C) and nonpermissive (32°C) temperatures (Fig. 9). In contrast, temperature shift-mediated growth arrest at 32°C is linked with enhanced cell survival. Much of the existing data implicates p53 in G_1 checkpoint control. However, in some systems, p53-dependent growth arrest may inhibit apoptosis and favor viable cell cycle arrest (46, 49). A central question related to p53 and optimization of anti-cancer therapies is how a cell decides

whether to undergo either a viable growth arrest and/or apoptosis when p53 is activated (56). It has been suggested that the outcome of wild-type p53 activation could be dependent on the timing of p53 nuclear translocation. p53-dependent apoptosis requires nuclear translocation of the protein during a critical period in early G_1 (14, 48). Similarly, we would like to propose that in S100B-REF cells, S100B and cPKC act in concert to activate a p53-dependent G_1 checkpoint by synchronizing nuclear translocation and transcriptional activation of the wild-type p53 in early G_1 . At this stage, p53 is probably capable of the transactivation of genes linked with both growth arrest and engagement of cells into a preapoptotic program (47). This model fits with the fact that UV-irradiated S100B-REF cells proceeding from G_1 enter apoptosis in the absence of de novo transcription (Fig. 9C, lane 4). When shifted to 32°C, REF cells and S100B-REF cells overexpressing the p53 Val135 stop growing, and this growth arrest protects cells from UV-mediated apoptosis (Fig. 9D). It is noteworthy that growth arrest at 32°C also protects cells from apoptosis mediated by the DNA-dam-

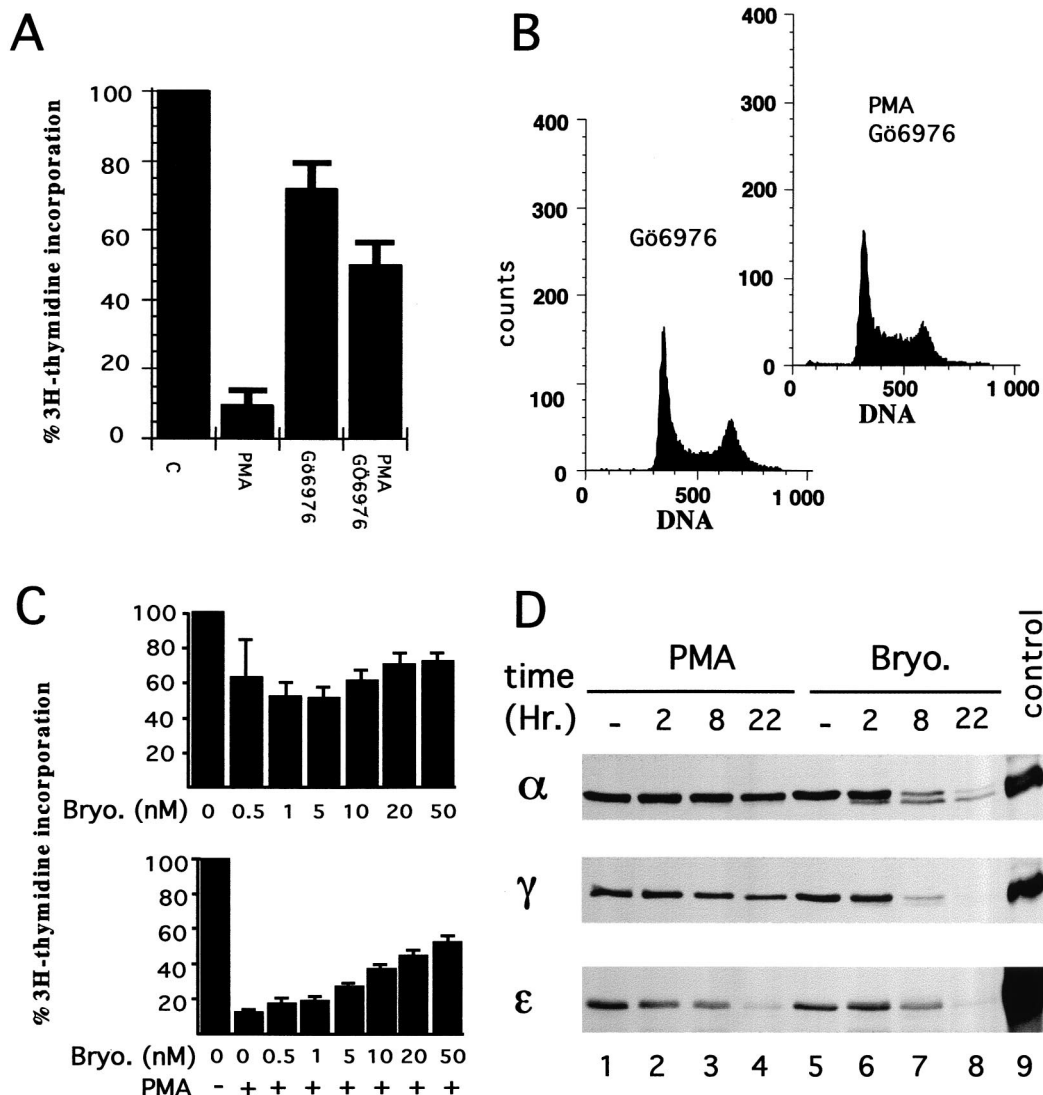


FIG. 8. cPKC inhibition suppresses the long-term cytostatic effect of PMA. (A) Subconfluent S100B-REF clone 6β cells were treated for a total of 20 h with 15 nM PMA in the absence or in the presence of the PKC inhibitor Gö6976 (1 μM) as indicated, and [³H]thymidine uptake was measured during the last 2 h. Results are the averages of values from three experiments performed in duplicate. C, control. (B) Effect of Gö6976 (1 μM) on the cell cycle parameters of clone 6β cells that were not stimulated or stimulated with 15 nM PMA for 20 h as indicated. (C) Upper panel, effect of bryostatin (Bryo.) concentration on the rate of DNA synthesis of clone 6β cells grown at 37.5°C; lower panel, effect of bryostatin concentration on PMA-mediated inhibition of DNA synthesis of clone 6β cells. Subconfluent cells were treated for 20 h with a single dose of bryostatin without (upper panel) or with (lower panel) 15 nM PMA as indicated, and [³H]thymidine uptake was measured during the last 2 h. (D) Comparison of the effects of PMA (PMA) and bryostatin (Bryo.) on down regulation of PKC isoenzymes in clone 6β cells. Cells grown at 37.5°C were not stimulated (lanes 1 and 5) or stimulated with PMA (15 nM) (lanes 2 to 4) or bryostatin (20 nM) (lanes 6 to 8) for 2 h (lanes 2 and 6), 8 h (lanes 3 and 7), and 22 h (lanes 4 and 8). Lane 9 is bovine brain extract, which was used as control. Total cell extracts (50 μg) were analyzed by Western blotting using anti-PKCα, anti-PKCγ, and anti-PKCε antibodies as indicated.

aging agent doxorubicin (unpublished data). The antiapoptotic activity of wt p53Val135 at 32°C could be linked to the fact that p53Val135 accumulates passively in the nucleus in mid or late G₁ subphases, triggering cell growth arrest after the G₁ restriction point. The ability of overexpressed p53 to bind to and inhibit the function of the cellular DNA replication factors such as RP-A could be one mechanism by which p53Val135 functions to suppress cell growth at 32°C beyond the G₁ restriction point at the G₁/S boundary (15). That arrest can also involve p53-mediated transactivation of a target gene like *p21*. p53-mediated transactivation of *p21* after the G₁ restriction point is indeed possible (35). The ability of p21 to inhibit proliferating cell nuclear antigen, a factor which is involved in

DNA replication, could also be one other mechanism by which p53Val135 functions in late G₁ by preventing cells progression to S phase (62). That model would also explain why, in contrast to PMA-mediated G₁ arrest, cell growth arrest at 32°C is associated with enhanced synthesis of the B99 protein (Fig. 7D). B99, which is normally down regulated in G₁, is thought to play a role in mediating specific activities of wild-type p53 in later phases of the cell cycle (61).

Conclusion. p53 does not appear to play an essential function in normal cell growth and development but plays a critical role in protection from neoplasia (33). One of the principal mechanisms by which wild-type p53 becomes activated is through its stabilization. One avenue of anticancer therapy

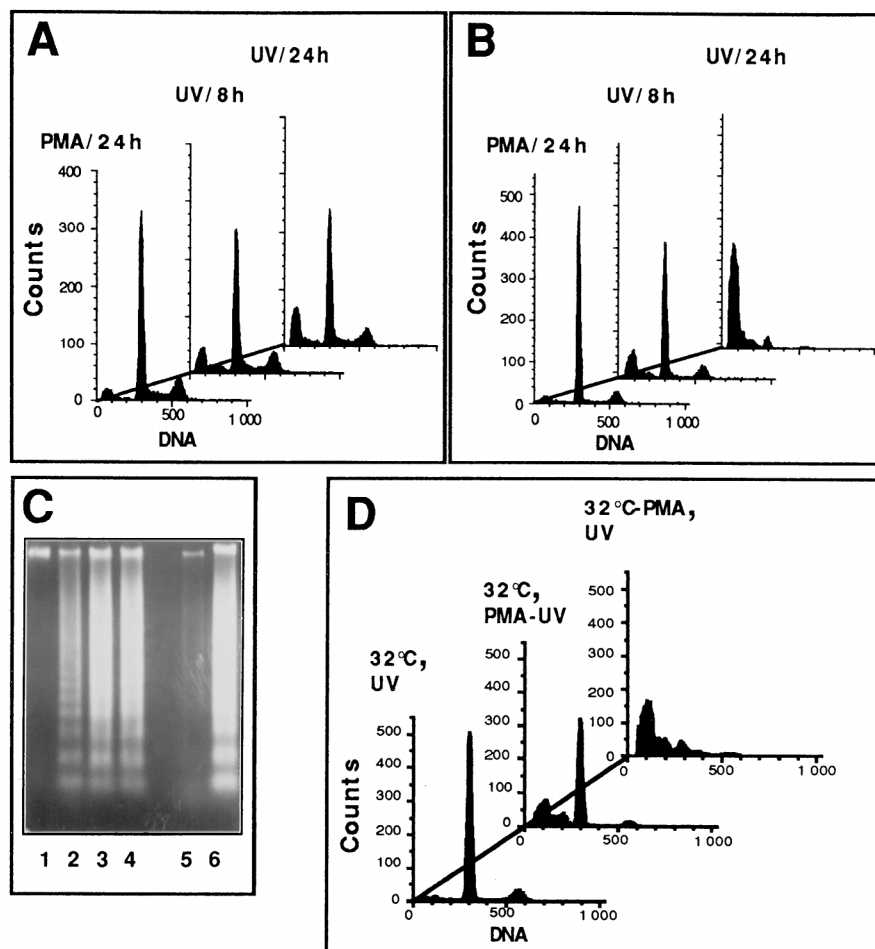


FIG. 9. S100B cooperates with PMA in triggering apoptosis of clone 6 cells upon UV irradiation. (A and B) Time course of induction of apoptosis in clone 6 (A) and clone 6 β (B) cells by UV irradiation. Clone 6 and clone 6 β cells were stimulated for 24 h with 4 nM PMA (PMA/24h). Cells were then irradiated (10 J/m^2), changed to fresh medium without PMA, and collected 8 h (UV/8h) or 24 h (UV/24h) after irradiation. (C) Agarose gel analysis of DNA fragmentation in apoptotic clone 6 β cells. Lane 1, control cells. Lanes 2 and 3, cells were first stimulated with 4 nM PMA, UV irradiated (10 J/m^2), and analyzed after 8 h (lane 2) or 24 h (lane 3). Lane 4, cells were as in lane 3 but incubated with actinomycin D (2.5 mg ml^{-1}) for 1 h prior to irradiation. After irradiation, actinomycin D was kept in the medium for another 24 h prior to cell analysis. Lanes 5 and 6 correspond to cells in panel D (32°C , UV and 32°C -PMA, UV). (D) PMA stimulation but not temperature shift restores full G₁ checkpoint control. Clone 6 β cells were growth arrested by shifting the temperature to 32°C . After 24 h at 32°C , cells were UV irradiated (32°C , UV). Cells were first growth arrested at 32°C ; after 24 h, cells were stimulated with PMA for another 20 h and UV irradiated (32°C , PMA-UV). Cells were stimulated with PMA at the time of the temperature shift to 32°C . After 24 h, cells were UV irradiated (32°C -PMA, UV). In all experiments, PMA was used at an 8 nM final concentration, the irradiation dose was 10 J/m^2 , and the culture media were replaced by media without PMA after irradiation. Cells were analyzed 24 h postirradiation.

might be to exploit mechanisms involved in the normal regulation of p53 conformation and stabilization. We have shown here that forced S100B expression coupled to cPKC activation can promote wild-type p53 nuclear translocation and accumulation. Moreover, we have demonstrated that the dominant negative activity of mutant p53 can be suppressed by forcing the wild-type p53 to translocate into the cell nuclei prior to mutant protein. Our results may constitute a basis for the rational design of p53 coactivators in the development of p53 gene therapy to restore wild-type p53 function in tumor cells harboring wild-type and mutant p53 alleles.

ACKNOWLEDGMENTS

This work was supported by grants from the Association pour la Recherche sur le Cancer, Ligue Nationale Contre le Cancer, to J.B.

We thank Licio Collavin and Claudio Schneider for the generous gift of B99 antibodies.

REFERENCES

- Aloni-Grinstein, R., D. Schwartz, and V. Rotter. 1995. Accumulation of wt p53 protein upon γ -irradiation induces a G2 arrest-dependent immunoglobulin κ light chain gene expression. *EMBO J.* **14**:1392–1401.
- Bates, S., and K. Vousden. 1996. p53 in signalling checkpoint arrest or apoptosis. *Curr. Opin. Genet. Dev.* **6**:12–19.
- Baudier, J., N. Glasser, and D. Gérard. 1986. Ions binding to S100 protein. Calcium and zinc-binding properties of bovine brain S100 $\alpha\alpha$, S100 $\alpha\beta$ ($\alpha\beta$), and S100B ($\beta\beta$) protein: Zn^{2+} regulates Ca^{2+} binding on S100B protein. *J. Biol. Chem.* **261**:8192–8203.
- Baudier, J., C. Delphin, D. Grunwald, S. Khoshbin, and J. J. Lawrence. 1992. Characterization of the tumor suppressor protein p53 as a protein kinase C substrate and a S100B-binding protein. *Proc. Natl. Acad. Sci. USA* **89**:11627–11631.
- Baudier, J., E. Bergeret, N. Bertacchi, H. Weintraub, J. Gagnon, and J. Garin. 1995. Interactions of myogenic bHLH transcription factors with calcium-binding calmodulin and S100a ($\alpha\alpha$) proteins. *Biochemistry* **34**:7834–7846.
- Beham, A., M. C. Marin, A. Fernandez, J. Herrmann, S. Brisbay, A. M. Tari, G. Lopez-Berestein, G. Lozano, M. Sarkiss, and T. J. McDonnell. 1997. Bcl-2 inhibits p53 nuclear import following DNA damage. *Oncogene* **15**:2767–2772.

7. Blagosklonny, M. V. 1997. Loss of function and p53 protein stabilization. *Oncogene* **15**:1889–1893.
8. Caelles, C., A. Heimberg, and M. Karim. 1994. p53 dependent apoptosis in the absence of transcriptional activation of p53-target genes. *Nature* **370**:220–224.
9. De la Monte, S. M., Y. K. Sohn, N. Ganju, and J. R. Wands. 1998. p53- and CD95-associated apoptosis in neurodegenerative diseases. *Lab. Investig.* **78**:401–411.
10. Deloulme, J. C., M. Sensenbrenner, and J. Baudier. 1990. Interactions of S100 proteins with protein kinase substrates, biological implication, p. 153–157. *In* R. Pochet, E. M. Lawson, and K. Heizmann (ed.), Calcium binding proteins in normal and transformed cells. Plenum Press, New York, N.Y.
11. Delphin, C., and J. Baudier. 1994. The protein kinase C activator, phorbol ester, cooperates with the wt p53 species of ras-transformed embryo fibroblasts growth arrest. *J. Biol. Chem.* **269**:29579–29587.
12. Delphin, C., K. P. Huang, C. Scotto, A. Chapel, M. Vincon, E. Chambaz, J. Garin, and J. Baudier. 1997. The *in vitro* phosphorylation of p53 by calcium-dependent protein kinase C. Characterization of a protein kinase C-binding site on p53. *Eur. J. Biochem.* **245**:684–692.
13. Delphin, C., M. Ronjat, J. C. Deloulme, G. Garin, L. Debussche, Y. Higashimoto, K. Sakaguchi, and J. Baudier. 1999. Calcium-dependent interaction of S100B with the C-terminal domain of the tumour suppressor p53. *J. Biol. Chem.* **274**:10539–10544.
14. Di Leonardo, A., S. P. Linke, K. Clarkin, and G. M. Wahl. 1994. DNA damage triggers a prolonged p53-dependent G1 arrest and long-term induction of Cip1 in normal human fibroblasts. *Genes Dev.* **8**:2540–2551.
15. Dutta, A., S. M. Ruppert, J. C. Aster, and E. Winchester. 1993. Inhibition of DNA replication factor RPA by p53. *Nature* **365**:79–82.
16. El-Deiry, W. S., S. E. Kern, J. A. Pietenpol, K. W. Kinzler, and B. Vogelstein. 1992. Definition of a consensus binding site for p53. *Nat. Genet.* **1**:45–49.
17. Fiscella, M., H. L. Zhang, S. Fan, K. Sakaguchi, S. Shen, W. E. Mercer, G. F. Vande Woude, P. M. O'Connor, and E. Appella. 1997. Wip1, a novel human protein phosphatase that is induced in response to ionizing radiation in a p53-dependent manner. *Proc. Natl. Acad. Sci. USA* **94**:6048–6053.
18. Frey, M. R., M. L. Saxon, X. Zhao, A. Rollins, S. S. Evan, and J. D. Black. 1997. Protein kinase C isozyme-mediated cell cycle arrest involves induction of p21waf1/cip1 and p27kip1 and hypophosphorylation of the retinoblastoma protein in intestinal epithelial cells. *J. Biol. Chem.* **272**:9424–9435.
19. Gannon, J. V., and D. P. Lane. 1991. Protein synthesis required to anchor a mutant p53 protein which is temperature-sensitive for nuclear transport. *Nature* **349**:802–805.
20. Graeber, T. G., J. F. Peterson, M. Tsai, K. Monica, A. J. Fornace, and A. Giaccia. 1994. Hypoxia induces accumulation of p53 protein, but activation of a G₁-phase checkpoint by low-oxygen conditions is independent of p53 status. *Mol. Cell. Biol.* **14**:6264–6277.
21. Griffin, W. S. T., J. G. Sheng, and R. E. Mrak. 1998. Senescence-accelerated overexpression of S100b in brain of SAMP6 mice. *Neurobiol. Aging* **19**:71–76.
22. Hocevar, B. A., and A. P. Fields. 1991. Selective translocation of p11-protein kinase C to the nucleus of human promyelocytic (HL60) leukemia cells. *J. Biol. Chem.* **266**:28–33.
23. Hofmann, J. 1997. The potential for isoenzyme-selective modulation of protein kinase C. *FASEB J.* **6**:649–669.
24. Karnell, R., E. Von Schoultz, L. O. Hansson, B. Nilsson, K. Arstrand, and B. Kagedal. 1997. S100B protein, 5-S-cysteinyldopa and 6-hydroxy-5-methoxyndole-2-carboxylic acid as biochemical markers for survival prognosis in patients with malignant melanoma. *Melanoma Res.* **7**:393–399.
25. Kernohan, N. M., and R. Rankin. 1987. S100 protein: a prognostic indicator in cutaneous malignant melanoma? *Histopathology* **11**:1285–1293.
26. Kitamura, Y., S. Shimohama, W. Kamoshima, Y. Matsuoaka, Y. Nomura, and T. Taniguchi. 1997. Changes of p53 in the brains of patients with Alzheimer's disease. *Biochem. Biophys. Res. Commun.* **232**:418–421.
27. Ko, L. J., and C. Prive. 1996. p53: puzzle and paradigm. *Genes Dev.* **10**:1054–1072.
28. Kraft, A. S., J. B. Smith, and R. L. Berkow. 1986. Bryostatin, an activator of the calcium phospholipid-dependent protein kinase, blocks phorbol ester-induced differentiation of human promyelocytic leukemia cells HL-60. *Proc. Natl. Acad. Sci. USA* **83**:1334–1338.
29. Kubbutat, M. H., R. L. Ludwig, M. Ashcroft, and K. Vousden. 1998. Regulation of Mdm2-directed degradation by C terminus of p53. *Mol. Cell. Biol.* **18**:5690–5698.
30. Kuo, T. H., H.-R. C. Kim, L. Zhu, H.-M. Lin, and W. Tsang. 1998. Modulation of endoplasmic reticulum calcium pump by Bcl2. *Oncogene* **17**:1903–1910.
31. Lam, M., G. Dubyak, L. Chen, G. Nunez, R. L. Miesfeld, and C. W. Distelhorst. 1994. Evidence that bcl-2 represses apoptosis by regulating endoplasmic reticulum-associated Ca²⁺ fluxes. *Proc. Natl. Acad. Sci. USA* **91**:6569–6573.
32. Lane, D. P. 1992. p53, guardian of the genome. *Nature* **358**:15–16.
33. Levine, A. J. 1997. p53, the cellular gatekeeper for growth and division. *Cell* **88**:323–331.
34. Liang, S. H., D. Hong, and M. F. Clarke. 1998. Cooperation of a single lysine mutation and a C-terminal domain in the cytoplasmic sequestration of the p53 protein. *J. Biol. Chem.* **273**:19817–19821.
35. Linke, S. P., M. P. Harris, S. E. Neugebauer, K. C. Clarkin, H. P. Shepard, D. C. Maneval, and G. M. Wahl. 1997. P53-mediated accumulation of hypophosphorylated pRb after the G1 restriction point fails to halt cell cycle progression. *Oncogene* **15**:337–345.
36. Lucas, M., and V. Sanchez-Margalet. 1995. Protein kinase C involvement in apoptosis. *Gen. Pharmacol.* **26**:881–887.
37. Martinez, J., I. Georgoff, J. Martinez, and A. J. Levine. 1991. Cellular localization and cell cycle regulation by a temperature-sensitive p53 protein. *Genes Dev.* **5**:151–159.
38. Martiny-Baron, G., M. G. Kazanietz, H. Mischak, P. M. Blumberg, G. Kochs, H. Hug, M. Dieter, and C. Schachtele. 1993. Selective inhibition of protein kinase isozymes by the indolocarbazole Gö6976. *J. Biol. Chem.* **268**:9194–9197.
39. McConkey, D. J., and S. Orrenius. 1994. Signal transduction pathways to apoptosis. *Trends Cell Biol.* **4**:370–375.
40. Michalovitz, D., O. Halevy, and M. Oren. 1990. Conditional inhibition of transformation and of cell proliferation by a temperature-sensitive mutant of p53. *Cell* **62**:671–680.
41. Millward, T. A., C. W. Heizmann, B. W. Schäfer, and B. A. Hemmings. 1998. Calcium regulation of Ndr protein kinase mediated by S100 calcium-binding proteins. *EMBO J.* **17**:5913–5922.
42. Morii, K., R. Tanaka, Y. Takahashi, and R. Kuwano. 1992. Cloning of cDNA encoding human S100 a and b subunits and their differential expression in human tumor cell lines. *J. Neurosci. Res.* **32**:27–33.
43. Nakajima, T., S. Watanabe, Y. Sato, T. Kameya, T. Hirota, and Y. Shimamoto. 1982. An immunoperoxidase study of S100 protein distribution in normal and neoplastic tissues. *Am. J. Surg. Pathol.* **6**:715–727.
44. Nishizuka, Y. 1992. Intracellular signalling by hydrolysis of phospholipids and activation of protein kinase C. *Science* **258**:607–614.
45. Nishizuka, Y. 1995. Protein kinase C and lipid signaling for sustained cellular responses. *FASEB J.* **9**:484–496.
46. Polyak, K., T. Waldman, T. C. He, K. Kinzler, and B. Vogelstein. 1996. Genetic determinants of p53-induced apoptosis and growth arrest. *Genes Dev.* **10**:1945–1952.
47. Polyak, K., Y. Xia, J. L. Zweier, K. W. Kinzler, and B. Vogelstein. 1997. A model for p53-induced apoptosis. *Nature* **389**:300–305.
48. Ryan, J. J., E. Prochownik, C. A. Gottlieb, I. J. Apel, R. Merino, G. Nunez, and M. Clarke. 1994. c-myc and bcl-2 modulate p53 function by altering p53 subcellular trafficking during the cell cycle. *Proc. Natl. Acad. Sci. USA* **91**:5878–5882.
49. Ryan, K. M., and K. H. Vousden. 1998. Characterization of structural p53 mutants which show selective defects in apoptosis but not cell cycle arrest. *Mol. Cell. Biol.* **18**:3692–3698.
50. Sabapathy, K., M. Klemm, R. Jaenisch, and E. F. Wagner. 1997. Regulation of ES cell differentiation by functional and conformational modulation of p53. *EMBO J.* **16**:6217–6229.
51. Schneider, S. A., K. Fukuyama, J. Maceira, and W. L. Epstein. 1985. Effect of ultraviolet B radiation on S100 protein antigen in epidermal Langerhans cells. *J. Invest. Dermatol.* **84**:146–148.
52. Scotto, C., J. C. Deloulme, D. Rousseau, E. Chambaz, and J. Baudier. 1998. Calcium and S100B regulation of p53-dependent cell growth arrest and apoptosis. *Mol. Cell. Biol.* **18**:4272–4281.
53. Serrano, M., A. W. Lin, M. E. McCurrach, D. Beach, and S. W. Lowe. 1997. Oncogenic ras provokes premature cell senescence associated with accumulation of p53 and p16INK4a. *Cell* **88**:593–602.
54. Sheng, J. G., R. E. Mrak, and W. S. T. Griffin. 1994. S100b protein expression in Alzheimer's disease: potential role in the pathogenesis of neuritic plaques. *J. Neurosci. Res.* **39**:398–404.
55. Sherbet, G. V., and M. S. Lakshmi. 1998. S100A4 (MTS1) calcium binding protein in cancer growth, invasion and metastasis. *Anticancer Res.* **18**:2415–2422.
56. Smith, M. L., and A. J. Fornace. 1997. p53-mediated protective responses to UV irradiation. *Proc. Natl. Acad. Sci. USA* **94**:12255–12257.
57. Szallasi, Z., C. B. Smith, G. R. Pettit, and P. M. Blumberg. 1994. Differential regulation of protein kinase C isozymes by bryostatin 1 and phorbol 12-myristate 13-acetate in NIH 3T3 fibroblasts. *J. Biol. Chem.* **269**:2118–2124.
58. Tan, M., C. W. Heizmann, K. Guan, B. W. Schafer, and Y. Sun. 1999. Transcriptional activation of the human S100A2 promoter by wild-type p53. *FEBS Lett.* **445**:265–268.
59. Tronnier, M., U. Missler, K. Grotrian, and N. Kock. 1998. Does ultraviolet radiation exposure influence S100b protein plasma level? *Br. J. Dermatol.* **138**:1098–1100.
60. Tsoporis, J. N., A. Marks, H. J. Kahn, J. Butany, P. P. Liu, D. O'Hanlon, and T. G. Parker. 1997. S100β inhibits α1-adrenergic induction of the hypertrophic phenotype in cardiac myocytes. *J. Biol. Chem.* **272**:31915–31921.
61. Utrera, R., L. Collavin, D. Lazarevic, D. Delia, and C. Schneider. 1998. A novel p53-inducible gene coding for a microtubule-localized protein with G2-phase-specific expression. *EMBO J.* **17**:5015–5025.
62. Waga, S., G. J. Hannon, D. Beach, and B. Stillman. 1994. The p21 inhibitor of cyclin-dependent kinases controls DNA replication by interaction with PCNA. *Nature* **369**:574–578.
63. Wang, E., A. N. Murphy, D. E. Bredesen, G. Cortopassi, and G. Fiskum.

1996. Bcl-2 potentiates the maximal calcium uptake capacity of neural cell mitochondria. *Proc. Natl. Acad. Sci. USA* **93**:9893–9898.
64. **Whitaker-Amitia P., M. Wingate, A. Borella, R. Gerlai, J. Roder, and E. Azmitia.** 1997. Transgenic mice overexpressing the neurotrophic factor S100b show neuronal cytoskeletal and behavioral signs of altered aging processes: implication for Alzheimer's disease and Down's syndrome. *Brain Res.* **776**:51–60.
65. **Yahanda, A. M., J. M. Bruner, L. A. Donehower, and R. S. Morrison.** 1995. Astrocytes derived from p53-deficient mice provide a multistep in vitro model for development of malignant gliomas. *Mol. Cell. Biol.* **15**:4249–4259.
66. **Zeveloff, J., V. Sexl, C. Hutter, A. Karel, W. Schutz, and M. Freissmuth.** 1997. The cyclin-dependent kinase inhibitor p21cip1 mediates the growth inhibitory effect of phorbol esters in human venous endothelial cells. *J. Biol. Chem.* **272**:29967–29974.
67. **Zhao, X., J. E. Gschwend, T. Powell, R. G. Foster, K. C. Day, and M. L. Day.** 1997. Retinoblastoma protein-dependent growth signal conflict and caspase activity are required for protein kinase C-signaled apoptosis of prostate epithelial cells. *J. Biol. Chem.* **272**:22751–22757.

A Small Ubiquitin-Related Polypeptide Involved in Targeting RanGAP1 to Nuclear Pore Complex Protein RanBP2

Rohit Mahajan, Christian Delphin, Tinglu Guan, Larry Gerace, and Frauke Melchior
Department of Cell Biology
The Scripps Research Institute
10550 North Torrey Pines Rd
La Jolla, California 92037

Summary

We have found that the mammalian Ran GTPase-activating protein RanGAP1 is highly concentrated at the cytoplasmic periphery of the nuclear pore complex (NPC), where it associates with the 358-kDa Ran-GTP-binding protein RanBP2. This interaction requires the ATP-dependent posttranslational conjugation of RanGAP1 with SUMO-1 (for small ubiquitin-related modifier), a novel protein of 101 amino acids that contains low but significant homology to ubiquitin. SUMO-1 appears to represent the prototype for a novel family of ubiquitin-related protein modifiers. Inhibition of nuclear protein import resulting from antibodies directed at NPC-associated RanGAP1 cannot be overcome by soluble cytosolic RanGAP1, indicating that GTP hydrolysis by Ran at RanBP2 is required for nuclear protein import.

Introduction

Import of protein into the nucleus is a complex multistep process that coordinates nuclear and cytoplasmic functions. Transport is mediated by nuclear pore complexes (NPCs), elaborate supramolecular structures that span the nuclear envelope (NE) (reviewed by Rout and Wenthe, 1994; Bastos et al., 1995; Panté and Aebi, 1996a). Although some small proteins (<40 kDa) and metabolites can diffuse passively through aqueous channels in the NPC, most proteins are transported by signal- and energy-dependent mechanisms. Mediated import of proteins containing nuclear localization signals (NLSs) is proposed to involve binding of transport substrates to cytoplasmic fibrils of the NPC, movement to the central NPC region, and translocation through a central gated channel to the nuclear interior (reviewed by Melchior and Gerace, 1995; Görlich and Mattaj, 1996; Panté and Aebi, 1996b). However, most molecular details of these transport steps are not understood.

Analysis of nuclear protein import *in vitro* has led to the identification of five conserved soluble factors involved in this process: the NLS receptor (importin α , karyopherin α , Srp1p), p97 (importin β , karyopherin β , Kap95), hsp/hsc70, NTF2 (p10, pp15), and the small Ras-like GTPase Ran (for review, see Sweet and Gerace, 1995). In addition, at least one other GTPase appears to be involved in nuclear import (Sweet and Gerace, 1996).

The GTPase Ran has been implicated in a variety of cellular processes (reviewed by Sazer, 1996), but up to now the only pathway to which it has been directly linked

is nuclear protein import (Melchior et al., 1993a; Moore and Blobel, 1993). Like all Ras-related GTPases, Ran operates as a molecular switch by cycling between GTP and GDP bound conformations. Interconversion between these two states is regulated by guanine nucleotide exchange proteins (GEPs), which stimulate exchange of GDP for GTP, and GTPase-activating proteins (GAPs), which activate GTP hydrolysis (Bourne et al., 1990). Both a Ran GEP, the RCC1 protein (Ohtsubo et al., 1987; Bischoff and Ponstingl, 1991), and a Ran GAP, RanGAP1 (Bischoff et al., 1994, 1995a), have been identified. At least most of the detectable GEP and GAP activity for Ran in cell extracts can be attributed to RCC1 and RanGAP1, respectively (Bischoff et al., 1994; Dasso et al., 1994). Ran can engage in nucleotide-specific interactions with several cytosolic factors and NPC proteins implicated in nuclear transport. Ran-GDP preferentially binds NTF2 (Nehrbass and Blobel, 1996; Paschal et al., 1996). Ran-GTP specifically interacts with the soluble components RanBP1 (Bischoff et al., 1995b) and p97 (Rexach and Blobel, 1995; Paschal et al., 1996), and the NPC protein RanBP2/Nup358 (Wu et al., 1995; Yokoyama et al., 1995). RanBP1 stimulates RanGAP1-induced GTP hydrolysis by Ran (Bischoff et al., 1995b), while yeast p97 (importin β /karyopherin β) inhibits RanGAP activity (Floer and Blobel, 1996). How these various interactions are linked to different nuclear transport steps is still unclear. While it is widely accepted that GTP hydrolysis by Ran is required for nuclear import, several different models involving one or multiple rounds of GTP hydrolysis by Ran in various regions of the NPC have been proposed (Melchior et al., 1995a; Rexach and Blobel, 1995; Nehrbass and Blobel, 1996; Görlich and Mattaj, 1996).

To distinguish among these models, we decided to analyze the localization of RanGAP1 (the only known GAP for Ran in mammalian cells), because any site where GTP hydrolysis by Ran occurs should be characterized by the presence of a RanGAP. RanGAP activity has been found both in cytosolic and in nuclear fractions of HeLa cells, but immunolocalization of the 64-kDa mammalian RanGAP1 has not been reported as far as we know (Bischoff et al., 1994). RanGAP1 is related in sequence to the *Saccharomyces cerevisiae* and *Schizosaccharomyces pombe* RanGAP Rna1p (Bischoff et al., 1995a; Becker et al., 1995; Figure 1A), which is localized predominantly in the cytoplasm, although a small fraction might also be present at the NE (Hopper et al., 1990; Melchior et al., 1993b). Strong evidence for a role of the *S. cerevisiae* RanGAP Rna1p in nuclear import comes from *in vitro* assays using the temperature-sensitive *S. cerevisiae* strain *ma1-1* (Corbett et al., 1995). Therefore it seemed likely that mammalian RanGAP1 might also be involved in nuclear protein import.

We find that RanGAP1 is highly concentrated at the cytoplasmic periphery of the NPC, where it forms a stable complex with RanBP2. The interaction of RanGAP1 with RanBP2 involves a covalent conjugation of RanGAP1 with a novel 101-residue ubiquitin-related polypeptide. Antibody treatment of NPC-associated RanGAP1 leads to an inhibition of nuclear protein import that

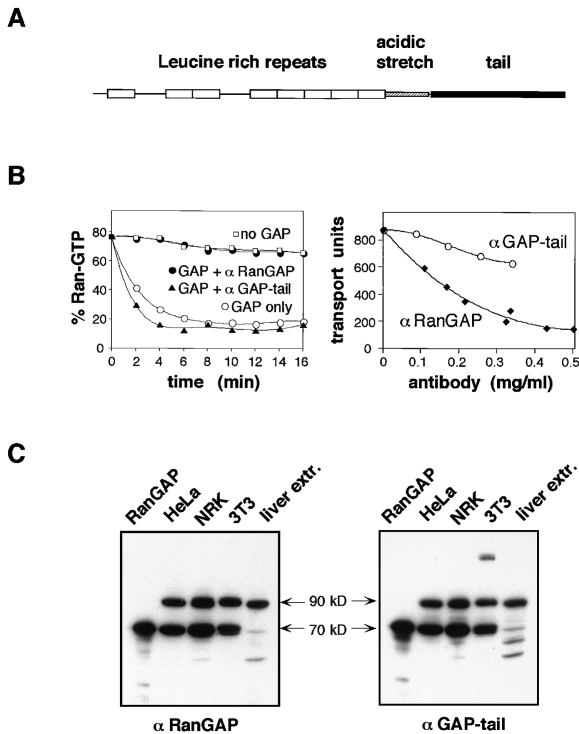


Figure 1. Characterization of Antibodies against Full-Length RanGAP1 and against the C-Terminal Domain of RanGAP1

(A) Structural motifs of the RanGAP1 protein. The schematic representation is based on a sequence comparison among human RanGAP1 (Bischoff et al., 1995a), its mouse homolog Fug1 (DeGregori et al., 1994), *S. cerevisiae* Rna1p (Traglia et al., 1989), and *S. pombe* rna1p (Melchior et al., 1993b). All proteins contain eight leucine-rich repeats and a highly acidic stretch, while the C-terminal tail domain of 185 amino acids is specific to mammalian RanGAP1.

(B) Antibodies to RanGAP1 inhibit RanGAP1-induced GTP hydrolysis by Ran as well as *in vitro* nuclear import. Left: RanGAP1 (1 μ g/ml)-stimulated GTP hydrolysis by Ran was measured in the absence (GAP only) or presence of 20 μ g/ml antibodies raised against full-length RanGAP1 (GAP plus α RanGAP) or 100 μ g/ml antibodies raised against the C-terminal tail domain (GAP plus α GAP-tail). No GAP: endogeneous hydrolysis rate of Ran-GTP in the absence of RanGAP1. Right: *in vitro* nuclear protein import was measured in the presence of increasing concentrations of α RanGAP1 or α GAP-tail antibodies.

(C) Antibodies to RanGAP1 reveal both the 70-kDa and the 90-kDa RanGAP1-related proteins in several cell extracts. Samples resolved on an 8% SDS gel were immunoblotted with α RanGAP1 or α GAP-tail antibodies. RanGAP1, 3 ng of recombinant RanGAP1. Cell extracts from HeLa, NRK, and NIH 3T3 tissue culture cells were prepared by lysis of cells in boiling SDS gel-loading buffer, whereas rat liver extract was prepared by homogenization of rat liver in a physiological buffer prior to addition of 2 \times SDS gel loading buffer.

cannot be overcome by addition of soluble RanGAP1. These findings suggest that GTP hydrolysis by Ran occurs at RanBP2 during nuclear protein import.

Results

Mammalian RanGAP1 Is Involved in Nuclear Protein Import

Rna1p, the only identified *S. cerevisiae* RanGAP, is required for nuclear protein import (Corbett et al., 1995). The 64-kDa mammalian RanGAP1 (Bischoff et al., 1995a) and the 44-kDa Rna1p proteins from fission and baker's

yeasts are approximately 30% identical over a shared domain consisting of eight leucine-rich repeats followed by a highly acidic stretch (Figure 1A). Whether mammalian RanGAP1, which contains an additional C-terminal extension (Figure 1A, tail), was a true functional homolog of Rna1p remained to be established.

To analyze a possible role of mammalian RanGAP1 in nuclear protein import, we prepared two affinity-purified antibodies: one directed against full-length RanGAP1, and one directed against the mammalian-specific tail domain. We first investigated their effect on RanGAP1-induced GTP hydrolysis by Ran (Figure 1B, left). Addition of 100 μ g/ml α GAP-tail antibodies had no measurable effect on RanGAP-stimulated GTP hydrolysis. In contrast, addition of only 20 μ g/ml α RanGAP1 antibodies completely abolished RanGAP-induced hydrolysis (Figure 1B, GAP + α RanGAP). We then measured the effect of these antibodies on nuclear import. α RanGAP1 antibodies strongly inhibited *in vitro* nuclear import in HeLa cells (Figure 1B, right), with maximal inhibition (>90%) at 0.4 mg/ml antibody. This inhibition could be reversed by the addition of excess recombinant RanGAP1 prior to antibody addition (see Figure 7). While the maximal level of inhibition varied somewhat from experiment to experiment, we routinely obtained >70% inhibition. In contrast, α GAP-tail antibodies had a much weaker inhibitory effect on import (Figure 1B, right). The differential effects of these two antibodies on RanGAP1-stimulated GTP hydrolysis by Ran correlated well with their differential effects in inhibition of nuclear protein import, suggesting that the decrease in transport was at least partly mediated by inhibition of RanGAP activity. Taken together, these data demonstrate that mammalian RanGAP1 is required for nuclear protein import.

Antibodies to RanGAP1 Recognize Two Proteins with Apparent Molecular Masses of 70 kDa and 90 kDa

Biochemical fractionation of HeLa cells has raised the possibility that mammalian cells may contain several related RanGAP proteins (Bischoff et al., 1994). We investigated this question by performing Western blot analysis of several cell extracts (see Figure 1C). Interestingly, both α RanGAP1 and α GAP-tail antibodies consistently recognized two proteins: one with an apparent molecular mass of 70 kDa that comigrated with recombinant mouse RanGAP1, and one that migrated at an apparent molecular mass of 90 kDa. The staining pattern obtained with both antibodies was virtually identical (Figure 1C), suggesting that the 70-kDa and 90-kDa bands are both related to RanGAP1. The ratio of the two bands was dependent on the method of sample preparation. When tissue culture cells were scraped directly into boiling SDS-polyacrylamide gel electrophoresis (PAGE) loading buffer, both bands were present in approximately equal abundance (Figure 1C). In contrast, when rat liver (Figure 1C) or HeLa cells (data not shown) were lysed under nondenaturing conditions prior to addition of SDS, the 90-kDa band predominated.

The 90-kDa RanGAP1-Related Protein Is Highly Enriched in NEs

To characterize further the 90-kDa RanGAP-like protein, we analyzed its subcellular distribution by fractionation

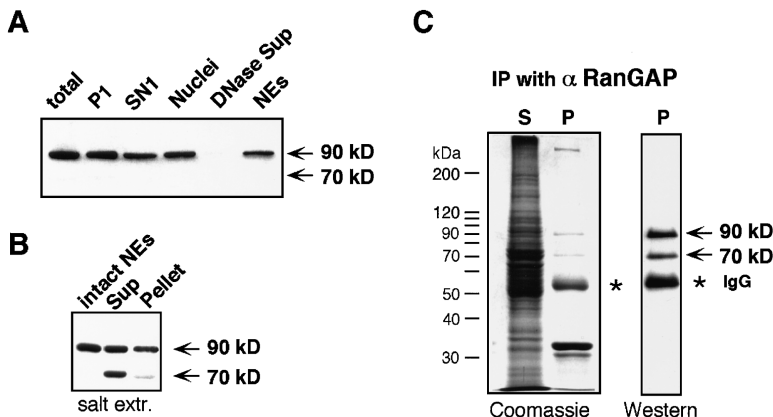


Figure 2. Purification of the 70 kDa and 90 kDa RanGAP1-Related Proteins from Rat Liver NEs

(A) The 90-kDa RanGAP1-related protein is highly enriched in rat liver NEs. Equivalent amounts of subcellular fractions of rat liver were resolved on an 8% SDS gel and immunoblotted with α RanGAP1 antibodies. Total was taken after homogenization of rat liver. P1 and SN1, pellet and supernatant of the first low speed centrifugation; Nuclei, purified nuclei; DNase Sup, the supernatant of the first DNase/RNase digest of the nuclei; NEs, the final NE fraction. NE proteins were enriched \sim 250-fold. Note that under these conditions, the 90-kDa protein is the only α RanGAP1-reactive species detected.

(B) Appearance of the 70-kDa α RanGAP1-reactive species upon salt extraction of the NE fraction. NEs containing the 90-kDa protein were incubated with 500 mM NaCl and centrifuged, and the supernatant (Sup) and pellet (Pellet) were analyzed by Western blotting.

(C) Immunoprecipitation with α RanGAP1 antibodies from solubilized rat liver NEs. NEs were solubilized and incubated overnight with α RanGAP1 antibodies preadsorbed to Protein A beads. Antibody-antigen complexes and the remaining supernatant were separated on 8% gels and either stained with Coomassie blue or immunoblotted with α GAP-tail antibodies. The lower band (\sim 32 kDa) results from a nonspecific interaction with the Protein A beads (see Figure 6). Asterisk, IgG heavy chain.

of rat liver homogenates (Figure 2A). Whereas a fraction of the protein was present in the low speed supernatant (and remained in a subsequent high speed supernatant; data not shown), the majority of the protein was present in the nuclear fraction. DNase/RNase digestion of nuclei, which releases most nuclear contents, did not solubilize a significant amount of the 90-kDa protein, indicating that a major fraction of the 90-kDa protein is associated with the NE. Extraction of NEs with high salt resulted in the appearance of a 70-kDa band in addition to the expected 90-kDa band (Figure 2B). About 50% of the 90-kDa band remained in the pellet after salt extraction, but the 70-kDa band was specifically enriched in the supernatant (Figure 2B; compare supernatant with pellet). The appearance of the 70-kDa protein suggested that this species might derive from the 90-kDa protein by proteolysis or by loss of a hypothetical posttranslational modification.

The 90-kDa RanGAP1-Related Protein Contains a Domain Absent from the Recombinant 70-kDa RanGAP1

To investigate the relationship between the 90- and 70-kDa protein bands, we solubilized rat liver NEs in radioimmunoprecipitation assay (RIPA) buffer, immunoprecipitated the two bands with α RanGAP1 antibodies (Figure 2C), and analyzed tryptic digests of the two species on a C18 high pressure liquid chromatography (HPLC) column. While the HPLC profiles of tryptic digests from the 70- and 90-kDa protein were virtually identical to each other (data not shown), the profile of the 90-kDa species contained a few peaks missing from the profile of the 70-kDa species. Several fractions from the HPLC column profiles were selected for peptide sequencing (Table 1). A peptide from the 90-kDa digest that was common to both species yielded a sequence found in the published RanGAP1 sequence (Table 1, P1), confirming that the 90-kDa protein is closely related to RanGAP1. Sequencing of three HPLC peaks (Table 1, P2-P4) specific to the 90-kDa protein demonstrated that none of these sequences was present in, or related to, the published RanGAP1 sequence.

This suggested that the 90-kDa protein might represent an alternatively spliced form of the previously identified 70-kDa RanGAP1, or an SDS-PAGE-resistant protein complex of the 70-kDa RanGAP1 with another protein.

Identification of a Novel Ubiquitin-Related Protein

The peptide sequences obtained from the 90-kDa-specific HPLC peaks (Table 1, P2-P4) were used to search for related sequences in the DNA databases. While no homology to known protein sequences was found, 30 overlapping expressed sequence tag (EST) cDNAs from the Human cDNA Database were identified that encoded all three peptides. The three longest of these clones were sequenced and found to contain the same putative open reading frame (ORF) of 101 amino acids that included the three unique peptide sequences present in the 90-kDa RanGAP protein. The cDNA sequence and the deduced protein sequence of the ORF are shown in Figure 3A. The small calculated size of the protein (11.5 kDa) suggested that the protein could be post-translationally coupled to RanGAP1 to yield the 90-kDa species. However, since the cDNAs contained no upstream stop codons, it was formally possible that this sequence represented an ORF downstream of the original published *RanGAP1* mRNA sequence, and that a hypothetical 5' section encoding a RanGAP1-related

Table 1. Amino Acid Sequences of Tryptic Peptides Derived from the 70-kDa and 90-kDa Proteins

Peptide	Sequence	70 kDa	90 kDa
P1	VINLNDNTFTEK	+	+
P2	ELGMEEEDVIEVY	-	+
P3	FLFEGQR	-	+
P4	VIGQDSSEIHFK	-	+

The 70-kDa and 90-kDa RanGAP proteins obtained by immunoprecipitation from solubilized NEs were separated by SDS-PAGE, transferred onto polyvinylidene difluoride membrane, and subjected to microsequencing (Paschal and Gerace, 1995). P1 is present in both proteins as well as in the published sequence of human RanGAP1; P2-P4 are specific for the 90-kDa protein.

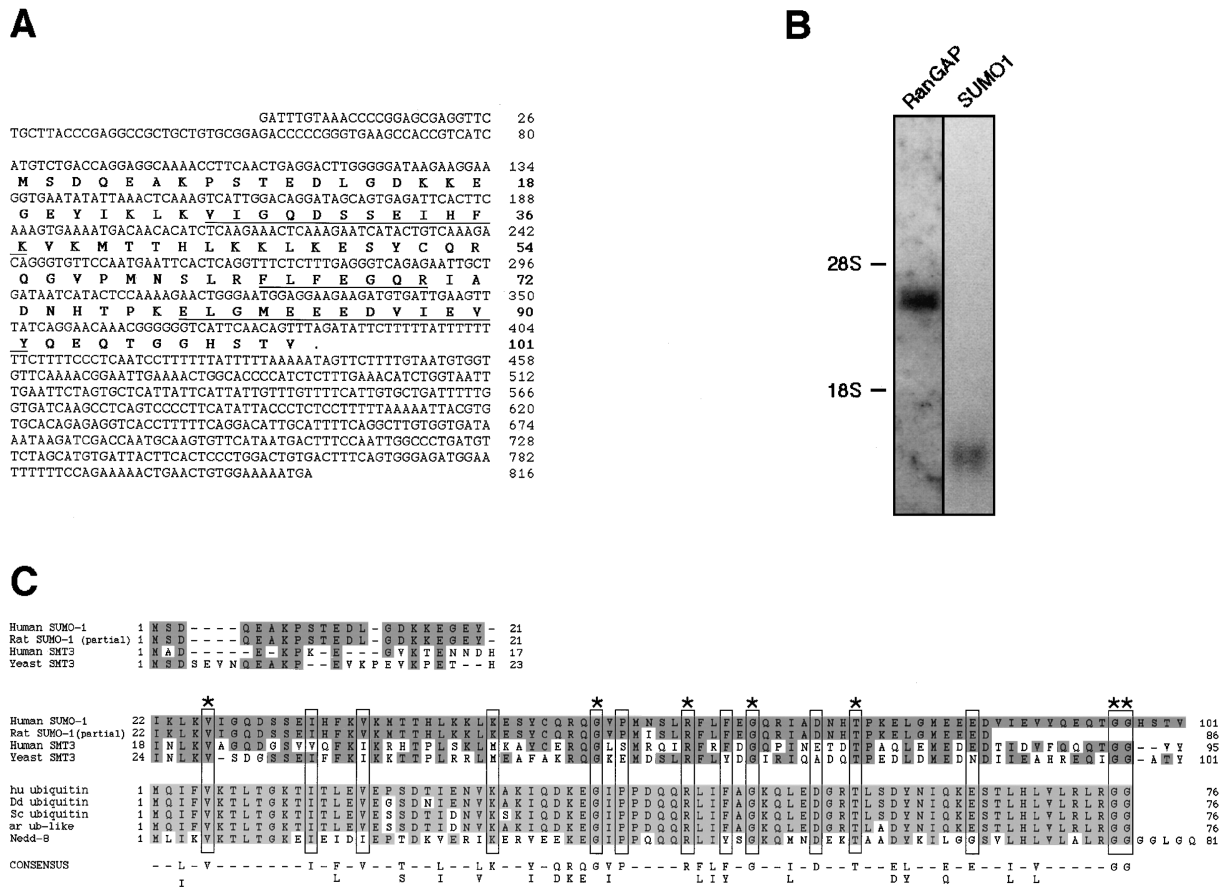


Figure 3. A Novel Ubiquitin-Related Protein (SUMO-1) Contains Peptide Sequence Present in the 90-kDa RanGAP1
(A) cDNA sequence and deduced amino acid sequence of SUMO-1. The ORF codes for a protein of 101 amino acids with a predicted molecular mass of 11.5 kDa. The three unique peptides detected in the 90-kDa RanGAP1 protein are present in the ORF (underlined; see also Table 1).
(B) Northern blot analysis of *RanGAP1* and *SUMO-1* mRNAs. HeLa total RNA (20 μg) was separated on a formaldehyde gel, transferred onto nitrocellulose, and probed with ³²P-labeled DNA fragments of *RanGAP1* or *SUMO-1*.
(C) SUMO-1 is a member of a ubiquitin-related protein family. The BLAST search algorithm was used to identify proteins homologous to SUMO-1. The following proteins were aligned: the deduced protein sequence of a partially sequenced rat EST cDNA clone that is virtually identical to human SUMO-1 (Rat SUMO-1, EST108203); human and *S. cerevisiae* SMT3; ubiquitins from human, *Dictyostelium discoideum*, *S. cerevisiae*, and *Arabidopsis thaliana*; and Nedd-8 from mouse. Dark shading, residues in rat SUMO-1 and the SMT3 proteins that are identical to corresponding positions of human SUMO-1. Light shading, residues in ubiquitins and Nedd-8 that are identical to human ubiquitin. Box, residues identical among human and rat SUMO-1 and ubiquitins. Asterisks, residues identical in all proteins compared. Consensus sequence below is defined by residues that are either identical or highly homologous among members of the SUMO-1, SMT3, and ubiquitin families.

sequence was missing from all the EST clones. This possibility was addressed by Northern blot analysis of total HeLa RNA with a 1.1 kb fragment of *RanGAP1* cDNA and a 430 bp fragment of the EST clones, including the entire ORF (Figure 3B). As reported previously for mouse *RanGAP1* (DeGregori et al., 1994), only a single band was detected for HeLa *RanGAP1*. Moreover, the only band obtained by hybridization with the EST fragment was similar to the size of the longest EST clone (1.42 kb). These data indicate that the *RanGAP1* sequence and the 90-kDa protein-specific sequence are encoded by two separate mRNAs, implying that the 90-kDa band observed after immunoprecipitation and SDS-PAGE contains a stable complex between the 70-kDa *RanGAP1* and the putative 11.5-kDa protein.

Using the basic local alignment search tool (BLAST) algorithm, we found that this protein (and a partially

sequenced EST cDNA encoding a nearly identical protein from rat) shows 18% identity to ubiquitin. Our database search revealed three additional proteins related both to the 11.5-kDa protein and to ubiquitin: the ubiquitin-like mouse protein Nedd8, of unknown function (Kumar et al., 1993), with 58% identity to ubiquitin and 20% identity to the 11.5-kDa protein; human SMT3 (Mannen et al., 1996), with 16% identity to ubiquitin and 47% identity to the 11.5-kDa protein; and *S. cerevisiae* SMT3 (Meluh and Koshland, 1995; GenBank accession number U27233), with 16% identity to ubiquitin and 52% identity to the 11.5-kDa protein. While the level of identity among the ubiquitin/11.5-kDa, ubiquitin/SMT3, and Nedd8/11.5-kDa pairs is very low, sequence alignment clearly revealed that these proteins are related. Of the 76 amino acid residues in ubiquitin, 32 (42%) are either identical or highly conserved in all proteins (Figure 3C,

consensus). Since the 11.5-kDa protein is functionally related to ubiquitin (see below), we have named it small ubiquitin-related modifier (SUMO-1).

SUMO-1 Converts the 70-kDa RanGAP1 to a 90-kDa Protein

The homology of the 11.5-kDa SUMO-1 to ubiquitin suggested that it might be involved in converting the 70-kDa RanGAP1 to the 90-kDa form through a posttranslational covalent modification. To address this question, we used affinity-purified α SUMO-1 antibodies in Western blot analysis of nuclear fractions (Figure 4A) and in immunoprecipitates of RanGAP1 from solubilized NEs (Figure 4B). SUMO-1 antibodies strongly react with 90-kDa RanGAP1 but not with 70-kDa RanGAP1, supporting the idea that 90-kDa RanGAP1 is modified with SUMO-1. Interestingly, while 90-kDa RanGAP1 is the major immunoreactive band in nuclei, α SUMO-1 antibodies detected three additional nuclear proteins with molecular masses of \sim 120 kDa and 140–150 kDa that are specifically enriched in the nuclear content fraction (Figure 4A, DNase supernatant).

Ubiquitination is accomplished by an ATP-dependent process (reviewed by Ciechanover, 1994; Hochstrasser, 1995) and can be achieved *in vitro* because cells contain an excess of the ubiquitin moiety. To determine whether SUMO-1 modification of RanGAP1 showed similar characteristics, we incubated recombinant RanGAP1 with a HeLa cell extract that had either been preincubated with ATP or depleted of ATP. Figure 4C shows that the 70-kDa recombinant RanGAP1 was shifted in a time-dependent fashion to a 90-kDa band in the cell extract containing ATP. This reaction was extremely rapid, as a significant fraction of the protein was already converted 10 s after mixing. Conversion was ATP dependent, as pretreatment of the cell extract with hexokinase-glucose (Figure 4C, minus ATP) prevented the shift almost completely. The apparent 20-kDa size shift is consistent with the addition of one SUMO-1 per RanGAP1, as recombinant SUMO-1 itself migrates with an apparent molecular mass of 17 kDa, both on SDS-PAGE and by molecular sieving (data not shown). Moreover, when GST-SUMO-1 (43 kDa) was added to the *in vitro* shift assay, some RanGAP1 was shifted to an apparent mass of \sim 110 kDa, consistent with the addition of one GST-SUMO-1 (data not shown). Western blot analysis with α SUMO-1 antibodies on a 1:1 mixture of 70- and 90-kDa protein prepared by incubation of recombinant RanGAP1 with HeLa extracts (Figure 4D) showed specific reaction with the 90-kDa band, but not with the 70-kDa species, demonstrating that the 90-kDa RanGAP1 contained SUMO-1.

RanGAP1 Is Localized Predominantly at the NPC

To localize the 70/90-kDa RanGAP1, we analyzed normal rat kidney (NRK) cells by double immunofluorescence staining with α RanGAP1 antibodies and with the NPC-specific RL1 monoclonal antibodies, which recognize a family of O-linked glycoproteins of the NPC (Snow et al., 1987). Immunofluorescence microscopy (Figure 5A) showed that like RL1, α RanGAP1 antibodies decorate predominantly the NE. However, in contrast with

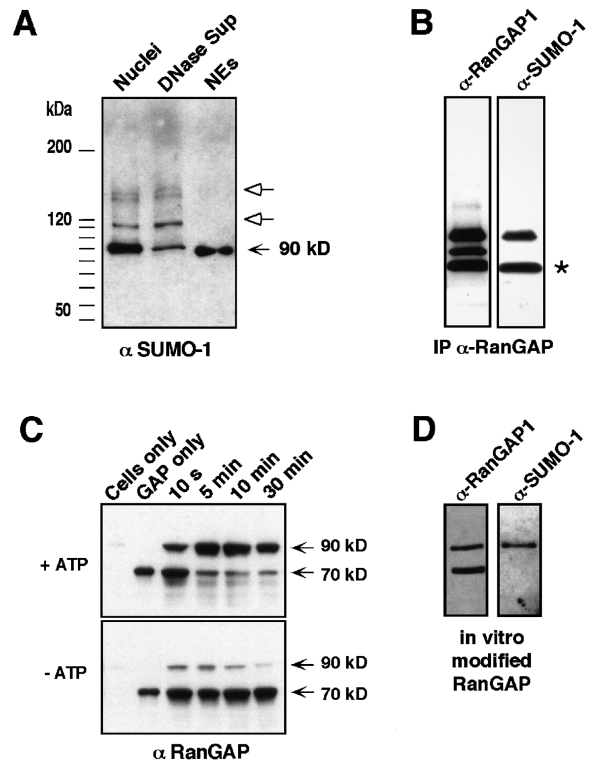


Figure 4. The 90-kDa RanGAP1 Is Formed by Covalent Modification of 70-kDa RanGAP1 with SUMO-1

(A) Antibodies raised against SUMO-1 react with a 90-kDa band in rat liver nuclei. Antibodies raised against recombinant SUMO-1 were used to probe rat liver nuclear fractions. Nuclei, DNase supernatant, and NEs were prepared as before (see Figure 2A) and subjected to immunoblotting. α SUMO-1 antibodies react with a 90-kDa band and with three additional bands (open arrows) that are released with the contents of nuclei (DNase Sup). (B) Immunoprecipitated 90-kDa RanGAP1 contains SUMO-1. NEs were solubilized and incubated with α RanGAP1 antibodies preadsorbed to Protein A beads. Antibody-antigen complexes were separated on a 5%–15% gradient gel and immunoblotted with α RanGAP1 and α SUMO-1 antibodies. Asterisk, IgG heavy chain. (C) Recombinant 70-kDa RanGAP1 can be shifted to the 90-kDa form in an ATP-dependent manner. HeLa cells were permeabilized with digitonin and preincubated for 30 min at room temperature with 1 mM ATP (plus ATP) or with hexokinase and glucose (minus ATP). Recombinant RanGAP1 was added and incubated at room temperature, and samples were mixed with SDS loading buffer at times indicated. Proteins were analyzed by immunoblotting with α RanGAP1 antibodies. (D) *In vitro* generated 90-kDa RanGAP1 contains SUMO-1. A mixture of 70-kDa and 90-kDa RanGAP1 was prepared as described in Experimental Procedures and analyzed by immunoblotting with α RanGAP1 and α SUMO-1 antibodies.

RL1, α RanGAP1 also stained the cytoplasm. The same staining pattern was obtained with α GAP-tail antibodies (data not shown). Cytoplasmic staining was lost when cells were permeabilized with digitonin prior to fixation (data not shown), indicating that the cytoplasmic pool of RanGAP1 is soluble. Confocal images of the cells (Figure 5B) showed nuclear rim staining in an equatorial view and punctate labeling in a nuclear surface view. This is virtually identical to the pattern of RL1 staining and suggests localization of RanGAP1 to NPCs. The

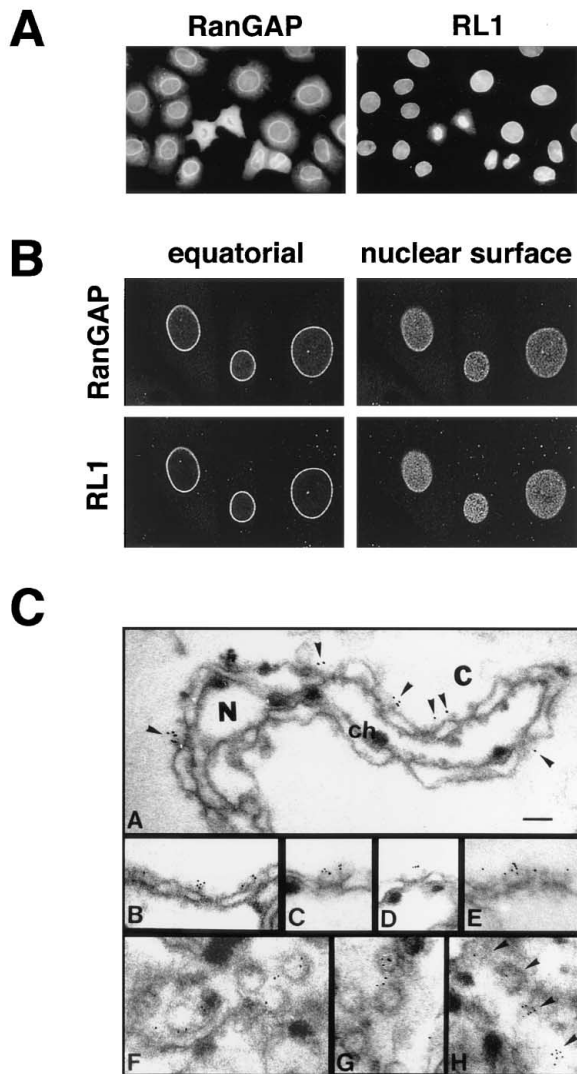


Figure 5. RanGAP1 Is Localized at the Cytoplasmic Surface of the NPC

(A) Detection of RanGAP1 in NRK cells by immunofluorescence microscopy. Cells were double stained with α RanGAP1 (left) and RL1 (right) and analyzed by light microscopy.

(B) Detection of RanGAP1 by confocal immunofluorescence microscopy of NRK cells. Cells were double stained with α RanGAP1 (top panels) and RL1 (bottom panels). Single sections through the equatorial plane (left) or nuclear surface plane (right) are shown.

(C) Immunogold localization of RanGAP1 in isolated rat liver NEs. Shown are thin section electron micrographs of isolated rat liver NEs displaying NPCs either in cross sections (A–E) or in tangential sections (F–H). Note that gold particles are found exclusively at the cytoplasmic side of NPCs (arrowheads). Cytoplasmic (C) and nuclear (N) faces of the NEs are easily distinguished by the presence of residual chromatin (ch) on the nucleoplasmic side.

Scale bar, 100 nm.

absence of cytoplasmic staining in optical sections obtained with confocal microscopy suggests that the cytoplasmic concentration of RanGAP1 is significantly lower than the concentration at the NE. This interpretation is consistent with the biochemical fractionation of rat liver, which revealed a strong enrichment of RanGAP1 in NEs (at least 100-fold over SN1; see Figure 2A).

Immunogold labeling of isolated rat liver NEs with α RanGAP1 antibodies (Figure 5C) resulted in the exclusive decoration of the cytoplasmic surface of the NE, specifically at NPCs. Most of the labeling was found in peripheral regions of the NPC, at a distance of $52 (\pm 14)$ nm ($n = 101$) from a plane bisecting the NPC into nucleoplasmic and cytoplasmic halves. This is very similar to the localization of the Ran-GTP-binding site at the NPC (Melchior et al., 1995a) and to the localization of RanBP2/Nup358 (Wu et al., 1995; Yokoyama et al., 1995), which is the putative site of initial substrate binding during nuclear import.

The 90-kDa SUMO-1–RanGAP1 Conjugate but Not 70-kDa RanGAP1 Stably Interacts with RanBP2

The similar localizations of RanGAP1 and RanBP2 at the cytoplasmic periphery of the NPC, and the presence of a >300-kDa protein in the immunoprecipitate of RanGAP1 from NEs (see Figure 2C, Coomassie P), suggested that RanGAP1 might be associated *in vivo* with the 358-kDa RanBP2. To address this possibility, we investigated whether these two polypeptides could be coimmunoprecipitated from samples of NEs solubilized in RIPA buffer by α RanGAP1 and α RanBP2 antibodies. Figure 6A shows that both α RanGAP1 and α RanBP2 antibodies precipitate the 90-kDa RanGAP1–SUMO-1 conjugate and RanBP2. This demonstrates that RanBP2 is indeed present in a stable complex with RanGAP1. Interestingly, this stable association seems to be specific for the 90-kDa modified RanGAP1 species, since α RanBP2 antibodies failed to precipitate the 70-kDa un-conjugated form of RanGAP1, even though a significant amount of 70-kDa protein was generated upon solubilization of the envelopes (Figure 6A, right; compare S and P). This suggests that the interaction between RanGAP1 and RanBP2 involves the SUMO-1 modification. This interaction is likely to be direct, as no additional specific bands could be detected in the α RanGAP1 immunoprecipitate (Figure 6A, Coomassie). Additional proteins present in the α RanBP2 immunoprecipitate are most likely proteolytic fragments of RanBP2, since this protein is extremely sensitive to proteolysis (Bischoff et al., 1995b, Melchior et al., 1995).

To investigate directly whether SUMO-1 modulates the binding to RanBP2, we carried out *in vitro* binding assays with modified and unmodified RanGAP1. We prepared a 1:1 mixture of these proteins by incubating recombinant RanGAP1 with digitonin cytosol and ATP under conditions in which only 50% of the protein was shifted to the 90-kDa species (as shown in Figure 4C, all recombinant RanGAP1 is competent to be shifted). To ensure stability of both forms and to rule out indirect binding via other cytosolic components, the RanGAP1 proteins were partially purified by ion exchange chromatography followed by molecular sieving. As shown by silver staining (Figure 6B, 70/90 mix), only a few additional proteins are present in the final 70/90 mixture. These proteins are unlikely to interact with RanGAP1, as they elute in different peak fractions from the 90-kDa RanGAP1. Moreover, the 70-kDa and the 90-kDa RanGAP1 elute very close together, and the 70-kDa protein in the 70/90 mix elutes in exactly the same position as untreated recombinant RanGAP1 (data not shown).

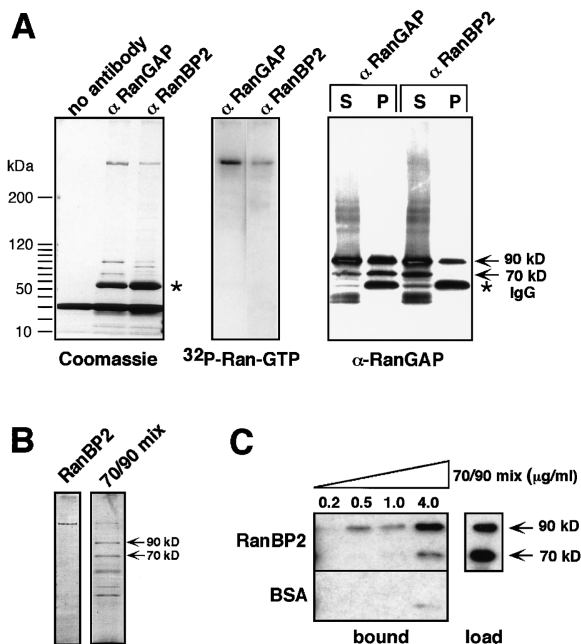


Figure 6. The 90 kDa Modified Form of RanGAP1 Is Stably Associated with RanBP2

(A) Immunoprecipitation from solubilized NEs using both α RanGAP1 and α RanBP2 antibodies was carried out as in Figure 2C. A control reaction with Protein A–Sepharose beads alone (no antibody) was carried out in parallel. Immunoprecipitates were resolved on a 5%–15% gradient SDS gel and analyzed by Coomassie blue staining (left) and blot overlay analysis with [32 P]GTP–Ran to identify RanBP2 (middle). Distribution of the 70-kDa and 90-kDa RanGAP1 was determined by immunoblotting of supernatants (S) and pellets (P) with α RanGAP1 antibodies (right). Asterisk, IgG heavy chain.

(B) RanBP2 and an in vitro generated mixture of 70-kDa and 90-kDa RanGAP1 were used in the binding assay. RanBP2 was purified from rat liver NEs, resolved on a 5%–15% SDS gel, and identified by silver staining. The 70/90 mix of RanGAP1 was generated from recombinant RanGAP1 (see Experimental Procedures), and the components of the partially purified mix were identified by silver staining.

(C) The 90-kDa RanGAP1 binds to immobilized RanBP2. The 70/90 mix was immunoblotted with α RanGAP1 antibodies to identify the relative ratio of the two forms of RanGAP1 (load). RanBP2 or BSA immobilized on microtiter wells was incubated with increasing amounts of the 70/90 mix. The bound fractions were washed, resuspended in SDS gel loading buffer, and analyzed by immunoblotting with α RanGAP1 antibodies (bound).

We purified the 358-kDa protein RanBP2 from rat liver to homogeneity by using affinity chromatography followed by ion-exchange chromatography (Figure 6B, RanBP2). The purified protein was bound to microtiter wells and incubated with increasing concentrations of the 70/90-kDa RanGAP1 mixture (0.2 μ g/ml to 4.0 μ g/ml, equivalent to 3–60 nM; Figure 6C). After washing, the bound fraction was solubilized with SDS gel loading buffer and analyzed by immunoblotting (Figure 6C, bound). As a specificity control, the 70/90-kDa mix was also incubated with BSA-coated microtiter wells. Even though the 70/90 mix contained more than 50% unmodified RanGAP1 (Figure 6C, load), nearly all of the RanGAP1 that bound to RanBP2 was of the 90-kDa modified form. This binding was not competed by addition of a

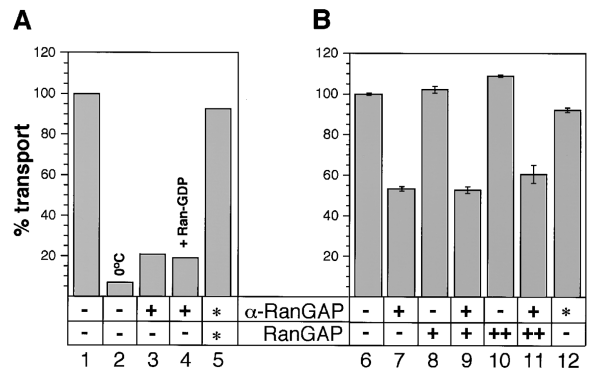


Figure 7. NE-Associated RanGAP1 Is Required for Nuclear Protein Import

(A) Complete transport reactions were incubated in the presence (3–5) or absence (1–2) of a final concentration of 0.5 mg/ml α RanGAP1 antibodies for 30 min at 4°C before initiation of nuclear protein import at 30°C. Lane 1, normal transport. Lane 2, ice control. Lane 3, antibody-inhibited transport. Lane 4, addition of 50 μ g/ml Ran-GDP to antibody-inhibited transport. Lane 5, antibodies preincubated (asterisk) with recombinant RanGAP1 (50 μ g/ml final concentration in the transport assay) for 15 min demonstrate specificity of the inhibition.

(B) Digitonin-permeabilized HeLa cells were incubated for 1 hr on ice in the presence (lanes 7, 9, 11, 12) or absence (lanes 6, 8, 10) of 0.5 mg/ml α RanGAP1 antibodies. Unbound antibodies were removed, and cytosol, substrate, and ATP-regenerating system were added before initiating nuclear protein import at 30°C. Lanes 8 and 9, addition of 2 μ g/ml recombinant RanGAP1 to the transport mix. Lanes 10 and 11, addition of 10 μ g/ml recombinant RanGAP1. Lane 12, antibodies preincubated (asterisk) with recombinant RanGAP1 (50 μ g/ml final concentration on the permeabilized cells) for 15 min prior to addition to the permeabilized cells demonstrate specificity of the inhibition. Mean values are shown; error bars indicate actual values of duplicate experiments.

100-fold excess of SUMO-1 (data not shown). The binding of the 70-kDa unmodified RanGAP1 to RanBP2-coated wells, observed primarily at the highest concentration tested (4.0 μ g/ml, equivalent to 60 nM), appeared to be largely or completely nonspecific, because similar amounts were also found in the BSA-coated wells.

RanBP2-Associated RanGAP1 Is Required for Nuclear Protein Import

The existence of a cytosolic pool of RanGAP1 (approximately 30%–40% of the total RanGAP1) raised the question of whether this pool has a specific role in nuclear protein import. It has been proposed that Ran-GDP is required at the cytoplasmic side of the NPC (Nehrbass and Blobel, 1996). According to this model, RanGAP1 might simply be required to recycle Ran-GDP. In this case, exogenously added Ran-GDP would be expected to relieve α RanGAP-mediated inhibition. As shown in Figure 7A, the addition of 50 μ g/ml Ran-GDP had no effect on antibody-inhibited nuclear protein import. However, since Ran is readily able to diffuse in and out of the nucleus (Melchior et al., 1995), we could not exclude the possibility that rapid exchange of GTP for GDP by nuclear RCC1 was reducing the effective concentration of exogenous Ran-GDP. To address this question, we performed a second experiment, shown in Figure 7B, in which only NPC-bound RanGAP1 was

inhibited by preincubation of permeabilized cells with the antibodies. Antibody-treated cells were washed to remove unbound antibodies, combined with untreated cytosol or cytosol plus recombinant RanGAP1, and used for transport assays. This pretreatment of cells led to a significant (~50%) inhibition of nuclear import, which could not be relieved by addition of either a 10- or a 50-fold excess of recombinant RanGAP1 over the inhibited NPC-associated RanGAP1. This experiment clearly demonstrates that inhibition of import by antibodies to RanGAP1 is not simply caused by depletion of Ran-GDP or accumulation of Ran-GTP, because recombinant RanGAP1 is very effective in converting Ran-GTP to Ran-GDP (see Figure 1B). The reduced level of inhibition in this case, compared with experiments where high concentrations of antibodies were present throughout the import reaction (see Figures 1B and 7A), is likely to be due to dissociation of antibodies during the transport reaction or to limited access of antibodies to RanGAP1 in the preincubation step. Transport inhibition by α RanGAP1 antibodies was also observed in reconstituted assays lacking cytosolic RanGAP1, in which cytosol was replaced with recombinant cytosolic factors (Ran-GDP, NTF2, p97, and Srp1 α). These results indicate that RanBP2-associated RanGAP1 is required for nuclear import, and that cytosolic RanGAP1 cannot substitute for this requirement.

Discussion

SUMO-1, a Novel Ubiquitin-Related Protein

We have identified a novel polypeptide of 101 amino acids (SUMO-1) that is covalently linked to RanGAP1 in an ATP-dependent reaction. SUMO-1 shows a low, but significant, homology to ubiquitin, a highly conserved 76-residue protein found in eukaryotes that is conjugated via its C-terminal carboxyl group to lysine ϵ -amino groups of acceptor proteins (reviewed by Ciechanover, 1994; Hochstrasser, 1995). The ATP-dependant ubiquitination reaction, which involves a cascade of enzymatic reactions, is best known for its ability to initiate regulated protein degradation by a complex called the 26S proteasome. Commitment of a target protein to the degradation pathway involves assembly of a polyubiquitin chain on the target, often via isopeptide bonds between lysine 48 of one ubiquitin and the C-terminus of the neighboring ubiquitin (Ciechanover, 1994). However, examples of metabolically stable ubiquitin conjugates containing a single ubiquitin moiety, such as Ub-histone H2A, have been documented, and it is becoming increasingly evident that the role of the ubiquitin modification is not limited to a degradation signal (reviewed by Hochstrasser, 1996).

This theme is extended by the present study, in which we demonstrate that SUMO-1 is a ubiquitin-related protein modifier that appears to be involved in protein targeting and not degradation. Immunoblot analysis indicates that at least three additional intranuclear proteins are modified with SUMO-1 or with a protein very closely related to it. Our database search revealed three proteins related to ubiquitin, the Nedd8 protein from mouse (Kumar et al., 1993), the human SMT3 (Mannen et al.,

1996), and the *S. cerevisiae* SMT3. No function has yet been established for these proteins, and we speculate that they may also function as covalent modifiers.

Stable Modification of RanGAP1 by SUMO-1

In contrast with most ubiquitinated proteins, RanGAP1 modified by SUMO-1 seems to be metabolically stable. No higher molecular mass RanGAP1 conjugates, indicative of polyubiquitination and a ubiquitin-mediated degradation pathway, can be detected in intact cells or upon *in vitro* modification. Moreover, the predominant site required for assembly of polyubiquitin chains on target proteins, lysine residue 48 in ubiquitin, is absent in SUMO-1. These findings suggest that modification of RanGAP1 by SUMO-1 does not target RanGAP1 for degradation.

Modified and unmodified forms of RanGAP1 are likely to be present in a dynamic equilibrium *in vivo*, as interconversion is possible *in vitro* (see Figures 2B and 4C). Complete conversion to the 70-kDa form occurs upon fractionation of cytosol or high salt extracts of NEs over molecular sieving columns, presumably owing to separation of free SUMO-1 protein (unpublished data). Our data suggest that both conjugating and cleaving enzymes are present in cell extracts. However, in total cell extracts, the modification of RanGAP1 is much more rapid than its demodification, suggesting that *in vivo* the RanGAP1-SUMO-1 conjugate is a long-lived species.

SUMO-1 Is Involved in Targeting RanGAP1 to the NPC Protein RanBP2

We found that RanGAP1 is highly concentrated at the NPC and forms a stable complex with RanBP2. Three lines of evidence argue that this interaction requires the modification of RanGAP1 with SUMO-1. First, when NEs are solubilized with RIPA buffer and a significant fraction of modified RanGAP1 becomes demodified, α RanBP2 antibodies coprecipitate only the modified RanGAP1. Second, when NEs are extracted with high salt (conditions that do not solubilize a significant amount of RanBP2), modified RanGAP1 distributes evenly between supernatant and pellet, while 70-kDa RanGAP1 is nearly completely soluble. Third, in binding assays with purified rat liver RanBP2 and a mixture of modified and unmodified RanGAP1, only modified RanGAP1 binds to RanBP2. Taken together, these data indicate that the ubiquitin-related modification of RanGAP1 serves to target RanGAP1 to RanBP2. Saitoh et al. (1996) recently reported that an 88-kDa protein that coimmunoprecipitates with RanBP2 from a *Xenopus laevis* egg extract contains peptide sequences found in RanGAP1 as well as some additional unique sequences. It seems likely that this 88-kDa protein is in fact modified RanGAP1.

RanBP2-Associated RanGAP1 Is Required in Nuclear Protein Import

Although the requirement for GTP hydrolysis by Ran during nuclear import is well established, the site of GTP hydrolysis has remained a matter of dispute. Models involving either single (Melchior et al., 1995a) or multiple sites (Rexach and Blobel, 1995; Nehrbass and Blobel,

1996; Görlich and Mattaj, 1996) of GTP hydrolysis have been proposed. The data presented here suggest that the localization of RanGAP1 at RanBP2 is essential for its function in nuclear protein import, as inhibition of NPC-bound RanGAP1 by antibodies to RanGAP1 leads to an inhibition of nuclear protein import that cannot be rescued by exogenously added RanGAP1. Furthermore, efficient *in vitro* import can be reconstituted when cytosol is replaced with soluble transport factors in the absence of soluble RanGAP1 (e.g., Görlich et al., 1995; our unpublished data). Taken together, these findings show that cytosolic RanGAP1 is not required for nuclear import, while RanBP2-bound RanGAP1 is essential. This strongly suggests that GTP hydrolysis by Ran at RanBP2 is an essential part of nuclear protein import. Together with our previous finding that Ran accumulates at RanBP2 when it cannot hydrolyze its GTP (Melchior et al., 1995), these data support a model in which nuclear import involves a single round of Ran-GTP hydrolysis at RanBP2. While we cannot rule out that GTP hydrolysis by Ran may also occur at other sites, there is currently no direct evidence to support this, as far as we know.

RanBP2 is localized at fibrils emanating from the cytoplasmic periphery of the NPC (Wu et al., 1995; Yokoyama et al., 1995), which are implicated in initial binding of transport substrates to the NPC (Panté and Aebi, 1996b). RanBP2 contains Ran-GTP-binding domains as well as FG repeat domains, which can interact with a complex containing NLS receptor, p97, and substrate *in vitro* (e.g., Hu et al., 1996). Several possible functions for Ran-GTP and the hydrolysis step can be envisioned. For example, the NLS receptor-substrate-p97 complex and Ran-GTP might initially interact with RanBP2 at the cytoplasmic fibrils (Melchior et al., 1995a, Panté and Aebi, 1996b). After receptor-substrate-p97 and RanGTP have bound to RanBP2, RanGAP1 would stimulate GTP hydrolysis by Ran to commit the transport complex to more distal steps of the import pathway. In another scenario, Ran-GTP might form a complex with p97 inside the nucleus during disassembly of a transport complex. The p97-Ran-GTP complex could then exit the nucleus and bind to RanBP2, where RanGAP1-induced GTP hydrolysis would release Ran-GDP from the complex and thereby allow RanBP2-bound p97 to interact with a NLS receptor-substrate complex. In any case, the data presented here strongly favor models of nuclear protein import in which the localization of RanGAP1 at the cytoplasmic periphery of the NPC imparts vectoriality to the import pathway.

Experimental Procedures

DNA Cloning and Northern Blot Hybridization

RanGAP1 cDNA obtained by reverse transcription of NIH 3T3 mRNA and subsequent polymerase chain reaction (PCR) was cloned into the pET-11d vector (Novagen). Amino acids 400-589 of the coding sequence were cloned into the pGEX-2T plasmid (Pharmacia) to create a GST-GAP-tail fusion protein, and amino acids 1592-1766 of RanBP2 were cloned into pGEX-2T to create a GST-RanBP2 fusion protein. A cDNA fragment encoding the ORF of SUMO-1 was obtained by PCR from the I. M. A. G. E. Consortium cDNA clone number 49768 and was cloned into pGEX-2T to create a GST-SUMO-1 fusion protein. I. M. A. G. E. Consortium cDNA clones (numbers 49768, 51818, and 199507; Lennon et al., 1996), containing the SUMO-1 ORF, were sequenced at the core facility of The Scripps

Research Institute. HeLa total RNA was prepared with TriReagent (Molecular Research Center, Incorporated). Northern blot hybridization was performed according to standard protocols. Radiolabeled probes were generated by using the full-length coding sequence for SUMO-1 or a 1.1 kb fragment of RanGAP1 as templates for random priming with the Prime-it II kit (Stratagene).

Expression and Purification of Recombinant Proteins

RanGAP1 was bacterially expressed as described for Ran (Melchior et al., 1995b). After lysozyme lysis the bacterial pellet was washed twice with buffer 1 (Melchior et al., 1995b), 1% Triton X-100, once with 2 M urea, 50 mM Tris-HCl (pH 7.4), and solubilized with 8 M urea. The supernatant was dialyzed against 50 mM Tris-HCl, 100 mM NaCl (pH 7.4), centrifuged at $100,000 \times g$ for 1 hr, applied to a Q-Sepharose column (Pharmacia) that had been washed with 200 mM NaCl, and eluted with 1 M NaCl. Final purification was achieved by molecular sieving (Superdex 200, Pharmacia) in transport buffer (TB; Melchior et al., 1995b). Expression and purification of GST-GAP-tail, GST-RanBP2, and GST-SUMO-1 fusion proteins followed standard procedures. Pure SUMO-1 was obtained by thrombin digestion of GST-SUMO-1 bound to glutathione beads and gel filtration of the resulting supernatant. Recombinant Ran/TC4 was expressed as described by Melchior et al. (1995b).

Antibodies

Rabbits were injected with 500 μ g of protein (RanGAP1, GAP-tail, RanBP2, or SUMO-1) emulsified with Titermax (Vaxcel, Incorporated). Boosts were with 200 μ g of protein emulsified with incomplete Freund's adjuvant. Antibodies were affinity purified from serum by adsorption to affinity columns containing recombinant protein and subsequent elution with 0.2 M acetic acid (pH 2.7), 0.5 M NaCl. RL1 monoclonal antibodies are described by Snow et al. (1987). Peroxidase-conjugated goat α rabbit immunoglobulin G (IgG) was from Pierce, rhodamine-conjugated donkey α rabbit IgG and FITC-conjugated goat α mouse IgG from Jackson ImmunoResearch, and 5-nm colloidal gold conjugated to goat α rabbit IgG from Zymed.

Preparation of Rat Liver NEs and Immunoprecipitation

NEs were prepared as described by Snow et al. (1987). For immunoprecipitation, NEs were solubilized at an OD₂₆₀ of 100 in RIPA buffer (50 mM Tris-HCl [pH 8.0], 150 mM NaCl, 1% Nonidet P-40, 0.5% deoxycholate, 0.1% SDS, 1 mM DTT, 0.1 mM PMSF, 1 μ g/ml each of leupeptin, pepstatin A, and aprotinin) for 2 hr on ice and centrifuged at $100,000 \times g$ for 30 min. Antibodies (10 μ g) (α RanGAP1 or α RanBP2) prebound to 5 μ l of protein A-Sepharose beads (Pierce) were added to each 100 OD of solubilized NEs and incubated overnight on ice. After three washes in RIPA buffer, antigen-antibody complexes were solubilized in SDS-PAGE loading buffer.

Immunoblotting, Indirect Immunofluorescence, and Immunogold Electron Microscopy

Detection of RanGAP1 on immunoblots was performed with 0.5 μ g/ml α RanGAP1 or α GAP-tail, 5 μ g/ml α SUMO-1, and 1 μ g/ml α RanBP2 antibodies in 5% milk powder in PBS, 0.2% Tween 20 for 1 hr at room temperature. Detection was by enhanced chemiluminescence (Amersham).

For indirect immunofluorescence using light or confocal microscopy, NRK cells were fixed on coverslips with 3.7% formaldehyde in PBS and processed as described by Melchior et al. (1995b). Antibodies were used at 0.5 μ g/ml (α RanGAP1) and at a 1:200 dilution (RL1 ascites fluid). For immunogold electron microscopy, rat liver NEs (200 OD₂₆₀/ml) were incubated with 10 μ g/ml α RanGAP1 in PBS/Mg, 0.5% BSA for 2 hr at room temperature, and processed as described by Melchior et al. (1995a).

Blot Overlay and GAP Assays

Recombinant Ran was loaded with [α -³²P]GTP and blot overlays with [α -³²P]Ran-GTP were carried out as described by Melchior et al. (1995a). GAP assays were initiated by adding 2 μ l of [α -³²P]Ran-GTP (40 μ g/ml final concentration) to 8 μ l of recombinant RanGAP1 (1 μ g/ml final concentration) in TB in the absence or presence of 20 μ g/ml α RanGAP1 or 100 μ g/ml of α GAP-tail antibodies. At the

times indicated, 1- μ l samples were spotted onto cellulose polyethyleneimine thin-layer chromatography plates (J. T. Baker) and chromatographed in 1.0 M formic acid, 0.5 M LiCl. Amounts of GTP and GDP were determined with a Phosphorimager (Molecular Dynamics), and percent GTP was calculated.

Nuclear Import Assays and In Vitro Modification of RanGAP1

In vitro nuclear import into HeLa cells followed protocols described by Paschal and Gerace (1995). For in vitro modification of RanGAP1, HeLa cells were permeabilized with digitonin at 4×10^7 cells/ml and with 0.07% digitonin. ATP (1 mM) or 400 U/ml hexokinase plus 5 mM glucose (to deplete cellular ATP) were added to the cell lysate, which was then incubated 30 min on ice. Reactions received 4 μ g/ml recombinant RanGAP1, were incubated at room temperature, and were quenched by the addition of $2 \times$ SDS loading buffer.

A 1:1 mixture of 70-kDa and 90-kDa RanGAP1 was prepared by incubating 50 μ g of recombinant RanGAP1 for 10 min at room temperature in 1.8 ml of digitonin supernatant (from a $200 \times g$, 5-min supernatant of 7×10^7 cells) and ATP. The mixture was diluted 10-fold with ice-cold TB, 300 mM NaCl, incubated with Q-Sepharose beads, washed, and eluted with 1 M NaCl in TB. The 70/90-kDa mix was further purified by gel filtration (S200-FPLC, Pharmacia). The 70- and 90-kDa RanGAP1 eluted at an apparent molecular mass of ~ 120 kDa, similar to the behavior of pure recombinant RanGAP1 (unpublished data) and RanGAP1 purified from HeLa cells (Bischoff et al., 1994).

Binding Assay

The 358 kDa RanBP2 was purified from rat liver NEs by Ran-affinity chromatography (adapted from protocols described by Saitoh and Dasso [1995]) and a Mono Q FPLC column. Microtiter plates were coated with 20 ng of RanBP2 per well and blocked overnight with 3% BSA, 0.05% Tween 20 in PBS. After washing with TB, 0.05% Tween 20, 2% BSA, increasing concentrations of the 70/90 RanGAP1 mixture were added and incubated at room temperature for 1 hr. The wells were washed four times and extracted with SDS-PAGE loading buffer. Samples were analyzed by immunoblotting with α RanGAP1.

Acknowledgments

We are grateful to Dr. C. Fritze, Dr. A. Dickmanns, Dr. S. Lyman, and A. Sapphire for critical reading of the manuscript. We would also like to thank Dr. K. Furukawa for providing NIH 3T3 mRNA, and Drs. T. Nishimoto and N. Yokoyama for providing a partial cDNA clone of *RanBP2*. This work was supported by postdoctoral fellowships from the Jane Coffin Childs Memorial Fund for Medical Research to R. M., the Human Frontiers in Science Program (HFSP) to C. D., and an American Cancer Society (California division) Senior Fellowship, number 1-15-95, to F. M., as well as by grants from the National Institutes of Health and HFSP to L. G. We also acknowledge support from the Lucille P. Markey Charitable Trust.

Received August 16, 1996; revised November 14, 1996.

References

Bastos, R., Pante, N., and Burke, B. (1995). Nuclear pore complex proteins. *Int. Rev. Cytol.* 162B, 257-302.

Becker, J., Melchior, F., Gerke, V., Bischoff, F.R., Ponstingl, H., and Wittinghofer, A. (1995). *RNA1* encodes a GTPase-activating protein specific for Gsp1p, the Ran/TC4 homologue of *Saccharomyces cerevisiae*. *J. Biol. Chem.* 270, 11860-11865.

Bischoff, F.R., and Ponstingl, H. (1991). Catalysis of guanine nucleotide exchange on Ran by the mitotic regulator RCC1. *Nature* 354, 80-82.

Bischoff, F.R., Klebe, C., Kretschmer, J., Wittinghofer, A., and Ponstingl, H. (1994). RanGAP1 induces GTPase activity of nuclear Ras-related Ran. *Proc. Natl. Acad. Sci. USA* 91, 2587-2591.

Bischoff, F.R., Krebber, H., Kempf, T., Hermes, I., and Ponstingl, H.

(1995a). Human RanGTPase-activating protein RanGAP1 is a homologue of yeast Rna1p involved in mRNA processing and transport. *Proc. Natl. Acad. Sci. USA* 92, 1749-1753.

Bischoff, F.R., Krebber, H., Smirnova, E., Dong, W., and Ponstingl, H. (1995b). Co-activation of RanGTPase and inhibition of GTP dissociation by Ran-GTP binding protein RanBP1. *EMBO J.* 14, 705-715.

Bourne, H.R., Sanders, D.A., and McCormick, F. (1990). The GTPase superfamily: a conserved switch for diverse cell functions. *Nature* 348, 125-132.

Ciechanover, A. (1994). The ubiquitin-proteasome proteolytic pathway. *Cell* 79, 13-21.

Corbett, A.H., Koepp, D.M., Schlenstedt, G., Lee, M.S., Hopper, A.K., and Silver, P.A. (1995). Rna1p, a Ran/TC4 GTPase activating protein, is required for nuclear import. *J. Cell Biol.* 130, 1017-1026.

Dasso, M., Seki, T., Ohba, T., and Nishimoto, T. (1994). A mutant form of the Ran/TC4 protein disrupts nuclear function in *Xenopus laevis* egg extracts by inhibiting the RCC1 protein, a regulator of chromosome condensation. *EMBO J.* 13, 5732-5744.

DeGregori, J., Russ, A., von Melchner, H., Rayburn, H., Priyaranjan, P., Jenkins, N.A., Copeland, N.G., and Ruley, H.E. (1994). A murine homolog of the yeast *RNA1* gene is required for postimplantation development. *Genes Dev.* 8, 265-276.

Floer, M., and Blobel, G. (1996). The nuclear transport factor karyopherin beta binds stoichiometrically to Ran-GTP and inhibits the Ran GTPase activating protein. *J. Biol. Chem.* 271, 5313-5316.

Görlich, D., and Mattaj, I.W. (1996). Nucleocytoplasmic transport. *Science* 271, 1513-1518.

Görlich, D., Vogel, F., Mille, A.D., Hartmann, E., and Laskey, R.A. (1995). Distinct functions for the two importin subunits in nuclear protein import. *Nature* 377, 246-248.

Hochstrasser, M. (1995). Ubiquitin, proteasomes, and the regulation of intracellular protein degradation. *Curr. Opin. Cell Biol.* 7, 215-223.

Hochstrasser, M. (1996). Protein degradation or regulation: Ub the judge. *Cell* 84, 813-815.

Hopper, A.K., Traglia, H.M., and Dunst, R.W. (1990). The yeast *RNA1* gene product necessary for RNA processing is located in the cytosol and apparently excluded from the nucleus. *J. Cell Biol.* 111, 309-321.

Hu, T., Guan, T., and Gerace, L. (1996). Molecular and functional characterization of the p62 complex, an assembly of nuclear pore complex glycoproteins. *J. Cell Biol.* 134, 589-601.

Kumar, S., Yoshida, Y., and Noda, M. (1993). Cloning of a cDNA which encodes a novel ubiquitin-like protein. *Biochem. Biophys. Res. Commun.* 195, 393-399.

Lennon, G.G., Auffray, C., Polymeropoulos, M., and Soares, M.B. (1996). The I.M.A.G.E. consortium: an integrated molecular analysis of genomes and their expression. *Genomics* 33, 151-152.

Mannen, H., Tseng, H.M., Cho, C.L., and Li, S.S. (1996). Cloning and expression of human homolog *HSMT3* to yeast *SMT3* suppressor of *MIF2* mutations in a centromere protein gene. *Biochem. Biophys. Res. Commun.* 222, 178-180.

Melchior, F., and Gerace, L. (1995). Mechanisms of nuclear protein import. *Curr. Opin. Cell Biol.* 7, 310-318.

Melchior, F., Paschal, B., Evans, J., and Gerace, L. (1993a). Inhibition of nuclear protein import by nonhydrolyzable analogues of GTP and identification of the small GTPase Ran/TC4 as an essential transport factor. *J. Cell Biol.* 123, 1649-1659.

Melchior, F., Weber, K., and Gerke, V. (1993b). A functional homologue of the *RNA1* gene product in *Schizosaccharomyces pombe*: purification, biochemical characterization, and identification of a leucine-rich repeat motif. *Mol. Biol. Cell* 4, 569-581.

Melchior, F., Guan, T., Yokoyama, N., Nishimoto, T., and Gerace, L. (1995a). GTP hydrolysis by Ran occurs at the nuclear pore complex in an early step of protein import. *J. Cell Biol.* 131, 571-581.

Melchior, F., Sweet, D.J., and Gerace, L. (1995b). Analysis of Ran/TC4 function in nuclear protein import. *Methods Enzymol.* 257, 279-291.

Meluh, P.B., and Koshland, D. (1995). Evidence that the *MIF2* gene of *Saccharomyces cerevisiae* encodes a centromere protein with

- homology to the mammalian centromere protein CENP-C. *Mol. Biol. Cell* 6, 793–807.
- Moore, M.S., and Blobel, G. (1993). The GTP-binding protein Ran/TC4 is required for protein import into the nucleus. *Nature* 365, 661–663.
- Nehrbass, U., and Blobel, G. (1996). Role of the nuclear transport factor p10 in nuclear import. *Science* 272, 120–122.
- Ohtsubo, M., Kai, R., Furuno, N., Sekiguchi, T., Sekiguchi, M., Hayashida, M., Kuma, K., Miyata, T., Fukushige, S., Murotsu, T., Matsu-
bara, K., and Nishimoto, T. (1987). Isolation and characterization of the active cDNA of the human cell cycle gene (*RCC1*) involved in the regulation of onset of chromosome condensation. *Genes Dev.* 1, 585–593.
- Panté, N., and Aebi, U. (1996a). Toward the molecular dissection of protein import into nuclei. *Curr. Opin. Cell Biol.* 8, 397–406.
- Panté, N., and Aebi, U. (1996b). Sequential binding of import ligands to distinct nucleopore regions during their nuclear import. *Science* 273, 1729–1732.
- Paschal, B.M., and Gerace, L. (1995). Identification of NTF2, a cytosolic factor for nuclear import that interacts with nuclear pore complex protein p62. *J. Cell Biol.* 129, 925–937.
- Paschal, B.M., Delphin, C., and Gerace, L. (1996). Nucleotide specific interaction of Ran/TC4 with nuclear transport factor NTF2 and p97. *Proc. Natl. Acad. Sci. USA* 93, 7679–7683.
- Rexach, M., and Blobel, G. (1995). Protein import into nuclei: association and dissociation reactions involving transport substrate, transport factors, and nucleoporins. *Cell* 83, 683–692.
- Rout, M.P., and Wentz, S.R. (1994). Pores for thought: nuclear pore complex proteins. *Trends Cell Biol.* 4, 357–365.
- Saitoh, H., and Dasso, M. (1995). The RCC1 protein interacts with Ran, RanBP1, hsc70, and a 340-kDa protein in *Xenopus* extracts. *J. Biol. Chem.* 270, 10658–10663.
- Saitoh, H., Cooke, C.A., Burgess, W.H., Earnshaw, W.C., and Dasso, M. (1996). Direct and indirect association of the small GTPase Ran with nuclear pore proteins and soluble transport factors: studies in *Xenopus laevis* egg extracts. *Mol. Biol. Cell* 7, 1319–1334.
- Sazer, S. (1996). The search for the primary function of the Ran GTPase continues. *Trends Cell Biol.* 6, 81–85.
- Snow, C.M., Senior, A., and Gerace, L. (1987). Monoclonal antibodies identify a group of nuclear pore complex glycoproteins. *J. Cell Biol.* 104, 1143–1156.
- Sweet, D.J., and Gerace, L. (1995). Taking from the cytoplasm and giving to the pore: soluble transport factors in nuclear protein import. *Trends Cell Biol.* 5, 444–447.
- Sweet, D.J., and Gerace, L. (1996). A GTPase distinct from Ran is involved in nuclear protein import. *J. Cell Biol.* 133, 971–983.
- Traglia, H.M., Atkinson, N.S., and Hopper, A.K. (1989). Structural and functional analyses of *Saccharomyces cerevisiae* wild-type and mutant *RNA1* genes. *Mol. Cell. Biol.* 9, 2989–2999.
- Wu, J., Matunis, M.J., Kraemer, D., Blobel, G., and Coutavas, E. (1995). Nup358, a cytoplasmically exposed nucleoporin with peptide repeats, Ran-GTP binding sites, zinc fingers, a cyclophilin A homologous domain, and a leucine-rich region. *J. Biol. Chem.* 270, 14209–14213.
- Yokoyama, N., Hayashi, N., Seki, T., Panté, N., Ohba, T., Nishii, K., Kuma, K., Hayashida, T., Miyata, T., Aebi, U., Fukui, M., and Nishimoto, T. (1995). A giant nucleopore protein that binds Ran/TC4. *Nature* 376, 184–188.

GenBank Accession Number

The accession number for the sequence reported in this paper is U67122.

RanGTP Targets p97 to RanBP2, a Filamentous Protein Localized at the Cytoplasmic Periphery of the Nuclear Pore Complex

Christian Delphin, Tinglu Guan, Frauke Melchior, and Larry Gerace*

Department of Cell Biology, The Scripps Research Institute, La Jolla, California 92037

Submitted July 14, 1997; Accepted September 10, 1997

Monitoring Editor: Suzanne R. Pfeffer

RanBP2, a protein containing FG repeat motifs and four binding sites for the guanosine triphosphatase Ran, is localized at the cytoplasmic periphery of the nuclear pore complex (NPC) and is believed to play a critical role in nuclear protein import. We purified RanBP2 from rat liver nuclear envelopes and examined its structural and biochemical properties. Electron microscopy showed that RanBP2 forms a flexible filamentous molecule with a length of ~36 nm, suggesting that it comprises a major portion of the cytoplasmic fibrils implicated in initial binding of import substrates to the NPC. Using *in vitro* assays, we characterized the ability of RanBP2 to bind p97, a cytosolic factor implicated in the association of the nuclear localization signal receptor with the NPC. We found that RanGTP promotes the binding of p97 to RanBP2, whereas it inhibits the binding of p97 to other FG repeat nucleoporins. These data suggest that RanGTP acts to specifically target p97 to RanBP2, where p97 may support the binding of an nuclear localization signal receptor/substrate complex to RanBP2 in an early step of nuclear import.

INTRODUCTION

In eukaryotic cells, molecular transport between the cytoplasm and the nucleus is mediated by the nuclear pore complex (NPC), a supramolecular structure of ~125 MDa that spans the nuclear envelope. The framework of the NPC consists of nucleoplasmic and cytoplasmic rings flanking eight central spokes, which surround a gated channel involved in the signal-mediated transport of macromolecules (Hinshaw *et al.*, 1992). In addition, eight fibrils, 30–50 nm in length, emanate from the cytoplasmic ring (Ris, 1991; Jarnik and Aebi, 1991; Goldberg and Allen, 1993), and eight fibrils, 50–100 nm in length, extend into the nucleus from the nucleoplasmic ring (for review see Panté and Aebi, 1996a). Metabolites and small molecules cross the NPC by passive diffusion, whereas most macromolecules appear to be transported by signal-dependent, active processes. The signals that specify nuclear protein import (nuclear localization sequences or NLS) are most commonly short stretches of basic

amino acid sequences (for review see Dingwall and Laskey, 1991), although at least one additional class of protein NLS is known to exist (Michael *et al.*, 1995; Pollard *et al.*, 1996).

The nuclear import of proteins containing basic type NLS has been characterized in considerable detail (for reviews see Melchior and Gerace, 1995; Görlich and Mattaj, 1996; Panté and Aebi, 1996a; Nigg, 1997). It is a multistep process that involves the binding or “docking” of transport substrates at the cytoplasmic fibrils of the NPC, followed by their movement to the central gated channel and translocation into the nuclear interior. These events are orchestrated by interactions between soluble import factors and components of the NPC. Nuclear protein import in digitonin-permeabilized mammalian cells can be reconstituted with four cytosolic factors: the NLS receptor, p97, Ran, and NTF2. The NLS receptor (also called importin α and karyopherin α) recognizes NLS-containing import substrates in the cytosol and carries them into the nucleus; after dissociation of the substrate in the nucleus, the NLS receptor is subsequently recycled back to the cytoplasm (reviewed in Sweet and Gerace, 1995;

*Corresponding author.

Görlich and Mattaj, 1996; Nigg, 1997). The association of the cytosolic NLS receptor/substrate complex with the NPC during the import process appears to involve p97 (also known as importin β and karyopherin β), which directly interacts with the NLS receptor (Adam and Adam, 1994; Görlich *et al.*, 1994; Chi *et al.*, 1995; Görlich *et al.*, 1995a, 1995b) as well as with a number of NPC proteins containing FG (phenylalanine, glycine) repeats (Iovine *et al.*, 1995; Kraemer *et al.*, 1995; Moroianu *et al.*, 1995b; Radu *et al.*, 1995b; Hu *et al.*, 1996). FG repeat nucleoporins are localized in many regions of the NPC and are thought to represent sites for the binding of the substrate/NLS receptor complex during its progressive movement from the cytoplasmic to the nuclear side of the NPC.

The small guanosine triphosphatase Ran/TC4 (Melchior *et al.*, 1993; Moore and Blobel, 1993) and NTF2/p10 (Moore and Blobel, 1994; Paschal and Gerace, 1995) are suggested to promote the vectorial movement of the transport substrate/NLS receptor complex through the NPC, but the functions of these proteins are not well understood. Ran acts as a molecular switch that cycles between guanosine triphosphate (GTP)- and guanosine diphosphate (GDP)-bound forms. The nucleotide state of Ran is regulated by its guanine nucleotide exchange factor RCC1 (Ohtsubo *et al.*, 1987; Bischoff and Ponstingl, 1991a, 1991b), and its guanosine triphosphatase-activating protein RanGAP1 (Bischoff *et al.*, 1994, 1995a). RCC1 is localized in the nucleoplasm (Ohtsubo *et al.*, 1989), whereas RanGAP1 is localized in the cytosol and on the cytoplasmic surface of the NPC (Matunis *et al.*, 1996; Mahajan *et al.*, 1997). The differential nucleocytoplasmic localizations of these two regulators is likely to be of key importance for the vectoriality of the nuclear import pathway.

Ran binds to three additional cytosolic proteins that may contribute to its transport functions: RanBP1, NTF2, and p97. The GTP-bound form of Ran binds to p97 (Rexach and Blobel, 1995; Floer and Blobel, 1996) as well as to RanBP1 (Bischoff *et al.*, 1995b), a 28-kDa protein that is suggested to have a direct role in nucleocytoplasmic transport (Schlenstedt *et al.*, 1995; Chi *et al.*, 1996; Lounsbury *et al.*, 1996; Richards *et al.*, 1996). The GDP-bound form of Ran interacts with NTF2 (Nehrbass and Blobel, 1996; Paschal *et al.*, 1996) as well as with a complex containing RanBP1 and p97 (Chi *et al.*, 1996, 1997). The precise stages in the nuclear transport cycle at which these nucleotide-specific interactions of Ran take place remain controversial (Melchior *et al.*, 1995; Rexach and Blobel, 1995; Görlich *et al.*, 1996).

The initial binding of transport substrate to the NPC during nuclear import is proposed to occur at RanBP2 (Melchior *et al.*, 1995), which is localized at the cytoplasmic fibrils of the NPC (Wilken *et al.*, 1995; Wu *et al.*, 1995; Yokoyama *et al.*, 1995). RanBP2 is a large

protein of 358 kDa that contains a number of distinct structural domains including four RanGTP-binding regions, several areas with FG repeat motifs, a zinc-finger domain, a leucine-rich region, and a cyclophilin-like domain (Wu *et al.*, 1995; Yokoyama *et al.*, 1995). However, the potential roles of these various domains of RanBP2 in the nuclear import process have yet to be defined. The FG repeat domains of some other nucleoporins mediate an interaction with p97 *in vitro* (Iovine *et al.*, 1995; Kraemer *et al.*, 1995; Radu *et al.*, 1995b; Hu *et al.*, 1996) and may serve a similar function in RanBP2. Consistent with this possibility RanBP2 is able to bind to p97 in a blot overlay assay (Moroianu *et al.*, 1995b).

The four RanGTP-binding domains of RanBP2 are 46–60% identical to the RanGTP-binding domain of RanBP1 (Yokoyama *et al.*, 1995). The binding of RanGTP to RanBP2 has not yet been characterized and may be very different from the binding of RanGTP to RanBP1. This is because of the sequence differences between the RanGTP-binding domains of RanBP1 and RanBP2 and because of the large surrounding regions in which the RanGTP-binding domains of RanBP2 are embedded. The presence of both RanGTP-binding domains and FG repeat domains in RanBP2 suggests that it plays a more complex role in nuclear import than the other nucleoporins.

Several lines of evidence indicate that binding and hydrolysis of RanGTP at RanBP2 are required for transport. First, when nuclear import is inhibited by nonhydrolyzable GTP analogues, Ran accumulates at the cytoplasmic fibrils of the NPC, at a site coincident with the localization of RanBP2 (Melchior *et al.*, 1995). In addition, the NPC-bound RanGAP1 is tightly associated with RanBP2, and binding of antibodies to this population of RanGAP1 strongly inhibits nuclear protein import (Mahajan *et al.*, 1997). This inhibition cannot be relieved by the addition of active cytosolic RanGAP1, implying that the localization of RanGAP1 at RanBP2 is central to the function of RanGAP1 in import and that RanGAP1 does not exist solely to generate cytosolic RanGDP (Mahajan *et al.*, 1997). However, the lack of purified RanBP2 has thwarted any detailed characterization of its interaction with nuclear import factors and its putative role in nuclear import.

Here we present a procedure for purifying RanBP2 from rat liver nuclear envelopes. We present structural data suggesting that RanBP2 is the primary component of the cytoplasmic fibrils of the NPC, which may undergo conformational changes to carry the transport substrate from the periphery of the NPC to the central channel. We have biochemically characterized the interaction of RanBP2 with Ran and p97 and demonstrate that RanGTP acts in selectively targeting p97 to RanBP2, where p97 may support the binding of a

substrate/NLS-receptor complex to RanBP2 in an early step of nuclear import at the NPC.

MATERIALS AND METHODS

RanBP2 Purification from Rat Liver Nuclei

RanBP2 was purified from 2000 OD₂₈₀ of salt-washed rat liver nuclear envelopes (NE). NE were solubilized for 2 h in 40 ml Buffer A (20 mM Tris-HCl, pH 8.8, 2% Triton X-100, 1 M NaCl, 2 mM dithiothreitol (DTT), and 5 µg/ml of each of the following protease inhibitors: aprotinin, leupeptin, pepstatin, E64, Pefabloc). Solubilized proteins were diluted 10-fold in buffer B (50 mM HEPES, pH 7.4, 2 mM DTT, protease inhibitors) and centrifuged at 100 000 × g for 1 h. The supernatant was incubated overnight with Ran-coated agarose beads (see below). The beads were washed four times with buffer B plus 0.2% Triton X-100, once with buffer B plus 0.2% Triton X-100 and 0.1% Empigen BB, and once with buffer C (20 mM HEPES, pH 7.4, 110 mM KOAc, 2 mM MgOAc, 1 mM EGTA). Proteins were eluted with buffer C plus 10 mM EDTA, 0.2 M NaCl, and 1% Empigen BB. RanBP2 was further purified by fast protein liquid chromatography (FPLC) using a Mono-Q column in 50 mM HEPES, 1% Empigen BB, 2 mM DTT, and eluted with a 100–700 mM NaCl gradient. Fractions (200 µl) were analyzed by SDS-PAGE and silver staining. Fractions containing RanBP2 were pooled, and aliquots were stored at –70°C. During fractionation, protein concentrations were estimated using the Bio-Rad protein assay (Bio-Rad, Richmond, CA) and Coomassie blue staining of SDS-PAGE using bovine serum albumin (BSA) as a standard. Yield of RanBP2 purification was determined by comparative Western blots.

Preparation of Ran-coated Agarose Beads for RanBP2 Purification

The coding sequence of 86 C-terminal amino acids of the bacterial biotin carboxy carrier protein (BCCP; Chapman-Smith *et al.*, 1994) were amplified by polymerase chain reaction from *Escherichia coli* and fused to the N-terminal end of the Ran cDNA. The construct was introduced into the pGEX-KG vector (Pharmacia LKB, Piscataway, NJ) in which the glutathione S-transferase (GST) coding sequence at the *Eco*NI/*Bam*HI sites has been deleted. BCCP-Ran expression in DH5α was induced at 37°C with 0.1 mM isopropyl-β-D-thiogalactopyranoside for 14 h in Luria-Bertani medium. The cells (500 ml) were then harvested at 6000 × g, 4°C, for 30 min and washed in lysis buffer (50 mM Tris-HCl, pH 8.0, 200 mM NaCl, 1 mM MgCl₂, 1 mM EGTA, 2 mM DTT, 1 µg/ml phenylmethylsulfonylfluoride, 2 µg/ml aprotinin, leupeptin, and pepstatin) and centrifuged. The pellet was then resuspended in 20 ml lysis buffer and frozen at –70°C. The frozen cells were thawed at room temperature and lysed with 1 mg/ml of lysozyme for 1 h at 4°C. Cell debris was pelleted at 100 000 × g for 1 h. Triton X-100 was added to the supernatant at 1% final concentration, and the solution was incubated with 4 ml of streptavidin-agarose beads (Sigma Chemical, St. Louis, MO) for 4 h at 4°C. The beads were then washed four times with 1% Triton X-100 in lysis buffer and twice with 50 mM HEPES, pH 7.4, 2 mM DTT. The bead-bound Ran was loaded with GDP by incubation for 30 min at 30°C with 200 µM GDP in 50 mM HEPES, pH 7.4, 2 mM DTT, 10 mM EDTA. The reaction was stopped at 4°C by addition of 20 mM MgCl₂, and the beads were washed in 50 mM HEPES, pH 7.4, 2 mM DTT, 1 mM MgCl₂.

Expression of Recombinant Proteins

Recombinant proteins were expressed in *E. coli* BL21 (DE3) and purified as described by Melchior *et al.* (1995) for Ran or as described by Hu *et al.* (1996) for GST-p97, (His)₆-p97, and (His)₆-SRP1.

Micro Plate Assay

Microtiter plates were coated with 2.5 ng purified RanBP2 or 25 ng GST-p62 per well by incubation for 24 h in coating buffer (phosphate-buffered saline [PBS] plus 4 mM DTT and 2 µg/ml of the protease inhibitors [E64, phenylmethylsulfonylfluoride, aprotinin, leupeptin, and pepstatin]). After coating, the plates were incubated overnight with binding buffer (3% BSA and 0.1% Tween 20 in coating buffer). Binding reactions involving Ran and/or 6xHis-p97 were carried out for 1 h at room temperature with 100 µl/well of the indicated protein, and the wells were subsequently washed three times with binding buffer without BSA. For analysis of p97 binding, proteins were cross-linked for 15 min with 1 mg/ml EDC (Pierce Chemical, Rockford, IL) in the same buffer. The wells were then washed for 20 min with PBS-T (PBS, 0.2% Tween 20), 10 min with PBS-T plus 100 mM ethanolamine, and 10 min with PBS-T plus 3% BSA. The bound 6xHis-tagged p97 was detected using antiXpress antibody (Invitrogen, San Diego, CA) and horseradish peroxidase-conjugated secondary antibody (Pierce Chemical). Colorimetric detection was carried out using 0.4 mg/ml *O*-phenylenediamine (Sigma Chemical) in 0.0012% H₂O₂, 50 mM Na₂HPO₄, 27 mM Na-citrate, pH 5. The reaction was stopped by addition of 2 M H₂SO₄, and the signal was measured at 490 nm using a microplate reader (Bio-Rad model 3550). For analysis of Ran binding, bound Ran was recovered from the plates with a 2% SDS solution, and the radioactivity was counted in a liquid scintillation counter.

Loading of Ran with GTP or GDP

To study the effect of RanGTP or RanGDP on p97 binding to RanBP2 or p62, 1 µM of recombinant Ran (essentially Ran-GDP) was incubated with 1 mM of nucleotide in the presence of 10 mM EDTA, 2 mM ATP, 4 mM DTT, 50 mM HEPES, pH 7.4, for 30 min at 30°C. The reaction was stopped at 4°C by addition of 15 mM MgCl₂. To study the binding of Ran to RanBP2, Ran was loaded using 6 µM of 40 µCi/mmol GTPγ³²P or GDPβ³²P. Loaded Ran was separated from free nucleotides using a NAP5 column (Pharmacia Biotech, Piscataway, NJ) that had been equilibrated in Buffer C (50 mM HEPES, 2 mM MgCl₂, 4 mM DTT, 0.1% BSA, 0.005% Tween 20). For loading of Ran with GTPγ³²P, the final RanGTP concentration was adjusted with cold RanGTP.

p97 Blot Overlay

For blot overlay procedures, proteins present in 2 OD₂₆₀ of salt-washed NE were separated on a 5–15% gradient SDS-PAGE and transferred to nitrocellulose membrane. Proteins were denatured in 6 N Guanidine HCl, 50 mM Tris-HCl, pH 7.4, 4 mM DTT and slowly renatured by three rounds of dropwise addition of 10 volumes of 50 mM Tris-HCl, pH 7.4, 150 mM NaCl, 2 mM MgCl₂, 2 mM CaCl₂, 0.2 mM ZnCl₂, 4 mM DTT. The membrane was then blocked with PBS containing 3% BSA plus 4 mM DTT. Binding reactions were carried out with 20 nM GSTp97 in the absence or presence of 40 nM Ran in 1 ml of 0.5% BSA, 0.1% Tween 20 in PBS/4 mM DTT for 30 min at room temperature. After incubation, the membrane was washed in incubation buffer without BSA, and the bound GST-p97 was cross-linked with 5 mM EDC (Pierce). GST-p97 was then detected by using anti-GST antibodies (Pharmacia), peroxidase-conjugated anti-mouse antibodies (Pierce), and ECL reagents (Pierce).

Electron Microscopy and Immunogold Labeling

Electron microscopy of purified RanBP2 utilized negative staining: 2 µl of RanBP2 (at 2.5 µg/ml) were dropped on carbon-coated grids, and the excess solution was blotted on the edge with a piece of filter paper. The grids were immediately washed three times with 15 µl of 2% uranyl acetate and then finally incubated with the 2% uranyl acetate for 1 min. Excess stain was removed, and the grid was air-dried before visualization. For immunogold labeling, isolated rat liver nuclear envelopes (NE) at a concentration of 250 OD₂₆₀/ml

were incubated for 30 min on ice either with GST-p97 (5 $\mu\text{g/ml}$) or with GST-p97 premixed with RanGTP (10 $\mu\text{g/ml}$). After incubation, NE were centrifuged at $6000 \times g$ and washed with PBS. p97 bound to NE was labeled by incubation with anti-GST antibody followed by anti-goat IgG conjugated to 5-nm gold particles for 2 h at room temperature. The pellets were fixed with 2% glutaraldehyde in PBS for 30 min at room temperature, washed with PBS, and postfixed with 1% osmium tetroxide in PBS for 1 h. Finally, samples were dehydrated and embedded in Epon 812 resin. Sections were stained with 2% uranyl acetate for 1 min (Guan *et al.*, 1995). All micrographs were recorded with a Hitachi 600 electron microscope at 80 kV.

RESULTS

Purification and Structural Analysis of RanBP2

We established a procedure to purify RanBP2 from salt-washed rat liver NE (Figure 1). The initial preparation of NE from intact rat liver results in an approximate 200-fold enrichment of NPC proteins versus total proteins (Snow *et al.*, 1987; our unpublished observations). NE (Figure 1A, lane 2) were first incubated in a buffer containing Triton X-100 and high salt at pH 8.8 to solubilize RanBP2 (Figure 1A, lane 3). We then used an affinity purification step to take advantage of the four functional Ran-binding domains in RanBP2. A fusion protein containing the biotinylated region of the *E. coli* BCCP was expressed in *E. coli*, and the resultant Ran-BCCP was bound to streptavidin

agarose beads. Solubilized NE proteins were incubated with this affinity matrix, and RanBP2 was eluted with a buffer containing the zwitterionic detergent EmpigenBB, which was stringent enough to efficiently elute RanBP2 without removing Ran-BCCP (Figure 1A, lane 5; and our unpublished observations). The eluted RanBP2 fractions were then purified on a MonoQ column (Figure 1A, lane 6). The final pool from the MonoQ contained no contaminants detectable by silver staining (Figure 1B). The yield of RanBP2 from purified rat liver NE with this procedure was $\sim 5\%$, and about 2.5 μg of RanBP2 was obtained from 2000 OD₂₆₀ of NE (Table 1).

We characterized the structure of purified RanBP2 by electron microscopy using negative staining (Figure 2). We observed two distinct but related structural views of RanBP2, depending on the specific electron microscopic (EM) sample examined. In some EM samples (Figure 2A), most of the particles were filaments with a length of ~ 36 nm and a diameter of about 5 nm and were usually bent or curved in an irregular manner. In other preparations (Figure 2B), most of the particles existed as spherical structures that appeared to be coiled or spiral conformations of the filamentous particles. A gallery of particles that appeared as spiral filaments is shown in Figure 2C. Each type of sample showed some particles with a structure that was intermediate between the two morphologies, suggesting that RanBP2 forms a flexible filamentous protein that is able to undergo conformational changes, such as coiling (Figure 2, A and B, arrows). Because the same biochemical preparations of purified RanBP2 yielded EM samples that contained either predominantly spiral particles or curved filaments, it appears that the conformation of RanBP2 on EM grids is determined by some aspect of the EM sample preparation (e.g., grid surface charge). Interestingly, the length of purified RanBP2 is very similar to the length of the cytoplasmic fibrils of the NPC that are visualized in freeze-dried, rotary shadowed preparations (35–50 nm, Jarnik and Aebi, 1991), and that also appear to be flexible structures (Panté and Aebi, 199b). Considered together, our

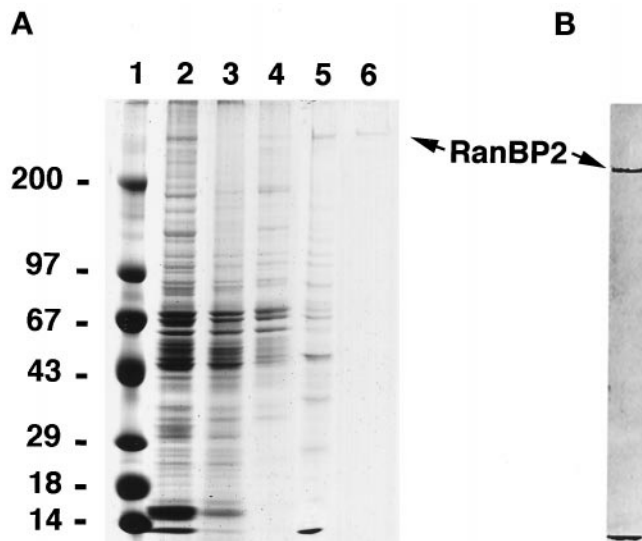


Figure 1. Purification of RanBP2 from rat liver NE. Proteins obtained during different steps of the purification were analyzed by SDS-PAGE on a 5–20% gradient gel followed by staining with Coomassie blue. (A) Lane 1, molecular weight standards (molecular weights indicated to the left of lane 1); lane 2, total NE; lane 3, salt-washed NE; lane 4, solubilized NE proteins; lane 5, proteins eluted from Ran affinity beads; lane 6, purified RanBP2. Proteins in lanes 2–4 were derived from 1 OD₂₆₀ NE, and proteins in lanes 5–6 were derived from 20 OD₂₆₀ NE. (B) Purified RanBP2 (from 20 OD₂₆₀ NE) was analyzed by silver staining after SDS-PAGE as in panel A

Table 1. Purification of RanBP2

Step	Proteins (μg)	RanBP2 (μg)	Fold-purification		Yield (%)
			Step	Cumulative	
Starting material (NE)	22,000	50			100
Salt wash	15,000	48	1.4	1.4	98
Solubilization	10,000	37	1.1	1.6	74
Ran affinity	200	17	23	37	34
Mono Q	2.5	2.5	11.7	440	5

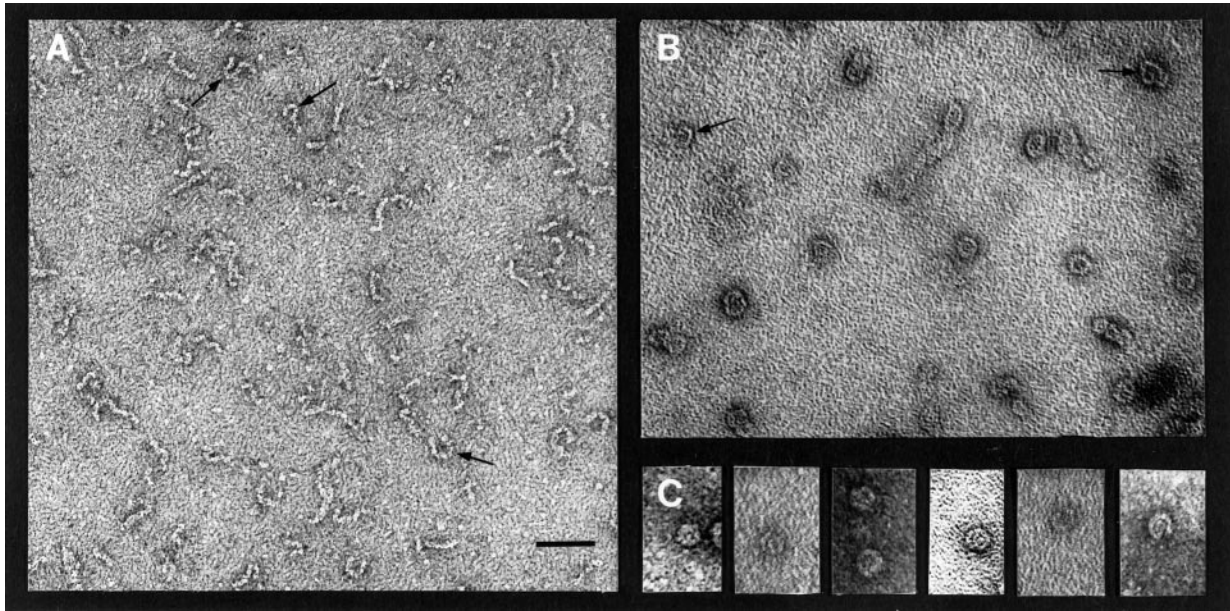


Figure 2. Electron microscopy of negatively stained RanBP2. Purified RanBP2 was adsorbed to glow-discharged carbon-coated grids and was negatively stained with uranyl acetate. Panels A and C are electron micrographs of two different grid preparations that show predominantly an extended (panel A) or folded (panel B) conformation of RanBP2. Arrows indicate examples of partially folded conformations of RanBP2 found in both preparations. Panel C is a gallery of folded RanBP2 molecules selected from the same preparation as panel B. Bar, 100 nm.

data indicate that RanBP2 is a primary component of the cytoplasmic fibrils of the NPC.

RanGTP Restricts the Binding of p97 to RanBP2 at the Cytoplasmic Surface of the NPC

Previous studies have shown that p97 interacts with multiple FG repeat nucleoporins *in vitro*, supporting the notion that p97 mediates the binding of the transport substrate/NLS receptor complex to multiple regions of the NPC (Moroianu *et al.*, 1995a; Radu *et al.*, 1995a; Hu *et al.*, 1996). Because RanGTP inhibits the formation of a complex between p97 and certain yeast nucleoporin fragments and/or dissociates this complex (Rexach and Blobel, 1995), we investigated whether RanGTP interferes with the binding of p97 to RanBP2 and other nucleoporins of mammalian cells. As shown in the blot overlay assay in Figure 3 (lane 1), p97 by itself binds to numerous nuclear envelope proteins representing FG repeat-containing nucleoporins, as previously reported by Moroianu *et al.* (1995b). The presence of RanGTP in the binding reaction abolished all detectable interaction of p97 with most of these proteins (Figure 3, lane 3), while RanGDP had no effect (Figure 3, lane 2). Interestingly, the presence of RanGTP enhanced the binding of p97 to a ~350-kDa protein that comigrates with RanBP2 (Figure 3, lane 3). We obtained the same result using purified RanBP2 (Figure 3, lanes 4 and 5) confirming the

identity of the ~350-kDa band. Thus, under these conditions RanBP2 is the only NPC protein whose interaction with p97 persists (and is enhanced) in the presence of RanGTP.

To assess the effect of RanGTP on the binding of p97 to native NPCs, we carried out p97 binding experiments with isolated rat liver nuclear envelopes and then localized the bound p97 by immunogold EM. As shown in Figure 4, p97 bound to both the nucleoplasmic and cytoplasmic sides of the NPC in the absence of RanGTP (panels A and B). Sixty-eight percent of the gold particles were localized on the cytoplasmic side of the NPC at an average distance of approximately 50 nm from the NPC midplane, whereas 32% of the gold particles were on the nucleoplasmic side of the NPC at an average distance of about 45 nm from the pore midplane (Figure 4E). In contrast, in the presence of RanGTP, p97 bound almost exclusively (92% of the gold particles) to the cytoplasmic side of the NPC at an average distance of about 50 nm, where RanBP2 is localized (Melchior *et al.*, 1995; Wilken *et al.*, 1995; Wu *et al.*, 1995; Yokoyama *et al.*, 1995). These results are consistent with the demonstration that the presence of RanGTP restricts binding of p97 to RanBP2 in blot overlay assay (Figure 3) and support the notion that RanGTP targets p97 to RanBP2 in the context of the native NPC structure.

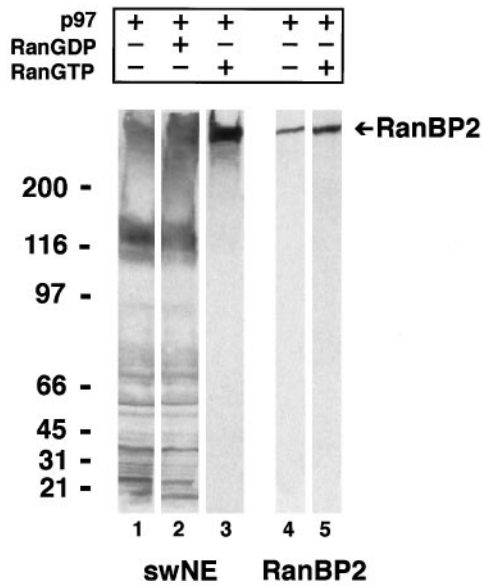


Figure 3. p97 binds selectively to RanBP2 in the presence of RanGTP. A blot overlay approach was used to analyze the binding of p97 to proteins of salt-washed NE (swNE, 2 OD₂₆₀, lanes 1–3), or to purified RanBP2 (10 ng, lanes 4–5). Protein samples were separated by SDS-PAGE on a 5–15% gradient gel, electrophoretically transferred to nitrocellulose, and the nitrocellulose membrane was renatured. Nitrocellulose strips were incubated with GSTp97, RanGDP, and RanGTP as indicated. After cross-linking, bound p97 was detected using anti-GST antibodies.

Characterization of the Binding of p97 and Ran to RanBP2

To investigate the molecular basis for the binding of p97 to RanBP2 in the presence of RanGTP, we quantitatively analyzed the binding of p97 and RanGTP to RanBP2 using a microtiter plate-binding assay. Figure 5A shows that the interaction of RanGTP with purified RanBP2 is saturable and of high apparent affinity ($K_{dapp} = 0.5$ nM). Because there are four distinct Ran-binding sites in RanBP2, this must be regarded as an average affinity. This affinity is significantly higher than that of RanGTP for RanBP1 under the same conditions ($K_{dapp} = 1.4$ nM; our unpublished results), and may either be caused by sequence differences between the RanBP1 and RanBP2 Ran binding domains, by the presence of adjacent domains in RanBP2 that are not found in RanBP1 or by the presence of four Ran binding sites in RanBP2 as opposed to one in RanBP1, which could lead to a higher local concentration of Ran (Wu *et al.*, 1995; Yokoyama *et al.*, 1995). RanGDP did not bind significantly to RanBP2 (Figure 5A) or to RanBP1 (our unpublished results) under these conditions. We also used the microtiter plate-binding assay to compare the binding affinity of p97 for RanBP2 and for p62, a nucleoporin that does not bind Ran but that also contains FG repeats (Starr *et al.*, 1990). We found that p97 bound both to RanBP2 (Figure 5B) and to p62

(Figure 5C) with an apparent K_d of 14 nM. Thus, RanGTP binds to RanBP2 with an apparent affinity that is nearly 30 times higher than the affinity of p97 for RanBP2 or p62.

We next investigated the effect of Ran on the binding of p97 to RanBP2 and p62 under the above conditions. Figure 6 shows that a low concentration of RanGTP stimulated the interaction of p97 with RanBP2 by approximately 50% (panel A) but had no stimulatory effect on the binding of p97 to p62 (panel B). As the RanGTP concentration was further increased, the extent of interaction of p97 with both RanBP2 and p62 decreased and was eventually abolished, although the binding of p97 to p62 was more strongly inhibited at a given concentration of RanGTP than was the binding of p97 to RanBP2. RanGDP had no significant effect on the binding of p97 to RanBP2 and p62.

A simple interpretation of these data is that Ran-binding sites and FG-repeat regions comprise two different classes of binding sites for p97, and that Ran differentially affects the binding of p97 to these two classes of sites. In the case of the FG-repeat regions, free p97 could bind to these regions in both RanBP2 and p62, and RanGTP could inhibit this binding through the formation of a RanGTP/p97 complex. This was observed previously for yeast nucleoporin fragments (Rexach and Blobel, 1995). In the case of the Ran-binding sites, RanGTP could stimulate the binding of p97 to RanBP2 by forming a RanGTP/p97 complex. Because the Ran-binding motifs of RanBP2 are similar to those of RanBP1 and because previous experiments have shown that a stable heterotrimeric complex can form between RanGTP, p97, and RanBP1 (Chi *et al.*, 1996; Lounsbury *et al.*, 1996), it is plausible that a similar trimeric complex could form between RanGTP, p97, and RanBP2. However, at high RanGTP concentrations, excess RanGTP would compete with the RanGTP/p97 complex for binding to the Ran-binding sites on RanBP2.

To directly test whether a complex between p97 and RanGTP is important for regulating the binding interactions of p97 with RanBP2 and p62, we analyzed a p97 mutant deficient in Ran binding (Görlich *et al.*, 1996) for its ability to interact with RanBP2 and p62 in the absence and presence of RanGTP. The $\Delta 54N$ -p97 used in these experiments was slightly shorter than the $\Delta 44N$ -p97 mutant characterized by Görlich and co-workers (1996). We confirmed that RanGTP did not bind to the $\Delta 54N$ -p97 mutant (Figure 7A). In the absence of RanGTP, the binding of $\Delta 54N$ -p97 to both RanBP2 and p62 was similar to that of the wild-type (wt) p97 (Figure 7, B and C). However, in contrast to wt p97, the binding of $\Delta 54N$ -p97 to RanBP2 was not stimulated by low concentrations of RanGTP, and the binding of $\Delta 54N$ -p97 to either RanBP2 or p62 was not diminished by higher concentrations of RanGTP (Figure 7, B and C). These results clearly indicate that

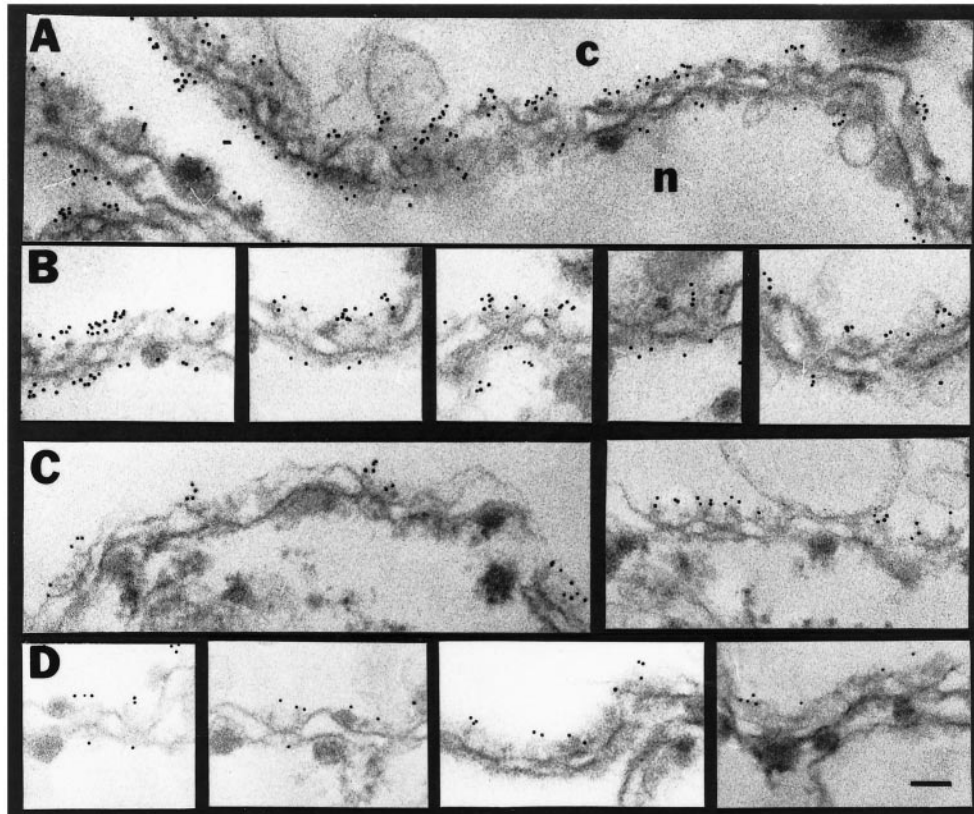
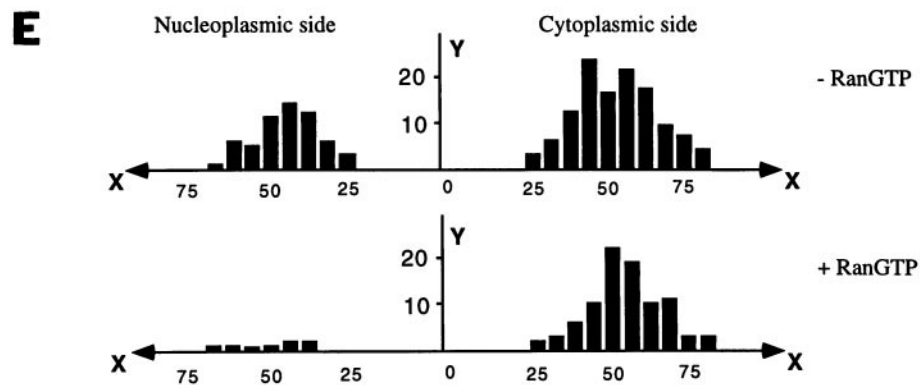


Figure 4. RanGTP selectively targets p97 to the cytoplasmic side of the NPC. GST-p97 was incubated with isolated rat liver NE in the absence (A and B) or presence (C and D) of RanGTP. Bound p97 was visualized by labeling with goat anti-GST antibodies followed by rabbit anti-goat antibodies coupled with 5 nm gold. Samples were then processed for thin section electron microscopy. (E) Histograms showing the distance of gold particles from the midplane of the NPC for the binding of p97 in the absence (top) or presence (bottom) of RanGTP. X axis: distance of gold particles from the midplane; Y axis: number of gold particles counted; c, cytoplasm; n, nucleoplasm.



RanGTP regulates the binding of p97 to RanBP2 and p62 through formation of a complex with p97.

DISCUSSION

We have developed a procedure for the purification of RanBP2 from rat liver NE under relatively mild conditions. Electron microscopy of negatively stained RanBP2 revealed it to be a flexible filamentous protein capable of adopting a tightly coiled spiral conformation. RanBP2 has previously been localized to the cy-

toplasmic NPC fibrils, which appear to be flexible structures (Panté and Aebi, 1996b) with a length of 35–50 nm in freeze-dried, rotary-shadowed preparations (Jarnik and Aebi, 1991; Goldberg and Allen, 1993). Purified RanBP2, after negative staining, had a length of about 36 nm. Thus, the localization, size, and flexibility of RanBP2 are similar to the properties of the cytoplasmic fibrils of the NPC. In addition, RanBP2 in its coiled conformation quite closely resembles the granules observed at the periphery of isolated

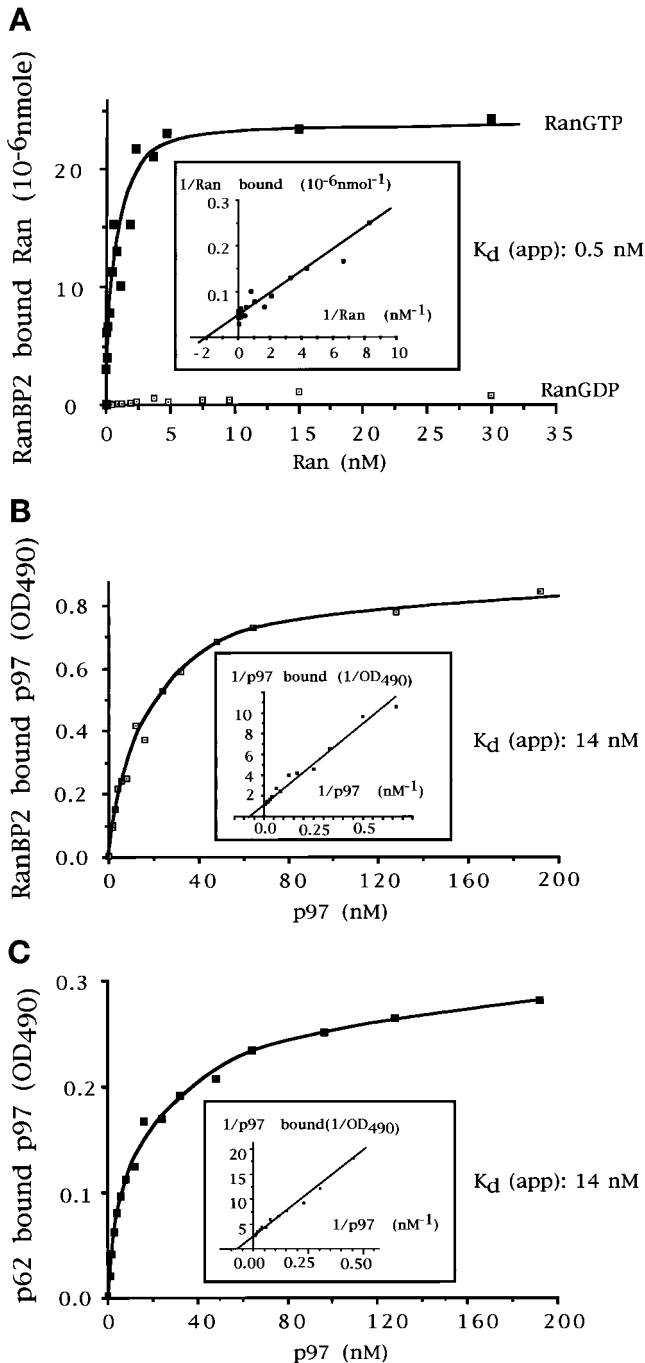


Figure 5. Characterization of the interactions of Ran and p97 with nucleoporins RanBP2 and p62. (A) Titration of Ran binding to RanBP2. Increasing concentrations of Ran loaded with either [³²P]GTP or [³²P]GDP were incubated with RanBP2 adsorbed to microtiter wells. After washing, the radioactivity was recovered from the wells with SDS and counted in a liquid scintillation counter, and the amount of Ran bound to RanBP2 was calculated from the [³²P]GTP-specific activity. (B and C) Titration of p97 binding to RanBP2 and p62, respectively. Increasing concentration of His-p97 were incubated with RanBP2 (B) or p62 (C) and adsorbed to microtiter wells. The 6xHis-p97 that remained after washing was

NPCs (Unwin and Milligan, 1982; Stewart and Whytock, 1988; Goldberg and Allen, 1993), which may represent a compacted/collapsed form of the cytoplasmic fibrils as suggested by Jarnik and Aebi (1991). Considered together, these observations suggest that RanBP2 may form the backbone of the cytoplasmic fibrils of the NPC.

One model for the movement of a transport complex from an initial docking side at the cytoplasmic fibrils of the NPC to central pore regions proposes the involvement of fibril bending (Melchior and Gerace, 1995; Panté and Aebi, 1995). This hypothesis has gained support from a recent electron microscopy study analyzing the movement of gold-coupled substrate through the NPC of *Xenopus* oocytes (Panté and Aebi, 1996b). Our present data lend further credence to this hypothesis, as indicated by the ability of RanBP2 to adopt an extended or bent/coiled conformation in vitro. The process leading to these conformational changes may be unregulated (as proposed by Panté and Aebi, 1996b), or could be controlled in the native NPC by interactions with cytosolic import factors such as p97 and Ran. Future analysis of conformational changes of RanBP2 in vitro should provide valuable mechanistic insight on the movement of an import complex from the periphery of the NPC to the central channel.

Using blot overlay and microtiter plate binding assays, we demonstrated that RanGTP at appropriate concentrations both promotes the binding of p97 to RanBP2 and inhibits the binding of p97 to p62 and to other FG repeat nucleoporins. In agreement with these data, EM analysis showed that RanGTP can restrict the binding of p97 to the cytoplasmic periphery of the NPC, where RanBP2 is found. Using a p97 mutant unable to bind RanGTP, we found that the ability of RanGTP to modulate the binding of p97 to RanBP2 and p62 is dependent upon the formation of a RanGTP/p97 complex. In agreement with these results, the ability of anti-RanBP2 antibodies to coimmunoprecipitate p97 and Ran from a *Xenopus* egg extract is nucleotide dependent (Saitoh *et al.*, 1996).

Our data suggest that two different classes of binding sites for p97 are responsible for these effects. First, the FG repeat domains present in both RanBP2 and p62 appear to be able to bind to p97 alone, each with an apparent K_d of about 14 nM. The presence of RanGTP, which promotes formation of a RanGTP/p97 complex, appears to inhibit the binding of p97 to this class of sites on both RanBP2 and p62. These results are in agreement with a previous study on the binding

Figure 5 (cont). then cross-linked to the adsorbed protein and detected with antibodies (see MATERIALS AND METHODS). The Lineweaver-Burk plots used to determine the apparent binding constants (K_{dapp}) are shown in the insets.

of p97 to fragments of yeast nucleoporins containing FG repeats (Rexach and Blobel, 1995). In addition, RanBP2 contains specific binding sites for RanGTP ($K_{dapp} = \sim 0.5$ nM) that are absent from p62 and from other FG repeat nucleoporins. These sites on RanBP2 are homologous to those of RanBP1 (Wu *et al.*, 1995; Yokoyama *et al.*, 1995) and appear to be capable of binding p97 in the form of a RanGTP/p97 complex as was previously described for RanBP1 (Chi *et al.*, 1996; Lounsbury *et al.*, 1996). Thus, in the case of this class of p97-binding sites, the presence of RanGTP leads to formation of a RanGTP/p97 complex and has a positive effect in promoting the binding of p97 to RanBP2. Because this second class of binding sites for p97 is present in RanBP2 but in no other FG repeat nucleoporins, appropriate concentrations of RanGTP can suppress the binding of p97 to all nucleoporins except RanBP2, to which the binding is enhanced.

In vivo, a complex of RanGTP and p97 could be formed in the late stages of a nuclear import cycle and exported to the cytoplasm from the nucleoplasm (see Görlich *et al.*, 1996) or could be created in the cytoplasm after RanGTP exits the nucleus in another form. Our in vitro binding experiments indicate that the RanGTP/p97 complex would be selectively targeted to RanBP2 via its RanGTP-binding sites and would not interact with FG repeat nucleoporins in other regions of the NPC. We propose that in vivo, the p97 bound to RanBP2 in this manner provides a docking site for a transport substrate/NLS receptor complex that is initially formed in the cytosol. This would explain how the initial binding of transport substrates to the NPC is restricted to the cytoplasmic fibrils, as indicated by previous work (Newmeyer and Forbes, 1988; Richardson *et al.*, 1988; Panté and Aebi, 1996b).

The hydrolysis of RanGTP during nuclear import very likely occurs at RanBP2 due to the action of RanGAP1 bound to this protein (Mahajan *et al.*, 1997) and could have two different functions in the proposed substrate/NLS receptor docking reaction at RanBP2. In one case, the GTP would be hydrolyzed upon binding of RanGTP/p97 to RanBP2 and, in so doing, would provide a binding site consisting of RanGDP, p97, and RanBP2 for the substrate/receptor complex at the NPC. In a second case, p97 would suppress hydrolysis of RanGTP that is bound to RanBP2, similar to the inhibition of RanGTP hydrolysis by p97 in solution (Floer and Blobel, 1996). In this scenario, RanGTP hydrolysis would be triggered by binding of the substrate/NLS receptor complex to RanBP2-associated p97. In either of these cases, RanGTP hydrolysis would allow formation of a "committed" transport complex at RanBP2. It is plausible that the resulting RanGDP would remain stably associated with the substrate/NLS receptor/p97 transport complex after GTP hydrolysis. This association could "mark" the transport complex as having passed

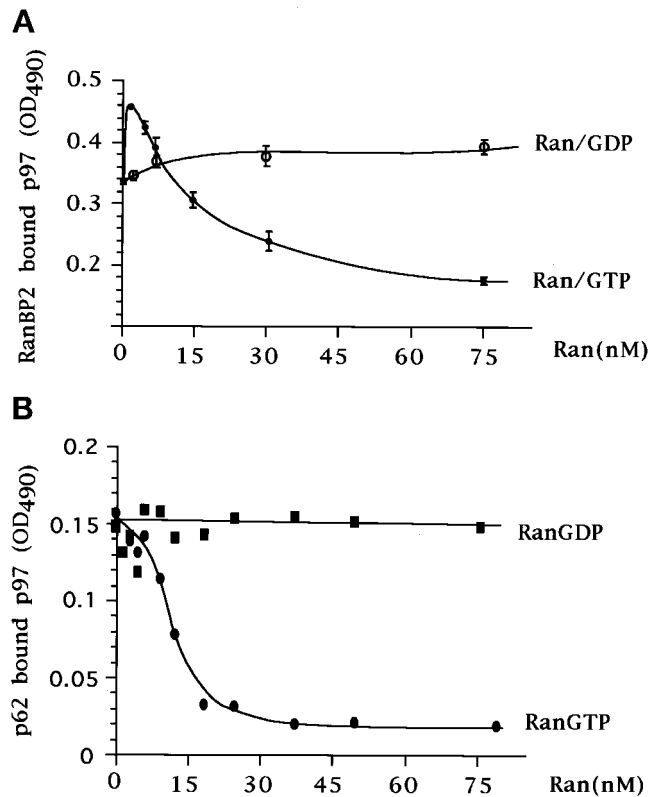


Figure 6. RanGTP modulates the interaction of p97 with RanBP2 and p62. (A) Effect of Ran on the binding of p97 to RanBP2. RanBP2-coated microtiter wells were incubated with 10 nM His-p97 and with an increasing amount of RanGTP or RanGDP. After incubation and washing, proteins were cross-linked, and the amount of bound p97 was quantified using antibodies (see MATERIALS AND METHODS). (B) Effect of Ran on the binding of p97 to p62. The analysis was carried out as in panel A, except that p62-coated microtiter wells were used.

through an initial commitment step and facilitate its movement to downstream binding sites in the NPC, possibly by the ability of RanGDP to interact with NTF2 (Nehrbass and Blobel, 1996; Paschal *et al.*, 1996) or with other factors.

Whatever the precise function of RanGTP hydrolysis, one key feature of the above models is that a complex between the substrate/NLS receptor and p97 first forms at the NPC at RanBP2, and not in the cytosol as was previously proposed by Imamoto and coworkers (1995). Although complexes between the NLS receptor and p97 can be detected in a soluble fraction of cell lysates (Görlich *et al.*, 1995a; Imamoto *et al.*, 1995), this could be attributed to the conversion of RanGTP to RanGDP in the cell extract. Hydrolysis of RanGTP during the in vitro incubation could convert an initial p97/RanGTP complex (which is incapable of binding the substrate/NLS receptor complex [Rexach and Blobel, 1995]) to a form that can interact with the substrate/NLS receptor. At present, there is

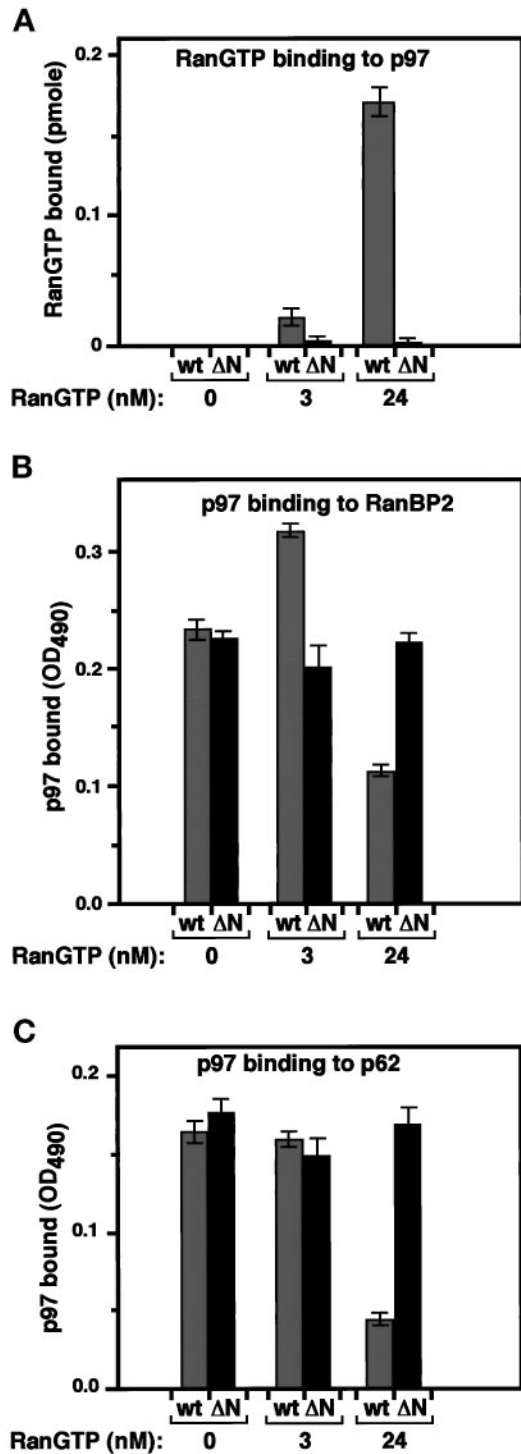


Figure 7. The ability of RanGTP to modulate the binding of p97 to RanBP2 and p62 requires the RanGTP/p97 interaction. (A) 3 nM or 24 nM [32 P]GTP-Ran was incubated with wt p97 or Δ N p97 bound to microtiter wells. After binding and washing, the radioactivity was recovered from the plate by elution with SDS and was counted in a liquid scintillation counter. The amount of bound RanGTP was calculated from the [32 P]RanGTP-specific activity. (B) The binding of

no clear evidence that cytosolic complexes of NLS receptor/p97 occur in living cells. A second key feature of these models is that RanGTP, in the form of a RanGTP/p97 complex, is required at the cytoplasmic side of the NPC for transport. This predicts that a high concentration of free RanGTP would inhibit import, as has been shown previously (Görlich *et al.*, 1996), since RanGTP would compete with a RanGTP/p97 complex for binding to RanBP2.

In conclusion, the data we present here suggest a specific mechanism by which RanGTP could mediate the formation of an import complex at RanBP2 in an early step of nuclear import. This is consistent with previous proposals that RanGTP hydrolysis at RanBP2 is important for defining the vectoriality of nuclear protein import involving basic-type NLS substrates (Melchior *et al.*, 1995; Mahajan *et al.*, 1997).

ACKNOWLEDGMENTS

We are grateful to Dr. S. Lyman, Dr. R. Mahajan, and Dr. C. Fritze for critical reading of the manuscript. We also thank Dr. T. Hu for providing GST-p62 protein and expression vectors for p97. This work was supported by postdoctoral fellowships from the Human Frontiers in Science Program (HFSP) to C.D., and by a California Division-American Cancer Society, Senior Fellowship 1-15-95 to F.M., as well as by a grant from the National Institutes of Health (6 M41955) to L.G. We also acknowledge support from the Lucille P. Markey Charitable Trust.

REFERENCES

- Adam, E.J., and Adam, S.A. (1994). Identification of cytosolic factors required for nuclear location sequence-mediated binding to the nuclear envelope. *J. Cell Biol.* 125, 547-555.
- Bischoff, F.R., Klebe, C., Kretschmer, J., Wittinghofer, A., and Ponstingl, H. (1994). RanGAP1 induces GTPase activity of nuclear Ras-related Ran. *Proc. Natl. Acad. Sci. USA* 91, 2587-2591.
- Bischoff, F.R., Krebber, H., Kempf, T., Hermes, I., and Ponstingl, H. (1995a). Human RanGTPase-activating protein RanGAP1 is a homologue of yeast Rna1p involved in mRNA processing and transport. *Proc. Natl. Acad. Sci. USA* 92, 1749-1753.
- Bischoff, F.R., Krebber, H., Smirnova, E., Dong, W., and Ponstingl, H. (1995b). Co-activation of RanGTPase and inhibition of GTP dissociation by Ran-GTP binding protein RanBP1. *EMBO J.* 14, 705-715.
- Bischoff, F.R., and Ponstingl, H. (1991a). Catalysis of guanine nucleotide exchange on Ran by the mitotic regulator RCC1. *Nature* 354, 80-82.
- Bischoff, F.R., and Ponstingl, H. (1991b). Mitotic regulator protein RCC1 is complexed with a nuclear ras-related polypeptide. *Proc. Natl. Acad. Sci. USA* 88, 10830-108304.

Figure 7 (cont). wt p97 and Δ N p97 to RanBP2 adsorbed to microtiter wells was analyzed in the absence of Ran, or in the presence of 3 nM or 24 nM RanGTP, and the bound p97 was quantified as in Figure 4. (C) The binding of wt p97 and Δ N p97 to p62 adsorbed to microtiter wells was analyzed as in panel B.

- Chapman-Smith, A., Turner, D.L., Cronan, J.E., Morris, T.W., and Wallace, J. (1994). Expression, biotinylation and purification of a biotin-domain peptide from the biotin carboxy carrier protein of *Escherichia Coli* acetyl-CoA carboxylase. *Biochem. J.* 302, 881–887.
- Chi, N.C., Adam, E.J., and Adam, S.A. (1995). Sequence and characterization of cytoplasmic nuclear protein import factor p97. *J. Cell Biol.* 130, 265–274.
- Chi, N.C., Adam, E.J.H., Visser, G.D., and Adam, S.A. (1996). RanBP1 stabilizes the interaction of Ran with p97 in nuclear protein import. *J. Cell Biol.* 135, 559–569.
- Chi, N.C., Adam, E.J.H., and Adam, S. (1997). Different binding domains for Ran-GTP and Ran-GDP/RanBP1 on nuclear import factor p97. *J. Biol. Chem.* 272, 6818–6822.
- Dingwall, C., and Laskey, R.A. (1991). Nuclear targeting sequences - a consensus? *Trends Biochem. Sci.* 16, 478–481.
- Floer, M., and Blobel, G. (1996). The nuclear transport factor karyopherin beta binds stoichiometrically to Ran-GTP and inhibits the Ran GTPase activating protein. *J. Biol. Chem.* 271, 5313–5316.
- Goldberg, M.W., and Allen, T.D. (1993). The nuclear pore complex: three-dimensional surface structure revealed by field emission, in-lens scanning electron microscopy, with underlying structure uncovered by proteolysis. *J. Cell Sci.* 106, 261–274.
- Görllich, D., Kostka, S., Kraft, R., Dingwall, C., Laskey, R.A., Hartmann, E., and Prehn, S. (1995a). Two different subunits of importin cooperate to recognize nuclear localization signals and bind them to the nuclear envelope. *Curr. Biol.* 5, 383–392.
- Görllich, D., Kutay, P.N.U., Aebi, U., and Bischoff, F.R. (1996). Identification of different roles for RanGDP and RanGTP in nuclear protein import. *EMBO J.* 15, 5584–5594.
- Görllich, D., and Mattaj, I.W. (1996). Nucleocytoplasmic transport. *Science* 271, 1513–1518.
- Görllich, D., Prehn, S., Laskey, R.A., and Hartmann, E. (1994). Isolation of a protein that is essential for the first step of nuclear protein import. *Cell* 79, 767–778.
- Görllich, D., Vogel, F., Mills, A.D., Hartmann, E., and Laskey, R.A. (1995b). Distinct functions for the two importin subunits in nuclear protein import. *Nature* 377, 246–248.
- Guan, T., Muller, S., Klier, G., Panté, N., Blevitt, J.M., Haner, M., Paschal, B., Aebi, U., and Gerace, L. (1995). Structural analysis of the p62 complex, an assembly of O-linked glycoproteins that localizes near the central gated channel of the nuclear pore complex. *Mol. Cell Biol.* 6, 1591–1603.
- Hinshaw, J.E., Carragher, B.O., and Milligan, R.A. (1992). Architecture and design of the nuclear pore complex. *Cell* 69, 1133–1141.
- Hu, T., Guan, T., and Gerace, L. (1996). Molecular and functional characterization of the p62 complex, an assembly of nuclear pore complex glycoproteins. *J. Cell Biol.* 134, 589–601.
- Imamoto, N., Tachibana, T., Matsubae, M., and Yoneda, Y. (1995). A karyophilic protein forms a stable complex with cytoplasmic components prior to nuclear pore binding. *J. Biol. Chem.* 270, 8559–8565.
- Iovine, M.K., Watkins, J.L., and Went, S.R. (1995). The GLFG repetitive region of the nucleoporin Nup116p interacts with Kap95p, an essential yeast nuclear import factor. *J. Cell Biol.* 131, 1699–1713.
- Jarnik, M., and Aebi, U. (1991). Toward a more complete 3-D structure of the nuclear pore complex. *J. Struct. Biol.* 107, 291–308.
- Kraemer, D.M., Strambio-de-Castillia, C., Blobel, G., and Rout, M.P. (1995). The essential yeast nucleoporin NUP159 is located on the cytoplasmic side of the nuclear pore complex and serves in karyopherin-mediated binding of transport substrate. *J. Biol. Chem.* 270, 19017–19021.
- Lounsbury, K.M., Richards, S.A., Perlungher, R.R., and Macara, I.G. (1996). Ran binding domains promote the interaction of Ran with p97/beta-karyopherin, linking the docking and translocation steps of nuclear import. *J. Biol. Chem.* 271, 2357–2360.
- Mahajan, R., Delphin, C., Guan, T., Gerace, L., and Melchior, F. (1997). A small ubiquitin-related polypeptide involved in targeting RanGAP1 to nuclear pore complex protein RanBP2. *Cell* 88, 97–107.
- Matunis, M.J., Coutavas, E., and Blobel, G. (1996). A novel ubiquitin-like modification modulates the partitioning of the Ran-GTPase-activating protein RanGAP1 between the cytosol and the nuclear pore complex. *J. Cell Biol.* 135, 1457–1470.
- Melchior, F., and Gerace, L. (1995). Mechanisms of nuclear protein import. *Curr. Opin. Cell Biol.* 7, 310–318.
- Melchior, F., Guan, T., Yokoyama, N., Nishimoto, T., and Gerace, L. (1995). GTP hydrolysis by Ran occurs at the nuclear pore complex in an early step of protein import. *J. Cell Biol.* 131, 571–81.
- Melchior, F., Paschal, B., Evans, J., and Gerace, L. (1993). Inhibition of nuclear protein import by nonhydrolyzable analogues of GTP and identification of the small GTPase Ran/TC4 as an essential transport factor. *J. Cell Biol.* 123, 1649–1659.
- Michael, W.M., Siomi, H., Choi, M., Pinol-Roma, S., Nakielny, S., Liu, Q., and Dreyfuss, G. (1995). Signal sequences that target nuclear import and nuclear export of pre-mRNA-binding proteins. *CSH Symp.*, CSHL press, vol. LX, Pp 663–668.
- Moore, M.S., and Blobel, G. (1993). The GTP-binding protein Ran/TC4 is required for protein import into the nucleus. *Nature* 365, 661–3.
- Moore, M.S., and Blobel, G. (1994). Purification of a Ran-interacting protein that is required for protein import into the nucleus. *Proc. Natl. Acad. Sci. USA* 91, 10212–10216.
- Moroianu, J., Blobel, G., and Radu, A. (1995a). Previously identified protein of uncertain function is karyopherin alpha and together with karyopherin beta docks import substrate at nuclear pore complexes. *Proc. Natl. Acad. Sci. USA* 92, 2008–2011.
- Moroianu, J., Hijikata, M., Blobel, G., and Radu, A. (1995b). Mammalian karyopherin alpha 1 beta and alpha 2 beta heterodimers: alpha 1 or alpha 2 subunit binds nuclear localization signal and beta subunit interacts with peptide repeat-containing nucleoporins. *Proc. Natl. Acad. Sci. USA* 92, 6532–6536.
- Nehrbass, U., and Blobel, G. (1996). Role of the nuclear transport factor p10 in nuclear import. *Science* 272, 120–122.
- Newmeyer, D.D., and Forbes, D.J. (1988). Nuclear import can be separated into distinct steps in vitro: nuclear pore binding and translocation. *Cell* 52, 641–653.
- Nigg, E.A. (1997). Nucleoplasmic transport signals, mechanisms and regulation. *Nature* 386, 779–787.
- Ohtsubo, M., Kai, R., Furuno, N., Sekiguchi, T., Sekiguchi, M., Hayashida, M., Kuma, K., Miyata, T., Fuukushige, S., Murotsu, T., Matsubara, K., and Nishimoto, T. (1987). Isolation and characterization of the active cDNA of the human cell cycle gene (RCC1) involved in the regulation of onset of chromosome condensation. *Genes Dev.* 1, 585–593.
- Ohtsubo, M., Okazaki, H., and Nishimoto, T. (1989). The RCC1 protein, a regulator for the onset of chromosome condensation locates in the nucleus and binds to DNA. *J. Cell Biol.* 109, 1389–1397.
- Panté, N., and Aebi, U. (1995). Exploring nuclear pore complex structure and function in molecular detail. *J. Cell Sci.* 19, 1–11.
- Panté, N., and Aebi, U. (1996a). Molecular dissection of the nuclear pore complex. *Crit. Rev. Biochem. Mol. Biol.* 32, 153–199.

- Panté, N., and Aebi, U. (1996b). Sequential binding of import ligands to distinct nucleopore regions during their nuclear import. *Science* 273, 1729–1732.
- Paschal, B.M., Delphin, C., and Gerace, L. (1996). Nucleotide specific interaction of Ran/TC4 with nuclear transport factor NTF2 and p97. *Proc. Natl. Acad. Sci. USA* 93, 7679–7683.
- Paschal, B.M., and Gerace, L. (1995). Identification of NTF2, a cytosolic factor for nuclear import that interacts with nuclear pore complex protein p62. *J. Cell Biol.* 129, 925–937.
- Pollard, V.W., Michael, W.M., Nakielny, S., Siomo, M.C., Wang, F., and Dreyfuss, G. (1996). A novel receptor-mediated nuclear protein import pathway. *Cell* 86, 985–994.
- Radu, A., Blobel, G., and Moore, M.S. (1995a). Identification of a protein complex that is required for nuclear protein import and mediates docking of import substrate to distinct nucleoporins. *Proc. Natl. Acad. Sci. USA* 92, 1769–1773.
- Radu, A., Moore, M.S., and Blobel, G. (1995b). The peptide repeat domain of nucleoporin Nup98 functions as a docking site in transport across the nuclear pore complex. *Cell* 81, 215–222.
- Rexach, M., and Blobel, G. (1995). Protein import into nuclei: association and dissociation reactions involving transport substrate, transport factors, and nucleoporins. *Cell* 83, 683–692.
- Richards, S.A., Lounsbury, K.M., Carey, K.L., and Macara, I.G. (1996). A nuclear export signal is essential for the cytosolic localization of the Ran Binding Protein RanBP1. *J. Cell Biol.* 134, 1157–1168.
- Richardson, W.D., Mills, A.D., Dilworth, S.M., Laskey, R.A., and Dingwall, C. (1988). Nuclear protein migration involves two steps: rapid binding at the nuclear envelope followed by slower translocation through nuclear pores. *Cell* 52, 655–664.
- Ris, H. (1991). The three-dimensional structure of the nuclear pore complex as seen by high voltage microscopy and high resolution low voltage scanning electron microscopy. *EMSA Bull.* 21, 54–56.
- Saitoh, H., Cooke, C.A., Burgess, W.H., Earnshaw, W.C., and Dasso, M. (1996). Direct and indirect association of the small GTPase Ran with nuclear pore proteins and soluble transport factors: studies in *Xenopus laevis* egg extracts. *Mol. Biol. Cell* 7, 1319–1334.
- Schlenstedt, G., Wong, D.H., Koepf, D.M., and Silver, P.A. (1995). Mutants in a yeast Ran binding protein are defective in nuclear transport. *EMBO J.* 14, 5367–5378.
- Snow, C.M., Senior, A., and Gerace, L. (1987). Monoclonal antibodies identify a group of nuclear pore complex glycoproteins. *J. Cell Biol.* 104, 1143–1156.
- Starr, C.M., D’Onofrio, M., Park, M.K., and Hanover, J.A. (1990). Primary sequence and heterologous expression of nuclear pore glycoprotein p62. *J. Cell Biol.* 110, 1861–1871.
- Stewart, M., and Whytock, S. (1988). The structure and interactions of components of nuclear envelopes from *Xenopus* oocyte germinal vesicles observed by heavy metal shadowing. *J. Cell Sci.* 90, 409–423.
- Sweet, D.J., and Gerace, L. (1995). Taking from the cytoplasm and giving to the pore: soluble transport factors in nuclear protein import. *Trends Cell Biol.* 5, 444–447.
- Unwin, P.N.T., and Milligan, R.A. (1982). A large particle associated with the perimeter of the nuclear pore complex. *J. Cell Biol.* 93, 63–75.
- Wilken, N., Senecal, J.L., Scheer, U., and Dabauvalle, M.C. (1995). Localization of the Ran-GTP binding protein RanBP2 at the cytoplasmic side of the nuclear pore complex. *Eur. J. Cell Biol.* 68, 211–219.
- Wu, J., Matunis, M.J., Kraemer, D., Blobel, G., and Coutavas, E. (1995). Nup358, a cytoplasmically exposed nucleoporin with peptide repeats, Ran-GTP binding sites, zinc fingers, a cyclophilin A homologous domain, and a leucine-rich region. *J. Biol. Chem.* 270, 14209–14213.
- Yokoyama, N., Hayashi, N., Seki, T., Panté, N., Ohba, T., Nishii, K., Kuma, K., Hayashida, T., Miyata, T., Aebi, U., Fukui, M., and Nishimoto, T. (1995). A giant nucleopore protein that binds Ran/TC4. *Nature* 376, 184–188.

Nucleotide-specific interaction of Ran/TC4 with nuclear transport factors NTF2 and p97

(GTPase/nuclear pore complex/protein import)

BRYCE M. PASCHAL, CHRISTIAN DELPHIN, AND LARRY GERACE*

Departments of Cell and Molecular Biology, The Scripps Research Institute, La Jolla, CA 92037

Communicated by Peter K. Vogt, The Scripps Research Institute, La Jolla, CA, April 17, 1996 (received for review February 9, 1996)

ABSTRACT The use of permeabilized cell models to study nuclear protein import has led to the identification of cytosolic components of the import machinery, including the NLS receptor, p97, Ran/TC4, and nuclear transport factor 2 (NTF2). These proteins are required to reconstitute docking of transport ligand at the nuclear pore complex and subsequent translocation through the nuclear pore. However, a detailed molecular understanding of how these factors mediate protein import is lacking. Here we describe the results of solution and solid phase binding assays, which demonstrate that the small GTPase Ran/TC4 interacts directly with the cytosolic transport factors p97 and NTF2. By preloading recombinant Ran/TC4 with [γ - 32 P]GTP or [3 H]GDP, we show that the interactions with p97 and NTF2 are specific for the GTP- and GDP-bound forms, respectively. These data together with previous studies lead us to suggest that the interaction of the GTP-bound form of Ran/TC4 with p97 is linked to an early step in the nuclear protein import pathway and that the association of the GDP-bound form of Ran/TC4 with NTF2 helps define vectorial transport.

The integration of nuclear functions with biosynthetic and signaling events in the cytoplasm requires rapid and selective nucleocytoplasmic transport. Molecular trafficking between the nuclear and cytoplasmic compartments is mediated by large supramolecular structures that span the nuclear envelope known as nuclear pore complexes (NPCs; reviewed in refs. 1–3). Ions and small molecules cross the NPC by passive diffusion, while most proteins and ribonucleoprotein complexes are transported by signal- and ATP-dependent mechanisms. There are multiple steps in the nuclear protein import pathway, including the docking of a nuclear localization sequence (NLS)-containing protein at the cytoplasmic periphery of the NPC, accumulation near the central gated channel, and translocation into the nucleus (reviewed in refs. 4 and 5).

The development of simple, quantitative assays for measuring nuclear protein import *in vitro* (6, 7) has led to the identification of several cytosolic factors that play direct roles in this process. These factors[†] are the NLS receptor (8–11), p97 (12–15), Ran/TC4 (17, 18), and nuclear transport factor 2 (NTF2; refs. 7 and 16). One of the earliest events in the protein import pathway occurs when the NLS receptor binds to the NLS of a protein ligand destined for import and mediates ligand docking at the cytoplasmic periphery of the NPC in a complex with p97 (reviewed in ref. 5). The function of p97 in this step of transport seems to be that of an adaptor protein, which binds directly to both the NLS receptor and to the NPC (12–15, 19). While addition of the NLS receptor and p97 is sufficient to reconstitute docking of NLS ligand in permeabilized cells, Ran/TC4 and NTF2 must also be present to reconstitute delivery of the NLS ligand into the nucleoplasm (7, 16). How Ran/TC4 and NTF2 facilitate transport steps

downstream of docking is unknown, though the fractionation behavior of the *Xenopus* homologues of these proteins leads to the suggestion they may interact with each other (16). It is clear that obtaining a detailed understanding of nuclear protein import requires defining how the cytosolic transport factors interact with each other and with proteins of the NPC to mediate discrete transport steps.

A number of NPC proteins have been characterized in vertebrates, among them a group of O-linked glycoproteins whose primary structures contain degenerate repeats involving the dipeptide sequence FG (phenylalanine-glycine; reviewed in ref. 3). The O-linked glycoproteins appear to have a direct role in nuclear import, since the binding of wheat germ agglutinin and monoclonal antibodies to them inhibits nuclear protein import, and NPCs assembled in their absence are transport-deficient (reviewed in ref. 1). Furthermore, our laboratory found that this group of polypeptides can specifically deplete cytosol of an *N*-ethylmaleimide-insensitive activity required for protein import (20). We further found that this depletion could be partly ascribed to one of these O-linked glycoproteins, p62 (7). The activity that restores transport to cytosol pretreated with immobilized p62 was purified. This activity is NTF2, a low molecular weight homodimeric protein (subunit mass = 14,478 Da) that seems to be conserved in phylogenetically diverse species (7).

Here we describe the results of a biochemical screen for cytosolic factors that interact with NTF2. We found that the nuclear transport factors Ran/TC4 and p97 were specifically depleted from HeLa cell cytosol by treatment with NTF2-Sepharose. Using purified recombinant proteins, we show that NTF2 interacts directly with the GDP-bound form of Ran/TC4, while p97 interacts directly with the GTP-bound form of Ran/TC4. Together with previous studies, our data suggests that Ran/TC4 is required for at least two distinct steps in the pathway of nuclear protein import which are defined by its nucleotide state.[‡]

MATERIALS AND METHODS

Preparation of HeLa Cell Cytosol and Affinity Depletion of Transport Factors. A high-speed cytosolic extract (150,000 × *g* supernatant fraction) was prepared from HeLa cells grown in suspension culture as described (7). The concentration of

Abbreviations: NLS, nuclear localization sequence; NPC, nuclear pore complex; NTF2, nuclear transport factor 2; GST, glutathione *S*-transferase; RanBP2, Ran/TC4 binding protein 2.

*To whom reprint requests should be addressed at: The Scripps Research Institute, Departments of Cell and Molecular Biology, 10666 North Torrey Pines Road, La Jolla, CA 92037.

[†]The NLS receptor has also been referred to as importin α , karyopherin α , and SRP1 (8–11). The protein p97 has also been referred to as importin β and karyopherin β (12–15). NTF2 has also been referred to as p10 (7, 16).

[‡]The results of this study were presented at the 35th Annual Meeting of the American Society for Cell Biology and published in abstract form (21).

The publication costs of this article were defrayed in part by page charge payment. This article must therefore be hereby marked "advertisement" in accordance with 18 U.S.C. §1734 solely to indicate this fact.

protein in the cytosolic extract was ≈ 10 mg/ml, in a buffer containing 20 mM Hepes (pH 7.4), 110 mM potassium phosphate, 2 mM magnesium acetate, 0.5 mM EGTA, and 2 mM DTT (transport buffer). The matrix for affinity depletion was prepared by coupling recombinant human NTF2 to CNBr-activated Sepharose (Pharmacia LKB) at a concentration of ≈ 2 mg of protein per ml of beads. After coupling the beads were quenched with 1 M ethanolamine, washed extensively with transport buffer, and transferred to a 10-ml disposable column. The column was treated with several volumes of 100 mg of BSA per ml to block nonspecific binding and washed again with transport buffer. Cytosol was passed over the column (volume ratio 1:1) three times, the unbound fraction was concentrated by vacuum dialysis, frozen in liquid N_2 , and stored at $-80^\circ C$. The depletion of known transport factors was examined with antibodies against p97 (13), SRP1 (11), and Ran/TC4 (22). A rabbit antibody to human NTF2 was prepared by using the recombinant protein both as the antigen and as the substrate for affinity purification.

Solution Binding of NTF2 and Ran/TC4. Human NTF2 and Ran/TC4 were expressed in bacteria and purified as described (7, 17). Based on the basal GTP hydrolysis rate, the recombinant Ran/TC4 should be a mixture of GTP- and GDP-bound forms, the latter constituting $\approx 80\%$ of the total protein. Recombinant proteins (stored at $-80^\circ C$) were thawed and clarified for 5 min in an air-driven ultracentrifuge (28 psi). Samples containing Ran/TC4 alone, NTF2 alone, or a mixture of the two proteins (25 μg each) were incubated on ice for 60 min in transport buffer containing 5 mM DTT and 100 μg of BSA in a total volume of 200 μl . Chromatography was performed in transport buffer on a Superdex 75 FPLC column at a flow rate of 0.5 ml/min. The elution profiles of the proteins were examined by immunoblotting with an anti-peptide antibody specific for Ran/TC4 (22) and with a monoclonal antibody (Novagen) reacting with the N-terminal T7 epitope tag on recombinant NTF2.

Chemical Crosslinking of NTF2 and Ran/TC4. The crosslinking reactions involved NTF2 and Ran/TC4, each at a final concentration of 100 $\mu g/ml$ in transport buffer. The proteins were incubated on ice for 60 min, and the crosslinker disuccinyl suberate (Pierce) was added from a 20 mM stock (in DMSO) to a final concentration of 0.2 mM. The reactions were quenched by the addition of excess Tris-Cl, and the products were analyzed by immunoblotting. Note the blot containing the crosslinked products of Ran/TC4 and NTF2 was probed, stripped, and reprobed with the relevant antibodies.

Determination of the Nucleotide State of Ran/TC4 That Interacts with NTF2. Recombinant Ran/TC4 (25 μg) was loaded with 20 μM guanine nucleotide ($[^3H]GDP$ or $[\gamma\text{-}^{32}P]GTP$) in the presence of 10 mM EDTA, 2.5 mM DTT, 2 mM ATP, and 15 mM Hepes (pH 7.4) in a total volume of 50 μl for 20 min at $30^\circ C$. The reaction was diluted with excess magnesium ions and chromatographed on a PD-10 gel filtration column (Pharmacia LKB) to remove unbound nucleotide. The nucleotide-loaded Ran/TC4 (10 μg) was incubated in the absence or presence of NTF2 (50 μg) along with BSA (2 mg) for 60 min on ice. The samples were chromatographed on a Sephacryl S100 HR column (40 ml) at a flow rate of 20 ml/hr in transport buffer. The elution position of the radiolabeled GDP- or GTP-Ran/TC4 was then determined by scintillation counting 50 μl of each 1-ml fraction. The components of the nucleotide exchange reactions were Ran/TC4 (1.2 μg) preloaded with $[^3H]GDP$, RCC1 (2.8 μg), NTF2 (16 μg), and 2 mM GTP in a total volume of 100 μl . The reactions (duplicate points) were performed in transport buffer at $30^\circ C$ for 10 min. $[^{32}P]GTP$, which remained bound to Ran/TC4, was quantitated by a nitrocellulose binding assay.

Binding Assays Featuring Glutathione S-Transferase (GST)-Fusions of Ran/TC4 and p97. Human Ran/TC4 and rat p97 were expressed as N-terminal GST fusions in bacteria

and immobilized on glutathione beads at a protein concentration of 1–5 mg/ml. Soluble recombinant Ran/TC4 (5 μg), NTF2 (5 μg), or both were mixed with 20 μl of packed beads in a total volume of 200 μl for 60 min at $4^\circ C$. The assays were performed in transport buffer containing 2.5 mM DTT and included 100 μg of BSA as a blocking agent. The beads were recovered by centrifugation and washed four times in transport buffer, and the bound proteins were eluted and detected by immunoblotting. To determine the nucleotide state of Ran/TC4 that interacts with p97, we preloaded Ran/TC4 with radiolabeled GDP or GTP as described above and carried out binding reactions (triplicate points) with immobilized GST or GST-p97. The bound fractions were eluted with 5% SDS/20 mM EDTA and assayed by scintillation counting.

RESULTS

We showed previously that HeLa cell cytosol pretreated with Sepharose-immobilized NTF2 was strongly deficient ($\approx 30\%$ of control) in its ability to support protein import in the permeabilized cell assay, indicating that NTF2 interacts with additional soluble factors (7). The addition of individual cytosolic fractions from sucrose density gradients failed to restore transport to cytosol pretreated with NTF2-Sepharose, suggesting this procedure may have removed more than one rate-limiting factor (B.M.P., unpublished observations). To determine whether NTF2-Sepharose removed any of the previously characterized transport factors, the unbound fractions of cytosol treated in this manner were examined by immunoblotting (Fig. 1). We found that the levels of p97 and Ran/TC4 in cytosol were drastically reduced under these conditions, while the levels of the NLS receptor and NTF2 were not detectably changed (Fig. 1).

To determine whether the depletion of cytosolic Ran/TC4 was due to a direct interaction with NTF2, binding experiments using recombinant forms of both proteins were performed (Fig. 2). Purified preparations of recombinant Ran/TC4 and NTF2 eluted from a Superdex 75 FPLC column with apparent molecular weights of ≈ 25 and ≈ 30 kDa, respectively (Fig. 2A, *Top* and *Middle*). This agrees with the apparent native sizes of

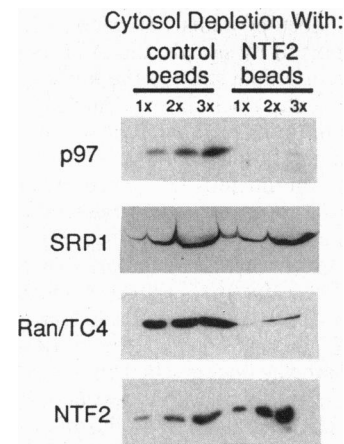


FIG. 1. Affinity depletion of transport factors from HeLa cell cytosol using Sepharose-immobilized NTF2. Cytosol was passed three times over Sepharose beads coupled with either 2 mg of BSA per ml or 2 mg of recombinant NTF2 per ml (5). The relative levels of the nuclear protein import factors [p97, SRP1 (NLS receptor), Ran/TC4, and NTF2] in the unbound fraction were then examined by immunoblotting. For comparative purposes, 10, 20, and 30 μl (denoted 1x, 2x, and 3x) of the unbound fraction from each column was analyzed. The transport factors p97 and Ran/TC4 were effectively removed from cytosol by this treatment, while the levels of the NLS receptor and NTF2 were relatively unchanged. Note that cytosol treated in this manner supports transport at $\approx 30\%$ of control cytosol (7).

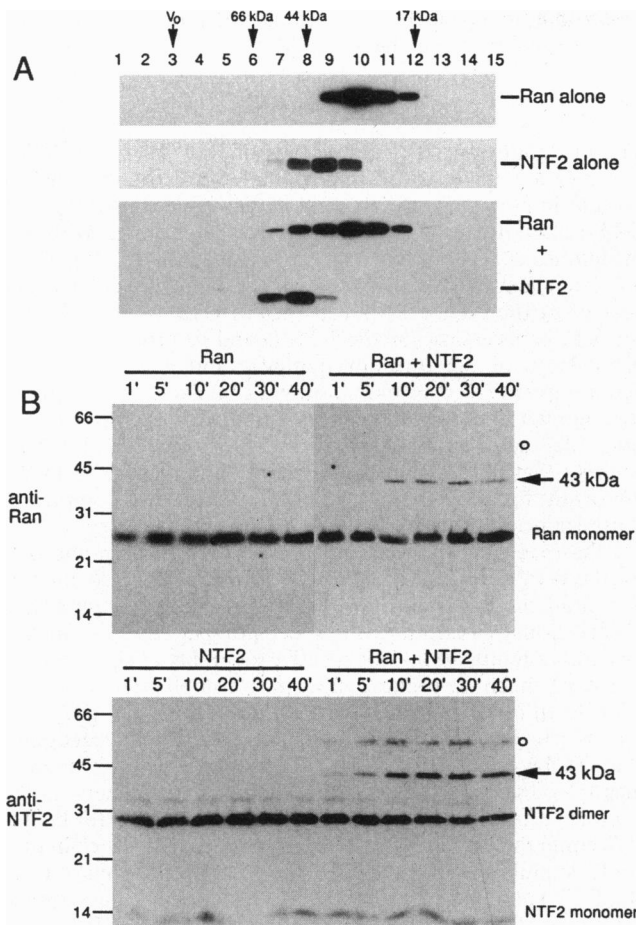


FIG. 2. Direct interaction of NTF2 with the GTPase Ran/TC4. (A) Purified recombinant Ran/TC4 and NTF2 alone and in combination were chromatographed on a Superdex 75 FPLC column and detected by immunoblotting. The two proteins form a complex that elutes with an apparent molecular mass of 44 kDa. (B) Purified recombinant NTF2 and Ran/TC4 were crosslinked using disuccinimidyl suberate for the indicated times, and the products were analyzed by immunoblotting. Crosslinking a mixture of NTF2 and Ran/TC4 resulted in the formation of a 43-kDa species with a predicted stoichiometry of 1:1 (NTF2:Ran/TC4). The ≈ 55 -kDa product generated by crosslinking (open circle) was recognized by the NTF2 antibody (Lower) but not by the Ran/TC4 antibody (Upper).

Ran/TC4 and the NTF2 homodimer. Gel filtration analysis of a mixture of the two proteins resulted in the appearance of higher molecular weight species of both NTF2 and Ran/TC4, suggesting the formation of a complex *in vitro* (Fig. 2A, Bottom). While Ran/TC4 eluted in fractions 9–12 when chromatographed alone, it appeared also in fractions 7 and 8 when combined with NTF2. The elution position of NTF2 was altered as well, as the actual peak shifted from fraction 9 to fraction 8. Interestingly, the peak fraction of the complex (fraction 8) elutes with an apparent molecular mass of ≈ 40 kDa, which could reflect the binding of Ran/TC4 to an NTF2 monomer.

Further evidence for the formation of a Ran/TC4-NTF2 complex was obtained in chemical crosslinking experiments. Recombinant proteins alone and in combination were treated with the crosslinker disuccinyl suberate for up to 40 min, and the products were examined by immunoblotting with mono-specific antibodies. Ran/TC4 alone remained a monomeric species during the entire time course (Fig. 2B, Upper), whereas NTF2 alone was nearly quantitatively crosslinked into a dimer during the first minute of incubation (Lower). Crosslinking of a mixture of the proteins generated an ≈ 43 -kDa species, which

was recognized by antibodies to both Ran/TC4 and epitope-tagged NTF2. These conditions also produced an ≈ 60 -kDa species (indicated by the open circle), which was recognized by the anti-NTF2 antibody but not by the anti-Ran/TC4 antibody. The 60-kDa product may be a tetramer of NTF2, or it could represent a product composed of one copy of Ran/TC4 and a dimer of NTF2 that is not recognized by our anti-Ran/TC4 antibodies (22).

We then examined whether the binding of NTF2 to Ran/TC4 is nucleotide-specific. In this experiment, Ran/TC4 was preloaded with either [3 H]GDP or [32 P]GTP and chromatographed on a S100 gel filtration column in the absence and presence of NTF2 (Fig. 3). A size shift of the [3 H]GDP-bound form of Ran/TC4 from ≈ 25 kDa to ≈ 40 kDa was observed when chromatography was carried out in the presence of NTF2 (Fig. 3A). In contrast, the [32 P]GTP-bound form of Ran/TC4 eluted at the same position whether chromatographed in the absence or presence of NTF2 (Fig. 3B). These data clearly demonstrate that NTF2 binds stably to the GDP-bound form of Ran/TC4 under conditions where no interaction with the GTP-bound form of Ran/TC4 is measured.

The interaction of NTF2 with the GDP-bound form of Ran/TC4 could serve to stabilize this state and consequently

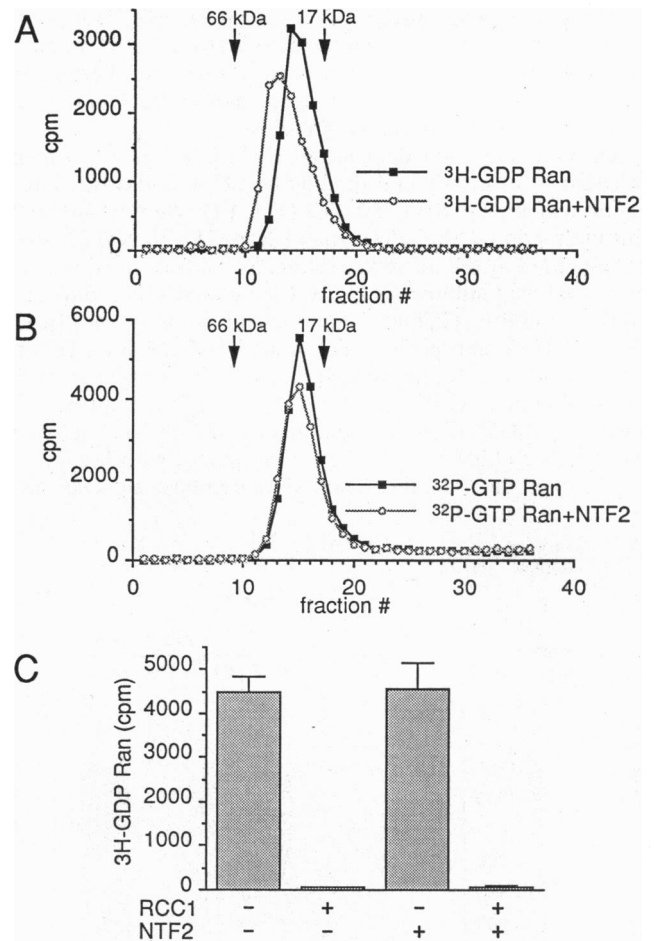


FIG. 3. Interaction of NTF2 with the GDP-bound form of Ran/TC4. (A) Recombinant Ran/TC4 was preloaded with [3 H]GDP and chromatographed in the absence or presence of recombinant NTF2. Under these conditions, GDP-Ran/TC4 displays a size shift from ≈ 25 to ≈ 40 kDa when chromatographed in the presence of NTF2. (B) Recombinant Ran/TC4 was preloaded with [32 P]GTP and chromatographed in the absence or presence of recombinant NTF2. The elution position of GTP-Ran/TC4 is unaffected by the presence of NTF2. (C) The nucleotide exchange activity of recombinant RCC1 was measured (23) in the absence and presence of NTF2. The exchange activity was not detectably affected by NTF2.

act as a guanine nucleotide dissociation inhibitor. Catalyzed nucleotide exchange on the GTPase rho can be inhibited by its guanine nucleotide dissociation inhibitor (23). We therefore tested whether NTF2 could inhibit the nucleotide exchange on Ran/TC4 catalyzed by its exchange factor RCC1 (24), using Ran/TC4 preloaded with [³H]GDP and a filter binding assay. This showed that the RCC1-mediated exchange of GTP for bound GDP was not detectably inhibited, even when carried out in the presence of a 10-fold molar excess of NTF2 (Fig. 3C). We also found that the dissociation of bound nucleotide with 10 mM EDTA was affected only slightly by including NTF2 in the reaction (B.M.P., unpublished observations). Thus, it seems unlikely that the function of NTF2 is to protect Ran/TC4 from nucleotide exchange.

The depletion of p97 from HeLa cell cytosol with NTF2-Sepharose (Fig. 1) suggested that NTF2, or perhaps a complex of NTF2 and Ran/TC4, might interact with p97. To probe for interactions between these proteins, we immobilized GST fusions of p97 and Ran/TC4 on Sepharose and tested whether soluble NTF2, Ran/TC4, or a combination of these proteins could bind to these matrices. As expected, NTF2 bound to Ran/TC4, but it did not bind to p97 either in the absence or presence of Ran/TC4. This suggests that the cytosolic depletion of p97 obtained using NTF2-Sepharose (Fig. 1) is mediated by an additional soluble factor. However, it remains possible that the use of recombinant proteins in the binding experiment does not reconstitute an interaction that is observed in cytosol with native proteins.

An interesting and unexpected finding in this experiment was that Ran/TC4 bound directly to p97 and that this interaction was independent of NTF2 (Fig. 4A). We reasoned that this interaction, like the binding of Ran/TC4 to NTF2, might be regulated by the nucleotide state. To address this issue, we measured the binding of Ran/TC4 preloaded with radioactive GDP or GTP to GST-p97 immobilized on Sepharose beads (Fig. 4). Only nonspecific binding of [³H]GDP-Ran/TC4 to GST-p97 (23.8 ± 6.2 ng) was obtained, as this was comparable to the binding to GST alone (17.2 ± 11.6 ng). In contrast, the level of [³²P]GTP-Ran/TC4 binding to GST-p97 was substantially higher (1204 ± 16.08 ng) as compared with binding to GST alone (7.0 ± 3.1 ng). These data demonstrate a specific,

direct interaction of the GTP-bound form of Ran/TC4 with the cytosolic transport factor p97.

DISCUSSION

The nucleotide-specific interactions of Ran/TC4 with NTF2 and p97 are likely to be important features of the nuclear protein import pathway. Recent studies have shown that the GTP-bound form of Ran/TC4 directly interacts with the protein Ran/TC4 binding protein 2 (RanBP2) (25, 26), which is located near the initial ligand docking site on the cytoplasmic surface of the NPC (22). Hydrolysis of GTP by Ran/TC4 at this site is necessary for the NLS ligand to proceed to more distal steps of the transport pathway and may represent a "commitment" step in the pathway (22). These observations, together with our new data showing mutually exclusive nucleotide dependent binding of Ran/TC4 to p97 and NTF2, suggest that these nucleotide-specific interactions may be important for the assembly and dissociation of a complex of these transport factors at RanBP2 (Fig. 5).

It has been shown that RanBP2 contains four binding sites for the GTP-form of Ran/TC4 (25, 26). RanBP2 also appears to contain binding sites for p97 and NTF2 (ref. 27; unpublished observations), prompting us to speculate that this NPC protein provides a template for cooperative assembly of the cytosolic transport machinery into a transport complex (Fig. 5). The GTP form of Ran/TC4 could facilitate binding of p97/NLS receptor to RanBP2 (step 1). Furthermore, the interaction of Ran/TC4 with p97 could allow GTP hydrolysis to be communicated to the p97/NLS receptor/ligand complex (step 2). The conformational change in Ran/TC4 induced by GTP hydrolysis could then abrogate its interaction with p97, which in turn could stimulate dissociation of the transport complex from RanBP2 (step 3). NTF2 could play several roles in these events. NTF2 could augment release of the GDP form of Ran/TC4 from p97, or promote the dissociation of a multisubunit transport complex from RanBP2 (step 3; see legend of Fig. 5). In addition, assembly of the heterodimer containing NTF2 and GDP-Ran/TC4 into the transport complex could provide a molecular marker that specifies vectorial transport, perhaps for targeting the transport complex to subsequent steps in the pathway (ref. 4 and below).

We have shown previously that NTF2 binds directly to NPC protein p62, an interaction which requires the amino terminal half of p62 (7). This region of p62 is notable because it contains multiple FXFG repeats, a feature shared by other O-linked NPC glycoproteins (reviewed in refs. 3 and 4). Indeed, at least nine different O-linked NPC glycoproteins released from nuclear envelopes by detergent and high salt are bound by Sepharose-immobilized NTF2 (unpublished observations). While it remains to be established whether these all represent direct interactions, our laboratory has determined that NTF2 binds directly to recombinant forms of NPC proteins p62 (7) as well as p58 and p54 (T. Hu and L.G., unpublished data). Blot overlay (27) and solution binding (T. Hu and L.G., unpublished data) experiments have shown that p97 also interacts directly with multiple NPC O-linked glycoproteins. The interaction of NTF2 and p97 with the same subset of O-linked glycoproteins, all of which contain FXFG repeats, provides a clue about the mechanism of protein import. Since the O-linked glycoproteins are localized at various cytoplasmic and nucleoplasmic regions of the NPC, p97 and NTF2 may function at multiple steps in the import pathway. Forward progress of the transport complex (after dissociation from RanBP2; Fig. 5) could rely on cooperative and/or sequential interactions of p97 and NTF2 with O-linked glycoproteins in the NPC.

Whether Ran/TC4 serves to stimulate assembly and/or disassembly of transport complexes at steps downstream of RanBP2 is presently unknown. The GTP-form of Ran/TC4 was recently shown to stimulate the release of NLS ligand from

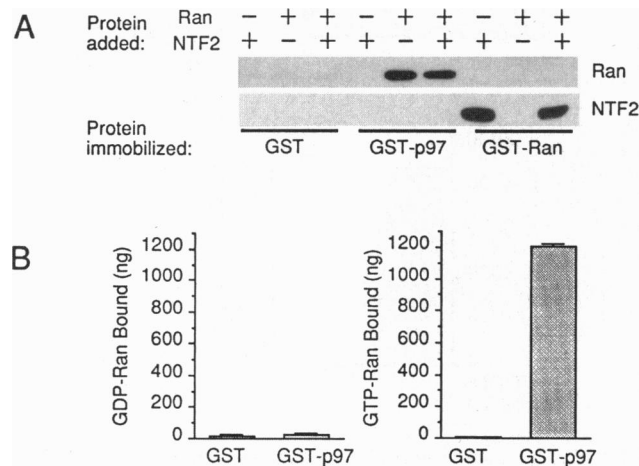


FIG. 4. Direct interaction of cytosolic transport factors NTF2 and p97 with Ran/TC4. (A) GST fusions of p97 and Ran/TC4 were expressed in *E. coli*, recovered on glutathione beads, and used for binding assays (25). Ran/TC4 bound specifically to immobilized p97, and NTF2 bound specifically to immobilized Ran/TC4. (B) GST and GST-p97 were incubated with recombinant Ran/TC4 preloaded with either [³H]GDP (specific activity, 5895 cpm/ μ g) or [γ -³²P]GTP (specific activity, 10^6 cpm/ μ g). The interaction of p97 with Ran/TC4 is specific for the GTP-bound form of the latter protein.

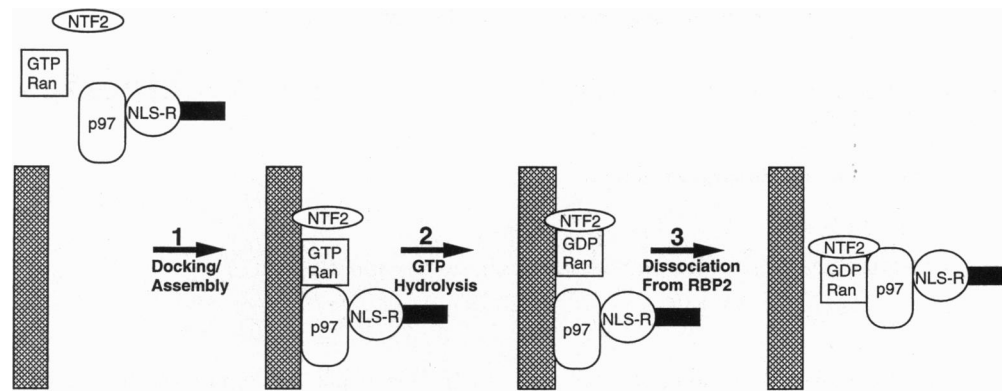


FIG. 5. Hypothetical model depicting interactions of the cytosolic transport factors Ran/TC4, NTF2, NLS receptor (NLS-R), p97, NLS-containing transport ligand (black), and RanBP2 (stippled) during early transport steps at the NPC. The interaction of p97 with NTF2 and the GDP form of Ran/TC4 (step 3) is speculative and has not been reconstituted with recombinant proteins. However, the fact that Ran/TC4 and p97 are depleted from cytosol using NTF2-Sepharose suggests that these proteins interact, either directly or indirectly.

an NLS receptor/p97 heterodimer (28). However, since the addition of an FXFG-containing protein (Nup1) was also reported to release NLS ligand from this complex (28), the implications of these findings remain to be determined. Defining the polypeptide composition of the transport complex, which ultimately translocates through the NPC, remains one of the key questions related to understanding nuclear protein import.

In summary, we have demonstrated that the GTP- and GDP-bound forms of Ran/TC4 interact directly with the cytosolic transport factors p97 and NTF2, respectively. These nucleotide-specific interactions could promote the assembly of a multisubunit transport complex and its dissociation from RanBP2. We envision that the transport factors p97 and NTF2 play dual roles in the import pathway, those of modulating the assembly of the complex and its subsequent targeting to distinct sites in the NPC.

We thank S. Adam, J. Becker, T. Hu, A. Lamond, F. Melchior, and D. Sweet for generous gifts of reagents, T. Guan for assistance with FPLC, and F. Melchior for helpful discussions and comments on the manuscript. This work was supported by postdoctoral fellowships from the Damon Runyon-Walter Winchell Cancer Research Fund (DRG-1179) to B.M.P. and the European Molecular Biology Organization (ALTF 539-1994) to C.D., a grant from the National Institutes of Health to L.G., and a grant from the Lucille P. Markey Charitable Trust.

- Forbes, D. J. (1992) *Annu. Rev. Cell Biol.* **8**, 495–527.
- Panté, N. & Aebi, U. (1993) *J. Cell Biol.* **122**, 977–985.
- Rout, M. P. & Wente, S. R. (1994) *Trends Cell Biol.* **4**, 357–365.
- Goldfarb, D. S. (1994) *Curr. Biol.* **4**, 57–60.
- Melchior, F. & Gerace, L. (1995) *Curr. Opin. Cell Biol.* **7**, 310–318.
- Adam, S. A., Sterne-Marr, R. E. & Gerace, L. (1990) *J. Cell Biol.* **111**, 807–816.
- Paschal, B. M. & Gerace, L. (1995) *J. Cell Biol.* **129**, 925–937.
- Adam, S. A. & Gerace, L. (1991) *Cell* **66**, 837–847.

- Gorlich, D., Prehn, S., Laskey, R. A. & Hartmann, E. (1994) *Cell* **79**, 767–778.
- Moroianu, J., Blobel, G. & Radu, A. (1995) *Proc. Natl. Acad. Sci. USA* **92**, 2008–2011.
- Weis, K., Mattaj, I. W. & Lamond, A. I. (1995) *Science* **268**, 1049–1053.
- Adam, E. J. & Adam, S. A. (1994) *J. Cell Biol.* **125**, 547–555.
- Chi, N. C., Adam, E. J. & Adam, S. A. (1995) *J. Cell Biol.* **130**, 265–274.
- Gorlich, D., Kostka, S., Kraft, R., Dingwall, C., Laskey, R., Hartmann, E. & Prehn, S. (1995) *Curr. Biol.* **5**, 383–392.
- Radu, A., Blobel, G. & Moore, M. (1995) *Proc. Natl. Acad. Sci. USA* **92**, 1769–1773.
- Moore, M. & Blobel, G. (1994) *Proc. Natl. Acad. Sci. USA* **91**, 10212–10216.
- Melchior, F., Paschal, B., Evans, J. & Gerace, L. (1993) *J. Cell Biol.* **123**, 1649–1659.
- Moore, M. & Blobel, G. (1993) *Nature (London)* **365**, 661–663.
- Gorlich, D., Vogel, F., Mills, A. D., Hartmann, E. & Laskey, R. A. (1995) *Nature (London)* **377**, 246–248.
- Sterne-Marr, R., Blevitt, J. M. & Gerace, L. (1992) *J. Cell Biol.* **116**, 271–280.
- Paschal, B.M., Fritze, C. & Gerace, L. (1995) *Mol. Biol. Cell* **6**, 82a (abstr.).
- Melchior, F., Guan, T., Yokoyama, N., Nishimoto, T. & Gerace, L. (1995) *J. Cell Biol.* **131**, 571–581.
- Leonard, D., Hart, M. J., Platko, J. V., Eva, A., Henzel, W., Evans, T. & Cerione, R. (1992) *J. Biol. Chem.* **267**, 22860–22868.
- Bischoff, F. R. & Ponstingl, H. (1991) *Nature (London)* **354**, 80–82.
- Yokoyama, N., Hayashi, N., Seki, T., Panté, N., Ohba, T., Nishii, K., Kuma, K., Hayashida, T., Miyata, T., Aebi, U., Fukui, M. & Nishimoto, T. (1995) *Nature (London)* **376**, 184–188.
- Wu, J., Matunis, M. J., Kraemer, D., Blobel, G. & Coutavas, E. (1995) *J. Biol. Chem.* **270**, 14209–14013.
- Moroianu, J., Hijikata, M., Blobel, G. & Radu, A. (1995) *Proc. Natl. Acad. Sci. USA* **92**, 6532–6536.
- Rexach, M. & Blobel, G. (1995) *Cell* **83**, 683–692.